26th edition

ISSN 1454 - 8003

Proceedings of International Conference on HYDRAULICS, PNEUMATICS, SEALING ELEMENTS, TOOLS, PRECISION MECHANICS, SPECIFIC ELECTRONIC EQUIPMENT & MECHATRONICS

HERVEX 2022

November 9-10 | Băile Govora, ROMANIA

November 2022
26th Edition

INTERNATIONAL CONFERENCE

HERVEX 2022

Hydraulics| Pneumatics| Sealing Elements| Tools| Precision Mechanics| Specific Electronic Equipment & Mechatronics

Baile Govora, ROMANIA | November 9 - 10, 2022

HERVEX 2022

ORGANIZERS

HYDRAULICS AND PNEUMATICS RESEARCH INSTITUTE
BUCHAREST, ROMANIA

CHAMBER OF COMMERCE AND INDUSTRY VALCEA, ROMANIA

ORGANIZING PARTNERS

WROCLAW UNIVERSITY OF SCIENCE AND TECHNOLOGY, POLAND

KOMAG INSTITUTE OF MINING TECHNOLOGY, POLAND

TECHNICAL UNIVERSITY OF MOLDOVA IN CHISINAU, REPUBLIC
OF MOLDOVA

NATIONAL INSTITUTE OF RESEARCH & DEVELOPMENT FOR MACHINES
AND INSTALLATIONS DESIGNED TO AGRICULTURE AND FOOD INDUSTRY
– INMA BUCHAREST, ROMANIA

"POLITEHNICA" UNIVERSITY OF BUCHAREST, ROMANIA

"POLITEHNICA" UNIVERSITY OF TIMISOARA, ROMANIA

TECHNICAL UNIVERSITY OF CLUJ-NAPOCA, ROMANIA

MEDIA PARTNERS

HIDRAULICA
HYDRAULICS-PNEUMATICS-TRIBOLOGY-ECOLOGY-SENSORICS-MECHATRONICS

Partener European
CAMERA DE COMERȚ ȘI INDUSTRIE VÂLCEA

HERVEX 2022

INTERNATIONAL CONFERENCE

HERVEX 2022

HELD UNDER HONORARY AEGIS OF

Comité Européen des Transmissions Oléohydrauliques et Pneumatiques

cetop
The Voice of the European Fluid Power Industry

SUPPORTED BY

National Professional Association of Hydraulics and Pneumatics in Romania - "FLUIDAS"

Conference Proceedings is **indexed by:**

EBSCO PUBLISHING Google scholar TIB LEIBNIZ INFORMATION CENTRE FOR SCIENCE AND TECHNOLOGY UNIVERSITY LIBRARY

Published by Hydraulics and Pneumatics Research Institute, Bucharest, Romania

COMMITTEES

HONORARY PRESIDENT

PhD.Eng. Hubertus MURRENHOFF – Institute for Fluid Power Drives and Controls at Aachen University, Germany

HONORARY COMMITTEE

Dr. Stefan KÖNIG – President of European Fluid Power Committee – CETOP

Prof. PhD. Eng. Viorel BOSTAN – Rector of Technical University of Moldova, Republic of Moldova

PhD.Eng. Petrin DRUMEA – President of National Professional Association of Hydraulics and Pneumatics – FLUIDAS, Romania

Dipl.Eng. Valentin CISMARU – President of Chamber of Commerce and Industry Valcea, Romania

ORGANIZING COMMITTEE

Dipl. Eng. Gheorghe RIZOIU – General Manager of Chamber of Commerce and Industry Valcea, Romania

PhD. Eng. Gabriela MATACHE – Hydraulics and Pneumatics Research Institute in Bucharest, Romania

PhD. Eng. Krzysztof KEDZIA – Wroclaw University of Technology, Poland

Prof. PhD. Eng. Dan OPRUȚA – Technical University of Cluj-Napoca, Romania

Prof. PhD. Eng. Ilare BORDEAȘU – Politehnica University of Timisoara, Romania

Prof. PhD. Eng. Adrian CIOCĂNEA – Politehnica University of Bucharest, Romania

PhD. Phys. Mihai VARLAM - General Manager of National Research & Development Institute for Isotope & Cryogenics Technologies (ICSI) Râmnicu Vâlcea, Romania

PhD.Eng. Sergiu NICOLAIE – General Manager of R&D National Institute for Electrical Engineering ICPE-Advanced Researches, Bucharest, Romania

PhD.Eng. Nicolae-Valentin VLĂDUȚ – General Manager of National Institute of Research and Development for Machines and Installations Designed to Agriculture and Food Industry – INMA Bucharest, Romania

PhD.Eng. Ioan LEPĂDATU – Hydraulics and Pneumatics Research Institute in Bucharest, Romania

PhD.Eng. Cătălin DUMITRESCU – Director of Hydraulics and Pneumatics Research Institute in Bucharest, Romania

SCIENTIFIC PROGRAMMEE COMMITTEE

PhD.Eng. Zygmunt DOMAGALA – Wroclaw University of Technology, Poland

Prof. PhD.Eng. Pavel MACH – Technical University of Praga, Czech Republic

PhD.Eng. Mohamed HAJJAM – University of Poitiers – IUT Angouléme, France

Prof. PhD.Eng. Valeriu DULGHERU – Technical University of Moldova, Republic of Moldova

Dipl. Eng. Nicolae TASU – HANSA FLEX Romania

PhD.Eng. Iulian-Claudiu DUȚU – Politehnica University of Bucharest, Romania

Prof. PhD.Eng. Mihail SAVANIU – Technical University of Civil Engineering in Bucharest, Romania

Assoc. Prof. PhD.Eng. Nicuşor BAROIU – "Dunarea de Jos" University of Galati, Romania

PhD.Eng. Mircea CHINTOANU – Director of Research Institute for Analytical Instrumentation INCDO INOE 2000 - ICIA Cluj-Napoca, Romania

Prof. PhD.Eng. Mircea POPOVICIU – Politehnica University of Timisoara, Romania

EXECUTIVE SECRETARIAT

Ana-Maria POPESCU – Hydraulics and Pneumatics Research Institute in Bucharest, Romania

SPECIALIZED REVIEWER COMMITTEE

PhD.Eng. Petrin DRUMEA – President of National Professional Association of Hydraulics and Pneumatics – FLUIDAS, Romania

PhD.Eng. Mohamed HAJJAM – University of Poitiers – IUT Angouléme, France

Prof. PhD.Eng. Valeriu DULGHERU – Technical University of Moldova, Republic of Moldova

Prof. PhD.Eng. Pavel MACH – Technical University of Praga, Czech Republic

PhD. Eng. Teodor Costinel POPESCU – Hydraulics and Pneumatics Research Institute in Bucharest, Romania

Assoc. Prof. PhD.Eng. Adinel GAVRUS – Institute National des Sciences Appliquees de Rennes, France

PhD. Eng. Marian BLEJAN – Hydraulics and Pneumatics Research Institute in Bucharest, Romania

EDITORIAL STAFF

Editor-in-Chief

- PhD. Eng. Gabriela MATACHE - Hydraulics and Pneumatics Research Institute in Bucharest, Romania

Executive Editor

- Ana-Maria POPESCU - Hydraulics and Pneumatics Research Institute in Bucharest, Romania

CONTENTS

ISSN 1454 - 8003
Proceedings of 2022 International Conference on Hydraulics and Pneumatics - HERVEX
November 9-10, Băile Govora, Romania

PNEUMATIC EQUIPMENT FOR MICRO-DEFORMATION OF WIRES AT AN ELECTRIC MICROMOTOR IN THE AUTOMOBILE INDUSTRY

Nicușor BAROIU[1], Daniela DANCI (MÂNCILĂ)[1], Mihăiță MÂNCILĂ[1], Georgiana-Alexandra MOROȘANU[2], Silvian BAROIU[3], Cătălin DUMITRESCU[4]

[1] Department of Manufacturing Engineering, "Dunărea de Jos" University of Galaţi, Romania
Nicusor.Baroiu@ugal.ro, dd189@student.ugal.ro, mm376@student.ugal.ro

[2] Research Center in Manufacturing Engineering Technology (ITCM), "Dunărea de Jos" University of Galaţi, Romania, Alexandra.Costin@ugal.ro

[3] Faculty of Electronics, Telecommunications and Information Technology, Politehnica University of Bucharest, Romania, silvianbar@gmail.com

[4] Hydraulics and Pneumatics Research Institute INOE 2000-IHP, Bucharest, Romania
dumitrescu.ihp@fluidas.ro

Abstract: *The design of technical solutions and the serial execution of electrical subassemblies to be integrated into the production of electronic components in the automotive industry requires adaptation to new working conditions and technologies, doubled by the quality of services and products, which must be competitive on a global scale. This can also be achieved by choosing the optimal variants of machines or equipment that are the most profitable from a qualitative and economic point of view for a fully automated technological process, as well as by a maintenance of these systems, which must be performed in accordance with the instructions manufacturer and at regular intervals. In this context, the appearance of new technical resources, of new trends and especially automation, gave to pneumatic technology an ever-rising development, most of the time, pneumatic drives constituting a basic component in intensive production systems. This paper aims to present a description of a pneumatic equipment for microdeformation of wires in the automotive industry, the technological process for obtaining microdeformed components (wires), as well as a calculation of the characteristic parameters of the pneumatic equipment.*

Keywords: *Pneumatic equipment, wires, microdeformation, tehnological process*

1. Introduction

In the last decades, there has been a growing evolution of the automotive industry at the global and European level, correlated with the increase in the share of electrical and electronic components in the construction of vehicles, with the aim of perfecting their performance, the European Commission estimating that the European automotive market will be fully electrified by 2050, as an essential contribution to the future of mobility and the technological base of the automotive industry [1, 2]. This led to the development of automated systems for making numerous elements in the area of microelectronics, such as digital processors, logic and analog integrated circuits, power integrated circuits, sensors, various actuation systems etc. [3]. At the same time, autonomous technology and connectivity, hybridization and electrification of motorization, as well as digitization along the production chain will lead to fundamental transformations in the way the entire automotive ecosystem operates [4, 5, 6]. Their facilitation could be done both by optimizing processes and workflows or data management and control, but also by adopting hardware and software technologies for the automation and robotization of manufacturing processes [7, 8, 9]. Romania is among the European states in Central and Eastern Europe that has a good increase in car production, with significant investments from the manufacturers of various components and car subassemblies and aligns with the trends regarding the production and sales of vehicles, employment, environmental protection or road safety [10, 11]. The production of electrical and electronic equipment that is included in the micromotors for raising-lowering windows, adjusting car seats, opening-closing the tailgate, actuating the wipers etc. from the automotive industry aligns itself with these current trends.

In this entire context, the new automation requirements and the development of technical resources gave pneumatic technology a strong development, placing it as a basic component in intensive production systems. The concept that was initially based only on the execution of the command and the power generating by the compressed air is gradually being replaced by the concept that associates the electrical and electronic control elements with the pneumatic execution elements. The association of the two technologies is done in order to accumulate the advantages offered by each of them in the field of control and power [12, 13].
Since in a pneumatic system the energy-carrying agent is the compressed air, the energy source is the pneumatic generator *GP*, the compressor, Figure 1. It receives the mechanical energy from an electric motor *ME* or thermal and, aspirating air from the atmosphere, *at*, achieves a first energy conversion, the mechano-pneumostatic one. The second element of the converter will be a linear pneumatic motor *MPL* (pneumatic cylinder or membrane chamber) or rotary, *MPR*. The pneumatic motor performs the second energy conversion, in this case pneumo-mechanical, and transmits the mechanical energy thus obtained to an *EE* execution element. In the case of pneumatic systems, the *ACR* apparatus is completed by the apparatus for the preparation of compressed air, which provides it with the necessary qualities to perform the function of energy carrier.

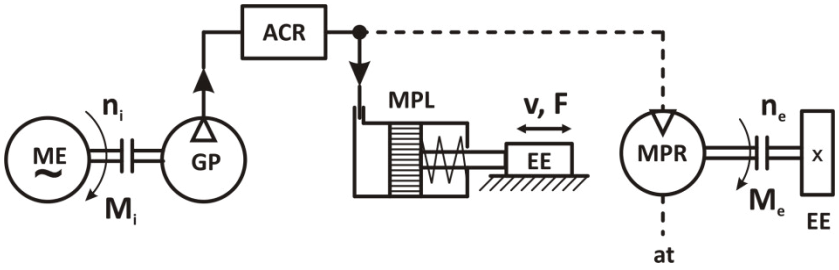

Fig. 1. General structure of a pneumatic system: *ME* - electric motor; *GP* - pneumatic generator; *ACR* - control and regulation equipment; *MPR* - rotary pneumatic motor; *MPL* - linear pneumatic motor; *EE* - execution element; n_i - input speed; M_i - moment of entry; n_e - output speed; M_e - exit moment; *v* - velocity; *F* - force [14]

Pneumatic actuators have found applications in extremely varied fields of technology, for multiple and diverse purposes, the profitability assessment of a pneumatic actuator being made both on the basis of the cost of the energy consumed and on the basis of the installation cost and maintenance and operation expenses. The paper presents a pneumatic equipment for the microdeformation of electrical and electronic components [15, 16, 17], with reference to the electric micromotor for raising the windows that is a part of a vehicle, taken as an assembly from the class of electric micromotors or mechanical-electrical systems.

2. Pneumatic equipment for microdeformation of electrical and electronic components in the automotive industry

The equipment for microdeformation (folding-cutting) of components is a system with a pneumatic drive, which aims to fold the metal arms of the components, as well as to cut the excess material, so that the component element obtains the special shape required for assembly [18]. In general, such equipment operated with compressed air requires a continuous air flow for flawless operation, which is achieved by using a correctly sized compressed air tank. The tank is vertical and galvanized inside and outside. It is equipped with a safety valve, which must be adjusted so that it opens when the air pressure has exceeded the nominal pressure by 10%, with a manometer and a device for purging, mounted in the lower part of the container. The access possibility to the safety valves for their adjustment and verification must be ensured.
The component parts of the wire microdeformation equipment are: the machine basis; air control group; pneumatic cylinder; component insertion unit by clamping; the preforming group, the pneumatic button and the protective housing, Figure 2.

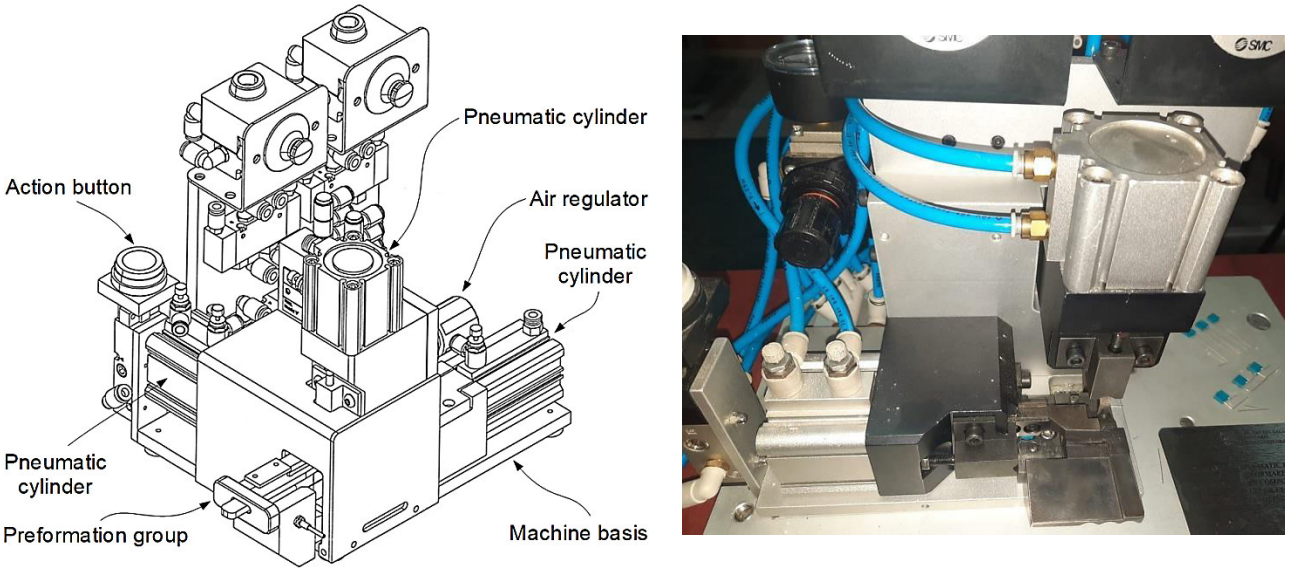

a. b.

Fig. 2. Wire microdeformation equipment: industrial model (a) [18]; laboratory model (b).

3. The components of the microdeformation equipment from the automotive industry

3.1 Air control group

The compressed air reaches into the wire microdeformation equipment through the pressure regulator, which adjusts the pressure received from the compressor group, according to the technical specifications. Figure 3 shows the pneumatic drive system of the wire microdeformation equipment.

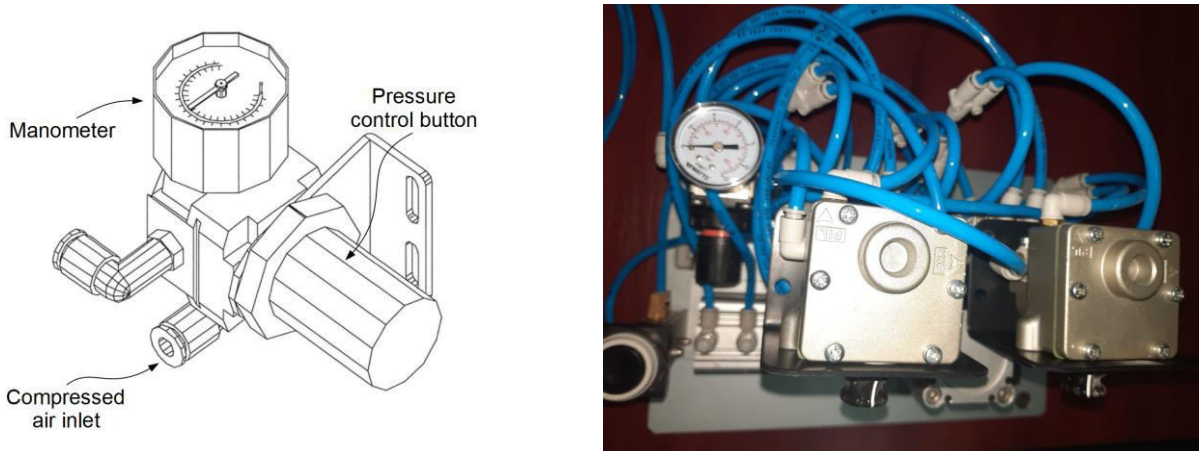

Fig. 3. The pneumatic drive system of the wire microdeformation equipment

3.2 Pneumatic cylinders

The wire microdeformation equipment has in its structure two pneumatic cylinders, Figure 4: a vertical cylinder with a diameter of Ø40 mm, having a stroke of 15 mm and a horizontal cylinder with a diameter of Ø32 mm and a stroke of 4 mm.

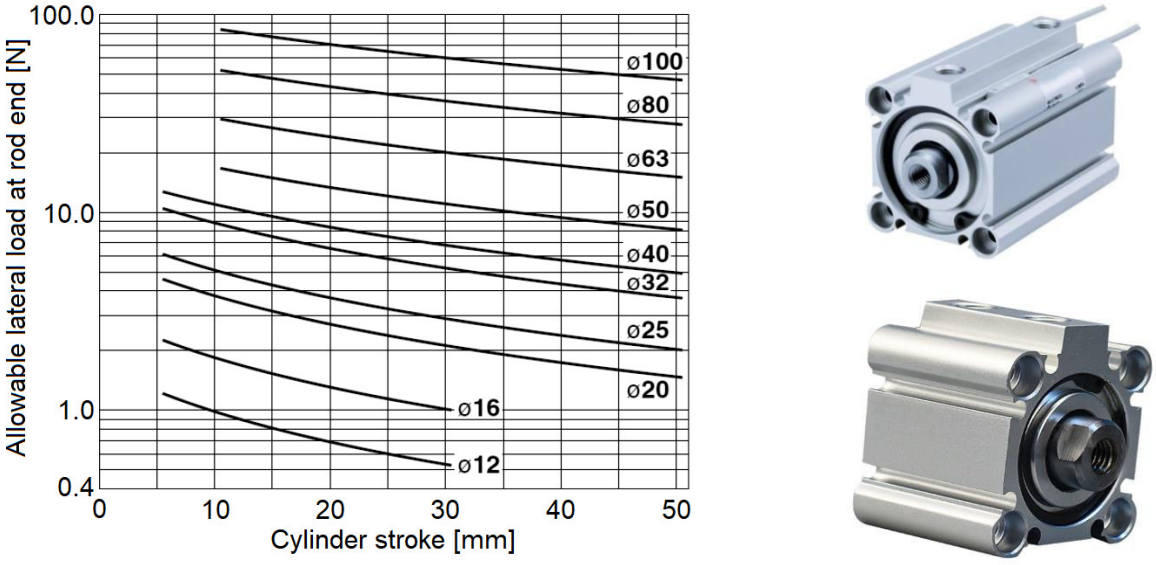

Fig. 4. Pneumatic cylinders: cylinder stroke and allowable lateral load at rod end [19]

The technical characteristics of the cylinders are presented in Table 1 [19].

Table 1: Technical characteristics of pneumatic cylinders

	Cylinder 1	**Cylinder 2**
Diameter of the cylinder [mm]	Ø40	Ø32
Stroke [mm]	15	4
Cylinder action	Double	
Speed range [mm/s]	30-500	30-500
Absolute maximum pressure [bar]	15	
Maximum operating pressure [bar]	10	
Minimum/ Maximum operating temperature [°C]	-10/70	-10/70

3.3 Pneumatic valves

The purpose of the pneumatic valves is to direct the compressed air along certain directions depending on the commands received from the outside. In an actuation system, the valve is primarily tasked with reversing the direction of movement of the engine's output and, in certain situations, stopping it. The valves used for this purpose are also called main valves. Valves can also be used to generate pneumatic control signals, in which case they are called auxiliary valves; this category includes: pneumatic buttons, stroke limiters and solenoid valves [19]. Table 2 and Figure 5 show the types of pneumatic valves included in the wire microdeformation equipment from the automotive industry, respectively, their technical characteristics.

Table 2: Technical characteristics of pneumatic valves [19]

	Pneumatic valve	**No. crt.**	**Pneumatic valve**
Mounting style	stand-alone	**Maximum flow rate**	578 Nl/min
Number of ports	5/2	**Minimum operating pressure [bar]**	1
Thread size [mm]	G 1/8	**Maximum operating pressure [bar]**	7
Actuation type	pilot/pilot	**Maximum operating temp. [°C]**	60

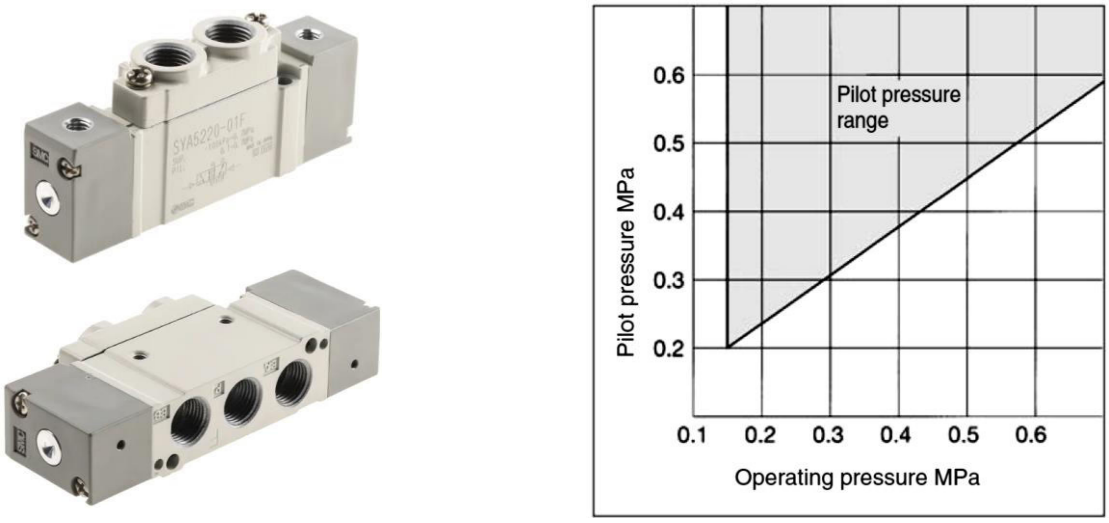

Fig. 5. Pneumatic valves: operating and pilot pressure [19]

3.4 The electric drive system of the pneumatic equipment and the mechanical system

The wire microdeformation equipment of components is manually controlled by pressing a button and is equipped with a mechanical preforming system, Figure 6.

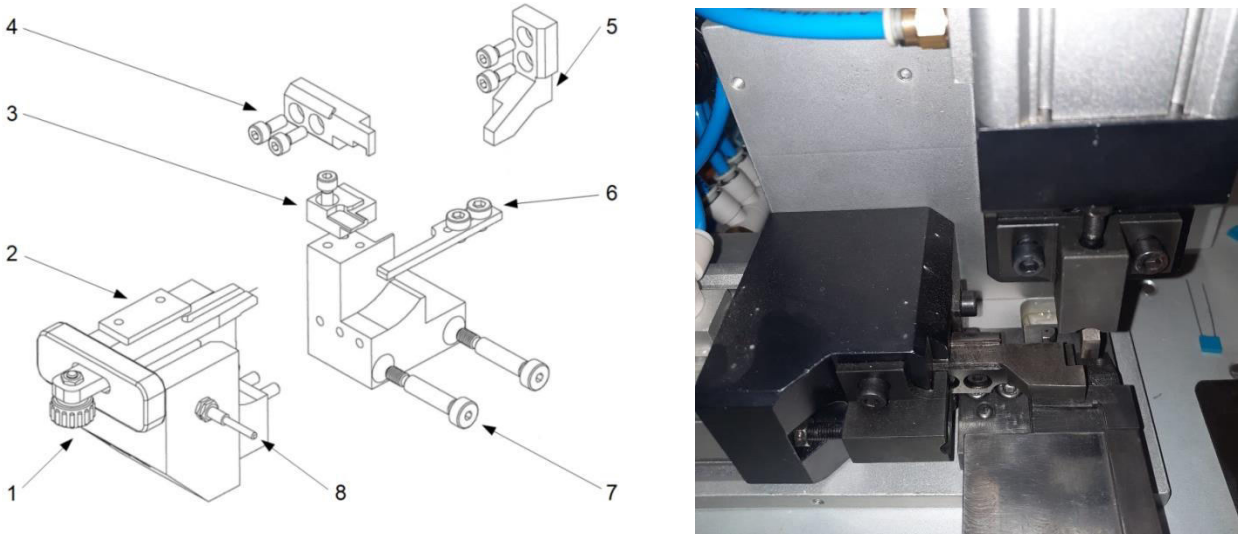

Fig. 6. The mechanical system of the folding-cutting equipment [18]: *1* - support; *2* - guide plug; *3* - matrix; *4* - bending profile at a *90°* angle; *5* - cutter for folding and cutting excess material; *6* - cutter for folding at an angle of *180°*; *7* - profiled support for microdeformation; *8* - stud bolt.

The structure of the actuation group includes both the elements necessary for the command and those for the protection of the actuation. Avoiding incidents that lead to damage to materials and installations is mandatorily fulfilled by protection against short circuits and protection against overload, which are ensured by anti-short circuit and/or anti-overload fuses, protection relay and circuit breaker. Switches and circuit breakers have the role of connecting or disconnecting direct current or alternating current circuits, the contact system comprising two elements, one fixed and one mobile. The switching consists in establishing or interrupting the energy from a receiver and is ensured by switches and contactors, the fuses being the switching elements that have the role of opening the circuit when the current passing through it exceeds the safety value.

The technological process of microdeformation of the wires for the capacitors within the micromotor for acting the window of vehicles, has the following stages, shown in Figure 7.

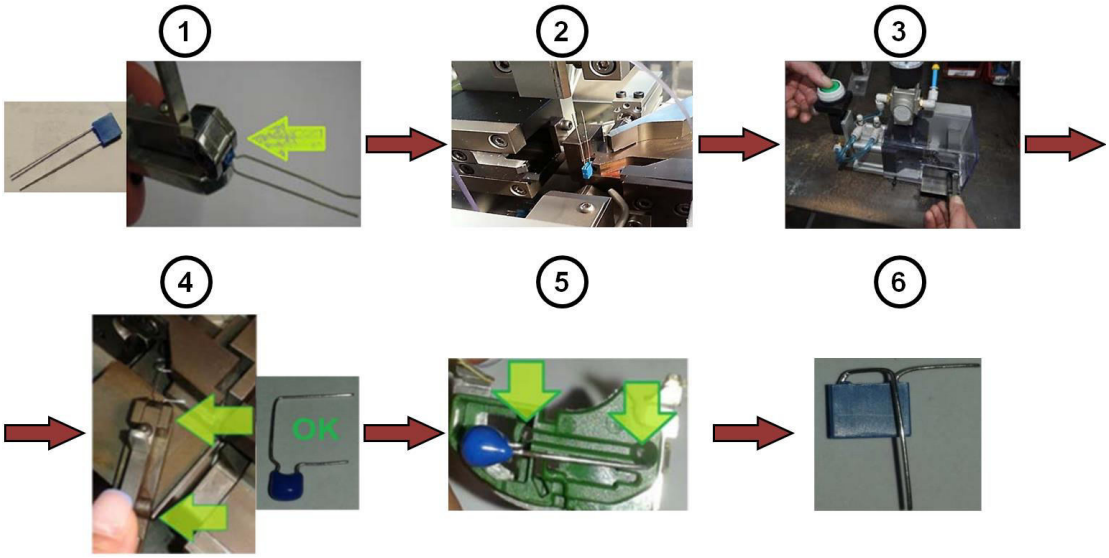

Fig. 7. The technological process of microdeformation of the wires for the capacitors within the micromotor for acting the window of vehicles

The blank is inserted into the tweezers provided with a special fixing channel (1), Figure 8. It is placed in a horizontal position with the arms facing forward and by pressing the machine button, the cutter system executes the cutting and folding of the arms of the blank according to the technical specifications (2 and 3). After bending and cutting, the caliper of the pliers is actuated to the right to be removed from the rail and the part is released with the help of the stud bolt fixed on the module housing, specially intended (4 and 5). A visual check of the cutting-folding operation is made by comparing it with a reference product (6). The final result is shown in Figure 8.

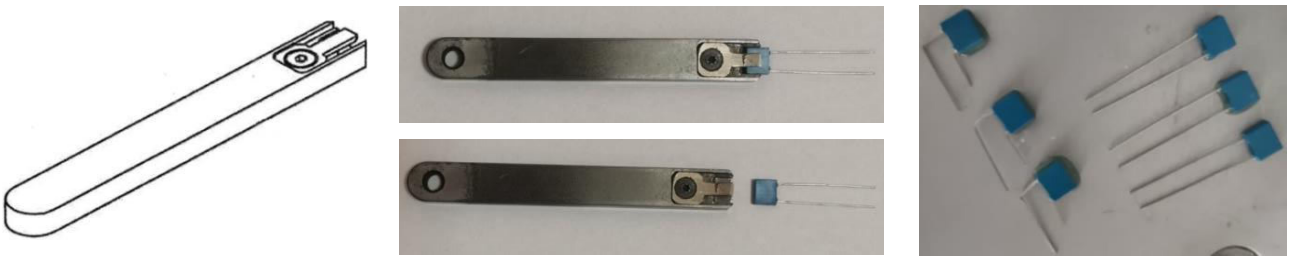

Fig. 8. Inserting the capacitors into the tweezers and the result after deformation

If the force acting on the capacitors is not optimal, component microdeformation defects can occur, Figure 9.

a. b. c.

Fig. 9. Component microdeformation defects:
deformed arms (a); arms cut too short (b); arms cut too long (c).

3.5 Calculation of the axial forces developed by the rod-piston subassembly

In order to perform the correct cutting and bending of the condenser arms, the axial displacement force of the rod-piston subassemblies must be determined, depending on the diameter of the piston and its stroke. The axial force *F* is defined as a theoretical effort available at the output of the rod depending on the direction of movement of the rod-piston subassembly and is calculated with the relation:

$$F = p \cdot S \left[\text{daN}\right], \tag{1}$$

where: *p* is the required pressure in the surface chamber *S* of the pneumatic cylinder.
Since the frictions due to the piston and rod seals are neglected, a coefficient τ, called the load coefficient, can also be used in the calculations to evaluate the real effort obtained. If it is considered that the double-action pistons each push a load - the cutters for folding and cutting the excess material, then the axial force is obtained by a displacement, in the form of dynamic effort. The load coefficient used under these conditions has the value $\tau = 0.6$.

$$F = p \cdot S \cdot \tau \ \left[\text{daN}\right]. \tag{2}$$

The active surface *S* depends on the piston diameter, *D*, Table 1:

$$S = \frac{\pi \cdot D^2}{4} \ \left[\text{mm}^2\right]. \tag{3}$$

Table 3 and Table 4 show the values of the axial forces associated with the movement of pneumatic cylinders in the range of Ø40 mm and stroke *l* = 15 mm, respectively Ø32 mm and stroke *l* = 4 mm, for working pressure values between 5÷10 [bar].

Table 3: The force values of the vertical pneumatic cylinder, D=40 mm

No. crt.	*p* [bar]	*D* [mm]	*l* [mm]	τ [mm]	*F* [daN]
1.	5	40	15	0.6	37.68
2.	6				45.22
3.	7				52.75
4.	8				60.29
5.	9				67.82
6.	10				75.36

Table 4: The force values of the horizontal pneumatic cylinder, D=32 mm

No. crt.	*p* [bar]	*D* [mm]	*l* [mm]	τ [mm]	*F* [daN]
1.	5	32	4	0.6	24.12
2.	6				28.94
3.	7				33.76
4.	8				38.58
5.	9				43.41
6.	10				48.23

In general, the effective useful force developed by a pneumatic cylinder at a given pressure is, as a rule, lower than the theoretical value. The efficiency of the cylinder η_c is defined as the ratio between the real useful force and the theoretical force. The efficiency of pneumatic cylinders is considered to have values in the $\eta_c = 0.7 \div 0.95$ range, increasing the higher the working pressure and the larger the cylinder diameter are. Figure 10 shows, in comparison, the force values of pneumatic cylinders of diameter *D*=40 mm, respectively *D*=32 mm.

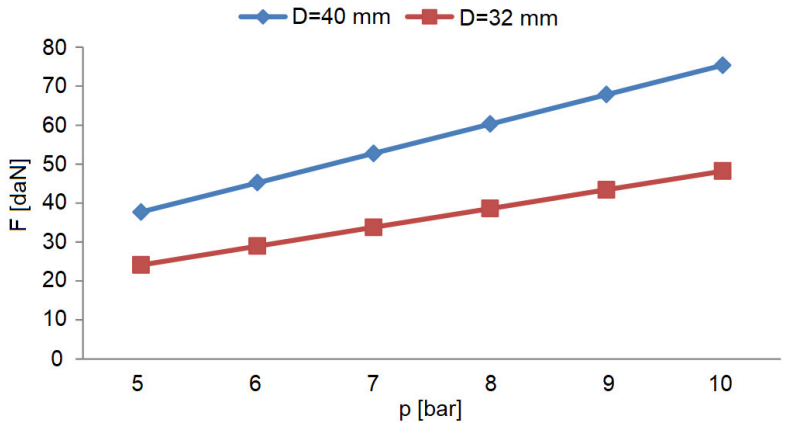

Fig. 10. Values of axial forces *F* for pneumatic cylinders of diameter *D*=40 mm and *D*=32 mm

4. Technological flow for assembling a micromotor for the automatic raising-lowering system of a vehicle windows

The purpose of the wire microdeformation machine is to bend the metal arms of some capacitors in the construction of a mechanism for the automatic raising-lowering of some vehicles windows, Figure 11.

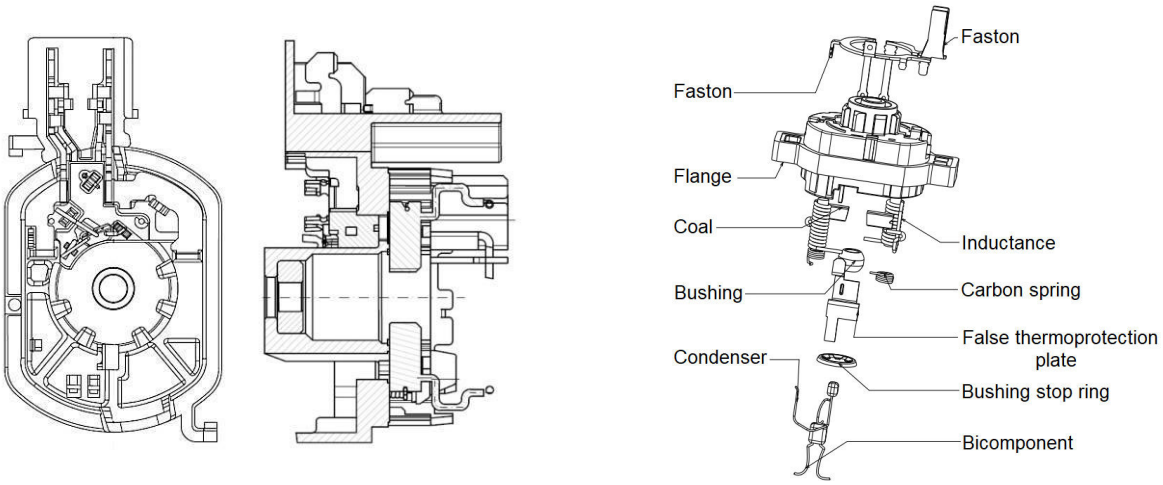

Fig. 11. The micromotor from the construction of the mechanism for the automatic raising and lowering windows of a vehicle [20]

Regardless of the type of motor, it is built from two component parts: the stator and the rotor. The stator is the fixed part of the motor, generally external, which includes the housing, the power terminals, the stator ferromagnetic armature and the stator enveloping. The rotor is the moving part of the engine, usually placed inside. It consists of a shaft and a rotor armature that supports the rotor enwrapping. Between the stator and the rotor there is a portion of air called the air gap that allows the movement of the rotor relative to the stator. Air gap thickness is an important indicator of engine performance. When is actuated from a constant frequency power supply, the electric motor is essentially a constant velocity drive, with the velocity dropping only 1% to 5% as the load torque is increased from zero to rated value.

Usually the starting current is thus limited to about four to seven times the rated current when started at full voltage. The starting torque is usually in the range of 1.75 to 2.5 times the rated value. If the stator has a higher starting current than is allowed from the electrical supply system, the motor can be started on a reduced voltage of about 70% to 80% using a step-down transformer. Alternatively, the stator envelopings may be connected at the start and switched as the speed approaches the rated value. Such measures reduce the starting torque substantially.

A reduction in starting voltage to 75% results in a reduction in supply current to 56%, but results in only 56% of the starting torque that would be provided at full voltage.
The flow of the assembly process of the parts from the construction of the electric micromotors used for the automatic raising and lowering of the windows of a vehicle is presented in Figure 12.

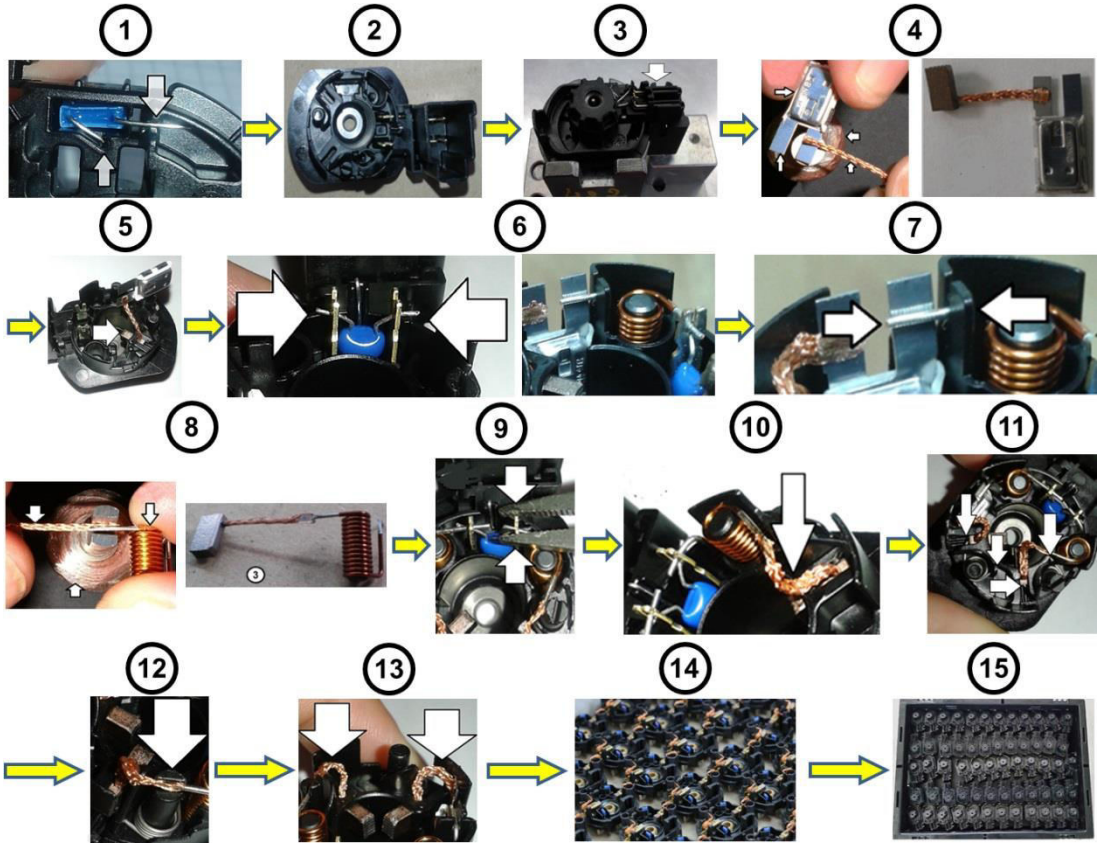

Fig. 12. The process flow for the realization of the parts

The capacitor is mounted on the cutting-folding machine, the operation being performed manually (1). At the same time, the bushing and the connector will be mounted in the flange (2 and 3). An electric welding will be performed by heating with coal wire. The metal blade expands by heating and will make contact (4). Both the group thus welded and the capacitor will be mounted on the flange, the operation being performed manually (5 and 6). Next, a non-welded resistance will be mounted on the flange, with the help of tweezers, and an electric welding of the resistance with carbon wire will be performed again (7 and 8). The assembly of the resistance-carbon welded group will be manually mounted on the flange, with a minimum of 1 mm space between the impedance arms (9 and 10). The springs will be mounted with the help of a special device (11) and the carbon-welded wires will be positioned with the help of the tweezers (12 and 13). Finally, a visual control of the assembly will be done, based on a standard product and, for packaging, barcode labels and special packaging will be used, after which it will be stored until the transport to the customer (14 and 15).

Conclusions

In order to carry out the technological process of microdeformation of the wires, a device containing pneumatic, electrical and mechanical working components was created. In order to provide a constant compressed air pressure, calculations were made of the characteristic parameters of the pneumatic cylinders - the effort to move some loads, such as vertical axial cutting force, respectively horizontal axial force of deformation of the arms of some capacitors.

In order to ensure the tightness and guidance of a pneumatic cylinder, it is necessary to use seals and guide rings. However, these elements will generate friction that will influence the operation of the cylinder. In order to take these frictions into account when determining the forces developed by a cylinder, a load factor was taken into account. The determination of the effort provided by the cylinder when the rod is withdrawn was not taken into account, since the efforts provided at the output of the rod are important for cutting and deforming the capacitor arms.
The continuous verification of the work flow, as well as the quality of the execution of the microdeformation operation determines the productivity of the work by completing this operation on time and sending the components to the next operation, namely the assembly of the micromotor flange.

References

[1] Agostino, M., A. Nifo, S. Ruberto, D. Scalera, and F. Trivieri. "Productivity changes in the automotive industry of three European countries. An application of the Malmquist index decomposition analysis." *Structural Change and Economic Dynamics* 61 (20220: 216-226.
[2] Guga, Şt. "Industria auto, încotro? Tendințe globale, perspective periferice", *Syndex, Friedrich-Ebert-Stiftung România*, Accessed September 12, 2022. http://library.fes.de/pdf-files/bueros/bukarest/15195.pdf.
[3] Măgdoiu, A. "Quality Improvement Using Poka Yoke Systems." PhD Thesis. "Lucian Blaga" University of Sibiu, 2014.
[4] Yang, Y., K. Arshad-Ali, J. Roeleveld, and A. Emadi. "State-of-the-art electrified powertrains – hybrid, plug-in, and electric vehicles." *International Journal of Powertrains* 5, no. 1 (2016): 1-29.
[5] Un-Noor, F., S. Padmanaban, L. Mihet-Popa, M.N. Mollah, and E. Hossain. "A Comprehensive Study of Key Electric Vehicle (EV) Components, Technologies, Challenges, Impacts, and Future Direction of Development." *Energies* 10 (2017): 1-82.
[6] Chiver, O., N. Burnete, I.R. Şugar, L. Neamț, and E. Pop. "Study on gear ratio of battery electric vehicles." *Ingineria automobilului* 59 (2021): 11-16.
[7] Djurdjanovic, D., L. Mears, F.A. Niaki, A.U. Haq, and L. Li. "State of the art review on process, system, and operations control in modern manufacturing." *Journal of Manufacturing Science and Engineering* 140, no. 6 (2018): 061010.
[8] Universal Robots. Accessed September 16, 2022. https://www.universal-robots.com/.
[9] Robital Industrial Supplier. Accessed September 16, 2022. https://robital.ro/en/home-en/.
[10] European Automobile Manufacturers' Association (ACEA). *Automobile Industry Pocket Guide 2022-2023*, Accessed October 3, 2022. https://www.acea.auto/publication/automobile-industry-pocket-guide-2022-2023/.
[11] Ispas, N., M. Năstăsoiu, and T.D. Ioniță. "Assessing potential cars occupant's injuries in three different collision scenarios between a car and a truck." *Ingineria automobilului* 62 (2022): 5-8.
[12] Abela, K., P. Refalo, and E. Francalanza. "Design and implementation of an energy monitoring cyber physical system in pneumatic automation." *Procedia CIRP* 88 (2020): 240-245.
[13] Taheri, K., and R. Gadow. "Industrial compressed air system analysis: Exergy and thermoeconomic analysis." *CIRP Journal of Manufacturing Science and Technology* 18 (2017):10–7.
[14] Baroiu, N., D. Vișan, and O.D. Ciocan. *Technological hydrostatics and pneumatics - laboratory guide* / *Hidrostatică și pneumatică tehnologică - îndrumar pentru laborator*. Galați, Academica Publishing House, ISBN 978-606-606-007-3, 2018.
[15] Gujar, A.N., T.D. Kadam, V.V. Shinde, G.E. Chavan, and A.J. Mane. "Design and Development of Pneumatic Stirrup Bending Machine." *International Journal of Advance Engineering and Research Development* 4, no. 3 (2017): 479-485.
[16] Suryawanshi, V.N., N.V. Wakade, and P.A. Narwade. "Design and Development of Pneumatic Punching Machine." *International Research Journal of Engineering and Technology* 6, no. 5 (2019): 1140-1145.
[17] Tambat, V., N. Rane, O. Savant, and P. Yadav. "Pneumatic Shearing and Bending Machine." *International Journal of Recent Research in Civil and Mechanical Engineering* 2, no. 1 (2015): 9-18.
[18] Olamef. Manuale d'uso e manutenzione macchina mod. SP 20.08, Accessed October 3, 2022. https://www.olamef.net/.
[19] SMC Pneumatics. Accessed September 16, 2022. https://www.smcpneumatics.com/.
[20] Moroșanu, G.A., V.G. Teodor, V. Păunoiu, R.S. Crăciun, and N. Baroiu. "Quality characteristics analysis for the assembly of the elements from the construction of a mechanism for adjusting the seats in the automotive industry." Paper presented at The 7th International Conference on Advanced Manufacturing Engineering and Technologies - NewTech, Rennes, France, September 08-10, 2022.

ISSN 1454 - 8003
Proceedings of 2022 International Conference on Hydraulics and Pneumatics - HERVEX
November 9-10, Băile Govora, Romania

INCREASING PERFORMANCE OF VERTICAL AXIS WIND TURBINES

Marius PARASCHIVOIU[1,*], Belkacem BELABES[1], Robert Alexis L. MINETTO[1], Farshad REZAEI[1]

[1] Concordia University, Montreal, Quebec, Canada

*marius.paraschivoiu@concordia.ca

Abstract: *The research presented in this work addresses the performance of Vertical Axis Wind Turbines (VAWT). The aerodynamic performance of the turbine is measured by the power coefficient (Cp) which is calculated by simulating the flow around the entire turbine with Computational Fluid Dynamics (CFD). The analysis is focused on evaluating the effect on the performance of the turbine for three different cases. In the first case, flows with different turbulence intensities are simulated. The turbulence intensity is increased from almost zero to 40% which leads to an increase of the Cp of about 27% for small turbines. In the second case, we change the camber of the blade during a quarter of the rotation of the VAWT. The proposed morphing methodology increases the Cp by 46%. In the third case, the placement of a small turbine on the frontal windward corner for three different building heights is studied. The Cp is increased by 80% on the highest building compared to the baseline case of the turbine in an unperturbed flow.*

Keywords: *Vertical Axis Wind Turbine, Computational Fluid Dynamics, Power Coefficient, Turbulence Intensity, Morphing Blade, Roof-mounted Turbines*

1. Introduction

VAWTs extract power as the airfoil blade generates a torque due to the lift force while rotating. For Darrieus or H-Type VAWT the axis of rotation is perpendicular to the flow direction, which leads to complex aerodynamics because the angle of attack of the blade is continuously changing. In this paper, mainly micro-scale VAWTs defined as an installed power of less than 2.5 kW [1] are investigated but we also examine a large 500 kW turbine.
Micro-scale turbines are mainly interesting for urban applications. Wind flow over a single building offers some locations where the wind accelerates considerably and therefore provides a greater potential for energy extraction by a wind turbine. Nevertheless, in dense urban locations, the wind is both slower and more turbulent. The complexity of this wind flow is due to the presence of the buildings themselves and their various effects on the wind flow's aerodynamic behavior. In this paper, the turbulence intensity of the flow is analyzed as it has been shown that it is able to increase the performance of the turbine. Experimental results reported in [2] show that the power coefficient can increase by 20% when the turbulence intensity is increased to 14.8%. A larger turbine is also analyzed and compared with field studies available in [3].
CFD has emerged as the most common tool to conduct design and analysis of the aerodynamic performance of VAWT [4]. It is cost effective and accurate but is still computationally expensive and cannot be used for all analyses. This paper will first show that the effect of the turbulence intensity on the Cp is well captured. CFD is then used to model a morphing blade simulation. The blade shape has a dominant effect on the wind generated turbine torque. In section 3, a case study is presented when the blade changes its shape during the rotation cycle. Finally, the location of a micro-scale turbine on the roof of a building is also studied. It is clear that the building has an enormous influence on the flow speed which requires dedicated analysis. Very accurate but computation expensive LES simulations were performed in [5] to examine the flow on the roof on cuboid buildings of different sizes and different wind directions. Though, the frontal windward corner was not recommended for placement of wind turbines while the other two windward corners showed significantly higher velocities, in this work we only investigate the frontal windward corner.
This paper is organized as follows. Section 2 discusses the effect of turbulence intensity on the Cp value for a small and a large turbine. Section 3 presents the results of a test case of a morphing

blade and section 4 reports on the effect of the building height on the performance of a small turbine placed on the corner of the building.

2. Effect of turbulence intensity

Turbulence intensity (Iu) is a measure of the wind turbulence. It is defined as the standard deviation of wind speed over the mean wind velocity. Turbulence intensity decreases with increasing wind speed but the wind in an urban environment will typically have values of turbulence intensity ranging from 20% to 30%. In this section, the effect of Iu on the performance of a VAWT is examined using CFD. Computational results based on a commercial CFD code (Star CCM+) using full URANS calculations of the turbine are performed. To demonstrate the accuracy of the approach wind tunnel results are reproduced numerically. A two-bladed H-type Darrieus turbine of diameter 0.5 m and swept area of 0.4 m^2 is simulated. The two NACA0018 blades rotate at angular speeds of 1200 rpm. The free stream wind speed is 10 m/s. The details of the computational methodology are reported in [6]. Numerical values of the power coefficient are compared with experimental measurements from [2] as shown in Figure 1.

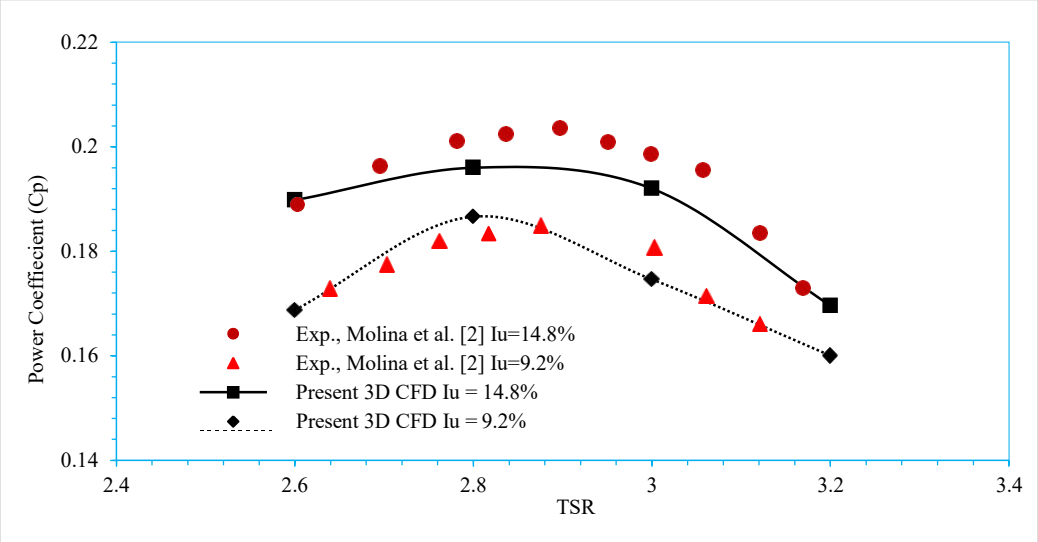

Fig. 1. Cp comparison between CFD results and experimental measurements of Molina et al. [2] for a small 0.5 m diameter turbine

The Figure 1 shows a good comparison for both values of the turbulent intensity of the flow. At Iu=9.2% the highest numerical Cp values of 0.187 is very close to the experimental value of 0.185. At Iu=14.8%, the numerical Cp values of 0.196 is a little less than the experimental value of 0.203, nevertheless the overall trend is well captured. Note that the higher turbulent intensity Iu=14.8% leads to an increase in Cp of 4.8%. We now perform the same simulation for different values of Iu ranging from 0.7% to 40%. Table 1 provides the numerical Cp values for each simulation at different Iu values. We can see a significant increase in the value of Cp from 0.175 at Iu=0.7% to Cp=0.222 at Iu=20%. This increase in Cp is about 27%, which is quite significant. However, the Cp does not increase for Iu values larger than 20% as shown in Table 1.

Table 1: The obtained Power coefficient against different intensity levels

Turbulence Intensity (%)	0.7	9.2	14.8	20	30	40
Power Coefficient (Cp)	0.175	0.177	0.192	0.222	0.229	0.230

We now investigate a larger turbine. The large turbine also has two NACA 0018 blades but the rotor diameter is 35 m. The swept area of this turbine is 850.5 m^2. Note that much of the literature is only addressing small turbines which are often less performant. Figure 2 reports the CFD results for the Fine Mesh (20 million elements) and Medium Mesh (15 million elements) as well as field measurements data. First, note that the Cp for this turbine reaches 0.33, which is higher than for smaller turbines. Note also the importance of the mesh size. The Medium Mesh is not able to capture the correct Cp at low Tip Speed Ratios (TSR). Therefore, the Fine Mesh is used to study the effect of the turbulence intensity on this large turbine. Figure 3 reports that the same Cp is obtained for three different turbulent intensity ranging from Iu = 1%, 15% and 30%. This work does show that small turbines can benefit from an increase in turbulence intensity but not large turbines. Indeed, the Cp can increase by as much as 20% but large turbines do not see any effect of the turbulence intensity.

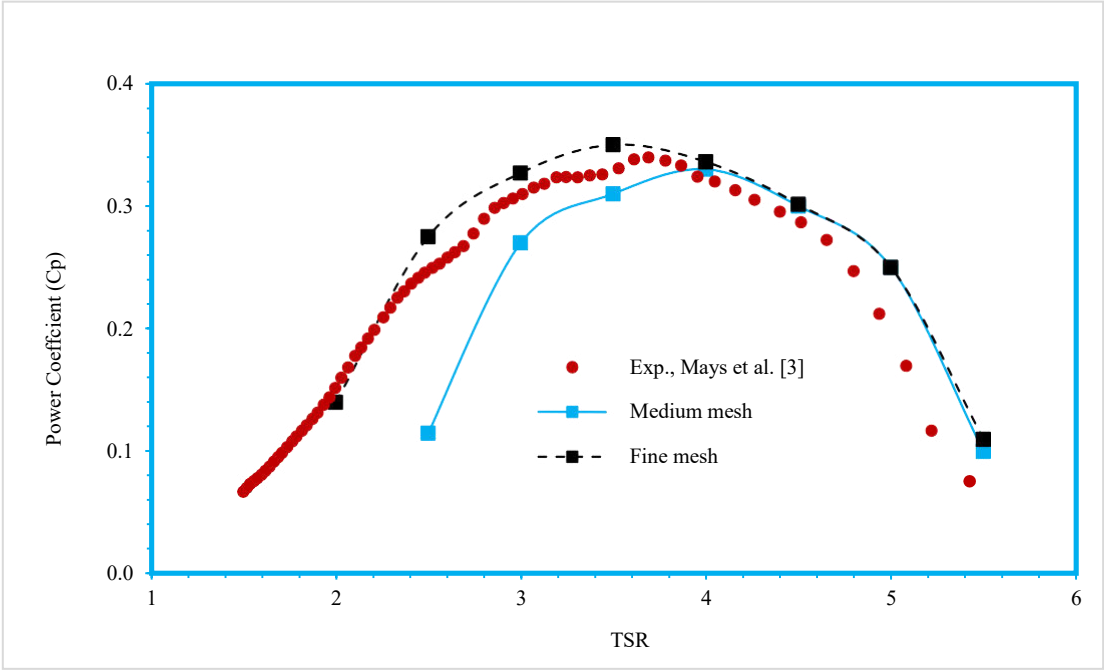

Fig. 2. Cp comparison between CFD and experimental data [3] for a large turbine 35 m diameter turbine

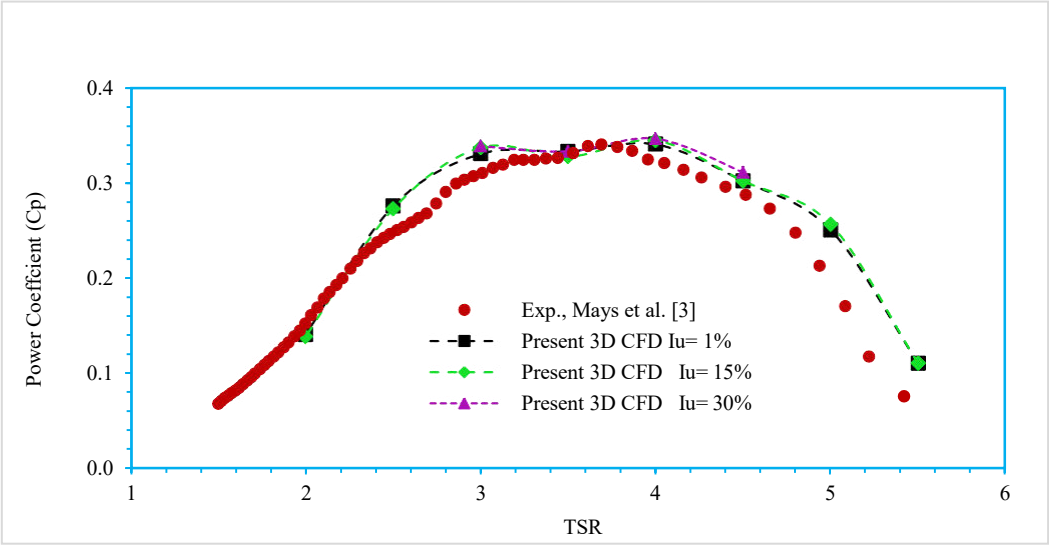

Fig. 3. Effect of the turbulence intensity on the Cp of a large turbine

3. Effect of blade morphing

The blade of a VAWT has a significant effect on the performance of the turbine. As the turbine rotates the angle of attach of each blade changes. If this angle reaches a large value, dynamic stall of the blade can occur which creates a large change of the forces on the blade. One interesting techniques to control the dynamic stall situation is to change the blade geometry by changing its camber. The overall benefit is that the performance of the turbine is improved. Robust and well controlled morphing airfoils have been designed. In particular, Pankonien et al. [7] have designed an airfoil mechanism that controls the trailing edge as shown in Figure 4. The baseline shape is a NACA 0012 airfoil. The inward shape is the trailing edge flexed with a deflection of 13.4 degrees.

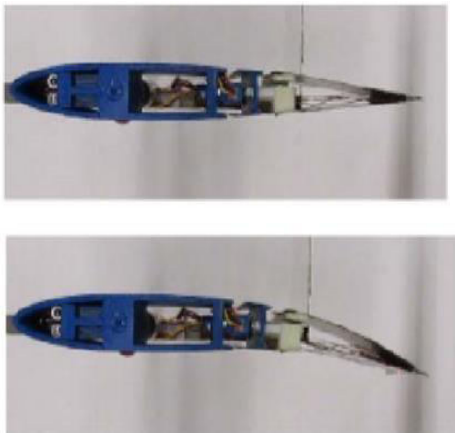

Fig. 4. The Synergetic Smart Morphing Aileron (SSMA) designed by Pankonien et al [7]; top) baseline shape, bottom) inward shape

A numerical simulation of a turbine with a single blade is performed to calculate the Power Coefficient. Details of the simulation are reported in [8]. The blade rotates at 90 RPM at TSR 3.17. The turbine has a rotor diameter of 5.395 m and the wind speed velocity is 8 m/s. A two dimensional simulation with a mesh of 416 000 elements with a time step of 2.222E-4 s equivalent to 3000 time steps per rotation is performed. The Cp for this baseline case is reported in Figure 5 as the solid line. The average Cp after 15 cycles is 0.096. When the blade is in the first quadrant, the Cp increase and as it reaches the 80 degrees azimuthal angle it start falling. In the second quadrant, which in Figure 5 is identified as a blue dash lined box, the Cp is negative and undergoes many fluctuations as vortices are shed over the blade. In quadrant 3 and 4, the Cp is smooth with maximum values around 270 degrees. For this specific case, it is suggested to morph the blade to control the complex flow which may be due to dynamics stall that occurs in the second quadrant. Therefore, a simple morphing strategy is investigated such as to only morph the blade very rapidly at the start of the second quadrant and keep its inward shape until the azimuthal angle of 180 degree, which is the end of the quadrant. The resulting Cp which is reported as the dashed line in Figure 5 shows two spikes, one upward at 90 degrees and one downward at 180 degrees. The spikes are related to the morphing motion. The first is when the blade changes from the baseline to the inward shape and the second is when the shape is changed back to the baseline position. Once the inward shape is fixed during the second quadrant, we can see from the Cp curve that only small vortices are shed. The Cp is only slightly negative. The performance of the turbine in this quadrant is significantly improved. The average Cp for the entire cycle is also increase to 0.14 due to this approach. This represents a 46% increase, which demonstrated the high benefit of a morphing approach. Table 2 reports the average CP for both cases.

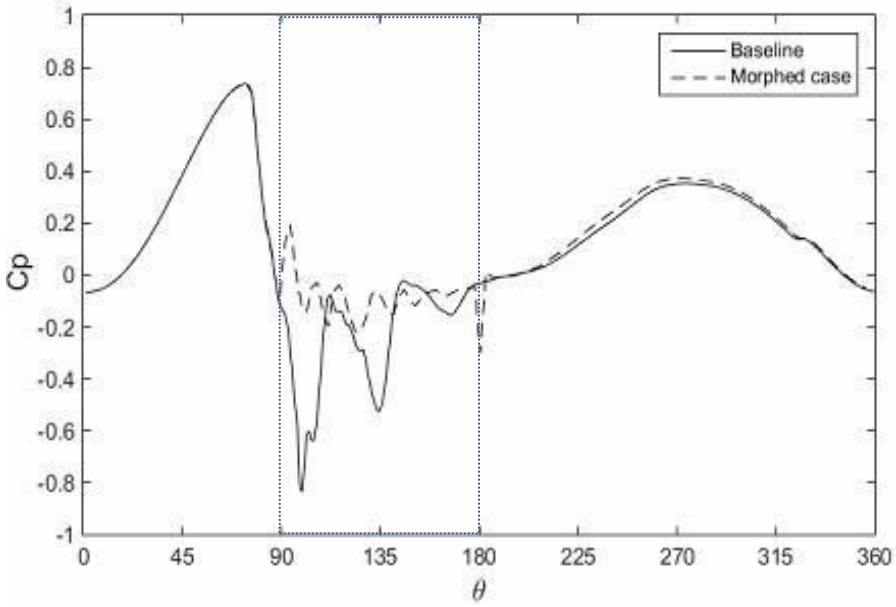

Fig. 5. Power Coefficient versus azimuthal angle for a turbine with the baseline blade and the morphing blade

Table 2: Average Cp values for baseline and morphed cases

Case	Cp
Baseline	0.096
Morphed case	0.140

4. Effect of building size

The study in section 2 indicates that small turbines, which are interesting for urban applications, would benefit from the high turbulence intensity in urban areas. But the best location to place a vertical axis wind turbine on a single building is not yet fully identified. It is well known that the wind flow over a single building offers some locations where the wind accelerates considerably, providing a greater potential for energy extraction by a wind turbine. Nevertheless, Drew et al. [9] reported that 38 building-mounted wind turbines in the UK performed below expectations during field tests. The study found that the wind speed data used for assessing these small wind turbines' performance was obtained from low-resolution wind speed databases that do not accurately reflect the local changes in wind resources. Thus, it is clear that a need to understand the different effects of wind flows disturbed by buildings on roof-mounted wind turbines' performance is required to have the turbines perform adequately. Herein, CFD analysis is performed on a roof-mounted VAWT.

It was shown that placement of a VAWT on the side of a building can led to a 120% increase of the Power Coefficient compared with the reference value [10]. Numerical and experimental analysis in [11] also show that the performance of a Savonius turbine placed above a small 5 m high structure increases the performance by 60%. Furthermore, investigating the placement on a 30 m cubic building, a new design, based on drag type blades with 120-degree arcs, led to a Cp of 0.25, which was significantly better than the original Savonius turbine but remained quite modest [12]. On the same building configuration, the placement of a Darrieus turbine in the middle of the roof edge facing the wind gave a max Cp of 0.40 [13]. By varying the placement of this turbine on the same building for different wind direction, the best result was a Cp of 0.54 [14]. In this section, we investigate an H-type Darrieus placed on the frontal windward corner, the corner facing the wind as shown in Figure 6.

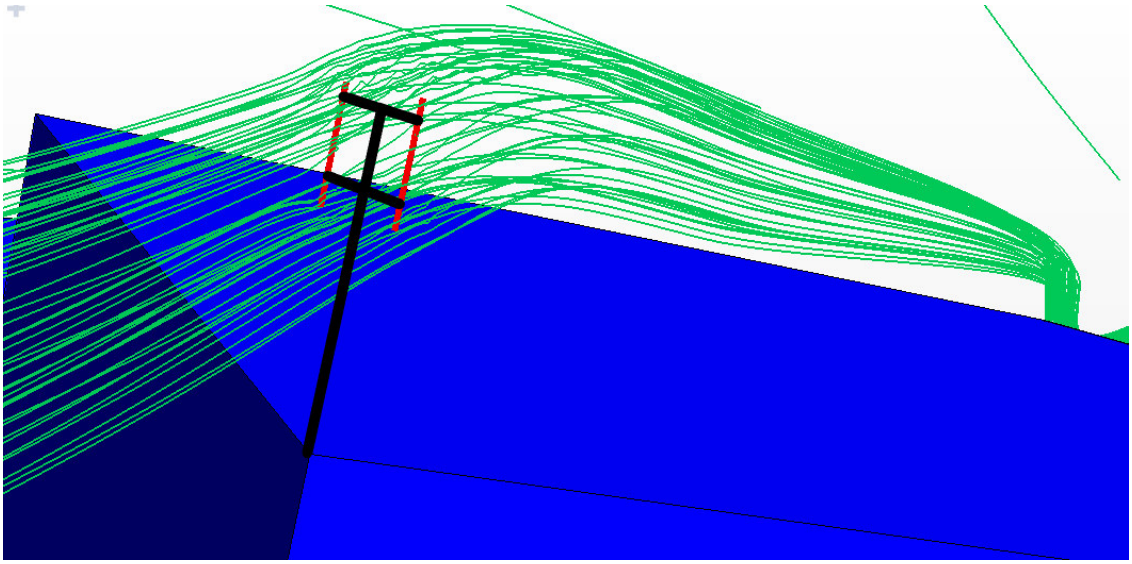

Fig. 6. Placement of a small VAWT on the corner of the building when the wind is facing this corner

It is clear that the building has an enormous influence on the flow speed, which requires dedicated analysis. The size of the building also has a significant effect on the performance of the turbine. We perform CFD simulations using STAR CCM+ to understand the effect of the building size. To do so, a two-bladed H-type VAWT is used with the turbine's diameter (D) and height (H) of 1 m, which provides an aspect ratio (H/D) of 1. The NACA 0018 airfoil section is used for the blades with the chord size (c) of 0.06 meters. This geometry gives the turbine's solidity (σ=nc/D, where n is the number of blades) equal to 0.12. Simulations have been done for three different building heights: 100 ft (30.48 m), 200 ft (60.96 m), and 300 ft (91.44 m). To eliminate the reverse flow effect, the computational domain has the building placed at a 5H distance from the inlet, 10H from the outlet, 5H from the sides, and 10H at the top, where H is the height of the building. The velocity inlet and pressure outlet boundary conditions have been used for the inlet and outlet faces of the domain, respectively. The wall boundary condition is used for the ground and surfaces of the building, and the symmetry boundary condition is used for the other boundaries. In this study, the turbine is placed on the roof-top corner of the building. The distance between the roof and the bottom of the turbine is 1.8 meters. To change the value of the Tip Speed Ratio ($TSR=R\omega/U_\infty$, where R is the turbine radius and ω is the angular velocity of the turbine) in this study, the angular velocity is changed.
Since the wind turbine operates in the atmospheric boundary layer, a velocity profile is defined for the inlet boundary to account for this effect. In this profile, the wind velocity is a function of the height of the building, defined as follows:

$$V_Z=V_{mid}(Z/H_t)^{0.31} \quad (1)$$

In this equation, V_{mid} is referred to the wind velocity at the middle plane of the turbine, Z is the height from the ground, and H_t is the height from the ground to the center plane of the turbine. The inlet velocity profile describing the atmospheric boundary layer is depicted in Figure 7—this velocity profile is used firstly for the building height of 100 ft. Therefore, the V_{mid} was considered as 9.3 m/s. Moreover, the same velocity profile is used for the taller buildings, i.e., 200 ft and 300 ft.

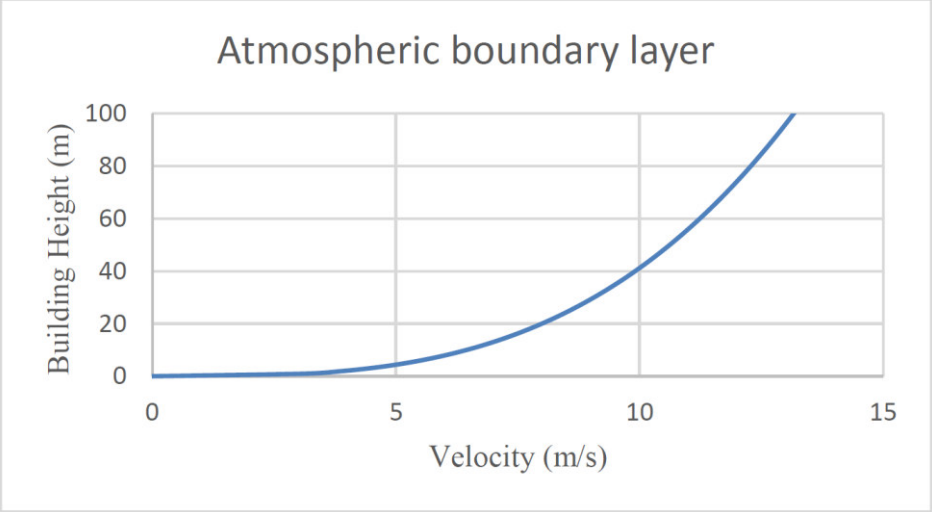

Fig. 7. Velocity profile showing the atmospheric boundary layer

To solve the equations of motion and capture all flow field features, a commercial CFD solver named STAR CCM+ is used. The SIMPLE algorithm (Semi-Implicit Method for Pressure Linked Equations) is utilized to couple the pressure-velocity equations. For the convection term, a second-order upwind scheme is used. In this study, a time step that is equal to 0.48° rotation of the blade per time step was used. Simulations continued until the moment coefficient, and the power coefficient became stable. The stability here is defined as less than 1% changes in the power coefficient in two consecutive rotations of the VAWT.

Figure 8 shows the moment coefficient (C_M) for the building height of 100 ft at a TSR of 5, where the max power is attained. This Figure depicts 16 rotations of the VAWT, where it has been stable at the 10th rotation. Moreover, Figure 9 compares the C_M of the turbine for different building heights at the TSR values that the maximum power is obtained. For comparison, one rotation of each turbine is shown at the rotation number when the results have been their stable state. This figure shows the 15th rotation of the VAWT for the 100ft building height. However, since the velocity is increased for higher buildings and the time step is decreased for them due to the higher rotational velocity in which the maximum power occurs, the 15th rotation does not have the same time for taller buildings. This graph shows that the highest value of the moment coefficient is higher for taller buildings.

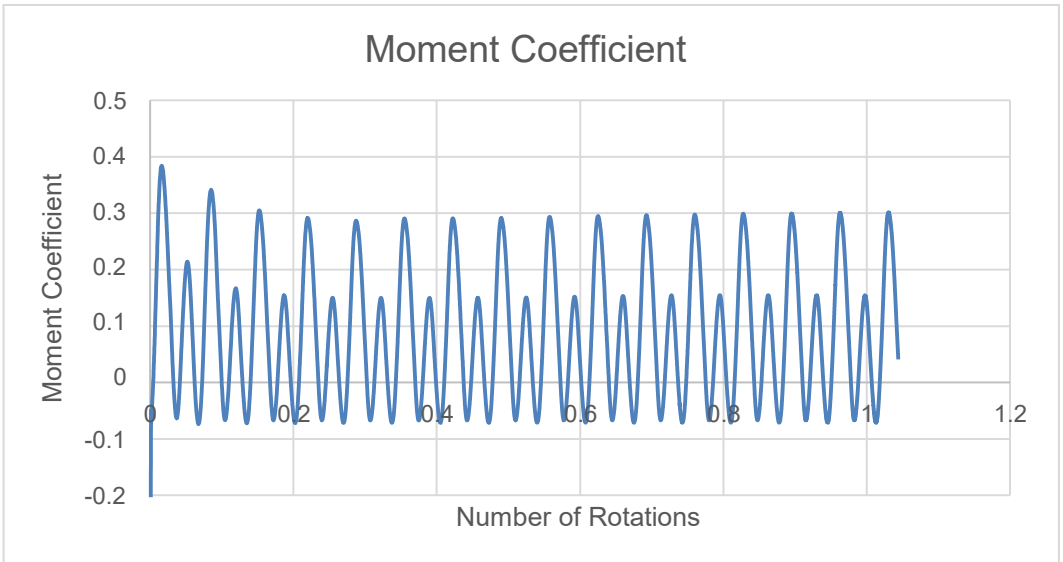

Fig. 8. Moment coefficient for the 100 ft height building at the TSR of 5 in which the maximum power for this building is obtained

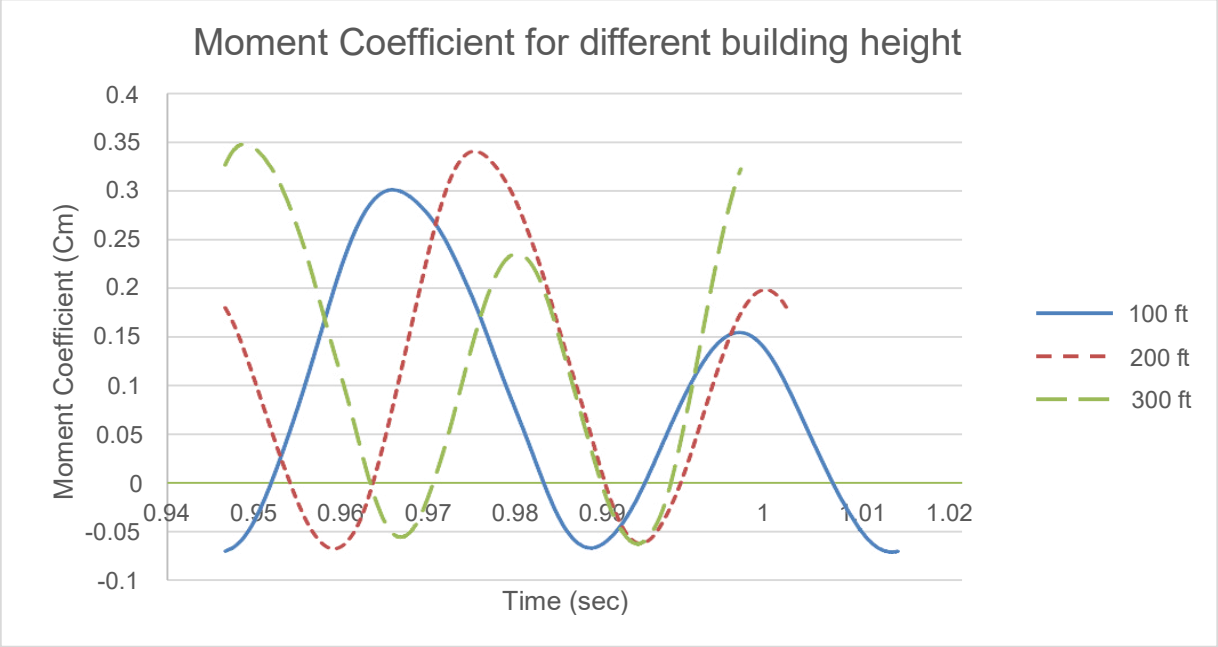

Fig. 9. Comparison of the instantaneous moment coefficient for different building heights at the TSR values for which the maximum power is generated

Figure 10 shows the power coefficient for different building heights at varying values of TSR. It shows that the maximum Cp is increased for taller buildings, while the maximum Cp occurs at lower TSR values for taller buildings. It is important to mention that since the velocity is increased for taller buildings, the values of TSR are decreased. However, the maximum Cp is obtained at higher rotational velocities for taller buildings. The Cp is increased from 0.426 for the turbine on placed on the building of height 100 ft to 0.578 for the turbine installed on the building of height 300 ft. This increase is significant and improves the performance of the turbine by 36%.
Table 3 shows the maximum power values for different building heights. The following equation is used to calculate power.

$$P_{Turbine} = C_P\, 0.5 \rho A_S U_\infty^3 \tag{2}$$

where ρ is the air density, U_∞ is the free stream velocity, and A_S is the swept area equal to the turbine diameter multiplied by the blade span. Since the power is proportional to the velocity cubed, taller buildings can generate more power due to the higher velocity on the roof-top and higher Cp values. This table shows that the maximum power for the 200 ft building is increased by 134% in comparison to the 100 ft building height results. On the other hand, the maximum power for the 300 ft building is increased by 260% and 54% in comparison to the 100 ft and 200 ft building height results, respectively. The increment rate of power from 100 ft to the 200 ft building height is 282 W, which is almost the same as the 266 W from 200 ft to 300 ft building height. It shows that although the building height increased equally, the power increment just slightly decreases.

Fig. 10. Power coefficient (C_P) for different building heights to varying values of TSR

Table 3: Maximum power generated for different building heights

Building Height (ft)	TSR value for maximum power	Maximum Power (W)
100	5	210
200	4.89	492
300	4.69	758

5. Conclusions

This paper presents CFD investigations related to unsteady simulations of vertical axis wind turbines. The analysis is focused on evaluating the effect on the performance of the turbine for three different cases. In the first case, we show that the turbulence intensity can increase the Cp about 27% for small turbines. In the second case, we illustrate that a morphing blade can increase the Cp by 46%. In the third case, we show that when placing of a small turbine on the frontal windward corner the Cp of that turbine is increased by 80% compared to the baseline case without a building. These studies show that the Cp can reach high values and can lead to very performant VAWTs, in particular for urban installation.

Acknowledgments

The authors gratefully acknowledge the financial support from Natural Sciences and Engineering Research Council of Canada (NSERC). Computing resources were provided by Calcul Quebec and Compute Canada.

References

[1] Peacock, Andrew, D. Jenkins, M. Ahadzi, A. Berry, and S. Turan. "Micro wind turbines in the UK domestic sector." *Energy and Buildings* 40, no. 7 (2008): 1324-1333.

[2] Carbo Molina, Andreu, Tim De Troyer, Tommaso Massai, Antoine Vergaerde, Mark Runacres, and Gianni Bartoli. "Effect of turbulence on the performance of VAWTs: An experimental study in two different wind tunnels." *Journal of Wind Engineering and Industrial Aerodynamics* 193 (2019): 103969.

[3] Mays, I. D., C. A. Morgan, M. B. Anderson, and S. J. R. Powles. "Experience with the VAWT 850 demonstration project." *Proceedings of European Community Wind Energy Conference* (1990): 482 – 487.

[4] Barnes, Andrew, Daniel Marshall-Cross, and Ben Richard Hughes. "Towards a standard approach for future Vertical Axis Wind Turbine aerodynamics research and development." *Renew Sustain Energy Rev* 148 (2021): 111221.

[5] Kono, Takaaki, Tetsuya Kogaki, and Takahiro Kiwata. "Numerical Investigation of Wind Conditions for Roof- Mounted Wind Turbines: Effects of Wind Direction and Horizontal Aspect Ratio of a High-Rise Cuboid Building." *Energies* 9, no. 11 (2016): 907.

[6] Belabes, Belkacem, and Marius Paraschivoiu. "Numerical study of the effect of turbulence intensity on VAWT performance." *Energy* 233 (2021): 121139.

[7] Pankonien, Alexander M., Cassio T. Faria, and Daniel J. Inman. “Synergistic smart morphing aileron.” Paper presented at the 54th AIAA/ASME/ASCE/AHS/ASC Structures, Structural Dynamics, and Materials Conference, Boston, Massachusetts, April 8-11, 2013.

[8] Minetto, Robert Alexis Leonczuk, and Marius Paraschivoiu. “Simulation based analysis of morphing blades applied to a vertical axis wind turbine.” *Energy* 202 (2020): 117705.

[9] Drew, Daniel R., Janet F. Barlow, Tim T. Cockerill, and Maria M. Vahdati. "The importance of accurate wind resource assessment for evaluating the economic viability of small wind turbines." *Renewable Energy* 77 (2015): 493-500.

[10] Xu, Wenhao, Gaohua Li, Xiaobo Zheng, Ye Li, Shoutu Li, Chen Zhang, and Fuxin Wang. "High-resolution numerical simulation of the performance of vertical axis wind turbines in urban area: Part I, wind turbines on the side of single building." *Renewable Energy* 177 (2021): 461-474.

[11] Liu, Xiran, Dan Zhao, and Nay Lin Oo. “Numerical prediction of the power coefficient improvements of three laterally aligned Savonius wind turbines above a forward-facing step.” *Journal of Wind Engineering and Industrial Aerodynamics* 228 (2022): 105112.

[12] Larin, Patrick, Marius Paraschivoiu, and Cevdet Aygun. “CFD based synergistic analysis of wind turbines for roof-mounted integration.” *Journal of Wind Engineering and Industrial Applications* 156 (2016): 1-13.

[13] Victor, Samson, and Marius Paraschivoiu. "Performance of a Darrieus turbine on the roof of a building." *Transactions of the Canadian Society for Mechanical Engineering* 42, no. 4 (2018): 341-349.

[14] Allard, Marc Alexandre, and Marius Paraschivoiu. "Power enhancement CFD based study of Darius wind turbine via roof corner placement." *Journal of Renewable and Sustainable Energy* 14, no. 3 (2022): 033301.

ISSN 1454 - 8003
Proceedings of 2022 International Conference on Hydraulics and Pneumatics - HERVEX
November 9-10, Băile Govora, Romania

VARIATION OF TRIBOLOGICAL PARAMETERS DEPENDING ON THE THICKNESS OF THE THIN FILMS USED FOR BIOMEDICAL APPLICATIONS

Liliana-Laura BĂDIŢĂ-VOICU[1], Aurel ZAPCIU[1], Cătălin VIȚELARU[2], Arcadie SOBETKII[3]

[1] National Institute of Research and Development in Mechatronics and Measurement Technique, INCDMTM Bucharest, badita_l@yahoo.com, zapciu.aurel@yahoo.com

[2] National Institute of Research and Development for Optoelectronics, INOE 2000, Bucharest, catalin.vitelaru@inoe.ro

[3] SC MGM Star Construct SRL, Bucharest, sobetkii@yahoo.com

Abstract: *This paper presents the results obtained from a project that had as main objective to improve the tribological characteristics of biomedical components in order to increase their lifetime. A solution for optimizing the constructive characteristics and increasing the operational duration for orthopaedic implants components is the deposition of micro and nanostructured thin films through intelligent mechatronic processes and technologies. TiO_2, TiN and CrN thin films with thicknesses of 0.5 μm, 1 μm and 1.5 μm were deposited by Direct Current (DC) sputtering, High Power Impulse Magnetron Sputtering (HiPIMS) and cathodic arc, on two types of substrates: CoCr and M30NW steel. The variation of the friction coefficient as a function of time and the wear traces profiles for all samples in each type of thin film were analysed. Following the tribological characterization, and the comparative analysis of the experimental results, information regarding the quality of the deposited material and the degree of influence of thin films thickness were obtained. The main conclusion of the study was that the friction coefficient and the wear rate decrease with an increase of the layer thickness. This means that a thicker layer will be more sustainable and can be used to improve the quality of biomedical components, like hip prostheses.*

Keywords: *Thin films, tribological characterization, friction coefficient, wear rate, implants*

1. Introduction

Substantially improving the quality of life of patients with severe motor disabilities by using partial or total arthroplasty is an important topic of current research in the field of materials engineering and biotribology. [1] This because, over time, the movement of the body causes the wear of the material, loose of fixation and destruction of the implant, most failures occurring due to improper properties or incorrect choice of materials. [2]
Deposition of micro and nanostructured thin films on the biomedical metallic implants and their components, is a solution for reducing the wear rate and increasing the operational time without changing the surface geometry. [3, 4, 5] Generally, coatings applied for improving the implants resistance must have a high adhesion to the substrate and a low friction coefficient to prevent detachment from the substrate, overheating and accelerated wear. Presently, there are studies regarding the use of nitride-based compounds [6], amorphous carbon [7], calcium-phosphate [8], diamond-like carbon [9] as coatings for increasing the implants resistance.
Based on this information and with the aim to improve the technical and functional properties of implants, micro- and nanostructured thin films with various thicknesses, deposited on materials with high mechanical strength and low wear, currently used in orthopaedics, were tested and analysed in the present project.
Tribological tests were performed to determine the friction coefficient and the wear rate of these micro-nanostructured thin films and the dependence on the thickness was assessed by characterization and comparative analysis of the experimental results.

2. Experiments

2.1 Preparation of the samples

In this study, materials with an increased wear resistance were tested and analysed in order to determine their capability to improve the tribological properties of biomedical components. Thus, thin layers of TiN, CrN si TiO_2 were deposited on substrates with a composition similar to the prostheses one, respectively CoCr and M30NW steel substrates [10, 11]. Studying nitrides and oxides with antimicrobial properties, it is possible to determine which of these have an increased resistance and will be more efficient for biomedical components.
Thin films were deposited on substrate disks of 8 mm thick and 10 mm in diameter. CoCr samples disks had been produced by 3D printing technique, using a laser metal sintering prototyping equipment – the Shining 3D EP M250 3D Printer (Fig. 1) – from the Research Centre for Intelligent Mechatronic Systems used for Securing Objectives and Intervention – CERMISO of INCDMTM. [12]

Fig. 1. Shining 3D EP M250 3D Printer

M30NW steel samples disks had been produced by mechanical processing techniques, respectively machining from M30NW steel bars, using the MECATOME T202 micro-cutting machine and polishing by using the MECATECH SPI machine. [12]

2.2 Thin films deposition

Micro and nanostructured biocompatible thin films were deposited on CoCr and M30NW steel substrates by physical techniques. TiO_2, TiN and CrN layers with thicknesses of 0.5 μm, 1 μm and 1.5 μm were deposited by Direct Current (DC) sputtering, High Power Impulse Magnetron Sputtering (HiPIMS) and cathodic arc techniques.
Cathodic arc is a technique in which the material from a cathodic target is vaporized, in vacuum, using an electric arc, then condenses on the substrate, forming thin film. [13]
Sputter deposition is based on ion bombardment of a source material, the target, where ion bombardment results in a vapor due to a purely physical process, i.e., the sputtering of the target material. DC sputtering is a deposition technique where a target material is bombarded with ionized gas molecules that hit the target, sputtering off the atoms into the plasma. The vaporized atoms condense, forming a thin film on a substrate. [14]
HiPIMS uses the magnetic field created inside a deposition system. Increased plasma densities are created near the target, which increase the spraying rate. [15]
The deposition of thin layers by cathodic arc, DC sputtering and HiPIMS was performed at SC MGM Star Construct SRL using two equipment: a DC and HiPIMS equipment Leybiold Z-550-S and a Cathodic-Arc UVN-MGM equipment. [12]. Cathodic arc deposition was performed using a power Wt = 1000, Current = 40 A, Voltage = 24-26 V and Pressure = $4x10^{(-1)}$ Pa. For thin films deposition by using the HiPIMS and DC sputtering methods the technological parameters were: power, Wt = 1000, BIAS = 100 V and pressure = $10^{(-3)}$ mbar.
Deposition processes were performed over a period of 5, 10 and 15 minutes to obtain layers of CrN, TiN and TiO_2 with thicknesses of 0.5 μm, 1 μm, and 1.5 μm on CoCr substrate and biocompatible M30NW steel substrate.

2.3 Tribological tests

Tribological tests were performed at National Institute for Research and Development in Optoelectronics (INOE 2000) with the aim to determine the friction coefficient and wear rate of the biocompatible thin films deposited.
The TriboLab UMT Bruker ball on disc tribometer for universal mechanical and tribological testing was used to perform these tribological tests (Fig. 2). The main types of measurements involve parameters like resistance to breaking, bending and scratching, and offer the possibility of measuring very low friction forces.

Fig. 2. Ball on disc tribometer

The variation of the friction coefficient as a function of time was determined applying a pressure force of 0.7N, on a sliding distance of 7,9m (300 cycles), during 80sec, with a speed of 10cm/s. The wear traces profiles were analysed using a Dektak 150 electro-mechanical probe profilometer, performing the tests on a scanning length of 1000 μm and applying a contact force of 49 μN.

3. Results

3.1 Thin films

Using the deposition systems with the technological parameters presented, TiO_2, TiN and CrN thin films were obtained, with thicknesses of 0.5 μm, 1 μm and 1.5 μm, deposited on CoCr and M30NW steel substrates (Fig. 3).

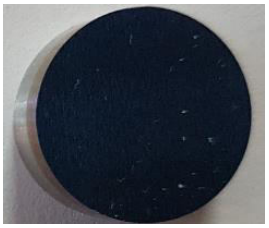

0.5 μm TiO_2 deposited on M30NW steel by DC sputtering

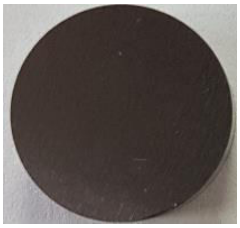

1 μm CrN deposited on CoCr by DC sputtering

1.5 μm TiN deposited on CoCr by DC sputtering

Fig. 3. Thin films deposited on CoCr and M30NW steel substrates by cathodic arc, DC sputtering and HiPIMS

3.2 Tribological tests

Following the tribological tests, the average value of the friction coefficient μ and the average value of the wear rates k were obtained. The variation of the friction coefficient as a function of time (Table 2) was also obtained for all samples from each type of layer (respectively each layer thickness). The wear traces profiles (Table 3, Table 4) were obtained for each type of deposition (respectively each layer thickness).

Table 2: Variation of the friction coefficient as a function of time

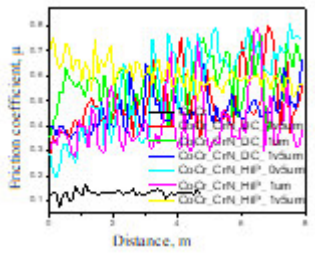	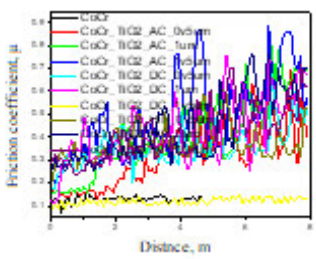	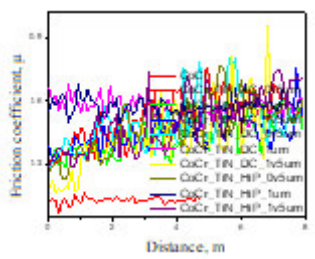
CoCr_CrN	CoCr_TiO_2	CoCr_TiN
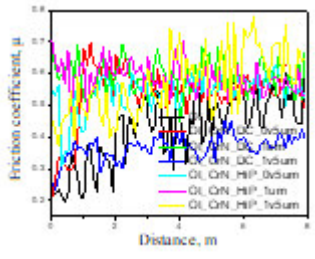	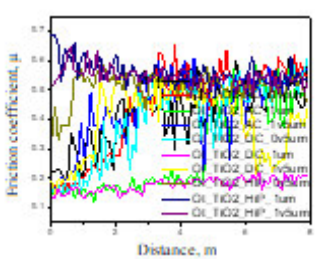	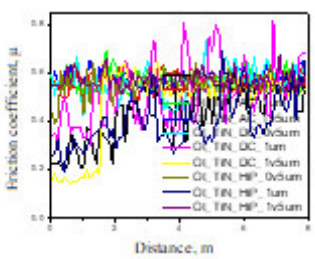
Ot_CrN	Ot _TiO_2	Ot _TiN

Table 3: Wear traces profiles of the thin films deposited on CoCr substrate

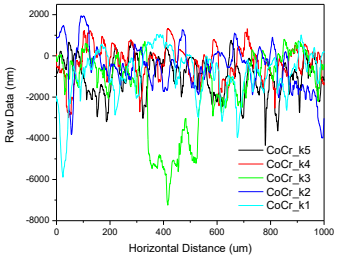		
CoCr		
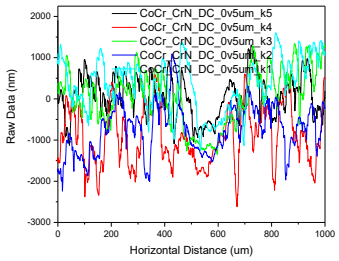	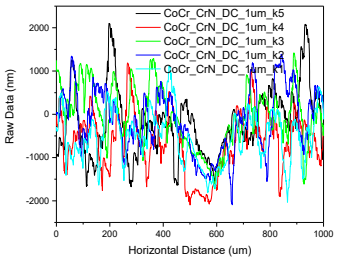	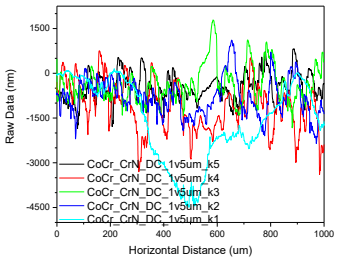
CrN - DC 0.5	CrN - DC 1	CrN - DC 1.5
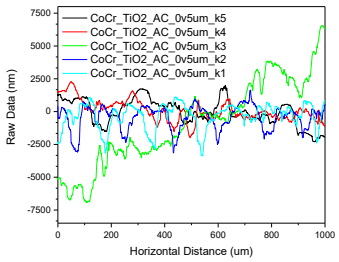	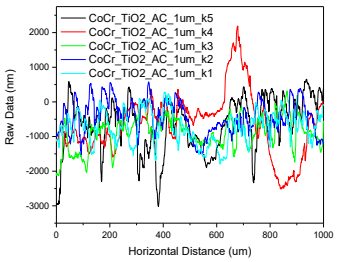	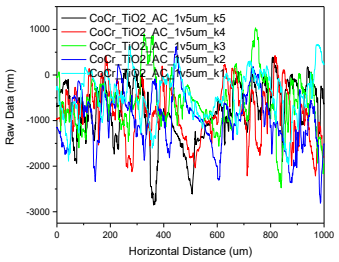
TiO_2 - AC 0.5	TiO_2 - AC 1	TiO_2 - AC 1.5

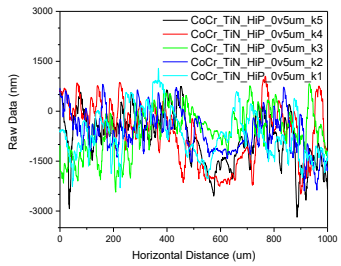	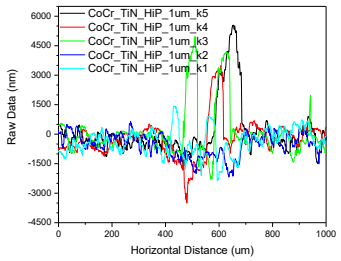	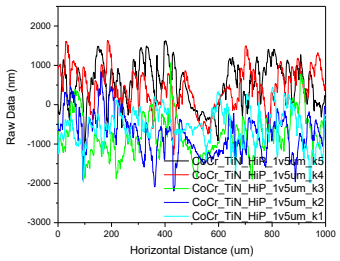
TiN - HIP 0.5	TiN - HIP 1	TiN - HIP 1.5

Table 4: Wear traces profiles of the thin films deposited on M30NW steel substrate

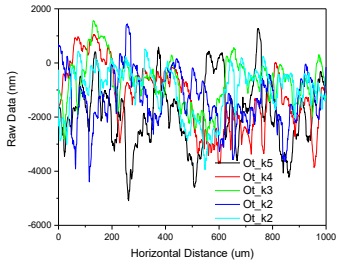		
M30NW steel		
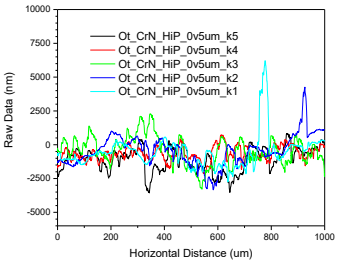	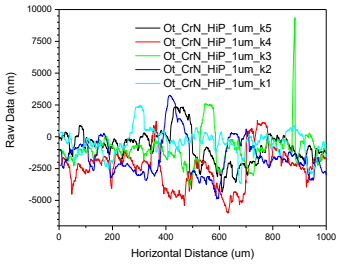	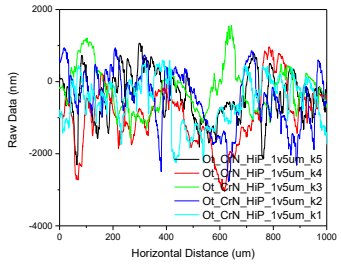
CrN - HIP 0.5	CrN - HIP 1	CrN - HIP 1.5
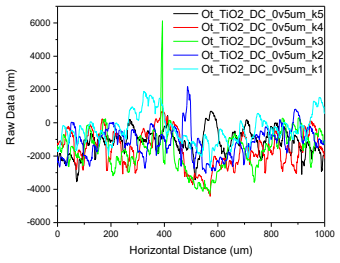	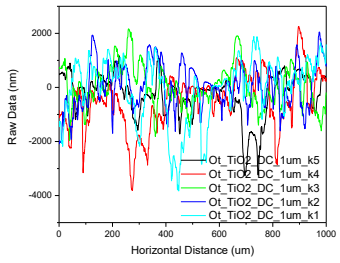	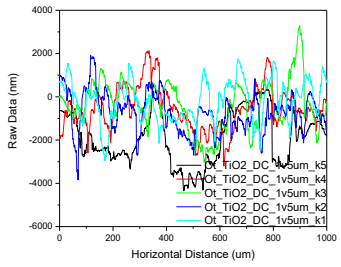
TiO_2 - DC 0.5	TiO_2 - DC 1	TiO_2 - DC 1.5
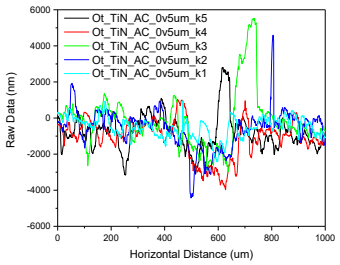	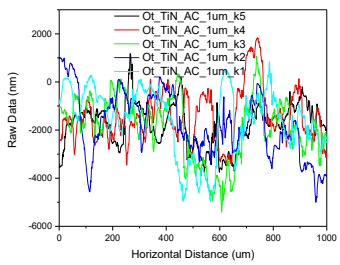	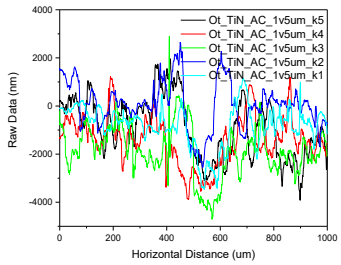
TiN - AC 0.5	TiN - AC 1	TiN - AC 1.5

Among the curves obtained, those with smaller errors were selected (presented grouped in the graph) to calculate the average values of the friction coefficient μ and of the wear rate k.
The friction coefficient and the wear rate of the deposited thin layers were analysed from the influence of the layer thickness and the deposition method point of view.

Friction coefficient μ – the influence of the thin films' thickness. The friction coefficient of the TiN layers deposited on the two types of substrates (Fig. 4) had a small variation, oscillating with the increase of the layer thickness (between 0.5 and 1.5 μm), having values between 0.132 and 0.649. The TiN layer with a thickness of 0.5 μm, deposited on the CoCr substrate by cathodic arc, has a maximum value of the friction coefficient. As the thickness of this layer increases, the value of the friction coefficient decreases. Increasing the layer's thickness from 1 μm to 1.5 μm also leads to a decrease of the friction coefficient when DC sputtering deposition method is used. However, the friction coefficient increases with the increase of the thickness, when the HiP sputtering method is used.
Regarding the friction coefficient of this layer when it is deposited on the M30NW steel substrate, although its values fall within a smaller range (0.504 and 0.593), there is a much more oscillating variation for the layers deposited by all the three methods. The TiN layer deposited by DC sputtering is the only one that shows a decrease of friction coefficient as the thickness increases. In the case of the other two layers, an increase of friction coefficient is observed as the layer thickness increases. If a uniform variation is taken into account, the increase of the friction coefficient also occurs proportionally to the increase of the thickness.

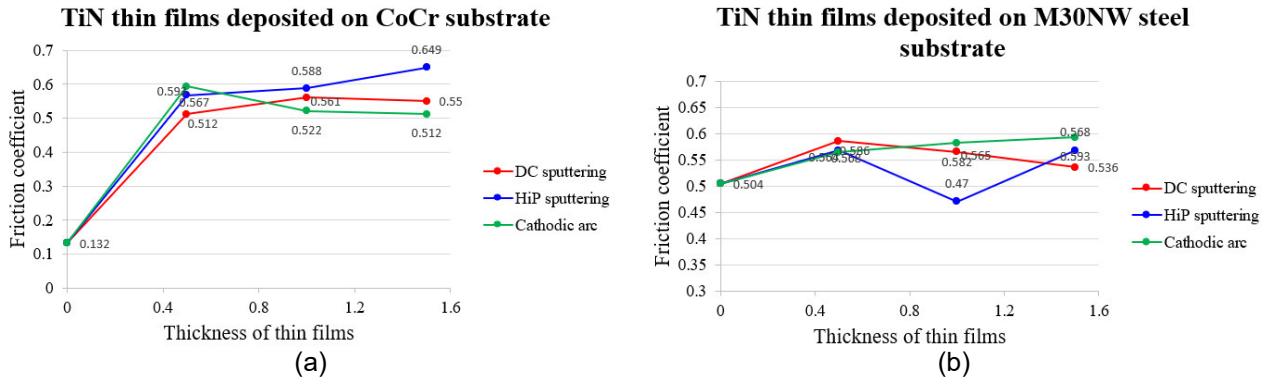

Fig. 4. Variation of the friction coefficient depending on the thickness of the TiN thin films deposited on CoCr substrate (a) and M30NW steel substrate (b)

The friction coefficient of the TiO_2 layers deposited on the CoCr substrate (Fig. 5) had a uniform increase with the increase of the layer thickness (between 0.5 and 1 μm) and a decrease with the increase of the layer thickness up to 1.5 μm.
In the case of TiO_2 layers deposited on M30NW steel substrate, it was observed that as the layer thickness increases from 0.5 μm to 1.5 μm, there is a decrease in the friction coefficient of the layers deposited using the cathodic arc and DC sputtering methods. The decrease in the value of the friction coefficient occurs with the increase of the layer thickness from 1 μm to 1.5 μm when using the HiP sputtering method.

The friction coefficient of CrN layers deposited on both types of substrates (Fig. 6) had different variations with the increase of the thickness in both cases. Thus, increasing the thickness of the CrN layer deposited on the CoCr substrate led to a decrease of friction coefficient when both deposition methods were used. In the case of the layer deposited on M30NW steel, friction coefficient decreases as the layer thickness increases when the DC sputtering method is used. The value of the friction coefficient increases for the layer deposited by HiP sputtering once the layer thickness increases up to 1.5 μm.

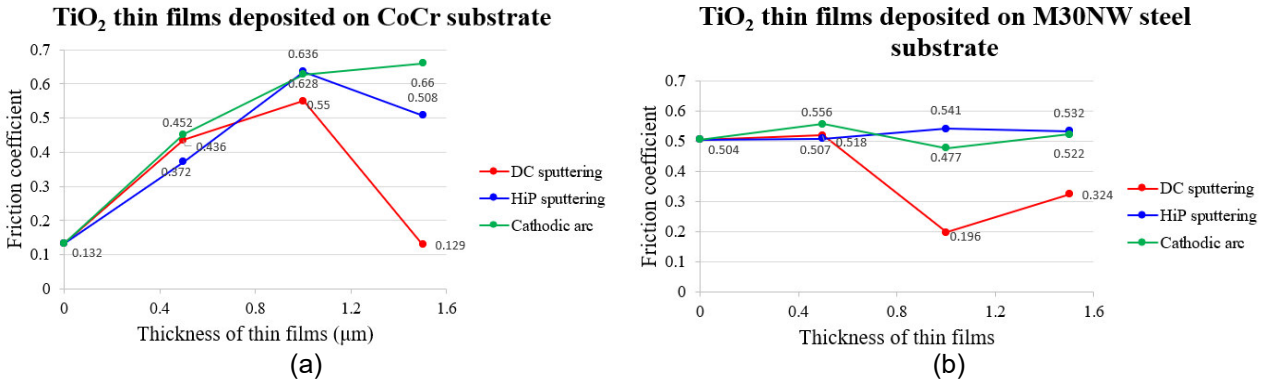

Fig. 5. Variation of the friction coefficient depending on the thickness of the TiO_2 thin films deposited on CoCr substrate (a) and M30NW steel substrate (b).

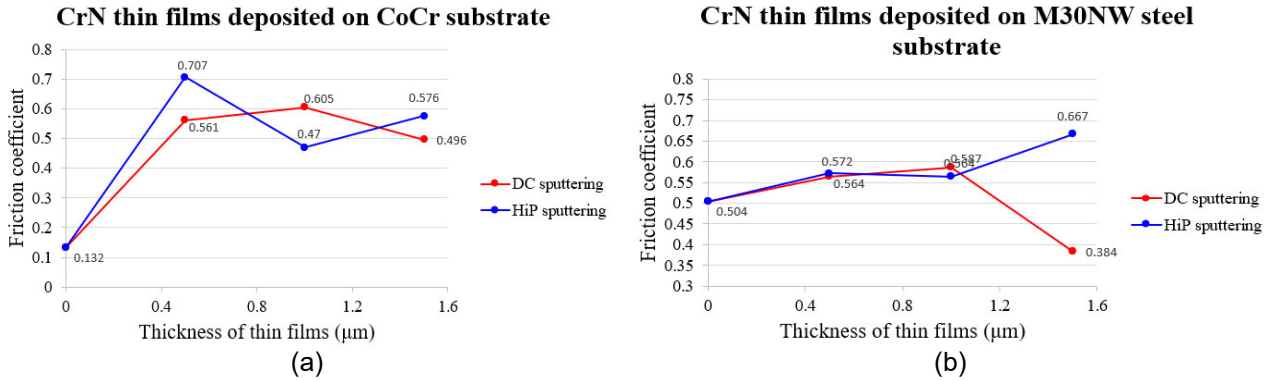

Fig. 6. Variation of the friction coefficient depending on the thickness of the CrN thin films deposited on CoCr substrate (a) and M30NW steel substrate (b).

Wear rate k – the influence of the thin films' thickness. The wear rate of the deposited TiN layers (Fig. 7) had an uneven variation as the thickness increased (between 0.5 and 1.5 µm) for both types of substrates, the values being between $207*10^{-6}m^3N^{-1}m^{-1}$ and $3510*10^{-6}m^3N^{-1}m^{-1}$. The 1 µm thick TiN layer, deposited on the CoCr substrate by DC sputtering, has a maximum wear rate value. Once the thickness of this layer increases to 1.5 µm, the value of the wear rate decreases, being an important result in the use of this material, demonstrating the increased resistance to wear. The wear rate of the TiN layers deposited by the other two methods had an oscillatory increase depending on the layer thickness.

The TiN layers deposited on the M30NW steel substrate using all 3 deposition methods showed a wear rate with a completely uneven variation once the thickness increased from 0.5 to 1.5 µm. The TiN layer with a thickness of 1 µm, deposited on M30NW steel substrate by cathodic arc, has a maximum value of the wear rate. Once the layer thickness increases from 1 µm to 1.5 µm, the value of the wear rate decreases when the cathodic arc and HiP sputtering methods were used. Taking into account a uniform average variation, there is a decrease of the wear rate proportional to the increase of the layers thickness between 0.5 and 1.5 µm, when using the cathodic arc method and the HiP sputtering method. In the case of the layer deposited by DC sputtering, the decrease of the wear rate occurs only up to a layer thickness of 1 µm, the 0.5 µm thicker layer showing an increase of the wear rate value.

The wear rate of the TiO_2 layers deposited on CoCr and M30NW steel substrates (Fig. 8) also had an uneven variation with the increase of thickness (between 0.5 and 1.5 µm) for all the three methods

used, the values being between 62*10^{-6}m^{3}N^{-1}m^{-1} and 3510*10^{-6}m^{3}N^{-1}m^{-1}. The 0.5 μm thick TiO_2 layer, deposited on the CoCr substrate by DC sputtering, has a maximum wear rate value.

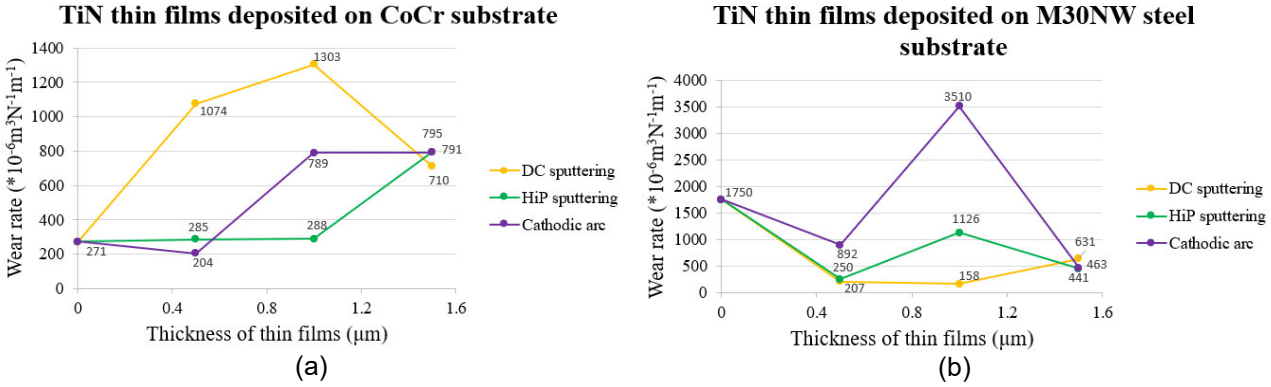

Fig. 7. Variation of the wear rate depending on the thickness of the TiN thin film deposited on CoCr substrate (a) and M30NW steel substrate (b).

Once the layer thickness increases from 0.5 μm to 1.5 μm, the wear rate value decreases when the DC sputtering and HiP sputtering methods were used. The TiO_2 layer deposited on the CoCr substrate by cathodic arc has an increase of the wear rate with the increase of the layer thickness between 0.5 and 1 μm, followed by a decrease with the increase of the thickness up to 1.5 μm. Taking into account a uniform average variation, there is an increase of the wear rate proportional to the increase of the layers thickness, when the cathodic arc method is used.
The wear rate of the TiO_2 layers deposited on the M30NW steel substrate also had an uneven variation with the increase in thickness (between 0.5 and 1.5 μm) for all three methods used. The TiO_2 layer with a thickness of 1 μm, deposited on M30NW steel substrate by cathodic arc, has a maximum wear rate value. Once the layer thickness increases from 1 μm to 1.5 μm, the value of the wear rate decreases when the cathodic arc and HiP sputtering methods were used. The TiO_2 layer deposited on the M30NW steel substrate by DC sputtering shows a decrease in the wear rate as the layer thickness increases between 0.5 and 1 μm, followed by an increase as the layer thickness increases up to 1.5 μm. Taking into account a uniform average variation, all three deposited layers show a decrease in the wear rate proportional to the increase of the deposited layers thickness. These results show that the TiO_2 layers deposited on the M30NW steel substrate present an increase of the wear resistance as their thickness increases.

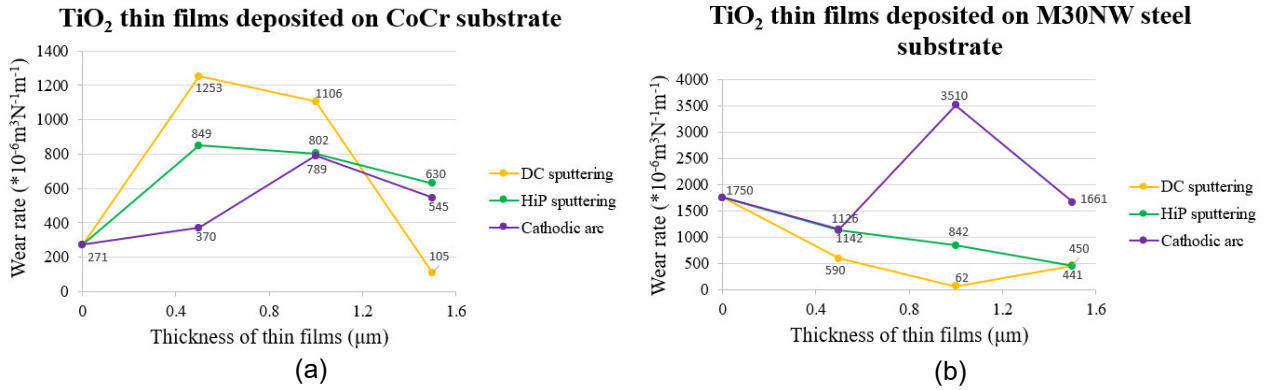

Fig. 8. Variation of the wear rate depending on the thickness of the TiO_2 thin film deposited on CoCr substrate (a) and M30NW steel substrate (b).

The wear rate of the CrN layers deposited on the two types of substrates (Fig. 9) had uneven variations, the values being between 119*10^{-6}m^{3}N^{-1}m^{-1} and 1750*10^{-6}m^{3}N^{-1}m^{-1}, depending on the

thickness. On the CoCr substrate, the wear rate had an uneven variation once the thickness increased (between 0.5 and 1.5 μm), the CrN layer with a thickness of 1 μm, deposited on the substrate by DC sputtering, having the maximum value of the wear rate. The wear rate of this layer shows an increase with the increase of the layer thickness up to 1 μm, followed by a decrease with the increase of the layer thickness up to 1.5 μm. The value of the wear rate of the CrN layer deposited by HiP sputtering has an oscillatory variation with the increase of the layer thickness between 0.5 and 1.5 μm. Taking into account a uniform average variation, the layer deposited by HiP sputtering has an increase in the value of the wear rate.
The wear rate value of the CrN layers deposited on the M30NW steel substrate decreases proportionally with the increase in thickness (between 0.5 and 1.5 μm) for the two methods used. These results show that the CrN layers deposited on the M30NW steel substrate show an increase in wear resistance as their thickness increases.

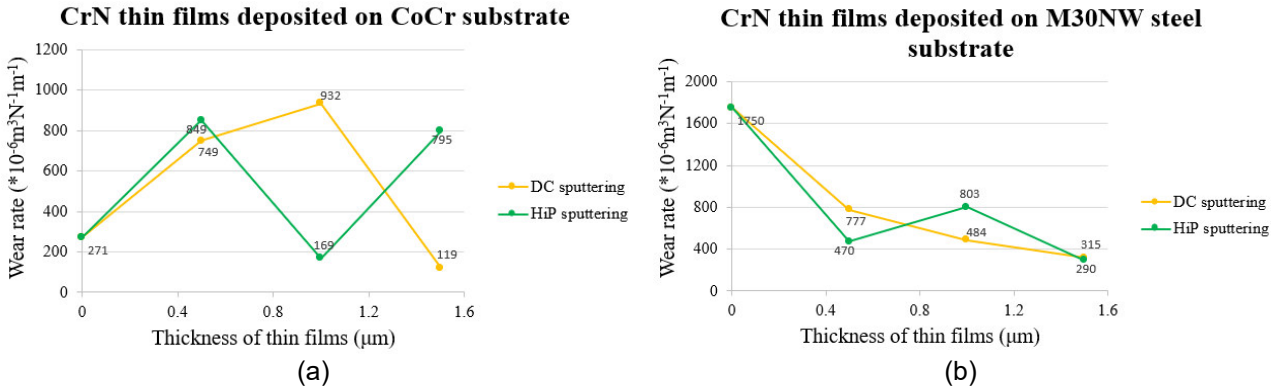

Fig. 9. Variation of the wear rate depending on the thickness of the CrN thin film deposited on CoCr substrate (a) and M30NW steel substrate (b)

For a comparative analysis of the obtained results and to determine the layers with the best tribological characteristics, the lowest values of the friction coefficient and of the wear rate were selected for each layer deposited on the two types of substrates used. (Table 5, Table 6)

Table 5: Comparative analysis of the parameters of the TiN, TiO_2 and CrN layers deposited on the CoCr substrate obtained after tribological tests. (The minimum values of the friction coefficient and of the wear rate. The comparison according to the material is marked with red, and the one according to the method is marked with blue).

Material	Layer thickness	Deposition method					
		DC sputtering		HiP sputtering		Cathodic arc	
		Friction coefficient	Wear rate	Friction coefficient	Wear rate	Friction coefficient	Wear rate
TiN	500 nm	0.512	1074	0.567	285	0.593	204
	1 μm	0.561	1303	0.588	288	0.522	789
	1.5 μm	0.550	710	0.649	795	0.512/met	791
TiO_2	500 nm	0.436	1253	0.372/met	40/849	0.452	370
	1 μm	0.550	1106	0.636	802	0.628	496/ 789
	1.5 μm	0.512/0.129	105/met	0.508	173/630	0.660	392/ 545
CrN	500 nm	0.561	127/749	0.707	849		
	1 μm	0.605	932	0.470	150/169		
	1.5 μm	0.496	119	0.576	795		

Table 6: Comparative analysis of the parameters of the TiN, TiO_2 and CrN layers deposited on the M30NW steel substrate obtained after tribological tests. (The minimum values of the friction coefficient and of the wear rate. The comparison according to the material is marked with red, and the one according to the method is marked with blue).

Material	Layer thickness	Deposition method					
		DC sputtering		HiP sputtering		Cathodic arc	
		Friction coefficient	Wear rate	Friction coefficient	Wear rate	Friction coefficient	Wear rate
TiN	500 nm	0.586	207	0.568	250	0.564	892
	1 µm	0.565	158	0.47/met	1126	0.582	3510
	1.5 µm	0.536	631	0.568	463	0.593	441
TiO_2	500 nm	0.518	590	0.507	112/772	0.556	627/1142
	1 µm	0.196/met	62	0.541	305/1126	0.477	952/3510
	1.5 µm	0.324	450	0.532	842	0.522	1161
CrN	500 nm	0.564	779	0.572	470		
	1 µm	0.587	484	0.564	803		
	1.5 µm	0.384	290/315	0.667	222/290		

Following the analysis of these values and comparisons, the following results were obtained.

TiN deposited on CoCr substrate

- The layer with the lowest friction coefficient is the one with a thickness of 1.5 µm deposited by cathodic arc, respectively the layer of 0.5 µm deposited by DC sputtering;
- The layer with the lowest wear rate is the one with a thickness of 1.5 µm deposited by DC sputtering.

From a tribological point of view, the TiN layer with a thickness of 1.5 µm deposited on a CoCr substrate by the cathodic arc method has superior properties.

TiO_2 deposited on CoCr substrate

- The layer with the lowest friction coefficient is the one with a thickness of 1.5 µm deposited by DC sputtering;
- The layer with the lowest wear rate is the one with a thickness of 1.5 µm deposited by DC sputtering.

From a tribological point of view, the TiO_2 layer with a thickness of 1.5 µm deposited on a CoCr substrate by the DC sputtering method has superior properties.

CrN deposited on CoCr substrate

- The layer with the lowest friction coefficient is the one with a thickness of 1 µm deposited by HiP sputtering, respectively 1.5 µm deposited by DC sputtering;
- The layer with the lowest wear rate is the one with a thickness of 1.5 µm deposited by DC sputtering.

From a tribological point of view, CrN layers with a thickness of 1 µm deposited by HiP sputtering, respectively 1.5 µm deposited by DC sputtering on a CoCr substrate have superior properties.

Considering these results, the main conclusion is that on the CoCr substrate, the TiN layer with a thickness of 1.5 µm deposited by the cathodic arc method, TiO_2 layer and CrN layer, both with a thickness of 1.5 µm deposited by DC sputtering method, have superior properties and are useful for continuing studies on real systems.

TiN deposited on M30NW steel substrate

- The layer with the lowest friction coefficient is the one with a thickness of 1.5 µm deposited by HiP sputtering;
- The layer with the lowest wear rate is the one with a thickness of 1.5 µm deposited by DC sputtering.

From a tribological point of view, the TiN layer with a thickness of 1.5 µm deposited on M30NW steel substrate by HiP sputtering, respectively DC sputtering has superior properties.

TiO_2 deposited on M30NW steel substrate

- The layer with the lowest friction coefficient is the one with a thickness of 1.5 µm deposited by DC sputtering;

- The layer with the lowest wear rate is the one with a thickness of 1.5 μm deposited by DC sputtering.
From a tribological point of view, the TiO_2 layer with a thickness of 1.5 μm deposited on M30NW steel substrate by the DC sputtering method has superior properties.

CrN deposited on M30NW steel substrate

- The layer with the lowest friction coefficient is the one with a thickness of 1.5 μm deposited by DC sputtering;
- The layer with the lowest wear rate is the one with a thickness of 1.5 μm deposited by DC sputtering, respectively the layer with a thickness of 1.5 μm deposited by HiP sputtering.

From a tribological point of view, CrN layers with a thickness of 1.5 μm deposited by DC sputtering, respectively HiP sputtering on M30NW steel substrate have superior properties.
Considering these results, the main conclusion is that on the M30NW steel substrate, the TiN layer, TiO_2 layer and CrN layer with a thickness of 1.5 μm deposited by DC sputtering method, have superior properties and are useful for continuing studies on real systems.

4. Conclusions

The tribological characterization of tree types of thin films deposited on two types of biocompatible substrates were realized in order to determine and analyse important parameters, like friction coefficient and wear rate. In this way it was possible to determine which is the most resistant substrate material – deposited material couple.
The 1.5 μm thick TiN layer − deposited on the CoCr and M30NW steel substrates – has displayed superior tribological parameters when using the cathodic arc deposition method. The superior quality of the TiO_2 layer deposited by DC sputtering on both types of substrates was demonstrated by the analyses performed. The 1.5 μm thick CrN layer exhibited superior tribological characteristics when deposited on both substrate types using DC sputtering.
The main conclusion of the study was that thin layers of TiN, TiO_2, and CrN, with a thickness of 1,5 μm, deposited on CoCr and M30NW substrates, had superior tribological characteristics. This means that a thicker layer will be more sustainable and can be used to improve the quality of biomedical components, like hip prostheses.

Acknowledgments

This work was supported by the Ministry of Research, Innovation and Digitization, through the PN19240401-17N/2019 research grant.
The authors would like to present their sincere gratitude to the SC MGM Star Construct SRL for layers deposition and gratefully acknowledge to the employees of Research Center for Advanced Surface Processing and Analysis by Vacuum Technologies from National Institute of Research and Development for Optoelectronics - INOE 2000, who have done the nanoindentation and tribological tests.
Also, the authors would like to thank Dr. Eng. Dorin Angelescu for his collaboration in the realization of CoCr substrate disks in the Research Center for Intelligent Mechatronic Systems used for Securing Objectives and Intervention – CERMISO of INCDMTM

References

[1] Javaid, Mohd, Suresh Babu, Shanay Rab, Raju Vaishya, and Abid Haleem. “Tribological Review of Medical Implants Manufactured by Additive Manufacturing.” In: Katiyar, Jitendra Kumar, Mir Irfan Ul Haq, Ankush Raina, S. Jayalakshmi, and R. Arvind Singh (eds.). *Tribology and Sustainability*. 1st Edition. Boca Raton, CRC Press, 2021.
[2] Bloch, Benjamin V., Jonathan J.E. White, Hosam E. Matar, Reshid Berber, and Andrew R.J. Manktelow. “Should Patient Age Thresholds Dictate Fixation Strategy in Total Hip Arthroplasty?” *The Bone & Joint Journal* 104-B (February 2022): 206–211.
[3] Shen, Gang, Jufan Zhang, Chengwei Kang, and Fengzhou Fang. "Study on surface texture patterns for improving tribological performance of bioimplants.” *Surface and Coatings Technology* 422 (September 2021): 127567.

[4] Rahmouni, Khaoula, Aurélien Besnard, Kafia Oulmi, Corinne Nouveau, Aissam Hidoussi, Linda Aissani, and Mourad Zaabat. “In vitro corrosion response of CoCrMo and Ti-6Al-4V orthopedic implants with Zr columnar thin films.” *Surface and Coatings Technology* 436 (April 2022): 128310.
[5] Montazerian, Maziar, Fatemeh Hosseinzadeh, Carla Migneco, Marcus V.L. Fook, and Francesco Baino. “Bioceramic coatings on metallic implants: An overview.” *Ceramics International* 48, no. 7 (April 2022): 8987-9005.
[6] Skjöldebrand, Charlotte, Joanne L.Tipper, Peter Hatto, Michael Bryant, Richard M.Hall, and Cecilia Persson. “Current status and future potential of wear-resistant coatings and articulating surfaces for hip and knee implants.” *Materials Today Bio* 15 (June 2022): 100270.
[7] Rothammer, Benedict, Max Marian, Kevin Neusser, Marcel Bartz, Thomas Böhm, Sebastian Krauß, Stefan Schroeder, Maximilian Uhler, Simon Thiele, Benoit Merle, Jan Philippe Kretzer, and Sandro Wartzack. “Amorphous Carbon Coatings for Total Knee Replacements—Part II: Tribological Behavior.” *Polymers* 13, no. 11 (June 2021): 1880.
[8] Rafieerad, Alireza, A.R. Ashra, Reza Mahmoodian, and Abdul Razak Bushroa. “Surface characterization and corrosion behavior of calcium phosphate-base composite layer on titanium and its alloys via plasma electrolytic oxidation: a review paper.” *Materials Science and Engineering C* 57 (December 2015): 397–413.
[9] Ching, Hee Ay, Dipankar Choudhury, Md Julker Nine, and Noor Azuan Abu Osman. “Effects of surface coating on reducing friction and wear of orthopaedic implants.” *Science and Technology of Advanced Materials* 15 (February 2014): 014402.
[10] Hunt, John Alan, Jill T. Callaghan, Chris J. Sutcliffe, Rhys H. Morgan, Ben Halford, and Richard A. Black. “The design and production of Co-Cr alloy implants with controlled surface topography by CAD-CAM method and their effects on osseointegration.” *Biomaterials* 26 (October 2005): 5890-5897.
[11] Guezmil, Manel, Walid Bensalah, and Salah Mezlini. “Effect of bio-lubrication on the tribological behavior of UHMWPE against M30NW stainless steel.” *Tribology International* 94 (February 2016): 550-559.
[12] Badita, Liliana-Laura, Aurel Zapciu, Catalin Vitelaru, Anca Constantina Parau, Lidia Ruxandra Constantin, Arcadie Sobetkii, and Iulian Sorin Munteanu. “Influence of the deposition method on the hardness and elastic modulus of biocompatible thin layers deposited on metallic substrates.” In: Cioboata, Doina Daniela (ed.). *Lecture Notes in Networks and Systems. International Conference on Reliable Systems Engineering ICoRSE 2022* 534 (2022): 338-357.
[13] Anders, Andre. “A review comparing cathodic arcs and high-power impulse magnetron sputtering (HiPIMS).” *Surface and Coatings Technology* 257 (October 2014): 308-325.
[14] Wasa, Kiyotaka, Isaku Kanno, and Hidetoshi Kotera. *Handbook of sputter deposition technology: Fundamentals and Applications for Functional Thin Films, Nano-Materials and MEMS*. Elsevier Inc., 2012.
[15] Ehiasarian, Arutiun. “High-power impulse magnetron sputtering and its applications.” *Pure Applied Chemistry* 82, no. 6 (April 2010): 1247–1258.

ISSN 1454 - 8003
Proceedings of 2022 International Conference on Hydraulics and Pneumatics - HERVEX
November 9-10, Băile Govora, Romania

ANALYSIS OF DYNAMIC REGIME OF A HEAVY MACHINE FOR SUPPLEMENTARY POWER CONSUMPTION EVALUATION

Carmen Nicoleta DEBELEAC[1]

[1]"Dunarea de Jos" University of Galati, Engineering and Agronomy Faculty in Braila,

Research Center for Mechanics of Machines and Technological Equipments, carmen.debeleac@ugal.ro

Abstract: *In this paper the author proposed some indicators for performance evaluation in dynamic steady of working time in the case of heavy machines. Thus, it was monitored the hydraulic parameters of a wheel loader knowing it's as a machine with an intense and varied working regime characterized by over-pressurization occurred because of excessive loads that appear when execution different tasks during technological cycle on construction site. Based on hydraulic parameters, it were evaluated engine power required for loading phase and, taking into account by the performance indicators, the supplementary power needed for task execution.*

Keywords: *Loader, hydraulic system, power, performance, indicators*

1. Introduction

In the last years, a large number of performance indicators has been introduced to measure the quality of products from different fields of industry. In particular, in this paper, about quality evaluation of construction machines are addressed. A method has been proposed to use an algorithm for operational performance evaluation of wheel loader. In the first step, we need to identify which parameter is being analyzed to define level of machine performance. Literature references indicate the state of knowledge about this aspect and some case studies are developed around the analysis of following parameters: energy consumption, power needed, pressure into the hydraulic circuit, engine torque or resistant forces developed at working tool etc. The novelty of the study presented in this paper consists in developing the set of indicators in order to measure the performance as dynamically state condition from a wheel loader.

2. Power monitoring

The engine power of a wheel loader is generally diverted to the transmission system, the hydraulic system, and accessories. The hydraulic power and the drivetrain power are the two largest power consumers in the wheel loader, because both systems act together when the machine work into the pile. According to engineering experience [1], we have reduced the auxiliary power being around 10% from total engine power. The way the power is distributed between hydraulics and drivetrain depends on how much power is requested from the different systems. Working phases involve the complex interaction of the loader power train, hydraulics, implement linkage, and steering system. Machine behavior is a function of these systems and their interactions and how the operator uses them. It is difficult to determine how a change in an individual system can affect the overall machine performance [2]. These interactions are highly nonlinear and dynamic, making them difficult to understand completely. The hydraulic drives have many factors that affect the power losses and for performance improvement the modern wheel loaders use load sense hydraulics instead of the open-center hydraulic system. In addition, for hydraulic-driven machines (loaders lifting trucks etc.), operating in a cyclic manner the energy consumption can be considerably reduced, by using accumulators as energy storage devices. Thus, it possible to balance forces in lifting system and to be used for regenerative braking of loads. Combined with a secondary controlled unit, the energy transformation can be performed with low losses [3]. However, high-amplitude oscillations are found in the acquired pressure signals due to the dynamic behavior of the machine, especially during the phase of loading the bucket or moving towards unloading in the truck [4,5]. A more detailed

knowledge of these aspects is opportune and creates the prerequisites for the introduction of a new criterion for evaluating the performance of a construction machine [5, 6]. The identification of all phases of the working cycle of loader is needed to know the particularities of each of them, as variation of the load intensity. With the information of all the phases in the cycle, an adequate energy management can be optimized not only for one phase, but even over one cycle [7]. Thus, the following phases can be distinguished [8]: bucket filling, leaving bank, retardation, reversing, towards lead receiver, bucket emptying, leaving load receiver, retardation and reversing, towards bank and retardation at bank. However, in order to minimize the execution time of the loading and transport works, the short work cycle with the loader (in V-type) is recommended (it contains fewer working phases). Next, the case study it was developed on the LDH loader (45 CP) with hydraulic scheme given in the Figure 1. Details about experimental tests, setup used, acquisition and processing aspects were the subject of a previously published paper [9-11]. By using a high pass filtering of the load pressure and flow measured signals (Fig. 2), the effective power can be evaluated as global parameter that are included both excitation sources generated by the internal (depending on the type of hydraulic circuit and apparatus used, commands for execution tasks, the control of functional parameters etc.) and external perturbations (as response to the resistant forces developed when the bucket penetrates the pile), all induced into driven system of loader.

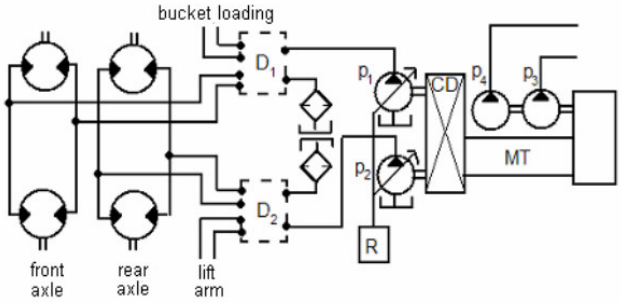

Fig. 1. Hydraulic wheel loader system circuit (MMT 45, Romania)

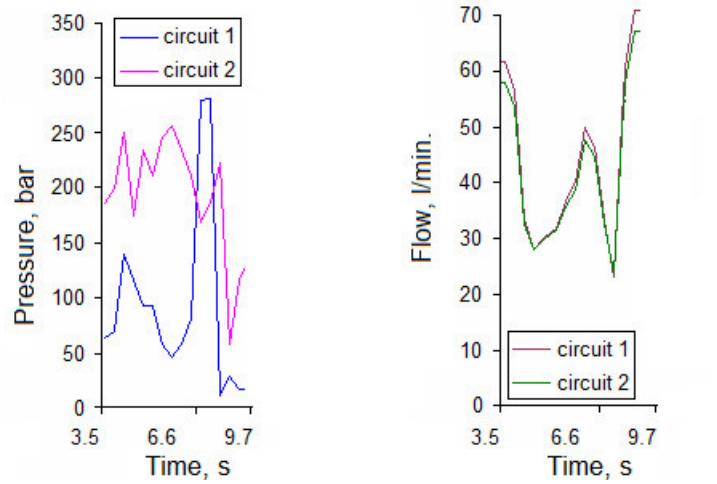

Fig. 2. Pressures and flows monitoring over the typical working cycle of loader (material: non-cohesive soil)

The hydraulic system power shows the various change in working cycle of loader and can be calculated as

$$P = \frac{\Delta p \cdot Q}{60 \cdot \eta} \tag{1}$$

where Δp is the differential pressure between the inlet and outlet pressures, Q is the volume flow rate, and η is the overall efficiency. After evaluating the total power (as the sum of the powers of both circuits), its average value is determined for each phase of the work cycle. The results obtained in

two cases of working (pile constituted from non-cohesive soil and, respectively, cohesive soil), only for loading bucket phase (noted as Phase 2) are shown in the Figure 3.

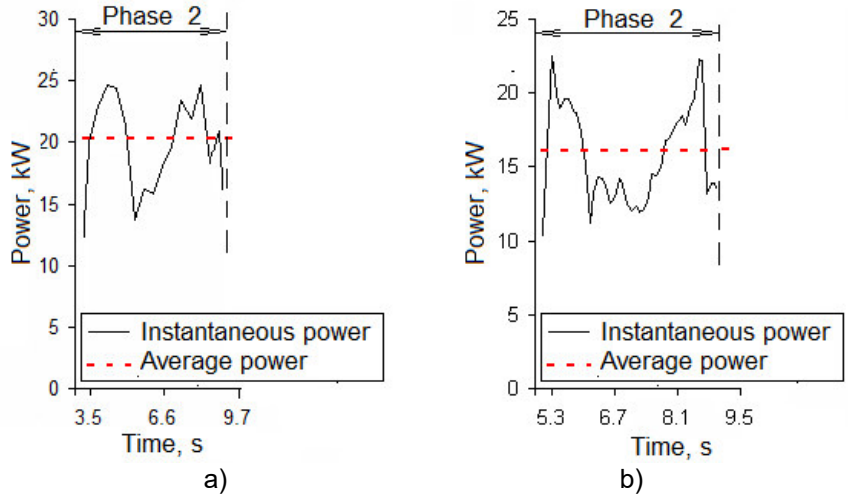

Fig. 3. Selecting and processing of the power signal from loading bucket phase, in two working cases: a) non-cohesive soil (wet sand); b) cohesive soil.

As consequence of the interactions between hydrostatic system, working equipment action, type of the displacement mechanism (on wheels) and irregular road on the construction site (in poor condition frequently) the power consumption have variations [12]. Based on these signals (represented in fig. 3), the working performance of the loader will be identified, for two different working environments, in order to supplementary power consumption evaluation (P).

3. Statistical signals processing

The statistical processing of the experimental data includes histograms, probability diagrams, and general statistics of data. Together, they provide means for analysis of the monitored data, especially for checking whether the data is normally distributed, because the control charts theory assumes normal probability distribution (Fig. 4). Control limits of the measured data can be calculated from sample points, but for improvement of processing quality, it is recommended to analyze the distribution of the average value compared to the individual values of the samples (Fig. 5).

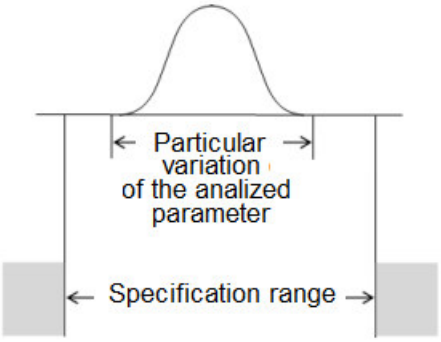

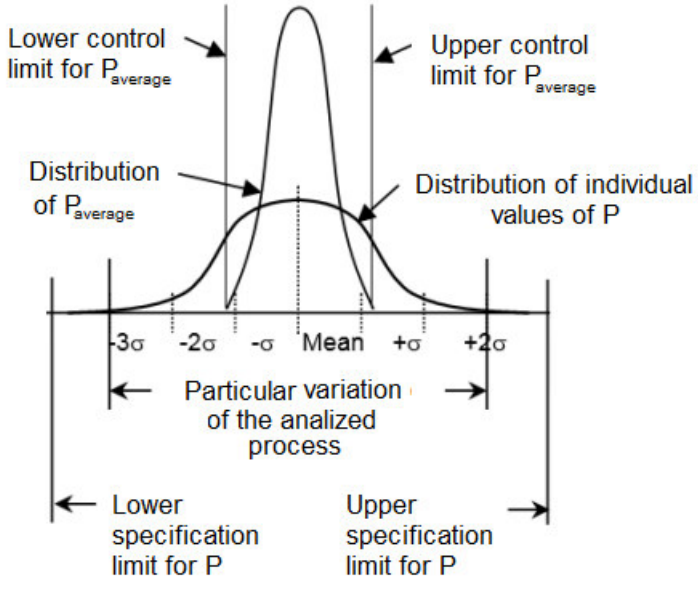

Fig. 4. Normal distribution of the samples points

Fig. 5. Comparative distribution limits of the sample points

These aspects will be taken into account when developing the data processing quality control algorithm, in the future work. At this stage, only the verification of the applicability of the proposed method will be demonstrated. For a basic evaluation, general statistics of the monitored parameters (pressure and flow) were carried out with the following operators: random variable (P_i), mean value ($\bar{P}$), root-mean-square (*RMS*), standard deviation (σ) and variance (σ^2). Based on these statistical operators, the following hypotheses can be stated necessary to formulate additional performance criteria in intense dynamic regime of a fast-speed loader, thus:

- random variable of power (P_i) differs from a working cycle to another. This operator quantifies stationary values of each phase;
- average value of power *($\bar{P}$)* leads to the highlighting of instantaneous dynamic stresses at the change from one phase to another. By evaluating of this statistical operator, the real power of the machine is quantified;
- root-mean-square of power *(RMS)* is used to quantify the overall energy content of the signal;
- standard deviation of power (σ), on the individual working phase, puts into evidence the transitory behaviour of each of them, and it quantifies the static power of the machine;
- variance of power (σ^2) it measures the degree of dispersion of the instantaneous power data around the power sample's mean. It is used to compare the relative performance of each working phase with imposed performance to achieve the best power consumption allocation.

4. Indicators for dynamic global performance

Based on a set of four indicators defined in the Table 1, the global (dynamic) performance of the charger is evaluated.

Table 1: Defining of indicators

Indicator name	Formula
Indicator for static power evaluation	$i_1 = \frac{P_s}{P_{max}}$
Indicator for dynamic power evaluation	$i_2 = \frac{P_d}{P_{max}}$
Indicator for real (effective) power evaluation	$i_3 = \frac{P_r}{P_{max}}$
Indicator for intensity of the dynamic power state	$i_4 = \frac{P_r}{P_s}$

It was introduced the next denotes with the following significations: P_s - power in steady regime and it is estimated by the statistical average of the instantaneous values purchased during the respective phase; P_d - additional power necessary for the transitory regime of the machine; P_r - the real needed power in to real loader conditions; P_{max} - maxim engine power.
The results of processing power data are centralized in the Table 2, for bucket loading phase and for two different material categories.

Table 2: Processing power data

Phase	Material	Operators	Power, kW
Loading bucket	Non-cohesive soil (wet sand)	RMS	36,631
		Standard deviation	9,041
		Mean	35,498
		Variance	81,746
	Cohesive soil	RMS	32,358
		Standard deviation	5,691
		Mean	31,853
		Variance	32,393

For example, Figures 6 and 7 show the four indicators (i_i, i = 1…4) for identifying the dynamic performance of a loader, in the bucket loading phase.

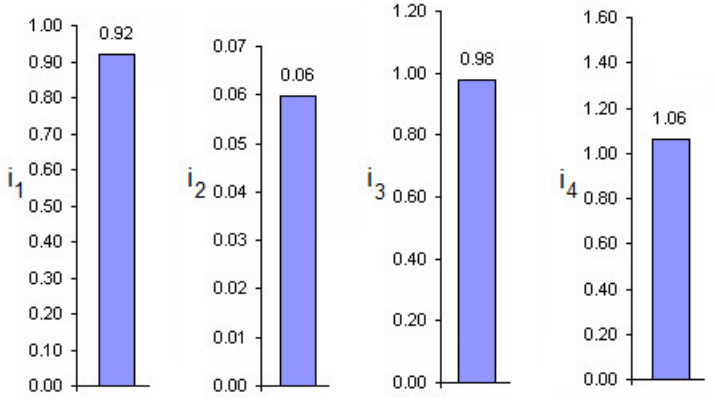

Fig. 6. Indicators values for global performance of dynamic working regime in the loading bucket phase (material: non-cohesive soil, wet sand)

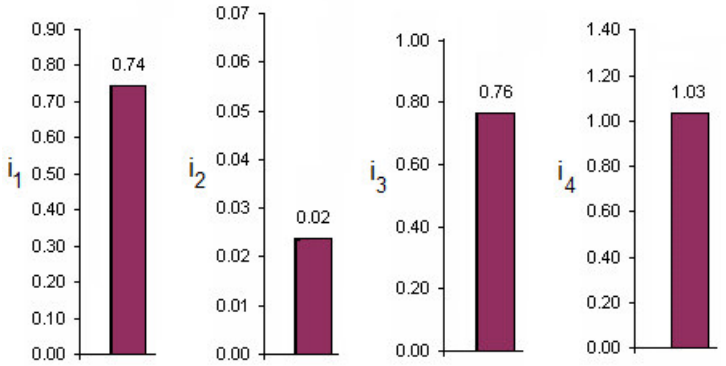

Fig. 7. Indicators values for global performance of dynamic working regime in the loading bucket phase (material: cohesive soil)

In demanding working conditions, comparing the performances of two different types of construction machines can be done by evaluating the i_4 indicator. Thus, in this case study, the difference caused by the type of material loaded in the bucket is noted, which is found in a percentage of 6% compared to 3% in the dynamic behavior of the loader's driven system and, implicitly, in the supplementary engine power consumption. Therefore, variance values indicate a significant difference of intensity of the bucket loading phase: 81,746 (non-cohesive soil) in respect with 32,393 (cohesive soil).

5. Conclusions

The topic of this work is part of the current trend of global identification of the performance of a machine, in general mode (by monitoring one or more reference parameters) and by specialization by types of machines (by elaborating valid reference standards for construction machines that have an intense and varied dynamic working regime).
In the study presented in the paper, the following conclusions were highlighted:
- static indicator (i_1) shows the percentage of the machine's power required for operation in stable working mode;
- dynamic indicator (i_2) quantifies the additional power required in transient regimes or with intense dynamics. Knowing the values of this indicator is of major importance in evaluating the additional power, being closely related to the size of the dynamic loads from the working phases of the technological process with fast chargers;
- real indicator (i_3) provides qualitative and quantitative information about the power reserve and its efficient use by the machine;

- indicator (i_4) characterizes the intensity of the dynamic state and, implicit, of the supplementary consumption of engine power as response of overloads into mechanic and hydraulic systems (sometimes also due to the operator's lack of experience).

Thus, the set of indicators described above can constitute a new reference criterion in the evaluation of the additional power consumed in the work phases of the construction machinery characterized by regimes with intense dynamics, with a view to an individual but also global characterization of the work performance.

References

[1] Ma, Wenxing, Yubo Zhang, Chunbao Liu, and Songlin Wang. "Prediction Method of the Fuel Consumption of Wheel Loaders in the V-Type Loading Cycle." *Mathematical Problems in Engineering* (2015): Article ID 538176.

[2] Järviluoma, M. "Driving situation identification based on vibration measurement in heavy work machines." VTT Technical Research Centre of Finland, Research report, VTT – R – 05388 - 06, 2006.

[3] Rydberg, Karl-Erik. "Design of Energy Efficient Hydraulic Systems - System Concepts and Control Aspects." Proc. of the 5th International Symposium on Fluid Power Transmission and Control, Beidaihe, China, June 6-8, 2007.

[4] Liu, Xiaojun, Dongye Sun, Datong Qin, and Junlong Liu. "Achievement of Fuel Savings in Wheel Loader by Applying Hydrodynamic Mechanical Power Split Transmissions." *Energies* 10, no. 9 (2017): Article ID 1267.

[5] Wang, F., M. Mohd Zulkefli, Z. Sun, and K. Stelson. "Energy management strategy for a power-split hydraulic hybrid wheel loader." *Part D: Journal of Automobile Engineering* 230, no. 8 (2016):1105–1120.

[6] Oh, K., H. Kim, K. Ko, P. Kim, and K. Yi. "Integrated wheel loader simulation model for improving performance and energy flow." *Automation in Construction* 58 (2015):129–143.

[7] Huang, J., D. Kong, G. Gao, X. Cheng, and J. Chen. "Data-Driven Reinforcement-Learning-Based Automatic Bucket-Filling for Wheel Loaders." *Applied Sciences* 11, no. 19 (2021):9191.

[8] Filla, R. "An Event-driven Operator Model for Dynamic simulation of Construction Machinery." The 9th Scandinavian International Conference of Fluid Power, Linköping, Sweden, 1-3 June, 2005.

[9] Debeleac C. "Vibratory diagnosis of the earthmoving machines for the additional necessary power level evaluation." Proc. of the 9th WSEAS International Conference on Acoustics & Music: Theory & Applications (AMTA '08), Bucharest, Romania, June 24-26, 2008, pp. 89-93.

[10] Debeleac, C. "Performances assessment from an earthmoving machine through power monitoring." *The Annals of "Dunarea de Jos" University of Galati, Fascicle XIV Mechanical Engineering* (2009):99-102.

[11] Debeleac, C. "Criteria to evaluation of the technological, functional and dynamic performances of the high-speed loaders." *Syntheses of Theoretical and Applied Mechanics* 10, no. 4 (2019):217-224.

[12] Axinti, A.S., S. Nastac, and G. Axinti. "First Order Virtual Prototype for Analysis of Complex Interactions between Hydrostatic Driving System, Wheel and Irregular Road at Construction Equipments." Proc. of the 18th International Conference on Hydraulics and Pneumatics HERVEX 2010, Calimanesti-Caciulata, Romania, November 10 – 12, 2010.

ISSN 1454 - 8003
Proceedings of 2022 International Conference on Hydraulics and Pneumatics - HERVEX
November 9-10, Băile Govora, Romania

DIGITAL HYDRAULICS CIRCUIT BASED ON PWM FUNCTION FOR CONTROLLING HYDRAULIC ACTUATOR POSITION

Ahmed Zubair JAN[1], Dr. hab. Eng. **Paweł ŚLIWIŃSKI[2],** Dr inz. **Krzysztof KEDZIA[1]**

[1] Department of Mechanical Engineering, Wroclaw University of Science and Technology, Wroclaw, Poland

[2] Department of Mechanical Engineering, Gdansk University of Technology, Gdansk, Poland

Abstract: *Hydraulic systems are used in many different industries, such as multi-source hydrostatic drive systems. In traditional hydraulic systems, a proportional servo valve is used to control the position of hydraulic actuators. The low energy efficiency and high cost of these control valves are two major problems with these systems. Digital hydraulics is one of the most unique ideas on how to solve these problems. Researchers like digital hydraulics because it is inexpensive, it saves energy, it is not sensitive to contamination, and it has low leakage. In this paper, a digital hydraulic circuit is suggested that uses a fast switching on/off valve instead of servo valves to control the position of a hydraulic actuator. Using a proper PWM duty cycle, the flow that passes through the fast-switching valve is controlled in this way. When the control valve is off, excess pump flow flows straight to the tank instead of going through the relief valve. Therefore, the waste of energy caused by the relief valve is greatly reduced. A robust sliding mode controller (SMC) is used to ensure position tracking even when there are uncertainties.*

Keywords: *SMC, Digital Hydraulics, PWM, Hydraulic Actuator Position*

1. Introduction

In this article, a discussion of the literature on the phenomena of DFP (Digital Fluid Power), particularly with respect to multisource hydraulic systems, is presented. In the investigation, the effective application of the phenomenon in multi-source hydraulic drive systems is also addressed. We will discuss a variety of factors related to this phenomenon, including hardware needs, control system design, and specifically whether servo valve technology is preferred as an alternative to proportional valves. The report also discusses the possibilities for further research in this area, as well as its limitations. The fundamental concept of digital fluid power is the design of a control system using hydraulic valves. "Digital fluid power is a new field of fluid power with tremendous scope for innovative solutions," claims Rudolf Scheidl [1]. For a successful implementation, new components, in-depth knowledge of the system, and new control concepts are required. In a book by Mc Cloy titled Control of Fluid Power: Analysis and design [2], Digital Hydraulic Power has been thoroughly described regarding its applicability in both hydraulic and pneumatic systems. Intelligent methods to reduce power consumption and improve energy recovery from hydraulic drives include multi-source hydraulic systems. According to a recent analysis completed in the year 2020 that examined the excavator's truck loading cycle, a thorough Multisource Network Hydraulic System (MSNHS) has also been suggested that significantly reduced the engine input power by about 60% and improved the overall system performance, highlighting the potential for further research in this area. While both proportional valves and servo valves are used to control fluidic flow, they differ from one another in several factors, like spindle overlap, frequency response, actuation mechanism, intended purpose, etc., each of which has advantages and disadvantages. Although proportional valves are continuously variable electrically modulated directional control valves with more than 3% center overlap, servo valves are continuously variable electrically modulated directional control valves with less than 3% center overlap, according to an article by Jack L. Johnson [3]. Keep in mind that this overlap leads to the length of the dead zone, which is essential for optimal control of hydraulic systems. Since the output of a dead zone is zero (the output is "dead" - (no action occurs), a dead zone is a band of input values in the domain of a transfer function in a control system or signal processing system [4]. In terms of intelligent control for hydraulic systems, servo valves are thus gaining greater research potential than proportional valves. A portion of closed-loop applications that

were previously only conceivable with servo valves can now be employed with high-performance proportional valves, sometimes known as servosolenoid valves [5]. According to the following findings [6], another study found that a proportional valve performed better when connected to the SMC (Siding Mode Control) than when coupled with a PI (Proportional Integral) controller.
The paper also discusses the digital fluid power as the use of simple hydraulic valves in place of a property valve to build a hydraulic system, control place proportional hydraulic in a multisource hydrostatic drive system to reduce energy consumption, and optimize the energy recovery of the hydraulic system. The main objective is to reduce the cost of building the system and its maintenance, improvements to the ecological perimeter such as energy, noise, emissions of harmful substances and carbon footprint, and so on.

2. Literature Review

Generation, monitoring, and control of power, as well as transmission of power, can be achieved using pressurized fluids, which is one of the many facets of the expansive field of engineering technology known as fluid power [1]. Because it has a low freezing point, a high boiling point, a significantly larger bulk modulus, and self-lubricating quality, hydraulic oil is often used [2]. Fluid power has a well-defined research domain and academic activities that benefit a wide variety of sectors, including agriculture, infrastructure, transportation, aerospace, marine and industrial, as well as many others that demand high power-to-weight ratios [3]. Fluid power is characterized by its transmission flexibility, user friendliness, simplicity of operation, comparatively low cost, controllability, and management [4], in addition to its ability to generate large power densities. Due to these advantages, fluid power technology is a viable solution for completing crucial activities that require a high power density and a high degree of reliability. Heavy-duty uses include construction trucks, material handling equipment, and military activities, as examples [5]. As a power-generating component, the hydraulic hybrid propulsion system may have one or two hydraulic pump/motor (P/M) units. Moreover, the components of the HHV that are responsible for the storage of energy are called hydropneumatics accumulators. There are three distinct configurations that can be applied to hydraulic hybrid vehicles: serial, parallel, and power-split. In a configuration known as a serial hydraulic hybrid, an internal combustion engine (ICE) serves the function of an accumulator charger, while a hydraulic power unit (P/M) supplies the vehicle with the necessary amount of power. However, in a parallel hydraulic hybrid architecture, the load is mechanistically connected to both the hydraulic P/M and the internal combustion engine (ICE). When compared to the series structure, the parallel HHV configuration is easier to implement and has lower costs because there are fewer modifications made to the conventional vehicle's mechanical components. A power-split hydraulic hybrid can switch between a parallel driveline and a serial driveline for power transmission. A power-split architecture is significantly more complicated than a parallel architecture. As a direct consequence of this, parallel HHV is a better option for businesses that manufacture vehicles. Because the speed of the internal combustion engine (ICE) depends on the speed of the wheels in the parallel configuration, the parallel configuration of the HHV has the disadvantage of having a higher fuel consumption than the series HHV. Previous demonstrations of parallel hydraulic hybrid powertrains for buses were conducted in Japan in the 1980s and early 1990s. These powertrains are currently being developed by Eaton Permo Drive and Bosch Rexroth and are described in [2]. Additionally, over the past ten years, several studies have been conducted on the modeling and simulation of parallel HHV [3, 4]. Between 2008 and 2010, Guo-Qing Liu and colleagues conducted research on the application of a parallel hydraulic hybrid powertrain for an urban bus [2, 5, and 6]. One of the most important contributors to the economy of the United States is the fluid power industry [6-8]. The National Fluid Power Association (NFPA) states that thousands of companies use hydraulic power systems in the United States. These companies are widely considered the most successful industrial enterprises in the United States [7-10], with more than 845,000 workers and a combined annual payroll of more than $60 billion.

3. System Model

The cutting-edge field of digital hydraulics [5-9] optimizes the performance of the hydraulic system, supports new kinds of fluid power application, and reduces energy consumption. This innovation allows efficient replacement of traditional fluid power components such as directional control valves with series of valves that operate in parallel [1]. Poppet-style actuation, as seen in the spool valves in Figure 1, prevents leakage across the valve, making such valve configurations ideal for this application. As a result, this configuration reduces system losses, grants more commands, increases performance and efficiency, and reduces the burden on maintenance budgets [2]. This technology has also been used to replace conventional check valves in fixed displacement pumps, among other configurations, with the aim of increasing the efficiency of traditional systems. It also allows conventional fixed displacement pumps to have variable displacements, which opens up the possibility of restriction and diversion [4]. Mechanical check valves in the inlet and outlet ports of the pump are used by some traditional piston pump/motor designs, such as reciprocating piston pumps, to isolate the high- and low-pressure halves of the system.

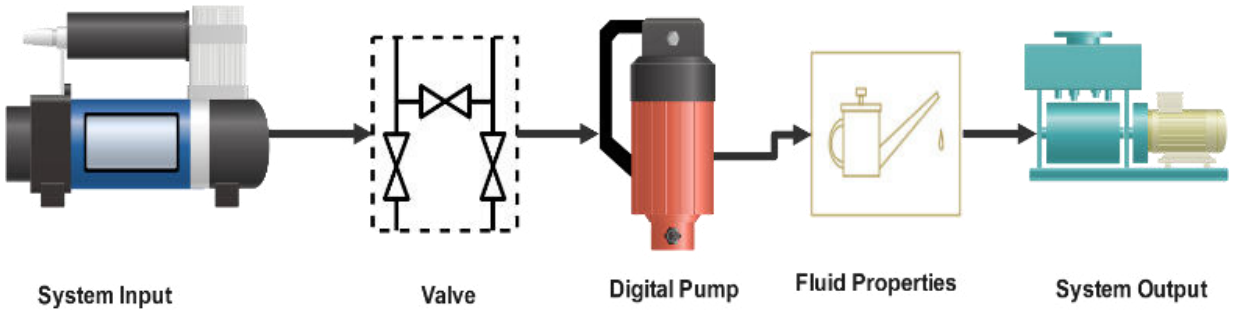

Fig. 1. Schematic of the series hydraulic system for multi-source hydro system configuration

The operation comprises three stages, start-up, cruising, and braking, similar to the parallel design. When the automobile is accelerated rapidly, the clutch (2) separates the engine shaft from the pump shaft. Therefore, it is possible that the hybrid hydraulic pump/motor (6) will do its job. When the accumulator is full, the hydraulic pump/motor will receive the pressurized fluid (5). (6). The acquired hydraulic energy is transformed into mechanical power and sent to the driveshaft (8). After the first burst of speed, the accumulator is allowed to return to its normal fluid level, and the cruising speed is then chosen. Since its pressure is now less than the nitrogen precharge pressure, the engine (1) is forced to run and the clutch (2) is engaged.
Therefore, the axles are driven by a hydraulic pump/motor (6), which is powered by the engine and pumps the fluid from a reduced pressure reservoir (3). The accumulator is where the overflow of high-pressure fluid from the hydraulic pump is temporarily maintained. Pressing the brake pedal causes the engine to break down, the clutch to disengage and the hydraulic pump/motor (6) to switch to pump mode, drawing fluid from low pressure storage and storing it in the accumulator. It is time to slow down now. The kinetic energy of the wheels is transferred into hydraulic energy and is kept in the accumulator in this fashion. Energy reserves will be used to accelerate the vehicle when it is time. When the pump is in the intake stroke, the low-pressure check valve allows the fluid to enter the system through the valve. When the pump cylinder is depleted, the fluid will be shifted to the high-pressure side of the system. This will cause the intake check valve to close, while the exhaust check valve will open due to pressure. In this arrangement, the pump can only produce fixed displacements because the activation of the intake and exhaust valves is exclusively dependent on the pressure difference in the chamber. Therefore, the authors of [6] suggest a digital inline 3-piston pump that is electronically activated and employs digital on/off valves in lieu of conventional valves. This pump would be inline and it would have three pistons. A digital pump/motor with a displacement of 28cc / rev, three displacement chambers, and two quick on / off valves is what the proposal calls for. Figure 4 shows that the pump and motor have been configured to be used with a single

displacement chamber. This configuration can be seen in the figure. Valve 1 is responsible for controlling the flow from the low-pressure side, while Valve 2 is responsible for controlling the flow coming from the high-pressure side. Using the suggested configuration, the operation of the valve may be regulated at any time throughout the pumping or driving cycle. Due to the improved controllability and flexibility of the system that this configuration makes feasible, a wide variety of digital pumping and driving approaches are now conceivable [7]. These techniques include flow-diverting and limiting operating strategies. In addition, our team came up with and implemented a mechanically actuated digital pump that, much like its electrically actuated version, can reach high efficiencies over a wide range of displacements. In the following sections, you will get an overview of the mechanical architecture of the digital pump that is actuated mechanically, you will learn about the most efficient operating strategy for the digital pump, that is, actuated electrically, and you will see the results of the experimental testing and validation of the digital pump. The following equations are given:

$$f_v = \frac{s_v * 1000}{v_g * n} \tag{1}$$

$$f_t = \frac{s_v * \partial p}{p_{max} * 600} \tag{2}$$

$$f_{mh} = \frac{f_t}{f_v} \tag{3}$$

$$A_{pump} = \frac{v_g * \partial p}{20 * \pi * f_{mh}} \tag{4}$$

$$A_{motor} = \frac{v_g * \partial p * f_{mh}}{20 * \pi} \tag{5}$$

The size of the accumulator is determined using the following formulae, which are based on the application for which it will be used.

$$\partial p_1 v_{g1}^k = \partial p_2 v g_2^k \tag{6}$$

$$p_0 * v_0^n = p_1 * v_1^n \tag{7}$$

$$p_2 * v_2^n = \partial p_n * v g_x^n \tag{8}$$

$$v g_1 = \frac{v g_x (^{p_3}/_{p_1})^{1/k}}{1 - (^{p_3}/_{p_2})^{1/k}} \tag{9}$$

The minimum operating pressure of the hydraulic circuit can be specified using these values using the following equation.

$$soc(\%) = \frac{v_x}{v\_max} * 100 \tag{10}$$

The most important output variable of the accumulator block is its State of Charge (SoC). SoC represents the ratio of fluid volume to its maximum by the following equation. The maximum fluid volume in the accumulator corresponds to the maximum gas pressure situation

4. Results and Discussion

In this section, we report the results of a simulation run on a series hydraulic hybrid drivetrain in MATLAB Sims cape, a graphical programming environment created by MathWorks [8]. MATLAB

Sims cape models the series hydraulic hybrid transmission seen in regular terrain hydraulic vehicles. The purpose of the model is to investigate whether a hydraulic hybrid transmission's performance might benefit from replacing its current pump/motor components with digital ones. The digital motor and pump data that was acquired at the tested displacements (25%, 50%, 75% and 100%), pressures (4 MPa, 10MPa and 18 MPa), and shaft speeds (300 RPM, 500 RPM, and 700 RPM) were applied to the physical simulation components to simulate the desired state-of-the-art digital units (pump and motor).

Therefore, the physical pump and motor contained, pressure compensated pump, and adjustable displacement motors are sized according to the maximum and minimum pressures and the needed flow rate of the system, using the imported lookup tables. Accumulator size, along with that of other hydraulic parts like valves, fittings, hoses, etc., is determined by the system's pressure and flow rate, which are measured during acquisition. The digital pumping/motoring data shows that at 300 and 700 RPM, the hydraulic units (5) and (11) are capable of a maximum displacement of 28 cc/rev. There will also be a maximum volumetric efficiency of 94% for hydraulic units, a minimum overall efficacy of 78%, and a pumping efficiency of up to 90%. However, while in the operation unit, (11) can achieve overall efficiency of up to 92.2% and volumetric efficiency of up to 99.99%. To provide additional flow at peak loads, a series hydraulic hybrid transmission uses a gas accumulator that expands and compresses its gas contents under adiabatic conditions (during the acceleration stage). Detailed testing was performed with a variety of duty cycles, one of which is shown in Figure 2.

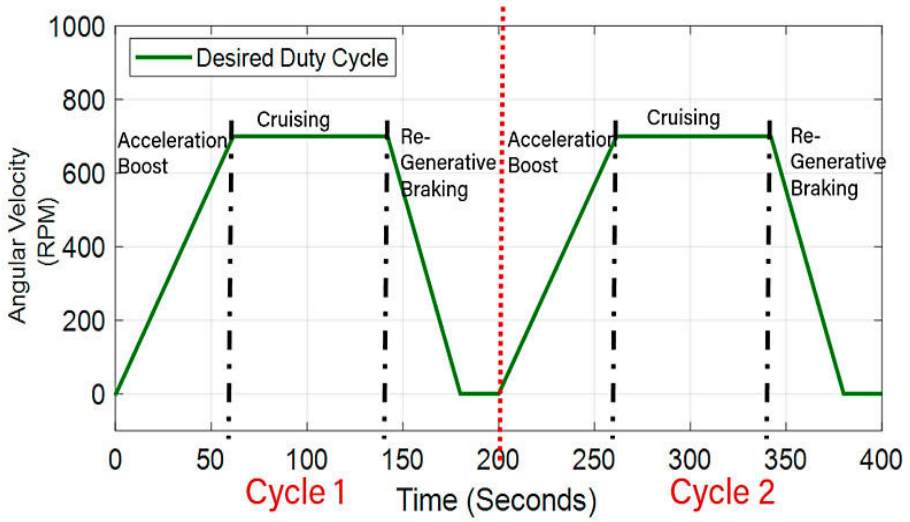

Fig. 2. The desired duty cycle

As a result, each tyre had a calculated moment of inertia of about 0.37 kg2 after being rotated once. Moments of inertia were determined for each tire, and a mild physical torque source was provided at the motor shaft to account for the values. Here, we break down the workings of the simulation model at each phase. The accumulator is shown in Figure 3 after being precharge with fluid to a pressure higher than that at which the system operates. Since the pump is turned off, the accumulator is used as a backup power source. When the vehicle is in motion, the energy stored in the accumulator is transferred to the motor (11). The stored pressure regulates the opening and closing of the valves. Because the accumulator nitrogen pressure is higher than the system pressure currently, the valve does not open (7). The flow is then directed through valve (9) and blocked at valve (8) by maintaining valve (7) in its unactuated position (10).

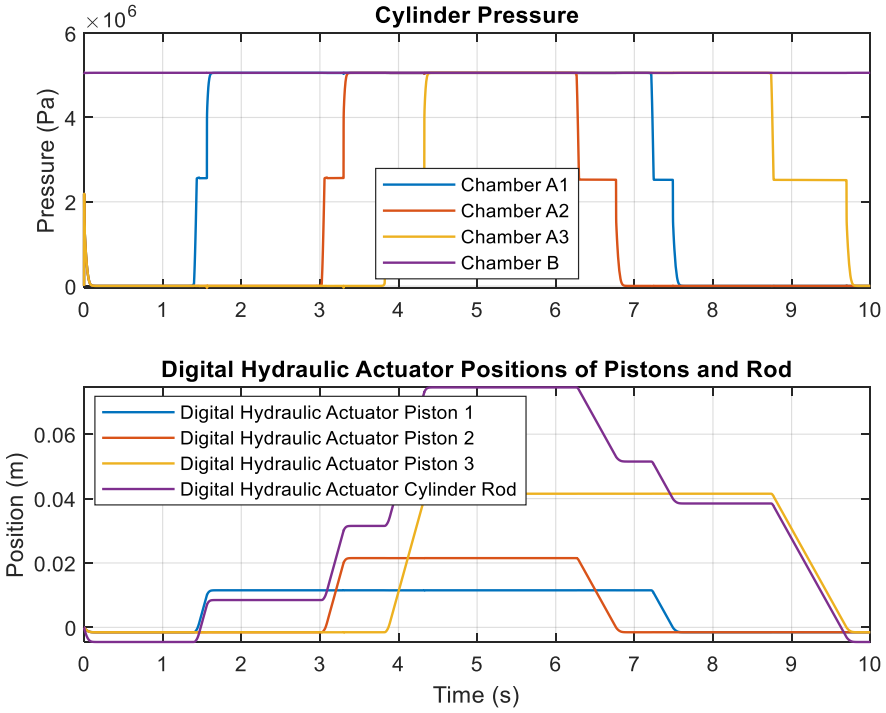

Fig. 3. The resulting pressure and flow simulation results at the pump's discharge and accumulator port throughout the duty cycle

As the acceleration phase ends, the accumulator's fluid level begins to drop, and the pressure of the recharged object falls below the pressure of the system. Since the accumulator has practically little energy left, a second hydraulic power source is required to drive the wheels. At this point (cruising), the clutch is engaged by an electrical signal from the engine after the precharge pressure has dropped. To put the motion into action on the wheels, the pump begins to push the fluid flow from the hydraulic tank (low-pressure reservoir) into the hydraulic motor (11), which still functions as a motor. Since valve (10) is still closed, fluid is supplied to the motor in the same way as it was during the acceleration phase: through valve (9).

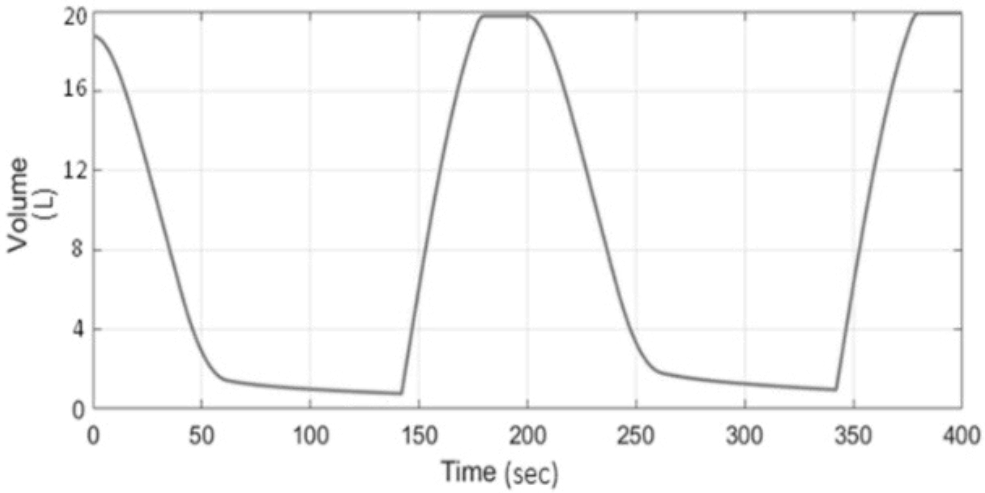

Fig. 4. Simulation outcomes for the fluid volume inside the accumulator

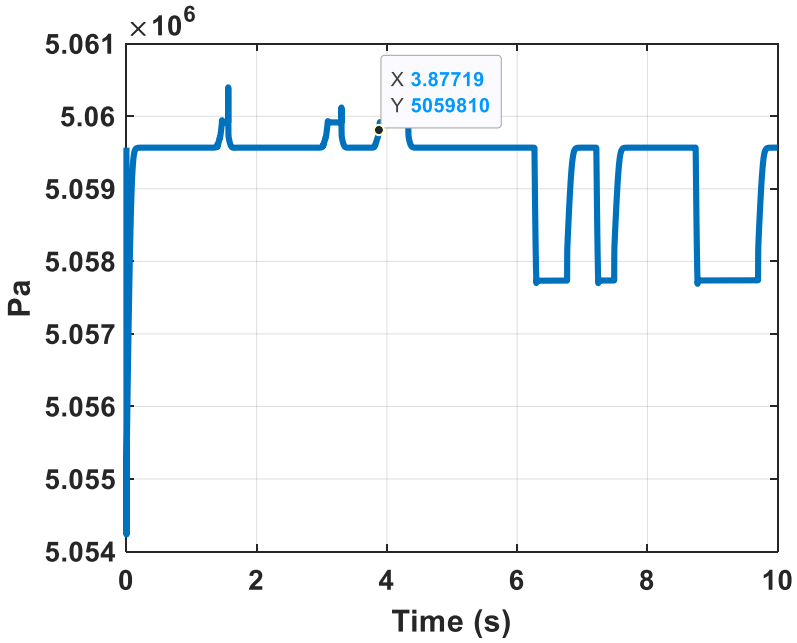

Fig. 5. Simulation of the pressure drop across the motor

Figures 4 and 5 illustrate the shifts that occur in the amount of fluid in the accumulator and, separately, the pressure drop that occurs in the motor throughout the period of the needed duty cycle for the different transmission stages (acceleration, cruising, and braking). Acceleration occurs when the stored energy is released into the intake port of the motor to increase the rotational velocity. Because of this, the motor operates in driving mode. 4.

5. Conclusions

It is apparent that fluid power is a critical part in almost every industry, including transportation, the construction of manufacturing facilities, etc. The development of models that can take the best advantage of the idea of digital fluid power is urgently needed in this era of intelligent technological systems. Due to the significant potential for energy recovery in multisource hydraulic drive systems, such models must be constructed as a first step. To determine system errors, the simulated model and the real system must be contrasted. This may lead to improved energy efficiency, less losses, and improved system performance. Due to the poor operation of conventional variable displacement pumps at partial displacements, the average efficiency of series hydraulic hybrid drivetrains is between 64% and 81%.

References

[1] Johnson, J.L. “What's the Difference Between a Servovalve and a Proportional Valve?”, 2012; Available from: https://www.hydraulicspneumatics.com/technologies/hydraulic valves/article/21882788/whats-the-difference-between-a-servovalve-and-a-proportional-valve.

[2] Taware, A., and G. Tao. “An adaptive dead-zone inverse controller for systems with sandwiched dead-zones.” *International Journal of Control* 76, no. 8 (2003): 755-769.

[3] Ferreira, J., F.G. De Almeida, and M.R. Quintas. “Semi-empirical model for a hydraulic servo-solenoid valve.” *Proceedings of the Institution of Mechanical Engineers, Part I: Journal of Systems and Control Engineering* 216, no. 3 (2002): 237-248.

[4] Lunge, S.P., S. Kurode, and B. Chhibber. “Proportional actuator from on off solenoid valve using sliding modes.” Paper presented at the 1st International and 16th National Conference on Machines and Mechanisms (iNaCoMM2013), Roorkee, India, December 18-20, 2013.

[5] Scheidl, R., M. Linjama, and S. Schmidt. “Is the future of fluid power digital?” *Proceedings of the Institution of Mechanical Engineers, Part I: Journal of Systems and Control Engineering* 226, no. 6 (2012): 721-723.

[6] McCloy, D., and H.R. Martin. *Control of fluid power: analysis and design*. 2d rev. ed. Chichester, Ellis Horwood Ltd. Publisher, 1980.
[7] Valmet. "Digital hydraulic concept reduces cost and increases reliability." Available from: https://www.valmet.com/media/articles/up-and-running/new-technology/FPDigHydr/.
[8] Chau, K., and Y. Wong. "Overview of power management in hybrid electric vehicles." *Energy conversion and management* 43, no. 15 (2002): 1953-1968.
[9] Doucette, R.T., and M.D. McCulloch. "Modeling the prospects of plug-in hybrid electric vehicles to reduce CO2 emissions." *Applied Energy* 88, no. 7 (2011): 2315-2323.
[10] Kim, N., and A. Rousseau. "A comparative study of hydraulic hybrid systems for class 6 trucks." SAE Technical Paper 2013-01-1472, 2013.
[11] Woon, M., S. Nakra, A. Ivanco, and Z. Filipi. "Series hydraulic hybrid system for a passenger car: Design, integration and packaging study." SAE Technical Paper 2012-01-1031, 2012.
[12] Zhang, Z., J. Chen, and B. Wu. "The control strategy of optimal brake energy recovery for a parallel hydraulic hybrid vehicle." *Proceedings of the Institution of Mechanical Engineers, Part D: Journal of Automobile Engineering* 226, no. 11 (2012): 1445-1453.
[13] Chen, J.-S. "Energy efficiency comparison between hydraulic hybrid and hybrid electric vehicles." *Energies* 8, no. 6 (2015): 4697-4723.
[14] Khadim, Q., et al. "Estimating the Characteristic Curve of a Directional Control Valve in a Combined Multibody and Hydraulic System Using an Augmented Discrete Extended Kalman Filter." *Sensors* 21, no. 15 (2021): 5029.
[15] Ketelsen, S., et al. "Thermo-Hydraulic Modelling and Experimental Validation of an Electro-Hydraulic Compact Drive." *Energies* 14, no. 9 (2021): 2375.

ISSN 1454 - 8003
Proceedings of 2022 International Conference on Hydraulics and Pneumatics - HERVEX
November 9-10, Băile Govora, Romania

EXPERIMENTAL STAND FOR IMPROVING THE ENERGY EFFICIENCY OF AIR SOURCE HEAT PUMPS

Claudiu RAFA[1], Daniel-Vasile BANYAI[1], Dan OPRUTA[1], Ioan-Lucian MARCU[1]

[1] Technical University of Cluj-Napoca, daniel.banyai@termo.utcluj.ro

Abstract: *The current climatic, political and economic situation, the constantly increasing price of electricity, requires the intensification of research in order to develop new methods of increasing the efficiency of heat pumps is an immediate desideratum. Because every percentage of efficiency has a major impact on the final operating costs, it is very important to design and make the most efficient system for heating and cooling installations. The paper presents the development of an experimental stand with air source heat pumps, which offers the possibility to control and determine the influence of the functional parameters so that the increase in efficiency is possible. The proposed solution increases the efficiency of the heat pump in the same climatic conditions, by heating or cooling the air taken by the evaporator's fan, but in the presented configuration it also eliminates the disadvantages of using the climatic well to ventilate the rooms.*

Keywords: *Heat pump, climatic well, energy saving, COP increase*

1. Introduction

In recent years, climate changes are felt more and more acutely through the occurrence of extreme weather phenomena with an increasing frequency, extreme heat waves are no longer isolated cases and with low frequency, but become periods of time with records in overcoming the most high temperatures, torrential rains with unusually high wind speeds, but also a continuous warming of the oceans, which implicitly leads to the melting of glaciers and the rise of sea levels, at a much faster rate than that observed in the last 50 years. The European average temperature for August 2022 was by far the warmest ever recorded for August, 1.72°C above the 1991-2020 average and 2.24°C above the 1981-2010 average. [1]
The "Fit 55" package includes a proposal to revise the Renewable Energy Directive. The proposal is to increase the current EU target of at least 32% of energy from renewable sources in the global energy mix to at least 40% by 2030, with a net greenhouse gas emissions by at least 55% by 2030. [2]
In order to decarbonize the economy but also to strengthen Europe's geopolitical energy independence, the solution with the highest energy efficiency in the use of electricity obtained with the help of renewable sources in applications for heating and / or cooling is the one with compressor heat pumps.
Despite the negative consequences of the coronavirus pandemic as well as challenges in global supply chains, demand for green air conditioning solutions continued to grow by around 30%. [3]
In the last two years, demand has exploded with the increase in energy prices, the war in Ukraine and the Russian gas crisis, and the upward trend is valid for the whole of Europe.
In these conditions where the price of electricity has a constantly increasing trend, the intensification of research in order to develop new methods of increasing the efficiency of heat pumps is an immediate desideratum. Each percentage of the efficiency has a major impact on the final operating costs and therefore the importance of designing and making a system as efficient as possible of heating and/or cooling installations with heat pumps is very high.
A solution for improving the energy efficiency in case of residential buildings is represented by heat pump systems (HPS), which are modern heating installations composed of the actual heat pump, the heat supply and distribution installation and the indoor central heating installation.
There are three main types of heat pumps used in residential HPS (figure 1):
- heat pumps with the outside air source
- heat pumps with the ground source,

- heat pumps with underground water source.

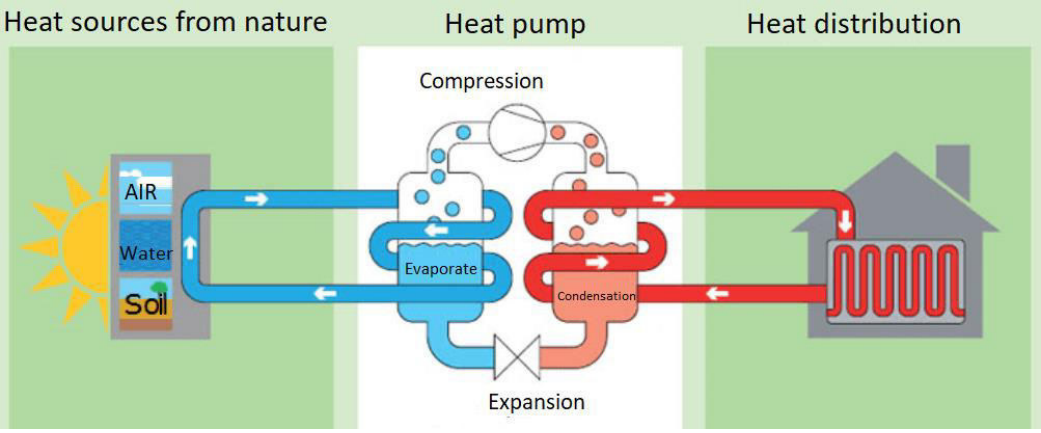

Fig. 1. Heat pump systems classification [www.ct1.ro]

The most affordable heat pumps, whose installation does not require drilling or complicated construction work, represent the first category, figure 2.

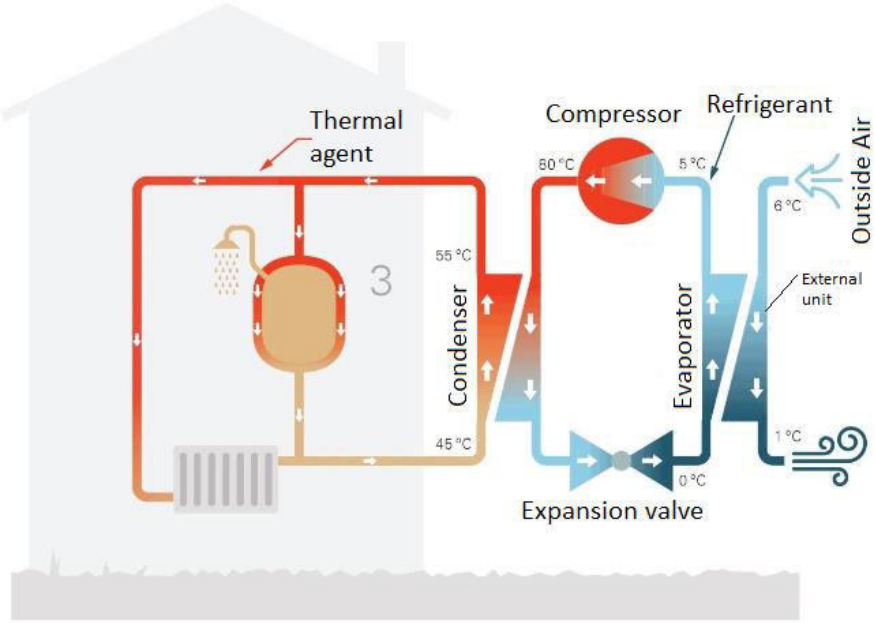

Fig. 2. Air source Heat pump [www.trust-expert.ro]

The energy consumption and the operating performance of air source heat pumps depend on many parameters such as: the climate zone, the thermal demand of the building, the indoor heating system, the number of hydraulic loops, thermal inertia, the size of the heat pump, the modulation of the pump and the automation adapted for each component of the HPS (terminal units, heat pump, circulation pumps, etc.).
For high efficiency, it is important that HPS are used both for heating and domestic hot water in the winter and in reversible mode during the summer, ensuring cooling and domestic hot water.
There are studies and analyses, in the literature, related to the operation of heat pumps with different types of heating installations: cast iron radiator, bimetal radiator (steel-aluminium), fan convectors and radiant floor. The operating costs of HPS with cast iron radiator, bimetal radiator, fan coil and radiant floor heating are 33%, 41%, 42% and 47% lower than the operating cost of an electric heating system. [4]

The performance of heat pumps can be assessed through a series of factors (specific electricity consumption, renewable energy supplied, seasonal performance coefficient) but the most important indicator that characterizes the operation of the heat pump is the coefficient of performance (COP). It is defined as the ratio between the useful thermal power produced ($E_{thermal}$) and the drive power of the heat pump ($E_{electrical}$). [5]

2. Objective

The reduction of electricity consumption for the same amount of thermal energy produced by an air-water type heat pump, in same climatic conditions, can be obtained by changing the temperature of the primary source (the air) that bathes the vaporizer (the heat exchanger from the primary source to refrigerant).
A passive method of heating or cooling the air taken from outside used in the ventilation of houses is climatic (Canadian or Provençal well, figure 3), is a simple and shallow geothermal system, capable of taking advantage of the stable temperatures of the subsoil surface layer. Its functioning is based on the fact that the underground temperature differs from that of the environment. This difference is accentuated at approximately two meters of depth, where it remains stable in increasingly lower temperature ranges (depending on the area at 10 m depth, the temperature variation throughout the year can be in the range of 9-11°C, figure 4 for Romania). As disadvantages of using climatic wells in ventilation, can mention those related to the possibility of infiltration of dangerous chemical substances in the case of the use of inappropriate materials or the poor installation of pipes and the creation of mold due to condensation.

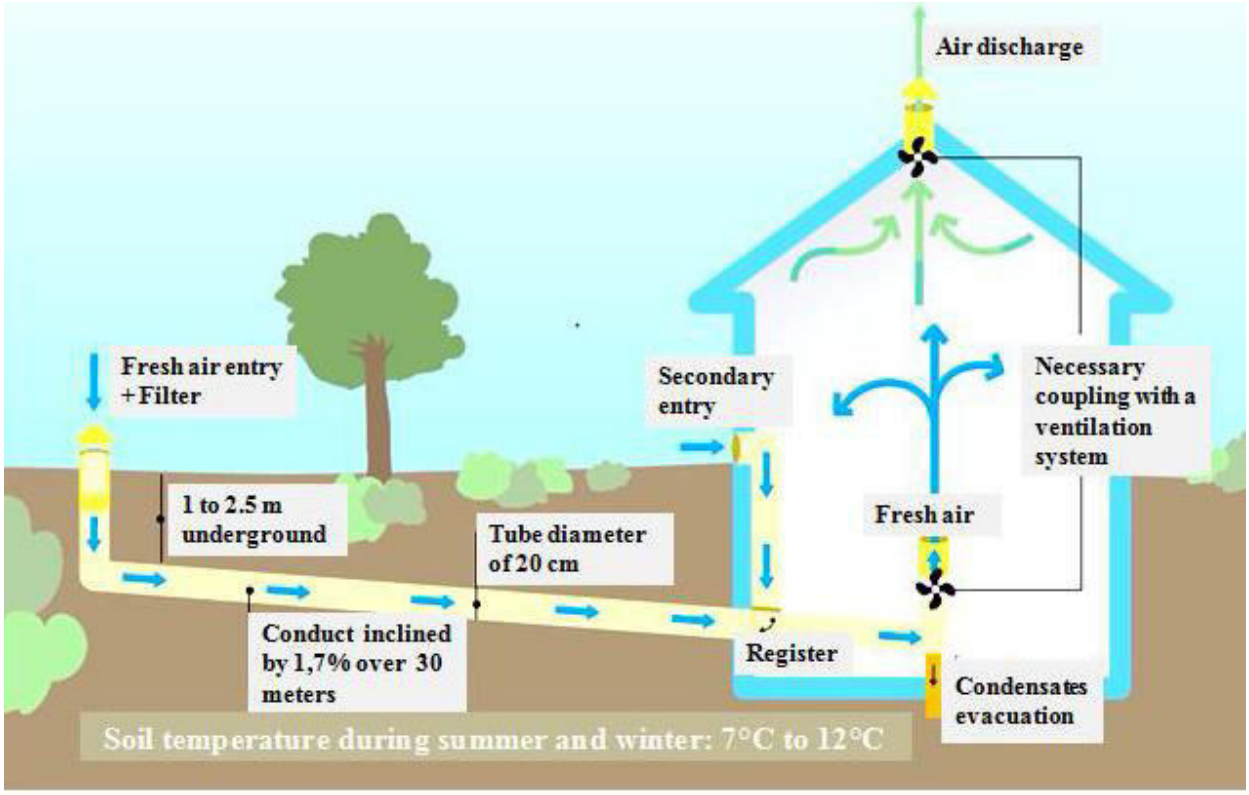

Fig. 3. Diagram of operation of a climate well. Source: ADEME-2012 (The French Agency for Ecological Transition)

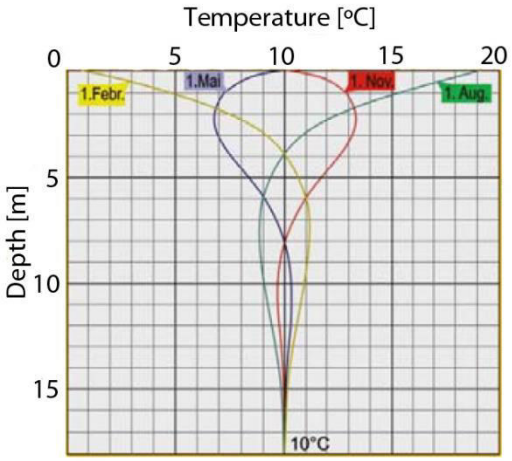

Fig. 4. Soil temperature variation [6]

Thus, the purpose of the work is the creation of an experimental stand, which, through temperature, humidity, pressure and speed sensors, allows establishing the influence of the physical quantities in the system that affect the consumption of electricity, as well as the variation of the functional parameters in different climatic scenarios, in the case coupling a heat pump whose source is outside air, with a climatic well. The system can be used in the passive version (without auxiliary fans), only the heat pump fan is used for the air flow from the Evaporator, or semi-passive in which the air flow through the underground pipes is created with the help of low power auxiliary fans.

3. Experimental setup

The components that are part of the experimental stand are shown in figure 5.

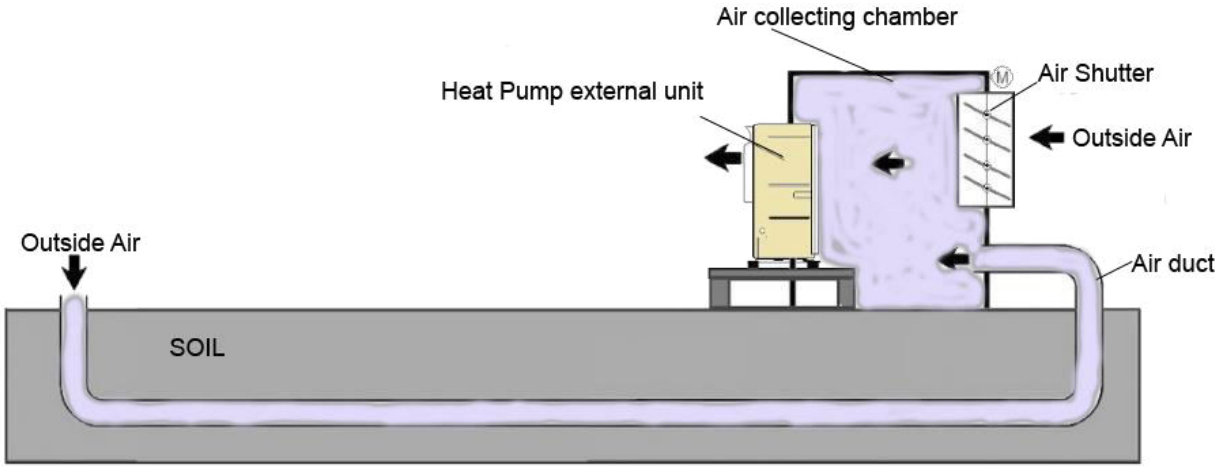

Fig. 5. Schematic experimental stand

The stand contains an air-water heat pump with a power of 6 kW, which provides the heat required for a residential house. The maximum air flow to the fan of the external unit of the heat pump in heating mode is 2530 m³/h. For an optimal thermal transfer through the piping below the ground level, the speed should be between 2 and 4 m/s, thus the required section is (A=Q/v) 0.17...0.35 m². For the stand described in the paper, a number of 6 pipes with an internal diameter of 190 mm, i.e., a total area of 0.17 m² was chosen. The speed of the air through the ducts, for different values of the flow rate, is presented in figure 6.

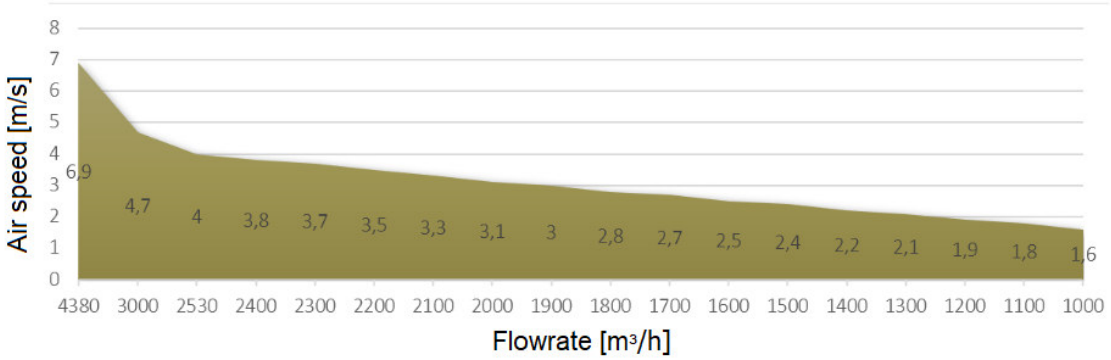

Fig. 6. Air speed in the climatic well depending on the flow rate

The total length of the pipes is 24 m, the depth below the ground surface is 2 m for three pipes and 1.5 m for the other three. The distance between them is 1 m. The useful volume of the collector chamber is 7 m³ and it is provided with an opening for the admission of outside air, without passing through the climatic well, controllable with a motorized shutter.
To calculate the total pressure loss in the air circuit, we must add up the pressure loss in each element of the circuit. The pressure loss due to the friction when air flows, is calculated according to the empirical known relationship:

$$\Delta P = f_a \cdot \frac{L}{d} \cdot \rho \cdot \frac{v^2}{2} \quad (1)$$

where: L - represents the length of the pipes [m]; d - inner diameter [m]; ρ - density of the fluid [kg/m3]; v - average flow velocity [m/s]; f_a - Darcy's coefficient of friction.
In order to ensure the flow rates entering the collection chamber at the entrance in the climatic well, auxiliary axial fans with a maximum power of 10 W were installed.
The propagation model of heat conduction in a semi-infinite solid (soil) proposes an analytical solution when the surface temperature of the solid is sinusoidal. The outside air temperature, T_{air} will be conveniently expressed [7]:

$$T_{air}(t) = m + A\sin(\omega t - \varphi) \quad (2)$$

Solving the heat equation for a transient semi-infinite environment whose surface temperature is imposed by equation (2) we obtain the soil temperature function of depth x, in equation (3). In this model the solutions are also sinusoidal with the same period and pulsation as the temperature signal but whose phase and amplitudes vary with the depth considered. [7]

$$T_{soil}(x,t) = m + A \cdot e^{-x\sqrt{\frac{\omega}{2\alpha}}} \cdot \sin\left(\omega t - \varphi - x\sqrt{\frac{\omega}{2\alpha}}\right) \quad (3)$$

where: α - thermal diffusivity, the ratio of the thermal conductivity to the volumetric heat capacity. It is an indicator of the rate at which a temperature change will be transmitted through the soil by conduction; m - mean period temperature [°C]; A - amplitude of the temperature variation [°C]; ω - pulsation [rad/s]; φ - phase shift [rad].
The experimental stand with the air source heat pump, climatic well and air collecting chamber was made at a residential building in Cluj County, Romania, as can be seen from figure 7. The experimental stand has just been completed and equipped with sensors and data acquisition so that the measurements that last a year will begin.

Fig. 7. Air source heat pump with climate well experimental setup

4. Conclusions

The efficiency of the climatic well upstream of the heat pump, will vary depending on the nature of the soil, its rate of aeration and moisture, the air flow speed in the pipes, pressure drop, etc.
The proposed solution increases the efficiency of the heat pump in the same climatic conditions, which uses the thermal inertia of the ground to preheat or cool the air taken by the evaporator fan.
The built stand allows the measurements for the four seasons and the determination of the coefficient of performance (COP) of the new system.

References

[1] Galey, Patrick. “2022 Was Europe's Hottest Summer on Record by a 'Substantial Margin.'” September 10, 2022. Accessed October 19, 2022. https://www.sciencealert.com/2022-was-europes-hottest-summer-on-record-by-a-substantial-margin.

[2] European Parliament and the Council. “Fit for 55.” June 29, 2022. Accessed October 20, 2022. https://www.consilium.europa.eu/en/policies/green-deal/fit-for-55-the-eu-plan-for-a-green-transition/.

[3] Trust Expert. “The demand for heat pumps increased by over 30% compared to last year” / „Cererea de pompe de căldură a crescut cu peste 30% faţă de anul trecut”. November 2, 2021. Accessed October 20, 2022. https://www.bursa.ro/trust-expert-cererea-de-pompe-de-caldura-a-crescut-cu-peste-30-procente-fata-de-anul-trecut-05917440.

[4] Hua, Bin, R.Z. Wanga, Biao Xiao, Lin He, Wei Zhang, and Shihang Zhang. “Performance evaluation of different heating terminals used in air source heat pump systems.” *International Journal of Refrigeration* 98 (2019): 274–282.

[5] Baran, Andreea Irina. *Optimization of systems equipped with heat pumps for the exploitation of renewable and recoverable forms of energy / Optimizarea sistemelor de instalații echipate cu pompe de căldură pentru valorificarea formelor de energie regenerabilă și recuperabilă*. PhD Thesis. “Gheorghe Asachi” University of Iasi, 2019.

[6] Dumitraşcu, Andrei, Dragoș Manea, Marinela Mateescu, and Marian Popescu. „System for air conditioning a house in a smart farm, using a heat pump” / „Sistem pentru climatizarea unei locuinţe dintr-o fermă smart, utilizând o pompă de căldură.” *Buletinul AGIR* no. 3 (2019): 13-17.

[7] Touzani, N., and J.E. Jellal. “Heating and cooling by geothermal energy: Canadian well-Case of Rabat.” *Journal of Materials and Environmental Science* 6, no. 11 (2015): 3268-3280.

ISSN 1454 - 8003
Proceedings of 2022 International Conference on Hydraulics and Pneumatics - HERVEX
November 9-10, Băile Govora, Romania

EMPIRICAL ASPECTS OF THE ANALYSIS OF THE DIGITIZATION OF MANUFACTURING

Elisabeta Mihaela CIORTEA[1]

[1] "1 Decembrie 1918" University of Alba Iulia, mciortea@uab.ro

Abstract: *The paper presents an empirical analysis for a digitized manufacturing system. It is part of Industry 4.0. for modeling we used schematically represented systems. Thus, the complete system includes, in addition to the manufacturing system, a manufacturing management location in the cloud. The role of cloud manufacturing is to connect internally with the manufacturing system and externally with RAMI 4.0. for the simulation we will use the empirical system and Petri nets. We use Petri nets because the modeling is relatively easy to analyze and simulate. Changes in terms of optimization and elimination of errors can be done relatively easily and the results are transmitted in real time. The resulting diagrams can be easily interpreted for decision-making so that no idle times are included in the technological process.*

Keywords: *Cloud manufacturing, digitization, Industry 4.0*

1. Introduction

According to specialized literature, industry, being one of the most critical sectors within any economy, is greatly affected by the digitization of production processes through the development of new technologies that can be used to increase productivity. Digital transformation in the industry plays a vital role in keeping the organization in pace with the competition. The only way of sustainability in any competitive market is to transform business processes into a digital one [1,3,4]. More and more companies accept the fact that digitization of production is the answer to increase competitiveness and try to find products or services to meet the needs. Investments in smart machines do not guarantee success without a vision for digitization [2].
According to specialized literature, the digitization of production is a development and adaptation strategy.
Digital is no longer just a tactical aspect of the manufacturing business – it becomes vital to pursue end-to-end digital transformation to achieve goals such as improving efficiency and quality, reducing costs and waste, and creating innovative products and services.
Digital transformation is about applying technologies to radically change traditional processes, products and services into data-driven, highly connected solutions that can be monetized through extreme efficiency gains and entirely new business models. With a digital approach, firms accelerate time to market, deliver new customer value through digital experiences, manage complex global value chains, and innovate to dramatically improve customer experience and create new revenue opportunities [5,6].
The starting point is a stochastic system. For the stochastic system, the performance evaluation area can be subdivided into two sub-areas. The first refers to measurement and includes three distinct domains that can be called measurements, benchmarks, prototypes.
Measurements are performed on a real system under real operating conditions. They provide the actual performance of the system in the particular state in which the system is observed. However, the measurement results have a very small generality because they are largely dependent on detailed characteristics measuring system workload imposed on the system during the measurement.
The benchmarks will require study system available, so they can be seen. There are cases where the performance study refers to a system that is not available, it is necessary to develop a representative approximation of it, either in hardware or software [7,8].
For the elaboration of the works, we have made a link to be able to do research in particular regarding the confidentiality of the cloud manufacturing, the analysis of the IoT resources in the manufacturing

systems and which can equal it for research purposes, namely RAMI 4.0. IoT is described in the literature as being anything connected to a network that can communicate autonomously without additional human intervention. This concept used in production and other industrial processes allows machine designers to create intelligent equipment and machines so that they can track, record, display, monitor and adjust parameters autonomously. For the cloud, we turned to the simple definition Cloud is an application available only to customers with active mobile Internet, which offers a solution for data storage. Cloud storage consists of archiving, organizing and distributing on demand data between virtualized storage volumes that have been consolidated into hardware [9,10,11].
In this paper have proposed a new architectural model of the intelligent factory that will allow the production experts to make a simpler planning, optimized using all the key technologies of the industry known until today.
Manufacturers can automate and schedule purchases to align with production schedules to reduce inventory costs and positions, while automating inventory and material control.

2. Model description and analysis

The impact of digital transformation in manufacturing includes improvements in safety, quality, production, efficiency, revenue and sustainability – all while reducing costs to remain competitive in the market.
Some major benefits of digitization for manufacturing companies
- digital solutions improve safety, fewer injuries and accidents occur at the workplace
- improvements in the quality of results, reduction of product repetition, reduction of warranty work and increase of customer satisfaction.
- effective process improvement, has a positive impact on employee productivity and production output.

The existing industry architecture model provides a good overview of the industrial environment architecture, but leads to some limitations for users. To overcome these limitations, we proposed based on RAMI 4.0 models a simple smart factory architecture model based on the concept of distributed systems with accurate information and data flows between them. The proposed architectural model enables more reliable and simple modeling of the smart factory. To solve many problems the solution can come from RAMI 4.0, which provides the reference architecture model for the industry, it is a three-dimensional map that shows how to approach the problem at the industrial level in a structured manner and last but not least it ensures that all participants involved reach a common denominator.
The key technology that enables the integration of distributed manufacturing resources, their transformation into manufacturing services and centralized service management is cloud manufacturing. This concept allows multiple users to request services at the same time by submitting the tasks of their requirements to a cloud production platform.
According to specialized literature, the integration of decentralized production resources and the establishment of a collaboration infrastructure between these units is fundamental. This idea requires building the networked manufacturing environment to integrate manufacturing resources and applications.
Manufacturing resources and knowledge can be put into the cloud and thus become accessible on demand by consumers.

3. Presentation of the system

In order to ensure good information management, I will use a tiered cloud system. Research using Petri nets has become very widespread due to the mathematical and graphical model used. Petri nets have at their disposal appropriate platforms in the field of modeling and design of concurrent systems, computer systems, manufacturing systems and performance analysis.

The present work is based on three objectives for IoT but also for the Cloud, these being key elements for RAMI 4.0 as well:
- fundamental study of Petri nets that can be analyzed and validated by a discrete system,
- petri nets are useful for modeling and analyzing systems with discrete events,
- validation methods and results obtained from the analysis of the subject model, deterministic and stochastic model that are used to reorganize and re-evaluate the system and increase its flexibility.

The figure 1 highlights the essential steps of a cloud manufacturing system in the ideal case. All the elements used in the simulation are discrete, which is difficult to obtain in practice.
The modeled system chosen is schematic and contains the basic components IoT, cloud, RAMI 4.0 and the connection between them. It is a generic system and has the role of highlighting the component elements.
In simulations, one can observe the intense activity throughout the requested period in the IoT area, because here the technological manufacturing flow takes place. In the Cloud area there is action at the required levels. Only three basic levels are represented in the scheme. These are at the beginning and end of the process and an intermediate level that can play a role in monitoring the activity.

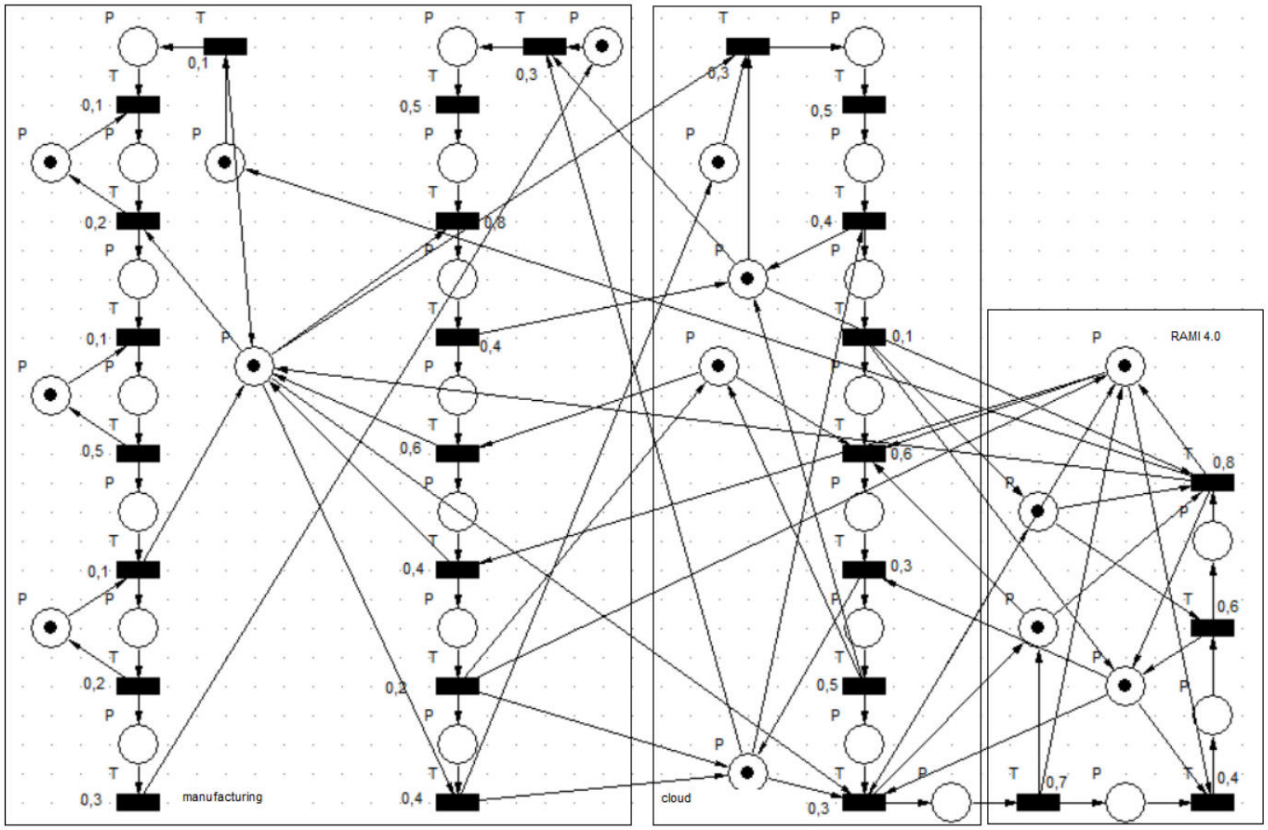

Fig. 1. The general model under analysis.

As for the times used in the simulation, they are comparable to those used in the work in which we dealt with Cloud systems and manufacturing systems. The times are chosen randomly to be able to see on the simulation result the variations that can occur as a result of using the three technologies and their own architectures, Cloud, manufacturing and RAMI.
As a result of the simulation it is observed that intense activity on the entire surface of the technological flow is only in the manufactuing area.
In the cloud, figure 2, and 3, area the activity from the beginning and the end of the model is actively

monitored, and the intermediate zone is the activity of tracking, the role of these areas is also to signal any possible defects that may occur in the technological process or errors that occur in the system.

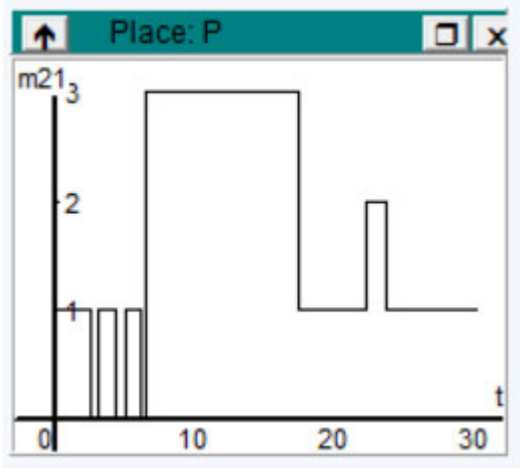

Fig. 2. Cloud-level simulation, as an intermediate control system.

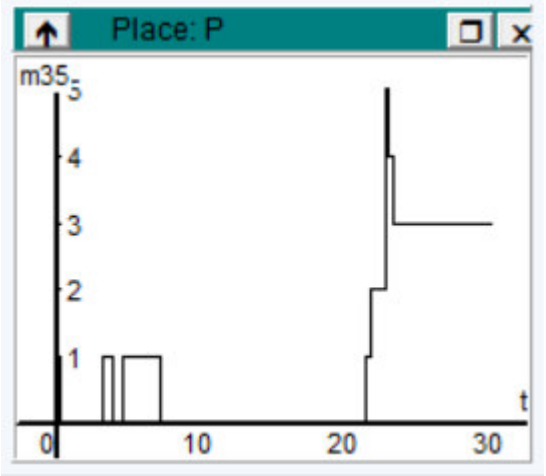

Fig. 3. Cloud-level simulation at the end of the stream.

In the area dedicated to RAMI 4.0 on the graphical representations, figures 4, 5, 6 and 7, we observe at the beginning a determined variation of relations, connections, internal and external requests. These are up to the stability of the system at the cloud level, and then everything unfolds linearly without any variations and sudden differences in representations. All this representation is until the end of the lot.

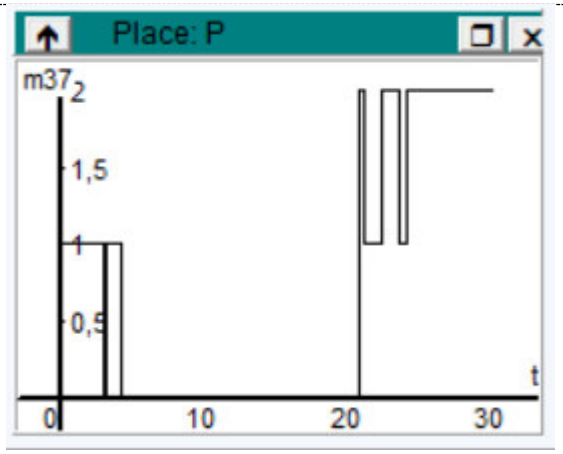

Fig. 4. Simulation at RAMI nodes with rules for manufacturing

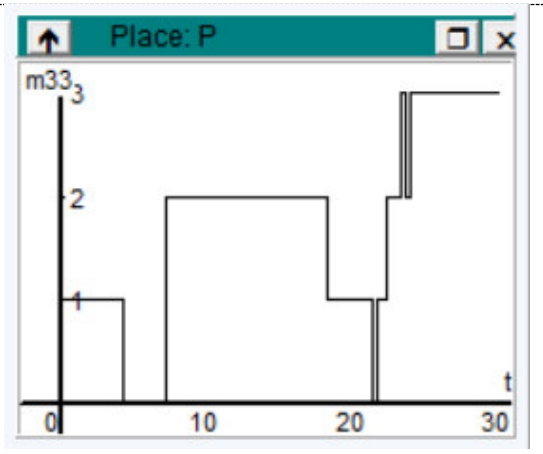

Fig. 5. Simulation at RAMI nodes with rules for Cloud.

At the beginning of a new manufacturing batch determined by the same type of product established for processing, the entire RAMI 4.0 system will again have variations determined by the internal actions of the system and the external actions due to the imposed specifications. This simulation refers only to the product life cycles, the orders with the hierarchical levels of the industry. The life cycles of the factories and machines are not debated because in the model we included only one working point.

All simulations were performed in the same time frame for a single batch, in order to be able to observe as explicitly as possible the variation corresponding to the production flow and the level of orders accessed by RAMI for the system chosen as the simulation model.

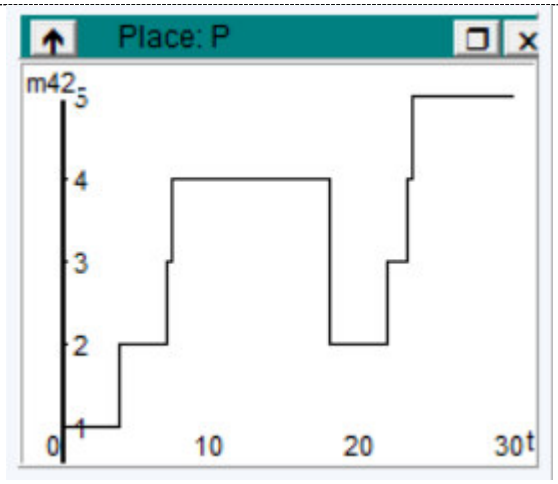

Fig. 6. Simulation at RAMI nodes with rules for manufacturing

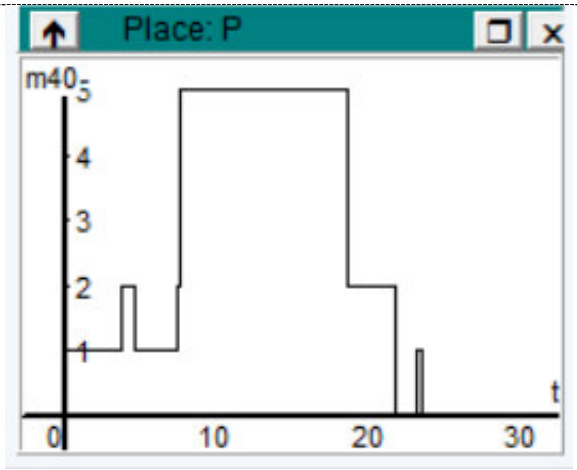

Fig. 7. Simulation at RAMI nodes with rules for Cloud.

4. Conclusions

Digitization is radically changing the face of manufacturing companies. Digital factories are transforming manufacturing as companies implement innovative technologies and seek employees with fundamentally different skill sets.

Leading manufacturing companies are implementing a number of key technologies to digitize manufacturing as well as their entire supply chain. These include end-to-end big data analytics solutions, real-time planning and connectivity, autonomous systems, digital twinning and worker augmentation, among many others. These technologies offer significant efficiency gains and enable companies to produce highly customized products, often at batch size. However, the full effect of digitization is only realized when companies are connected in real time to their key suppliers and critical customers.

Through digital trainings and a communication concept, it motivates employees to contribute to the digital success of their companies.

Digital change is easier said than done. While the benefits of digital transformation are tremendous, there is no one-size-fits-all approach.

Digital transformation is changing the structure of modern business, the scale of operation, consumer behavior, product life cycles, innovative behavior and company culture, legal regulation, promoting broader innovations to meet consumer demands, increasing efficiency and improving the quality of goods and services produced delivered.

References

[1] Abdallah, Yasser Omar, Essam Shehab, and Ahmed Al-Ashaab. “Understanding digital transformation in the manufacturing industry: a systematic literature review and future trends.” *Product, Management & Development* 19, no. 1 (2021): e20200021. https://doi.org/10.4322/pmd.2021.001.

[2] Ribeiro da Silva, Elias Hans Dener, Ana Carolina Shinohara, Edson Pinheiro de Lima, Jannis Angelis, Carla Goncalves Machado. “Reviewing Digital Manufacturing concept in the Industry 4.0 paradigm.” *Procedia CIRP* 81 (2019): 240-245.

[3] Ohrimenco, Serghei, and Grigori Borta. “Chapter 8 Challenges for Digital Transformation in the Manufacturing Industry.” In: Urbaniec, M., and Zur, A. (Eds.) *Socio-Economic Development - Interdisciplinary Ecosystems Perspective*, 2020, pp. 139- 154.

[4] Borangiu, Theodor, Octavian Morariu, Silviu Raileanu, Damien Trentesaux, Paulo Leitao, and Jose Barata. "Digital transformation of manufacturing. Industry of the Future with Cyber-Physical Production Systems." *Romanian Journal of Information Science and Technology* 23, no. 1 (2020): 3–37.

[5] Petrișor, Ioan, and Diana Cozmiuc. "The Stages of Digital Transformation in Manufacturing Industries according to Industry 4.0." In: Nicolescu, Ovidiu, Constantin Oprean, and Aurel Mihail Titu (Eds.). *The Best Romanian Management Studies 2017-2018*. Budapest, Trivent Publishing, 2020.

[6] Kupfer, David, João Carlos Ferraz, and Julia Torracca. "A comparative analysis on digitalization in manufacturing industries in selected developing countries: Firm-level data on Industry 4.0." United Nations Industrial Development Organization. Department of Policy, Research and Statistics. *Inclusive and Sustainable Industrial Development Working Paper Series*. Working Paper 16/2019.

[7] Lorenz, Rafael, Christoph Benninghaus, Thomas Friedli, and Torbjørn Netland. "Digitization of manufacturing: The role of external search." *International Journal of Operations and Production Management* 40, no. 7/8 (2020): 1129-1152. https://www.doi.org/10.1108/IJOPM-06-2019-0498.

[8] Molchanova, S. M. "Digital Transformation in Manufacturing, Infrastructure and Public Services." *The European Proceedings of Social and Behavioural Sciences* EpSBS (2020): 1285-1294. DOI: 10.15405/epsbs.2020.10.03.148.

[9] Siderska, J., and Khambi Mubarok. "Cloud manufacturing platform and architecture design." *Multidisciplinary Aspects of Production Engineering – MAPE* 1, no. 1 (2018): 673-680. doi:10.2478/mape-2018-0085.

[10] Mohammad, A., and B. Ranjit. "The Dependency of the Internet of Things on Cloud Computing." *International Journal of Trend in Scientific Research and Development (IJTSRD)* 2, no. 3 (April 2018): 2575-2581.

[11] Lydon, B. "RAMI 4.0 Reference Architectural Model for Industrie 4.0." *InTech* (March/April 2019). Accessed October 21, 2022. https://www.isa.org/intech-home/2019/march-april/features/rami-4-0-reference-architectural-model-for-industr.

ISSN 1454 - 8003
Proceedings of 2022 International Conference on Hydraulics and Pneumatics - HERVEX
November 9-10, Băile Govora, Romania

EXPERIMENTAL RESEARCH ON THE DEVELOPMENT OF A SALE SYSTEM (VENDING MACHINE), INDEPENDENT OF ENERGY, OF COLD AND HOT PRODUCTS

Mihail SAVANIU[1], Oana TONCIU[2] , Răzvan CALOTĂ[3], Alina GIRIP[4]

[1] UTCB – Faculty of Mechanical Engineering and Robotics in Constructions, mihai.savaniu@utcb.ro

[2] UTCB – Faculty of Mechanical Engineering and Robotics in Constructions, oana.tonciu@utcb.ro

[3] UTCB – Faculty of Building Services Engineering, razvan.calota@utcb.ro

[4] UTCB – Faculty of Building Services Engineering, alina.girip@utcb.ro

Abstract: *This paper presents considerations regarding the realization of the experimental model of a sale system (vending machine), independent of energy, of cold and hot products. In the current context, in which desiderata such as: reducing energy consumption and reducing physical interaction, in the field of sales between customer and seller, are particularly important, the present paper presents the experimental research platform realized in order to test an innovative system of storage and delivery of cold or hot products, system powered by electricity obtained from renewable sources. This paper presents the tests performed and the results obtained regarding the sustainability of the proposed innovative system.*

Keywords: *Renewable sources, vending machine, energy efficiency, environment*

1. Introduction

In the current geopolitical context in which the aim is to reduce energy consumption and use renewable energies, the creation of an automatic energy-independent sales system is particularly current. Vending machines are becoming more and more present in today's trade because they limit the contact between the trader and the customer. The COVID 19 pandemic has generated among traders an increased interest in autonomous vending machines, machines that limit contact between people and the spread of viruses in case of epidemics. In order to place a vending machine near the customer (near the home, workplace, playground, etc.), a problem is the connection to the electricity system. The creation of an energy-independent machine solves this problem and generates an increase in sales of this kind.

Fig. 1. Source https://solarstik.com/energy-storage-feature/

There have been several attempts regarding the supply of vending machines from renewable sources. The solutions presented by other manufacturers and which are in the spirit of our system are presented as a reference as follows:
Coca Cola has created a freestanding vending machine that runs entirely on solar power. This off grid machine is self-contained and fully functional. It is also very easy to install and easy to ship, thanks to its compact solar panels and internal batteries. The machine can turn out to be a great asset in open areas like promenades, boardwalks, beaches, ballparks, college campuses, amusement parks and even military bases. All that it needs is the sun to function. What if there is no sun? The machine simply stores surplus energy in its batteries, powering the machine for at least five days on this stored energy [10].
Disney's ESPN Wide World of Sports Complex deploys two Renewable Equipped Vending (REV) Machines following a successful initial deployment of six prototype REVs at SeaWorld in Orlando, Florida. The solar-powered machines are selling beverages at the following locations within Sea World: Shamu's Happy Harbor, Key West; Terrace Garden, Pacific Point Preserve; and Aquatica, SeaWorld's Waterpark.[14]

Fig. 2. Source https://www.springwise.com/solar_powered_vending_machines/

Fig. 3. Source: Media-Cdn.TimesFreePress

Springwise has also come up with its own unique plan to design a vending machine powered by solar energy. The machine incorporates a strong refrigeration system that can keep the foods and drinks inside it cool for hours. It is fitted with solar panels at the top to absorb the sun's rays. The

electricity thus generated is used to power the vending machine as well as recharge a battery that would keep the machine running at night and on cloudy/rainy days. An inbuilt wind turbine can substitute for solar energy in areas where the sun does not come out too often. [10]
Another company called Solar Vending has developed an entirely off-grid vending machine that uses solar power to power its refrigeration and vending mechanisms. The off-grid ability would allow the machine to be placed even in remote locations like in the middle of a golf course.
A number of companies have started developing solar powered vending machines to keep beverages in the most sustainable manner. Utilizing only the sun's energy for operation, these machines will be a blessing for people living or travelling remote, off-grid locations. [10]

Fig. 4. Source http://innovativevendingsolutions.com/case-studies/td-solar-powered/

In the age of Coronavirus, as more consumers rely on vending machines to get their food and beverages, solar–powered vending machines only enhances the value of vending machines. Consumers can have confidence in knowing that regardless of what's happening with the power grid, as long as the vending machine is solar–powered, it's always going to be working.
Vending owners who own solar–powered vending machines can also have confidence that their devices are offering consumers real value while they are also doing their part to lower their carbon footprint by owning an environmentally friendly vending machine.[15]
The energy independence of the sales system ensures the creation of a green product with a low impact on the environment and also allows its placement in areas where electricity cannot be provided from other sources.
Taking into account the existing models, we developed an autonomous vending-machine type equipment that would allow the analysis of the operation of a system for selling cold and/or hot products that would be powered with the help of solar panels. In order to study the problems that arise in the case of the creation of such equipment, we designed and created an experimental model made on a real scale. The trading of products with the help of automatic systems allows getting closer to the customer. The customer does not have to travel long distances, with the help of means of transport that emit CO2, to procure certain products. Also, trading with the help of vending machines allows them to be fed at night, when fuel consumption for transporting goods from the warehouse to the point of sale is reduced and the impact of CO2 emissions is lower.

The experimental model

The proposed experimental model has dimensions similar to those of the sales system to be designed and built for commercialization.

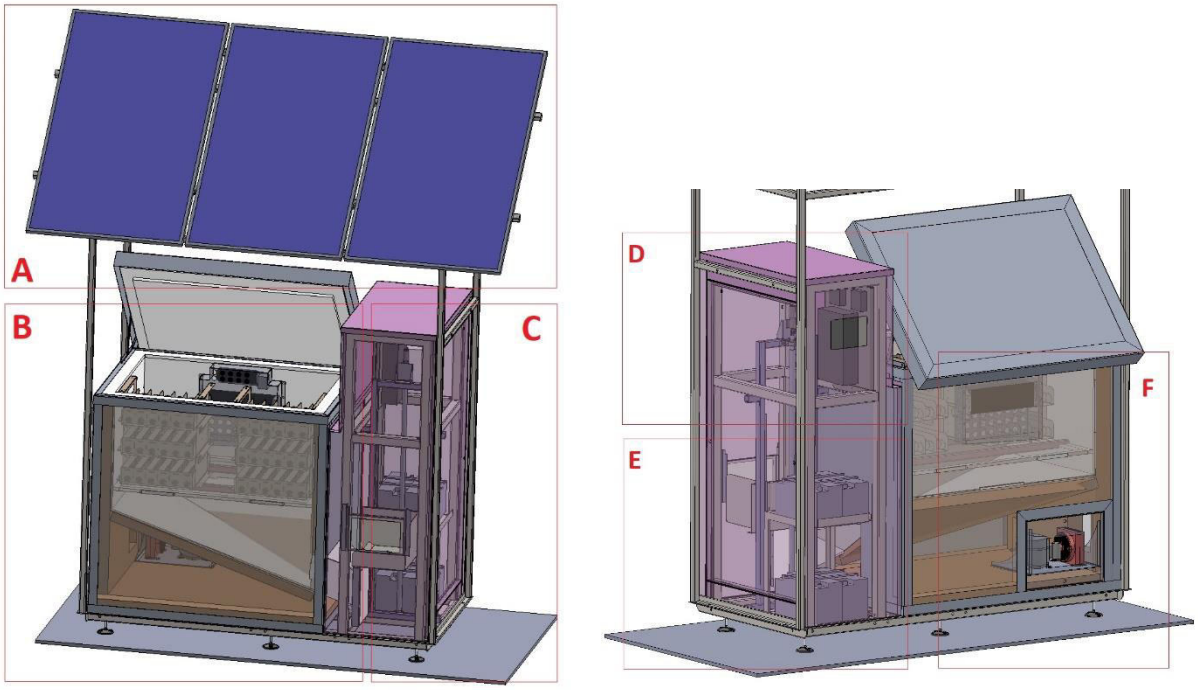

Fig. 5. Subsystems of the experimental model

Fig. 6. Experimental model

The experimental model designed and made has the following subsystems:

- Electricity production subsystem - A
- The thermally insulated enclosure subsystem - B;
- Product delivery subsystem - C;

- The command and control subsystem – D;
- The electricity storage subsystem – E;
- Refrigeration installation subsystem – F.

The efficient functioning of the entire system is determined by the structure and fulfillment of the functional roles of all the equipment components, as follows:

- the metallic structure of the experimental model ensures the support for the component elements;
- the subsystem - thermally insulated enclosure - is made of materials with low thermal transfer and represents the area where the products are stored for delivery.
- The products are fed on the upper part of the equipment and their delivery is carried out on the lower part; the product delivery function is ensured by a complex system consisting of two large components: the product tray in which the products are stored for delivery and the collection and transport system for delivery to the consumer;
- the refrigeration installation is the system that produces cold in a thermally insulated room;
- the production and storage of electricity is carried out by the system that uses photovoltaic panels for the conversion of solar energy into electricity which, through a management system, is either stored in accumulators or delivered to the consumers of the experimental model;
- the command and control functions are ensured by the electronic automation system that controls the thermal subsystem, the product delivery system, the communication of data received from the sensor systems, the remote control through an interface that the consumer accesses from a personal device.

The initial and final stages of the product's route inside the equipment are as follows: the product to be delivered to the consumer is loaded (by lifting the thermally insulated cover by tilting and inserting the trays with previously loaded products) in the upper area of the thermally insulated enclosure. The unloading of the product is carried out with the help of a spiral system, with which the product tray is equipped, in the collecting funnel of the thermally insulated enclosure that directs the mechanism for taking and delivering the products to the tray (see figure no. 1).

Fig. 7. Thermally insulated enclosure

The product is then lifted to the area where the product is picked up by the consumer, this area being equipped with a manually operated door.

The product delivery experimental model is energy independent and is designed in such a way as to use as efficiently as possible the electricity produced with the help of photovoltaic panels.
The main objective of this work is to analyze the consumption of the cold production installation in the thermally insulated premises, so that, in the following, it is presented how to achieve it.
In the design stage and later, in the manufacturing stage of the subsystem of the thermally insulated enclosure, the use of materials that have a heat transfer coefficient as low as possible was taken into account.
Thus, a new composite material (consisting of three different materials) was chosen for the construction of the enclosure, both for the product storage tank and for the tilting cover of the enclosure. On the inside, a Komacel expanded PVC [17] type plastic material was used, on the middle part we used a high-performance insulating material of the Termoconfort type [18], and on the outside, a material resistant to the weather and exposure to solar radiation, Bond PE type [16], was used.

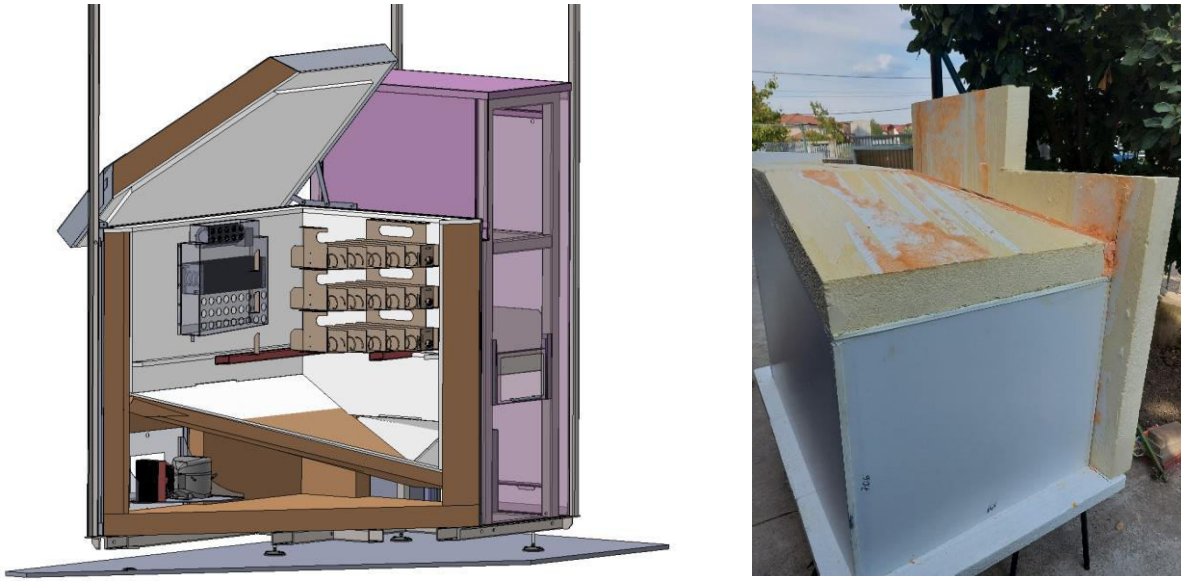

Fig. 8. Realization of a thermally insulated enclosure

The use of these materials was aimed at ensuring the highest possible energy efficiency, but also the possibility of recycling the materials in the post-use stage. The realization of the experimental model on a natural scale allowed the validation of the technology and the manufacturing costs of the energy-efficient vending machine that will be produced in series.

Fig. 9. Refrigeration installation subsystem

The application of these manufacturing technologies allows obtaining superior energy performances but also reduced manufacturing costs by using existing materials and technologies.
The following equipment was used for the cold production installation: Evaporator coil; Evaporator fan motor (electrical power 36 W) Condenser coil; Condenser fan motor (electrical power 38 W) Hermetical single speed compresor (cooling capacity 523 W, condensing temperature 45 C Evaporating temperature -10 C [19]). Refrigerant installation uses R290 as a refrigerant.
The experimental model is equipped with a complex system of sensors whose values are collected and sent continuously via the Internet to a server. The collected data are stored in the server so that they can later be analyzed either in real mode through an Internet browser, or to be downloaded in the form of a database. The data stored on the server are: temperatures on three levels in the thermally insulated enclosure; ambient temperature; consumption for the refrigeration system [W]; consumption for the product heating system [W]; consumption for the interphase product transport system [W]; data provided by the photovoltaic system through the MPPT solar charge controller (Baterry [mV]; Baterry injected current [mA]; Solar voltage [mV]; Solar power [W]; etc).

Fig. 10. Data server interface experimental model

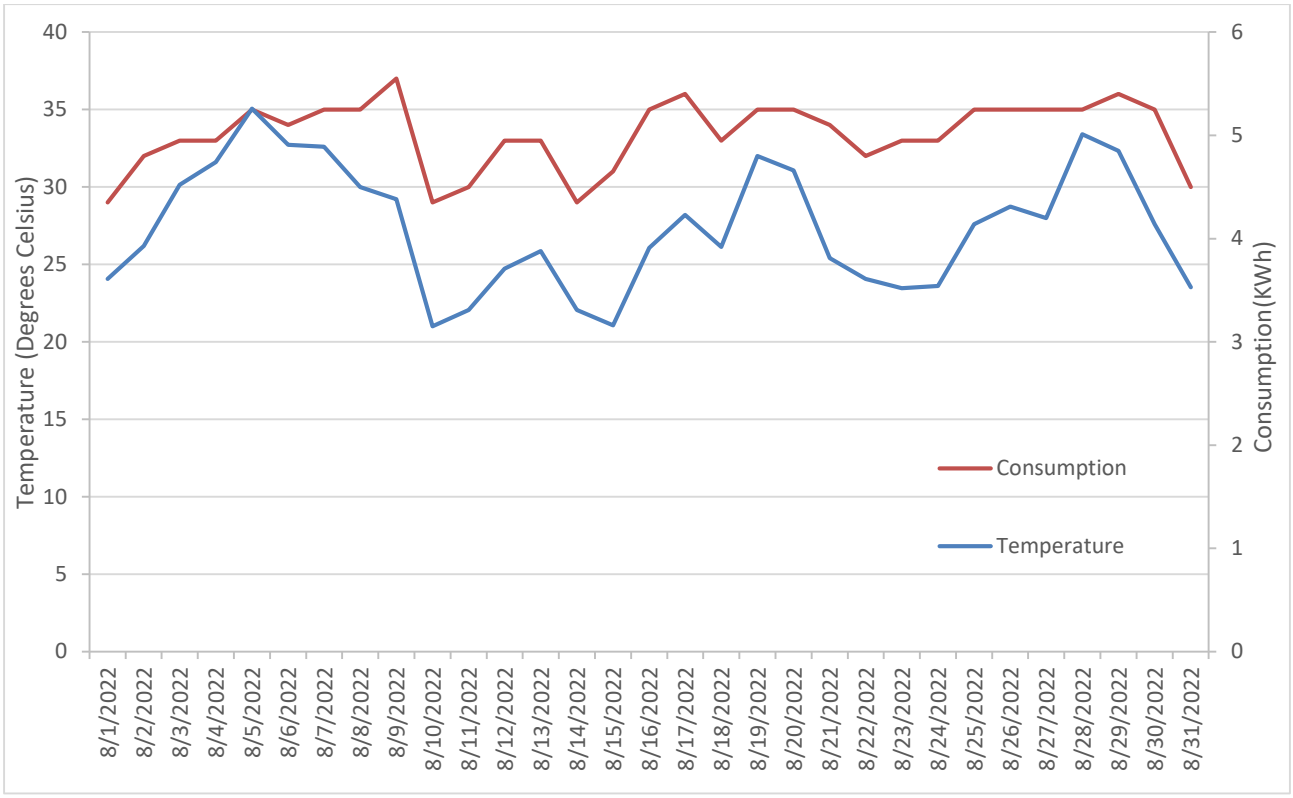
Temperature (Degrees Celsius)
Consumption(KWh)
Consumption
Temperature
40
35
30
25
20
15
10
5
0
6
5
4
3
2
1
0
8/1/2022
8/2/2022
8/3/2022
8/4/2022
8/5/2022
8/6/2022
8/7/2022
8/8/2022
8/9/2022
8/10/2022
8/11/2022
8/12/2022
8/13/2022
8/14/2022
8/15/2022
8/16/2022
8/17/2022
8/18/2022
8/19/2022
8/20/2022
8/21/2022
8/22/2022
8/23/2022
8/24/2022
8/25/2022
8/26/2022
8/27/2022
8/28/2022
8/29/2022
8/30/2022
8/31/2022

Fig. 11.

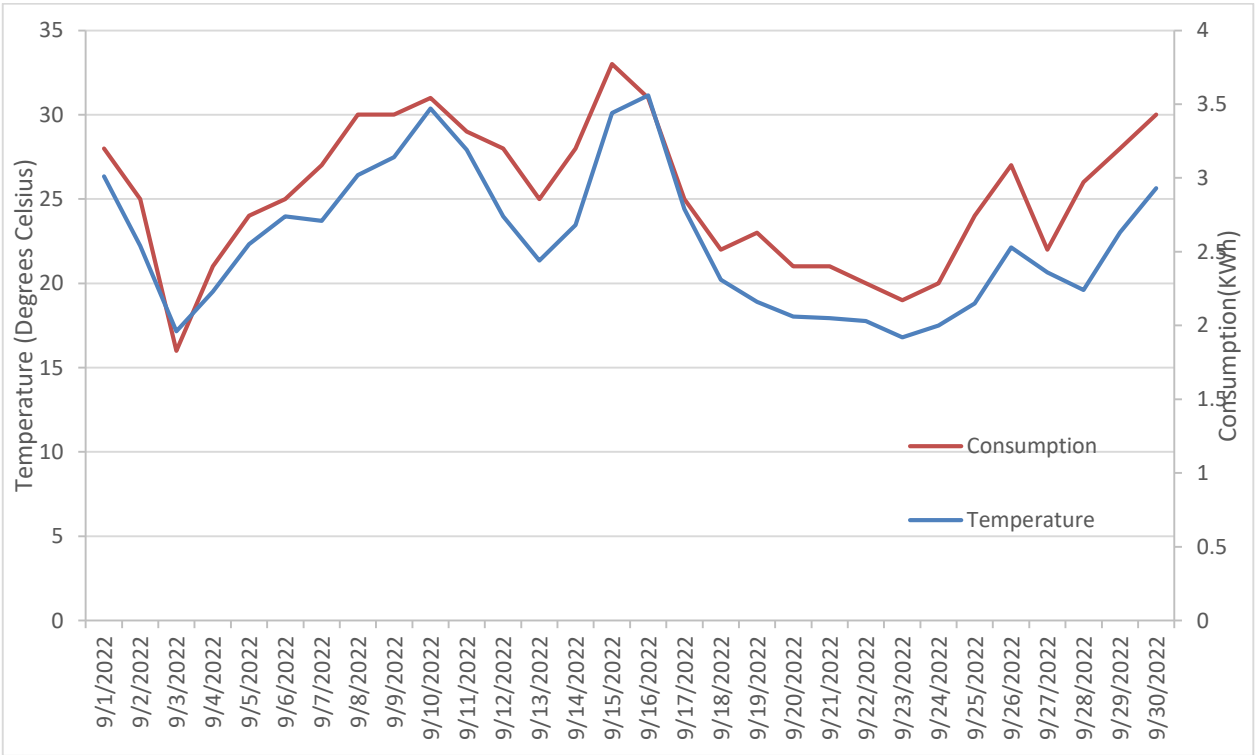
Temperature (Degrees Celsius)
Consumption(KWh)
Consumption
Temperature
35
30
25
20
15
10
5
0
4
3.5
3
2.5
2
1.5
1
0.5
0
9/1/2022
9/2/2022
9/3/2022
9/4/2022
9/5/2022
9/6/2022
9/7/2022
9/8/2022
9/9/2022
9/10/2022
9/11/2022
9/12/2022
9/13/2022
9/14/2022
9/15/2022
9/16/2022
9/17/2022
9/18/2022
9/19/2022
9/20/2022
9/21/2022
9/22/2022
9/23/2022
9/24/2022
9/25/2022
9/26/2022
9/27/2022
9/28/2022
9/29/2022
9/30/2022

Fig. 12.

Following the tests carried out with the help of the experimental model, we collected more data regarding the operation of a system for the automatic sale of cold and hot products, an energy independent system. From the complex of multidisciplinary data, this paper presents, in summary, an analysis of the electricity consumption of the refrigeration system in correlation with the ambient temperature. The presented data were extracted from the database in which the experimental model of the energy independent sales system stores the values recorded from the sensors it is equipped with. The analysis is carried out for August and September 2022, in fig. 11 and fig. 12, being presented in the form of graphs, the daily consumption (KWh) of the cooling subsystem and the ambient temperature (degrees Celsius).
Analyzing the graphs presented previously, we notice that there is a direct dependence between the electricity consumption and the energy consumption of the refrigeration system that ensures the internal temperature of around 6 degrees Celsius in the premises where the products to be delivered are stored. In August, the average outside temperature was 33.38 degrees Celsius, and in September, an average temperature of 25.30 degrees Celsius was reached.
In the analyzed period, the system consumed a total of 127.44 kWh for the month of August 2022. The daily average consumption was 4.11 KWh. Considering the value mentioned in the electricity label [] of an electricity supplier from Romania, for the production of electricity in the year 2021, the level of CO2 emissions was 217.24 g/KWh. Using this value of CO2 emissions, in determining the level of emissions for the cooling system of the experimental model, we conclude that by using solar panels we can obtain a reduction in CO2 emissions of 0.027685 tons of CO2 in August 2022.
In September 2022, the experimental model consumed a total of 77.58 kWh. The average daily consumption was 2.50 KWh. Considering the value mentioned in the electricity label [12] of an electricity supplier from Romania, for the production of electricity in the year 20211, the level of CO2 emissions was 217.24 g/KWh. Using this value of CO2 emissions, in determining the level of emissions for the cooling system of the experimental model, we conclude that by using solar panels we can obtain a reduction in CO2 emissions of 0.016853 tons of CO2 in September 2022.

Conclusions

The realization of an experimental model on a real scale for an automatic sales system of cold and hot products allowed the performance of tests that, in the case of a complex system, would not be conclusive for a reduced-scale model.
Following the presented analysis, we can say that the use of renewable sources to power an automatic sales system leads to a significant reduction in CO2 emissions. The reduction of CO2 emissions has a beneficial effect on the environment, which recommends these systems for use in the urban environment or in protected geographical areas.
For the two months analyzed in terms of consumption, a total consumption of 205.22 KWh was recorded, which corresponds to an average consumption of a house for one month [9]. The total value of reduced CO2 emissions is 0.0445 tons, equivalent to a road of about 280 km traveled by a mid-range gasoline car, with an emission level of 160 grCO2/km. Considering the large number of vending machines currently existing in the urban environment and the future regarding the use of these systems, the reduction of energy consumption and CO2 emissions will be significant in the energy balance and in terms of environmental protection from urban areas.

Acknowledgments

This work is part of the Competitiveness Operational Program Innovative Energy Efficient Sales Systems for Urban Use (acronym, SVIEE MySMIS code 121420), a project co-financed by the European Regional Development Fund.

References

[1] Matthews, M., and T. Horacek. “Vending machine assessment methodology. A systematic review.” *Appetite* 90 (2015): 176–186. http://dx.doi.org/10.1016/j.appet.2015.03.007.

[2] Martinez-Perez, N., and M. Arroyo-Izaga. “Availability, Nutritional Profile and Processing Level of Food Products Sold in Vending Machines in a Spanish Public University.” *Int. J. Environ. Res. Public Health* 18 (2021): 6842. https://doi.org/10.3390/ijerph18136842.
[3] https://ecofriend.com/solar-energy-powers-awesome-vending-machines.html. Accessed on 22 April 2022.
[4] Solano, A., N. Duro, R. Dormido, and P. González. “Smart vending machines in the era of internet of things.” *Future Generation Computer Systems 76* (2017): 215–220. http://dx.doi.org/10.1016/j.future.2016.10.029
[5] Sibanda, V., L. Munetsi, K. Mpofu, E. Murena, and J. Trimble. “Design of a high-tech vending machine.” *Procedia CIRP* 91 (2020): 678-683. http://dx.doi.org/10.1016/j.procir.2020.04.133.
[6] Ratnasri, Nilani, and Tharaga Sharmilan. “Vending Machine Technologies: A Review Article.” *International Journal of Sciences: Basic and Applied Research (IJSBAR)* 58, no. 2 (2021): 160-166.
[7] Sethi, A., E. Becerra, and S. Motta. “Low GWP R134a replacements for small refrigeration (plug-in) applications.” *International Journal of Refrigeration* (2016): 64–72. http://dx.doi.org/10.1016/j.ijrefrig.2016.02.005.
[8] Wongsuwan, W., R. Kallaka, and P. Chaiwiwatworakul. “Energy Efficiency of the Beverage Vending Machine Refrigeration System.” Paper presented at the International Conference on Power, Energy and Innovations (ICPEI), Nakhon Ratchasima, Thailand, October 20–22, 2021.
[9] https://sameday.ro/news/easybox-autonom/.
[10] https://ecofriend.com/solar-energy-powers-awesome-vending-machines.html.
[11] https://www.springwise.com/solar_powered_vending_machines/.
[12] https://www.enel.ro/enel-energie/ro/informatii-utile/reglementari/eticheta-energiei-electrice.html.
[13] https://www.solidworks.com/domain/simulation.
[14] https://www.springwise.com/solar_powered_vending_machines/.
[15] https://innovativevendingsolutions.com/td-solar-powered-vending-machine-enables-company-to-lower-carbon-footprint-from-vending-connection/.
[16] https://leykom.ro/catalog/product/view/id/2909/s/bond-pe/category/8/.
[17]https://www.komasheets.com/en/products/advertising-sector/koemacel-advertising/?tab=technical_documentation.
[18] https://joriside-thermoconfort.eu/wp-ontent/uploads/2022/02/Thermoconfort_Technical_EN.pdf.
[19] https://www.embraco.com/wp-content/uploads/2021/12/eweb-compressors-072020-en.pdf.

ISSN 1454 - 8003
Proceedings of 2022 International Conference on Hydraulics and Pneumatics - HERVEX
November 9-10, Băile Govora, Romania

THE INFLUENCE OF THE ROTORS SHAPE ON THE FLOW RATE CONVEYED BY A ROTATING VOLUMETRIC PUMP

Gabriel FISCHER- SZAVA[1], Georgiana DĂESCU (DUICULETE)[1], Nicolae BĂRAN[1], Rana ADIL ABDUL-NABE[1], Mihaela CONSTANTIN[1,*], Cătălina DOBRE[1]

[1] University Politehnica of Bucharest

*i.mihaelaconstantin@gmail.com

Abstract: *The paper presents a new type of rotating volumetric pump with two profiled rotors, which is based on a patent. The calculation relations for the pump flow rate and its driving power are deduced. The influence of the shape of the rotors on the flow conveyed by the rotary pump takes place in two ways:*
1- by the shape of the rotating pistons
2- through the influence of the main dimensions of the rotating machine (rotor length, rotor radius, rotating piston height).

Keywords: *Rotating machine, volumetric pump, profiled rotors*

1. Introduction

The machines are aggregates used to transform energy from one form to another with the help of a mobile organ (piston, profiled rotor, blade) [1-2].
Machines, according to their intended purpose, are divided into two large categories [3-5]:
1. Power machines (motor machines), which transform a certain form of energy into mechanical energy (internal combustion engines, steam, or gas turbines, etc.).
2. Working machines, which transform mechanical energy into potential pressure energy (fans, pumps, compressors).
Force and working machines that are traversed by fluids, according to the variation of the flow parameters, are classified as follows (table 1):
a. Hydraulic machines, which circulate or are actuated by liquids, where thermal phenomena are neglected.
b. Thermal machines, which circulate gases or vapors (or are acted upon by them) in which the thermal phenomena that occur are not neglected.
The realization of high-performance rotating machines (pumps, fans, blowers) is current.

Table 1: A general classification of rotating machines

Classification by purpose	Depending on the constructive solution	According to the working parameters
Working machines	Machines with profiled rotors	a) Fans, blowers, pumps
	Blade machines	b) Fans, blowers
Force machines	Machines with profiled rotors	c) Internal combustion engines, steam or gas engines, pneumatic engines
	Blade machines	d) Steam turbines, gas turbines

Researches aims to build machines that ensure the transformation of the engine torque received from the shaft into useful effects, but with as little energy loss as possible.
Table 2 presents the classification of rotating machines with profiled rotors according to the purpose pursued and the adopted constructive solution [6].

Table 2: Classification of rotating machines with profiled rotors

Rotating machines with profiled rotors	**Classification by purpose**	**Classification in terms of construction**
	Working machines	Pumps for driving fluids or with suspensions
		Fans for transporting gases or vapors
		Blowers for gas and vapor compression
	Force machines	Hydraulic motor
		Pneumatic motor
		Steam engine or combustion gases

From the category of rotating working machines for the circulation of liquids, rotating pumps are presented.
In technics, there are two main criteria for classifying pumps [7-9]:
I. According to the operation principle;
II. By training mode.
I. According to the principle of operation, two categories are distinguished:
A. Volumetric pumps;
B. Non-volumetric pumps.
II. According to the driving mode, three categories of pumps are distinguished [10]:
a) Electric pumps;
b) Motor pumps;
c) Turbo pumps.

Table 3: Categories of pumps

A) Volumetric pumps	Piston pumps	a) Single cylinder pumps
		b) Polycylindrical pumps
		c) Pumps with axial pistons
	Rotating pumps	d) Pumps with blades
		e) Gear pumps
		f) Screw pumps
		g) Lobe pumps
B) Non-volumetric pumps	Centrifugal pumps	
	Axial pumps	

A more difficult problem is to make a rotating machine that can be used as a working machine or a power machine, that is, in theory, a "reversible" machine [11,12].
Such a type of machine must ensure:
- transformation of the useful moment with minimal losses when it works as a working machine;
- the full use of the energy of the working agent to actuate the shaft when it works as a force machine.

2. Rotating volumetric pump with two profiled rotors with triangular-shaped rotating pistons

In this version, the rotating piston has the shape of a triangle due to the materials strength (figure 1). For the specified values for R_r, z, the base of the piston triangle (i.e., the piston section) was dimensioned.

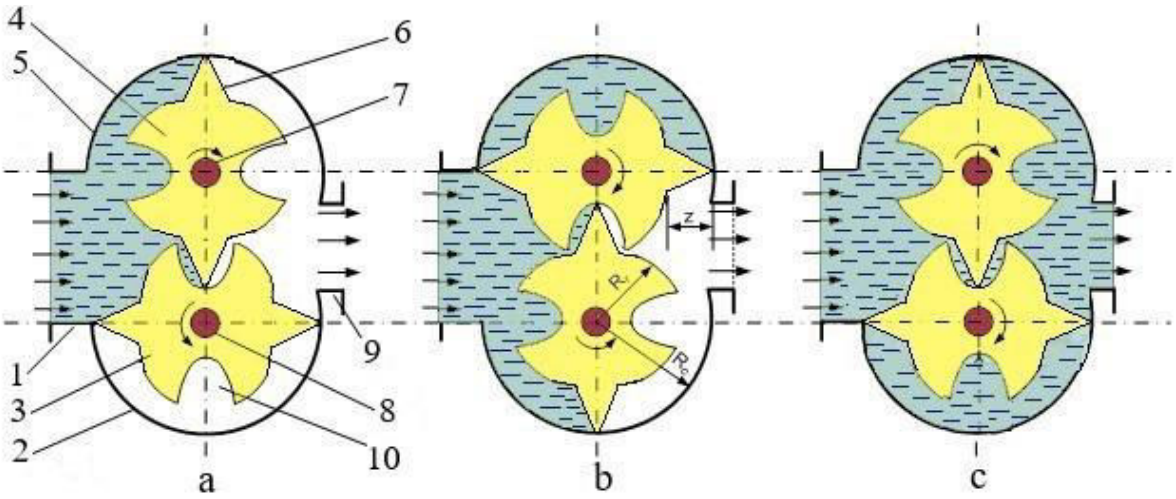

Fig. 1. The operating principle of the rotating volumetric machine
1- suction chamber; 2 - lower casing; 3- lower rotor; 4- upper rotor; 5- upper casing; 6 - rotating piston; 7- driven shaft; 8 - driving shaft; 9- discharge chamber; 10 - cavity into which the piston of the upper rotor enters.

The fluid in the chamber (1) is taken up by the rotating pistons (6) and transported to the discharge chamber (9).
On the shafts 7 and 8 two toothed wheels are mounted (figure 2) which form a cylindrical gear; thus, the penetration of the pistons 6 from the upper rotor into the cavities 10 from the lower rotor (3) is ensured.

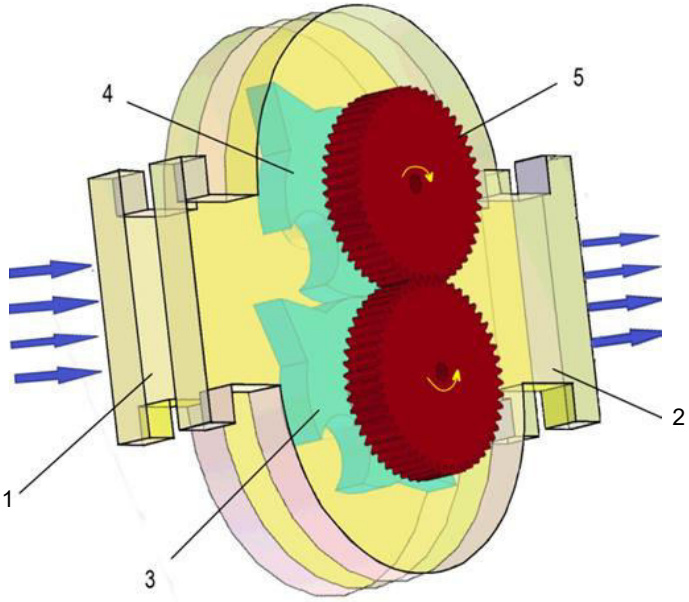

Fig. 2. Cylindrical gear mounted on the shafts of the two rotors

1 – suction chamber; 2 – discharge chamber; 3 – lower rotor; 4 – upper rotor; 5 – cylindrical gear.

Profiled rotors can have different shapes (figure 3):
Variant I: rectangular blades;
Variant II: an isosceles triangle;
Variant III: a curvilinear profile.

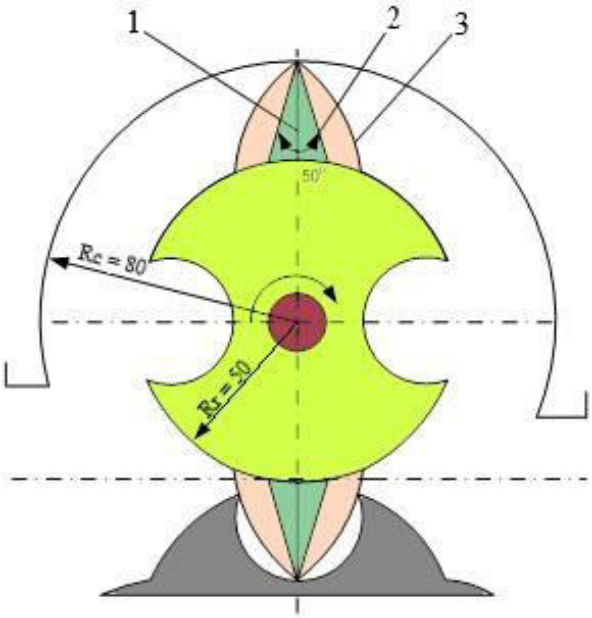

Fig. 3. Rotor with rotating pistons
1- rectangular lamella; 2- triangular profile; 3- curvilinear profile

3. Calculation of the flow rate transported by the machine with profiled rotors with rotating triangular pistons

Figure 4 shows a cross section through the rotating machine.

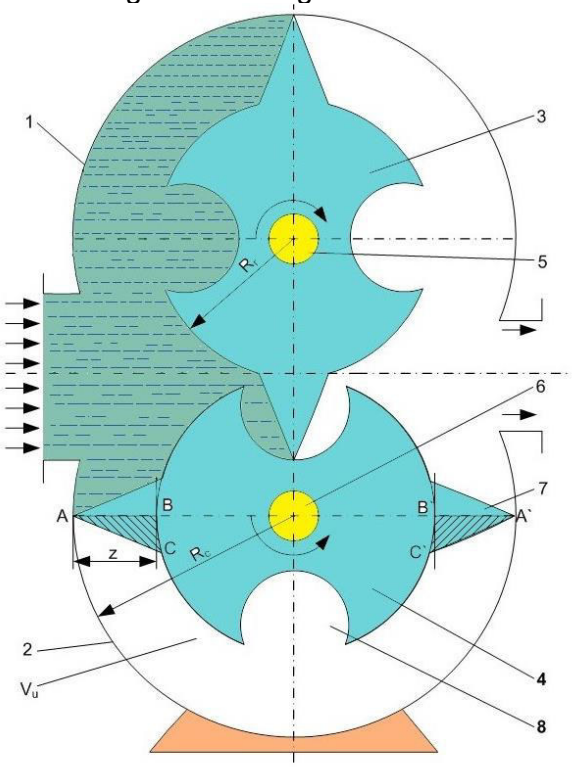

Fig. 4. Cross-section through the rotating working machine
1 - upper casing; 2 - lower casing; 3 - upper rotor; 4 - lower rotor; 5,6 – shafts;
7 - triangular piston; 8 - the cavity into which the piston enters.

The paper will analyze the case where the rotating pistons of the two rotors have a triangular shape.
The contour of the rotor was established after the elaboration of a very complicated calculation program and the construction of the rotors was carried out on a computer numerical control center (C.N.C) [13, 14].
The constructive solution ensures a good resistance of the piston and two sealing zones: between the piston tip and the inside of the casing and between the piston tip and the cavity.
As one can see in figure 4, the useful volume V_u is reduced by the volumes of prisms ABC and A'B'C'; it is equal and together will give the volume of a piston of triangular section, i.e., a prism with dimensions:
-height: z = 30 [mm];
-base: b = 30 [mm];
-length: l = 50 [mm].
The cross-sectional area between the base of the prism and the rotor is neglected. The volume of this prism will be [15]:

$$V_p = A_{base} \cdot l = \frac{1}{2} \cdot b \cdot z \cdot l = \frac{1}{2} \cdot 0.03 \cdot 0.03 \cdot 0.05 ; \quad V_p = 0.0225 \cdot 10^{-3} \ [m^3 / rot] \tag{1}$$

Compared to the theoretical flow transported by the machine, in version I: $\dot{V}_I = \pi l z (z + 2R_r) \cdot \frac{n_r}{30} \ [m^3/s]$, the theoretical flow of the machine in this version will be reduced by V_{pII}
The fluid flow rate transported by a rotor:

$$\dot{V}_u = \left[\pi l z \left(z + 2R_r \right) - V_{p,II} \right] \ \left[m^3 / rot \right] \tag{2}$$

The machine has two identical rotors, so the flow rate will be:

$$\dot{V}_u = \left[\pi l z (z + 2R_r) - \frac{1}{2} b z l \right] \cdot \frac{n_r}{30} \ \left[m^3 / s \right] \tag{3}$$

For the same data as in variant I, but in addition: b = 0.03 [m], and the same speed, a flow rate is obtained:

$$\dot{V}_u = \left[\pi \cdot 0.05 \cdot 0.03 \left(0.03 + 2 \cdot 0.05 \right) - \frac{1}{2} \cdot 0.03 \cdot 0.03 \cdot 0.05 \right] \cdot \frac{500}{30} \tag{4}$$

$$\dot{V}_u = 0.00983 \ [m^3/s] = 35.388 \ [m^3/h] \tag{5}$$

Table 4: The values of $\dot{V} = f(n_r)$ - Variant I

n_r [rev/min]	100	200	300	400	500
$\dot{V}_I$ [m³/s]	0.002041	0.004082	0.006123	0.008164	0.010205
$\dot{V}_I$ [m³/h]	7.3476	14.6952	22.0428	29.3904	36.738

Table 5: The values of $\dot{V} = f(n_r)$ - Variant II

n_r [rev/min]	100	200	300	400	500
$\dot{V}_{II}$ [m³/s]	0.001966	0.003932	0.005898	0.007864	0.00983
$\dot{V}_{II}$ [m³/h]	7.0776	14.1552	21.2328	28.3104	35.388

Table 6: The values of $\dot{V} = f(n_r)$ - Variant III

n_r [rev/min]	100	200	300	400	500
$\dot{V}_{III}$ [m³/s]	0.00190977	0.00381953	0.0057293	0.00763907	0.0095883
$\dot{V}_{III}$ [m³/h]	6.87516	13.75032	20.62548	27.50064	34.3758

Based on the data from table 4, 5 and 6, the function $\dot{V} = f(n_r)$ - was represented in figure 5.

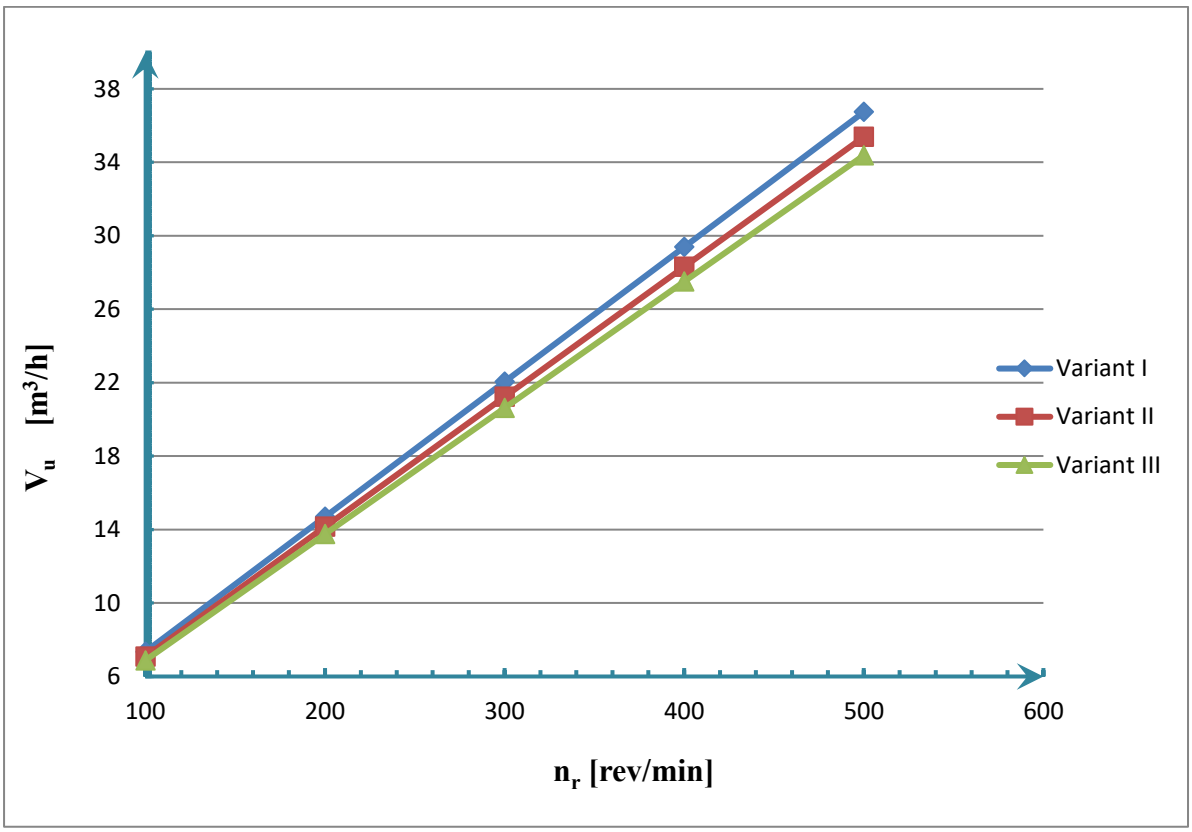

Fig. 5. Graphical representation of the function $\dot{V} = f(n_r)$ for different machine speeds
Variant I - rectangular blade shape piston, R_r = 50 [mm], z =30 [mm];
Variant II - piston in the form of an isosceles triangle, R_r = 50 [mm], z =30 [mm];
Variant III - curvilinear piston, R_r = 50 [mm], z =30 [mm].

From figure 5, one can see that the flow rate transported by the rotating machine is the highest in the case of variant I (the rotor is provided with rectangular blades).

4. Calculation of the theoretical driving power for the volumetric pump

The theoretical driving power of the rotary machine for the three constructive solutions can be calculated as follows [16,17]:

$$P = \dot{V} \cdot \Delta p = \pi \cdot l \cdot z \cdot (z + 2R_r) \cdot \frac{n_r}{30} \cdot \Delta p \quad [W] \tag{6}$$

$$\Delta p = \rho g \Delta H \quad [N/m^2] \tag{7}$$

where:

* $\dot{V}$ – volumetric flow rate [m³/s];

* Δp – pressure increase [N/m^2];
* ΔH – pumping height [m];
* ρ_l – density of the transported fluid [kg/m^3].

The total pressure increase achieved by the pump (Δp) changes when the pump speed increases; the hydrostatic load and pressure losses occurring in the hydraulic circuit of the pump are evaluated at about 4 mH_2O [18- 20]:

$$\Delta p = \rho_{H_2O} \cdot g \cdot H = 10^3 \cdot 9.81 \cdot 4 = 0.3924 \cdot 10^5 \ \ [Pa] \tag{8}$$

Next, based on the values of the flow rates previously obtained, the theoretical driving power is calculated.

For n_r = 500 [rev/min], substituting the values in relation (6) one can obtain:

Variant I - piston in the form of a blade:

$$P = \dot{V} \cdot \Delta p = 0.010205 \cdot 0.3924 \cdot 10^5 = 400.044 \ \ [W] \tag{9}$$

Carrying out similar calculations, the values of P are obtained for n_r = 100, 200, 300, 400 and 500 [rev/min] presented in table 7, 8 and 9.

Table 7: The values of $P = f(n_r)$ - Variant I

n_r [rev/min]	100	200	300	400	500
P [W]	80.088	160.177	240.266	320.355	400.444

Variant II - piston in the form of an isosceles triangle:

$$P = 0.00983 \cdot 0.3924 \cdot 10^5 = 385.729 \ \ [W] \tag{10}$$

Table 8: The values of $P = f(n_r)$ - Variant II

n_r [rev/min]	100	200	300	400	500
P [W]	77.145	154.291	231.437	308.583	385.729

Variant III - curvilinear shaped piston:

$$P = 0.00954883 \cdot 0.3924 \cdot 10^5 = 374.696 \ \ [W] \tag{11}$$

Table 9: The values of $P = f(n_r)$ - Variant III

n_r [rev/min]	100	200	300	400	500
P [W]	74.939	149.878	224.817	299.756	374.696

Based on the data in tables 7, 8 and 9 the function $P = f(n_r)$ was graphically represented in figure 6, for the three constructive variants.

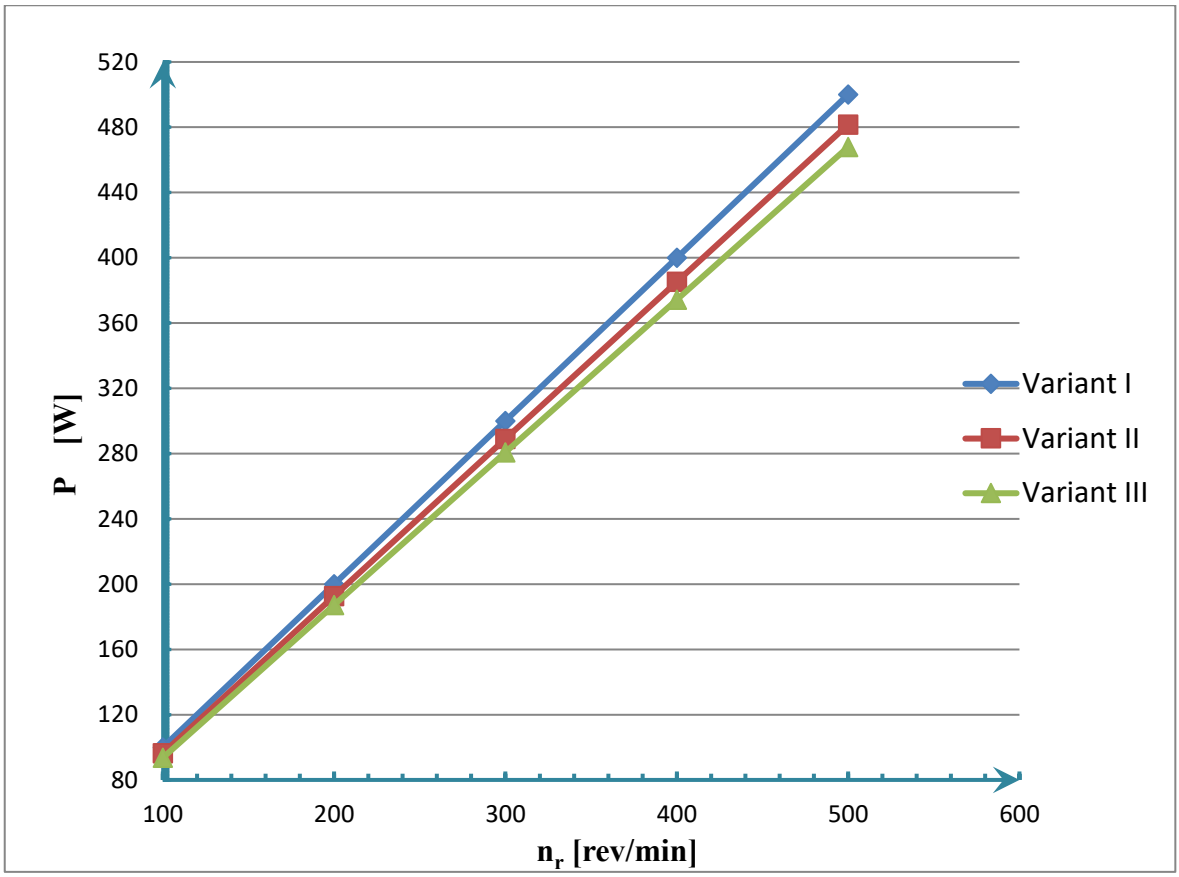

Fig. 6. Graphical representation of the function $P = f(n_r)$ for the three constructive variants
Variant I - rectangular blade shape piston, R_r = 50 [mm], z =30 [mm];
Variant II - piston in the form of an isosceles triangle, R_r = 50 [mm], z =30 [mm];
Variant III - curvilinear piston, R_r = 50 [mm], z =30 [mm].

From figure 6, a linear dependence is observed between the theoretical driving power and the speed of the rotating machine.
Obviously, if the flow rate for variant I is the highest, then the driving power will also be higher (variant I).

5. Conclusions

1. The flow rate transported by the rotating machine varies according to the following:
- the geometric parameters: l – rotor length [m]; R_r – rotor radius [m]; z – piston height [m];
- the functional parameters: n_r – machine speed [rev/min].
2. The driving power is influenced by the flow rate (that is, by the parameters mentioned above) by the increase in pressure (Δp) achieved by the rotating machine between suction and discharge, by the nature of the transported fluid. The pressure increase produced by the rotating machine must overcome the hydrostatic load and the pressure losses occurring on both the suction circuit and the discharge circuit of the pump.
3. In variant I (pistons in the form of rectangular blades) the flow rate transported by the rotating machine will be the highest compared to variant III.
This high flow rate will require a higher driving power of the machine: $P_I > P_{II} > P_{III}$ [W].

References

[1] Băran, N. *Rotating thermic machines. Working machines. Force machines / Masini termice rotative. Masini de lucru. Masini de forta*. Bucharest, MATRIXROM Publishing House, 2001.
[2] Băran, N. *Working rotating thermic machines. Machines with profiled rotors. Blade machines* / *Masini termice rotative de lucru. Masini cu rotoare profilate. Masini cu palete*. Bucharest, MATRIXROM Publishing House, 2003.
[3] Dobrovicescu, Al., N. Băran, Al. Chisacof, S. Petrescu, E. Vasilescu, D. Isvoranu, M. Costea, C. Petre, and A. Motorga. *Bases of Technical Thermodynamics. Vol. I. Technical Thermodynamics Elements* / *Bazele termodinamicii tehnice. Vol. I. Elemente de termodinamică tehnică*. Bucharest, Politehnica Press Publishing House, 2009.
[4] Exarhu, M. *Hydraulic and pneumatic machines and installations* / *Mașini și instalații hidraulice și pneumatice*. Bucharest, AGIR Publishing House, 2006.
[5] Hanlon, Paul C. (Ed.). *Compressor Handbook*. New York, McGraw Hill, 2001.
[6] Motorga, A. *Influenţa parametrilor constructivi şi funcţionali asupra performanţelor maşinilor rotative cu rotoare profilate* / *Influence of constructive and functional parameters on the performances of rotating machines with profiled rotors*. PhD Thesis. Faculty of Mechanical Engineering and Mechatronics, Politehnica University of Bucharest, 2011.
[7] Băran, N., Despina Duminica, Daniel Besnea, and Antonios Detzortzis. "Theoretical and Experimental Researches Regarding the Performances of a New Type of Rotating Machine with Profiled Rotors." *Advanced Materials Research* 488-489 (2012): 1757-1761.
[8] Burchiu, V., I. Santău, and O. Alexandrescu. *Pumping installations* / *Instalaţii de pompare*. Bucharest, Didactic and Pedagogical Publishing House, 1982.
[9] Hâncu, S. *Fluid Mechanics*. Bucharest, CONPRESS Publishing House, 2011.
[10] Reynolds, A.J. *Turbulent flows in Engineering* / *Curgeri turbulente în tehnică*. Bucharest, Technical Publishing House, 1982.
[11] Ţurcanu, C., and N. Ganea. *Volumetric Pumps for Liquids* / *Pompe volumice pentru lichide*. Bucharest, Technical Publishing House, 1980.
[12] Vasiliu, N., and D. Vasiliu. *Fluid Power* / *Acționări hidraulice și pneumatice*. Bucharest, Technical Publishing House, 2004.
[13] Hawas, M. *The influence of fluid viscosity on the performance of rotating machine with profiled rotors*. PhD Thesis. Politehnica University of Bucharest, 2015.
[14] Besnea, D., G. O. Donțu, and N. Alexandrescu. *Computer-aided manufacturing technologies for the production of mechatronic components* / *Tehnologii de fabricație asistate de calculator pentru execuția unor componente mecatronice*. Bucharest, Printech Publishing House, 2008.
[15] Stoican (Prisecaru), Mariana Mirela, Nicolae Băran, and Almaslamani Ammar Fadhil Shnawa. "Establishing the mathematical relation between the rotor radius and the height of the rotating piston for a rotating machine with profiled rotors." *Hidraulica Magazine* no.1 (2020): 64 - 69.
[16] Băran, N., D. Ion, and Al. Motorga. "A new type of machine that can work as a pump or as a hydraulic motor"/ "Un nou tip de mașină care poate funcționa ca pompă sau ca motor hidraulic." *Revista Hidrotehnica* 53, no. 7-8 (2008).
[17] Bansal, R. K. *A Textbook of Fluid Mechanics and Hydraulic Machines*. New Delhi, India, Laxmi Publications, 2005.
[18] Stoican (Prisecaru), M. M., N. Băran, D. Besnea, and A. Costache. "The influence the rotating piston shape on the sealing between two profiled rotors of a rotating machine that transports fluids.*"* Paper presented at the 4th Edition of the International Conference of Mechatronics and Cyber-Mixmechatronics – ICOMECYME, Bucharest, Romania, September 10-11, 2020.
[19] Stoican (Prisecaru), Mariana Mirela, Nicolae Băran, Daniel Besnea, and E. Moraru. "A constructive solution for a rotating machine with profiled rotors that transport fluids.*"* *Journal Fiability & Durability*, no. 1 (2020): 194 - 203.
[20] Stoican (Prisecaru), M. M., N. Băran, and A. Costache. "Calculation elements for establishing the design of a rotating machine that transports fluids." Paper presented at The 9th International Conference on Advanced Concepts in Mechanical Engineering, Iași, Romania, June 04-05, 2020.

ISSN 1454 - 8003
Proceedings of 2022 International Conference on Hydraulics and Pneumatics - HERVEX
November 9-10, Băile Govora, Romania

PLC IMPLEMENTATION OF 2-DOF CONTROLLER FOR HYDRAULIC DRIVES

Marian BLEJAN[1], Robert BLEJAN[1], Ioana ILIE[1]

[1]National R&D Institute for Optoelectronics, Subsidiary Hydraulics and Pneumatics Research Institute Bucharest, blejan.ihp@fluidas.ro

Abstract: *Two-Degree-of-Freedom control systems, abbreviated as 2-DOF, have two independent adjustable closed-loop transfer functions. One is feedback type PID control (proportional – integral – derivative) and the other one is feedforward type control. This kind of control combines the advantage of feedback and feedforward type controllers. On the other hand, the accessibility of programmable logic controller, abbreviated as PLC, with real-time signal processing performance for the control of fast systems (such as hydraulic drives), enables the implementation of high-performance control algorithms that are executed in real time. The paper presents the software implementation in a common PLC of a 2-DOF type controller as well as its monitoring and parameterization software application.*

Keywords*: Hydraulic drive, actuator, controller, PLC*

1. Preliminaries

This chapter presents a brief introduction to the theory of control systems with two degrees of freedom used to implement the controller. The specific requirements for using 2-DOF controllers in hydraulic drives are also presented.
A general form of the 2-DOF control system is shown in fig.1, where the controller consists of two compensators *C(s)* and $C_f(s)$, and the transfer function $P_d(s)$ from the disturbance *d* to the controlled variable *y* is assumed to be different from the transfer function *P(s)* from the manipulated variable *u* to *y*. *C(s)* is called the serial (or main) compensator and $C_f(s)$ - the feedforward compensator [1].

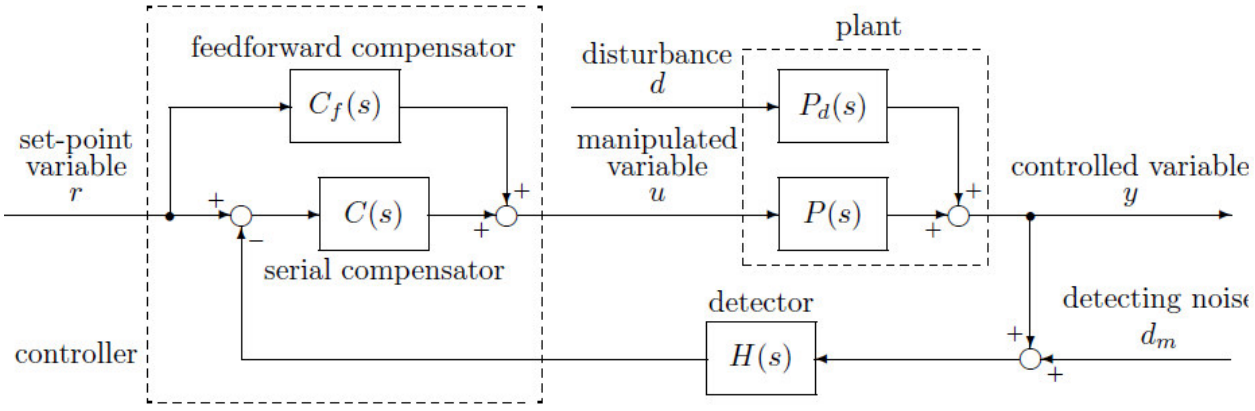

Fig. 1. Two degree of freedom (2-DOF) control system

We consider that

$$H(s) = 1, d_m = 0 \tag{1}$$

and

$$P_d(s) = P(s) \tag{2}$$

Under these assumptions, (1) and (2), a 2-DOF PID control system is shown in fig. 2. Considering that the major advantage of the PID controller lies in its simplicity, it was proposed to include only

the proportional and/or the derivative components in $C_f(s)$. The controller part is a two-input one-output system where the set-point variable *r* and the controlled variable *y* are the input signals and the manipulated variable *u* is the output signal. Thus the feedforward path from *r* to u is adding to the conventional PID command.

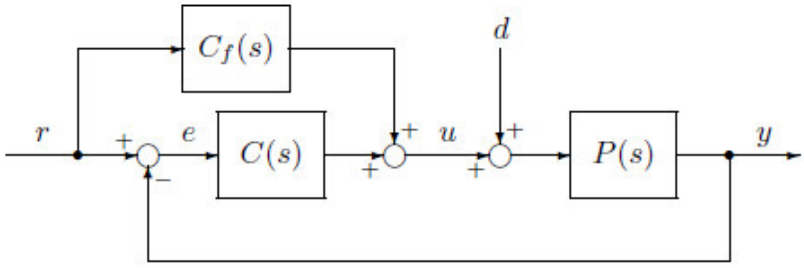

$$C(s) = K_P\left\{1 + \frac{1}{T_I s} + T_D D(s)\right\}$$

$$C_f(s) = -K_P\{\alpha + \beta T_D D(s)\}$$

Fig. 2. Feedforward type of the 2-DOF PID control systems

Mainly, hydraulic drives have two types of actuators, position-controlled linear actuators and speed-controlled rotary actuators. For position-controlled linear actuators, it is necessary to calculate the feedforward path command as the derivative of the reference point because this command value (derivative of the reference point) is proportional to the speed of the manipulated variable (*α=0*), while for speed-controlled rotary actuators the feedforward path command is proportional to the set-point value because the actuators speed (manipulated variable) is also proportional to it (*ß=0*).

2. Controller implementation - PLC software and hardware

Modicon IIoT-native edge controllers manage complex interfaces across assets and devices or directly into the cloud, with embedded safety and cybersecurity. Modicon provides performance and scalability for a wide range of industrial applications up to high-performance multi-axis machines and high-available redundant processes [2]. Modicon M221, an entry-level PLC, was used to implement the 2-DOF PID control algorithm. The software development platform for this PLC is EcoStruxureMachine Expert - Basic, free licence, programing software for M221 controllers.
The hardware platform was built around a TM221CE24T controller with the following characteristics: 14 digital inputs, 10 sources transistor outputs (0.5 A), 2 analog inputs, 1 serial line port, 1 Ethernet port, 24 Vdc power supply controller with removable terminal blocks. A TM3AM6 analogic expansion module is required to interface the actuator with the PLC. TM3AM6 has the following characteristics: 4 analog inputs (+- 10 V, 0-10V, 0-20 mA, 4-20mA) and 2 analog outputs (+- 10 V, 0-10V, 0-20 mA, 4-20mA), 12 bits, removable terminal blocks.
The program running on the PLC implements the operation of the 2-DOF controller and is developed in the ladder diagram language. Thus, the configuration of the controller is established by positioning some bits such as:
- enabling feedforward control
- enabling feedback control (PID or PI+feedforward)
- enabling S-curve generator [3] on set-point path
- sign reversal enabled for controlled variable
- derivative value of set-point for feedforward control, default is set-point value

The value of the process command, manipulated variable, is:

$$u(t) = K_P * [err(t) + T_D * \frac{d\,err(t)}{dt} + \frac{1}{T_I} * \int_0^t err(\tau)d\tau] + K_F * [\frac{d\,sp(t)}{dt}; sp(t)] \qquad (3)$$

where if feedforward control is enabled then $T_D=0$ and $K_F<>0$ else $T_D<>0$ and $K_F=0$.
Other parameters of the controller that can be set by the user are:
- proportional gain K_P
- derivative time T_D (if feedforward is disabled) or feedforward transfer factor K_F (if feedforward is enabled)
- integral time T_I
- proportional weight
- derivative weight
- integral weight
- maximum error for reference (if S-curve generator is enabled)
- maximum speed for reference (if S-curve generator is enabled)
- maximum acceleration for reference (if S-curve generator is enabled)
- maximum jerk for reference (if S-curve generator is enabled)
- scaling factor for reference an controlled variable values
- scaling factor for speed
- scaling factor for acceleration
- scaling factor for jerk

The establishment of these values is carried out through the Ethernet interface of the controller using the MODBUS over TCP/IP protocol.

3. Controller monitoring and parametrization - PC software

To monitor and parameterize the 2-DOF controller, it was necessary to develop a software that runs on a computer located in the same network as the controller. It was developed using the Lazarus free programming environment and the Free Pascal programming language [4].
The software main window is shown in fig. 3. This window enables one to monitor the process parameters in graphical form, measuring the values on the graph as well as viewing the controller configuration and the state of communication with it.

Fig. 3. PC software – main window

Fig. 4 shows the window of the program that allows the establishment of the functional parameters of the 2-DOF controller.

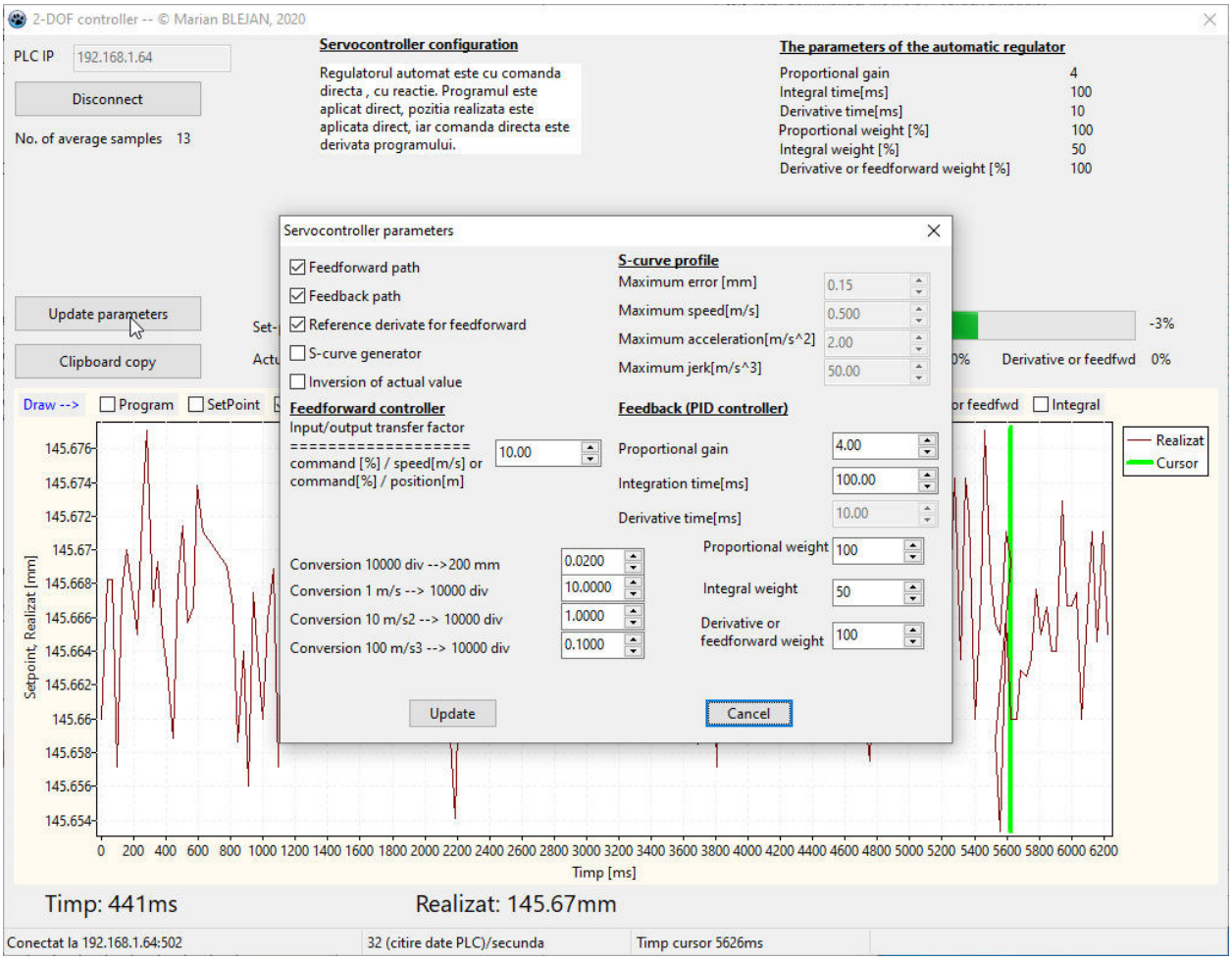

Fig. 4. PC software – 2-DOF controller parameters window

4. Experimental setup

The presented controller was tested on the experimental setup shown in fig. 5 and fig. 6, respectively on a position-controlled linear actuator.

Fig. 5. Experimental stand

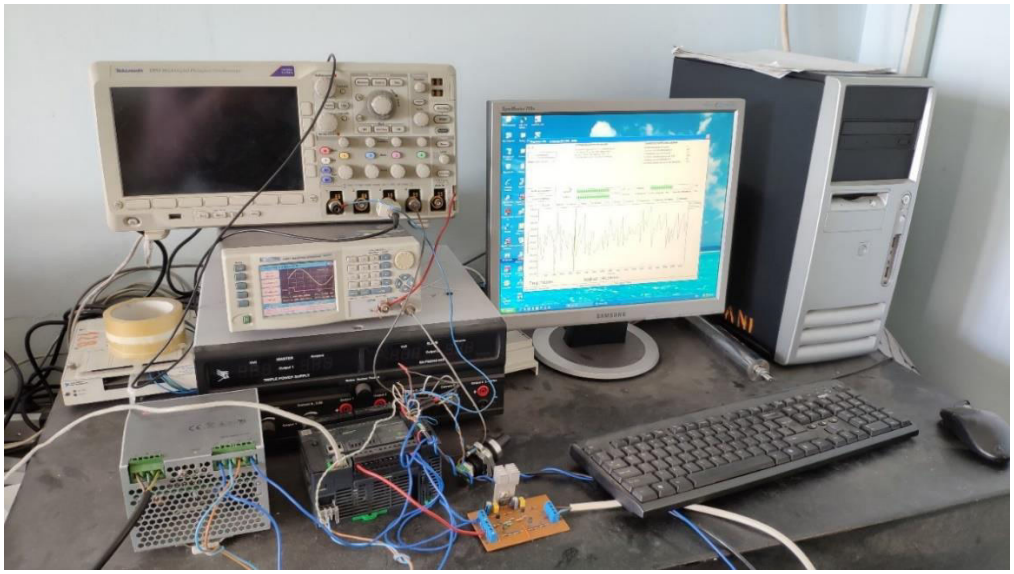

Fig. 6. Controller, waveform generator and PC

Fig. 7 shows the functional diagram of the test stand.

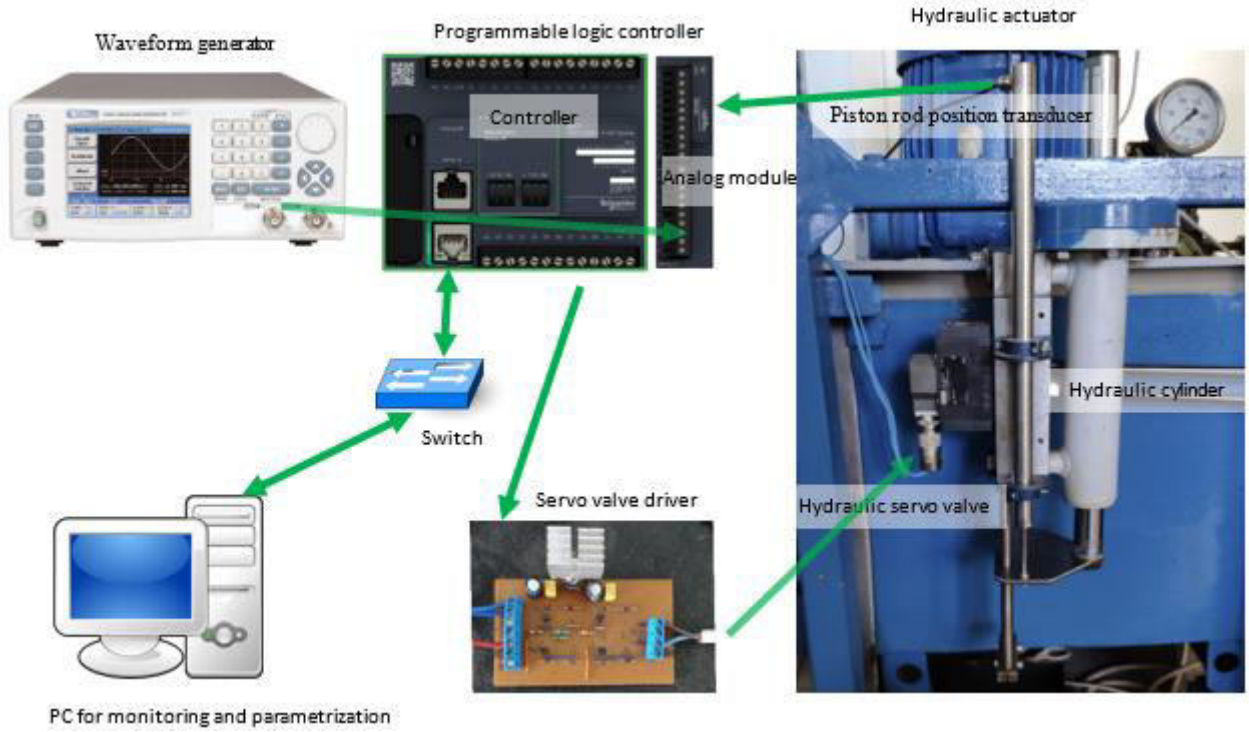

Fig. 7. Experimental stand diagram

The hydraulic cylinder is actuated by an electrohydraulic flow servo valve powered by a hydraulic station capable of providing a pressure of *150 bar* at a flow rate of *60 litres/min*, which allows a maximum speed of *0.66 m/s* to be obtained and a maximum force whose value is *1100 daN* at the level of the hydraulic cylinder rod. The position of the cylinder rod, which has a maximum stroke of *200 mm*, is monitored with the help of an LVDT type position transducer with a measurement range of *200 mm*. The control signals of the linear hydraulic axis are generated with the help of a WW5061 - TABOR ELECTRONICS digital signal generator [5] and allow the evaluation of the performance of the static and dynamic regime of the hydraulic axis.

5. Experimental results

To evaluate the position control performance of a hydraulic linear actuator, a step reference signal was applied and the response of the actuator was monitored.

Fig. 8. Set-point and actual value of position, *70 mm* step, 1-DOF PID regulator K_P*=4,* T_I*=100 ms,* T_D*=10 ms*

Fig. 9. Set-point and actual value of position, *70 mm* step, 2-DOF PI regulator K_P*=4,* T_I*=100 ms,* K_F*=10*

Fig. 10. Reference and actual value of position, *70 mm* step, 2-DOF PI regulator and S-curve generator on set-point path K_P*=4,* T_I*=100 ms,* K_F*=10,* v_{max}*=0.4 m/s,* a_{max}*=20 m/s2,* j_{max}*=175 m/s*^{3}

Three tuning algorithms were used: 1-DOF PID feedback (fig. 8), 2-DOF feedforward and PI feedback (fig. 9), respectively 2-DOF feedforward, PI feedback and S-curve generator on the set-point path shown in fig. 10. The blue trace is the reference position and the green trace is the actual position.
The maximum pressure of the hydraulic group is set to *50 bar*, which allows a maximum speed of *0.5 m/s* without load.
1-DOF PID feedback shown in fig. 8 has an aperiodic response with a rise time of *200 ms*. 2-DOF feedforward and PI feedback, fig. 9, has a periodic response with a rise time of *150 ms* and *3.5 mm* overshot (*5%* of step value of *70 mm*), while 2-DOF PI regulator and S-curve generator on set-point path (fig. 10) has an aperiodic response with a rise time of *160 ms*.

6. Conclusions

The two-degree-of-freedom controller developed as software on PLC hardware support has experimentally confirmed its functional performance in the field of hydraulic drives obtained by using advanced control algorithms. The authors have also demonstrated the functionality of the PC software for controller monitoring and parameterization.

Acknowledgments

This paper has been developed in INOE 2000-IHP, as part of a project cofinanced by the European Union through the European Regional Development Fund, under Competitiveness Operational Programme 2014–2020, Priority Axis 1: Research, technological development and innovation (RD&I) to support economic competitiveness and business development, Action 1.2.3 – Partnerships for knowledge transfer, project title: Development of energy efficient technologies in niche applications of the manufacture of on-demand mechanical-hydraulic subassemblies and maintenance of mobile hydraulic equipment, project acronym: MENTEH, SMIS code: 119809, Financial agreement no. 6 /25.06.2018.

References

[1] Araki, Mituhiko, and Hidefumi Taguchi. “Two-Degree-of-Freedom PID Controllers.” *International Journal of Control, Automation, and Systems* 1, no. 4 (December 2003): 401-411.
[2] Schneider Electric Global. “Modicon Master Range.” Accessed October 5, 2022. https://www.se.com/ww/en/work/products/master-ranges/modicon/.
[3] Ilie, Ioana, Marian Blejan, and Robert Blejan. “S-curve motion profiles generator for hydraulic actuators.” Paper presented at the 25th International Conference on Hydraulics and Pneumatics HERVEX, Băile Govora, Romania, November 13-15, 2019.
[4] ***. Lazarus Homepage. Accessed October 7, 2022. https://www.lazarus-ide.org/.
[5] Tabor Electronics. “Model WW5061.” Accessed October 7, 2022. https://www.taborelec.com/ww5061.

ISSN 1454 - 8003
Proceedings of 2022 International Conference on Hydraulics and Pneumatics - HERVEX
November 9-10, Băile Govora, Romania

VARIOUS OPERATION MODE OF CONSTRUCTION MACHINERY USING ENERGY OBTAINED FROM RENEWABLE SOURCES

Ioana Aristia POPOVICI[1], Mihail SAVANIU[2], Oana TONCIU[3] , Magdalena CULCEA[4], Andrei TEODORESCU[5]

[1] UTCB – Faculty of mechanical engineering and robotics in constructions, ioana.popovici@utcb.ro

[2] UTCB – Faculty of mechanical engineering and robotics in constructions, mihai.savaniu@utcb.ro

[3] UTCB – Faculty of mechanical engineering and robotics in constructions, oana.tonciu@utcb.ro

[4] UTCB – Faculty of building services engineering, magdalena.culcea@utcb.ro

[5] UTCB – Faculty of mechanical engineering and robotics in constructions, andrei-serban.teodorescu@phd.utcb.ro

Abstract: *The aim of the paper is to outline the potential solutions for operation of construction machinery using energy obtained from renewable sources. "Green" machines for construction have zero-emissions and are silent, therefore they are recommended to be used in the urban environment. This paper presents the proposed platform for the experimental study carried out in order to use solar energy as an energy source, which is stored in batteries with various capacities and its direct use in processes with energy consumption fluctuations, such as soil digging process.*

Keywords: *Renewable sources, construction machineries, energy efficiency, environment*

1. Introduction

Importance of the subject from a scientific, technologic, socio-economic or cultural point of view. Within the context of global warming, the energy crisis and the ever-increasing price of petroleum, there is a need to reduce the energy consumption and pollution of construction machinery. The current geopolitical context imposes the reduction of our dependency on fossil fuels and the identification of alternative solutions for the actuation of construction machinery. In order to fulfill these requirements, we can look towards the field of automobile development, where a variety of actuation solutions are currently being studied, some purely electrical and some hybrid. Some of these solutions can also be applied to construction equipment – one prime example being the hybrid excavator. Electric actuation technologies have become increasingly popular in the field of construction equipment over the past few years, with them being increasingly able of providing the necessary power, functional safety and reliability for such applications, while also offering reduced fossil fuel consumption and lowered pollution. Studies have been conducted on purely electrically actuated construction machinery systems, which are based on energy storage units (ESUs) and electromotors (EMs). In order to ensure a high enough autonomy of the equipment and proper dynamic performance under shocks, both the ESU and the EM need to have high energy capacity and power. Table 1 lists the characteristics of the most usual ESUs [1].

Table 1: Energy storage units (ESU)

ESU Type	Pb Battery	Flywheel	Supercondensator	Hydraulic Accumulator (HA)	NI-MH Battery	Li Battery
Specific power (W/kg)	75-300	400-1500	500-5000	2000-19.000	150-200	250-340
Specific energy (Wh/kg)	30-50	10-30	2.5-5.5	2	100-120	75-200
Energy capacity (Wh/L)	50-80	20-80	35	5	150-180	200-500
Nr.of cycles	500-1500	200.000	100.000	100.000	2500	2000-10.000
Efficiency	<80%	≤96%	≤95%	90%	90%	≤95%

2. Analysis of current state-of-the-art within the conetxt of the project's scope

The field of aviation is also strongly oriented towards electrical actuation solutions (usually called PBW – „Power-By-Wire" technologies). These PBW solutions are used to extend the applicability of electrical acuation systems towards aeronautic control systems. A PBW actuation system (fig.1) transports electrical energy between various systems using wires and cables, instead of hydraulic pipes, which increases aircraft performance.
The advantages offered by PBW actuation systems are increased reliability, due to the absence of hydraulic fluids which are flammable, reduced weight, volume and complexity of the energy transfer systems, reduced costs and complexity of maintenance, higher energetic efficiency and improved dynamic characteristics [2].

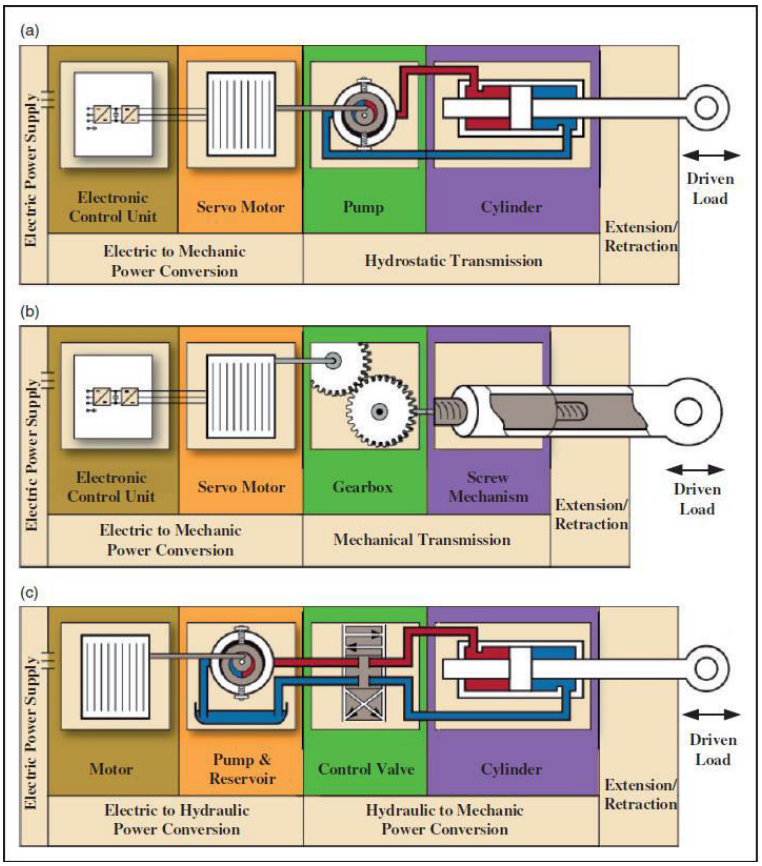

Fig. 1. Actuators using PBW technology: a) EHA, b) EMA, c) HSA

The innovative solution proposed by this project is the use of solar panels as main energy source, storing the energy in accumulators of various capacities (depending on desired autonomy) and using said energy directly for processes with large fluctuations of energy consumption (like digging operations), all without requiring intermediary power sources.
Green construction equipment (which are electrically powered and actuated) have zero polluting emissions [3][4] are far more silent, which would allow them to function continually in densely populated areas, even during night hours, without disturbing the local population [5]. All these characteristics translate to a positive impact to society through increased work efficiency, productivity, functional safety and reduced influence on the environment [6]. A variety of electrically powered and actuated construction equipment is presented in fig. 2-7.

Fig. 2. E10e Mini Excavator

The Bobcat E10e [7] has a state-of-the-art Lithium-Ion, maintenance-free battery pack with an advanced management system, designed to fit within the standard machine envelope to maintain the machine's ZTS profile. Following the daily working routine, the E10e can operate throughout a full 8-hour day, using operator breaks to recharge the batteries. Using an external super-charger functionality, the batteries can be recharged to 80% of battery capacity in around 1 hour. The battery can also be recharged overnight by using the on-board charger from a standard 230V grid. In addition, the new machine is easy to maintain and safe to operate – thanks to the exclusive use of low voltages, there is no need for operators to have special authorization to work with the E10e.

Fig. 3. The 19C-IE electric compact excavator

The new JCB 19C-IE [8] has maintenance free batteries, needs minimal daily checks and requires less servicing, saving rental companies, hirers and owner operators time and money. No engine and associated items significantly reduce servicing time and equipment. No need for emissions extraction saves on wages and equipment. No engine liquids to check saves you time and money. Electricity is a lot cheaper than fossil fuel. The new 19c-1e gives you the freedom to work anywhere, anytime with quick charging and long battery life. The machine's 4 battery pack lets you work for 5 hours on a standard application (equivalent to a full day). 3 charging options: 110V, 230V and 415V let you get to work when and where it suits.
The JCB 19c-1e electric mini excavator generates less noise than many household appliances, making it ideal for urban areas and indoor applications and allowing better communication with co-workers. Noise at the operator station is a huge 10 dB less than the diesel version. It allows for 'out-

of-hours' working, to maximise time on site and speed up the job. The 19C-1E is fitted with a blue light indicator to show the machine is running. Three single flanged bottom rollers allied with short pitch tracks ensure a quiet, smooth ride.
The JCB 19c-1e electric mini excavator is safer for the environment, operators and bystanders, and is ideal for working indoors and in urban areas. Zero emissions and low noise levels make for safer working conditions. The 19C-1E operates completely free of any trailing tethers. JCB's unique 2GO system safely isolates all the controls.

Fig. 4. XCMG Electric Excavator

Cummins collaborated with XCMG [9], the 4th largest construction machinery company in the world, to design and build the 3.5-ton electric excavator, which will serve as a technology demonstrator. Often operating on work sites in densely populated towns and cities around the globe, construction equipment must meet stringent emissions requirements and keep noise and disruption to a minimum while getting the job done. The new electric excavator is suitable for working conditions that require more stringent environmental standards and noise reductions.

Fig. 5. PC30E-5 Mini Electric Excavator

The Komatsu-original electric PC30E-5 [10] achieves a clean work environment. It can be deployed to a diverse range of workplaces, such as indoors, piping work, urban construction, and landscaping. As its power source is an electric motor, this model does not generate loud noise like internal combustion models. Even while the machine is in use, it is easy for the operator to communicate with workers near the machine, which improves workplace safety. This machine can also be deployed at workplaces where you need to consider construction noise, such as residential areas, near the hospitals and at night. Reducing the operator's fatigue, thanks to no engine vibrations. As no internal combustion engine is mounted on this machine, the vibrations which are transmitted to the operator are outstandingly improved. With low levels of stress or fatigue, the operator can perform work comfortably. Making the work environment comfortable by reducing the amount of heat generated Heat generated by the machine is very small, as it has no engines. As it also gives almost no heat around the machine, the machine also helps improve the work environment.

Fig. 6. Volvo ECR25 Electric Excavator

The lower noise levels that the ECR25 Electric offers enable you to work anytime, anywhere – even at night in populated areas [11]. This can lessen the disturbance inner city work can cause and reduce congestion at peak times, all the while increasing your efficiency. It also creates a more pleasant working environment for you and your colleagues with whom you can clearly communicate whilst operating. The ECR25 Electric features a zero-tail swing radius design making it perfect to confidently work in confined spaces. Moreover, thanks to zero emissions, the need for costly fumes extraction systems is eliminated in indoor jobs, such as basement groundworks and building demolition.

Fig. 7. EX02 electric excavator prototype

This opens up new business opportunities which in turn helps optimize utilization • No emission locally • Sound level down tremendously • Maintenance free battery • Low electricity cost • No power consumption when machine not working • Low vibration • Color display with jog wheel navigation • Intuitive and easier to operate • Full LED lighting • Blows less dust • Same performance as its diesel equivalent • Ultimate lifting capacity • Zero-tail swing radius • Front corner stays within tracks width • Wide range of Volvo attachments.
Volvo Construction Equipment (Volvo CE) [3] unveiled its latest concept machine – known as the EX02 – to industry specialists, policymakers, the media and academics at the Volvo Group Innovation Summit on May 2017. The 100% electric compact excavator prototype delivers zero emissions, 10 times higher efficiency, 10 times lower noise levels and reduced total cost of ownership compared to its conventional counterparts. It is believed to be the world's first fully electric compact excavator prototype.
The Volvo Group defines electromobility as 'commercial vehicles and machines that can utilize an electrical motor to propel or to perform the main purpose of the machine'. To make the EX2 prototype fully electric, the combustion engine has been replaced with two lithium-ion batteries, totaling 38KWh, which store enough electric energy to operate the machine for eight hours in an intense application, such as digging compact ground. The hydraulic architecture has also been replaced with electric architecture, which incorporates electromechanical linear actuators that help to optimize the transmission chain. Removing the hydraulic system and the combustion engine, as well as reducing the cooling needs, has led to significantly lower noise levels
The field of electrically actuated construction machinery is new and in continous development. Like in every new domain, there are emergent issues with the large scale implementations of such solutions, due to lack of experience and knowledge related to actuation solutions, energy storage systems, system reliability and lackluster training of maintenance personnel.
For the validation of an electrical actuation system, using solar panels and energy storage units, an experimental stand will be used in order to simulate the actuation of an excavator's arm during digging operations. The characteristics of the experimental stand are presented in fig. 8.

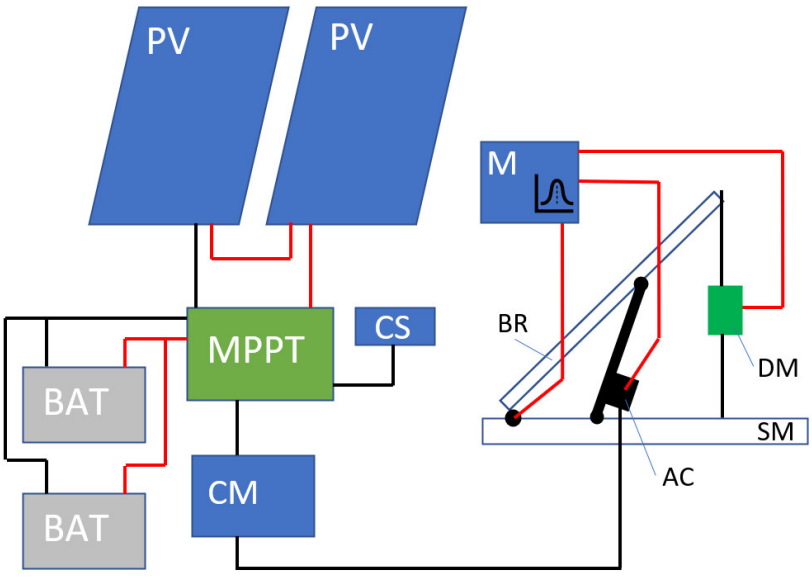

Fig. 8. Experimental Stand

The experimental stand is composed of the following elements (fig. 9-15):

1. PV – photovoltaic monocrystalline solar panels, with a maximum power of 375 W (fig. 9);

Fig. 9. Solar panels

2. BAT –Deep Cycle Gel type electric accumulators, with a 12 V voltage and an energy capacity of 150 Ah (fig. 10);

Fig. 10. Electric accumulator

3. MPPT –SmartSolar type solar charge controller with a maximum voltage of 100V and 50 A current , with Bluetooth connectivity (fig. 11);

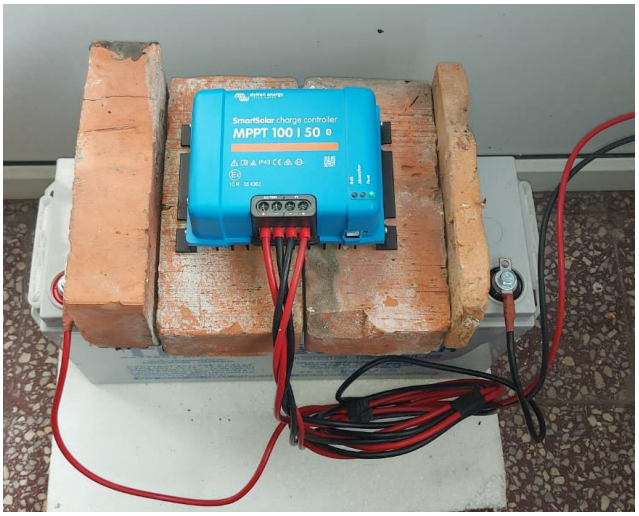

Fig. 11. MPPT charge controller

4. CS – solar system monitor – Victron app;
5. CM – electromechanic actuation command system, using a Controlino type PLC controller;
6. BR – metallic excavator arm – welded structure made out of S235 carbon steel (fig. 12);

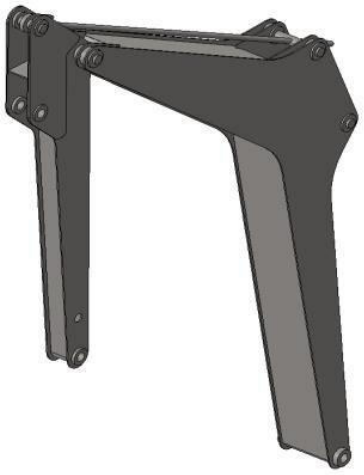

Fig. 12. Metallic excavator arm

7. M – actuator functionality monitoring system. This is composed of and Arduino Mega controller which collects and stores the data generated by a rotative encoder mounted on the mechanical joint of the excavator arm, by a linear encoder mounted on the electromechanic actuator and by a force transducer;
8. DM – force transducer with a capacity of 1000kg (fig. 13);

Fig. 13. Force transducer

9. AC – electromechanic actuator, with an optimum operating voltage of 12 V (fig.14);

Fig. 14. Electromechanic actuator

10. SM – metallic structural base – welded out of S235 carbon steel (fig. 15).

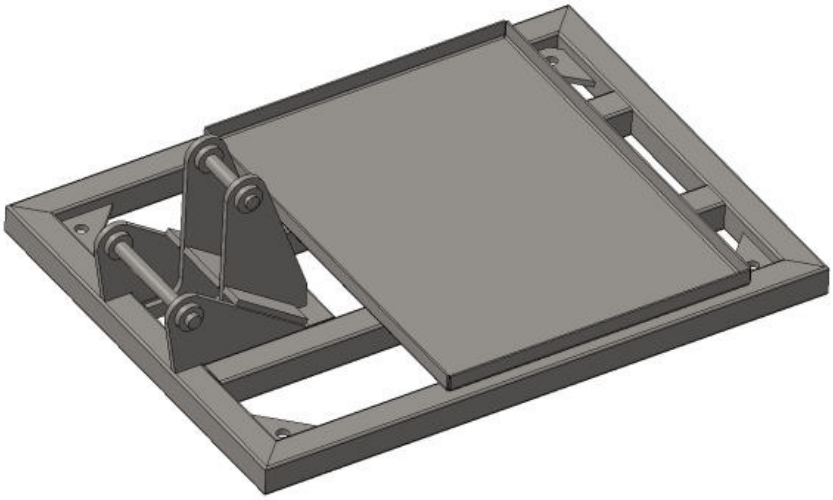

Fig. 15. Metallic structural base

The proposed solution does not necessarily imply the mounting of the solar panels directly on the construction equipment. The experimental stand could also be adapted into a stationary charging station.
The originality of the project stems from the use of green energy sources in the field of construction machinery with the intent of reducing fossil fuel and noise pollution, thus having a positive impact on the quality of life on a construction site and in nearby environments. There is a current demand for reduced pollution in urban construction sites. Real-estate developers are stimulated, from the very first stages of a construction project, to use alternative energy sources, such as solar panel arrays mounted in construction sites during initial organizational stages of a project.
This way, there is a source of alternative green energy on site, which can be used for the powering of construction equipment. The aim of the proposed project is to obtain an algorithm for the balance between the consumption of energy by construction equipment and the amount of energy stored in the electric accumulators.
The optimisation of the actuation system for an excavator arm fuelled by solar panel energy can be performed using an experimental model built for this purpose. The actuator must be driven in such a way that peak loads are as low as possible, while also taking into account the capacity and other performance characteristics of the electric accumulators.
In the case of a large number of very short, high peak electrical spikes, the batteries will undergo a rapid deterioration, which leads to premature discharge events. In order to limit the occurence of such phenomena during digging operations, a damping sequence for the power spikes absorbed by the actuators must be developed. This sequence must be able to be peformed in parallel with the other activities in which the operator of the equipment is involved and independent of the operator's control. Such a system could be succesfully implemented into predefined, automated digging programs offered by the construction equipment.
For the actuation system of the experimental model's excavator arm, various actuation sequences will have to be developed, which take real digging regimes into account and which feature the proper damping algorithms for peak loads. The first step to achieve this goal is to pergorm a SolidWorks simulation in which various digging sequences are tested. These sequences will then be later evaluated and validated by comparing theirs actual physical results obtained from the experimental stand. The SolidWorks simulation is presented in fig. 16.

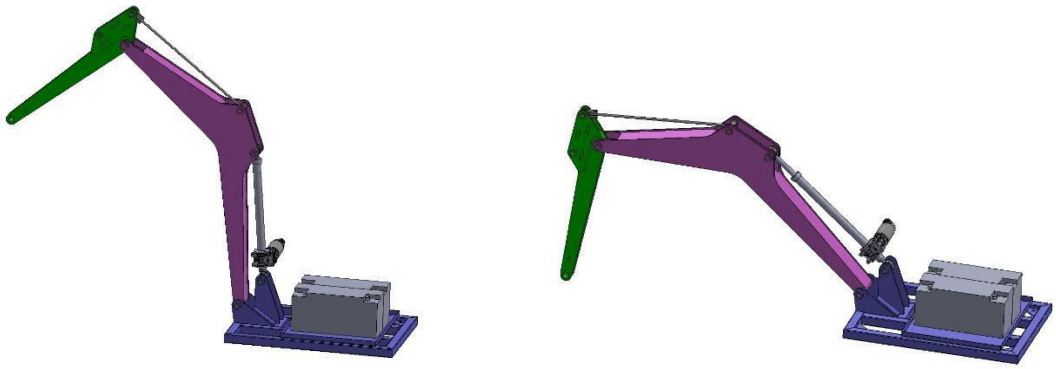

Fig. 16. SW simulation of the functionality of an actuation system for the arm of an excavator

Using SolidWorks Motion Analysis [12], the system was tested in a virtual environment, where several work scenarios were created. The following were taken into consideration:

- Different loads on the excavator's bucket an on the excavator's arm, which is driven by the electromechanic actuator;
- Different positions of the boom arm relative to the stick arm during digging operations;
- Various digging programs – in terms of velocities and accelerations applied at electromehcanical actuator level.

One possible scenario has been thus defined:
Following completion of the simulation we have obtained the following trajectory of the boom arm joint and the required force to properly acutate the arm (fig. 17).

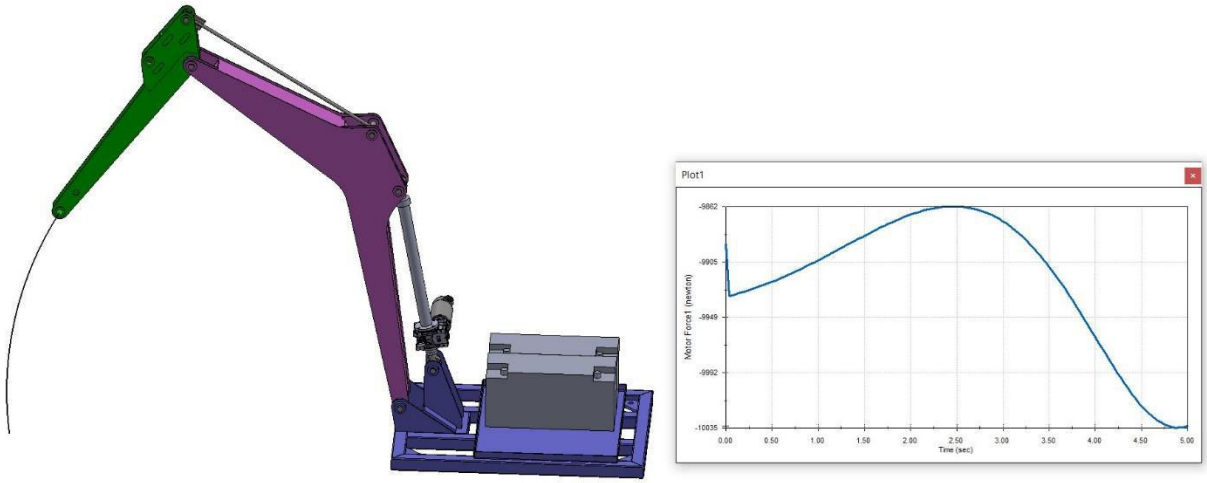

Fig. 17. Trajectory of the boom arm's joint

With the help of the simulation produced by SW Motion Analysis, the necessary power required to drive the electromechanic actuator has been estimated, together with the required energy which the actuator must draw from the batteries. Multiple iterations of the simulation were run, with various values for the load on the boom arm's final mechanical joint, as well as for the velocity and acceleration at the excavator arm level, which resulted in the simulation of real-life work scenarios (fig. 18). In figure 19 are presented the results of a simulation where 1000 N of force were applied to the final joint of the excavator arm. The model's own weight was also taken into account, which resulted in a 45 mm displacement at the actuator rod's level, the excavator arm being raised for a duration of 2 seconds, then lowered back to initial position in another 2 seconds, followed by yet another 5 mm raise of the arm in one second.

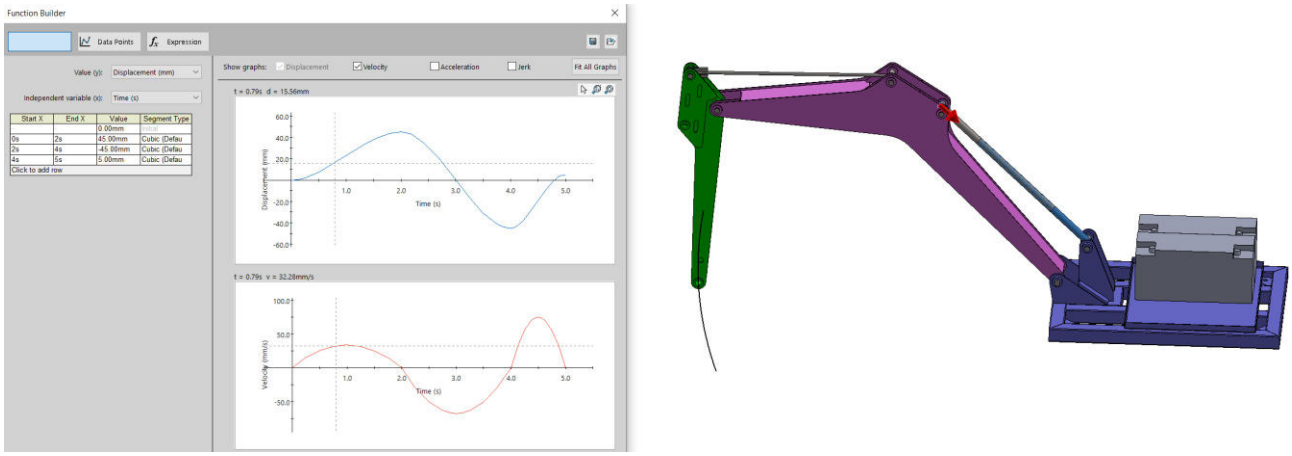

Fig. 18. Scenario for the electromechanical actuation of the excavator arm model

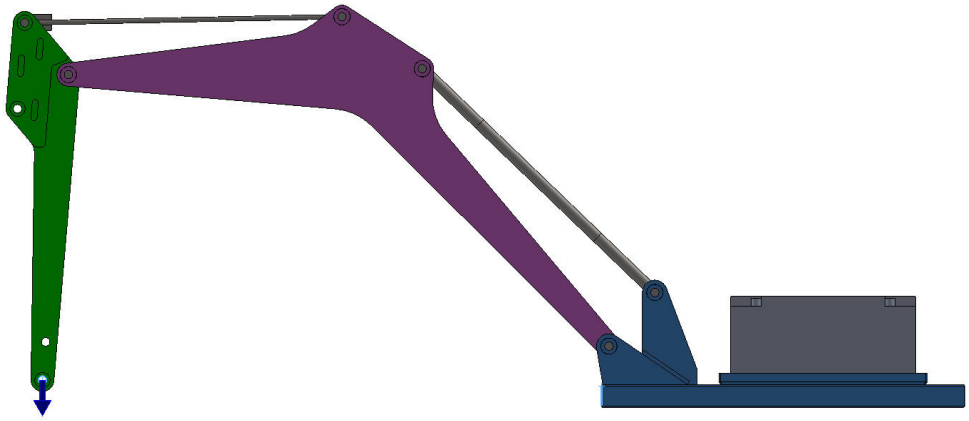

Fig. 19. 1000 N load applied to the final joint of the excavator arm

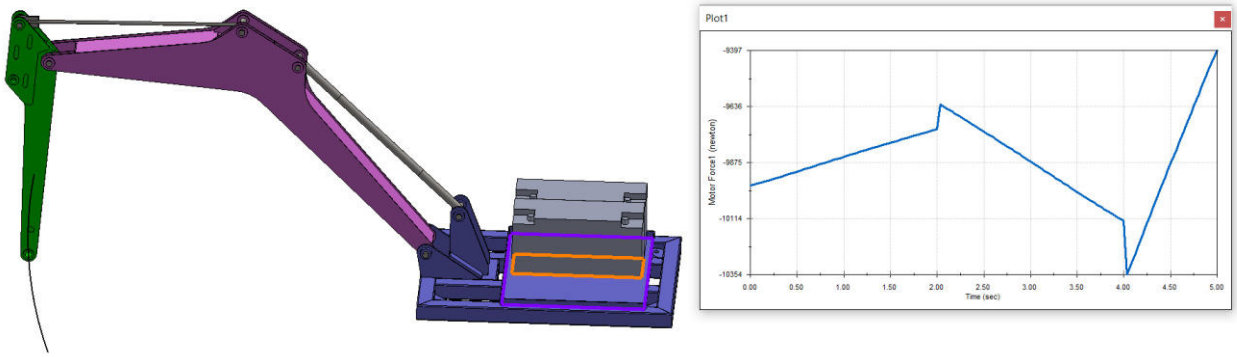

Fig. 20. Power at the electromechanic actuator level and the variation of the angle between arm and base

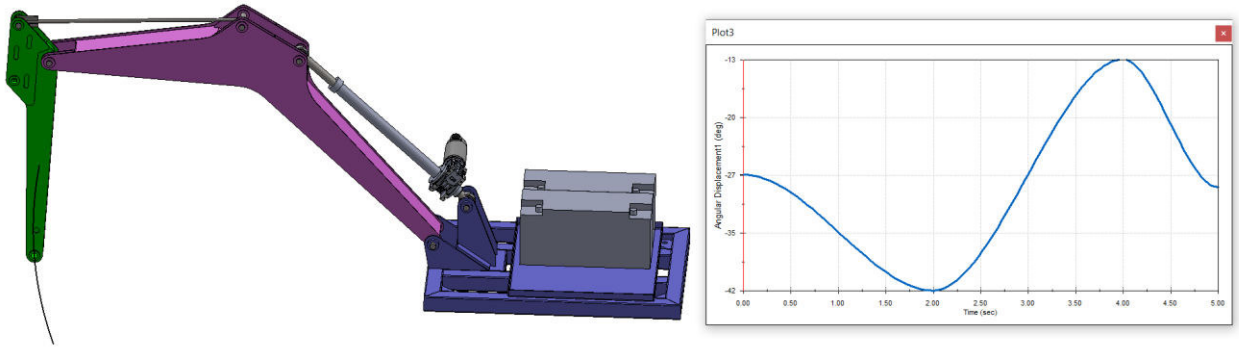

Fig. 20. (continued) Power at the electromechanic actuator level and the variation of the angle between arm and base

Following the simulation, the maximum necessary force for driving the electromechanic actuator has been calculated at 10354 N and power spikes have been detected during the simulation run (fig. 20) which must be optimised in the case of using photovoltaic panels and battery packs to power such an actuator. These power spike are present and detected even during fairly simple work scenarios. Simulations run for much more complex work sequences have determined the necessity of optimizing the functionality of the electromechanic actuator.
The optimisation will be performed through an actuation sequence which will be obtained by corellating results obtained from the simulation with future results obatined through experimental means.

3. Conclusion

Based on the performed research, the ever-increasing interest in electrical actuation solutions for construction machinery can be confirmed. The use of such equipment is well suited for urban areas and enclosed spaces where internal combustion engines can't be used due to polluting emissions. Such methods of actuation would also prove very welcome in the fields of food industry, agriculture and interior spaces of public buildings where the rupture of a hydraulic system component could cause oil contamination of aforementioned spaces. Various technological advances are currently being made in terms of development of electromehcanic actuation solutions for construction equipment. Electric actuation for such pieces of machinery is also being taken into consideration for far future applications, such as digging in low temperature vaccum environments, like space or exoplanets.
In order to validate the possibility of using an electromechanical actuation system, a series if simulations have been performed in a virtual environment. Following these simulations, load spikes were detected, which must be dampened when using our proposed solution for energy production and storage. In order to properly use solar panels to produce green energy and store said energy in rechargeable battery packs, some type of load spike correction must be implemented in the command and control module of the actuation system. In this way, the equipment will function properly, corecting the load spikes, independent of the commands issued by the operator. Corrections will be performed based on the position of the excavator arm and the measure load on the excavator bucket.

Acknowledgments

This work is part of the Internal Competition Program for the financing of the scientific research in UTCB (project acronym SOLUT, code UTCB-CDI-2022-016).

References

[1] Lin, T., Y. Lin, H. Ren, H. Chen, Q. Chen, and Z. Li. “Development and key technologies of pure electric construction machinery.” *Renewable and Sustainable Energy Reviews* 132 (2020): 110080, https://doi.org/10.1016/j.rser.2020.110080.

[2] Qiao, G., G. Liu, Z. Shi, Y. Wang, S. Ma, and T.C. Lim. “A review of electromechanical actuators for More/All Electrical aircraft systems.” *Journal of Mechanical Engineering Science* 232, no. 22 (2018): 4128-4151. DOI: 10.1177/0954406217749869.

[3] https://www.volvoce.com/global/en/this-is-volvo-ce/what-we-believe-in/innovation/prototype-electric-excavator/.

[4] Chen, Qihuai, Tianliang Lin, Haoling Ren, and Shengjie Fu. “Research on the control strategy of power train systems for hybrid hydraulic excavators.” *Advances in Mechanical Engineering* 10, no. 7 (2018): 1–10. DOI: 10.1177/1687814018790666.

[5] Dwibedia, Rajat Kumar, R. Jayaprakashb, T. Sivac, and N.P. Gopinath. “Hybrid electric vehicle using photovoltaic panel and chemical battery.” *Materials Today: Proceedings* 33, Part 7 (2020): 4713–4718. https://doi.org/10.1016/j.matpr.2020.08.351.

[6] Nevrly, Josef, Martin Fichta, Miroslav Jurik, Zdenek Nemec, Daniel Koutny, Pavel Vorel, and Petr Prochazka. “Battery Electric Drive of Excavator Designed with Support of Computer Modeling and Simulation.” *Proceedings* 58, no. 1 (2020): 25. https://doi.org/10.3390/WEF-06927.

[7] https://www.bobcat.com/eu/en/equipment/mini-excavators/0-1t-mini-excavators/e10e.

[8] https://www.jcb.com/en-us/products/compact-excavators/19c-1e.

[9] https://www.cummins.com/ro/news/2020/05/29/powered-cummins-xcmg-electric-excavator-makes-its-beautiful-debut.

[10] https://www.komatsu.jp/en/newsroom/2020/20200317.

[11] https://www.volvoce.com/europe/en/products/electric-machines/ecr25-electric/#specifications.

[12] https://www.solidworks.com/domain/simulation.

ISSN 1454 - 8003
Proceedings of 2022 International Conference on Hydraulics and Pneumatics - HERVEX
November 9-10, Băile Govora, Romania

DYNAMICAL ASPECTS OF PNEUMATIC PROPULSION OF A PELLET

Bogdan-Marian ȘERBAN[1,2], Andrei-Alexandru BENESCU[1,2,*], Alexandru-Polifron CHIRIȚĂ[1]

[1] Hydraulics and Pneumatics Research Institute INOE 2000-IHP, Bucharest, Romania

[2] Mechanical Engineering, Mechatronics and Robotics Department, Politehnica University of Bucharest, Bucharest, Romania

*benescu.ihp@fluidas.ro

Abstract: *In this paper, the dynamic aspects of the pneumatic propulsion of a pellet are presented. The numerical simulation was performed in the Simcenter AMESim program. Mechanical, pneumatic and signal component libraries were used; the air model used is an advanced (real) dry air model, namely the Redlich - Kwong - Soave model, in order to obtain results as close as possible to reality. The variation in time of the piston and pellet parameters with different masses, the variation of displacement versus velocity, the force exerted by the piston on the pellets and the pressure in the pneumatic chamber were determined.*

Keywords: *Pneumatic propulsion, numerical simulation, dynamical aspects*

1. Introduction

Nowadays, the most important aspect of air use is its ability to be compressed. Thus, since pressure is defined as force divided by surface area, pressure can be converted into force, which applied to a piston in a circular bore, can produce translational displacement [1].
The disadvantages of pneumatic equipment lie in its limitations: both the forces and moments produced by pneumatic motors are low and the compressibility of the air prevents precise adjustment of operating parameters [2].
Beater presented the basic concepts of pneumatic (air) propulsion [3]. In this paper, some of the more dynamic aspects of pneumatic propulsion will be addressed, in particular the use of mechanical components and pistons.
Pneumatic pistons are cylinders that convert air pressure into mechanical force. The study of this force includes the investigation of motion, velocity and the effect of friction. There are many ways to determine the dynamics of pneumatics, but researchers most often use either a vector or a moment-balance approach[4].
Special attention is paid to the effect of the piston's weight on the pellet's dynamics. According to the simulations, the pellet's acceleration and deceleration phases are affected by the weight of the piston. It fluctuates as a function of the system's compressional and thermal properties, and it is not possible to determine the precise force exerted by the system on the pellet without a detailed analysis. However, it is possible to make some general statements about the nature of the force. The force exerted by the system on the pellet will be greater when the system is close to its equilibrium state.
A typical spring-powered air propulsion system can be seen in figure 1. The trigger sear and its connection to the trigger blade are substantially simplified in the top example, which depicts the system action in the cocked position. Trigger geometry is far more complicated than what is seen in the figure. The system's motion is seen in the bottom picture after it has fired but before the projectile has made it all the way to the barrel's muzzle [5].

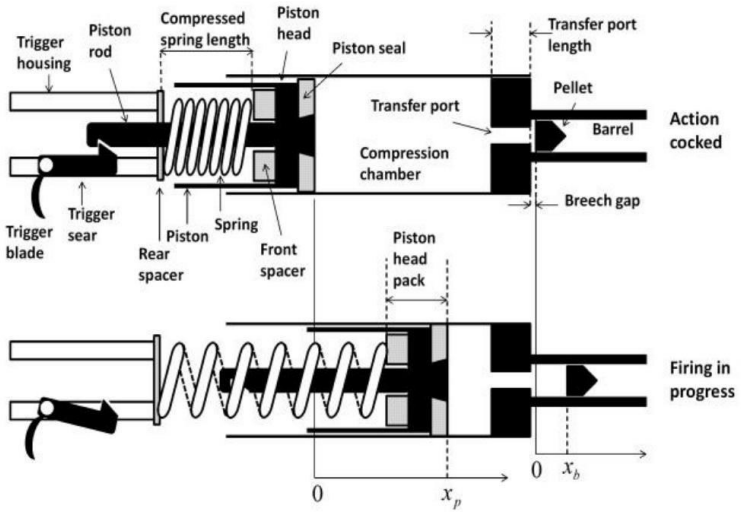

Fig. 1. Pellet propulsion diagram [5]

As seen in the image, a pellet is propelled forward by the compressed air resulted from the action of the spring. Frequently, the front of the spring contacts a spacer, whereas the back of the spring contacts a flat washer. The front spacer's function is to support the spring and increase the piston's total weight. Controlling the deflection energy held by the spring is the function of the rear spacer.
A transfer port is used to send high-pressure air to the breech. Through the transfer channel, the transfer port joins the breech and compression chamber.
The compression chamber will withstand some of the high-pressure air during firing, and the compression chamber model is created to include both cavities or pockets in the seal itself, where high-pressure air can become trapped when the firing mechanism is activated. The compression chamber model geometry is depicted in figure 2. It is obvious that seal cavities can be dealt with by effectively changing the chamber capacity, but the transfer channel needs further consideration [5].
If the piston's journey reaches its design-working stroke, it stops and bounces backward. For high-performance spring-piston propulsion systems, this is the most typical scenario, in which the piston physically hits the chamber end after reaching it. The pellet has not yet left the honed pipe at this point as the piston velocity reduces to zero. The piston then springs backward. As a result, the spring partially recompresses and its velocity acquires negative values [4]. This makes the piston and the spring oscillate and cause an increase in the pellet velocity.

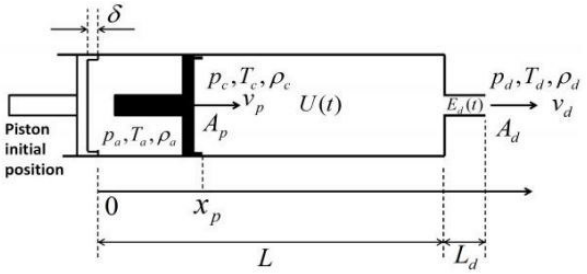

Fig. 2. Compression chamber diagram [5]

The thermodynamic parameters at the transfer port plane are computed beginning with the discharge pressure. Below a certain breech pressure, the flow at the transfer port turns sonic, and that value is:

$$p^*_d = p_c \left(\frac{2}{\gamma+1}\right)^{\frac{\gamma}{\gamma-1}} \quad (1)$$

Where:

$\gamma = \frac{\mathrm{Cp}}{\mathrm{Cv}}$
p_c – the pressure of the pressure chamber
p_d – pressure discharge

Figure 3 shows the design of the honed pipe and the pellet. This measurement considers the transfer port's spacing as well as the pellet's resting depth in the breech. This distance is crucial for thermodynamics and affects the numerical conditioning of the differential equations that characterize the issue.

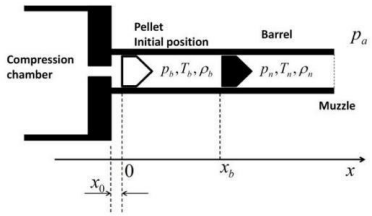

Fig. 3. Honed pipe diagram [5]

$$\frac{d}{dt}[(\mathrm{x}_0 - \mathrm{x}_b)\mathrm{p}_b] = \mathrm{C}_b * \eta_b * \dot{m} \tag{2}$$

Where:

$$\eta_b = \frac{A_d}{A_b}$$

$\dot{m}$ – mass flow rate

$$\frac{d\rho_b}{dt} = \frac{\mathrm{C}_d * \eta_b * \dot{m} - v_b * \rho_b}{(\mathrm{x}_0 + \mathrm{x}_b)} \tag{3}$$

Where:

$v_b = \frac{dx_b}{dt}$ – the speed of the pellet

Both a direct calculation from the model and the use of influence coefficients, which indicate the partial reaction of the model owing to the unit change in specific input parameters, can be used to estimate system performance, such as muzzle velocity, kinetic energy, reload duration, etc. [6, 7, 8, 9].

2. Material and method

The main part of this paper presents the simulation made in AMESim environment (Fig. 4). As so, the principle of the diagram from figure 1 has been transformed into a mathematical model that can be iterated in AMESim.
To create a numerical simulation on AMESim environment, first, a deep understanding of the mechanical and pneumatic phenomenon that occurred during the propelling process is needed. The simulation sketch is illustrated in figure 4, when the trigger is released, the helical compression spring 3, which was compressed, provides a force that is delivered to piston 4 with mass 5. The air within the pressure chamber 6 (a closed system that acts as an air spring) is compressed, propelling the pellet 9 inside the honed pipe 8, imprinting it an acceleration.

An advanced dried air model has been used (Redlich - Kwong – Soave) in combination with viscous friction for the moving parts to get results as close to reality as possible. The values used for the simulation can be found in Table 1.

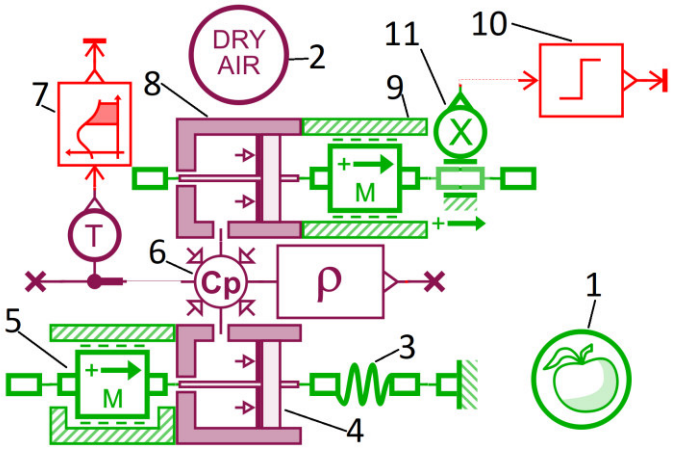

Fig. 4. Simulation model developed in AMESim

Table 1: Simulation model components

Number	Simulation component	Value	Unit
1	Gravitation force	g = 9.801	[m/s^2]
2	Dried air model	Advanced model: Redlich - Kwong - Soave	Null
3	Helical spring	spring rate = 3500	[N/m]
		spring pre-tension force = 400	[N]
4	Pneumatic chamber	piston diameter = Ø0.02	[m]
5	Piston mass	displacement = 0.08	[m]
		mass = 0.15	[kg]
		coefficient of viscous friction = 8	[N/(m/s)]
		restitution coefficient = 0.01	Null
		higher displacement limit = 0.08	[m]
6	Pneumatic volume	initial temperature = 19.85	[degree C]
		volume = 1e-05	[L]
7	Moving average	iteration period = 0.15	[s]
8	Honed pipe	diameter = Ø0.05	[m]
9	Pellet	**pellet mass = 0.0005 (reference value)** pellet mass = 0.0008 pellet mass = 0.001 pellet mass = 0.0015	[kg]
		coefficient of viscous friction = 3	[N/(m/s)]
10	Trigger	0.11	[m]
11	Displacement sensor	gain = 1	Null

3. Results of virtual experimentation

Based on the AMESim simulation network from the previous chapter and the parameters indicated in table 1, the results presented below were obtained:

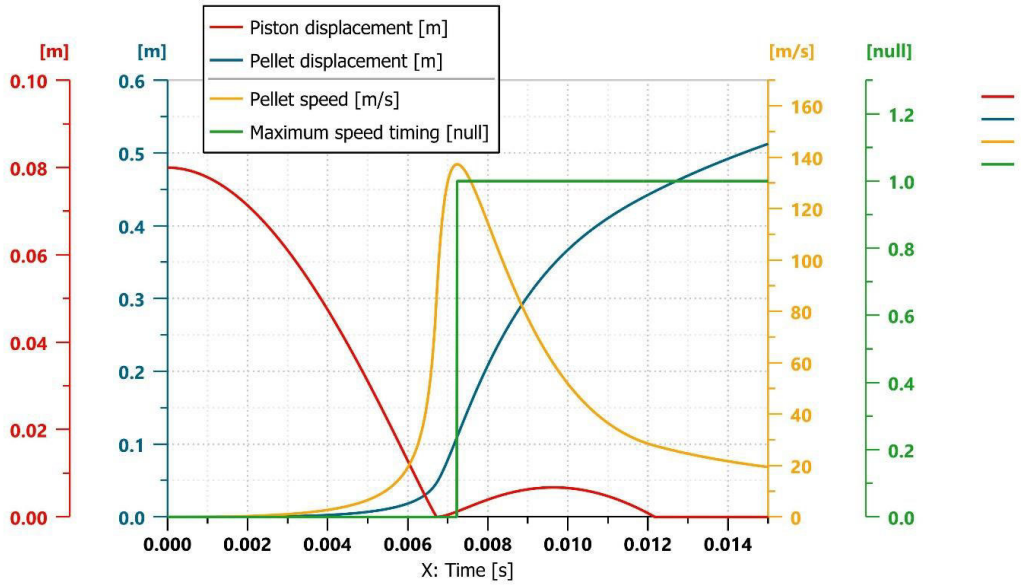

Fig. 5. Parameters time variation of piston and pellet

Figure 5 shows the evolution of displacement of both piston and pellet, also the speed of the pellet, which reaches its maximum value at the trigger point x = 0.00723 [s]. The graphic also highlights the restitution – movement of the piston after it reaches the higher displacement limit.

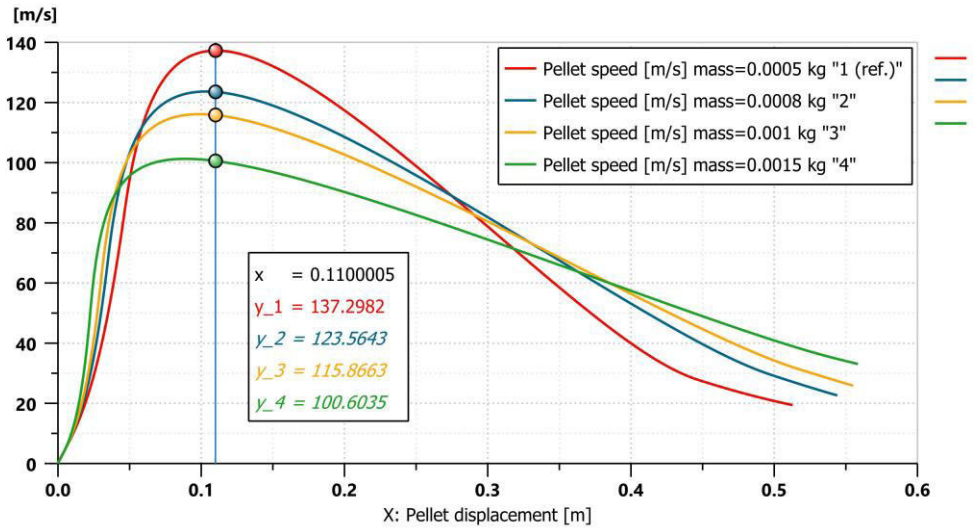

Fig. 6. XY Variation of displacement versus velocity

Figure 6 presents a set of simulations made to highlight the limit distance traveled by the pellet before losing speed (x = 0.11 [m]). The pellet mass also influences the maximum speed it can reach, the heavier the pellet results in a reduced threshold speed and a longer distance traveled.

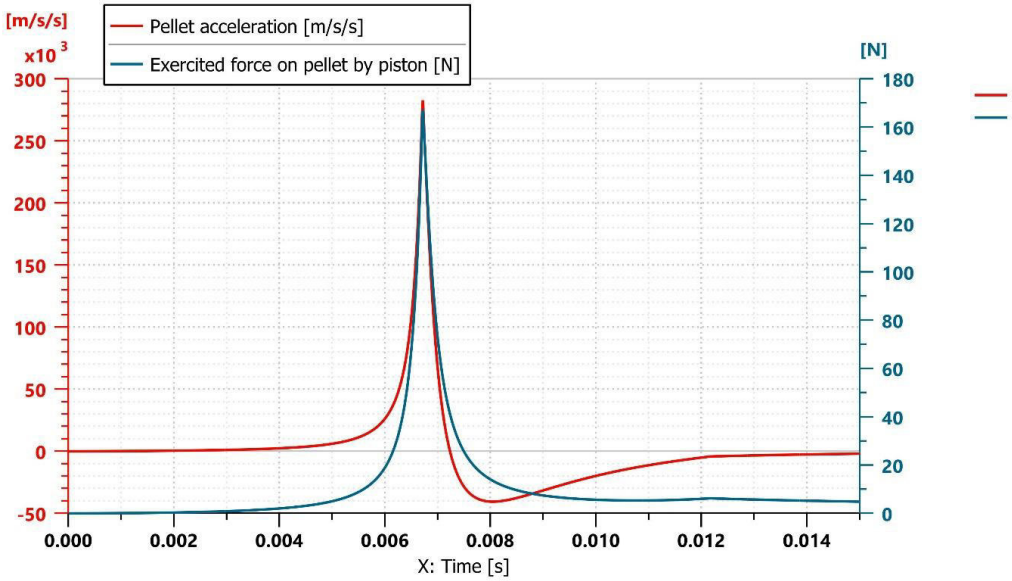

Fig. 7. XY Force exercised by the piston on the pellet and the pellet acceleration in time

In Fig. 7, it is shown that the pellet is accelerated by a net force imposed by the air compressed by the piston. The resistive force is proportional to the velocity of the pellet relative to the average force exerted by a piston on a pellet.

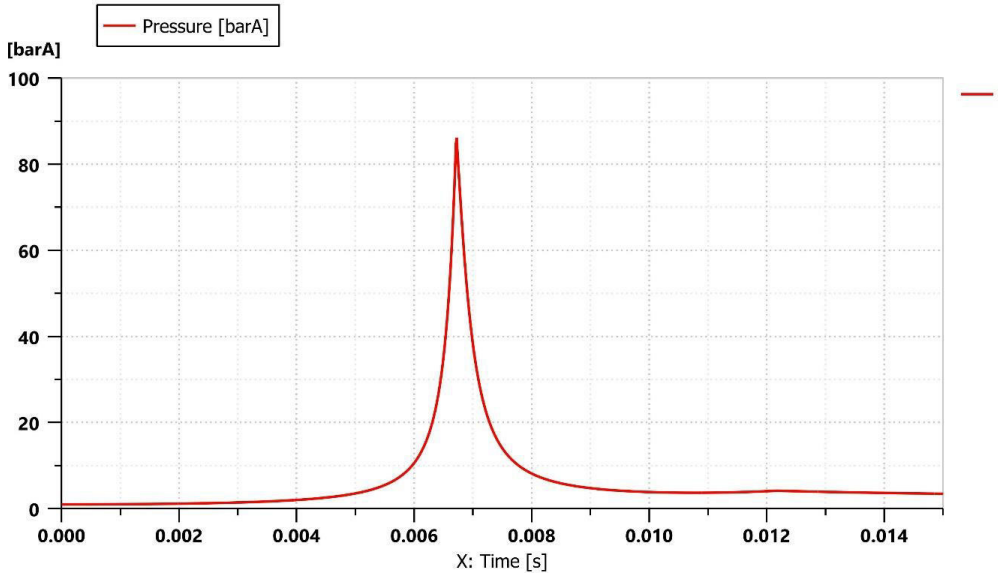

Fig. 8. Pressure in the pneumatic chamber

Because the pressure inside the chamber is greater than the atmospheric pressure. This pressure difference causes a decrease in air resistance and an increase in pneumatic power.
The maximum pressure that can be exerted on the pellet is determined by the ratio between the diameters of the pneumatic chambers and the honed pipe and the force generated by the helical compression spring.
After the pellet is propelled, the spring must be recompressed and the piston must be returned to its starting position (a displacement of 80 [mm]) in order to produce a repeatable occurrence. A lever

mechanism (lever ratio $^{0.25}/_{0.08}$) has been included since the amount of force required to perform this motion directly is just too great (Fr = 680 [N]).

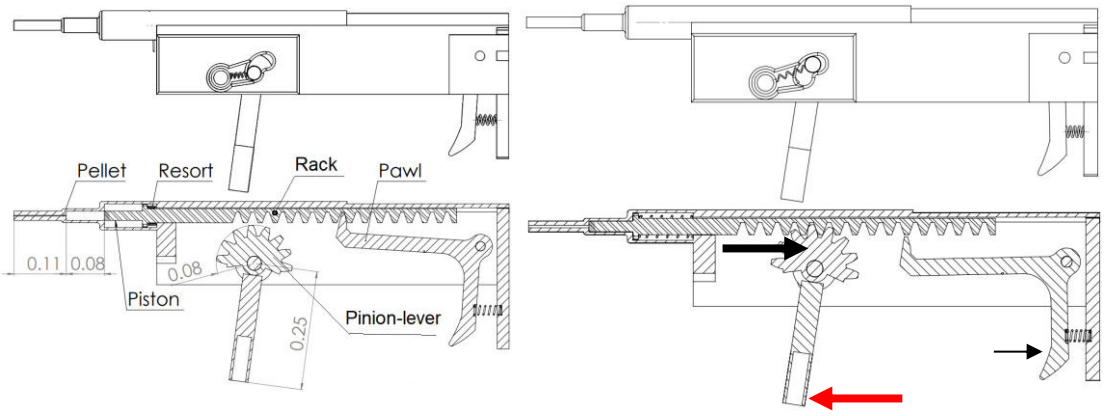

a. b.

Fig. 9. Section diagram of the lever–piston mechanism

Figure 9 shows the three components of the lever mechanism based on the Lifting-jack patent [10]: the rack, the pawn, and the pinion-lever. To prevent the pinion from restricting the rack movement, which is prevented by the pawl in figure 9.a, the torsion spring pulls the pinion-lever to the bottom of the slot. This allows the spring to remain compressed until the trigger is pulled. The forces, velocities and displacements of the mechanism can be seen in figure 10.
Figure 9.b shows the spring decompressing, the pellet being propelled, and the trigger is pushed. The lever-pinion is thus raised in the slot and engaged with the rack to recompress the spring. The rack slides easily because of the pawl design.

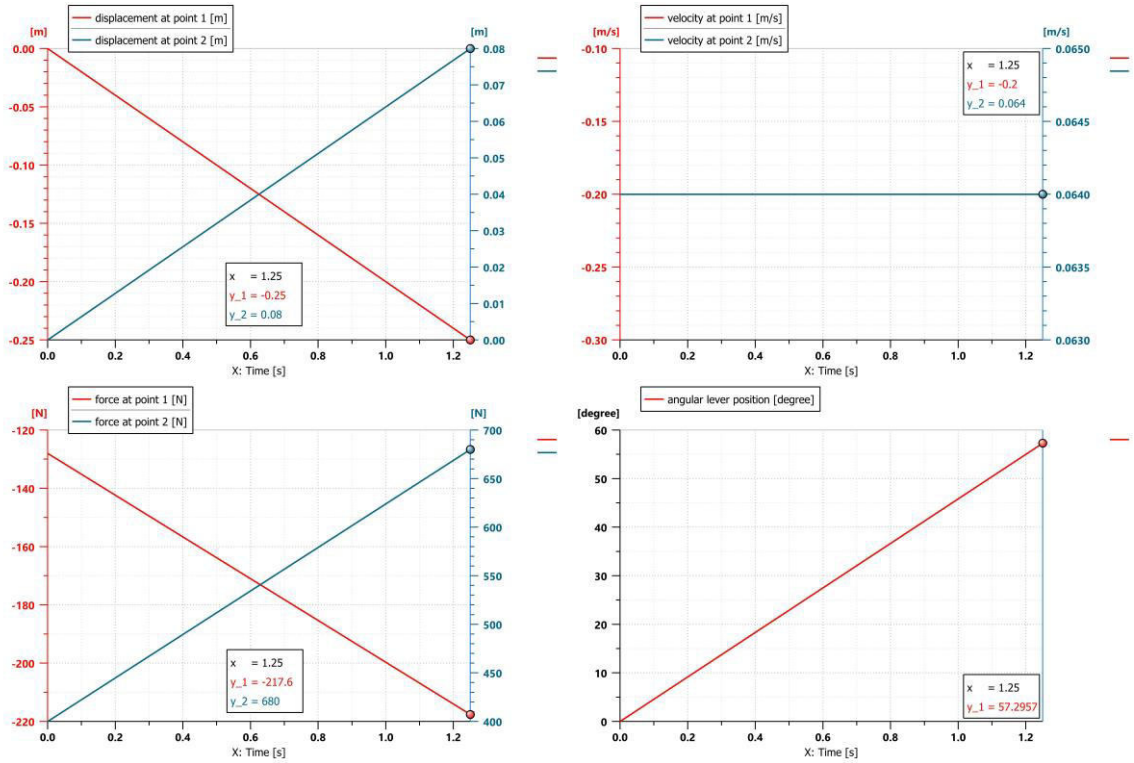

Fig. 10. Parameters of the lever – piston mechanism

4. Conclusions

In this study, the mathematical model of the spring-powered air propulsion system operation has been developed using AMESim simulation environment. Models used for the air, gravitation and friction are very complex and close to reality.
It has been demonstrated that the pellet mass influence the distance traveled by the pellet and its velocity, also the optimal length of the honed pipe until friction affects its speed.
The analysis enables us to understand how various design parameters and operating conditions influence the performance of spring-powered air propulsion systems, the simulation can be used to predict and help improve the performances of the system and may be used in an industrial design environment for optimization purposes.

Acknowledgments

This paper has been financed under a project funded by the Ministry of Research, Innovation and Digitalization through Programme 1- Development of the national research & development system, Sub-programme 1.2 - Institutional performance - Projects financing the R&D&I excellence, Financial Agreement no. 18PFE/30.12.2021. European funding has also been granted, under Competitiveness Operational Programme POC 2014-2020, call POC-A1-A.1.1.3-H-2016, Financial agreement no. 253/02.06.2020, signed between INOE 2000 and the Ministry of Education and Research for the project titled “Horizon 2020 Support Center for European project management and European promotion PREPARE”, MYSMIS2014 code 107874.

References

[1] Șerban, Bogdan. *Proportional pneumatic pressure regulator / Regulator de presiune pneumatic proportional*. Bachelor thesis. Politehnica University of Bucharest, 2022.
[2] Ryszard, Dindorf, Jakub Takosoglu, and Piotr Wos. *Development of pneumatic control systems.* Kielce, Publishing House of Kielce University of Technology, 2018.
[3] Beater, Peter. *Pneumatic Drives: System Design, Modelling and Control*. Springer Science & Business Media Publishing, 2007.
[4] Duc, Linh Do, Vladimir Horak, Roman Vítek, and Vladimir Kulish. “The internal ballistics of airguns Paper presented at the 2017 International Conference on Military Technologies (ICMT), Brno, Czech Republic, May 31- June 2, 2017.
[5] Tavella, Domingo. “Internal Ballistics of Spring Piston Airguns.” (April 2015). Available on ResearchGate, at https://www.researchgate.net/publication/274638905_Internal_Ballistics_of_Spring_Piston_Airguns.
[6] Horák, V., L. D. Duc, R. Vítek, S. Beer, and Q. H. Mai. “Prediction of the Air Gun Performance.” *Advances in Military Technology* 9, no. 1 (2014): 31–44.
[7] Plíhal, B., S. Beer, J. Komenda, L. Jedlička, and B. Kuda. *Ballistics*. Brno, Military Academy in Brno, 2003.
[8] Arsenjev, S.L., I.B. Lozovitski, and Y.P. Sirik. “The Flowing System Gasdynamics. Part 3: Saint-Venant – Wantzel’s formula modern form.” *arXiv: Fluid Dynamics* (February 2003): arXiv:physics/0302038.
[9] Johnston, I. A., and L. V. Krishnamoorthy. *A Numerical Simulation of Gas Gun Performance*. [Report DSTO-TN-0804]. Edinburgh, Defence Science and Technology Organisation, February 2008.
[10] Fraley, Robert M. *Lifting-jack*. US patent 964905A, 1909. https://patents.google.com/patent/US964905A/en?oq=US+patent+964905.

ISSN 1454 - 8003
Proceedings of 2022 International Conference on Hydraulics and Pneumatics - HERVEX
November 9-10, Băile Govora, Romania

BIOCHAR FOR EMERGENCY ENERGY STOCK AND NATURAL GAS REPLACEMENT

Erol MURAD[1], Florian DRAGOMIR[2], Manuela DRĂGHICESCU[3], Andrei PĂTRUȚ[4]

[1] EKKO OFFICE AG, Innovation Department, erolmurad@yahoo.com

[2] PROMECO SD, promeco@digiro.net

[3] SUNE, manuela.draghicescu@gmail.com

[4] CALORIS Group S.A., andrei.patrut@ymail.com

Abstract: *Energy and biochar (BCH) are produced from vegetable biomass, with thermo-chemical processes, without residues and with negative CO_2 emissions. Quality BCH with molar ratios O/H <0.2 and H/C < 0.2 contains at least 40% of biomass carbon, has 33% of input energy, is porous with a specific surface area of 150 – 400 m2/g.bc and has many non-energy uses. BCH with 10% moisture can be stored long-term as a carbon and energy stock. BCH as an agricultural amendment cheaply sequesters CO2 in the long term and ensures increased horticultural production. A stock of BCH ensures the production of cheap electricity and heat,* ***when and as much as needed****, with zero or negative CO_2 emissions, without or with low-capacity electric storage. Low-volatile BCH gasified in miniCHP unit produces electricity with 30% efficiency and thermal energy with 56%. For a CO_2 emission below zero, a maximum of 70% of the biochar produced is gasified. From the gasification of BCH with O2 and H2O, gas.bc is obtained as a cheap substitute for natural gas for local use in smart hybrid energy mini-grids.*

Keywords: *Biochar, energy stock, carbon footprint, natural gas*

1. Introduction

In the current period, bio-oil, biochar and pyrolysis gas can be produced from residual biomass through allothermal or autothermal pyrolysis on an industrial scale. On a midi scale, gas.bm and biochar (BCH) are obtained through gasification. Gas.py and gas.bm are burned to produce heat, and biochar for use as an agricultural amendment, filter material, or emergency energy stock [2, 3, 4, 5, 6, 15, 18].
The use of biochar as an agricultural amendment sequesters carbon in the soil for long periods of time with a negative carbon footprint CFP, is used as a filter material. The biochar is stored and gasified to recover energy, the toxic ash is embedded in concrete and stored for the long term, operation with positive CFP [1, 11, 12, 17, 19].
To decarbonize energy production with the CFP = 0 limit, it is necessary that part of the biochar be incorporated into agricultural soils to sequester carbon and contribute to increasing agricultural production, on average by 13% [8, 9, 10, 12].
Depending on the biomass from which the biochar is produced, for CFP =0 it would be necessary for at least 30% of the produced biochar to be used as an agricultural amendment [6, 7, 10].
Biochar with an average moisture content of 10% can be stored in maximum safety, building a decentralized energy stock that can be used – ***when and as much as needed*** – usually in emergency situations, without the grid, without photovoltaics or wind.
The residual or energetic biomass from which energy and biochar are produced is very diverse in chemical composition and ash content. Depending on the pyrolysis or gasification regime, different proportions of biochar with equally different properties are obtained.
In Romania, about 3500 thousand toe of energy is consumed annually for heating homes. 3 million homes are heated by burning wood, with thermal efficiencies below 30%, which represents a major national waste of energy. The efficient gasification of biomass and the use of biochar stocks for emergency situations are economically and ecologically viable alternatives, with great social impact.

2. Material and methods

Heat, bio-oil and biochar result from vegetable biomass with pyrolysis and gasification processes. Bio-oil and BCH can be stored, but the heat must be consumed efficiently and economically. A continuous production does not adapt to the real consumption of heat and electricity, which have a dominant random component. Producing energy when and as much as needed is the optimal economic and ecological option. Systems with the CHAB concept with discretized operation can produce heat when and as much as needed with a very small heat storage capacity [3, 4, 5, 7, 15].
The production of heat and biochar is done with CHAB concept installations equipped with GSIDD gas generators, with thermal power of 100kWth in hot water, called SEB.HW100, which can gasify a wide variety of chopped or pelletized vegetable biomass. The operating regimes are controlled to obtain a share of 20% biochar from dry biomass, i.e. 0.2 Mg.bc/Mg.bm.db, as well as maintaining the temperature in the OZ oxidation zone below the ash softening temperature.
A CHP.BC50 cogeneration unit is used for the production of gas.bc and electricity, it is equipped with a downdraft gasifier GBC.DD to obtain gas.bc with very little tar and high HHV.
For the simulation of biomass gasification, the MER.BM.GAZ.DD simulation program with the MUKMER model, produced by EROLSoft, was used for the oxypyrolysis and gasification processes with stratified downdraft or reversible front processes.
For the simulation of the SEB.HW100 unit, the MER.SEB.MESI simulation program, produced by EROLSoft, was used for the production of hot water/air and biochar.
For biochar gasification, the simulation program MER.BCH.GAZ.DD, produced by EROLSoft, was used for gasification with air, CO2, H2O and O2.
The results obtained have a margin of error of +5% to -10% due to the characteristics of the biomass used which have a large random dispersion due to the pedoclimate conditions and applied agricultural technologies.
Several types of residual, energetic or forestry biomass will be analyzed. Table 1 shows the types of nonwoody biomass, table 2 shows the types of woody biomass.

Table 1: Nonwoody biomass characteristics

Feature	U.M.	Values			
Biomass type		**wheat straw**	**corn stover**	**vegetables growing wastes**	**miscanthus**
Biomass price	€/Mg.bm	130.00	130.00	130.00	160.00
Water	kg.w/kg/bm	***0.080***	***0.080***	***0.080***	***0.080***
Carbon	kg.C/kg/bm	**0.4195**	**0.4444**	**0.4119**	**0.4407**
Hydrogen	kg.H/kg/bm	**0.0534**	**0.0476**	**0.0611**	**0.0552**
Oxygen	kg.O/kg/bm	**0.3938**	**0.3692**	**0.4191**	**0.3831**
Azote	kg.N/kg.bm	**0.0000**	**0.0000**	**0.0000**	**0.0055**
Sulfur	kg.S/kg.bm	**0.0000**	**0.0000**	**0.0000**	**0.0051**
Ash	kg.ash/kg.bm	**0.0534**	**0.0589**	**0.0280**	**0.0305**
HHV for BM.db	MJ/kg.bm.db	**18.158**	**18.635**	**18.574**	**19.317**
HHV	kWh/kg.bm	**4.641**	**4.762**	**4.747**	**4.937**
LHV for BM.db	MJ/kg.bm.db	**16.885**	**17.499**	**17.116**	**17.999**
LHV	kWh/kg.bm	**4.261**	**4.418**	**4.320**	**4.546**
Stoichiometric Flow	kg.air/kg.bm	**4.979**	**5.172**	**5.048**	**5.332**
Softening ash temperature	degree C	**840**	**990**	**1000**	**835**

Table 2: Woody biomass characteristics

Feature	U.M.	Values			
Biomass type		beech wood	energetic poplar	vine pruning	fruit growing pruning
Biomass price	€/Mg.bm	**200.00**	**200.00**	**130.00**	**140.00**
Water	kg.w/kg/bm	***0.080***	***0.080***	***0.120***	***0.120***
Carbon	kg.C/kg/bm	**0.4571**	**0.4385**	**0.4174**	**0.4421**
Hydrogen	kg.H/kg/bm	**0.0558**	**0.0526**	**0.0515**	**0.0524**
Oxygen	kg.O/kg/bm	**0.3938**	**0.3757**	**0.3883**	**0.3643**
Azote	kg.N/kg.bm	**0.0038**	**0.0396**	**0.0000**	**0.0079**
Sulfur	kg.S/kg.bm	**0.0002**	**0.0003**	**0.0000**	**0.0008**
Ash	kg.ash/kg.bm	**0.0093**	**0.0133**	**0.0229**	**0.0124**
HHV for BM.db	MJ/kg.bm.db	**19.904**	**18.986**	**18.635**	**20.027**
HHV	kWh/kg.bm	**5.087**	**4.852**	**4.555**	**4.896**
LHV for MB.db	MJ/kg.bm.db	**18.571**	**17.730**	**17.351**	**18.718**
LHV	kWh/kg.bm	**4.692**	**4.477**	**4.160**	**4.494**
Stoichiometric Flow	kg.air/kg.bm	**5.498**	**5.250**	**4.914**	**5.335**
Softening ash temperature	degree C	**1400**	**1200**	**1200**	**1200**

Agricultural residual biomass was chosen for the analysis – wheat straw, corn stover, vegetables growing wastes, vine pruning and fruit growing pruning; energetic biomass – miscanthus and energetic poplar; forest biomass - beech wood [2, 4, 8, 15].
Tables 3 and 4 present the parameters of the biomass gasification regimes in SEB.MESI, from which an average biochar share of 20% of the dry biomass is obtained and the ash softening temperature is not exceeded, in order not to block the propagation of the flaming pyrolysis and reduce the quality of the biochar produced.

Table 3: SEB.HW100 gasification regime for nonwoody biomass

Feature	U.M.	Values			
Biomass type		wheat straw pellets	corn stover pellets	vegetables wastes pellets	miscanthus pellets
Air ratio ER		**0.254**	**0.277**	**0.284**	**0.251**
Temperature in oxyzone	degree C	**779**	**823**	**823**	**775**
Biochar rate dry BM	kg.bc/kg.bm,db	**0.206**	**0.188**	**0.194**	**0.216**
Biochar rate	kg.bc/kg.bm	**0.189**	**0.173**	**0.179**	**0.198**
Carbon content in BCH	kg.C/kg.bc	**0.660**	**0.612**	**0.785**	**0.779**
Ash content in BCH	kg.ash/kg.bc	**0.281**	**0.339**	**0.156**	**0.153**
Molar ratio O/C	molO/molC	**0.033**	**0.027**	**0.027**	**0.034**
Molar ratio H/C	molH/molC	**0.310**	**0.302**	**0.302**	**0.311**
HHV for biochar	kWh/kg.bc	**6.711**	**6.175**	**8.085**	**8.022**
Biomass price	€/Mg.bm	**130.00**	**130.00**	**130.00**	**160.00**
Operating cost	€/y	**14885.85**	**14885.85**	**14885.85**	**14885.85**

Biomass consumption cost	€/y	**29215.43**	**33847.06**	**33838.49**	**30224.28**
Production costs	€/y	**44101.29**	**48732.91**	**48724.34**	**45110.13**
Thermal energy production	MWht/y	**485.050**	**639.687**	**532.441**	**397.898**
BCH mass production	Mg.bc/y	**39.895**	**42.171**	**43.545**	**35.105**
Thermal energy cost	€/MWht	**58.583**	**54.142**	**55.087**	**66.388**
BCH cost production	€/Mg.bc.db	**393.168**	**334.328**	**445.377**	**532.533**
Carbon from BCH cost	€/Mg.Cbc	**595.553**	**546.448**	**567.483**	**683.824**
Energy from BCH cost	€/MWh.bc	**58.58**	**54.14**	**55.09**	**66.39**

The biochar produced with SEB.HW100 unit has molar ratios O/C < 0.2 and H/C < 0.4 which is required for a biochar usable as an agricultural amendment, which produced at temperatures above 750 ºC is sterile, porous and pH >10.00 [1, 11, 12, 17, 18, 19, 20].
Very low volatile biochar is very good for gasification because very little tar is produced which is simple, safe and cheap to dispose of [13].
The prices for the analyzed biomass are estimated from the current supply in the market of pellets and wood chips, which can have large variations depending on the requirement, supply and demand for energy.

Table 4: SEB.HW100 gasification regime for woody biomass

Feature	**U.M.**	**Values**			
Biomass type		**beech wood pellets**	**energetic poplar pellets**	**vine pruning chopped**	**fruit pruning chopped**
Air ratio		**0.288**	**0.287**	**0.252**	**0.254**
Temperature in oxyzone	degree C	**819**	**823**	**856**	**877**
Biochar rate dry BM	kg.bc/kg.bm,db	**0.198**	**0.197**	**0.213**	**0.215**
Biochar rate	kg.bc/kg.bm	**0.182**	**0.181**	**0.187**	**0.189**
Carbon content in BCH	kg.C/kg.bc	**0.883**	**0.862**	**0.824**	**0.883**
Ash content in BCH	kg.ash/kg.bc	**0.051**	**0.073**	**0.122**	**0.0655**
Molar ratio O/C	molO/molC	**0.027**	**0.027**	**0.021**	**0.017**
Molar ratio H/C	molH/molC	**0.302**	**0.302**	**0.297**	**0.293**
HHV BCH	kWh/kg.bc	**9.172**	**8.947**	**8.524**	**9.177**
Biomass price	€/Mg.bm	***130.00***	***130.00***	***130.00***	***160.00***
Operating cost	€/y	**14885.85**	**14885.85**	**14885.85**	**14885.85**
Biomass consumption price	€/y	**48099.39**	**36562.25**	**25468.54**	**25576.92**
Production costs	€/y	**62985.25**	**51448.10**	**40354.40**	**40462.78**
Thermal energy production	MWht/y	**516.408**	**444.043**	**351.584**	**353.201**
BCH mass production	Mg.bc/y	**41.006**	**37.971**	**34.338**	**32.364**
Thermal energy cost	€/MWht	**70.57**	**65.44**	**62.63**	**62.23**
BCH cost production	€/Mg.bc.db	**647.29**	**589.67**	**533.89**	**571.10**
Carbon from BCH cost	€/Mg.Cbc	**732.79**	**678.91**	**647.66**	**646.57**
Energy from BCH cost	€/MWh.bc	**70.57**	**65.44**	**62.64**	**62.23**

Thermal energy can be produced with average costs in the range of 55 – 70 €/MWht depending on the price at which the gasified biomass enters production.
The production cost of BCH is lower for nonwoody biomass, as is the production cost of carbon from BCH, values that depend on the cost of the biomass processed.
BCH from nonwoody biomass contains a lot of ash and less carbon for which the main economically efficient use is as an agricultural amendment intended to increase the fertility of agricultural soils. A biochar with a high carbon content is indicated for gasification [1, 11, 12, 20].
Two representative types of biomass were chosen for the functional and energetic analysis. Poplar from intensive energy crops is used for woody biomass, which has a chemical composition similar to the average of forest resources [14, 16]. From the residual agricultural biomass, corn stover was chosen because it represents in RO and the EU about 40 of the collectable energy potential [5].
Table 5 shows the functional characteristics of the CHP.BC50 cogeneration unit with a nominal electrical power of 50 kWe. The CHP.BC50 produces cold gas.bc that can be used instead of natural gas and LPG, or to feed an electric power generator, when and as much as needed. The relatively low power was chosen to be usable in isolated locations with alternative operating regimes, low load with heat production, gas.bc production for consumption, electricity and heat production.
For maximum efficiency utilization, the generator set only regime in an optimal mode, the specialized heat engine is constructively optimized and extremely driven, with an efficiency of up to 50%, a common variant for hybrid cars with heat engine charging. The 27% electrical efficiency used in the simulation is still modest, but with a real basis.

Table 5: Operating characteristics of CHP.BC50 unit

Feature	**U.M.**	**Values**	
BCH from biomass type		**energetic poplar**	**corn stover**
HHV for BCH	MWh/Mg.bc	***8.944***	***6.175***
Carbon content	kg.C/kg.bc	***0.862***	***0.612***
BCH production cost	€/Mg.bc	***589.00***	***355.00***
Handling and storage	%	***5***	***5***
BCH user cost	€/Mg.bc.db	**618.45**	***372.75***
Cooled gas.bc efficiency	%	***75.0***	***75.0***
Gas.bc specific energy	MWh/kg.bc	***6.708***	***4.631***
Gas engine yield	%	***38***	***38***
Electric generator yield	%	***95***	***95***
Electro engine generator yield	%	***36.1***	***36.1***
Electricity production efficiency	%	***27.1***	***27.1***
Yield heat recovery gas.bc cooling	%	***0.213***	***0.213***
Yield heat recovery gas engine	%	***37.2***	***37.2***
Thermal energy efficiency	%	***58.5***	***58.5***
Cogeneration efficiency	%	***85.5***	***85.5***
Cogeneration Index	%	***46.3***	***46.3***
CFP emitted from operation	kg.CO2/Mg.bc	**35.000**	**35.000**

Table 6 shows the results of the economic estimation of the use of CHP.BC50 for a continuous operation of 7000 h/y and an operating life of 5 years, extendable through successive upgrades.

This results in an hourly operating cost of 7.10 €/h affected by input cost estimation errors of ± 10 %.

Table 6: Operating costs for CHP.BC50 unit

Feature	U.M.	Values
Specific power CHP price	€/kWe	**2500**
Electric power	kWe	**50.000**
CHP.BC50 price	€/system	**125000**
Installation and start-up ratio	%	**20**
Installation and start-up costs	€/system	***150000***
Live Cycle operating time	y/LC	**5.00**
Annual operating time	h/y	**7000.00**
Annual banking interest	%	**5.00**
Annual income from deposit	€/y	**7500.00**
Residual value ratio	%	**30.00**
Installment depreciable value	€/system	**149985**
Annual value to be amortized	€/y	**37497**
Annual maintenance rate costs	%	**15**
Annual maintenance costs	€/y	**5624.55**
Operator cost	€/month	**500.00**
Annual operating costs	€/y	**49121.55**
Hourly operating costs	€/h	**7.017**

3. Results

From the data obtained for operating regimes and production costs, the production costs for the production of electricity and heat, as well as for gas.bc intended for local replacement of PLG and in emergency cases of NG at network blockages, can be estimated accurately enough.

Table 7: Economic evaluation of CHP.BC50 unit

Feature	U.M.	Values	
Biomass type		**poplar**	**corn stover**
HHV for BCH	MWh/Mg.bc	**8.944**	**6.175**
BCH using cost	€/Mg.bc	**618.45**	**372.75**
Specific electricity production	MWhe/Mg.bc	**2.422**	**1.672**
Specific BCH consumption	kg.bc/kWhe	**0.413**	**0.598**
Hourly BCH consumption	kg.bc/h	**20.647**	**29.906**
Hourly BCH cost	€/h	**12.77**	**11.15**
CHP production hourly costs	€/h	**19.79**	**18.15**
Hourly input energy	MWh/h	**184.672**	**184.672**
Electricity production efficiency	%	**0.271**	**0.271**
Thermal energy efficiency	%	**0.585**	**0.585**

Cogeneration Index	%	**0.463**	**0.463**
Hourly electricity production	MWhe/h	**0.050**	**0.050**
Hourly thermal energy production	MWht/h	**107.941**	**107.941**
Equivalent energy produced annually	MWh/y	**108.049**	**108.049**
Specific cost thermal energy	€/MWht	**183.12**	**168.12**
Electricity cost	€/MWhe	**395.33**	**362.94**
ENEL tariff	€/MWhe	**246.00**	**246.00**
Difference from ENEL tariff	€/MWhe	**149.33**	**116.94**

Table 8: Economic evaluation gas.bc use

Feature	**U.M.**	**Values**	
Biomass type		**poplar**	**corn stover**
CHP.BC50 hourly consume	kg.bc/h	**20.647**	**29.9074**
BCH cost	€/Mg.bc	618.45	**372.75**
Hourly cost BCH consumption	€/h	**12.77**	**11.15**
HHV cooled gas.bc	MWh/Mg.bc	**6.708**	**4.631**
Gas.bc hourly energy production	MWh/h	**0.139**	**0.139**
Gas.bc energy cost	€/MWh	**80.65**	**60.36**
Hourly operating costs	€/h	**4.91**	**4.91**
Hourly gas.bc production cost	€/h	**17.68**	**16.06**
Gas.bc energy cost	€/MWh.gbc	**127.66**	**115.95**
NG average cost in 2022 year	€/MWh	**95.35**	**95.35**
Gas.bc to NG difference energy costs	€/MWh	**32.31**	**20.60**
PLG energy cost in 2022 year	€/MWh	**398.22**	**398.22**
Gas.bc to PLG difference energy costs	€/MWh	**-270.56**	**-282.27**

The cost of the produced electricity of 380 €/MWhe ± 10% is relatively high compared to the current one in the national network of 246 €/MWhe, but lower than that of the electricity produced by the intervention generators. For energetically isolated areas without an electrical network, the use of CHP.BC with biochar produced from locally available biomass is economical, ecological and with a positive social impact.
Table 8 presents the economic evaluation of the use of gas.bc to replace NG in emergency cases and PLG for local use.
The production cost of 120 €/MWh.gbc ± 10% is +25% higher than that of NG, but economically acceptable for emergency situations when the supply of energy for vital consumption is important.
In the case of replacing the local use of PLG with gas.bc, the cost difference is obvious, which is on average +255 €/MWh, that is, the use of gas.bc is 3.3 times cheaper, being an obvious economic alternative. However, the difference is mitigated by the need for a much higher initial investment, but with guaranteed long-term economic efficiency.

4. Conclusions

In the current energy crisis, the production of energy and biochar from residual plant biomass, **when and as much as necessary**, is a complementary solution when it is dark and the wind is not blowing, ensuring economically and ecologically the necessary energy consumption in real time.

This work is a contribution to the development of research and the design of systems for the production and efficient use of biochar produced from vegetable biomass for the production of energy when and as much as necessary and the increase of agricultural soil fertility.
A wide variety of plant biomass can be gasified with SEB.MESI with CHAB concept to produce when and how much thermal energy is needed with an average efficiency of 45% and to obtain 20% high quality biochar.
The biochar produced with SEB.MESI has molar ratios O/C < 0.2 and H/C < 0.4, which is required for a biochar usable as an agricultural amendment, which, being produced at temperatures above 750 ºC, is sterile, porous and with pH >10.0. The minimum commercial price in EU 2021 was 1250 €/Mg.bc with a maximum of 4000 €/Mg.bc.
The production costs for biochar are 350 – 450 €/Mg.bc for nonwoody biomass and 550 – 650 €/Mg.bc for woody biomass, much below the current prices on the BCH market, which ensures an advantageous capitalization.
It is worth mentioning the production cost of carbon from BCH, which is on average 550 – 650 €/Mg.Cbc for nonwoody biomass and 650 – 750 €/Mg.Cbc for woody biomass, strongly influenced by the cost of the biomass used.
Biochar can be stored as a carbon and energy stock, for long periods, usable as an agricultural amendment, as a filter material, but very important as a source of energy for emergency situations, **when and as much as needed**.
Energy can be produced from gas.bc 3 times cheaper than from PLG, thus being a cheap and safe source of fuel gas for isolated areas without a NG network.
The cost of electricity produced from BCH is higher than that from the network, by about 35-50%, acceptable for emergency situations, but much lower than that of emergency generators.
The biochar produced from residual agricultural plant biomass, which has a lot of ash, is indicated to be used effectively as an agricultural amendment, with which it produces an average increase in agricultural production by 13%, an action subsidized with green vouchers, now with the value of 180 €/Mg. Cbc.
The stock of biochar can be used when and as much as necessary as an agricultural amendment or for the production of energy in emergency situations or for continuous consumption, for a zero carbon footprint it is required that at least 30% of the stock be used as an agricultural amendment.

References

[1] Conte, Pellegrino, Roberta Bertani, Paolo Sgarbossa, Paola Bambina, Hans-Peter Schmidt, Roberto Raga, Giuseppe Lo Papa, Delia Francesca Chillura Martino, and Paolo Lo Meo. “Recent Developments in understanding Biochar’s Physical–Chemistry.” *Agronomy* 11, no. 4 (2021): 615.
[2] Greco, F., S. Righi, A.C. Dias, and L. Tarelho. “Wood pellet as biofuel: a comparative life cycle analysis of a domestic and industrial production chain.” Paper presented at the 12th Italian LCA Network Conference, Messina, Italy, June 11-12, 2018.
[3] Murad, Erol, and Florian Dragomir. “Heat generators with TLUD gasifier for generating energy from biomass with a negative balance of CO_2.” Paper presented at the International Conference on Hydraulics and Pneumatics HERVEX 2012, Călimăneşti-Căciulata, Romania, November 7-9, 2012.
[4] Murad, E., C. Dumitrescu, F. Dragomir, and M. Popescu. “CHAB concept in sustainable development of agriculture.” Paper presented at the International Symposium ISB-INMA TEH' 2016, Bucharest, Romania, October 27 – 29, 2016.
[5] Murad, Erol. “Production of energy and agribiochar without residues and with negative carbon footprint with CHAB and CHBAP concepts from the Romanian residual vegetable agricultural biomass.” Paper presented at the International Symposium ISB-INMA TEH’ 2021, Bucharest, Romania, October 29, 2021.
[6] Murad, Erol, Manuela Drăghicescu, Perino-Constantin Baraga, and Adrian-Ioan Drăghicescu. “Energy and Biochar production with a ZERO carbon foot print.” Paper presented at the National Conference of New and Renewable Energy Sources, CNSNRE 2022, Valahia University, Târgoviște, Romania, June 2 - 3, 2022.
[7] Murad, Erol. “Production of energy and agribiochar without residues and with negative carbon footprint with CHAB and CHPAB concepts from the annual residual vegetable agricultural biomass from

Romania.*" ANNALS of Faculty Engineering Hunedoara – International Journal of Engineering* XX, no. 1 (February 2022): 109-116.
[8] Murad, E. "Biochar from residual vegetable agricultural biomass amendment for increasing agricultural production and energy stock." Paper presented at the International Symposium ISB-INMA TEH' 2022, Bucharest, Romania, October 7, 2022.
[9] Hu, Qiang, Janelle Jung, Dexiang Chen, Ken Leong, Shuang Song, Fanghua Li, Babu Cadiam Mohan, Zhiyi Yao, Arun Kumar Prabhakar, Xuan Hao Lin, Ee Yang Lim, Le Zhang, Gupta Souradeep, Yong Sik Ok, Harn Wei Kua, Sam F.Y. Li, Hugh T.W. Tan, Yanjun Dai, Yen Wah Tong, Yinghong Peng, Stephen Joseph, and Chi-Hwa Wang. "Biochar industry to circular economy." *Science of the Total Environment* 757 (February 2021): 143820.
[10] San Miguel, G., A.M. Méndez, G. Gascó, and A. Quero. "LCA of alternative biochar production technologies." Paper presented at the15th International Conference on Environmental Science and Technology, Rhodes, Greece, August 31 - September 2, 2017.
[11] Schmid, Hans-Peter, Claudia Kammann, and Nikolas Hageman. *EBC-Guidelines for the Certification of Biochar Based Carbon Sinks. Version 2.1 from 1st February 2021*. Ithaka Institute for Carbon Strategies, Switzerland (www.ithaka-institut.org), 2020.
[12] Schmidt, Hans-Peter, Claudia Kammann, Nikolas Hagemann, Jens Leifeld, Thomas D. Bucheli, Miguel Angel Sánchez Monedero, and Maria Luz Cayuela. "Biochar in agriculture – A systematic review of 26 global meta-analyses." *GCB-Bioenergy* 13, no. 11 (November 2021): 1708-1730.
[13] Zhao, Shengguo, Liang Ding, Yun Ruan, Bin Bai, Zegang Qiu, and Zhiqin Li. "Experimental and Kinetic Studies on Steam Gasification of a Biomass Char." *Energies* 14 (2021): 7229. https://doi.org/10.3390/en14217229.
[14] Stolarski, M.J., K. Warminski, and M. Krzyzaniak. "Energy Value of Yield and Biomass Quality of Poplar Grown in Two Consecutive 4-Year Harvest Rotations in the North-East of Poland." *Energies* 13 (2020): 1495. doi:10.3390/en13061495 www.mdpi.com/journal/energies.
[15] Pröll, Tobias, and Florian Zerobin. "Biomass-based negative emission technology options with combined heat and power generation." *Mitigation and Adaptation Strategies for Global Change* 24, no. 7 (2019): 1307–1324.
[16] Townsend, P.A., S.P. Kar, and R. O. Miller. *Poplar (Populus spp.) Trees for Biofuel Production*. USDA National Institute of Food and Agriculture, September 5, 2019.
[17] Levine, Jonah (ed.). "U.S.-Focused Biochar Report. Assessment of Biochar's Benefits for the United States of America." Center for Energy and Environmental Security, June 2010, Colorado, USA.
[18] Bioenergy Europe. *Bioenergy Europe factsheet: Biomass for energy - Agricultural residues & energy crops*. October 15, 2019. Accessed October 12, 2022. https://bioenergyeurope.org/component/attachments/attachments.html?id=561&task=download.
[19] European Biochar Industry Consortium e.V. (EBI). *EBI Whitepaper. Biochar-based carbon sinks to mitigate climate change*. October 2020. Accessed October 10, 2022. http://www.biochar-industry.com/wp-content/uploads/2020/10/Whitepaper_Biochar2020.pdf.
[20] Verra. Etter, Hannes, Andrea Vera, Chetan Aggarwal, Matt Delaney, and Simon Manley. Verified Carbon Standard Program. *Methodology for biochar utilization in soil and non-soil applications*. Version 1.0. August 4, 2021. https://verra.org/wp-content/uploads/imported/methodologies/210803_VCS-Biochar-Methodology-v1.0-.pdf.

ISSN 1454 - 8003
Proceedings of 2022 International Conference on Hydraulics and Pneumatics - HERVEX
November 9-10, Băile Govora, Romania

EXPERIMENTAL RESEARCH ON THE INFLUENCE OF COMBUSTION AIR VELOCITY ON ENERGY EFFICIENCY AT TLUD GENERATOR

Ioan PAVEL[1,*], Gabriela MATACHE[1], Gheorghe ȘOVĂIALĂ[1], Kati PAVEL[1], Dragoș ANGHELACHE[2]

[1] INOE 2000-Subsidiary Hydraulics and Pneumatics Research Institute (INOE 2000-IHP) Bucharest/Romania

[2] National Institute of Research – Development for Machines and Installations Designed to Agriculture and Food Industry- INMA, Bucharest / Romania

* pavel.ihp@fluidas.ro

Abstract: *Biomass energy dates back to the beginnings of human civilization and is one of the most important resources to meet the daily energy requirements for many people in developing countries. Biomass gasification is an important branch of heat production, electricity or biofuels. With the help of the TLUD gasification process, applied to heating systems or for cooking, thermal energy and biochar can be produced, contributing to the reduction of deforestation pressure, to the improvement of soil productivity and to a sustainable development.*
The article presents experimental tests on the influence of the speed of the combustion air (secondary air) on the energy efficiency of a laboratory testing equipment, of gaseous type TLUD. The results show a substantial increase in the temperature in the flame in case of increasing the flow of combustion air and its speed by 30% compared to the ratio of 1/3 recommended in other scientific articles on this topic.

Keywords: *TLUD Gasification, biomass, biochar, greenhouse gases, stoichiometric combustion*

1. Introduction

Energy is an essential factor of socio-economic development and it is clear that in the future demand will increase worryingly much [1]. Problems with the need for energy are found in all developed or developing countries. For developed countries in the future, energy demand will be low compared to developing countries, where it is necessary first and foremost to improve energy accessibility [2].
Affordable energy for everyone is the starting point for poverty alleviation, and for the development of human capital [2]. For this desideratum, the economic cost is usually a priority, before the impact on the environment or the health of the population. This is shown in a United Nations report [4] which states that 3.2 billion people depend on solid fuels (wood, vegetable waste or coal) for heating. The imbalance between biomass supply and demand leads to massive deforestation and deforestation. It is worrying because these actions bring negative effects on the environment and on human health.
The negative effects of using biomass for energy production also result from the incomplete combustion of biomass and the release of CO2 and PM into the atmosphere, which results in an increase in global temperature and an increase in climate change [5]. Climate change mitigation and forest resource conservation have been two main motivations for most improved combustion system projects. In many developing countries, the cooking technique used is still the traditional open fire that has less than 10% energy efficiency. The percentage can be increased with the use of improved combustion systems, thus reducing the consumption of firewood and combating deforestation [6].
Energy consumption and economic growth have a two-way causality [2], as economic growth encourages energy consumption and the growth of energy consumption affects economic growth and the environment. The use of improved burn technology, such as the TLUD gasification process, which produces thermal energy and biochar, could help reduce deforestation pressure, improve soil productivity and heating systems, or for better performing and more environmentally

friendly cooking. Almost any form of natural organic material (woody) can be converted into biochar. Therefore, materials considered as wood waste can be efficiently transformed, through gasification, into energy and biochar which can be used as a basic material for the improvement of degraded soils, and to sequester carbon in the soil over a long period of time, contributing to the reduction of greenhouse gas emissions, to the achievement of an efficient protection of the environment and to the achievement of a sustainable energy development.
The name of TLUD was adopted due to the burning type Top Lit Up Draft [7, 8, 9], in which the ignition is made at the top, the pyrolytic front advances into the biomass layer and the gasification air (primary) penetrates through the biomass layer from the bottom up. More details about this process can be seen in various published articles [10,11, 12, 13].

2. Test device

The laboratory device on which the tests were performed (fig. 1) consists of a gas generator on the TLUD principle (1), equipped with air flowmeters (7.8) and adjustment throttles (5), seven temperature probes (2.3), four in the pyrolysis area, one for the supply air, one in the flame zone and one in the water bowl for power testing. All these elements are placed on an electronic scale (9) to establish the hourly consumption of biomass. For the measurement of the gasification air pressure (necessary for crossing the biomass layer) a pressure transducer is provided (10). Air is supplied by a compressed air source (6).

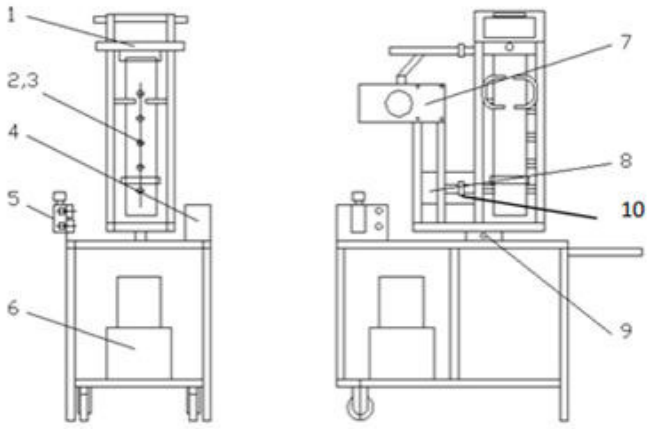

1-gasogen
2,3- temperature probes
4- electrical panel
5- adjustment throttles
6- compressed air source
7,8- air flowmeters
9- electronic scale
10- pressure transducer

Fig. 1. Test device component

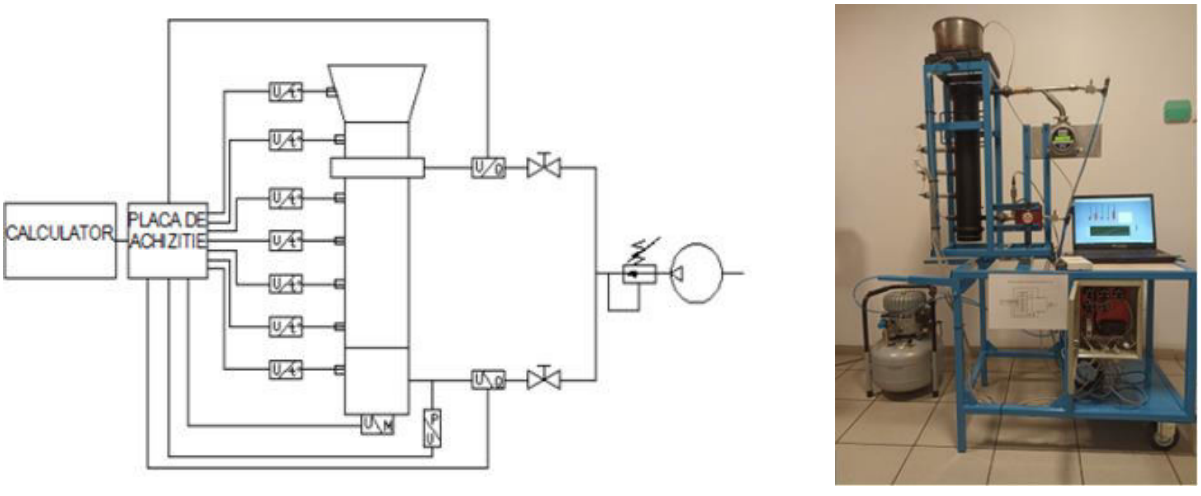

Fig. 2. Functional scheme / test device

According to the functional scheme (fig. 2) the data provided by the sensors are purchased and stored on the computer through a purchase board [13] [14].
A data acquisition program has been created in LabView, with a friendly graphical interface (fig. 3) that displays and records all the purchased parameters and their graphics in real time.

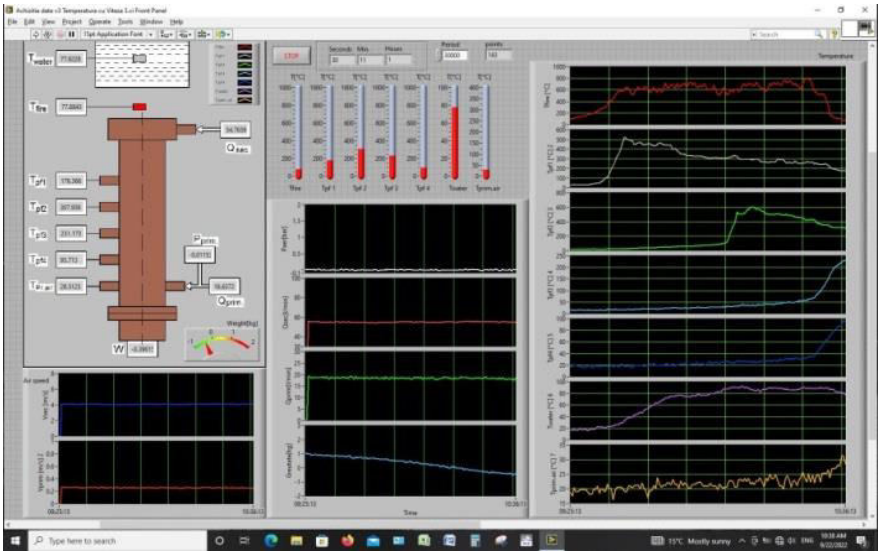

Fig. 3. Graphical interface created in LabView

Technical data of the test device:
- Di = Ø106 mm
- H max=450 adjustable by sieve positioning
- Biomass volume / 0.1 m = 0.78 dm³
- Hourly consumption: 0.8 kg/h
- Operating time / 0.1 m biomass layer height =0.7-1 h
- Thermal power at the burner = 2.7 kWth
- Gasification air section 12 cm²
- Combustion air section 2.3 cm² or optional 20.3 cm²

TLUD modules with powers of 3-4 KWth generally have a biomass consumption of 10-15 g/min and require a primary air flow (gasification) of 15-25 l/min and secondary air (combustion) of 30-50 l/min, for the reactor diameter of 100 mm.

3. The testing methodology refers strictly to this construction of TLUD gasifier

For each test, the TLUD type laboratory device is lit at the top and the pyrolytic front, initially formed, advances into the fixed bed of biomass. The primary air (gasification) is regulated using the flow meter at the value of 25 l / min and is introduced into the lower part through 130 holes with a total section of 12 cm². It penetrates through the biomass bed to the pyrolytic front area where the gas that rises is generated, due to the ascending current, at the top, and mixes with the secondary air, necessary for complete combustion, regulated to the value of 50;65 l/min, supplied through 18 holes with a total section of 2.3 cm². The mixture burns at the top with the flame open.
The values of the flows, of the primary/secondary air velocity and of the flame temperature are recorded in real time and stored in the computer through the data acquisition board.

4. Results

Two tests were made in order to track the influence of the primary air velocity (of combustion) or on the energy produced in the flame.

Test 1

For the first test, the primary/secondary air flow was adjusted with the ratio of 1/3 respectively of 25/50 l/min (fig. 4) and a ratio of speeds of 0.35/3.5 m/sec (fig. 5) was recorded (for this TLUD construction) and the average temperature recorded in the flame was about 700°C (fig. 6).

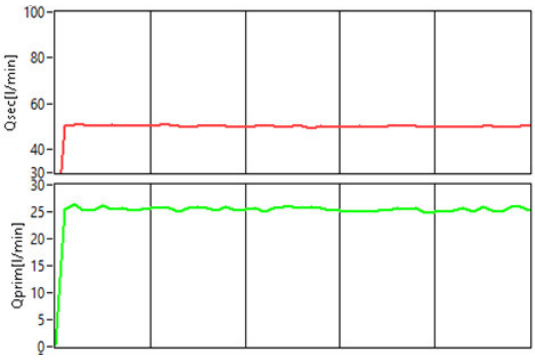

Fig. 4. Variation of primary/secondary air flow during the test (25/50 l/min)

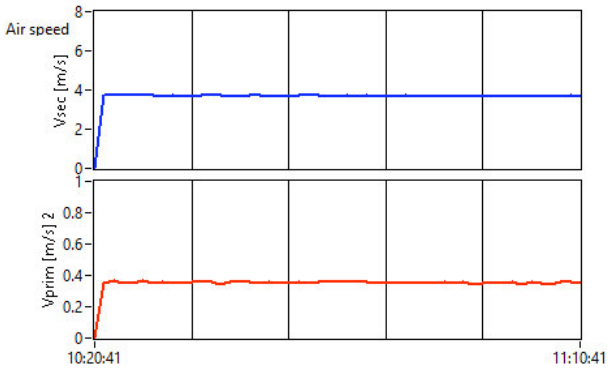

Fig. 5. Variation in primary/secondary air velocity during the test (25/50 l/min)

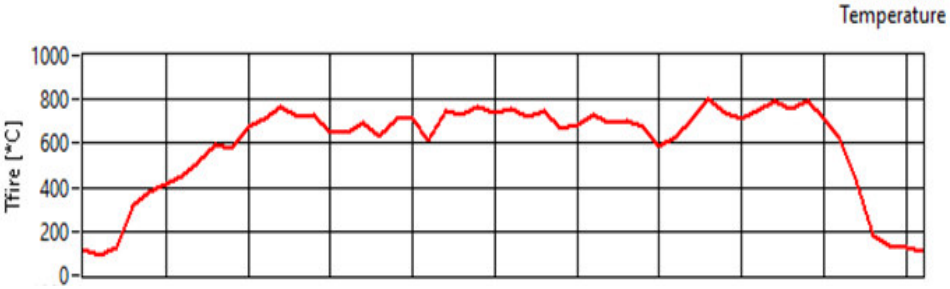

Fig. 6. Flame temperature variation during the test (25/50 l/min)

Test 2

For test 2, the primary air flow adjustment of 25 l/min was kept and the secondary air flow was supplemented by 30% i.e. 65 l/min (fig. 7) to increase the speed (turbulence) of the mixing air and a ratio of speeds of 0.35/4.5 m/sec (fig. 8) was obtained (for this TLUD construction) and the average temperature recorded in the flame was about 800°C (fig. 9).

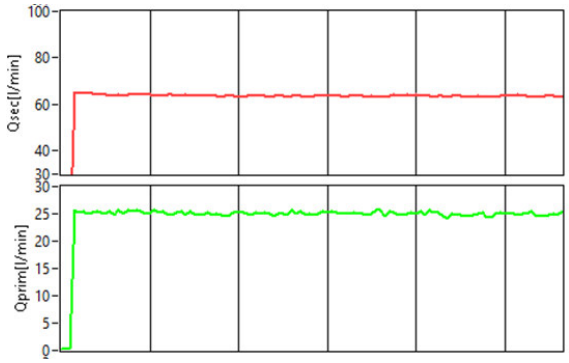

Fig. 7. Variation of primary/secondary air flow during the test (25/65 l/min)

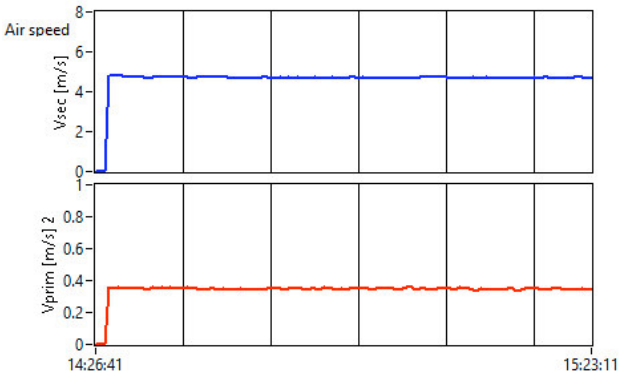

Fig. 8. Variation in primary/secondary air velocity during the test (25/65 l/min)

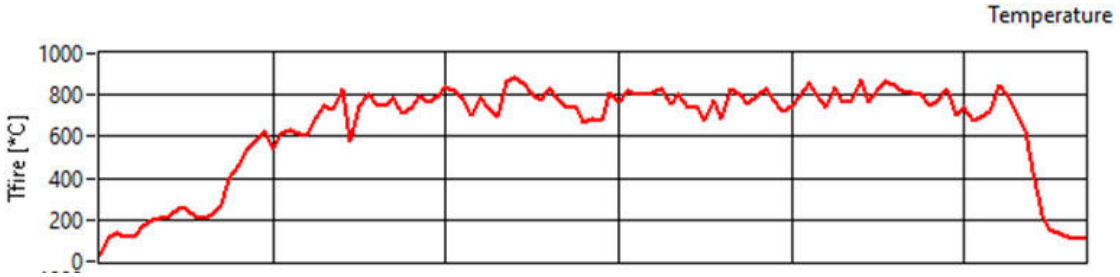

Fig. 9. Flame temperature variation during the test (25/65 l/min)

5. Conclusions

The increase of the secondary (combustion) air flow by 30% led to the increase of its speed from 3.5 m/sec to 4.5 m/sec on the same supply section and to the realization of a turbulent mixture with superior calorific value.
The test results indicate a higher efficiency of the equipment (flame temperature higher by 100°C) when the flow rate and speed of the combustion air has been supplemented by 30%.
Further studies and research are needed to obtain the best performance on this equipment that proves to be environmentally friendly, which can contribute to the reduction of greenhouse gas emissions, to the achievement of an efficient protection of the environment and to the achievement of a sustainable energy development.

Acknowledgments

This work was supported by a grant of the Ministry of Research, Innovation and Digitization, CCCDI - UEFISCDI, project number PN-III-P2-2.1-PTE-2021-0306, Financial Agreement no. 87PTE/ 21.06.2022, within PNCDI III. It has also received financing under a project funded by the Ministry of Research, Innovation and Digitization through Programme 1- Development of the national research & development system, Sub-programme 1.2 - Institutional performance - Projects financing the R&D&I excellence, Financial Agreement no. 18PFE/30.12.2021.

References

[1] Ministry of Lands and UNCRD. *Kwale District and Mombasa Mainland South Regional Physical Development Plan 2004–2034.* Nairobi, UNON Publishing Services Section, 2011.
[2] Toth, F.L., and M.L. Videla. *Energy for development: a key to long-term sustainability. Energy for Development*. Springer, 2012.
[3] United Nations. *The Sustainable Development Goals Report 2017*. In: JENSEN, L. (ed.). New York: United Nations, 2017.
[4] United Nations. *United Nations Decade of Sustainable Energy for All: Report of the Secretary General*. United Nations General Assembly, 2013.
[5] Ekouevi, K. “Household Energy for Cooking: Project Design Principles.” *Energy and Mining Sector Board Discussion Paper Series*, Paper no. 27, 2013.
[6] Mehetre, S.A., N. Panwar, D. Sharma, and H. Kumar. “Improved biomass cookstoves for sustainable development: A review.” *Renewable and Sustainable Energy Reviews* 73 (2017): 672-687.
[7] Jetter, J., Y. Zhao, K.R. Smith, B. Khan, T. Yelverton, P. Decarlo, and M.D. Hays. “Pollutant emissions and energy efficiency under controlled conditions for household biomass cookstoves and implications for metrics useful in setting international test standards.” *Environ. Sci. Technol.* 46 (2012): 10827–10834.
[8] Jetter, J., and P. Kariher. “Domestic solid fuel stoves: Characterization of performance and emissions.” *Biomass Bioenergy* 33 (2009): 294–305.
[9] Maccarty, N., D. Ogle, D. Still, T. Bond, and C. Roden. “A laboratory comparison of the global warming impact of five major types of biomass cooking stoves.” *Energy for sustainable development*, 12 (2008): 56-65.
[10] Maccarty, N., D. Still, and D. Ogle. “Fuel use and emissions performance of fifty cooking stoves in the laboratory and related benchmarks of performance.” *Energ. Sustain. Develop.* 14 (2010): 161–171.

[11] Roth, C. *Micro-gasification: Cooking with dry biomass gas: An introduction to wood gas concepts and applications. Combustion Technologies for Cooking*. Second ed. Bonn, GIZ-Deutsche Gesellschaft für Internationale, 2013.

[12] Tryner, J., J.W. Tillotson, M.E. Baumgardner, J.T. Mohr, M.W. Defoort, and A.J. Marchese. "Effects of Air Flow Rates, Secondary Air Inlet Geometry, Fuel Type, and Mode of Operation on Gasifier Stove Performance." *Environment. Sci. Tech.* 50 (2016): 9754–9763.

[13] Marchese, A., M. Defoort, X. Gao, J. Tryner, F.L. Dryer, F. Haas, and N. Lorenz. *Achieving level 4 emissions in biomass stoves*. Office of Scientific and Technical Information (OSTI): Oak Ridge, TN, USA, 2018.

[14] Pavel, Ioan, Alexandru-Polifron Chirita, Gabriela Matache, Ana-Maria Popescu, and Ioan Caba. "Combustion test equipment in low power TLUD gasifiers / Echipament de testare a arderii in gazogenele tip TLUD de putere mica." Proc. of ISB-INMA TEH' 2021 International Symposium, Bucharest, Romania, October 29, 2021, pp. 632-641.

ISSN 1454 - 8003
Proceedings of 2022 International Conference on Hydraulics and Pneumatics - HERVEX
November 9-10, Băile Govora, Romania

ELECTRO-MECHANICAL SIMULATION OF A HYBRID STEPPER MOTOR

Ilie-Constantin ROȘIANU[1,2,*], Edgar MORARU[2], Philip COANDĂ[2], Vlad-Andrei STĂNESCU[2], Daniel-Constantin COMEAGĂ[2]

[1] Siemens Industry Software SRL, *calin.rosianu@siemens.com

[2] Politehnica University of Bucharest, edgar.moraru@upb.ro; philip.coanda@gmail.com; stanescu.vlad1998@gmail.com; daniel.comeaga@upb.ro

Abstract: *In this paper modern simulation methods are used for modelling the functioning principles of a hybrid stepper motor, which is widely used in commercially available mechatronics systems, where exact positioning is necessary, such as the case of modern 3D printers. The simulation created and its results are presented, results from which further mechatronic simulations can be derived. From the standard black-box simulation and design of electric-machines, FEA simulations allow the engineers to create models that take into account the shape of the elements of an electric motor, shapes that have a great influence on the well-functioning of such motors. In the end, we present further simulation possibilities.*

Keywords: *Stepper motor, variable reluctance motor, switched reluctance motor, hybrid motor, electro-mechanical simulation, Simcenter3D, Simcenter MAGNET*

1. Introduction

Stepper motors are widely used to drive all kind of machines, from simple plotters to complex machines such as modern 3D printers [1] [2]. The versatility of this electrical machine, given by its ability to be driven in discrete steps, thus making it possible to position its shaft to the desired location. In addition, with the advent of the new and better IC drivers, using stepper motors became a lot easier.
Using a microcontroller to control the steps outputted by the stepper motor driver, gave these electrical machines the ability to be present all around us.
One important application in which stepper motors are essential is the field of additive manufacturing. When a component is created using Additive manufacturing [3] [4] techniques, a printing head or a mirror needs to be positioned with great precision, and stepper motors makes this possible. However, one element that really contributes to the precision of a working stepper motor is its driver, as this is the one that creates the waveforms that drives each phase of the stepper motor.
As stated earlier, an important field in which stepper motor show their power is the Additive manufacturing one, but there is one more reason why they are so important, and that is the apparition of the new generation of 3D printers, the ones that make use of more degrees of freedom to create the part, using the FDM process [5] [6].
In the usual case, a classical 3D printer using the FDM process makes use of only 3 degrees of freedom and thus it has 3 axes only which usually represent the 3 Cartesian axes. Other types of 3D printers with 3 axes are the Delta 3D printers or the Polar 3D printers, which make use of a cylindrical coordinate system. However, for the 3D printers of the new generation, which we believe will represent in a few years the new norm, is mandatory to use at least one new axis to increase the DOF's of the part.
The new axes used are usually rotation axes, as the only degrees of freedom remaining are the rotation ones. These rotations are created with the use of a stepper motor and thus a perfect positioning system is needed.
This calls for better motor design and better stepper motor driver design, as most of the parameters that govern the correct functioning of the stepper motor are dependent on the temperature.
Because the stepper motors will be subjected to varying loads, as the parts created will increase the moment of inertia that the motor has to overcome, this moment of inertia varies as well with the inclination of the printing bed.
In this paper, we propose a way to simulate the functioning of a hybrid stepper motor using the *FEA* software *Simcenter3D*, thus gaining an insight into how different parameters affect the motor

functioning. This is the basis for further development of a better stepper motor to be used in advanced mechatronics applications.

2. Stepper motor functioning principles

2.1. Classification of stepper motor electrical machines

A variety of electrical machines can be defined as stepper motors, meaning that the shaft is positioned in discrete steps, but what differentiates them is how the magnetic fields are produced that make it possible to move the shaft in discrete steps.
The working principle of all stepper motors is that of the variable reluctance. The main idea behind it is that if you let a bar of iron suspended in air, which is free to rotate around an axis, and if you apply a magnetic field, the bar will tend to align itself with the magnetic field. If the magnetic field is rotated, then the bar will tend to align accordingly.
Based on this principle, there exists two main types of stepper motors [7]:

- Variable Reluctance types
- Hybrid types

The only difference between them is the way that the magnetic field is created, but the working principle of them both is almost the same. Thus, in the Variable Reluctance type, the magnetic field is created by stationary coils wound around the stator teeth, whereas the hybrid type also has inside its rotor a permanent magnet. Although their function is almost identical, their use is different as the *Variable Reluctance* motors usually tend to be used in applications which need larger step angles (usually 15º, 30º or even 45º), whereas the *hybrid* ones tend to be used for smaller angle steps (0.9º, 1.8º).

2.2 How the hybrid stepper motor works

For additive manufacturing the stepper motor need to drive small angular increments, usually necessary in the case of 3D printers, thus it is better to describe the workings of the hybrid stepper motor.
In **Fig. 1.** several different sections of the inside structure of a hybrid stepper motor are presented, with a design specific to a *Variable Reluctance* motor, as it has some number of teeth (this number is

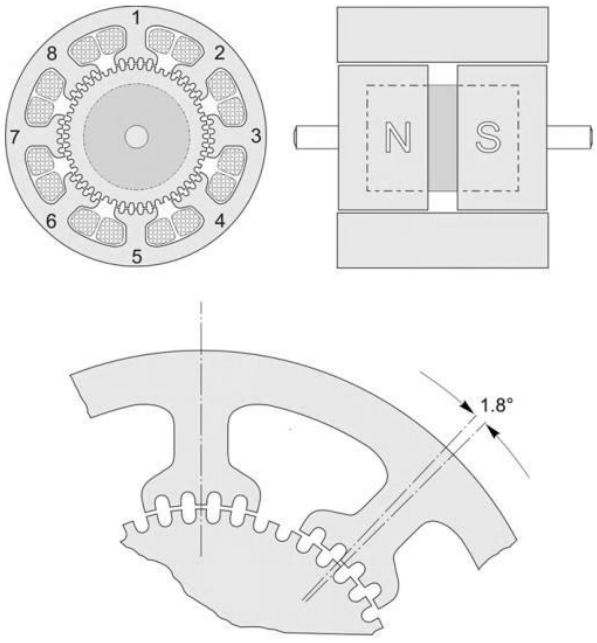

Fig. 1. Graphical description of a hybrid stepper motor [7]

important for the computation of the stepping angle). In the upper right corner of Fig. 1, we can see a section from the side view of the stepper motor, and we can see that inside the rotor, which is composed

of two cups, there is a permanent magnet. This permanent magnet has a uniform orientation along the axis of rotation, thus its magnetic field intersects the teeth on the stator.
The step angle is given by the following formula:

$$\theta_{step} = \frac{360\ °}{N_{rotor\ teeth} * N_{stator\ phases}} \quad (1)$$

For a common hybrid motor, such as a NEMA 17, used in a lot of commonly used 3D printers, the rotor has 50 teeth on each cup, which are rotated one to the other, with an angle equal to half a stepping angle (this is due to the aligning tendency of the teeth on the rotor to the ones on the stator), which makes for a total of 100 teeth on the rotor. Usually this kind of motor has two phases connected to 8 stator poles (4 poles per each phase) thus we get the common stepping angle of 1.8^{o} or 200 steps per full revolution of the motor.
It can be seen that in order to rotate the rotor a certain amount, the stator coils needs to be energized in a certain order that would tend to align the teeth in the correct position. In order to do this, usually a microcontroller is paired with an integrated circuit driver, which switches the current to the correct phase, thus we see that these types of motor, the stepper motors, need to have intelligent electronic devices accompanying them.
Coming back to Fig. 1, we can see in the left upper corner the front section of the hybrid stepper motor. As stated earlier, this motor usually has two phases and the coils that make up these windings are the following:

- Phase A : Coils 1, 3, 5 and 7
- Phase B : Coils 2, 4, 6 and 8

When Phase A is energized, the coils opposite (1 and 5) form a north pole whereas coils 3 and 7 form a south pole. The teeth on the north side of the rotor tend to align to the south pole created by the coils, and the teeth on the south side of the rotor tend to align with the north pole created. When the teeth tend to align themselves, phase A is switched off and phase B is energized either positively or negatively, depending on the direction of rotation wanted [7].
Thus we can observe that for the correct functioning of the motor, the phases needs to be energized in the sequence A+, B-, A- and A+ which gives a clockwise rotation of the shaft. For an anti-clockwise direction of rotation the phases should be energized as A+, B+, A-, A+ [7].

2.3. Control circuit

The usual control circuit is made out of a microcontroller, a supply source, a motor driver and the stepper motor as it can be seen in the following image.

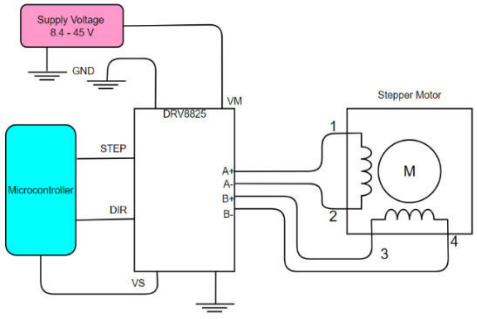

Fig. 2. Schematics of stepper motor control circuit

In Fig. 2, the driver represents the interface between the logic level, at which the microcontroller operates and the power level which represents the level at which the stepper motor works (usually 12V with 2A per each phase). This separation is needed, as to protect the microcontroller, who only just sends signals corresponding to the number of steps and the direction wanted. The driver does the real work, as it decides which phase to energize and at what rate to obtain the desired number of steps in the desired direction.

In the above figure, we have used the following notation:

- *STEP* : represents the input pin on the driver for the number of steps that the motor has to make
- *DIR* : represents the input pin on the driver for the direction of rotation of the stepper motor
- *VM* : represents the driving voltage which is usually in the range of 8.4 to 45 V
- *VS* : represents the logic power supply voltage which needs to have a value of 5V
- *A+, A-, B+, B-* : represents the output of the driver and their letters corresponds to the letters of the phases ends.

3. Simulation

3.1. Motivation behind creating an *FEA* analysis of a hybrid stepper motor

As stated in the introduction chapter, stepper motors are a companion to modern electro-mechanical devices, which by correct application of phase currents to the stator windings, these motors can be made to rotate in well-defined steps ranging down to a fraction of a degree per pulse [8].
Being able to analyze the complex working of such motors, can help with choosing the right motor for the specific application or it may help the electrical engineers in design better stepper motors, which work more efficiently.
Another reason in setting up this simulation is to be able to get the defining parameters of a stepper motor before it is being created. This way we can create a mechatronic model in Simulink where the stepper motor is defined as a black-box which only has the parameters obtained from the *FEA* analysis, thus making it easier for the mechatronic engineer to design a proper control system.

3.2 Model set-up

In order to create the simulation, it is necessary to create a correct 3D CAD model of the stepper motor with all the elements inside of it. For this, we used the capabilities of *Simcenter3D*, which allows its users to both design the motor and to also set-up the simulation inside the same environment.
To have a good understanding of what elements the stepper motor is composed of, an existing NEMA 17 motor was dismantled and measured, and based on it we created the following CAD model.
It can be seen that the stator has castellated poles, to better increase the accuracy of positioning of the

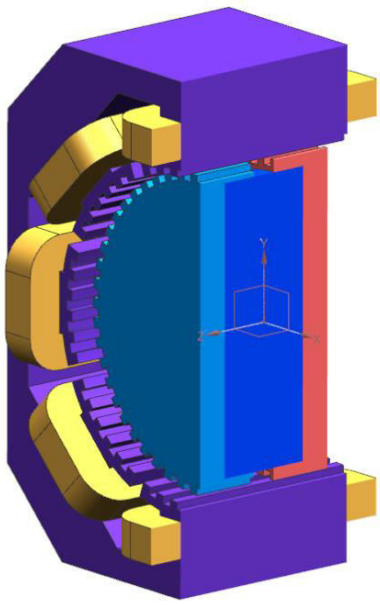

Fig. 3. CAD model of the stepper motor, created with the use of Simcenter3D

rotor. The stator coils are in number of eight and are represented with the yellowish colour. *Simcenter3D* allows to create the coils as simple blocks, and then assign them the correct parameters, such as number of turns, conductor area per turn and optionally the resistance and inductance of each coil. The

rotor is composed of two cups, each having 50 teeth on them, but the cups are rotated one with respect to another with an angle equal to half a step angle. Inside the cups, the permanent magnet resides, which has an uniform orientation of its magnetic field, parallel to the axis of rotation of the rotor.
Another element that it is not figured in the previous image is the airbox that surrounds the stepper motor. This is an important element in computing the magnetic field. Another important element is the remesh region, which represents the air gap between the rotor and stator. This is an important region as here are computed the magnetic forces and torque created.

3.3. *FEM* model set-up

In order to set-up the simulation, the CAD model must be divided into a mesh with specific materials, so that the solver can compute the correct parameters. In Fig. 4, the FEM model is presented.

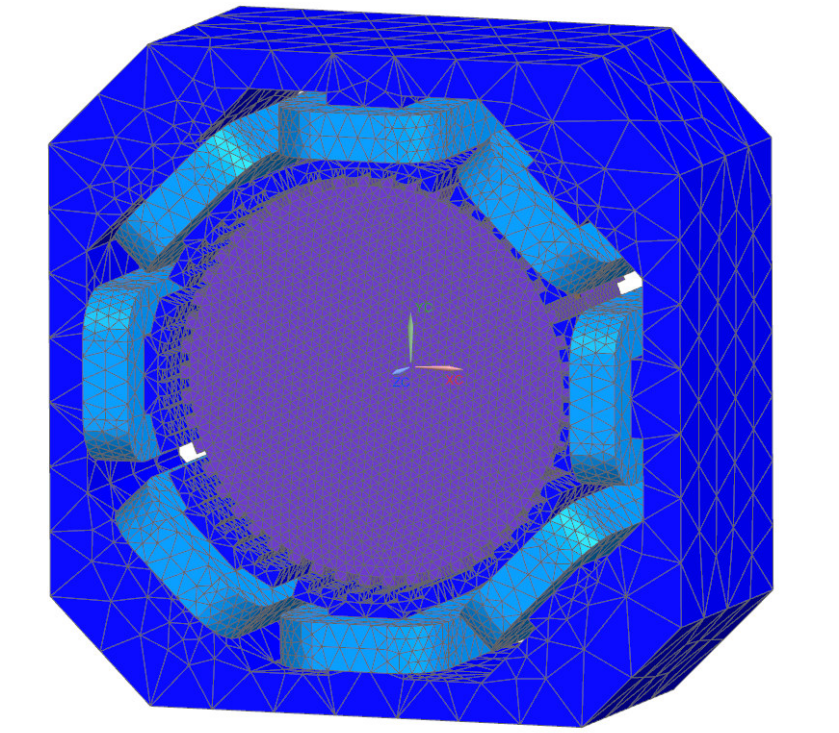

Fig. 4. FEM model of the stepper motor

Each mesh is represented with a different color, such that the properties of each material can be taken into account. The materials used are the following:

- M19 26 Ga : non-oriented steel for the stator and the two rotor cups
- N38 : neodymium – iron – boron (*NdFeB)* permanent magnet [9]
- Copper with a conductance of 5.77e7 Siemens / meter for the coils
- Air for the airbox and remesh regions.

These materials are commonly used in the creation of electric machines.
The remesh region is not represented again, because this region contains the biggest number of elements. This is due to the necessity of computational precision and due to the small air gap that exists between the rotor and the stator.
After setting-up the *FEM* model, the simulation model has to be set-up, in which the coils are connected according to the previous explanations, and the motion component, which is composed of the two rotor cups, the permanent magnet and the rotor airbox.

3.4. Simulation results

One important result obtained from the static simulation is that of how the teeth influence on the distribution of the magnetic field inside the rotor. Using the N38 permanent magnet, in the following image we can see the distribution of the magnetic field inside around the rotor.

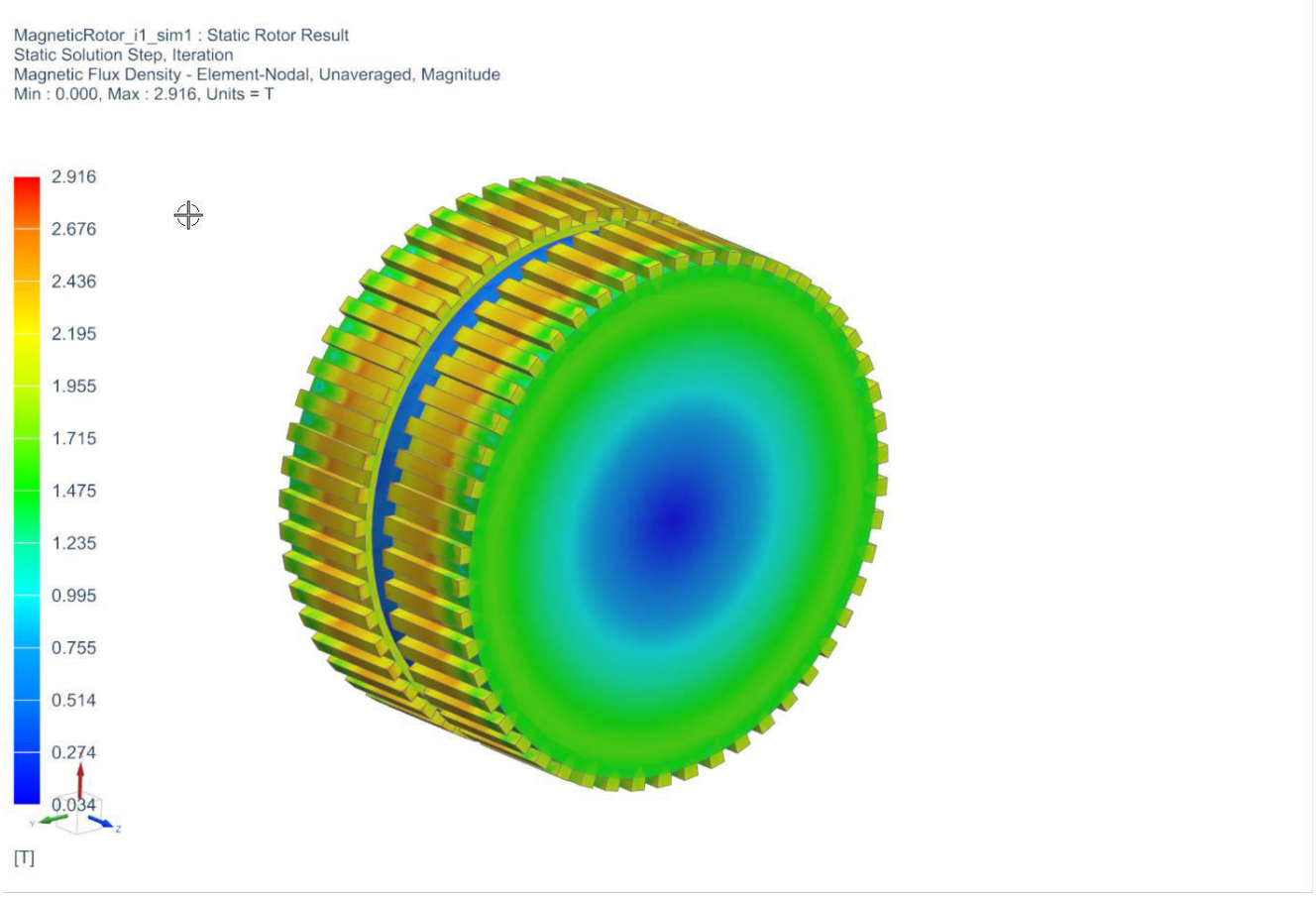

Fig. 5. Distribution of the magnetic field inside the rotor

It can be seen that the presence of teeth allow for a better flow of the magnetic field inside the rotor, thus making each teeth a pole. The magnetic field of the permanent magnet is directed along the Z-axis, represented in Fig. 5.
Another important result, obtained from the static solution, is that of the surface nodal forces distribution, as this one helps explain how the rotor teeth will be pulled into the correct position by the magnetic forces. These results are obtained by energizing the phase B coils, and by keeping the rotor fixed, thus the force acting on each element of the stator and rotor can be seen.
These forces are also relevant for further studies of acoustics problems, as these forces tend to modify both their magnitude and direction during the functioning of the motor. These forces create the noise usually heard during operation, and by careful study of them, coupled with physical measurements, improved control algorithms can be created.
In the following image, we can see that the greatest forces appear on the stator teeth of the stator poles that has the energized coils. Some forces also appear on the poles that are not energized, because the magnetic field flows to them as well, because the stator is made out of connected stator poles.

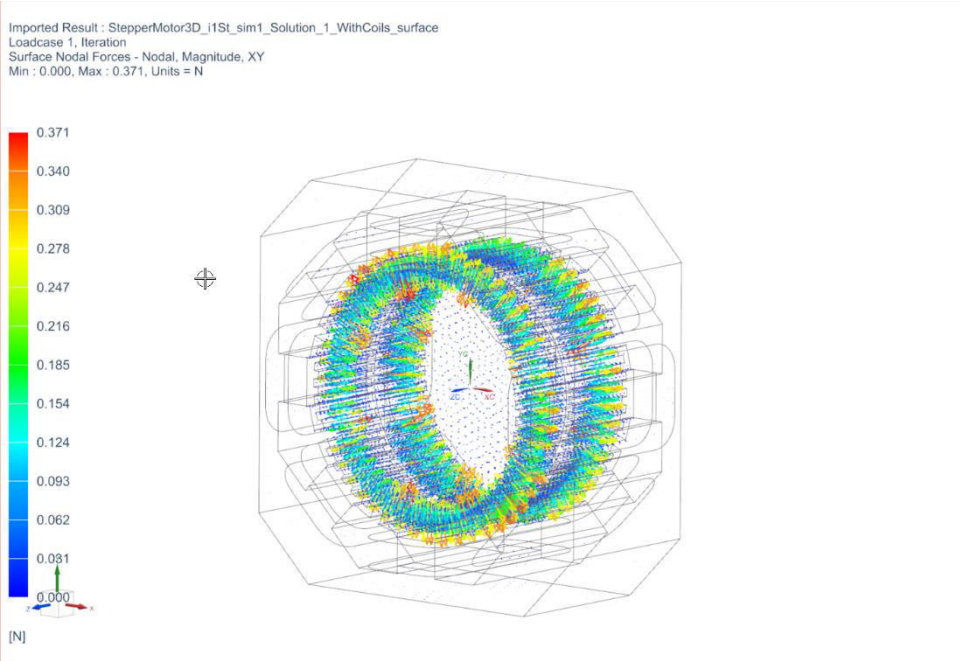

Fig. 6. Distribution of surface nodal forces on the stator

One important result, that represents the solution of the transient simulation, is the value of the back EMF. This constant, specific to a certain speed, represents one of the black-box parameters that can be used in a mechatronic simulation in Simulink.
This result is obtained by allowing the rotor to rotate with a certain speed and not energizing the coils. The non-energizing state of the coils can be modelled by connecting them to a current source whose output is null.

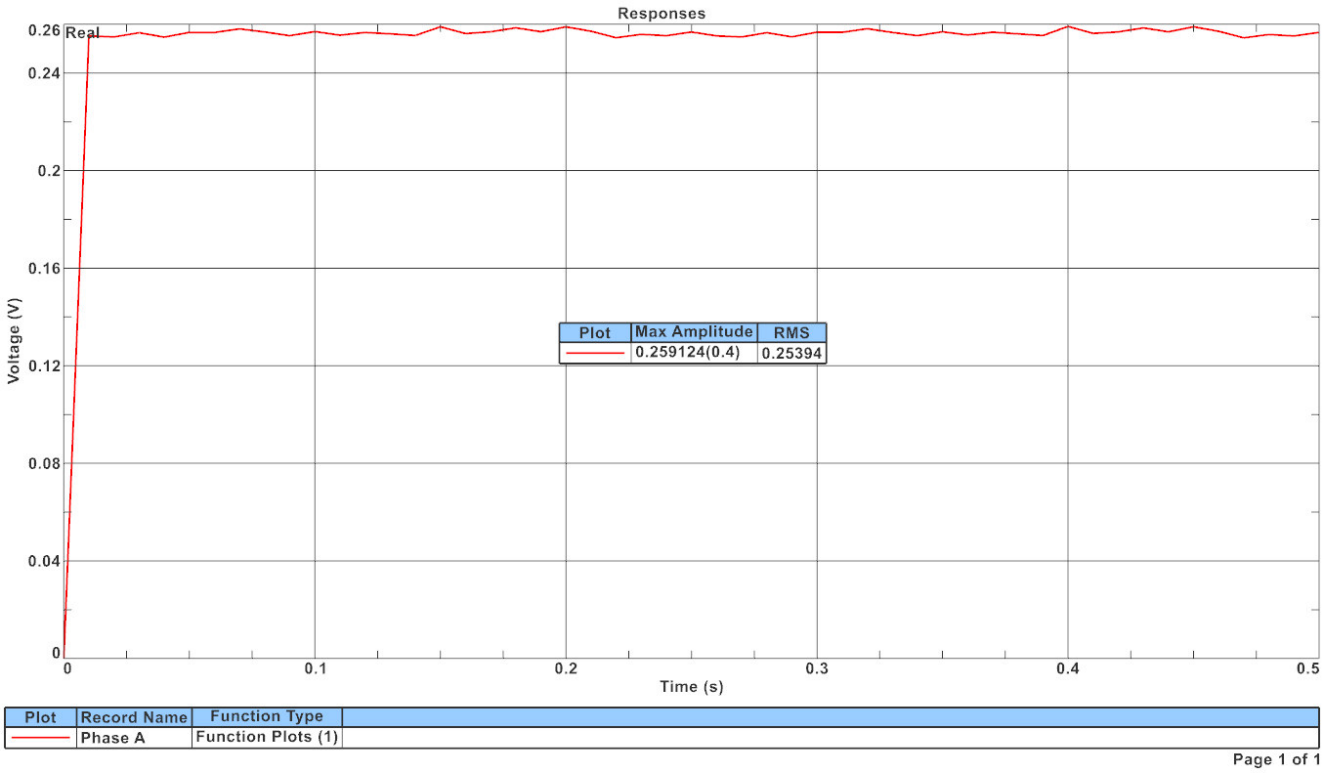

Fig. 7. Back-EMF corresponding to Phase A of the stepper motor

From Fig. 7, we can see that the maximum value of the back-EMF is equal to *0.259 V*. This parameter has an RMS value of *0.254 V*, and the peak value can be further used in the Simulink simulation.
This parameter is necessary to describe the functioning of the stepper motor, as it is governing the equivalent circuit of the stepper motor during constant operation, as can be seen in the following formulas [10]:

$$V_{supply} = iR + \frac{d\lambda(\theta)}{dt} \tag{2}$$

In equation (2) we used the following notation:

- V_{supply} : represents the voltage supply of a phase
- i : represents the current through the coils of the phase
- R : represents the resistance of the coils
- λ : represents the flux linkage through the coils, which is dependent of the rotation angle θ

From this equation, we can derive the exact differential equation that governs the functioning of the stepper motor:

$$V_{supply} = iR + L(\theta)\frac{di}{dt} + i\frac{dL(\theta)}{dt} = iR + L(\theta)\frac{di}{dt} + i\frac{dL(\theta)}{d\theta}\frac{d\theta}{dt} \tag{3}$$

The last term in equation (3) represents the back-EMF, which we will denote as ε, as can be seen in the following equation:

$$V_{supply} = iR + L(\theta)\frac{di}{dt} + i\frac{dL(\theta)}{dt}\,\omega_{rotor} \tag{4}$$

Thus, from Fig. 7, we can obtain the motor velocity constant, which is defined as following:

$$K_v = \frac{\omega_{no\ load}}{V_{peak}} \tag{5}$$

In our case, this constant has the following value:

$$K_v = 48.5188\frac{Vs}{rad} \tag{6}$$

This is useful as the stepper motor has the following equivalent circuit [10]:

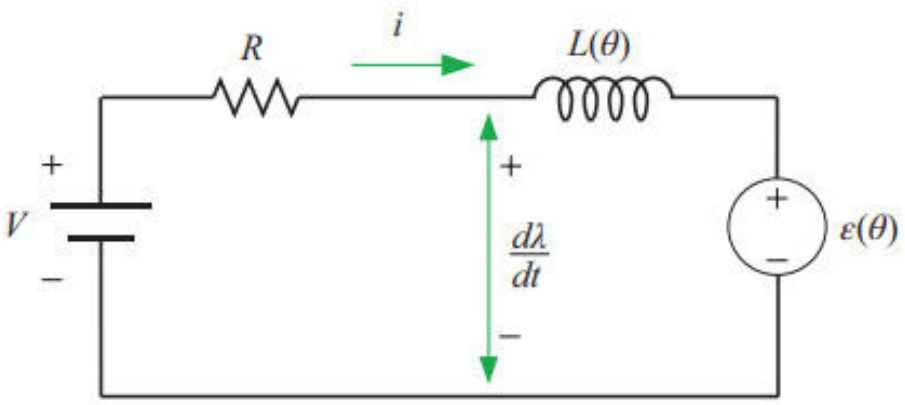

Fig. 8. The equivalent circuit for the hybrid stepper motor

This is an acceptable approximation of the stepper motor, as this type of motor is a type of brushless DC motor, during constant operation.

4. Conclusions

This paper is the basis for further *FEA* analysis of the hybrid stepper motor design, created to give the authors a better understanding of the electromagnetic phenomena that happens during the operation of said electric machines.
Further improvements are to be made, especially in the field of comparing the results obtained with physical measurements, which will help in the future to create better digital twins of real-world applications. This is an important step in the development of mechatronic systems, as it will allow the engineers to create and test different rigs, in the phase of design such systems.
One point that we think that will be of important study in the future, is the acoustic simulation, which will give an insight into how the stepper motor creates vibration and thus we can come up with better solutions to counteract its negative impacts on the functioning of systems that employ such electric machines.

Acknowledgements

We want to thank Siemens and **Siemens Industry Software SRL**, especially, for allowing us to use their software to create the simulations needed in this paper. We would also like to thank the teams from **Siemens Industry Software**, for the knowledge that shared with us, helping us to better understand the functionalities of **Simcenter3D**.

References

[1] Kiranlal, S., V. M. Brathikan, B. Anandh, and S. Vikash. “A Review on Electrical and Electronics Part of 3D Printer.” *IOP Conference Series: Materials Science and Engineering* 1228, no. 1 (2022): 012007.
[2] Soni S., and M. Taufik. “Design and assembly of fused filament fabrication (FFF) 3D printers.” *Materials Today: Proceedings* 46 (2021): 5233-5241.
[3] Gardan, J. “Additive manufacturing technologies: state of the art and trends.” In: *Additive Manufacturing Handbook*. CRC Press, 2017.
[4] Vafadar, A., F. Guzzoni, A. Rassau, and K. Haywar. “Advances in metal additive manufacturing: a review of common processes, industrial applications, and current challenges.” *Applied Sciences* 11, no. 3 (2021): 1213.
[5] Popescu, D., A. Zapciu, C. Amza, F. Baciu, and R. Marinescu. “FDM process parameters influence over the mechanical properties of polymer specimens: A review.” *Polymer Testing* 69 (2018): 157-166.
[6] Solomon, I. J., P. Sevvel, and J. Gunasekaran. “A review on the various processing parameters in FDM.” *Materials Today: Proceedings* 37 (2021): 509-514.
[7] Hughes, A., and B. Drury. *Electric motors and Drives Fundamentals, Types and Applications*. Oxford, Elsevier, 2013.
[8] Umans, S. D. *Fitzgerald & Kingsley's Electric Machinery*. New York, McGraw Hill, 2014.
[9] Arnold Magnetic Technologies. “Sintered Neodymium-Iron-Boron Magnets N38.” [Interactive]. Available: https://www.arnoldmagnetics.com/wp-content/uploads/2017/11/N38-151021.pdf.
[10] Bilgin, B., J. W. Jiang, and A. Emadi. *Switched Reluctance Motor Drives - Fundamentals to Applications*. Boca Raton, CRC Press, 2019.

ISSN 1454 - 8003
Proceedings of 2022 International Conference on Hydraulics and Pneumatics - HERVEX
November 9-10, Băile Govora, Romania

EXPERIMENTAL RESEARCH ON EQUIPPING LOW-PRESSURE PUMPING UNITS WITH MINIBOOSTERS

Teodor Costinel POPESCU[1], Ana-Maria Carla POPESCU[1], Andrei VLAD[2], Gheorghe Alexandru TRĂNECI[2], Alina Iolanda POPESCU[1]

[1]National R&D Institute for Optoelectronics, Subsidiary Hydraulics and Pneumatics Research Institute Bucharest, popescu.ihp@fluidas.ro

[2]S.C. HESPER S.A. Bucharest, vladandrei92@outlook.com

Abstract: *One of the effective methods of achieving high pressures in hydraulic drive systems is to equip low-pressure pumping units with minibooster-type hydraulic pressure intensifiers. These hydraulic devices, with pulsating mode of operation, consume low-pressure high flows rates to generate high-pressure low flow rates. This is why low-pressure pumping units equipped with miniboosters are used to generate high pressure rates in constant confined volumes or when moving hydraulic cylinders with heavy loads, over long distances and at low speed rates. Through experimental tests, carried out on a bench dedicated to the topic of this paper, the authors of the material comparatively analyse the displacement of a hydraulic cylinder, with constant load of 800 bar over the entire advance stroke, when the pumping unit that supplies the cylinder is equipped, successively, with three types of miniboosters.*

Keywords*: Low-pressure pumping unit, minibooster, high pressure, hydraulic cylinder*

1. Introduction

There are known two solutions for generating high pressure in hydraulic drive systems: an expensive one, based on pumps and equipment for adjusting / controlling high pressure hydraulic parameters, and a cheaper one, based on pumps and equipment for adjusting / controlling low pressure hydraulic parameters, plus hydraulic pressure intensifiers. For example, Fig. 1 shows the two drive solutions for a hydraulic cylinder with a 700-bar load.

Fig. 1. Generating 700-bar pressure for actuating a hydraulic cylinder: ***left side*** - with high-pressure pump; ***right side*** - with low-pressure pump and hydraulic pressure intensifier

In the hydraulic drive diagram [1] shown in Fig. 1-left side, motor **M** drives **high-pressure pump (1)**, to direct hydraulic oil, at a pressure of 700 bar, indicated on pressure gauge **(2)**, limited by pressure control valve **(3)**, via directional control valve **(5)**, switched to the field of parallel arrows, to the

cylinder rod chamber. The cylinder piston chamber discharges into the tank via return filter **(8)**, and the hydraulic cylinder moves to the right with a 700-bar load.
One can move the same hydraulic cylinder to the right, with a 700-bar load, according to the hydraulic drive diagram [1] shown in Fig. 1-right side, where **low-pressure pump (1)**, pressure control valve **(3)** and directional control valve **(5)** operate at 200 bar, indicated on pressure gauge **(2)**. Return filter **(8)** remains, while additional low pressure filter **(4)** and **pressure intensifier (6)** appear; the latter is fed via connecting fitting **P**, from the primary side, by pump **(1)**, and on the outlet of the secondary side, it delivers hydraulic oil at 700 bar in the cylinder rod chamber. Due to the pulsating mode of operation of the pressure intensifier, one uses this drive diagram for **short displacements under load** of the hydraulic cylinders or with the purpose of **achieving and maintaining the load at the stroke end**.
State of the art in the field of technical applications for the use of low-pressure pumping units equipped with oscillating hydraulic pressure intensifiers (miniboosters) does not include applications with displacements of hydraulic cylinders that have high loads over the entire stroke. ***The aim*** of this paper is to demonstrate experimentally the possibilities of using miniboosters in such applications, too, with reasonable limits of uniformity and continuity of displacement of the actuated cylinders, as well as the possibilities of equipping the same low-pressure pumping unit with miniboosters with different amplification factors, depending on the type of application in which it is used.

2. Materials and Methods

To achieve the proposed goal, the authors have used an experimental method by which they have monitored the dynamic behaviour of a hydraulic cylinder which, being fed into the piston chamber by a minibooster, moves with a constant load, equivalent to a pressure of **800 bar**, over the entire stroke. The minibooster has been integrated into a low-pressure pumping unit, and the hydraulic cylinder under testing - in a test bench. Three sets of tests have been performed, one for each of the miniboosters [2] shown in figure 2 and table 1.

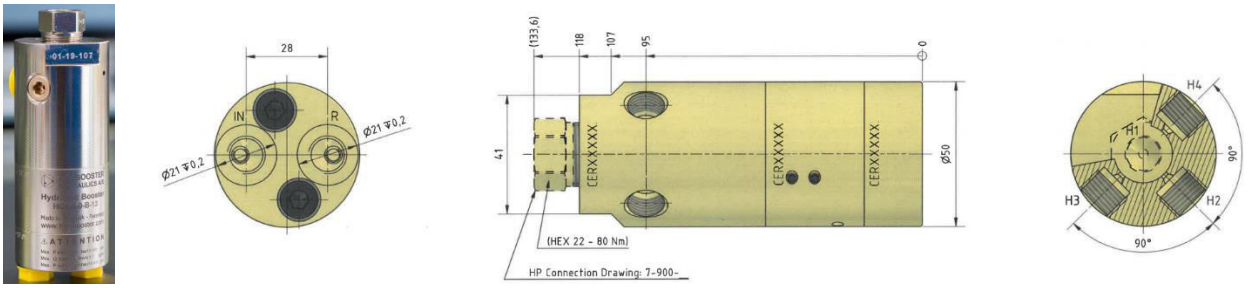

Fig. 2. HC7 miniboosters [2]

Table 1: Technical features of the miniboosters used in the set of three tests

Minibooster technical features	**Minibooster code**		
	HC7-5.0-B-12	**HC7-6.6-B-12**	**HC7-7.6-B-12**
Low pressure connecting fittings: **IN** (inlet) / **R** (return)	1/4" BSPP	1/4" BSPP	1/4" BSPP
High pressure connecting fitting **H1** (p_{HP})	M22 x 1.5	M22 x 1.5	M22 x 1.5
High pressure connecting fitting **H2** (p_{HP})	9/16-18 UNF	9/16-18 UNF	9/16-18 UNF
Amplification factor $\mathbf{i = p_{HP} / p_{IN}}$	5.0	6.6	7.6
Maximum inlet flow rate: $\mathbf{Q_{max\ IN}}$ [l/min]	14	13	13
Maximum outlet flow rate: $\mathbf{Q_{max\ H1}}$ [l/min]	1.6	1.3	1.1

Note:
Because the actual flow rate $\mathbf{Q_{max\ IN}}$ supplied by the low-pressure pumping unit (***10.5 l/min***) is less than the values in table1, the flow rates $\mathbf{Q_{max\ H1}}$ will have lower values as well.

2.1 Low-pressure pumping unit equipped with minibooster

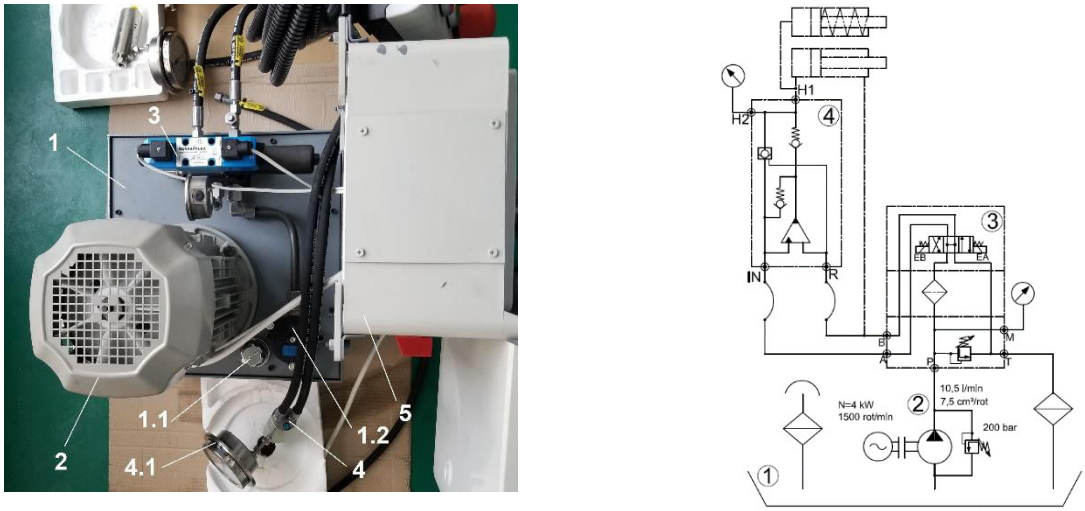

Fig. 3. Low-pressure pumping unit equipped with minibooster:
left side - overview; ***right side*** - hydraulic schematic diagram

The pumping unit in figure 2 comprises: **1**= oil tank (38 l volume); **1.1**= fill and vent filter; **1.2**= return filter; **2**= low-pressure electric pump (4 kW; 1500 rev/min; 7.5 cm^3/rev; 250 bar); **3**= block with hydraulic devices (pressure control valve; pressure filter; 4/3 hydraulic directional control valve, Dn6, electrically actuated; 250-bar pressure gauge); **4**= HC7 minibooster (technical features as in table 1); **4.1**= 2500-bar pressure gauge; **5**= electric panel.
Pressure adjustment on the circuit **H1**, which supplies the hydraulic cylinder actuated by the pumping unit, is done using the pressure control valve on the hydraulic block of the unit, and the adjusted value of this pressure can be read on the high pressure gauge, mounted in the connecting fitting **H2.**

2.2 Test bench for low-pressure pumping unit equipped with minibooster

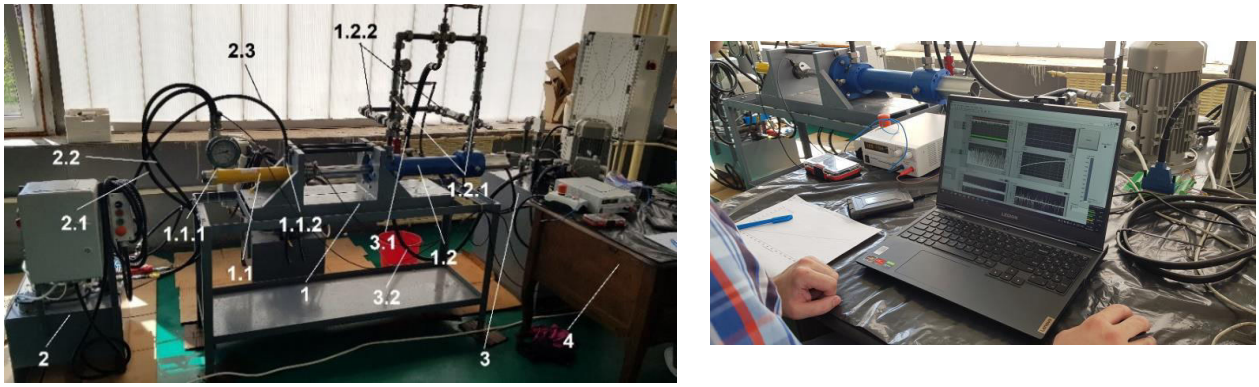

Fig. 4. Test bench for pumping unit equipped with minibooster

The structure of the test bench [3, 4] and the pumping unit in figure 4 is as follows:
1: Module for clamping the hydraulic cylinders; **1.1**: test cylinder with piston Ø= 38.1 mm, rod Ø= 25 mm, stroke length= 257 mm, p_{max}= 700 bar; **1.1.1**: fitting that connects cylinder piston chamber with secondary side of the minibooster; **1.1.2**: connecting fitting and hose for cylinder rod chamber; **1.2**= load cylinder with built-in stroke transducer and piston Ø= 80 mm, rod Ø= 45 mm, stroke length= 300 mm, p_{max}= 300 bar; **1.2.1**= cylinder chambers inlet check valves; **1.2.2**= cylinder chambers outlet check valves;
2: Low-pressure pumping unit (previously presented); **2.1, 2.2**= hoses connecting the primary side of the minibooster to the consumers of the hydraulic directional control valve of the unit;

3: Pumping station for filling the load cylinder equipped with: 2-kW, 10-bar, and 90-l/min electric pump; oil tank with V= 180 l; filling pressure control valve; proportional pressure control valve (acting as load); fill and vent filter; return filter; **3.1**= cylinder chambers fill fitting and hose; **3.2**= cylinder chambers drain fitting and hose;
4: Control and data acquisition module (figure 4 - right side) acquiring data from the transducers of: minibooster primary side pump pressure (**p1**); load cylinder pressure (**p2**); filling pump pressure (**p3**); minibooster primary side input flow rate (**Q1**); load cylinder flow rate (**Q2**); **stroke** (built into the load cylinder).

2.3 Test conditions

- Adjusted pressure at the safety valve of the pumping unit: **P_r = 190 bar**;
- Adjusted pressure in the load cylinder: **800 bar** (potentiometer adjustment value for load cylinder compression = **50%**), for the test cylinder advance, and **20 bar** (potentiometer adjustment value for load cylinder extension = **0%**);
- 3 sets of tests have been made, with the same load, one for each of the three miniboosters, item no. 2 in figure 5, which successively equipped the tested low-pressure pumping unit;

Fig. 5. High-pressure test cylinder (1), powered by the minibooster (2) equipping the low-pressure pumping unit

- The displayed (acquired) load pressure is amplified by the following factors: **4.41** (for compression); **5.3** (for extension);
- The parameters measured using the transducers have been as follows: minibooster primary side pressure (denoted **P1** on graphs); load pressure equivalent to minibooster secondary side pressure (denoted **P2** on graphs); load cylinder filling pressure (denoted **P3** on graphs); minibooster primary side flow rate (denoted **Q1** on graphs); load cylinder flow rate (denoted **Q1** on graphs); load cylinder stroke (denoted **C** on the graphs).

3. Results and discussions

The following is the set of tests carried out for the pumping unit equipped with the minibooster with amplification factor i=5.0. At the end of the chapter, a comparison is made, by superimposition, between the time-variations of the displacement of the cylinders on the test bench, for the three cases of equipping a low-pressure pumping unit with miniboosters (i=5.0, i=6.6 and i=7.6).

3.1 Testing of the pumping unit equipped with minibooster, i=5.0

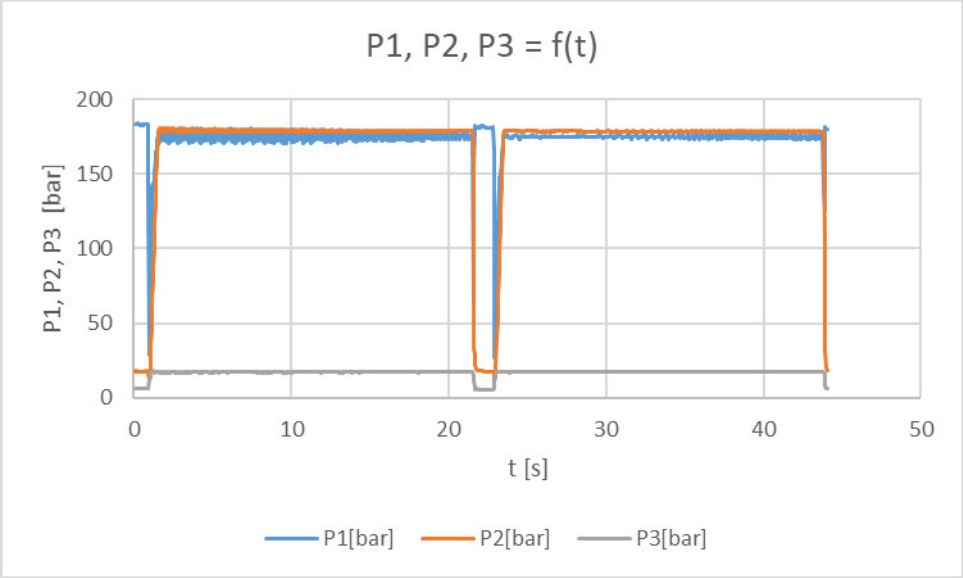

Fig. 6. Time-variation of pressures P1, P2, and P3

Figure 6 shows time-variations of the pressure in the minibooster primary side (P1), load pressure (P2) time-variations, and time-variations of the load cylinder filling pressure (P3), over two full strokes (extension + compression). On the first compression stroke, the P1 and P2 pressure pulsations are larger, because of the presence of air in the hydraulic circuits of the cylinders on the bench.

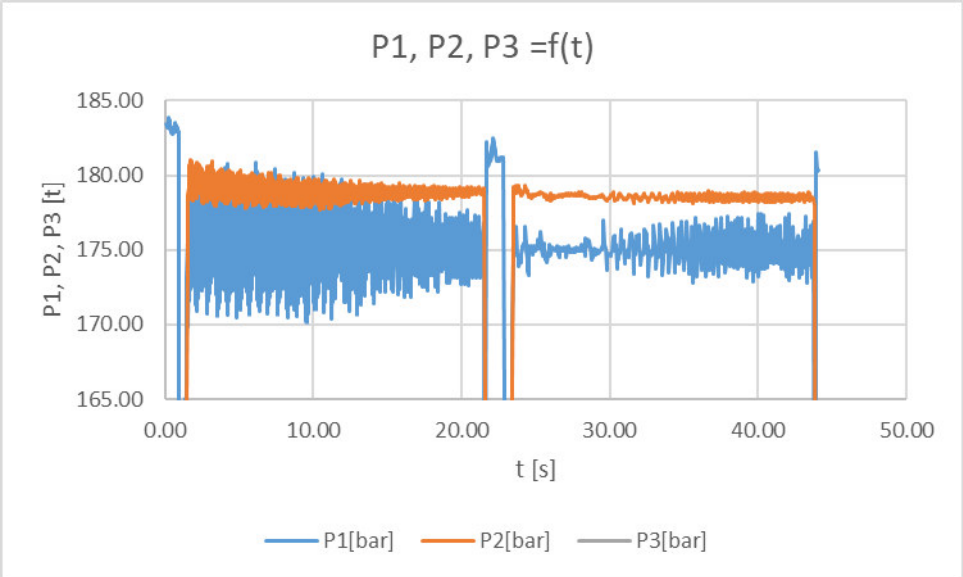

Fig. 7. Detail: time-variation of pressures P1 and P2

The detail in figure 7 shows the variations of pressures P1 and P2 [5], over two extension and compression strokes of the load cylinder. The detail has been made for the ***165-185 bar*** pressure range; this range that does not contain the pressure P3 variation, too. It is noted that the peaks of the pressures P1, ***183 bar*** roughly, are recorded when the direction of displacement of the load cylinder changes (transition from compression to extension), and equivalently the direction of displacement of the test cylinder changes (transition from advance stroke to retraction stroke).

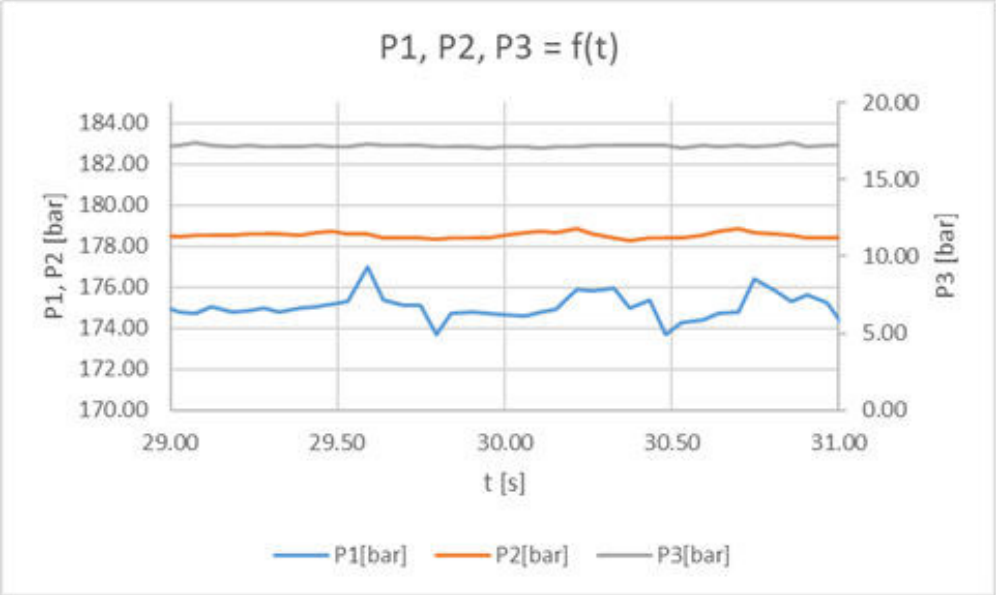

Fig. 8. Detail: time-variation of pressures P1, P2, and P3

The detail in figure 8 shows the variations of pressures P1, P2 and P3, over two compression strokes of the load cylinder. The detail has been made for a segment of the compression stroke of the load cylinder, corresponding to the ***29-31 s*** time range and the ***170-184 bar*** pressure range, for pressures P1 and P2, and the ***0-20 bar*** pressure range, for pressure P3.
One can notice that:
- Variation of the pressure in the minibooster primary (P1) is within the range ***174-177 bar***.
- Load pressure (that generates the resistive force of the test cylinder on the bench) variation is within the range ***178-179 bar***. Taking into account the ratio of the piston surfaces of the two cylinders on the bench, which is ***4.41***, this range becomes ***785-789 bar***.
- Variation of the load cylinder filling pressure is within the range ***17.5-18 bar***.

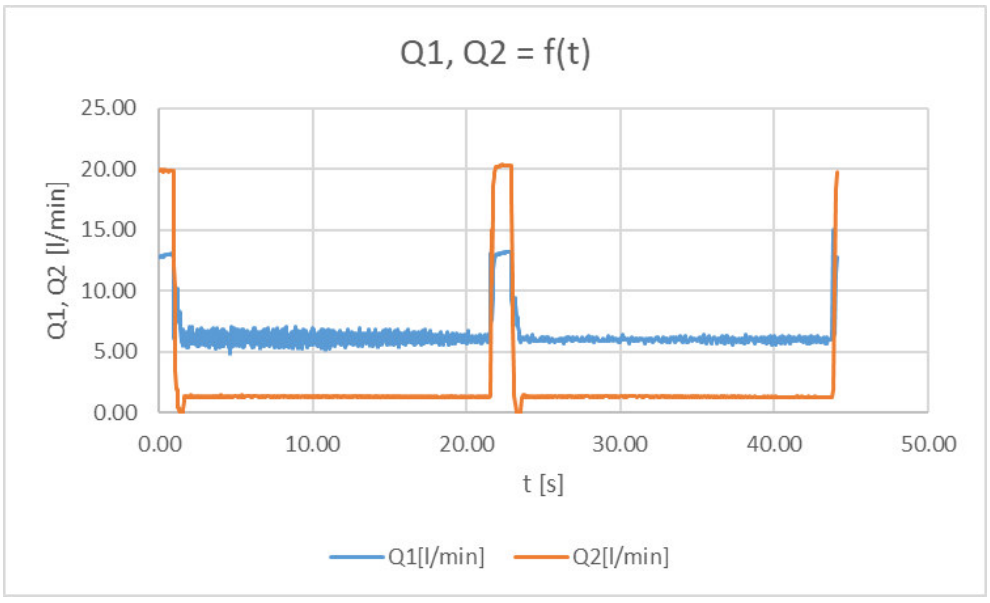

Fig. 9. Time-variation of flow rates Q1 and Q2

Figure 9 shows the time-variations of flow rates Q1 and Q2, over two full strokes of the load cylinder (extension + compression).

One can notice that:
- Maximum flow rate Q1, which is achieved on the extension stroke of the load cylinder (retraction of the test cylinder) is ***12.5 l/min***;
- Maximum flow rate Q2, which is achieved on the extension stroke of the load cylinder (retraction of the test cylinder) is ***20 l/min***.

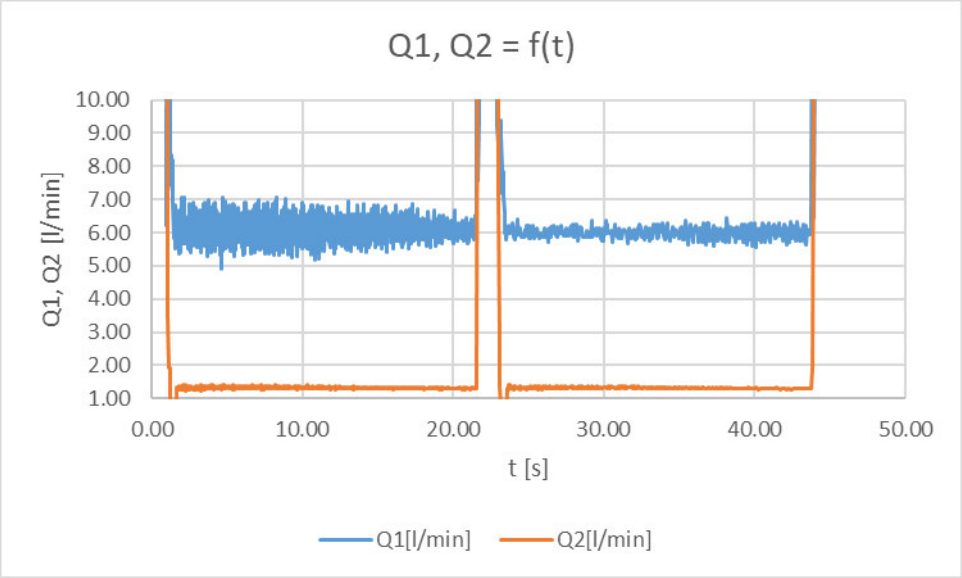

Fig. 10. Detail: time-variation of flow rate Q1

Figure 10 shows a detail of the flow rate Q1 variation [5], made for two full strokes of the load cylinder (extension + compression), over the ***1-10 l/min*** flow rate range; this range does not contain the flow rate Q2 variation, too.
One can notice that the flow rate Q1 variation, of ***maximum ± 1 l/min***, relative to the average value of ***6 l/min***, on the first compression stroke of the load cylinder, drops to a ***maximum of ± 0.5 l/min***, relative to the same average value, on the second compression stroke of the load cylinder. The explanation lies in the incomplete venting of the hydraulic circuits of the cylinders before the experimental tests began.

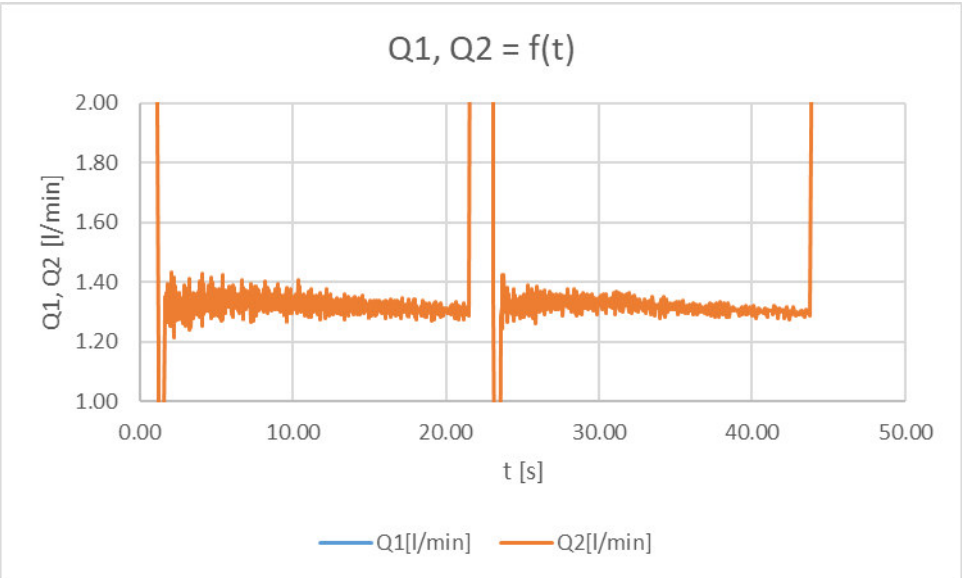

Fig. 11. Detail: time-variation of flow rate Q2

Time-variation of flow rate Q2 [5], over two compression strokes of the load cylinder, over the ***1-2 l/min*** flow rate range, is shown in detail in figure 11. One can notice that the flow rate Q2 variation is max. ***± 0.1 l/min*** relative to the average value of ***1.3 l/min***.

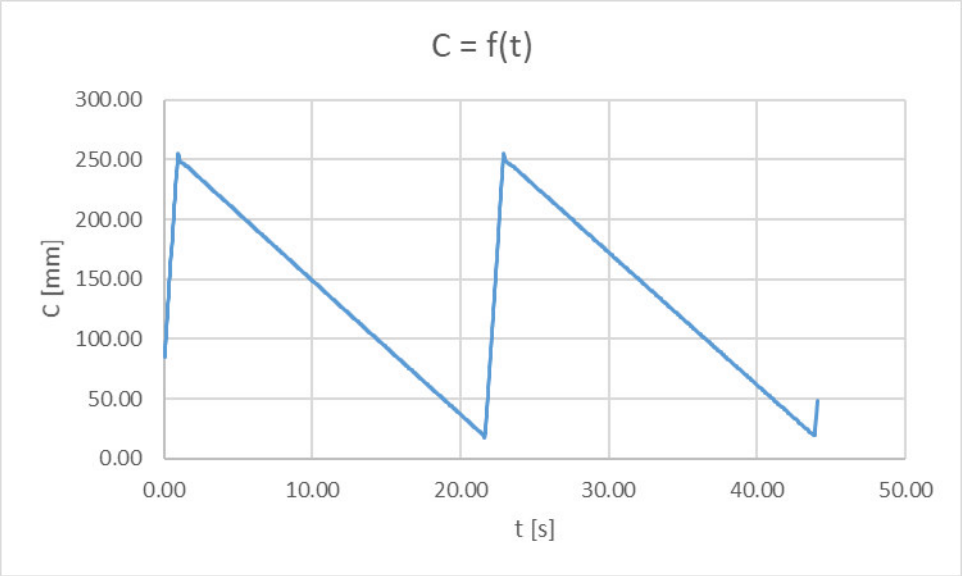

Fig. 12. Time-variation of cylinder stroke

Figure 12 shows the time-variation of the stroke of the two (test and load) hydraulic cylinders on the bench, when the load cylinder makes two full strokes (extension + compression). One can notice that the time to complete the compression stroke (test cylinder advance under constant load) is much longer than the time to complete the extension stroke (test cylinder idle retraction).
The advance speed of the test cylinder under load is about ***16 times lower*** than its idle retract speed because on the idle retraction stroke the test cylinder is fed with the full flow rate of the pump within the pumping unit, while on the advance under load stroke the same cylinder is fed only with the flow rate from the minibooster high-pressure connection.

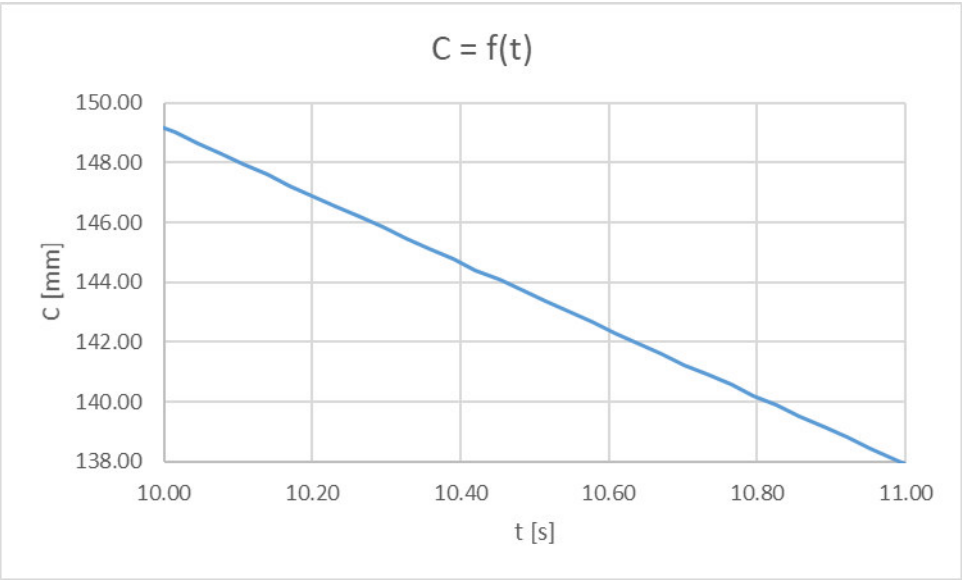

Fig. 13. Detail: time-variation of cylinder stroke

On the detail in figure 13, made for a time duration of ***1 second*** (in the range of ***10-11 s***) and a ***12-millimeter*** load cylinder compression stroke segment (in the range ***138-150mm***) one can notice that the displacement of hydraulic cylinders on the test bench is roughly linear [5].

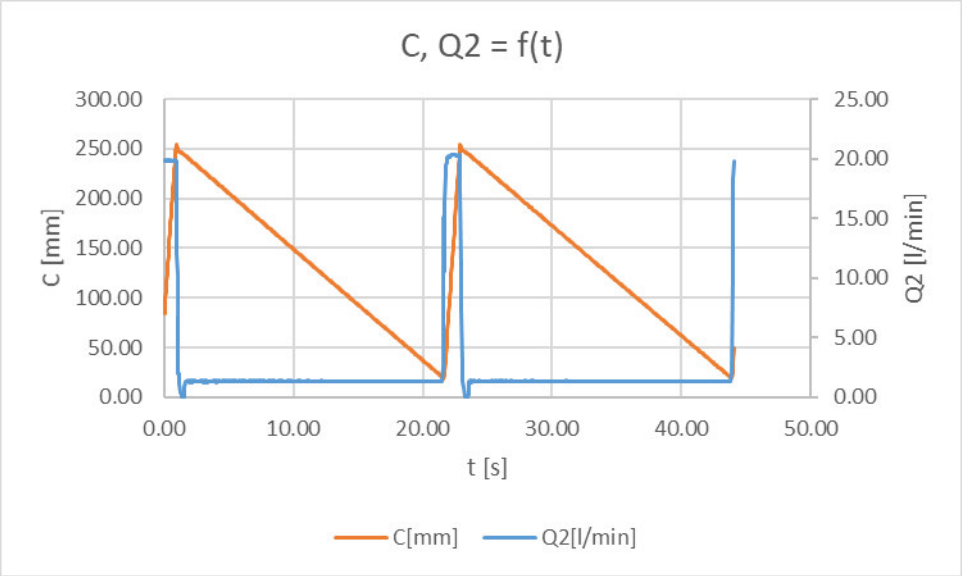

Fig. 14. Time-variation of load cylinder stroke and flow rate

Figure 14 shows the time-variation of the load cylinder stroke and flow rate over two full strokes (extension + compression). One can notice that:
- During load cylinder extension (approx. ***1.31 s***) the maximum flow rate is approx. ***20 l/min***;
- During load cylinder compression (approx. ***15.6 s***) the maximum flow rate is approx. ***1.3 l/min***;
- Small variations in the load cylinder flow rate cause small deviations from its linear displacement.

3.2 Comparative analysis between the variations of displacement of hydraulic cylinders on the test bench

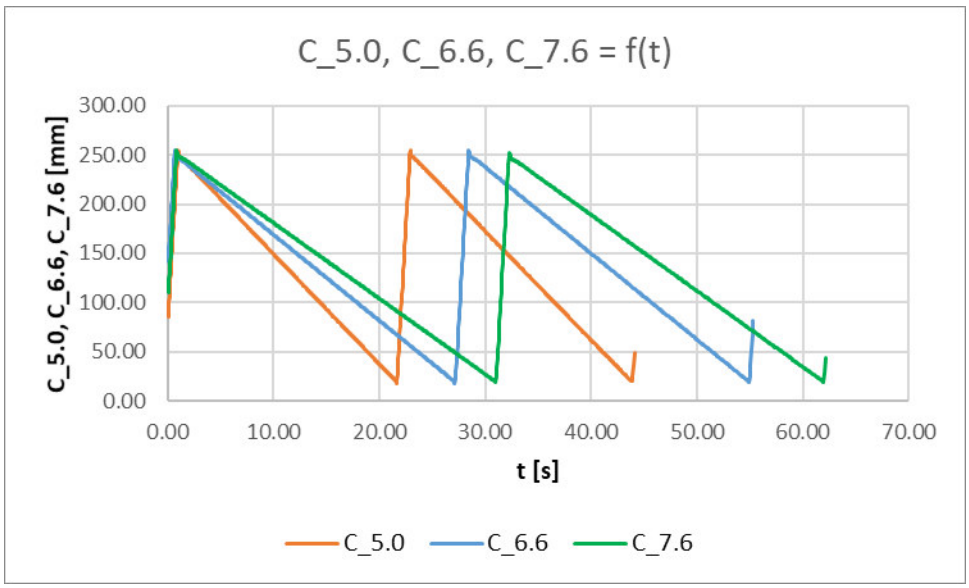

Fig. 15. Comparative analysis between the variations of displacement of hydraulic cylinders

After completing the ***1st set*** of tests for the pumping unit equipped with the minibooster ***i=5.0***, the following steps have been taken:
- The minibooster ***i=5.0*** has been replaced with a minibooster ***i=6.6*** and the ***2nd set*** of tests has been carried out under the same conditions;
- The minibooster ***i=6.6*** has been replaced with a minibooster ***i=7.6*** and the ***3rd set*** of tests has been carried out under the same conditions;
- The results from the three sets of measurements have been superimposed on the same graph of time-variation of the displacement of hydraulic cylinders, figure 15.
Figure 15 shows a comparison between the displacements of the load cylinder on the bench, equipped with displacement transducer, under the following conditions:
- The pumping unit, which supplies the test cylinder of the bench, is successively equipped with the three miniboosters, with different amplification factors (i=5.0; i=6.6; i=7.6);
- The (test and load) cylinders on the bench make two full strokes of ***250 mm*** each, for each direction of displacement;
- The load cylinder creates approximately equal and constant resistive forces for the test cylinder, on its advance stroke, and zero load on its retraction stroke.

4. Conclusions

- ***Displacement of the cylinders on the bench is approximately linear*** for the three cases of equipping the pumping unit with miniboosters;
- ***Advance speed rate under load*** of the test cylinder (displacement slope) decreases with increasing the minibooster amplification factor;
- ***Idle*** (no load) ***retraction speed rate*** does not depend on the amplification factor of the minibooster;
- ***The test cylinder moves slowly***, but with no restraint or stiffness, ***on the advance stroke***, and ***fast***, ***on the retraction stroke***;
- ***Resistive force*** that the test cylinder can overcome is ***directly proportional to the amplification factor of the minibooster***.
- The tested pumping unit can be equipped with any of the three miniboosters;
- For applications with hydraulic cylinders that need to move smaller loads at higher speed rates, the unit will be equipped with a minibooster with i=5.0, while for higher loads and lower displacement speed rates, the unit will be equipped with miniboosters with i= 6.6 or i=7.6.

Acknowledgments

The research presented in this paper has been developed under Financial Agreement no. 272/24.06.2020, signed by the Ministry of European Funds / Ministry of Education and Research and S.C. HESPER S.A. Bucharest for the Innovative Technological Project titled “Digital mechatronic systems for generating pressure of 1000 bar, using hydraulic pressure intensifiers” (SMGP), project under implementation from 01.07.2020 to 30.06.2023. Financial support has also been granted under a project funded by the Ministry of Research, Innovation and Digitalization through Programme 1- Development of the national research & development system, Sub-programme 1.2 - Institutional performance - Projects financing the R&D&I excellence, Financial Agreement no. 18PFE/30.12.2021.

References

[1] “Scanwill Fluid Power – Unique Hydraulic Pressure Intensifier Solutions.” Accessed October 05, 2022. https://www.luvra-hydraulik.de/fileadmin/web_data/downloads/Luvra-Hydraulik-Scanwill-0915.pdf.
[2] “HC7.” Accessed October 05, 2022. https://www.minibooster.com/hc7/.
[3] Popescu, T.C., A.-P. Chiriță, A.I. Popescu, A. Vlad, I.D. Vochin, and A.-M.C. Popescu. “Experimental demonstrations of extension of technical applications for pumping units equipped with miniboosters.” *“Hidraulica” Magazine*, no.1 (2022): 85-94.
[4] Bartnicki, A., and A. Klimek. “The research of hydraulic pressure intensifier for use in electric drive system.” *IEEE Access*, no.7 (2019): 20172-20177.
[5] Popescu, T.C., A.P. Chiriță, and A.-M.C. Popescu. “Research on the assessment of flow and pressure pulses in oscillating hydraulic intensifiers.” *Mining Machines*, no.4 (2020): 14-23.

ISSN 1454 - 8003
Proceedings of 2022 International Conference on Hydraulics and Pneumatics - HERVEX
November 9-10, Băile Govora, Romania

THE INFLUENCE OF HYDRAULIC FLUID TEMPERATURE ON THE ADJUSTMENT CAPABILITIES OF SERVO-MECHANISMS AND CLOSED-CIRCUIT HYDROSTATIC TRANSMISSIONS

Alexandru Polifron CHIRIȚĂ[1,2]

[1] Technical University of Civil Engineering of Bucharest (UTCB), Faculty of Mechanical Engineering and Robotics in Construction, Bucharest, Romania

[2] National Institute of Research & Development for Optoelectronics / INOE 2000 – Subsidiary Hydraulics and Pneumatics Research Institute / IHP, Bucharest, Romania

Abstract: *The present article presents the influence of insufficient cooling, the effects of high temperature on the hydraulic fluid and the influence of the fluid temperature on the hydrostatic transmission in the closed loop, with primary adjustment and its servo-mechanism. The hydrostatic transmission was studied with the help of the numerical simulation software AMESim, using the hydraulics library that also takes into account the effects of temperature on the hydraulic fluid.*

Keywords*: closed-circuit hydrostatic transmissions, fluid temperature influence, servo-mechanisms, CAE.*

1. Introduction

High working fluid temperatures are the result of heat generation in the hydraulic system. Because high working fluid temperatures can be so damaging to a hydraulic system, it is important to identify the source of heat generation [1]. Heat generation typically results from fluid flowing from an area of high pressure to an area of low pressure without performing useful mechanical work [2]. When hydraulic fluids are exposed to high temperatures for extended periods of time, they suffer a permanent deterioration in lubrication properties and a severe reduction in kinematic viscosity [3] (Fig. 1). Deterioration of hydraulic fluid leads to oxidation and sludge formation that clogs small flow sections [4]. At the same time, chemical reactions between the degrading additives will occur in the hydraulic fluid, all of which seriously compromise the performance of the fluid and the hydraulic drive and control system [5]. A significant decrease in viscosity, generated by higher working temperatures, also affects the behavior of the hydraulic fluid itself, negatively influencing the performance of the hydraulic system as a whole [6].

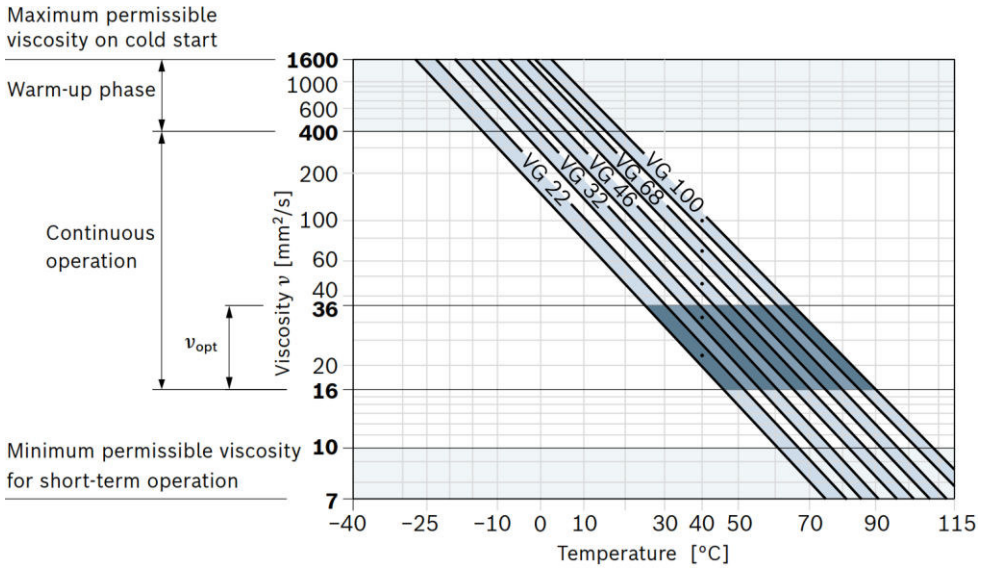

Fig. 1. Kinematic viscosity versus hydraulic fluid temperature and recommended intervals [7]

For an optimal operation of the hydraulic actuation systems, it is necessary that the viscosity of the hydraulic fluid falls within certain limits, between at least 16 and 36 cSt (Fig. 1) [8].

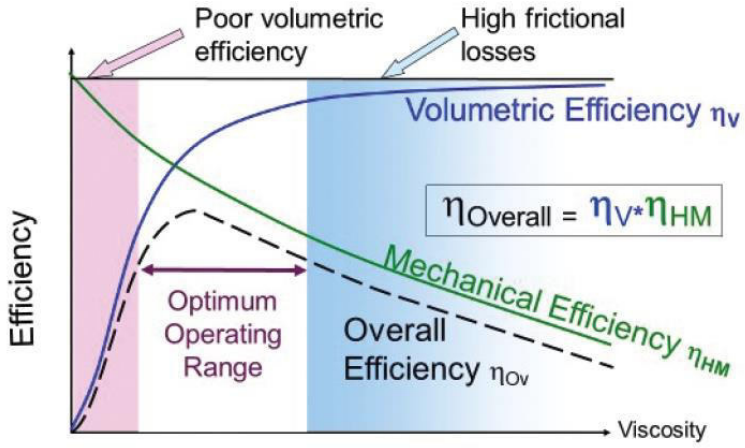

Fig. 2. Effects of Viscosity on Overall Efficiency [9]

The optimal viscosity range, previously mentioned, ensures adequate lubrication of the system, limits volumetric losses and ensures a very good efficiency of the system [10] (as in Fig. 2, too).

2. Material and method

To study the influence of temperature on the system parameters, two numerical simulations were performed in AMESim, the first of which includes a cooling circuit, and the second one does not. The simulation network is represented in Fig. 3; it includes: a closed-loop hydrostatic transmission with primary adjustment, a PID type controller with automatic tuning and feed forward, the transfer box of the truck and the motor truck. This is a multifunctional motor truck; it is used in the field of construction; it moves at normal road speed rates and also at technological speed rates.

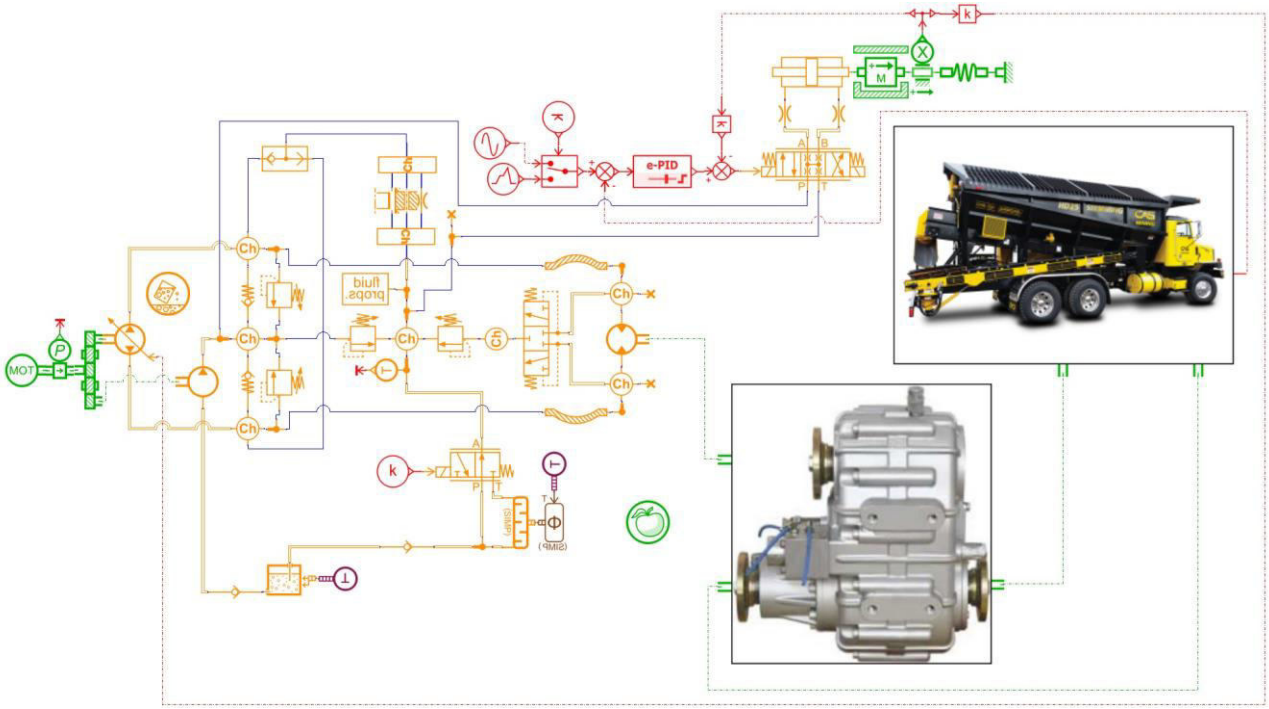

Fig. 3. Simulation network of a motor truck equipped with a closed-loop hydrostatic transmission

The components, operation and initial parameters of the numerical simulation:

- The thermal engine of the truck with a power of 240 kW operates at a constant speed of 1000 rev/min and at this speed it can produce a maximum torque of 1020 Nm; it drives the servo-pump with a displacement of 210 cc/rev and the auxiliary pump with a displacement of 33 cc/rev; the pressure relief valves acting as safety valves in the closed loop circuit are adjusted to 450 bar and the pressure relief valve of the compensating pump is set at 25 bar.
- The hydrostatic motor with radial pistons has a fixed capacity of 1352 cc/rev and is connected to the servo-pump; connected to the same ports, there is also the loop flushing valve, whose pressure relief valve is adjusted to 20 bar.
- The volumetric flow losses of the transmission together with most of the compensation pump flow rate is sent to the heat exchanger in order to cool the hydraulic fluid (ISO VG 46) or directly to the tank.
- The servo-mechanism system of the main pump is composed of a Dn6 proportional control valve, calibrated nozzles with a diameter of 1.1 mm, a spring with an elastic constant of 175 N/mm, a hydraulic cylinder with bilateral rods, with a piston diameter of 50 mm that controls the pump displacement and a PID controller.
- The transfer case of the motor truck has a transmission ratio of 1.652 and the transmission ratio of the two axles is 4.
- The motor truck has all-wheel drive and its velocity can be continuously variable, its total weight is 18 tons and it can carry a payload of 10 tons.

3. Results

After running the numerical simulation model of the hydrostatic transmission with primary adjustment of the motor truck, the following graphs result:

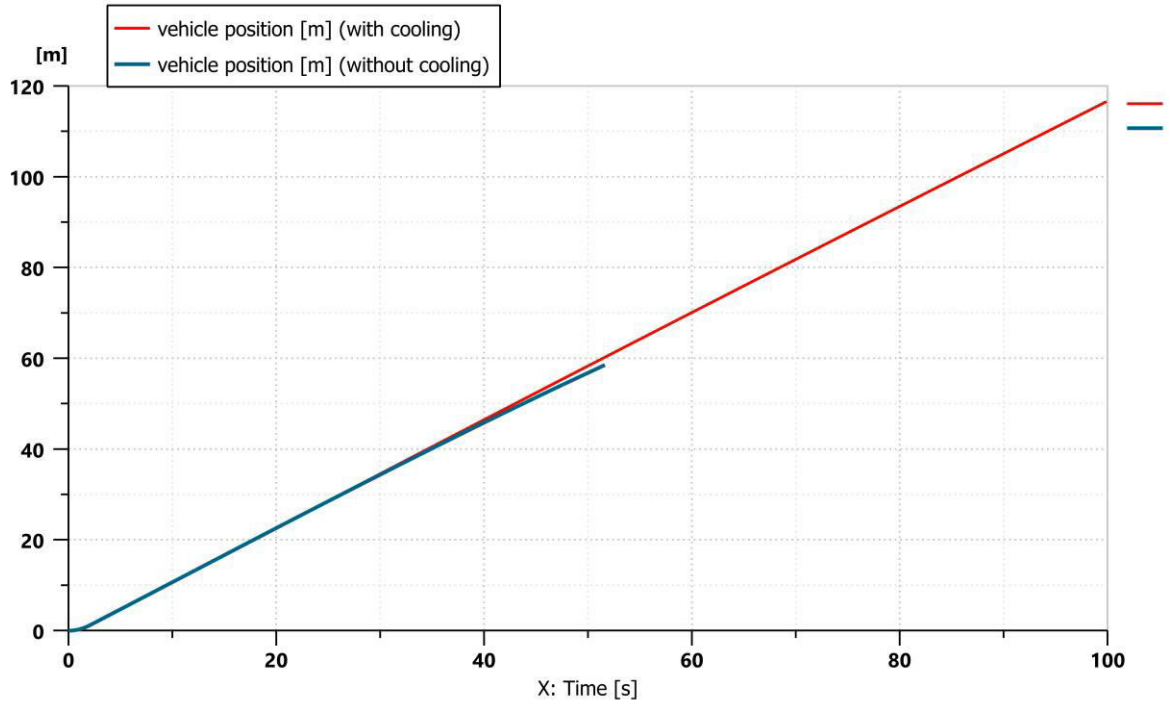

Fig. 4. Time-variation of the motor truck displacement

In Fig. 4 one can see how the displacement in the case of the system that does not benefit from cooling is limited.

In Fig. 5 one can notice that both motor trucks move on a road with the same slope, so the torque at the hydrostatic motor shaft is identical in both cases, as is the pressure of the two hydrostatic transmissions.

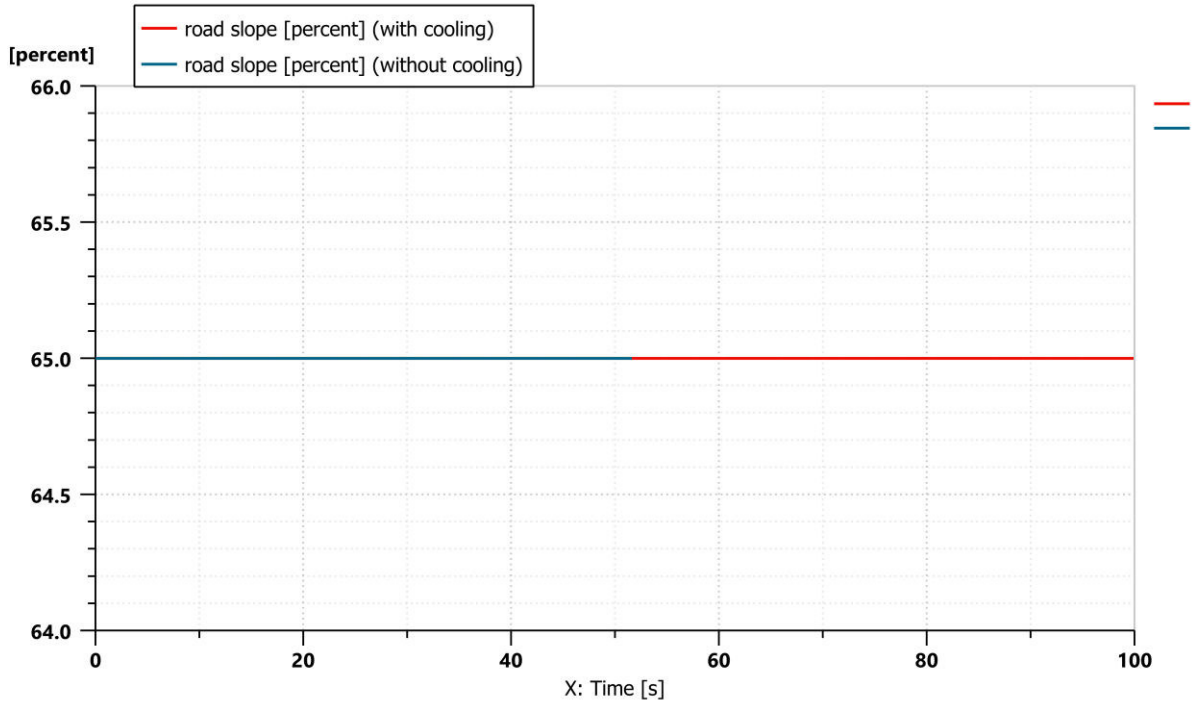

Fig. 5. The slope of the road

Fig. 6 shows how the velocity of the motor truck varies over time.

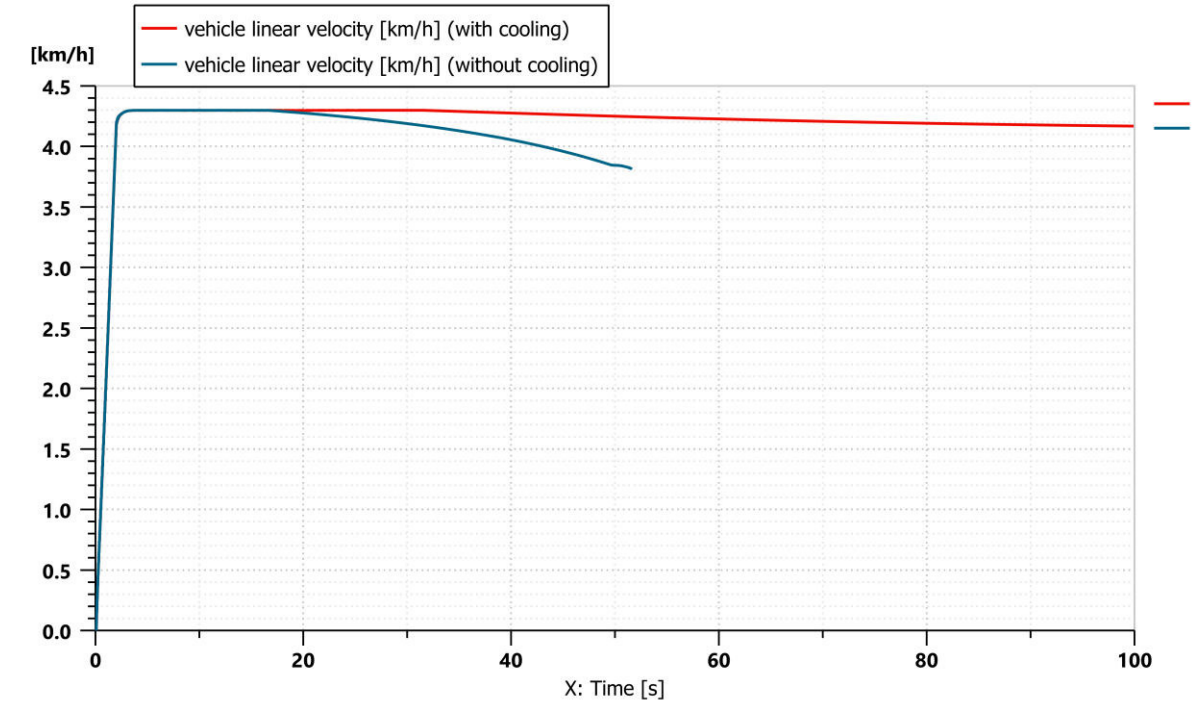

Fig. 6. The velocity of the motor truck

In Fig. 7 one can see how the speed of the hydrostatic motor shaft decreases, proportional to the travel speed; this decrease is due to the increase in volumetric losses (Fig 8.); these losses increase over time because the temperature of the hydraulic fluid increases and simultaneously with this increase, the viscosity of the hydraulic fluid also decreases.

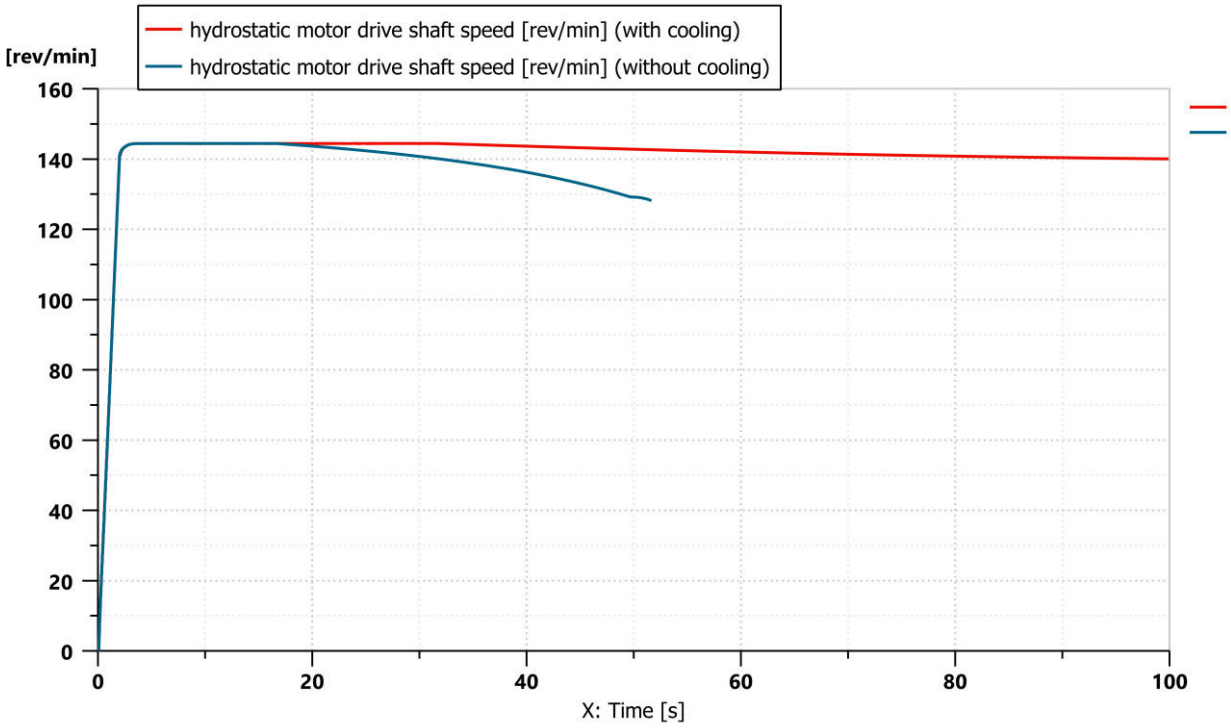

Fig. 7. The shaft speed of the hydrostatic motor

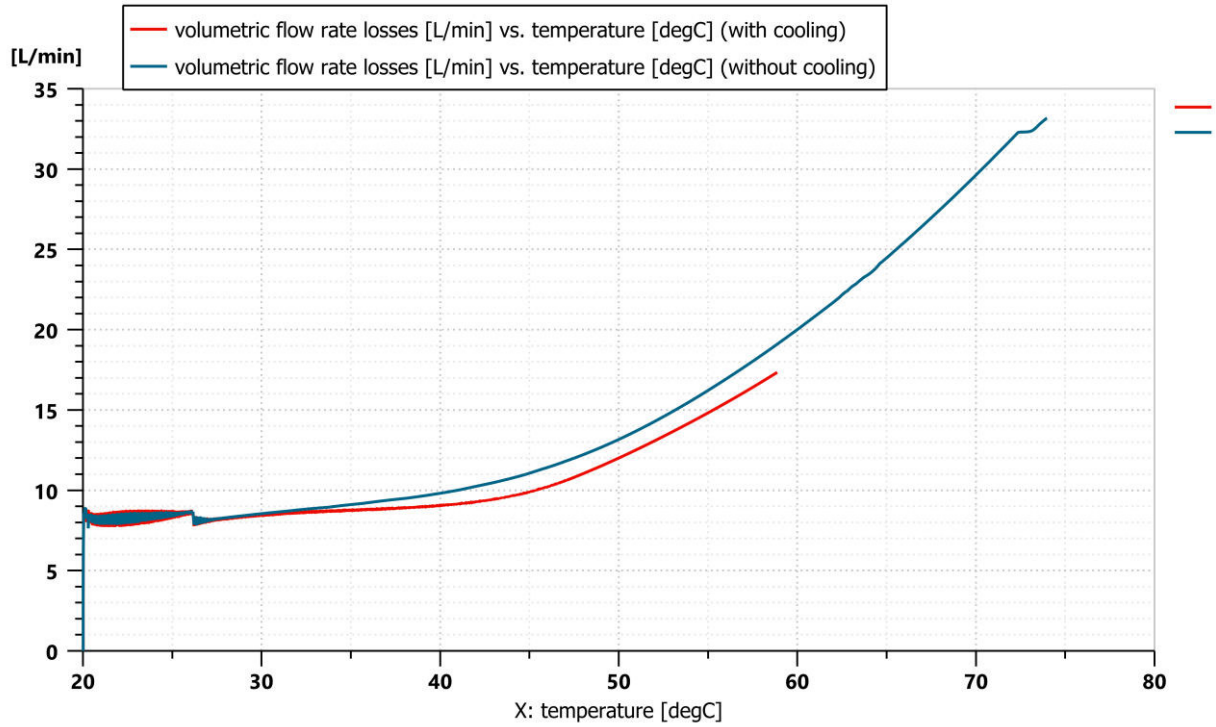

Fig. 8. Transmission volumetric flow rate losses versus hydraulic fluid temperature

Fig. 9 shows that the temperature of the hydraulic fluid affects the maximum speed of the motor truck. This limitation occurs because as the temperature of the fluid increases, the viscosity decreases and the volumetric losses of the transmission increase and a smaller flow rate reaches the port of the hydrostatic motor.

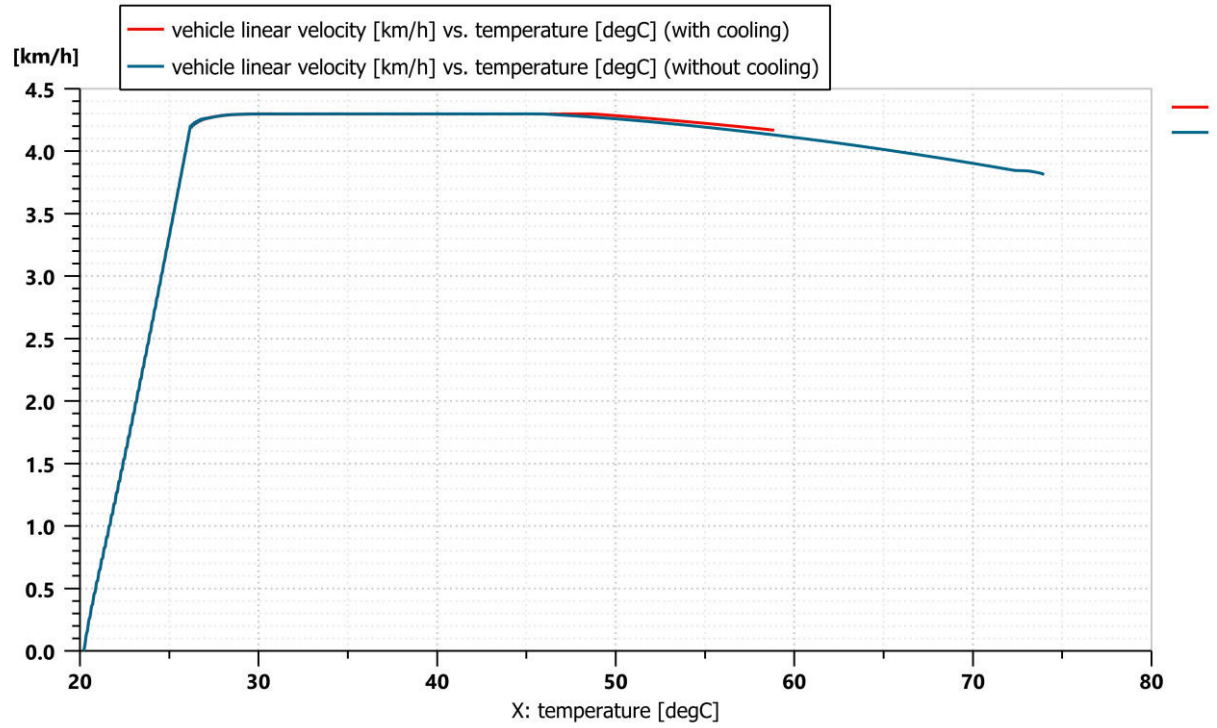

Fig. 9. Variation of the travel speed versus the temperature of the hydraulic fluid

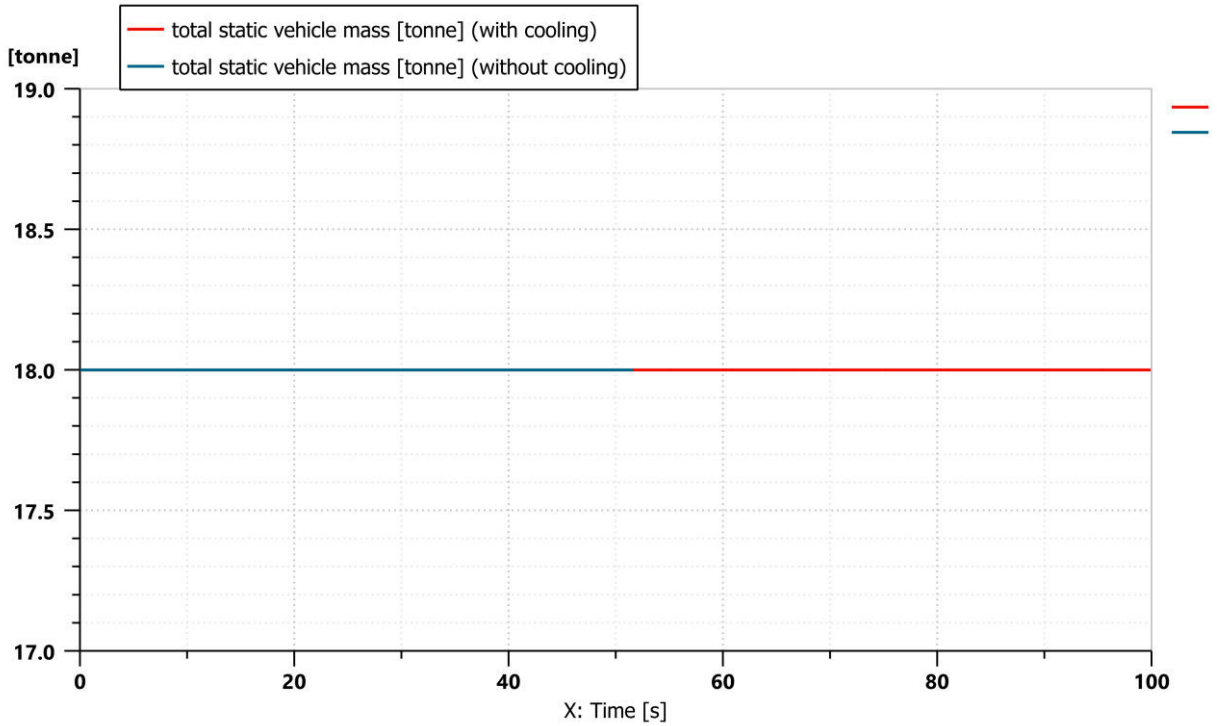

Fig. 10. Total mass of the motor truck

The total mass of the motor truck is constant during simulation (Fig. 10), as is the driving force (Fig. 11) with the exception of the acceleration period from the beginning of the simulation, as well as the torque on the two axles of the motor truck (Fig. 12).

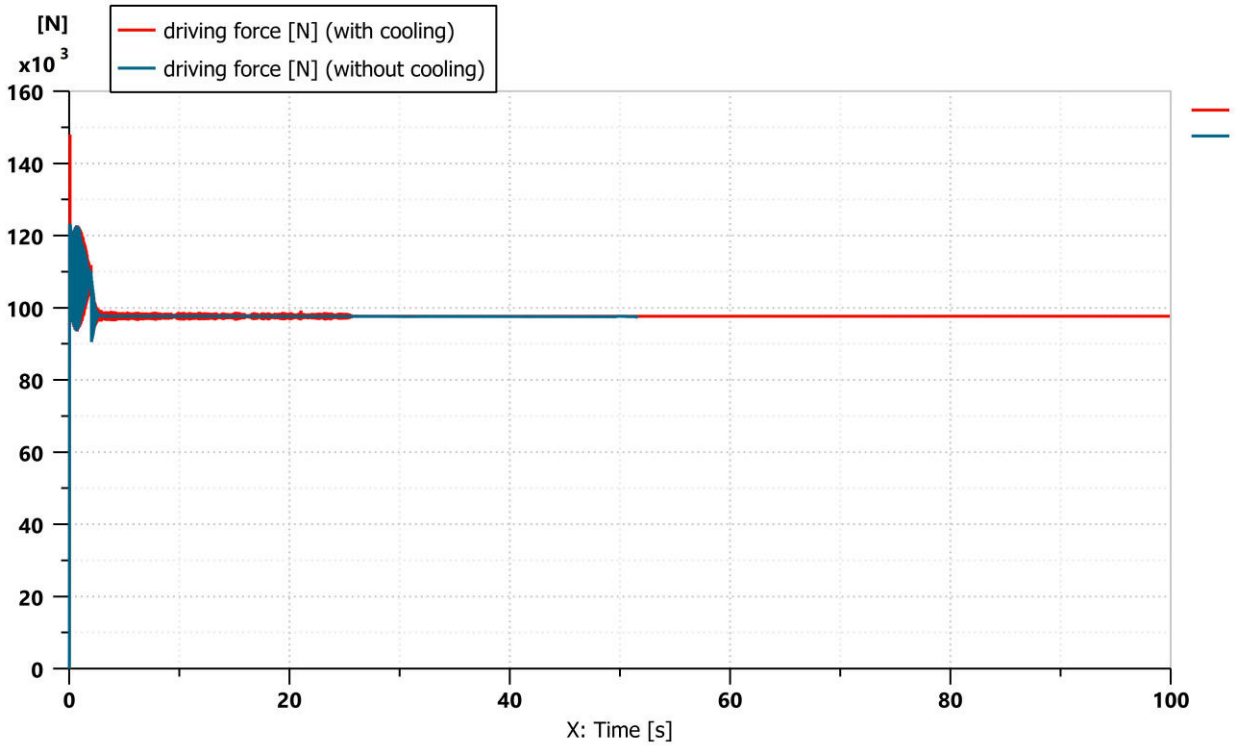

Fig. 11. The driving force of the motor truck

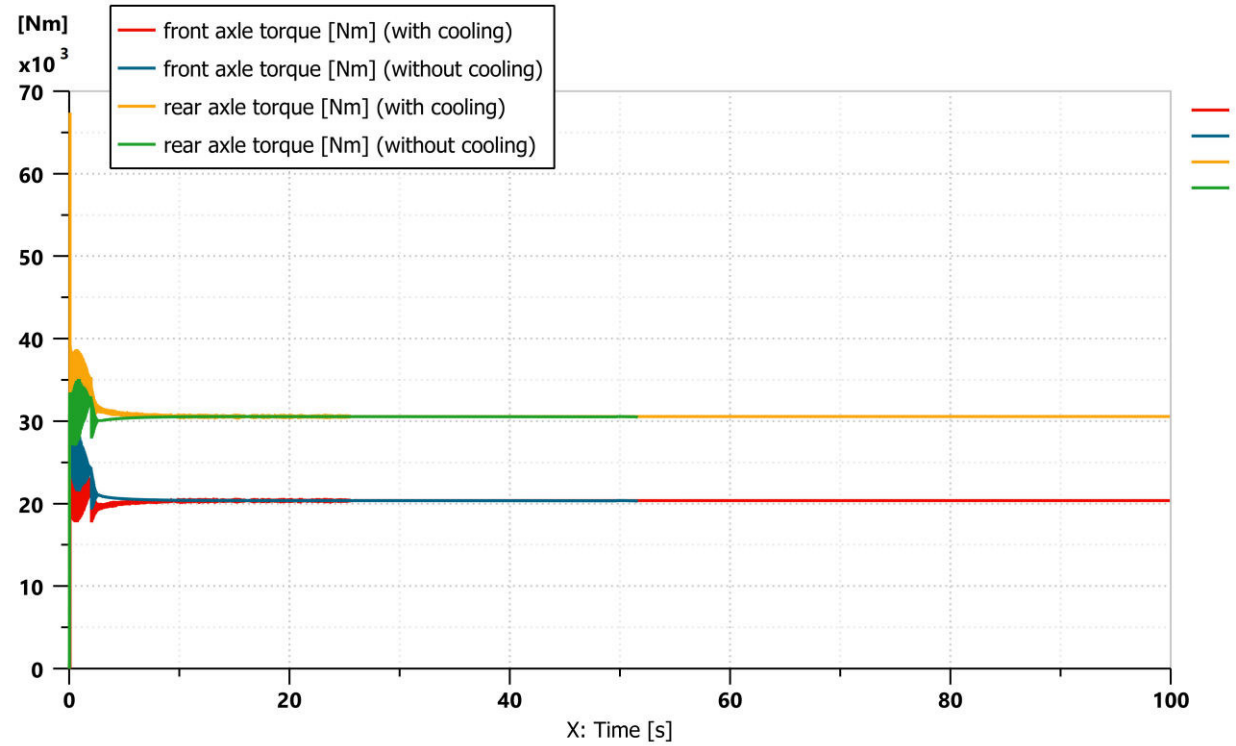

Fig. 12. The torque at the two axles of the motor truck

Fig. 13 shows the variation over time of the pressure at the port of the servo-mechanism for regulating the flow of the servo pump. It can be seen that the hydrostatic transmission that does not benefit from cooling no longer achieves the pressure required to control the flow of the pump because the density of the hydraulic fluid has decreased too much (Fig. 14).

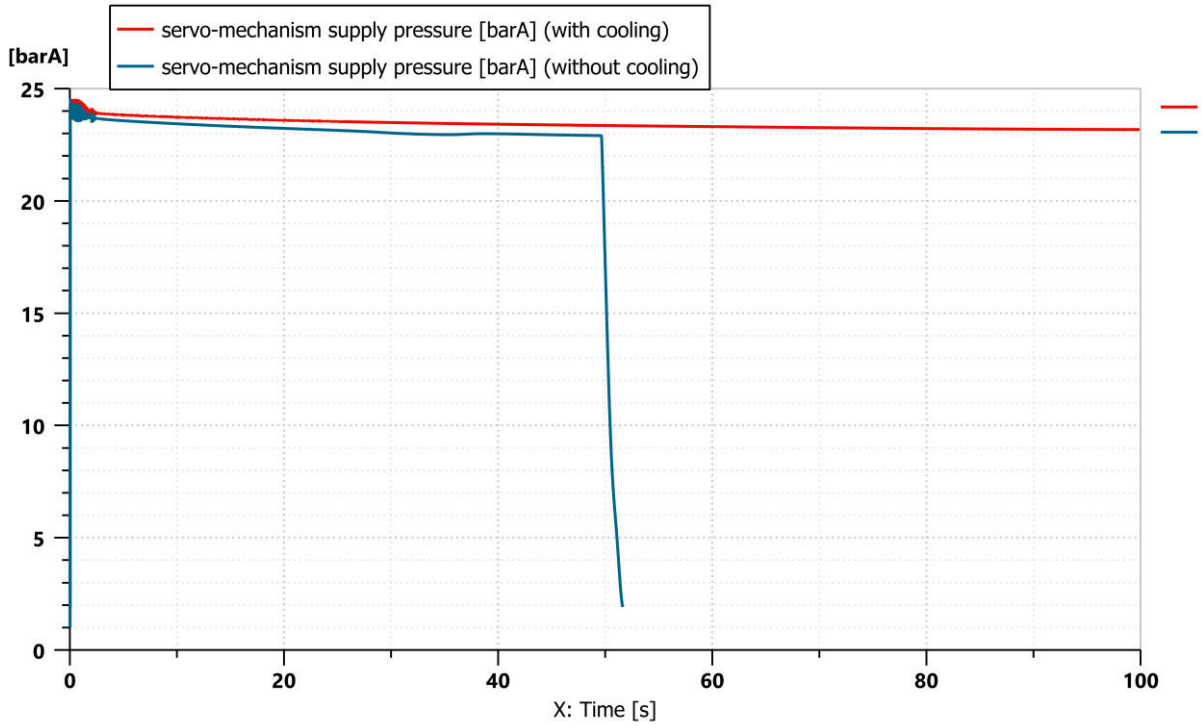

Fig. 13. The pressure at the port of the servo-mechanism for adjusting the displacement of the servo pump

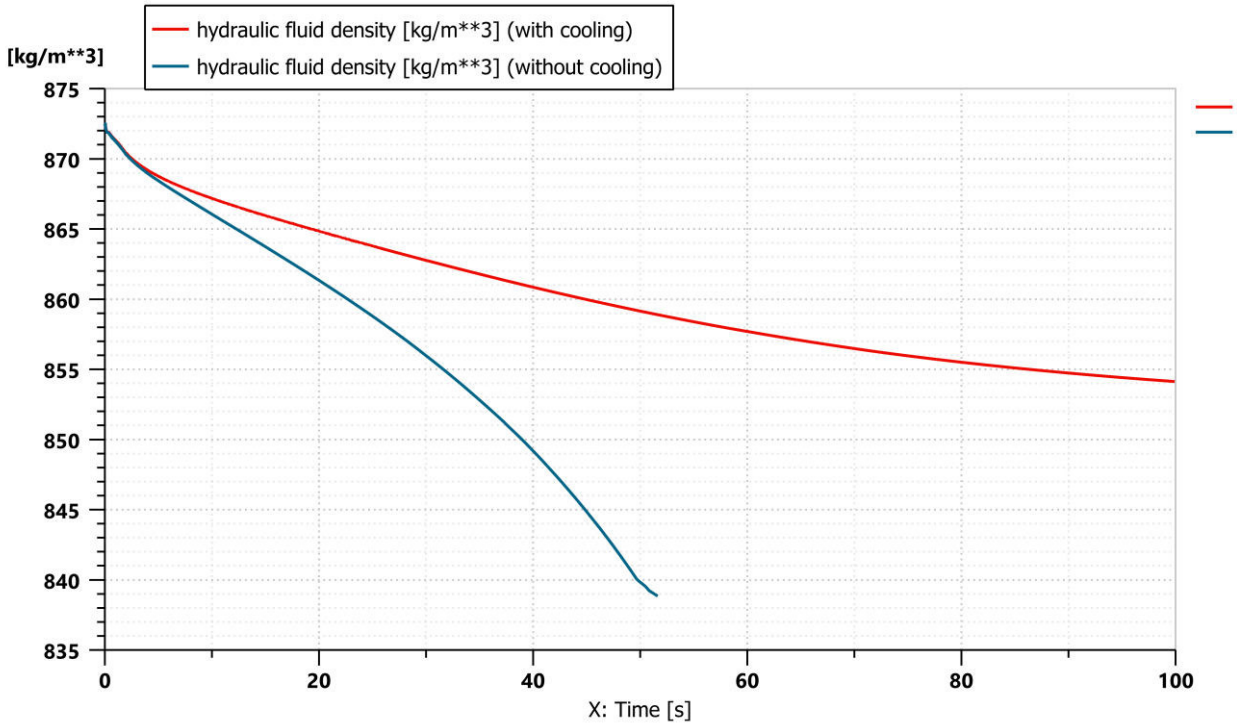

Fig. 14. The time variation of the hydraulic fluid density

The time-variation of the kinematic viscosity of the hydraulic fluid is shown in Fig. 16; this variation occurs due to the increase in the temperature of the hydraulic fluid; likewise, in the case of the void content of the hydraulic fluid (Fig. 15).

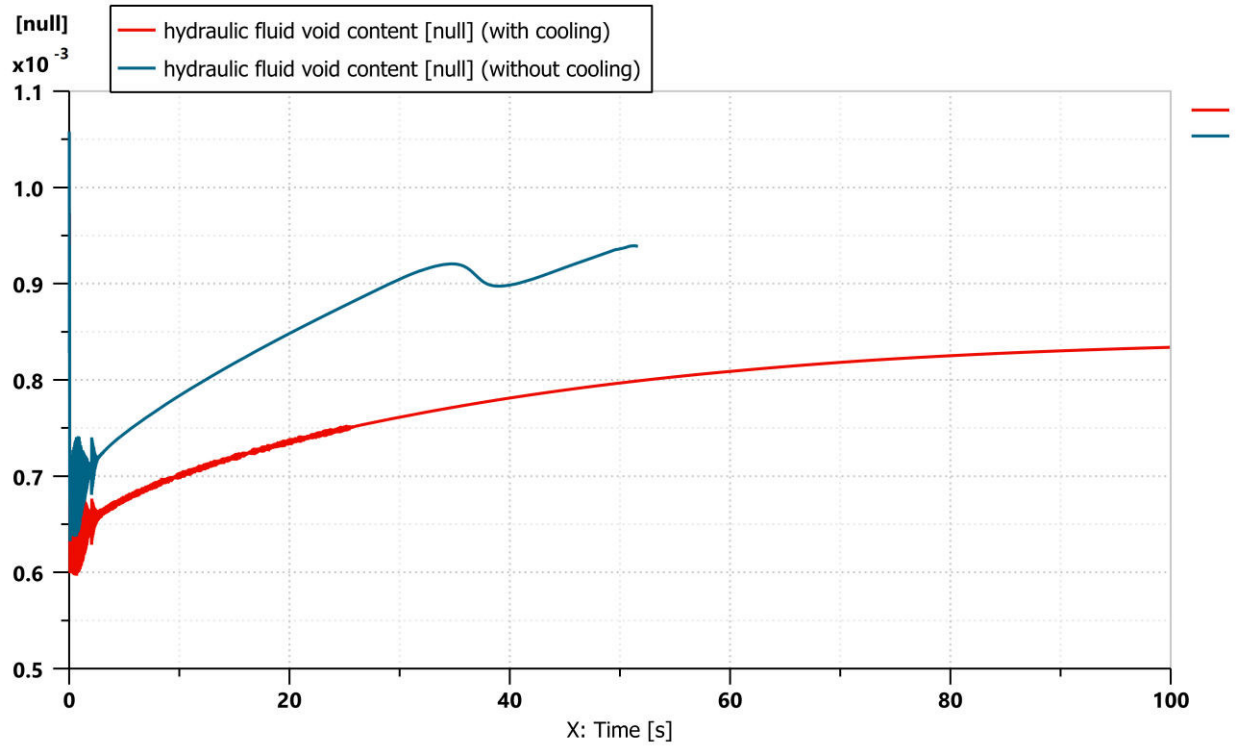

Fig. 15. The void content of the hydraulic fluid

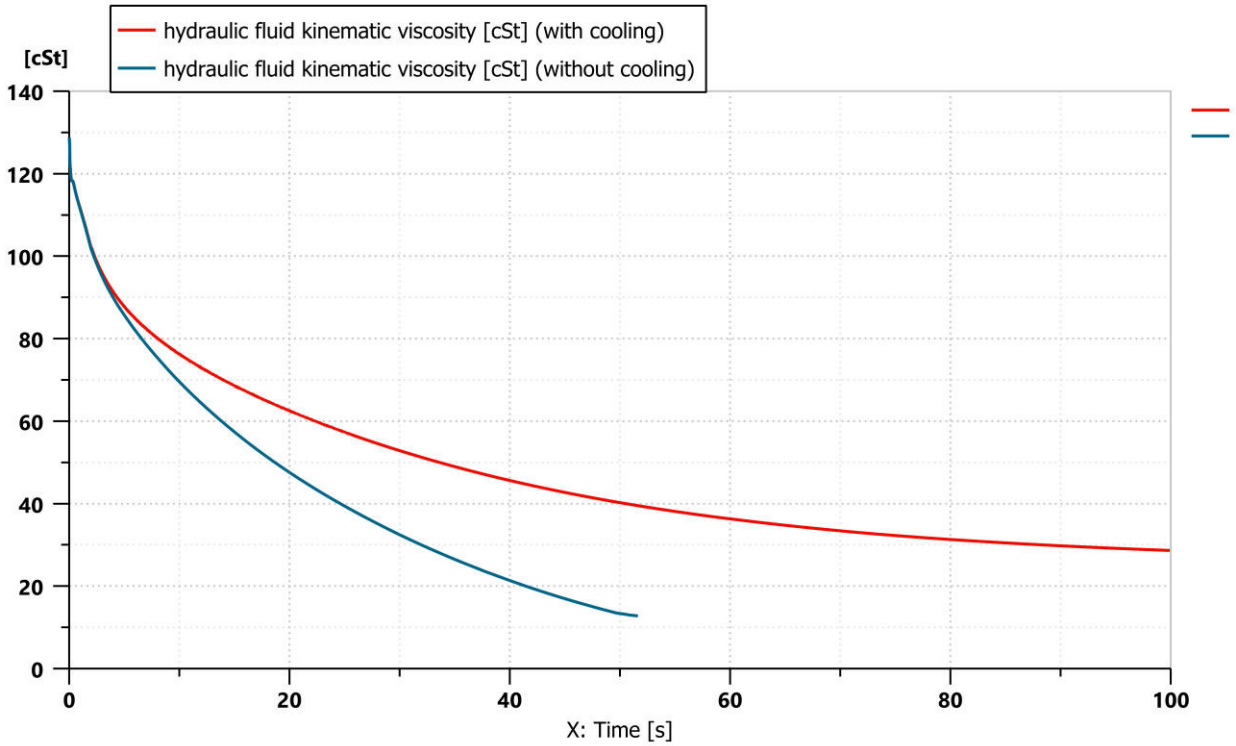

Fig. 16. Kinematic viscosity of the hydraulic fluid

The variation of the kinematic viscosity of the hydraulic fluid depending on the temperature is shown in Fig. 17, where one can see that the transmission that does not benefit from cooling worked up to a temperature of 74 °C and a kinematic viscosity of 12 cSt.

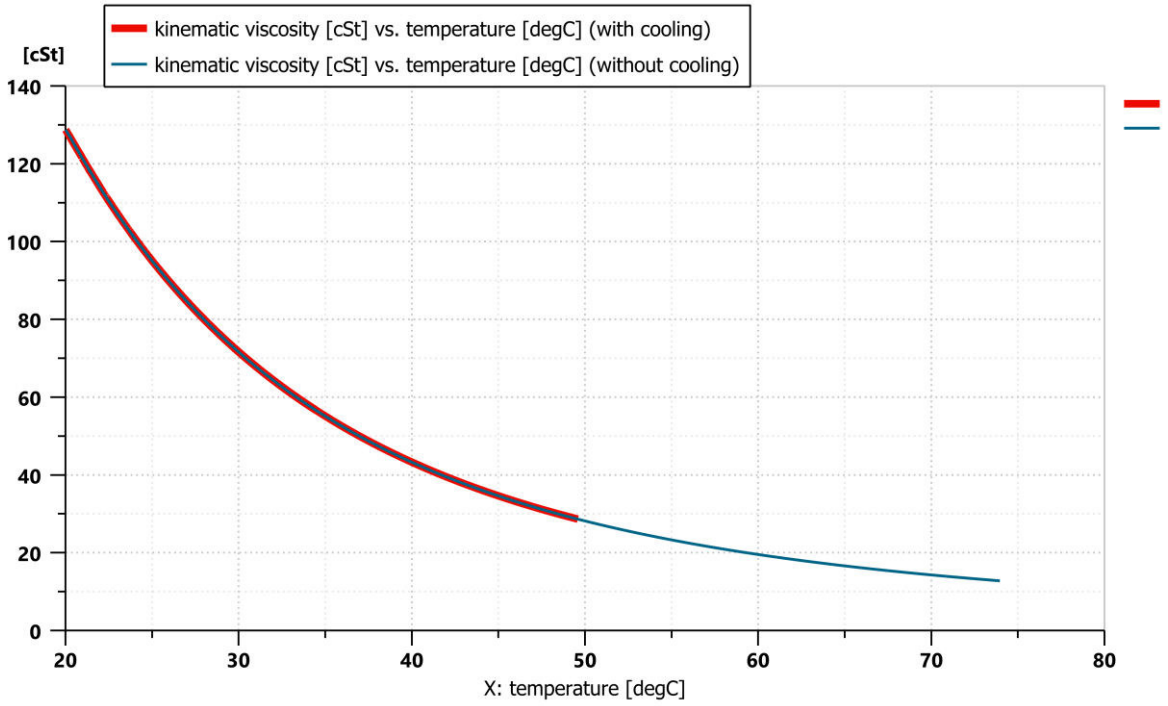

Fig. 17. The kinematic viscosity of the hydraulic fluid depending on its temperature

The heat flow rate between the heat exchanger and the environment is shown in Fig. 18.

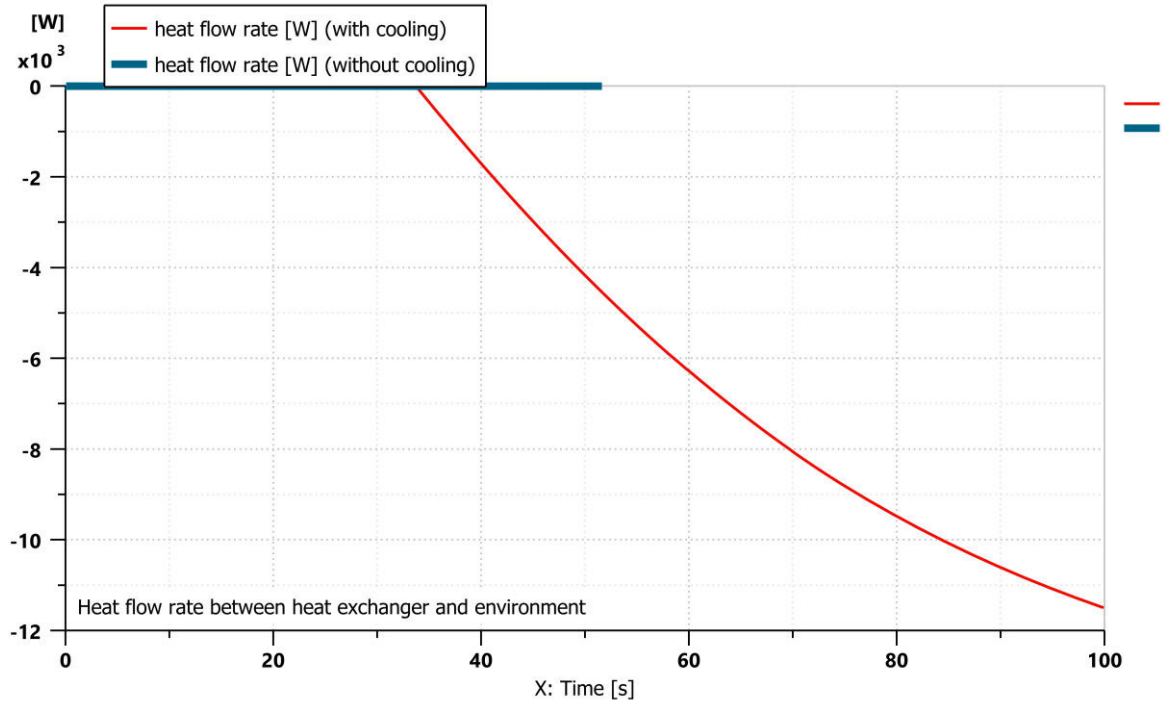

Fig. 18. Heat flow rate between heat exchanger and environment

4. Conclusions

- In the case of servo-mechanisms, the viscosity of the hydraulic fluid must not be strictly controlled, but must be kept within the limits specified by the manufacturer.

- If the cooling circuit of the transmission and the heat exchanger are not sized correctly, in certain situations when the temperature of the environment is very high or the transmission has not been optimized to cope with certain load conditions, the temperature of the hydraulic fluid can increase. Along with this increase, the viscosity decreases, and if it decreases too much, the volumetric losses will be too high and the servo-mechanism will no longer be able to control the flow rate of the pump.

- Unlike open loop transmissions that can operate at the limit even at temperatures of 80 degrees Celsius but with significant volumetric losses and for a short time, closed loop hydrostatic transmissions require a lower hydraulic fluid temperature during operation due to the sensitivity to the viscosity of the hydraulic fluid of the servo-mechanisms.

Acknowledgments

This paper has been financed under a project funded by the Ministry of Research, Innovation and Digitalization through Programme 1- Development of the national research & development system, Sub-programme 1.2 - Institutional performance - Projects financing the R&D&I excellence, Financial Agreement no. 18PFE/30.12.2021.

References

[1] Ma, Li, Hao Yan, Yukai Ren, Lei Li, and Cunkun Cai. "Numerical Investigation of Flow Force and Cavitation Phenomenon in the Pilot Stage of Electrical-Hydraulic Servo Valve under Temperature Shock." *Machines* 10, no. 6 (2022): 423. https://doi.org/10.3390/machines10060423.

[2] Niu, Yubo, Xingyuan Gu, Xuhui Yue, Yang Zheng, Peijie He, and Qijuan Chen. "Research on Thermodynamic Characteristics of Hydraulic Power Take-Off System in Wave Energy Converter." *Energies* 15, no. 4 (2022): 1373. https://doi.org/10.3390/en15041373.

[3] Siddique, Md. Abu Ayub, Wan-Soo Kim, Yeon-Soo Kim, Taek-Jin Kim, Chang-Hyun Choi, Hyo-Jai Lee, Sun-Ok Chung, and Yong-Joo Kim. "Effects of Temperatures and Viscosity of the Hydraulic Oils on the Proportional Valve for a Rice Transplanter Based on PID Control Algorithm." *Agriculture* 10, no. 3 (2020): 73. https://doi.org/10.3390/agriculture10030073.

[4] Lou, Weitao, Weifang Zhang, Tingzhu Jin, Xuerong Liu, and Wei Dai. "Synergistic Effects of Multiple Environmental Factors on Degradation of Hydrogenated Nitrile Rubber Seals." *Polymers* 10, no. 8 (2018): 897. https://doi.org/10.3390/polym10080897.

[5] Masser, Robin, and Karl Heinz Hoffmann. "Endoreversible Modeling of a Hydraulic Recuperation System." *Entropy* 22, no. 4 (2020): 383. https://doi.org/10.3390/e22040383.

[6] Deuster, Sebastian, and Katharina Schmitz. "Bio-Based Hydraulic Fluids and the Influence of Hydraulic Oil Viscosity on the Efficiency of Mobile Machinery." *Sustainability* 13, no. 14 (2021): 7570. https://doi.org/10.3390/su13147570.

[7] Bosch Rexroth AG. "Axial piston variable pump. A10VG series 10." *Installation instructions*. RE 92750/2020-03-03. Accessed August 22, 2022. https://www.boschrexroth.com/documents/12605/25209043/re92750_2020-03-03.pdf/dbb6b049-f973-d8b0-4654-e574803b104d?routed=true.

[8] Minav, Tatiana, Jani Heikkinen, Thomas Schimmel, and Matti Pietola. "Direct Driven Hydraulic Drive: Effect of Oil on Efficiency in Sub-Zero Conditions." *Energies* 12, no. 2 (2019): 219. https://doi.org/10.3390/en12020219.

[9] Society of Tribologists and Lubrication Engineers (STLE). Accessed August 22, 2022. https://www.stle.org/images/TLT/2019/October/Don%20Smolenski/Oct2019_Machinery_Figure1.jpg.

[10] Kauranne, Heikki. "Effect of Operating Parameters on Efficiency of Swash-Plate Type Axial Piston Pump." *Energies* 15, no. 11 (2022): 4030. https://doi.org/10.3390/en15114030.

ISSN 1454 - 8003
Proceedings of 2022 International Conference on Hydraulics and Pneumatics - HERVEX
November 9-10, Băile Govora, Romania

ONE SOLUTION FOR VINEYARDS IN ACTUAL ENERGY CRISIS

Erol MURAD[1], Ion MARIAN[2], Manuela DRĂGHICESCU[3], Florian DRAGOMIR[4], Perino BARAGA[5]

[1] EKKO OFFICE AG, Innovation Department, erolmurad@yahoo.com

[2] ICDVV, marian1367@yahoo.com

[3] SUNE, manuela.draghicescu@gmail.com

[4] PROMECO SD, promeco@digiro.net

[5] CTT PETAL, perino.c.baraga@gmail.com

Abstract: *In vineyard residual biomass is obtained that can be used locally to produce electricity, heat and biochar, when and as much as necessary, so necessary in this state of actual energy crisis. In RO 2021, 160000 ha were cultivated with vines and a minimum of 0.274 Tg.br.db dry vine ropes with an energy potential of 1.45 TWh/year would be collected. In farms from vine prunings, chopped and dried, with CHP equipment is produced electricity for own use with an efficiency of 19% and a thermal energy with efficiency of 52%. With CHAB systems heat and biocar is produced, biocar is used as an agricultural amendment or is gasified to produce gas.bc that can locally replace natural gas, or electricity production with a CHP. The vineyard activity is seasonal, the collection and storage of biomass for energy use is an investment and lock-up of capital, recoverable through lower costs and the supply of energy* ***when and as much as needed****. Ecological variants with energy and economic efficiency are analyzed. Chopped and dried vine prunings as well as biochar represent an energy stock that can be used when and as much as needed in wine growing units to ensure safe and economical operation.*

Keywords: *Vine prunings, power, heat, biochar, carbon footprint*

1. Introduction

In the current energy crisis, the utilization of local resources is essential to ensure operation **when and as much as necessary.**
One problem with systems that harness the solar and wind resource is that they cannot deliver energy immediately and as needed, that is, they are not dispatcable.
In Romania, in august 2022 there were 23,400 prosumers with a power of 200 MWe produced by photovoltaics and wind with a share of biomass below 2%. Energy is produced during the day and when there is wind, which loads the distribution network heavily because it is above the actual consumption, which has imposed restrictions.
A storable energy source is residual vegetable biomass from which, when and as much as needed, thermal energy, electricity and biochar are produced locally that can be used as an energy stock or as an agricultural amendment that sequesters carbon for long periods of time.
Romania has an annual reserve of residual vegetal agricultural biomass of at least 20 Tg.br/y to which viticulture contributes with 3% quality residual woody biomass.
From biomass local energy is produced by direct burning, pyrolysis or gasification **when and as needed.** Cogeneration is the most energy-efficient and economical option to produce electric and thermal energy.
For farms and small communities, the intelligent energetic network type **Smart Grid** concept represents the trend of decentralizing power supply from various sources of energy through the organization of energy network. The Smart Grid system identifies the status and charging of all network elements, it can provide basic loading and can prevent real-time overhead from managing network-connected power sources.
Locally, the most complete utilization of the residual biomass from vineyard represents a major contribution to sustainable development that also involves increasing the level of energy

independence of farms, which is desirable that correlates with the current ecological requirements of reducing CO2 emissions and economic sequestration of atmospheric carbon in agricultural soils.

2. Materials and methods

The chemical composition and heat of combustion of cut vine ropes is relatively uniform regardless of the vine variety grown. [1, 2, 4]
Table 1 shows the estimate potential of residual biomass from viticulture for Romania in 2021.

Table 1: Rezidual mass vine prunings in RO 2021

Feature	U.M.	Value
Cultivated area in RO 2021	Mha/an	**0.1656**
Vine prunings dry	Mg.br/ha	**1.828**
Collection rate	%	**90**
Usable collected dry vine prunings	Mg.br/ha	**1.645**
Annual dry vine prunings mass collected	Tg.br.db/an	**0.272**
Vine prunings average HHV	TWh/Tg.br.db	**5.320**
Energy potential at mass annual collected	TWh/an	**1.449**
Energy consumption for biomass chopping	MWh/MWh.br	**0.030**
Annual energy consumption for chopped mass	TWh/y	**0.008**
Annual usable energy from chopped mass	TWh/y	**1.441**

It is found that at 90% annual collection rate, **272 Gg.br/**y biomass would be obtained with an energy potential of **1.45 TWh/y**. Collection, transport, chopping and storage consume energy and produce CO_2 emissions. Energy consumption was found to be no more than 0.8–1% of string energy, for drying with waste heat and chopping with electricity produced from biomass.
For the production of energy from biomass, excluding direct combustion with a lot of PM2.5 and positive CFP, thermo-chemical conversion processes such as autothermal pyrolysis and gasification are currently used, which produce fuel gas, called gas.bm, as well as vegetable charcoal sterile and porous called biochar (BCH).
The current concept used called CHAB - Combined Heat and Biochar production - ensures a very good utilization of a large variety of plant biomass. [6, 7]. They are systems with batch operation to produce water or hot air, or hot gases for technological processes, **when and as much as needed**, reducing the need for heat storage. They are usable with powers from 20 to 200 kWth.
The installations named SEB.HW, systems for hot water and biochar production, gasify biomass and produce thermal energy with an efficiency of 45-50%, as well as high quality biochar with molar ratios O/C <0.2 and H/C < 0.4 with very few volatiles. [6, 7, 9]. In [8] are presented the performance of a SEB.HW.100 system for vine prunings.
For the production of electricity, the vine prunings (BVR) is gasified in the CHP with an energy efficiency of 20% and a thermal efficiency of 60%. [10, 13].
In [8, 13] are presented the performance of a CHP type HK45 Spanner that produces electricity with an energy efficiency of 19% and thermal energy with an efficiency of 52%.
Figure 1 shows the block diagram of a SEB.HW system and Figure 2 shows the block diagram of a CHP with vegetable biomass. [7, 8].
The biochar produced by SEB.HW can be used for energy production through gasification with a positive CFP, or as an agricultural amendment or filter material with a negative CFP. Typical is an electrical energy efficiency of 30% and thermal efficiency of 56%. Figure 3 shows the block diagram of the ways of using the biochar produced by systems with the CHAB concept, the production of gas.bc, electricity, heat or agricultural amendment and as filter material.

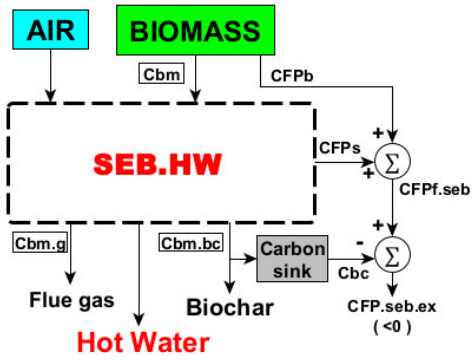

Fig. 1. Block diagram for a SEB.HW

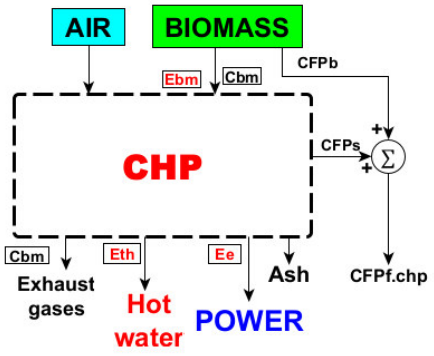

Fig. 2. Block diagram for a biomass CHP

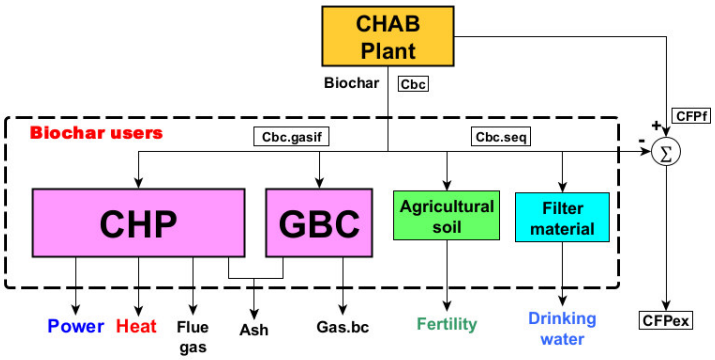

Fig. 3. Block diagram of biochar utilization for energy and amendment

The biochar obtained from the gasification of vineyard prunings has very few volatiles, it gasified with CO2, H2O and air produces a gas.bc with very little tar and high HHV, usable instead of methane gas in local Smart recipes.
Table 2 shows the results of the gas.bc production estimation in different versions by the share of gasified biochar, 100 % or zero. From the 100 % potential of **458 GWh/y**, gas can be obtained, which would replace about **34.3 million m^3** of natural gas.
If less than 75% of the biochar produced is gasified, the energy conversion operation is done with a negative CFP, the biochar used as an amendment sequesters the carbon taken from the biomass for long periods of time.
Gas.bc can be used to power generators, similar to CHP, with an electrical efficiency of 30% and a thermal efficiency of 56%. If less than 70% of the biochar produced is gasified the CFP is zero or negative.
Gasification of biochar with CO2, H2O and air produces a combustible gas with CO, H2 and CH4, similar in use to natural gas, which can be a substitute when and as needed in areas without a gas network where PLG is used.
Table 3 shows the functional performances of using biochar for the production of electricity and heat with CHP systems.
Modern electrical energy production systems with internal combustion engines use gas engines that operate in single mode, constructively optimized and with extremal autocontrol to operate around the economic pole. Real yields reach 50%, but for the case studied, 42% is a value confirmed by functional hybrid systems.
The functional advantage of the CHP with biochar is that it can operate at idle at 20% of the load, from gas.bc produced by producing usable heat. The system produces electricity when needed locally or in the grid where it is connected.

Table 2: Gas.bc from GBC WITH biochar for NG replacement

Feature	U.M.	Value				
Biochar relative mass gasified	%	**100**	**75**	**50**	**25**	**0**
Annual biochar input energy	TWh/y	**0.458**	**0.343**	**0.229**	**0.114**	**0.000**
Biochar Mass not gasified	Tg.bc/y	**0.000**	**0.014**	**0.027**	**0.041**	**0.054**
Carbon mass sequestered in soil	TgC/y	**0.000**	**0.011**	**0.022**	**0.033**	**0.044**
Mass of CO2 sequestered in soil	TgCO2/y	**0.000**	**0.040**	**0.081**	**0.121**	**0.162**
Energy efficiency of gas.bc cooled	%	**75**	**75**	**75**	**75**	**75**
Gas.bc specific HHV	MWh.gbc/Mg.bc	***6.300***	***6.300***	***6.300***	***6.300***	***6.300***
Annual energy gas.bc cooled	TWh/y	**0.343**	**0.257**	**0.172**	**0.086**	**0.000**
HHV of natural gas	kWh/m3	10.000	10.000	10.000	10.000	10.000
Volume of NG with equal energy	Mm3.ng/y	**34.328**	**25.746**	**17.164**	**8.852**	**0.000**

Table 3: CHP with biochar from vine prunings

Feature	U.M.	Value				
Biochar relative mass gasified	%	**100**	**75**	**50**	**25**	**0**
Biochar mass gasified	Tg.bc/an	**0.054**	**0.041**	**0.027**	**0.014**	**0.000**
Annual biochar energy for CHP	TWh/an	**0.458**	**0.343**	**0.229**	**0.114**	**0.000**
Energy efficiency cooled gas.bc	%	**75**	**75**	**75**	**75**	**75**
Gas.bc engine yield	%	42	42	42	42	42
Electric generator yield	%	95	95	95	95	95
Electrogenerator yield	%	**39.9**	**39.9**	**39.9**	**39.9**	**39.9**
Electricity production efficiency	%	**29.9**	**29.9**	**29.9**	**29.9**	**29.9**
Electricity annual production	TWhe/y	***0.137***	***0.103***	***0.068***	***0.034***	***0.000***
Yield heat recovery gas.bc cooling	%	**21.3**	**21.3**	**21.3**	**21.3**	**21.3**
Yield heat recovery from gas engine	%	34.8	34.8	34.8	34.8	34.8
Heat recovery yield	%	31.4	31.4	31.4	31.4	31.4
Recovered heat from cooling gas.bc	MWhth/Mg.bc	1.785	1.785	1.785	1.785	1.785
Recovered heat from gas engine	MWhth/Mg.bc	2.923	2.923	2.923	2.923	2.923
Heat production in CHP	MWhth/Mg.bc	4.708	4.708	4.708	4.708	4.708
CHP heat production efficiency	%	**56.1**	**56.1**	**56.1**	**56.1**	**56.1**
Heat annual production	TWh.th/y	**0.257**	**0.192**	**0.128**	**0.064**	**0.000**
Cogeneration efficiency	%	**86.0**	**86.0**	**86.0**	**86.0**	**86.0**
Cogeneration index		**0.534**	**0.534**	**0.534**	**0.534**	**0.534**
Annual energy production	TWh/y	**0.394**	**0.295**	**0.197**	**0.098**	**0.000**
CFP emitted from CHP operation	kg.CO2/Mg.bc	**35.000**	**35.000**	**35.000**	**35.000**	**35.000**
Annual CFP emitted from CHP operation	Mg.CO2/y	**1.907**	**1.430**	**0.954**	**0.477**	**0.000**

If all the 100 % of biochar produced annually is gasified, **137 GWh.e** of electric energy can be obtained, as well as **257 GWh.th** of thermal energy. For a zero or negative emission, a maximum of 70% of the biochar produced must be gasified.

3. Results

Table 4 shows the products obtained from gasification in SEB.HW systems from vine prunings. The calculations were made for the entire mass of BVR collectable at RO level, **650 GWh.th/y** thermal energy and **54 Gg.bc/y** quality biochar with positive CFP can be produced annually.
If more than 30% of the produced biochar is used as an agricultural amendment, a negative CFP is obtained for the entire energy conversion operation.

Table 4: Energy and biochar from SEB.HW systems

Feature	U.M.	Value
Energy efficiency heat production	%	**0.450**
Annual heat production	TWh/an	**0.652**
Average biochar production	g.bc/g.br.db	***0.200***
Biochar mass annually produced	Tg.bc/y	**0.054**
Average Carbon content of biochar	g.Cbc/g.bc	**0.810**
Annual Carbon mass from biochar	Tg.Cbc/y	**0.044**
Biochar HHV	kWh/kg.bc	**8.400**
Annual biochar energy potential	TWh/y	**0.458**
CFP emitted from CHAB plant operation	kgCO2/Mg.br	**135.000**
CFP emitted from CHAB plant operation	kgC/Mg.br	**36.818**
BCH incorporated into soil for CFP=0	kg.bc/Mg.br	**45.455**
Relative mass BCH gasified for CFP=0	%	***77.3***

The economic analysis of the use of an HK45 CHP manufactured by Spanner is presented in table 5. The usage period for the LCA study was chosen to be only 5 years to investigate whether extensive operation at full production capacity can be economic.
At maximum load, 285 tons of dry biomass are consumed annually, which would be harvested from 160 ha, so it would be feasible for a farm with at least 200 ha cultivated, or for a similar association.
Production costs below 150 €//MWhe depend a lot on the value of the collection, transport, chopping, drying and storage operations. The value of 120 €//Mg.bcr.db is relatively covering for a modern technology use, which requires investments recoverable in 5-8 years.
The important advantage of the HK45 type systems is that they can work with woody chips from different origins, forestry, energy crops, etc. [13]
For lower electrical powers, it is recommended to use ECO20X type CHP aggregates produced in Italy. It produces 20 kWe and 40 KWth with an average hourly consumption of 25 kg.br/h.

Table 5: Economic evaluation of HK45 with chopped vine prunings

Feature	U.M.	Value 1	Value 2
Live Cycle operating time	y/LC	5	7
Average load level	%	100	71
Annual operating time	h/y	7000	5000
Electricity produced annually	MWhe/y	315	225
Heat produced annually	MWh.th/y	700	500
Annual consumption of biomass	Mg.bm/y	283.5	202.5
Price chopped vine prunings	€/Mg/bm	120	120
CHP specific investment	€/kWe	2500	2500

Installation and start-up	%	10	10
Total investment for CHP	€	123750	123750
Biomass storage	€	6000	6000
Distribution electric block	€	4500	4500
Total investment	€	134250	134250
Feature	**U.M.**	**Value 1**	**Value 2**
Annual maintenance rate costs	%	10	10
Maintenance costs for live cycle	€/LC	13425	13425
Operator cost for live cycle	€/LC	60000	84000
Prices ratio MWh.th / MWh.e		0.376	0.376
Equivalent electricity production	MWhe.ech/y	578.038	412.923
Total operating costs	€/LC	207675	231675
Annual operating costs	€/y	41535.00	33096.43
Annual biomass expenses	€/y	34020.00	24300.00
Annual operating costs	€/y	75555.00	57396.43
Share of biomass expenses	%	45.03	42.34
Cost electricity production	€//MWhe	130.71	139.00
Cost heat production	€//MWhth	49.12	52.24
ENEL network tariff	lei /kWhe	1.230	1.230
ENEL network tariff	€//MWhe	246.000	246.000
Electricity tariff difference	€//MWhe	115.291	107.000
Heat tariff	€//MWh.th	64.000	64.000
Heat tariff difference	€//MWh.th	14.884	11.757
Investment recovery time	operating day	811.512	909.030
Investment recovery time	year	2.782	6.109
Annual saving electricity production	€/y	36316.52	24074.95
Annual saving heat production	€/y	10418.48	5878.62
Annual saving operating CHP	€/y	46735.00	29953.57
Saving from operating costs	%	61.86	52.19

It is worth noting that the cost of electricity production is similar to that of 2021, which made the use of CHP with biomass economical in terms of ensuring energy independence. In 2022, in the midst of the energy crisis, the production cost is below 60% of that practiced on the networks, which ensures real economic efficiency.
Since the production costs depend on the cost of using the residual biomass, it is economical to process and store it for larger quantities, corresponding to about 100 ha of cultivation, so for growers' associations.
For higher powers, systems with 150 kWe or 600 kWe can be used, which, however, are debited to the network and require large amounts of biomass.

Table 6: Economic evaluation for using gas.bc to replace natural gas

Feature	**U.M.**	**Value**			
Biochar relative mass gasified	%	**100**	**75**	**50**	**25**
Conversion rate euro/leu	lei/€	4.95	4.95	4.95	4.95

Energy price for 2022 natural gas	lei/MWh	472	472	472	472
Energy price for 2022 natural gas	€/MWh	95.35	95.35	95.35	95.35
Energy price for 2022 PLG	lei/MWh	1792	1792	1792	1792
Energy price from PLG	€/MWh	398.22	398.22	398.22	398.22
Production price gas.bc	€/Mg.bc	850	850	850	850
Price energy from gas.bc	€/MWh	134.92	134.92	134.92	134.92
Price energy between PLG and gas.bc	€/MWh	-263.30	-263.30	-263.30	-263.30
Additional annual income from gas.bc	M€/y	**90.386**	**67.790**	**45.193**	**22.597**

Table 7 shows the evaluations of carbon emissions produced by the energy recovery of BVR according to the share of BCH used for gasification in GBC or CHP.
For 100 % of biochar gasification the CFP is positive, but much lower than those produced by the use of fossil fuels. CFP ≈ 0 can be obtained for 25% BCH used as an agricultural amendment. The use as an agricultural amendment produces a long-term sequestration with the value of **-0.46 Tg.CO2/Tg.br**, which annually for viticulture would represent - 25 Gg.CO2/y equivalent for a consumption of **4100 tons of diesel**.

Table 7: Carbon footprints from energetic uses of vine prunings

Feature	U.M.	Value				
Annual biochar mass gasified	%	**100**	**75**	**50**	**25**	**0**
CFP from SEB.HW	Mg.C/Mg.br	0.037	0.037	0.037	0.037	0.037
Annual CFP from SEB.HW	Tg.C/y	**0.010**	**0.010**	**0.010**	**0.010**	**0.010**
Annual CFP from CHP operation	Tg.C/y	5.2E-04	3.9E-04	2.6E-04	1.3E-04	0
Annual CFP from energy production	Tg.C/y	0.011	0.010	0.010	0.010	0.010
Sequestered carbon from amendment	Tg.Cbc/y	0	**0.011**	**0.022**	**0.033**	**0.044**
Annual CFP for energy	TgC/y	**0.010**	**-0.001**	**-0.012**	**-0.023**	**-0.034**
Annual CFP for energy production	Tg.CO2/y	**0.037**	**-0.004**	**-0.044**	**-0.085**	**-0.125**
Specific CFP energy production	Tg.CO2/Tg.br	**0.135**	**-0.014**	**-0.162**	**-0.311**	**-0.459**

4. Conclusions

In the current energy crisis, the use of renewable, storable local energy resources is even more urgent, with which energy can be produced for productive or domestic use **when and as much as necessary**, preferably with a negative carbon footprint.
In RO viticulture, it is produced annually on 160,000 ha from which a minimum of **272 Gg.bvr.db/y** dry vine prunings with an energy potential of **1.45 TWh/**y would be collected, an energy resource from which through pyrolysis and gasification produces heat, electricity and biochar.
By gasifying BVR in systems with the CHAB concept, **650 GWh.th/**y of heat and **54 Gg.bc/y** of quality biochar can be obtained with the energy potential of **458 GWh/y**, without residues and with very low CFP.
From the biochar gasification, a gas.bc is obtained that could annually replace **34.3 million m of natural gas**, or about 137 GWh.e/y and 257 GWh.th/y of heat would be produced with CHP.
The economic estimate indicates that the use of gas.bc instead of PLG is economically efficient, reducing annual expenses by up to 90 million euros in wine farms.
At a use of 50% of biochar as an agricultural amendment the energetic and ecological use of BVR is made with a negative carbon footprint of **-44 Gg.CO2/y**.

A wine farm with **100 ha** can annually collect a BVR mass of 165 Mg.bvr.db/y from which a CHP produces 180 MWhe/y and 400 MWh.th/y. Gasified in SEB.HW systems, 390 MWh.th/y and 33 Mg.bc.y biochar are obtained.
It is economically feasible to use CHP with biomass for the production of electricity and heat, with lower energy costs than the current ones, with a maximum investment payback time of 4 years.
The paper highlights the current usefulness of harnessing the energy potential of the residual viticultural biomass, being the basis for the development of optimal variants, adapted to the real conditions of the viticultural farms.

References

[1] Cavalaglio, G., and S. Cotana. *Recovery of vineyards pruning residues in an agro-energetic chain*. University of Perugia – Biomass Research Centre, 2008.
[2] Giorio, Chiara, Sarah Pizzini, Enrico Marchiori, Rossano Piazza, Stefano Grigolato, Michela Zanetti, Raffaele Cavalli, Marco Simoncin, Lidia Soldà, Denis Badocco, and Andrea Tapparo. "Sustainability of using vineyard pruning residues as an energy source: Combustion performances and environmental impact." *Fuel* 243 (May 2019): 371-380.
[3] Genesio, Lorenzo, Franco Miglietta, Silvia Baronti, and Francesco P. Vaccari. "Biochar increases vineyard productivity without affecting grape quality: Results from a four years field experiment in Tuscany." *Agriculture, Ecosystems and Environment* 201 (March 2015): 20–25.
[4] Murad, Erol, M. Seiculescu, C. Sima, and G. Haraga. "Using the energy potential of vine ropes" / Utilizarea potenţialului energetic al corzilor de viţă." Paper presented at the Scientific communications session ICDVV Valea Călugărească, Romania, June 10, 2010.
[5] Murad, Erol, and Florian Dragomir. "Heat generators with TLUD gasifier for generating energy from biomass with a negative balance of CO_2." Paper presented at the International Conference on Hydraulics and Pneumatics HERVEX 2012, Călimăneşti-Căciulata, Romania, November 7-9, 2012.
[6] Murad, E., C. Dumitrescu, F. Dragomir, and M. Popescu. "CHAB concept in sustainable development of agriculture." Paper presented at the International Symposium ISB-INMA TEH' 2016, Bucharest, Romania, October 27 – 29, 2016.
[7] Murad, Erol. "Production of energy and agribiochar without residues and with negative carbon footprint with CHAB and CHBAP concepts from the Romanian residual vegetable agricultural biomass." Paper presented at the International Symposium ISB-INMA TEH' 2021, Bucharest, Romania, October 29, 2021.
[8] Murad, Erol, Manuela Drăghicescu, Perino-Constantin Baraga, and Adrian-Ioan Drăghicescu. "Energy and Biochar production with a ZERO carbon foot print." Paper presented at the National Conference of New and Renewable Energy Sources, CNSNRE 2022, Valahia University, Târgoviște, Romania, June 2 - 3, 2022.
[9] Schmidt, Hans-Peter, Claudia Kammann, Claudio Niggli, Michael W.H. Evangelou, Kathleen A. Mackie, and Samuel Abiven. "Biochar and biochar-compost as soil amendments to a vineyard soil: Influences on plant growth, nutrient uptake, plant health and grape quality." *Agriculture, Ecosystems and Environment* 191 (June 2014): 117-123.
[10] Pröll, Tobias, and Florian Zerobin. "Biomass-based negative emission technology options with combined heat and power generation." *Mitigation and Adaptation Strategies for Global Change* 24, no. 7 (2019): 1307–1324.
[11] Bioenergy Europe. *Bioenergy Europe factsheet: Biomass for energy - Agricultural residues & energy crops*. October 15, 2019. Accessed October 10, 2022. https://bioenergyeurope.org/component/attachments/attachments.html?id=561&task=download.
[12] European Biochar Industry Consortium e.V. (EBI). *EBI Whitepaper. Biochar-based carbon sinks to mitigate climate change*. October 2020. Accessed October 10, 2022. http://www.biochar-industry.com/wp-content/uploads/2020/10/Whitepaper_Biochar2020.pdf.
[13] Spanner Re² GmbH. "Biomass power plant from Spanner Re²." Accessed October 19, 2022. https://www.holz-kraft.com/en/products/biomass-chp.html.

ISSN 1454 - 8003
Proceedings of 2022 International Conference on Hydraulics and Pneumatics - HERVEX
November 9-10, Băile Govora, Romania

S-CURVE MOTION CONTROL IMPLEMENTATION USING 32-BIT MICROCONTROLLER

Andrei DRUMEA[1], Cristina Ioana MARGHESCU[1], Mihaela PANTAZICĂ[1], Gheorghe JITIANU[1], Andrei VLAD[2]

[1] Politehnica University of Bucharest, andrei.drumea@upb.ro

[2] S.C. HESPER S.A.

Abstract: *The paper presents the design, implementation and testing of a stepper motor controller with soft-start function based on 32-bit microcontroller. The soft-start is implemented using the S-curve due to its simplicity and its ability to control the maximum values of speed and acceleration, key parameters for many mechatronic systems. Theoretical aspects are briefly presented, as well as software and hardware solution and its testing and measurement on a specific test bench.*

Keywords: *S-curve, stepper motor, microcontroller*

1. Introduction

Many mechatronic applications require fast and precise movement of actuators from one point to another. Shocks in the actuator mechanism should be avoided and a smooth operation is preferred; these requirements are harder to meet at the start of the motion, especially in the case of actuators implemented with stepper motors that have movement divided in discrete parts. Soft-start operation is a good solution for such systems, and this technique involves slower movement at the beginning, with controlled (limited) speed and acceleration.
A good implementation of soft-start operation is the S-curve, which offers limited speed, acceleration and jerk ([1]). At the start of the motion, the speed is slow but gradually increases up to a maximal value; near the end of the movement, the speed starts to decrease in the same way. In typical mechanical movements, a 0.5 seconds timespan for the S-curve profile is a good value. Considering this parameter, the S-curve can be obtained from trigonometric functions, as follows in formula (1):

$$y(t) = \int_0^t sin^2(x)dx \tag{1}$$

This particular function offers S-type curve for a 0.5 seconds timespan. Calculating the integral, we can obtain the simplified equation for the S-curve, as formula (2):

$$y(t) = \frac{2}{\pi}\left(\pi t - \frac{1}{4}sin(4\pi t)\right) \tag{2}$$

This formula can be used by a microcontroller to generate a pulse train with variable period for driving a stepper motor; an integrated timer module simplifies this task. The period of the pulse can be calculated on the fly (for each pulse the microcontroller calculates its period, performing 4 multiplications and one difference) or, for improved speed but with larger memory consumption, this function can be tabulated (calculated before using a mathematical software and stored as a vector in microcontroller program memory). Because modern microcontrollers offer large program memory space, the second method is preferred due to its speed and easier software implementation (the program parses the pulse period vector and sets the timer to generate the pulse accordingly).

The S-curve described by equation (2) for a 0.5 seconds timespan is shown in figure 1.

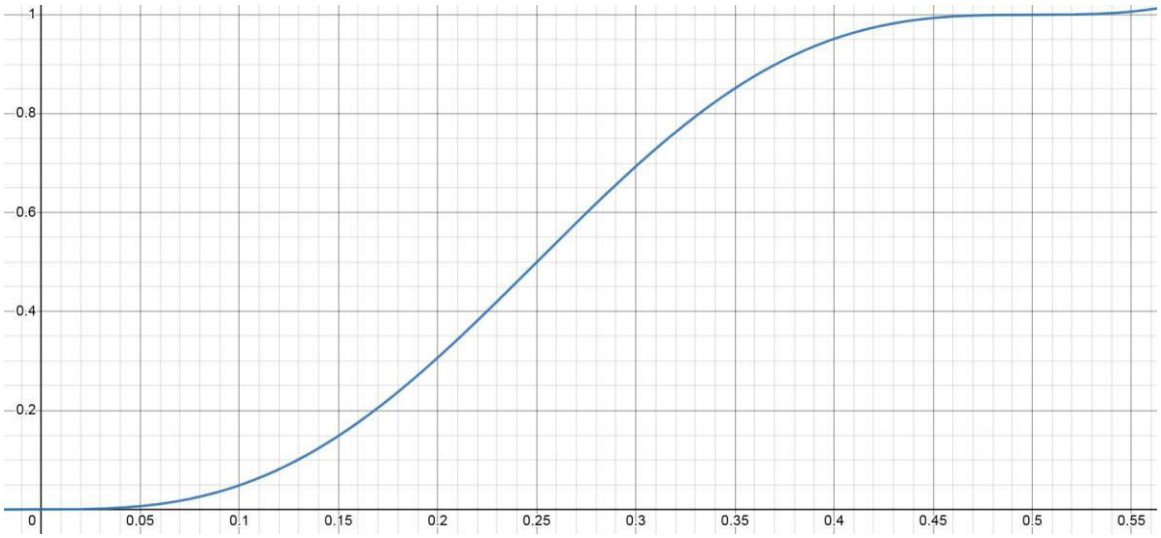

Fig. 1. Proposed S-curve with 0.5 seconds timespan

This curve will be used to generate variable period/frequency pulses for a stepper motor driver from lower frequencies (start frequency is in 100Hz...1kHz range) up to 30kHz.

2. Software Implementation

An Object-Pascal based Windows application was developed to generate the vector values for the presented S-curve. The application, shown in figure 2, generates the vector of configuration values for a microcontroller timer programmed for a 0.25microsecond ticks.

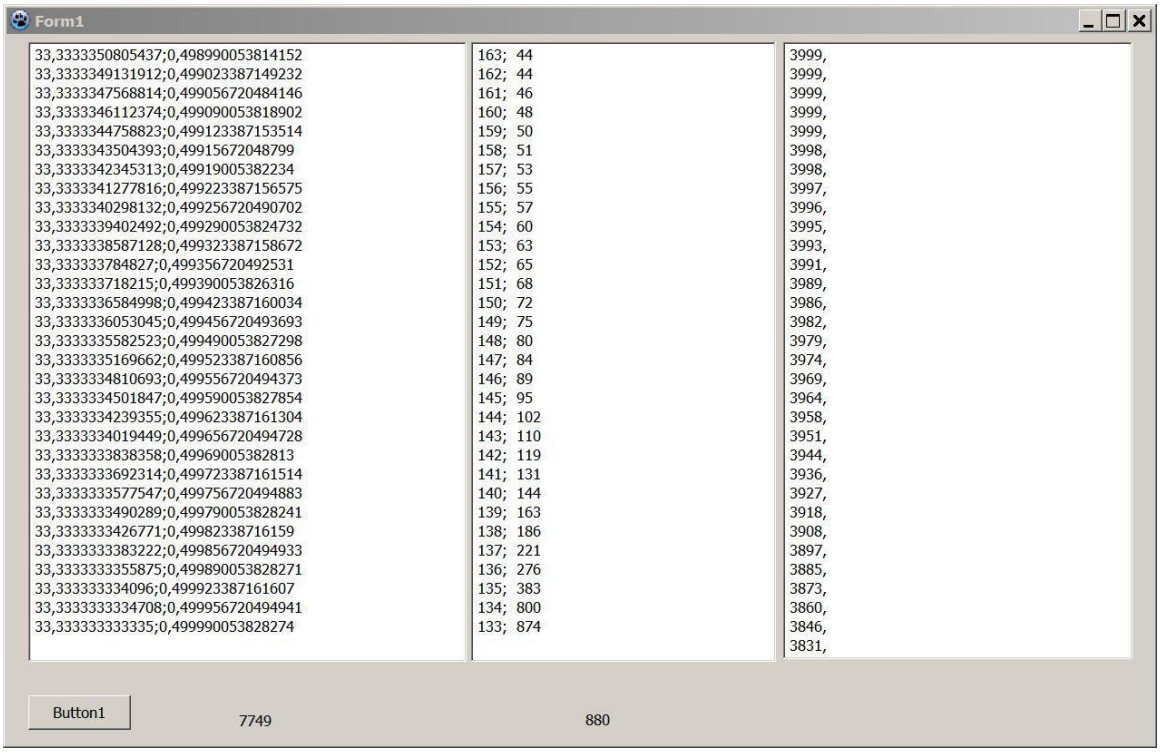

Fig. 2. Main window of Windows application for generating vector values for S-curve

This 0.25 microsecond value can be precisely generated using a standard 16bit timer of the STM32F205 microcontroller. The microcontroller is clocked at 120MHz so it has enough power for industrial process control and enough granularity for timer.
In the application, current pulse period (in microseconds) and time (in seconds) are stored on the left memo box; in the middle memo box is shown a statistics of values for the timer configuration (the value and the number of times it repeats), and the right memo box is the vector itself, that can be pasted into C source code of the microcontroller program. The bottom labels contain the total number of vector values and the number of different values. This information is useful when defining vector size or for other optimizations.
The generated S-curve values for frequencies between 100Hz and 30kHz are shown in figure 3.

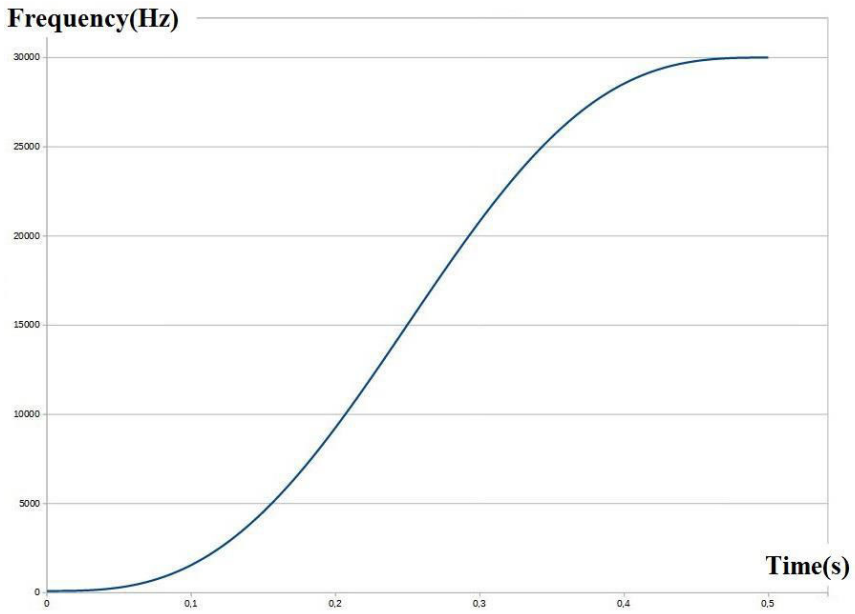

Fig. 3. Calculated S-curve for frequency sweep from 100Hz to 30kHz in 0.5 seconds

Figure 4 presents pulse width, which decreases from 10 miliseconds to 33.3 microseconds.

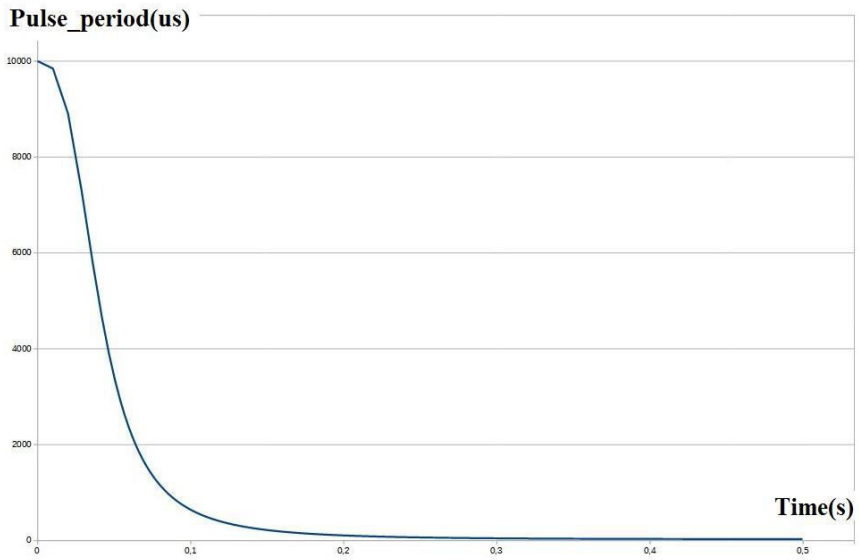

Fig. 4. Calculated period of pulses for frequency sweep from 100Hz to 30kHz in 0.5 seconds

Different vectors can be generated for other start frequencies (200Hz, 333Hz, 500Hz or 1kHz) and can be grouped in a matrix for more flexibility; each vector element requires 2 bytes of flash memory, about 16 kBytes for the entire vector ([4]). This memory requirement is not a problem for STM32F205 microcontroller that has a flash memory of 256kBytes...1MByte, depending on chosen chip version.
In our application we use an array of 8 S-curve vectors, but the microcontroller has enough memory for more vectors (up to 32).

3. Test and Measurements

The S-curve software was written in C language for ARM Cortex-M processors (STM32F205 belongs to this category) and implemented in an electromechanical system for electric discharge machining. This system moves the electrode for electric discharge using an actuator with stepper motor and rotary encoder, as shown in figure 5.

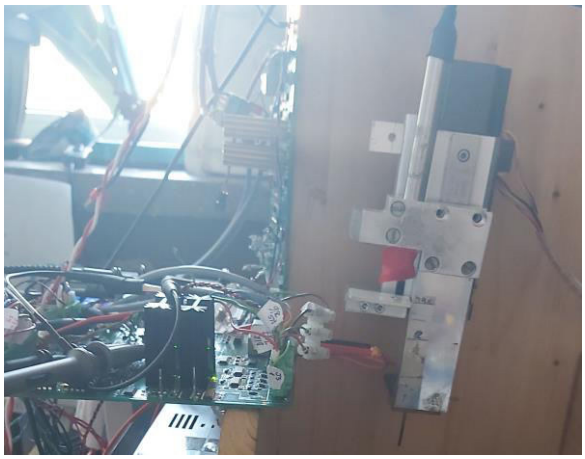

Fig. 5. System view, microcontroller board and actuator with stepper motor, rotary encoder and LVDT sensor

A LVDT displacement sensor ([3]) is fixed to the actuator to measure the real displacement and to observe if any motor steps are missing. The microcontroller board, shown on the left side, is detailed in figure 6.

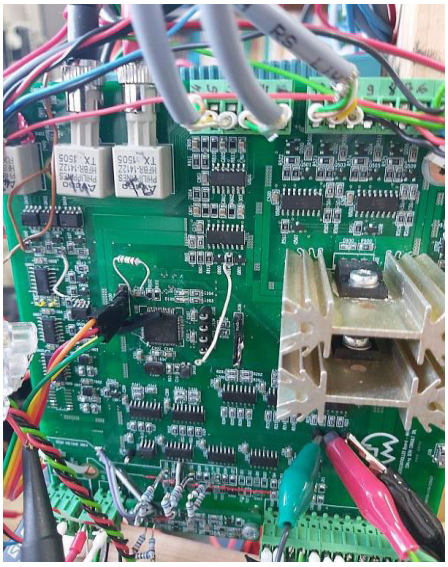

Fig. 6. Microcontroller board, detailed

The microcontroller board uses many optocouplers to isolate the digital command signals from the power signals ([2]); there is also a serial connection to a programmable logic controller (PLC) that offers human to machine interface using a touch panel.
The following pictures present the generated pulses for stepper motor driver (blue traces), measured displacement from LVDT sensor (green traces) and logic commands from master programmable logic controller – stop command (magenta traces) and slow command (orange traces). These signals were observed during an up-down periodic movement with 0.5 seconds pause at the end. Noise can be observed at the LVDT sensor output, due to the electric discharge process running in the same time.

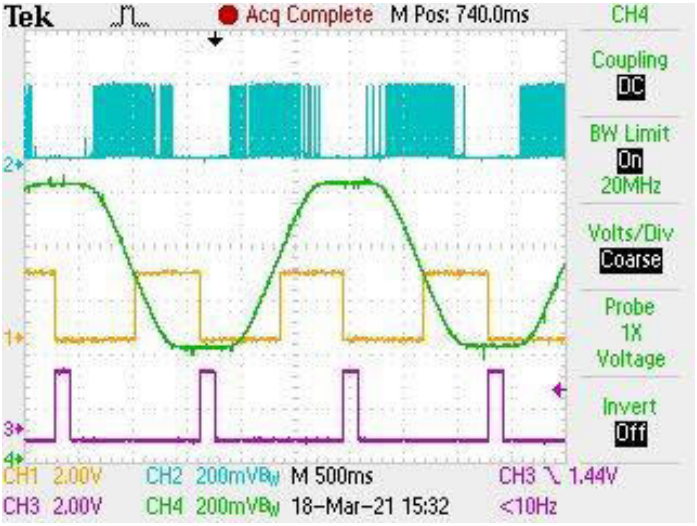

Fig. 7. Pulses from stepper motor controller for an up-down movement

Fig. 8. Pulses from stepper motor controller for an up-down movement, detailed

Presented traces for stepper motor traces have lower pulse density at the start and the end of the motion and higher density in the middle, but the limited number of memory points of the digital oscilloscope as well as aliasing affects the display of the trace when trying to show the pulses on a larger timespan.
Nevertheless, the system works as expected and each pulse has the correct timing.

4. Conclusions

Soft-start option is an important feature in mechatronic systems such as stepper motor based actuators because it reduces the number of lost steps at the beginning of the motion. Soft-start is usually implemented as a variable speed with an S-curve profile that can be easy implemented using a 32-bit microcontroller with enough memory resources. Our implementation, based on STM32 microcontroller from ST Microelectronics, was tested and fulfilled its requirements.

Acknowledgments

The research presented in this paper has been developed under Financial Agreement no. 272/24.06.2020, signed by the Ministry of European Funds / Ministry of Education and Research and S.C. HESPER S.A. Bucharest for the Innovative Technological Project titled “Digital mechatronic systems for generating pressure of 1000 bar, using hydraulic pressure intensifiers” (SMGP), project under implementation from 01.07.2020 to 30.06.2023. Financial support has also been granted under a project funded by the Ministry of Research, Innovation and Digitalization through Programme 1- Development of the national research & development system, Sub-programme 1.2 – Institutional performance – Projects financing the R&D&I excellence, Financial Agreement no. 18PFE/30.12.2021.

References

[1] Blejan, Marian, and Robert Blejan. "Mathematics for Real-Time S-Curve Profile Generator." *Hidraulica Magazine*, no. 4 (October 2020): 7-25.
[2] Drumea, Andrei, and Robert Dobre. “Analysis of power supply circuits for electroluminescent panels.” Paper presented at the Advanced Topics in Optoelectronics Microelectronics and Nanotechnologies VIII ATOM-N2016, Constanta, Romania, August 25-28, 2016.
[3] Drumea, Andrei, Marian Blejan, and Ciprian Ionescu. “Differential inductive displacement sensor with integrated electronics and infrared communication capabilities.” Paper presented at the Advanced Topics in Optoelectronics Microelectronics and Nanotechnologies VI ATOM-N2012, Constanta, Romania, August 23-26, 2012.
[4] Drumea, Andrei. “Low power aspects of a microcontroller-based module with wireless communication.” Paper presented at the 23rd International Symposium for Design and Technology in Electronic Packaging SIITME2017, Constanta, Romania, October 26-29, 2017.

ISSN 1454 - 8003
Proceedings of 2022 International Conference on Hydraulics and Pneumatics - HERVEX
November 9-10, Băile Govora, Romania

THE EFFECT OF HYDRAULIC ISOLATORS FOR CAB OF VIBRATORY ROLLERS ON RIDE COMFORT

Carmen Nicoleta DEBELEAC[1]

[1]"Dunarea de Jos" University of Galati, Engineering and Agronomy Faculty in Braila,

Research Center for Mechanics of Machines and Technological Equipments, carmen.debeleac@ugal.ro

Abstract: *In this paper, the author studied the characteristic of the hydraulic isolators regarding the vibration transmissibility under harmonic excitations developed in the working regime of roller. A nonlinear dynamics model of the vibratory roller under drum-terrain interaction can be established based, usually, on Matlab environment. The accelerations of the vertical driver's seat and the cab's pitch angle can be simulated with high accuracy. The research results available at technical literature indicate that the characteristics of non-linear damper of the hydraulic mounts can greatly reduce the vertical driver's seat vibration and cab comparative with the vibratory roller's cab using the traditional rubber mounts.*

Keywords: *Vibratory roller, hydraulic isolator, ride comfort, cab.*

1. Introduction

The purpose of this review consists on highlighting the isolation performances of hydraulic mounts of vibratory compactors equipments compared to solutions that have other insulation principles. As a consequence of the technical progress in the field of construction machines, over time, especially in the case of vibratory rollers, the performance requirements imposed on them (to ensure the ride comfort) have become very high according to the standard of ISO 2631-1 [1]. Knowing the characteristics of these anti-vibration systems embedded in the structure of the compactor, various models were developed to simulate the dynamic actions that occur during the working process, most of them with one degree of freedom based on the standard Kelvin-Voigt spring-damper model (with linear or nonlinear parameters) in combination with others rheological devices (Fig. 1).

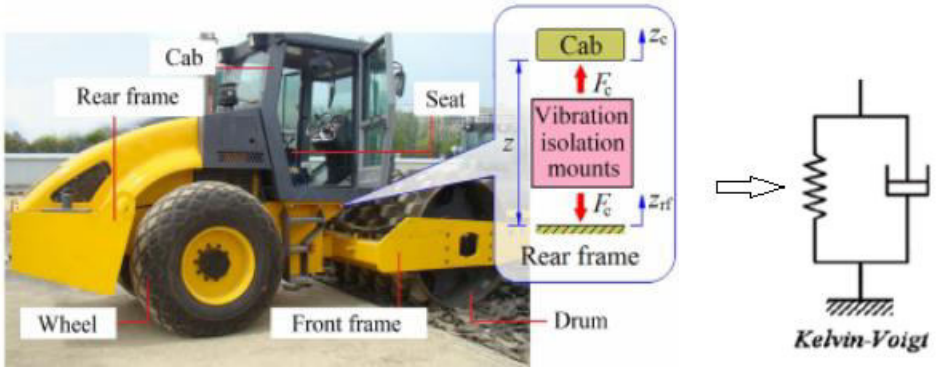

Fig. 1. Principle of isolation mounts modelling [2]

To isolate vibrations of compactor cab caused by vibratory roller excitations, low stiffness and low damping are needed because the dynamic force transmitted to the body is proportional to the stiffness and damping of the mount.

2. Modelling of the rubber and metal-rubber mounts for cab isolation

In order to isolate the vibration sources generated from the wheels and the vibratory drum of vibratory compaction machines to the operator, its seat and the cab were equipped with various isolation

systems. First solutions are based of rubber elements (Fig. 2) interposed between cab-chassis and, respectively, cab floor - operator seat.

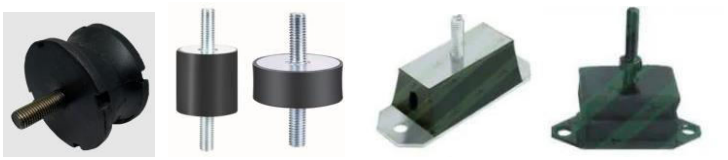

Fig. 2. Traditional rubber mounts for cab isolation

Later, metal rubber anti vibration cabin mounts (Fig. 3) are developed as industrial mounts with efficiency in vibration isolation of engines, cabs and other devices. These are available in different types of steel and rubber mesh and are use in common applications in earthmoving machinery fields, military vehicles, agricultural equipments, etc.

Fig. 3. Common rubber-metal mounts for cab isolation

The settlement of the cab of vibratory compactors on these rubber elements is illustrated in Figure 4, together with the lumped model with a degree of freedom for studying the behaviour of the analysed system.

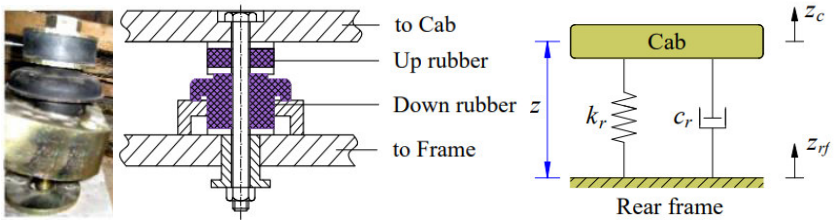

Fig. 4. Cab isolation with rubber mount:
a) Rubber mount; b) Lumped model of cab - rear frame isolation [3]

3. Modelling of the hydraulic mounts for cab isolation

Hydro mount models are more complex than rubber models. The model is designed to accurately predict the behaviour when the real design parameters like the fluid channel length and area are given [4, 5]. Figure 5 shows an example for this type of mount usually used for cab isolation.

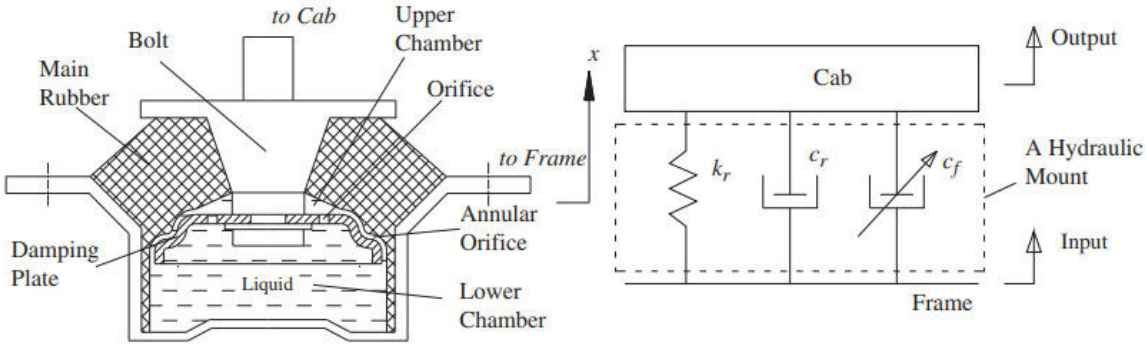

Fig. 5. Solutions for cab isolation with hydraulic mounts [6]

Hydraulically damped mounts use the tuned cab mass damping effect and additional fluid damping in order to assure high dynamic stiffness and damping around the tuned resonance frequency of vibrations generated by the vibratory roller (Fig. 6).

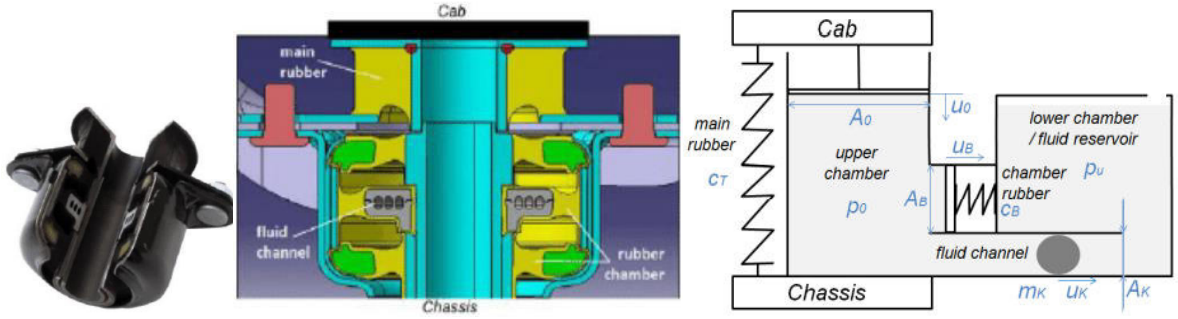

Fig. 6. Simple hydro mount model [7]

To characterize the mount's dynamic behaviour the force-displacement loops are measured at sinusoidal excitation with increasing frequency, for different amplitudes. The resulting average dynamic stiffness k_{dyn} at sinusoidal excitation is much higher than the static stiffness and depends on the frequency and amplitude (dynamic stiffness range: 2500-4500 N/mm; frequency range: 10-25 Hz). Thus, the evaluation of this isolation model under transient excitations has covered a large amplitude range and simulation put into evidence very good response to measured loads, being recommended for use on a large scale on a varied range of heavy machines [7].

4. Modelling of the hydro pneumatic mounts for cab isolation

The research results show that the cab shaking and the vertical vibration of the operator's seat were improved compared to the constructive solution of the cab's hydraulic mount without control [8] and we remark the various solution for the semi-active hydraulic mounts seat suspension and cab's horizontal damper [8, 9] illustrated in the Figure 7.

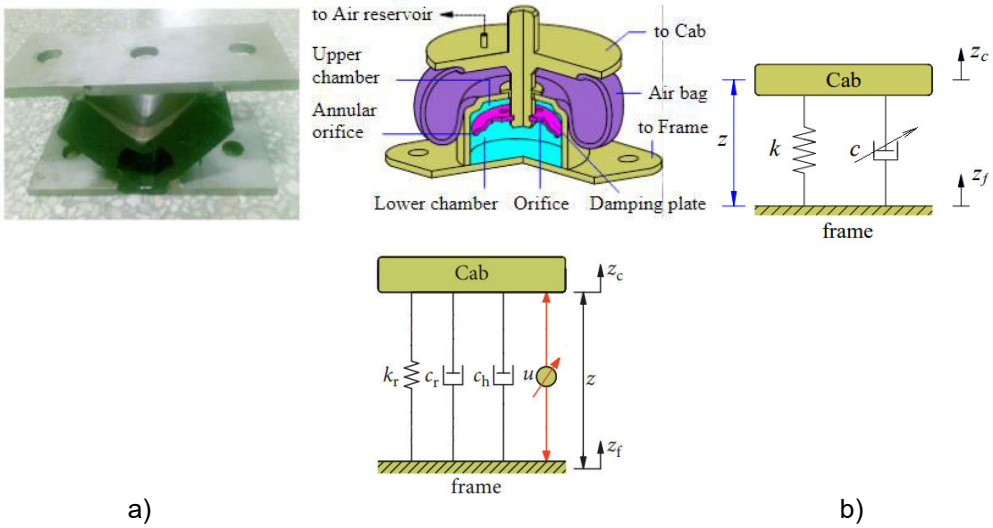

a) b)

Fig. 7. Modelling of vibratory roller for ride comfort simulation with hydro-pneumatic mounts:
a) Hydro pneumatic mount; b) Semi-active lumped models of cab - frame isolation [12]

The force output of the PID control is governed by the next law:

$$u(t) = K_p e(t) + K_i \int_0^t e(t)dt + K_d \dot{e(t)}, \quad (1)$$

where *e(t)* represents the displacement error the cab frame. The adequate values for K_p, K_i, and K_d, are chosen from a variable range as [K_{pmin}, K_{pmax}], [K_{imin}, K_{imax}], and [K_{dmin}, K_{dmax}], respectively, in function by the performance evaluation indexes regarding the ride comfort that we supposed to be achieved, for individual constructive and functional characteristics of each vibratory compactor type (with single or two vibratory rollers).

5. Methods for ride comfort simulation

To further improve the ride performance of the vibratory compactors, the cab insulation systems were controlled by multiple type of control: Fuzzy and PID-Fuzzy control applied in the frequency domain, in the time domain or in both [8-11]. The need for vibration control is based on the requirements of the Occupational Safety Standards that imposes maximum levels for the whole-body vibration (WBV) felts by the operator, to limited value 0.5 m/s^2. Therefore, it was suggested that a low-frequency range of 4–10 Hz for the vertical and of 0.5–2 Hz for the rotational vibrations seriously affected the driver's health and safety.
On the other hand, the root-mean-square (RMS) and power spectral density (PSD) acceleration responses on the vertical motion of the driver's seat and pitching cab angle were chosen as the objective functions (for performance evaluation indexes) under the working condition of the vibratory roller during the compaction process [12-15]. Thus, based on the international standard ISO 2631, the RMS of acceleration responses is determined by the formula:

$$a_{RMS} = \sqrt{\frac{1}{T}\int_0^T a^2(t)dt}, \quad (2)$$

where *a(t)* is the weighted acceleration (translational and rotational) as a function of time, in m/s^2; *T* is the duration of the measurements, in s.
Mostly, the numerical simulation of the vibratory behaviour of the cab in Matlab environment were performing with best accuracy results using dedicate modules for processing data measured or simulated. The processing algorithm on which the simulation is based derives from solving the differential equations of motion of the rheological model associated with the physical one, having multiple degrees of freedom. In some cases, only the damping element and the compactor cabin are considered, and in other cases, the heavy machine is approached as a whole system, subject to excitations given by the dynamic working regime or by the unevenness encountered on the terrain (as can be seen in the Fig. 8).

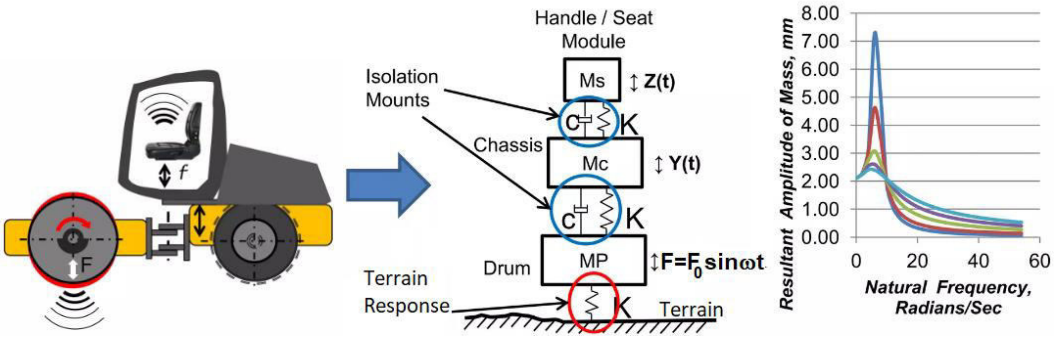

Fig. 8. Vibration mitigation at cab/operator's seat [16]

Generally, the motion equations of the vibratory compactor can be represented as matrix form thus:

$$[M]\{\ddot{Z}\} + [C]\{\dot{Z}\} + [K]\{Z\} = \{F(t)\}, \quad (3)$$

where: [M], [C], and [K] represent mass, damping, and stiffness matrices; {Z} is the displacement

vector; {F(t)} is the dynamic force vector. We have the number of lines and columns of the matrices equal to the number of degrees of freedom of the studied model.
Thus, taking into account by the Eq. (3), the dynamics of frame-cab systems and properties of the isolation system interpose between them can be surveyed and evaluated, from ride comfort of point of view, using the half-machine dynamic model or the complex 3-D nonlinear dynamic models. In this way, by detailing the component elements of the model with a significant influence on the comfort of the operator, results will be obtained with high accuracy and the model can be more easily verified and validated.

6. Conclusions

The isolation solution chosen to ensure ride comfort of operator in the case of vibratory compactors (when the frequencies and amplitudes are varied in different ranges of interest in function by the working conditions of the machine) are based on the next aspects:

- the establishment of technical solutions with the increased efficiency of reducing the harmful effects generated by the cumulative action of vibrations (generated by the working condition and/or the motion on uneven terrain);
- using of the modular anti-vibration devices, which offer to possibility of adjusting the isolation parameters in accordance with the effective values of the vibration parameters for each cabin type of the compactor equipment (using various method for vibration control, as Fuzzy or PID-Fuzzy control);
- system analysis (as lumped mass-stiffness model) and mathematical modelling of the motion equations (in function by the number of degrees of freedom of the proposed model);
- data processing for highlighting of the performances obtained compared to other systems used;
- the selection criteria of the isolation mounts: load capacity, stiffness, constructive type;
- the objective functions proposed to be achieved: RMS and PSD of the signal of the acceleration response on the vertical motion of the driver's seat and pitching cab angle;
- parameters adopted in the dynamic behaviour of the analysed model: mass, spring stiffness and damping coefficient;
- the parameter that requires to be controlled: natural frequency in order to avoid resonance vibration at roller's cab for low frequency (results obtained by the modal analysis of the system parameters);
- experimental verification and validation of the proposed isolation device.

All the aspects presented in this paper provide an overview of the design and work principle of the vibration isolation systems for vibratory compactors.

References

[1] International Organization for Standardization. "Mechanical Vibration and Shock-Evaluation of Human Exposure to Whole Body Vibration-Part 2: General Requirements." ISO 2631-1:1997, 1997.
[2] Jiao, R., V. Nguyen, and V. Le. "Ride comfort performance of hydro pneumatic isolation for soil compactors cab in low frequency region." *Journal of Vibroengineering* 22, no. 5 (2020): 1174-1186.
[3] Nguyen, V. and V. Le. "Development of cab isolation systems of off-road vibratory rollers: review research." *Mathematical Models in Engineering* 6, no. 2 (2020): 93–102.
[4] Scheiblegger, C., N. Roy, P. Pfeffer, and A. Hillis. "Modeling hydro mounts in vehicles for durability load analyses, ride comfort and vehicle dynamics simulation." Paper presented at the International Symposium on Advanced Vehicle Control, September 13-16, 2016, Munich, Germany.
[5] Scheiblegger, C. *Modelling of bushes and hydro mounts in vehicles using a multi body simulation environment*. Doctoral Thesis. University of Bath, 2018.
[6] Sun, X., and J. Zhang. "Performance of earth-moving machinery cab with hydraulic mounts in low frequency." *Journal of Vibration and Control* 20, no. 5 (2012): 724-735.
[7] Higuchi, T., and K. Miyaki. *Work machine with operator's cabin*. US Patent No. 5984036, 1999.
[8] Zhang, B., V. Nguyen, and Y. Wang. "Control the ride comfort of soil compactor with semi-active seat suspension and cab's horizontal damper." *Vibroengineering Procedia* 30 (2020): 91-96.

[9] Nguyen, V., R. Jiao, V. Le, and A. Hoang. "Performance of PID-Fuzzy control for cab isolation mounts of soil compactors." *Journal of Mathematical Models in Engineering* 5, no. 4 (2019): 137-145.
[10] Nastac, S. "On Fuzzy Logic Techniques for Vibration Isolation Active Systems." *Romanian Journal of Acoustics and Vibration* 4, no. 2 (2007): 97-102.
[11] Nguyen, V., R. Jiao, V. Le, and P. Wang. "Study to control the cab shaking of vibratory rollers using the horizontal auxiliary damping mount." *Mathematical Models in Engineering* 6, no. 1 (2020): 57-65.
[12] Nguyen, V., J. Zhang, V. Le, and R. Jiao. "Vibration analysis and modeling of an off-road vibratory roller equipped with three different cab's isolation mounts." *Shock and Vibration* (2018): ID 8527574.
[13] Jiao, R., and V. Nguyen. "Improving ride comfort for vibratory roller utilizing semi-active hydraulic cab mounts with control optimization." *Vibroengineering Procedia* 28 (2019): 75-80.
[14] Wang, Min, Guo-feng Yao, Jing-zhou Zhao, and Min Qin. "A novel design of semi-active hydraulic mount with wide-band tunable notch frequency." *Journal of Vibration and Control* 333 (2014): 2196-2211.
[15] Van Quynh, L., L.A. Vu, B. Van Cuong, H.A. Tan, and L.X. Long. "A Comparative Analysis of Ride Performance of Double-Drum Vibratory Roller with Two Cab Mount Systems." *Advances in Engineering Research and Application* 366 (2022):19-30.
[16] ***. "Design of vibration isolation for vibratory compactors." June 06, 2017. Accessed on October 24, 2022. https://www.slideshare.net/ManoharMHegde/design-of-vibration-isolation-for-vibratory-compactors.

ISSN 1454 - 8003
Proceedings of 2022 International Conference on Hydraulics and Pneumatics - HERVEX
November 9-10, Băile Govora, Romania

HIGH-PRESSURE POWER SOURCES – STATE OF THE ART, PERSPECTIVES

Cătălin FRÂNCU[1], Ion DAVID[1], Cristina SESCU-GAL[1]

[1] Technical University of Civil Engineering of Bucharest (UTCB), Faculty of Mechanical Engineering and Robotics in Construction, Bucharest, Romania

catalin.francu@utcb.ro; ion.david@utcb.ro; cristina.sescu-gal@utcb.ro

Abstract: *The paper presents the current status regarding the use of high pressures in the field of hydraulic drives as well as the possibility of adapting existing drive solutions in order to obtain these pressures at low costs. The trend of increasing the level of pressure used is complemented by the expansion of branches that use high operating pressures, which leads to beneficial results regarding the reduction of dimensions and weight of elements and systems, better manoeuvrability and reduction of manufacturing costs, a fact also complemented by the latest research in the field of materials and manufacturing technologies, it being known that some materials and technologies, currently used in the manufacture of medium pressure equipment, do not provide the desired performance, especially durability and reliability, in the field of high pressures. The technical solutions that can generate pressures of up to 1000 bar are identified, whose main advantages are satisfying the requirements of force, speed, manoeuvrability, precision, etc. as well as the automation of the work process: equipping the hydraulic systems with high-pressure radial pumps with all the related equipment and pipes, and the second solution is the creation of standard pumping units to which a pressure amplifier - miniBOOSTER - chosen according to the application is attached.*

Keywords: *High pressure, hydraulics, applications*

1. Introduction

In today's hydraulic systems, the term "high pressure" is increasingly used when referring to values greater than 450 bar. The use of these pressure values is required by mechanical applications that need to make precise and fast movements in tight spaces or generate high forces for handling/moving large and very heavy weights. The delimitation of values for medium pressures and high pressures is not clearly established globally, but it is accepted that operation at pressures above 315 and 350 bar respectively (depending on the established program) can be considered as operation at high pressures. If the lower limit of the high-pressure range is relatively established, the upper limit is more difficult to define; it starts at 500 bar and can go up to 1000...1200 bar. Beyond these values is considered the zone of ultra-high working pressures. Most companies producing hydraulic equipment produce both in the medium pressure range and in the high-pressure range; however, there are also companies specialized only in the production of high pressure equipment

2. Trends in the field of working pressures of hydraulic equipment

Currently, the development of hydraulic equipment is manifested in multiple directions, such as: increasing working pressures (concentration in time), ensuring multiple functions for a certain element-module construction (functional concentration), increasing energy indicators (power concentration), increasing reliability and durability. The use of equipment with high working pressures is found in various fields, exploiting their advantages and looking for solutions to minimize/reduce the disadvantages. Specialized companies focus their production on pressure levels in both the medium and high-pressure range. However, there are also companies specialized only in the production of high-pressure equipment. The most representative are:
- the HAWE company - produces hydraulic equipment with a maximum working pressure of 700 bar;

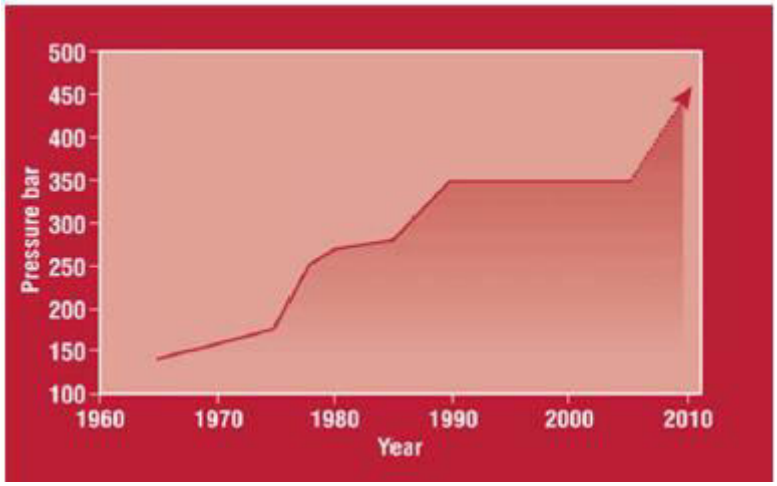

Fig. 1. Modern hydraulics working pressures evolution

- the company ATOS (Italy) - produces hydraulic equipment in the medium pressure range up to 350 bar and equipment with a maximum working pressure of 500 bar;
- the BIERI company (Switzerland) - belonging to HYDAC, specializes in high pressure hydraulic equipment (up to 700 – 1000 bar);
- the BOSCH – REXROTH company, one of the world leaders in the production of hydraulic equipment, produces in the medium pressure range (350 – 420 bar) or with a maximum pressure of 630 bar;
- the HYDAC company (Germany) produces medium pressure (320 bar) and high pressure (630 bar) equipment.

Limit values in the range of high pressure products 700-1000 bar and above this value are found at companies specialized in hydraulics for constructions, interventions in various situations, where the equipment works at pressures from 700 bar to 2500 bar and even more (LUKAS, ENERPAC, NIKE Hydraulics, etc.). In the current global context, regarding the protection of the environment by reducing emissions and optimizing energy consumption, the use of hydrostatic transmissions in the actuation of mobile machinery is of real benefit, as it is possible to conserve dynamic energy and reduce emissions, thanks to the possibilities of making the drives more efficient.

Ever since the widespread use of hydraulic drives, the values of working pressures have seen a continuous increase, the evolution shown in figure 1. The trend of increasing working pressures is also present in other fields, such as aviation, military and civil.

In the studies developed by various companies producing hydraulic equipment such as VICKERS, BOSCH - REXROTH, etc., working pressures of 500 and even 700 bar are indicated for the next years, and the current technical means allow pressure values of 1000...2000 bar to be achieved without difficulty; the problem that arises, however, is to ensure, simultaneously with the increase of the working pressure, the durability of the hydraulic equipment. Another consequence of increasing the working pressure in a system is the need to use working fluids with superior characteristics.

3. Equipment for generating high pressures

Obtaining high working pressures can be ensured by two types of pumping groups: a) pumping groups containing volumetric pumps and high-pressure hydraulic equipment; they directly feed linear or rotary volumetric hydraulic motors. These are used in dynamic applications, where the linear or rotary movement of large loads with uniform speeds is required. In static applications, they show reduced energy properties, and are not recommended.

b) pumping groups containing volumetric pumps and low-pressure hydraulic equipment; they feed the pressurized closed volumes or volumetric hydraulic motors by means of pressure amplifiers,

which are placed between the pumping group and the hydraulic consumers. This category is energy efficient in power-dissipating applications, but has disadvantages in high-load dynamic applications

3.1. High pressure hydraulic pumps

Hydraulic pumps do not generate pressure in a system, but have the role of supporting pressure requests through the assured flow. The main types of pumps used, are shown in figure 2.

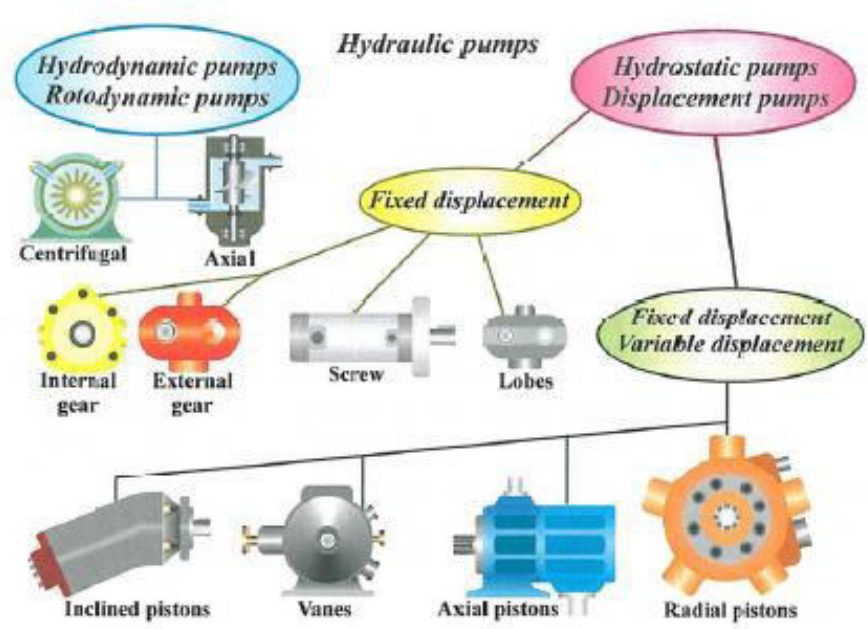

Fig. 2. Types of hydrodynamic and hydrostatic pumps

High-pressure pumps belong to the category of hydraulic generators, which, through a systematic dosing of the amount of fluid, achieve very high pressures. By the generated pressure level, from a constructive point of view the pumps can be (table 1):

Table 1: Pump types

No.	Constructive type of the pump	Working pressure
1.	Axial piston pumps	up to 350 bar
2.	In-line piston pumps	up to 1000 bar
3.	Radial piston pumps	up to 1500 bar
4.	Manual pumps	up to 2500 bar
5.	Piston pressure intensifiers	up to 5000 bar

3.2. Constructive examples of pumps

a) High-pressure radial piston pumps manufactured by Bosch – Rexroth, figure 3, ensure good sealing due to the spherical seating surface. They are pumps with a simple construction, they have a very good suction, but they ensure a lower volumetric efficiency when the working pressure is very high, a fact that determined the limitation of operation to a maximum pressure of 630 bar.

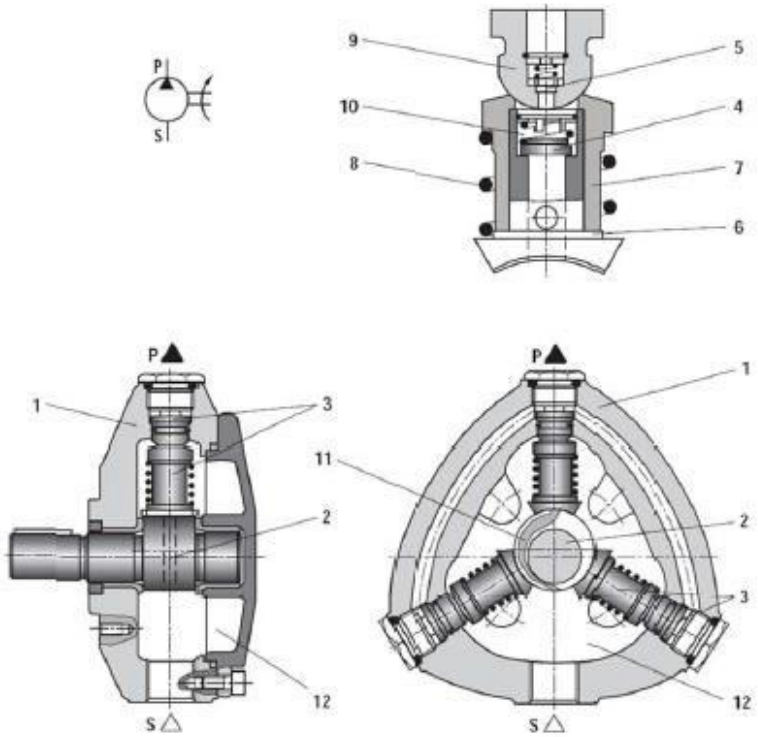

Fig. 3. Bosch – Rexroth radial piston pump [1]

b) Hydraulic pump controlled by air under pressure LP, figure 4.
This type of pump, not being powered by electricity, is recommended for working in environments with a risk of explosion, being able to be used up to pressures of 1500 bar. The operating principle is that of a pneumatic-hydraulic pressure booster.

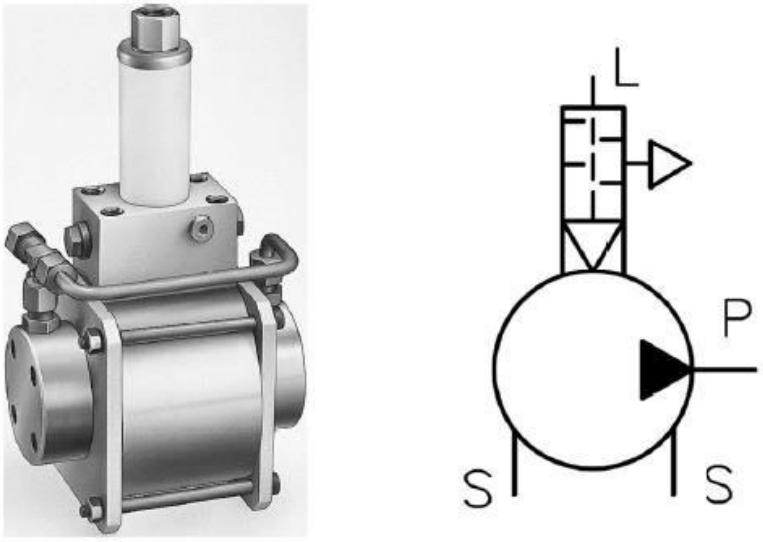

Fig. 4. Air driven pump under pressure, LP [2]

c) KKP combined pump
Combined pumps type KKP, figure 5, are radial pumps, with low weight and high compactness, with two stages (HP / LP) with tubular shaft, which allows obtaining a reduced dimension with the motor mounted directly on the pump.

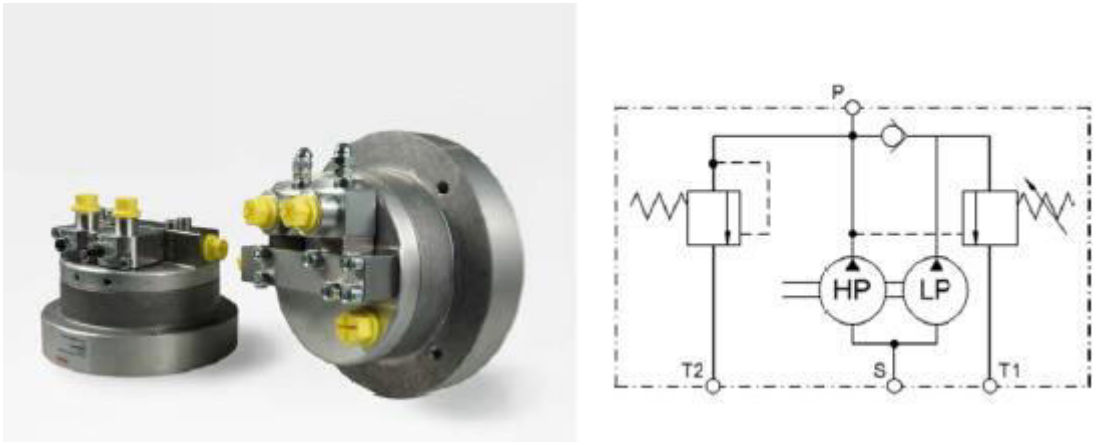

Fig. 5. KKP combined pump [3]

d) High pressure pump made by IHP Bucharest
It is a technical solution that brings together two pumps and contains the operating mode switching device attached to the outside of the pump, figure 6. It has six radial pistons, three large and three small, placed alternatively in the same plane, which realize the operation of both pumps.

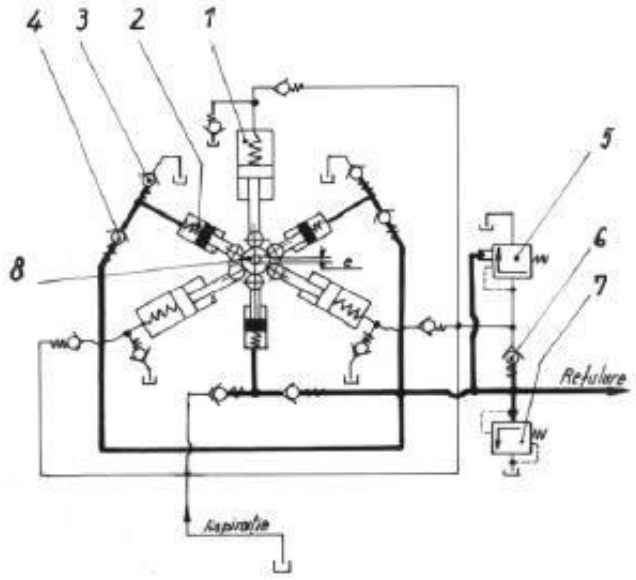

Fig. 6. High-pressure pump made by IHP Bucharest

e) LUKAS manual pumps
These are pumps that use muscle power as an energy source and have low flow rates, figure 7. These can be operated in two steps, including a valve that allows the automatic change of the working regime, from low pressure to high pressure. The HKP series pumps can reach a pressure of 2500 bar, have a single pressure stage, and are used for assembly/disassembly operations, test work, etc.

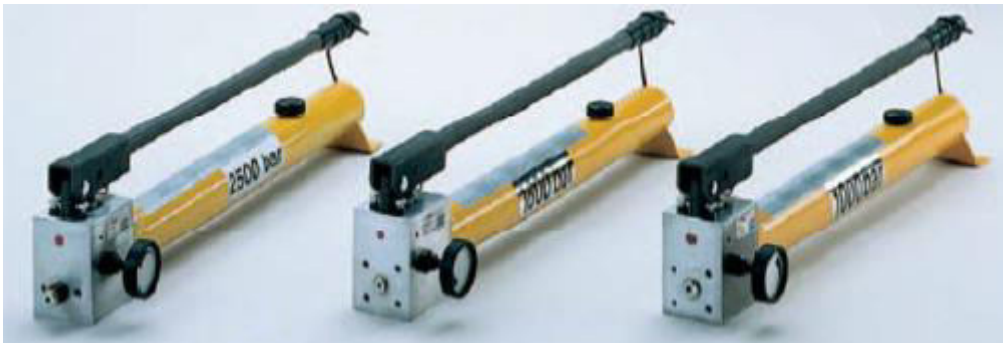

Fig. 7. LUKAS manual pumps for pressures up to 1000 ... 2500 bar [4]

4. Hydraulic pressure amplifiers

During the performance of a work cycle of a hydraulically operated installation or machine, there are certain work phases in which the powered volume motors, hydraulic cylinders or rotary hydraulic motors, are required to develop large, static or dynamic forces and moments, which requires their power supply at high pressures (over 450 bar). These pressures can be generated by two types of pumping groups:

a. pumping groups containing high-pressure (HP) volumetric pumps and high-pressure hydraulic equipment; they directly feed linear or rotary volumetric hydraulic motors. They are more expensive equipment due to the high price of pumps and command and control components. They are used in dynamic applications, where linear or rotary movement of large loads at uniform speeds is required.

b. pumping groups that contain volumetric pumps (LP) and low-pressure hydraulic equipment and feed the volumetric hydraulic motors by means of pressure amplifiers, which are placed between the pumping group and the hydraulic consumers with the role of raising the pressure to the value imposed by the demand at the level of the hydraulic motor. These pumping groups make energy-dissipating applications energy efficient, with the disadvantage of low and pulsating flows for dynamic applications.

The operation of fixed or mobile installations driven by hydraulic systems has phases of the work cycle which, in order to be achieved, require pressure increases of up to 1000 ... 2000 bar under low flow conditions. Classic solutions require the use of high-pressure radial pumps, which leads to high costs, so to avoid these costs, pressure amplifiers, also known as pressure intensifiers, boosters, miniboosters, were made.

The hydraulic pressure booster is a device used to increase the pressure intensity of any hydraulic fluid or water, with the help of the hydraulic energy available due to high values of the flow of water or hydraulic oil at low pressure. These devices are very important in the case of hydraulic machines, the best example being hydraulic presses, which require in their operation fluid at high pressure (HP) that the pumping group cannot provide directly; with their help, the existing pressure level is increased with minimal effort, resulting in minimal costs and maximum effect regarding the action of the hydraulic installation in achieving the work cycle. The basis of the operation of hydraulic pressure amplifiers is the simple principle of Pascal's law and the difference in area between the two pistons; even though the oil only acts at 15,000 psi, the area it presses on is huge compared to the small piston, and so a pressure of 150,000 psi appears. This increase is achieved with a ratio of the areas of the two pistons of 10:1. The material from which they are made is an alloy steel, heat treated to withstand high pressures and to preserve the surface quality and technological tolerances for as long as possible.

4.1. Pressure intensifier circuits – constructive types

Pressure intensifiers are circuits that generate high pressure from a low-pressure source. Pressure boosters can work with any type of fluid used in standard hydraulic installations. Among the most important benefits can be mentioned the low cost price, reduced space required for installation and

last but not least the energy saving of the system.
In figure 8, the schematics of some hydraulic air-oil pressure intensifiers are presented, which work on the principle of hydraulic cylinders, in which the cylinder operated by air has a larger diameter compared to the cylinder operating with hydraulic oil. The ratio between the two areas represents the pressure multiplication ratio, the volume of liquid expelled depending on the length of the cylinder stroke.

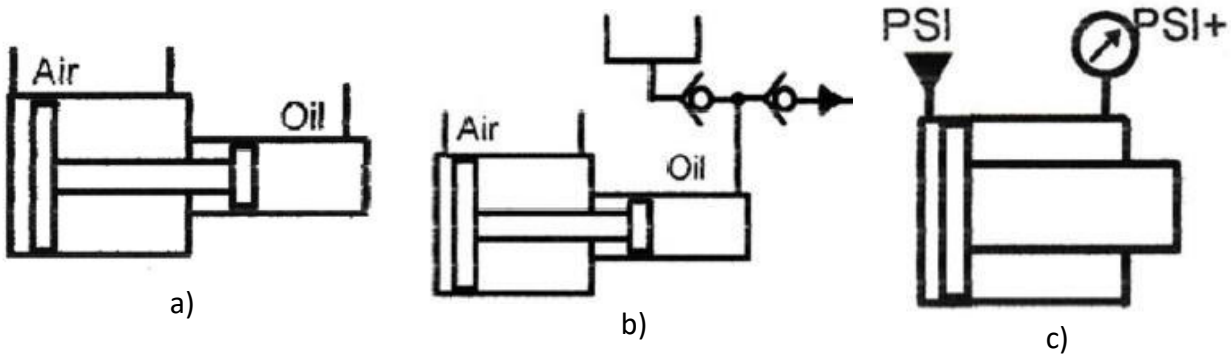

Fig. 8. Hydraulic air-oil pressure intensifiers - constructive types [5]

Pressure booster circuits, can also be made from cylinders of standard construction, being a way of obtaining the high pressure required for a defined action that requires a large force to be performed. The assembly of the circuit is done directly on the structure of the machine, hydraulic cylinders being able to perform the advance stroke both at high pressure, figure 9, and at low pressure.

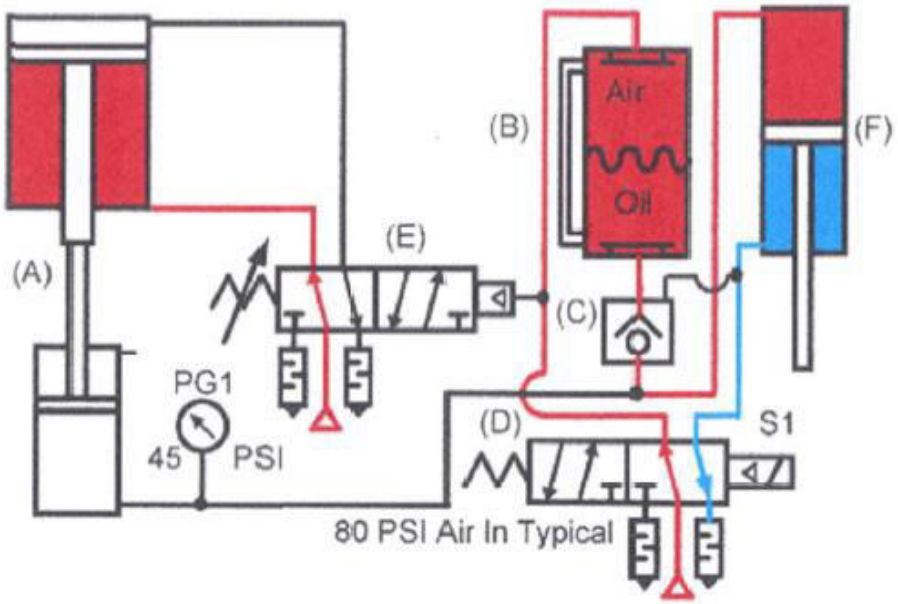

Fig. 9. Pressure amplifier circuit with standard cylinders: A – amplifier assembly; B – hydraulic air-oil reservoir; C – pilot valve; D- pneumatic distributor; E – electric distributor; F – working cylinder [5]

4.2. Oscillating hydraulic pressure intensifier - miniBOOSTER

In general, hydraulic pressure boosters are used to provide high pressure in applications where hydraulic cylinders must develop high-imposed forces. These types of amplifiers have optimal applicability in machinery and equipment used in construction, etc.

OHPI – oscillating hydraulic pressure intensifier mounted on a mobile crusher – ensures a high force with a small cylinder on the mobile wall of the crusher, figure 10.a. In figure 10.b., the pressure amplifier set used to increase the performance of the trailer pick-up system. The solution can be used for loading system with a capacity between 15 and 30 tons.

a) b)

Fig. 10. Examples of the use of pressure amplifiers [6]

For demolition machines with cutting and/or crushing materials equipment, during work due to the random variation of the resistance of the demolished elements, a high-pressure demand may occur at the engine level. The requirement is ensured by mounting a miniBOOSTER, figure 11.a, which ensures high speed and force, so minimum power consumption can be maintained. In figure 11.b, the pressure amplifier is mounted on an excavator, the aim being to optimize the drive systems to reach characteristics close to the maximum limit.

a) b)

Fig. 11. Pressure intensifiers mounted on construction machinery [6]

The miniBOOSTER pressure boosters also called HC, increase the low inlet pressure (ranging from 20 bar to 200 bar) to a high outlet pressure value (up to 800 bar / 2,000 bar). Adjusting the outlet pressure is done by adjusting the inlet pressure, being directly proportional. These boosters initially provide the consumer with low pressure at a high flow rate (for example, to quickly move a cylinder), then there is an automatic switching of operation in high-pressure pulses. Therefore, they allow both high flow rates at low pressures and low flow rates at high pressures, in figure 12 the hydraulic diagram of such a miniBOOSTER is being presented.

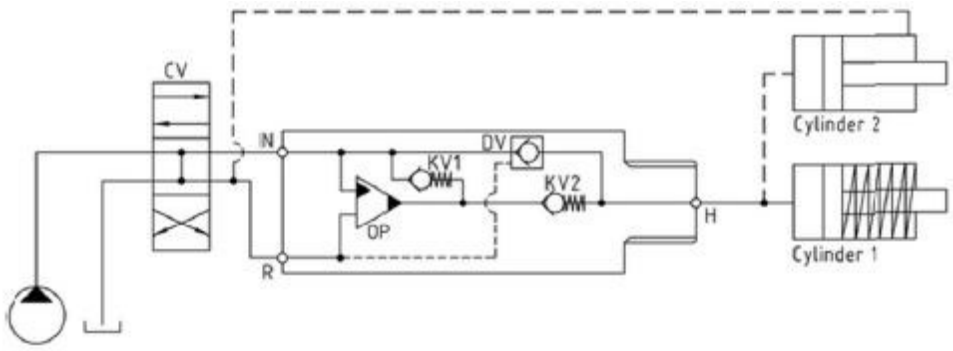

Fig. 12. Hydraulic diagram of a miniBOOSTER type HC1 [7]

This type of construction is used to amplify the pressure of low-pressure pumping groups that supply hydraulic cylinders with single or double action that move heavy loads linearly at the end of the advance stroke or achieve and maintain high pressure in a closed enclosure.

5. Conclusions

The general trend is to increase the level of pressure used and to expand the branches that use high operating pressures, with beneficial consequences in terms of reducing the size and weight of elements and systems, better manoeuvrability and reducing manufacturing prices. The latest research in the field of manufacturing materials and technologies contributes to this, as it is known that some materials and technologies, currently used in the manufacture of medium pressure equipment, do not provide the desired performance, especially durability and reliability, in the field of high pressures. The field of high pressures is increasingly attractive for various applications of mobile or fixed hydraulic drive systems.
The requirements of the internal market, but especially external, for equipment and systems to generate high pressures in hydraulic circuits (1000 bar) are still at a high level, because the production of fixed or mobile hydraulic installations that satisfy the conditions of force, speed, manoeuvrability, precision in movements, high reliability, automation of the work process, impose from the start of their design, the condition of their operation at high pressure, this being the main technical parameter that would lead to the realization of the parameters imposed by the beneficiary. The use of high-pressure generation systems with a low-pressure pump associated with a pressure amplifier as the power source ensures a low cost of the installation, its safety conditions and high reliability.

References

[1] Bosch Rexroth AG. “Radial piston pumps, fixed displacement. PR4-3X.” Accessed October 10, 2022. https://www.boschrexroth.com/en/xc/products/product-groups/industrial-hydraulics/pumps/radial-piston-pumps/pr4-3x.
[2] HAWE Hydraulik. “Hydraulic power pack type LP.” Accessed October 10, 2022. https://www.hawe.com/products/product-search-by-category/hydraulic-power-pack/standard-hydraulic-power-pack/lp/.
[3] Bieri Hydac International. “Combination pumps KKP.” Accessed October 10, 2022. https://www.bierihydraulics.com/en/pumps/radial-piston-pumps-hollow-shaft/combination-pumps-kkp/.

[4] Lukas Hydraulik GmbH. Accessed October 10, 2022. https://lukas.com/industrial/en/products/high-pressure-programme/244/ high-pressure-hand-pumps.
[5] ***. “Book 2, Chapter 13: Pressure intensifier circuit.” *Power & Motion*. April 13, 2009. Accessed October 10, 2022. https:/www.hydraulicspneumatics.com/technologies/other-techonogies/article/21884328/book-2-chapter-13-pressure-intensifiers-circuits.
[6] ***. “Mobile from miniBOOSTER Hydraulics A/S.” Accessed October 10, 2022. https://www.minibooster.com/mobile/.
[7] ***. “HC1.” Accessed October 10, 2022. https://www.minibooster.com/hc1/.
[8] Popescu, T.C., P.A. Chirita, and A.I. Popescu. “Increasing energy efficiency and flow rate regularity in facilities, machinery and equipment provided with high operating pressure and low flow rate hydraulic systems.” Paper presented at the 18th International Multidisciplinary Scientific GeoConference SGEM 2018, Albena, Bulgaria, June 30 – July 9, 2018.

ISSN 1454 - 8003
Proceedings of 2022 International Conference on Hydraulics and Pneumatics - HERVEX
November 9-10, Băile Govora, Romania

WORLD, EUROPEAN AND POLISH MACHINERY AND EQUIPMENT MARKET DURING THE ENERGY CRISIS

PhD. Eng. **Krzysztof KĘDZIA[1*],** MSc. Eng. **Jarosław PROKOPOWICZ[1]**

[1] Department of Technical Systems Operation and Maintenance, Faculty of Mechanical Engineering

Wrocław University of Science and Technology, 7/9 Łukasiewicza St., 50-371 Wrocław, Poland

* Corresponding author's e-mail address: krzysztof.kedzia@pwr.edu.pl

Abstract: *The global energy crisis initiated significant changes on the market of capital goods, in particular on the market of machinery and equipment. The article presents the machine industry and fluid power market and its main shareholders. Increases (decreases) in the production and sales of machinery and equipment were analysed in relation to important macroeconomic indicators such as: GDP (GNP), industrial production and unemployment. Based on the latest data obtained on the basis of CETOP, VDMA, OECD publications and data from selected countries, the situation in various branches of the machine industry in the World, Europe and Poland, in particular in the area of fluid power, was presented.*

Keywords: *Fluid power market, energetic crisis, conditions of fluid power companies, forecast of the future.*

1. The global engineering industry in times of the energy crisis

The COVID-19 pandemic and the ongoing war in Ukraine have caused a global energy, financial and related economic crisis. This situation affects the markets for industrial (investment) goods and services, and in particular the markets for machinery and equipment (Fig. 1 and 2).

Fig. 1. World: industrial production and Purchasing Managers' Index manufacturing (PMI) [1]

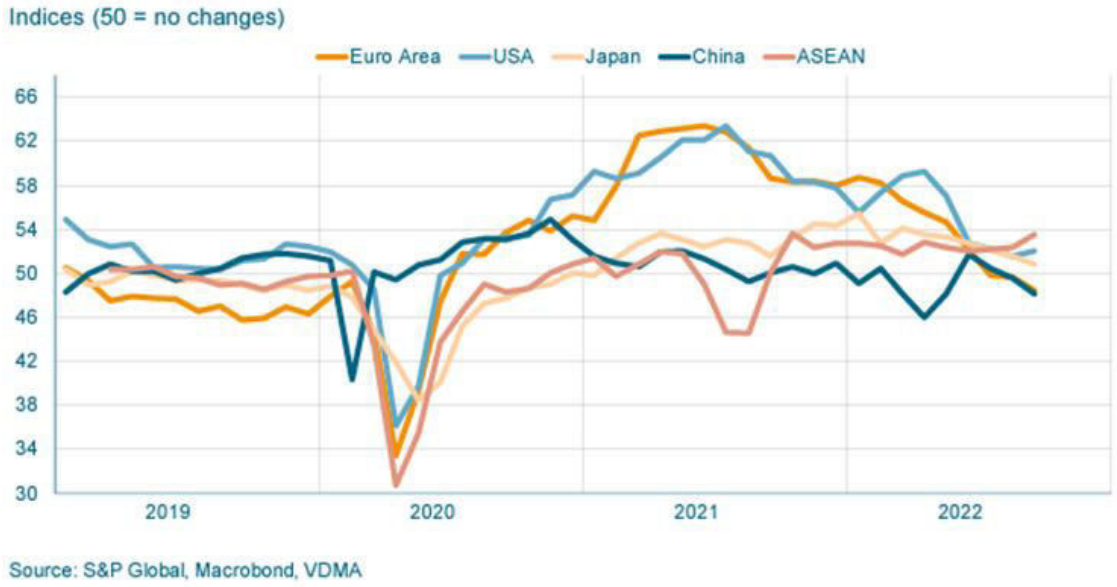

Fig. 2. Purchasing Managers' Index in manufacturing [1]

The situation faced by European countries during the COVID-19 pandemic, in particular the inability to manufacture the simplest products such as masks, significant increases of labour costs (in particular in China and other Asian countries) and political conditions - resulted in decisions of entrepreneurs to move production back to Europe. These decisions are in most cases supported by the governments of individual European countries, e.g. for strategic reasons - especially after the negative experiences related to the war in Ukraine and the related perturbations on the energy and food markets.

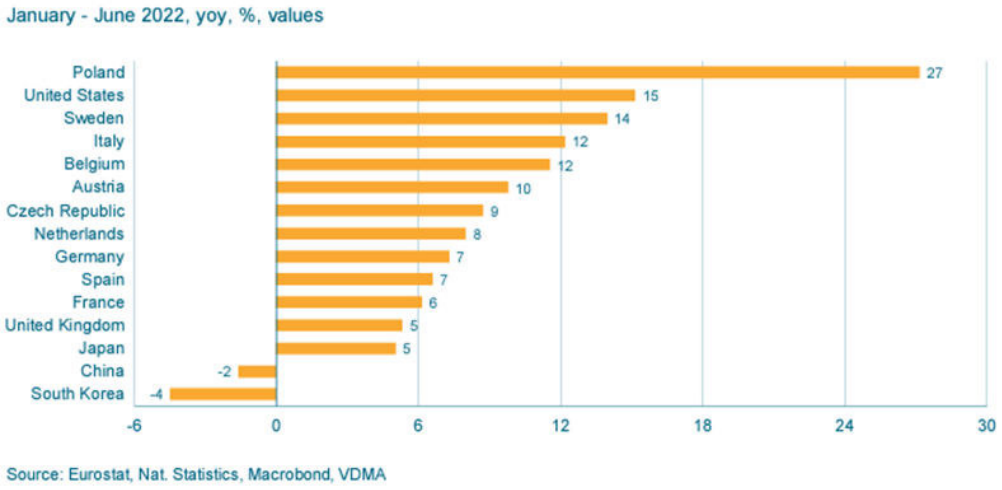

Fig. 3. Top machinery locations: current turnover development [1]

The above graphic shows the economic position of Poland at the moment. The largest increases in locating the transferred production are recorded in Poland (increase by 27%). This is undoubtedly influenced by: the competitiveness of the economy (low taxes), well-qualified staff at all levels and the growing geopolitical position in Europe (the Three Seas Initiative) and the world (an increasingly larger and more important US ally in Europe).
One of the factors having the greatest impact on the situation on the machinery and equipment market is the energy crisis - gradually intensified by Russia for over a year. As can be seen from

the graphs in Fig. 4, as many as 70% of respondents have problems related to increases in energy prices.

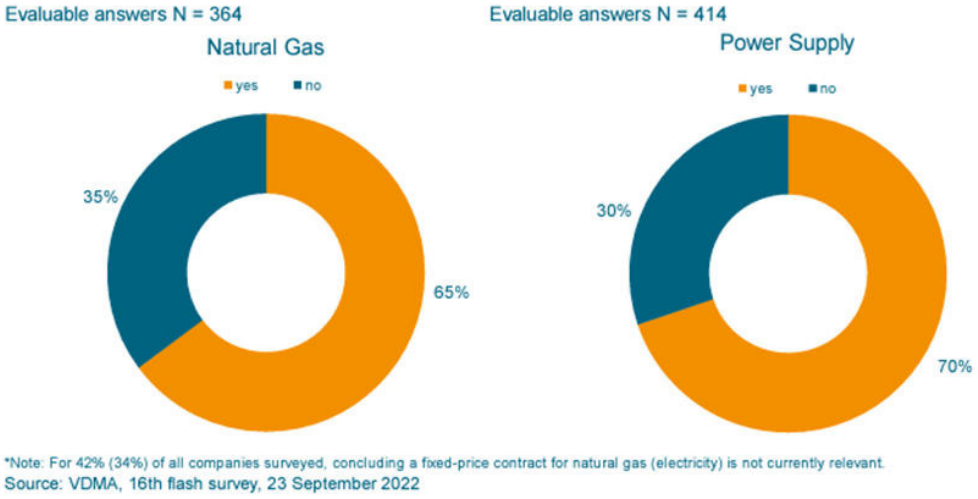

Fig. 4. Problems in obtaining fixed- price contracts for own company's energy supply [1]

The effect of the increase in energy and raw material prices is shown in Fig. 5. It shows that as many as 82% of respondents see the related problems as critical.

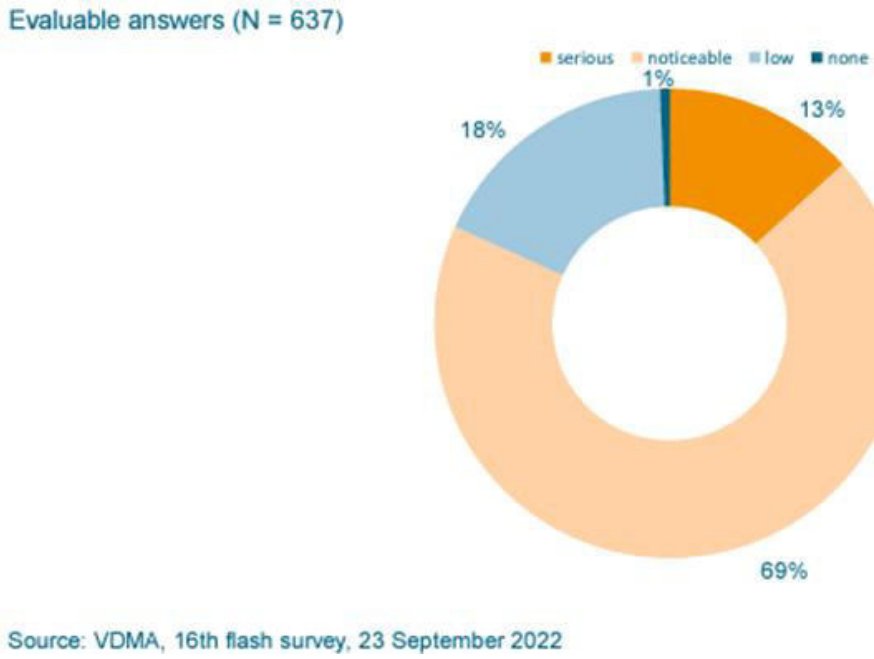

Fig. 5. Effects of rising prices for Energy and row materials on companies [1]

Some companies are trying to reduce their energy bills. Even 85% of respondents from enterprises implement energy saving, 35% intend to use other sources than those used so far, 32% change the way energy is ordered and 16% ban very energy-intensive production (e.g. artificial fertilisers).

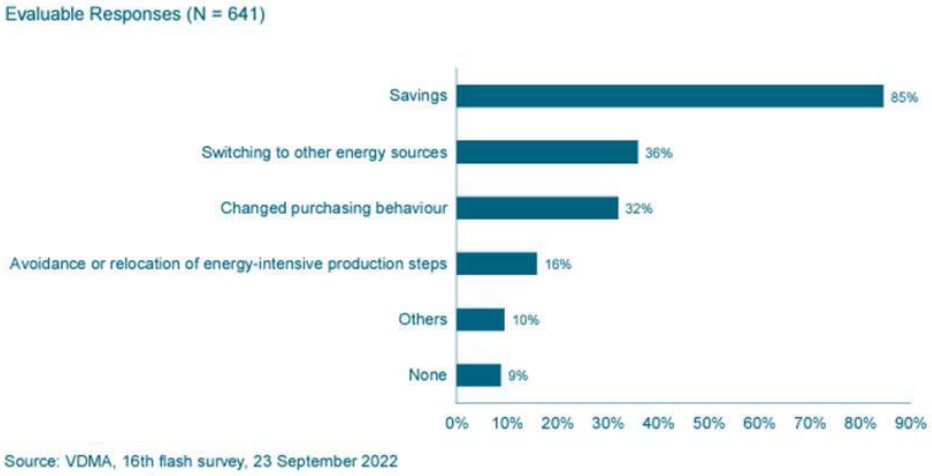

Fig. 6. Evasive actions regarding energy supply [1]

The survey on Expected nominal turnover development 2022 and 2023 (prior-year comparison) is presented in Fig. 7. As you can see, most of the respondents assume an increase in production orders.

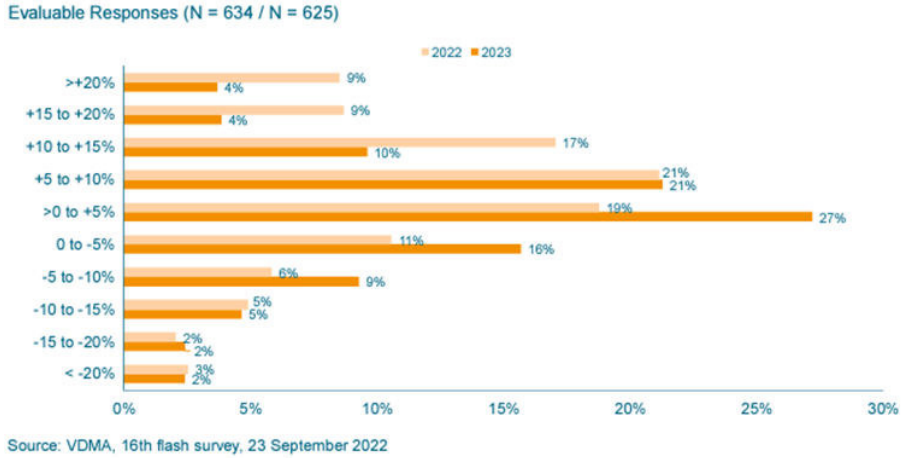

Fig. 7. Expected nominal turnover development 2022 and 2023 (prior-year comparison) [1]

Similarly happens, in the area of investment plans, Fig. 8.

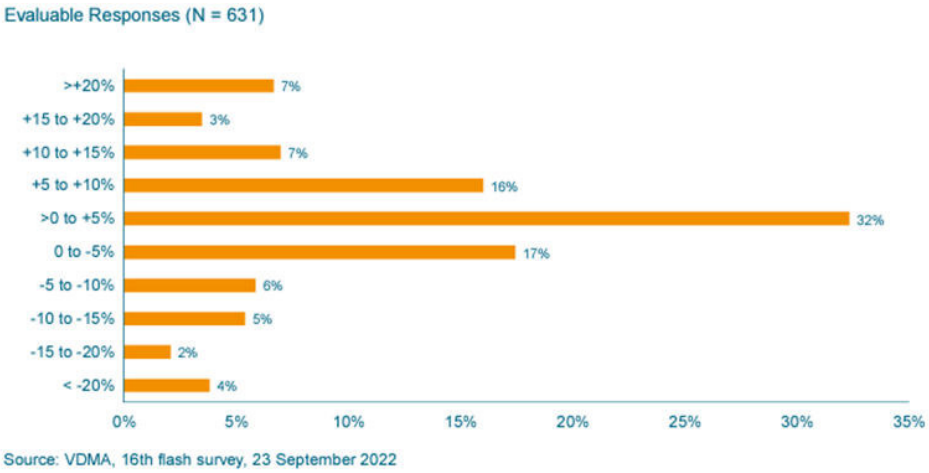

Fig. 8. Investment plans in 2023 (prior-year comparison) [1]

However, the situation on the global market next year is not so optimistic. Outside of China, the outlook for next year is worrying (Figure 9). Recession is forecast in the USA, Japan, the EU zone, Germany and Italy.

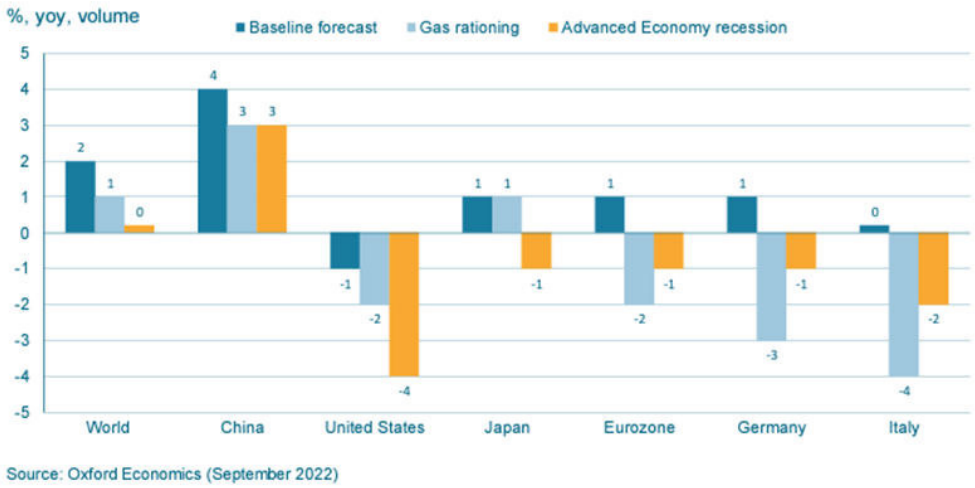

Fig. 9. Machinery turnover forecast for 2023 (selected countries by scenarios) [1]

Inflation is another factor that has a very large impact on the situation on the machinery and equipment market. In the countries of the European Union, the average inflation is currently at the level of 10.7% (Fig. 10).

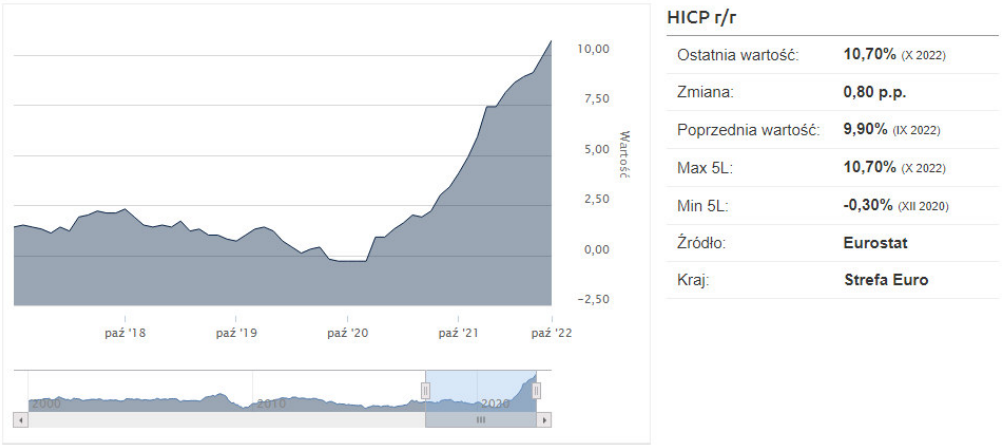

Fig. 10. Inflation in European zone [3]

2. Situation in the area of fluid power in selected European countries.

The situation in the broadly understood area of fluid power in selected countries associated in CETOP is extremely interesting.
In Belgium, sales growth in the hydraulics area was 13.51% through August. In September, -6% was recorded, the forecast for next year is -5%. In pneumatics, 1.38%, -0.8%, 0.5% and -5%, respectively (Tab. 1).

Table 1: Situation in fluid power in Belgium [1]

Hydraulics national home sales

• January to August 2022/2021	+ 13.51 %
• Trend for September	– 6 %

- Forecast for the year 2022 + 3.5 %
- Outlook for the year 2023 – 5 %

Pneumatics national home sales

- January to August 2022/2021 + 1.38 %
- Trend for September – 0.8 %
- Forecast for the year 2022 + 0.5 %
- Outlook for the year 2023 – 5 %

In the Czech Republic, the current situation as well as predictions for the next year in hydraulics and pneumatics are more promising. The good condition of industry in the Czech Republic is related to the unemployment rate. Currently, it is the lowest among the countries associated in the EU (Poland is ranked second in this ranking).

Table 2: Situation in fluid power in the Czech Republic [1]

Hydraulic Industry

- National Home sales 152.500 T EUR
- Recorder trend Jan/Aug. 2022 + 13%
- Trend for September 2022 + 9% (Mobile +10%, Industrial +8%)
- Forecast 2022 + 6%
- Outlook 2023 + 4%

Pneumatic Industry

- National Home sales 66.500 T EUR
- Recorder trend Jan/Aug.2022 + 9%
- Trend for September 2022 + 7%
- Forecast 2022 + 5%
- Outlook 2023 + 3%

In France, the situation in fluid power is also positive (fig. 11, fig. 12) - however, the Czech and French markets are significantly different in terms of market size. Last year, the French market rebuilt to the value of production revenues from 2017.

Hydraulics

2021/2020:	+ 17%
January-August 2022:	+9%
September Trend:	Good
2022:	+9%
2023:	+5% (Mobile + 6%, Industrial + 3%)

Fig. 11. French market in hydraulics from 2013 to 2021 [1]

Pneumatics

National Home Sales:	312 560 K€
2021/2020:	+14%
January-August 22/21:	+7%
September Trend:	Good
2022:	+ 8%
2023:	+4%

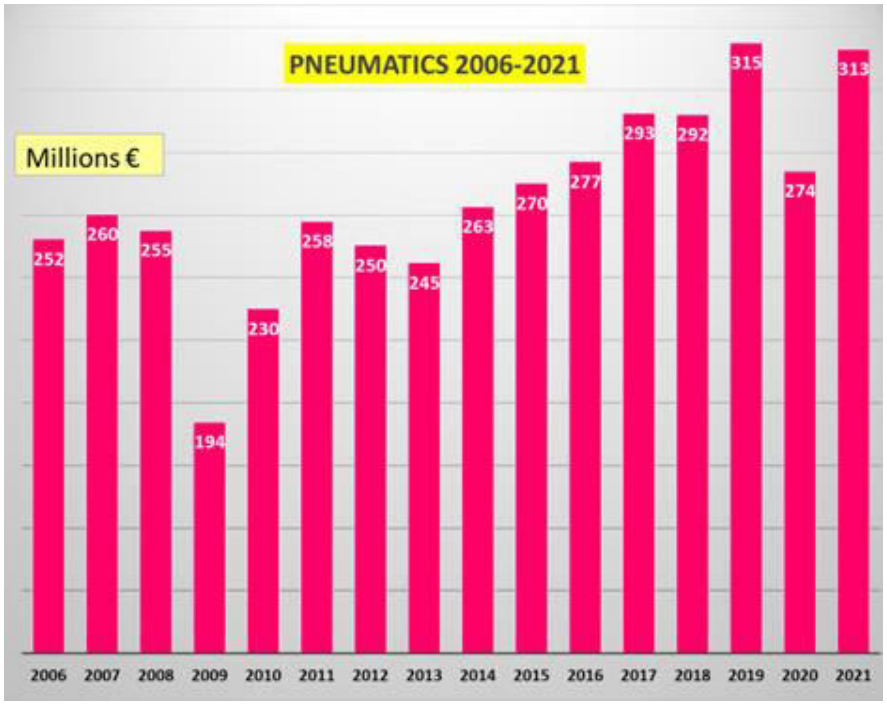

Fig. 11. French market in pneumatics from 2006 to 2021 [1]

Germany is the largest European producer in the field of hydraulics and pneumatics.
The CETOP Association in Germany - brings together 232 member companies. The history of sales and orders in the fluid power industry in Germany is shown in Figures 13, 14.

General data about fluid power in Germany:

– Turnover:	8.5 Billion Euro
» Hydraulics:	5.6 Billion Euro
» Pneumatics:	2.9 Billion Euro
– Export ratio:	61%
– Sealings–Turnover:	1.3 Billion Euro

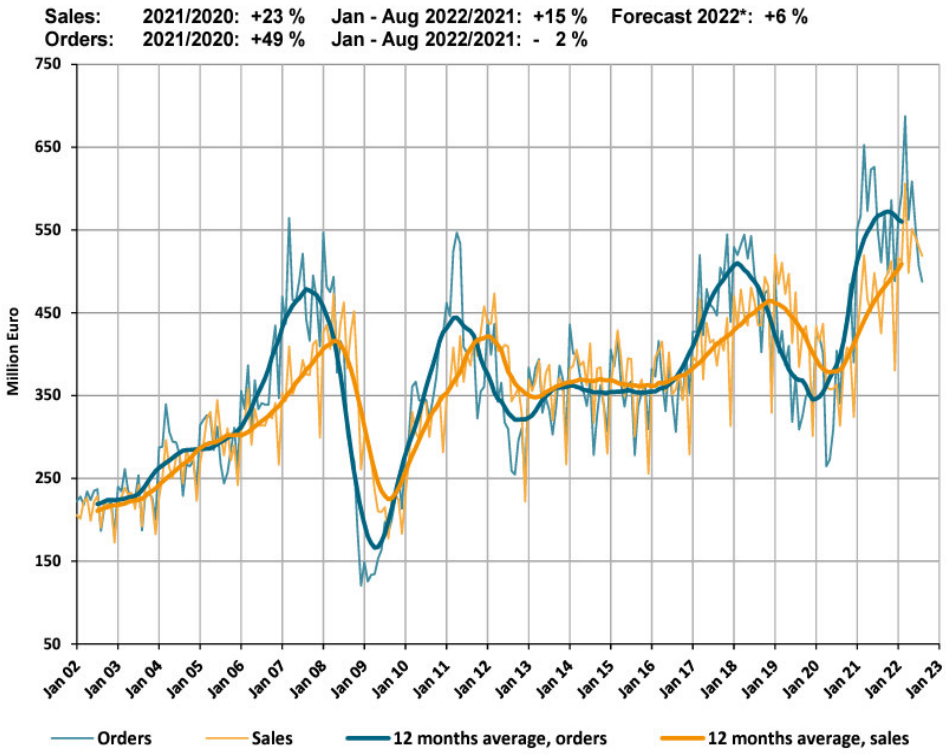

Fig. 12. German sales and orders in hydraulics from 2002 to 2022 [1]

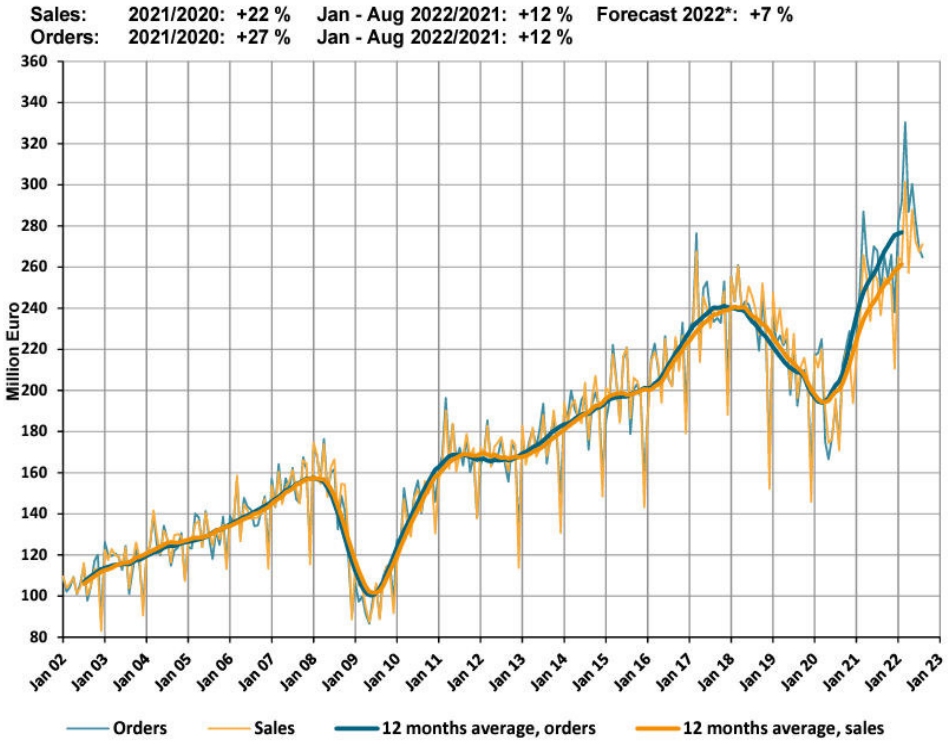

Fig. 13. German sales and orders in pneumatics from 2002 to 2022 [1]

The situation in fluid power in Italy is as follows (table 3, fig. 15).

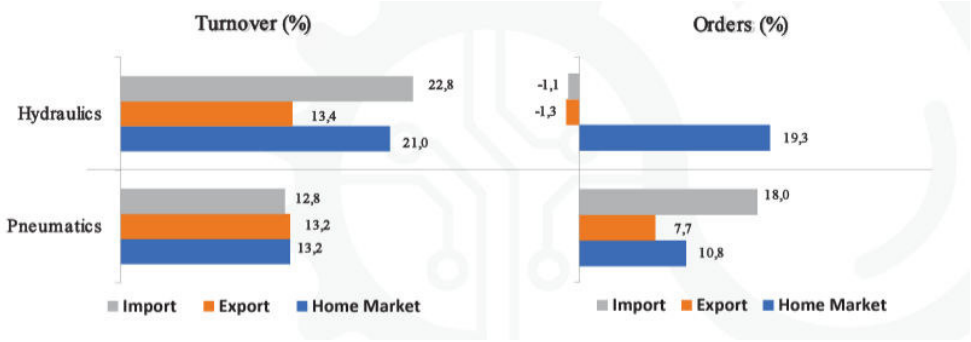

Fig. 14. Italian turnover and orders in fluid power (January –June 2022/ January –June 2021) [1]

Table 3: Italian fluid power market

	Hydraulic	Pneumatic
Total Home Market Sales 2021 (Million of euro)	1.851.000	982.000
Home Market Sales January to August 2021/2022	+17,4%	+12,4%
Trend for August	Sales - down Orders - down	Sales - down Orders – down

3. Polish machinery industry

The Polish machinery industry - less than other industries in Poland (e.g. construction) - felt the energy crisis, very high inflation (17.8%) and the effects of restrictions caused by the COVID-19 pandemic. This applies in particular to products constituting investment (industrial) goods. Figure 16 shows Poland's gross domestic product (GDP). Figure 17 shows the rate of inflation.

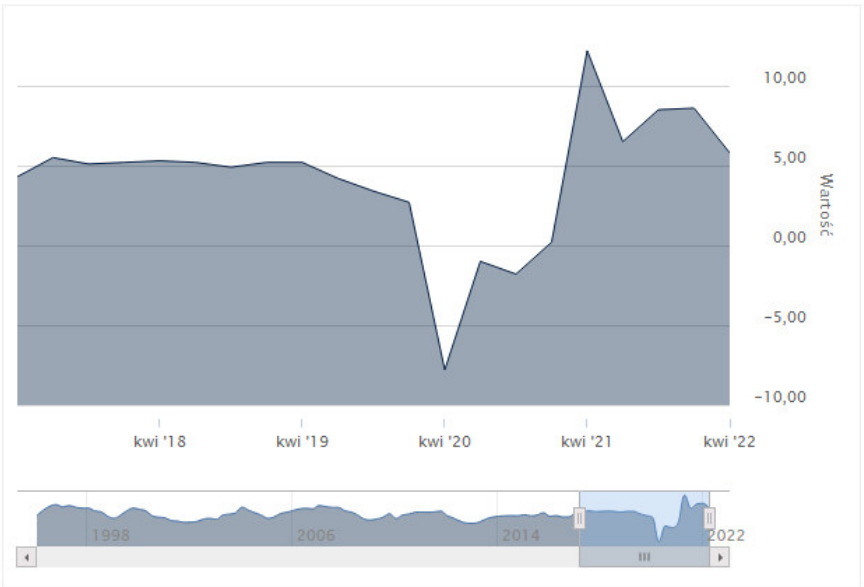

Fig. 16. Indices of gross domestic product (GDP) in current prices (5.8%) [2]

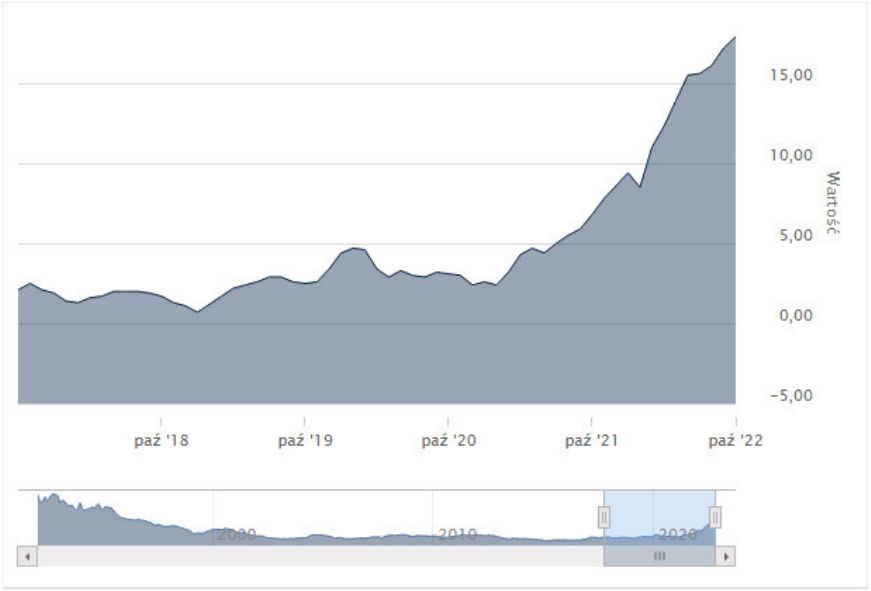

Fig. 15. Inflation in Poland (17.8%) y/y [2]

The domestic machinery industry consists of 50-60 large companies producing a wide range of machinery and equipment, ranging from engines of various power, including marine, cranes, agricultural machinery (tractors, combine harvesters and others) to many types of machine tools (including CNC) and machines and equipment for the mining, chemical, food, textile, paper, etc. industries. The PMI for Poland is shown in Fig. 18.

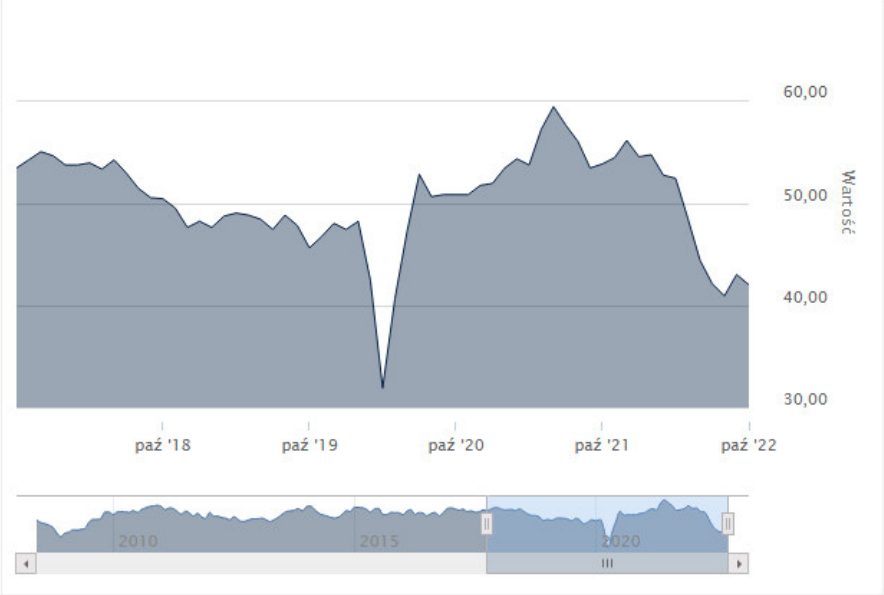

Fig. 16. Purchasing Managers' Index for Poland (42) [2]

Analyzing the unemployment rate (Fig. 19), it can be said that despite the very high inflation and the turmoil caused by the pandemic and the war in Ukraine, the labor market in Poland is still looking for employees.

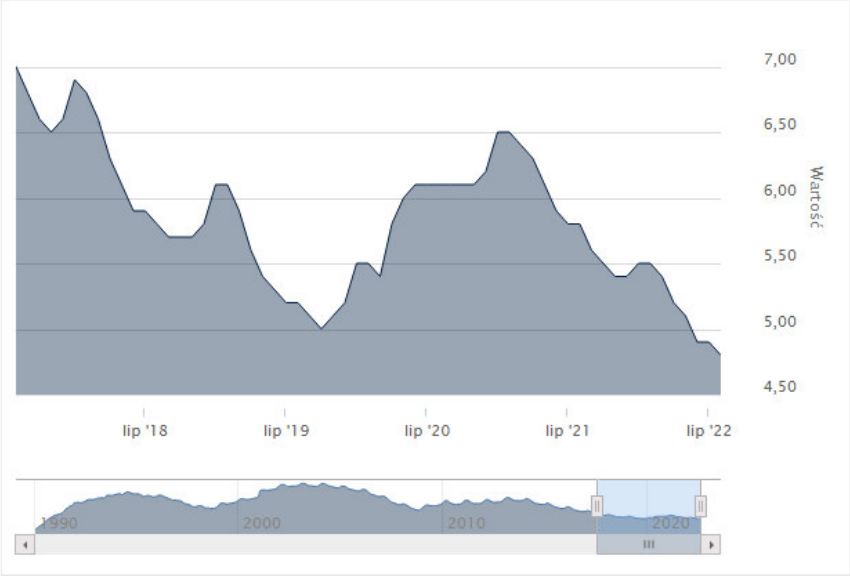

Fig. 17. Unemployment rate for Poland (4.8%) [2]

Industrial production, despite of many turbulences and macro and microeconomic problems, as well as preparations of European countries "for worse times", still fluctuates around 10%, which is a very good result (Fig. 20).

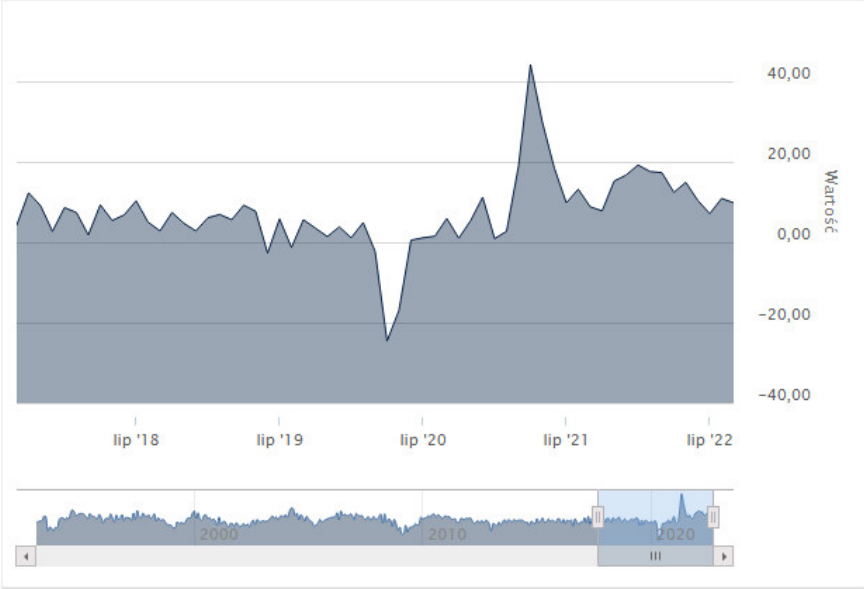

Fig. 18. Industrial production in Poland (9.80%) y/y [2]

4. Conclusions

The moods in the global, European and Polish machinery industry, where the indicators of the general economic climate were below the levels of the deep economic downturn in 2012-2013, do not look too good. A similar situation applies to construction and wholesale trade. Slightly better – but also below the line – indicators for the transport, catering and hotel industries. Only IT and communication, as well as the financial and insurance sectors, were on the plus side.

All these indicators suggest a hard autumn and a difficult winter 2022 for the Polish economy, but also for the European and global ones. So far, the downturn is not yet visible on the labour market, but it will probably change in the coming months and quarters. So before it gets better, it will clearly get worse. Currently, macroeconomic forecasts assume that the bottom of the business cycle will fall at the turn of the year (2022). However, it is not certain whether this will happen ...

References

[1] CETOP. “CETOP Market Outlook Presentations October 2022.” https://www.cetop.org/.
[2] ***. “Macroeconomic indicators – Poland / Wskaźniki makroekonomiczne – Polska.” https://www.bankier.pl/gospodarka/wskazniki-makroekonomiczne/polska.
[3] Economic Monitor September 2022. Polish Market 2022.

ISSN 1454 - 8003
Proceedings of 2022 International Conference on Hydraulics and Pneumatics - HERVEX
November 9-10, Băile Govora, Romania

HYDRAULIC WOOD SPLITTING SYSTEM

Andrei-Alexandru BENESCU[1,2], Bogdan-Marian ȘERBAN[1,2,*], Alexandru-Polifron CHIRIȚĂ[1], Mihai AVRAM[2], Mihai-Gabriel MATACHE[3]

[1] Hydraulics and Pneumatics Research Institute INOE 2000-IHP, Bucharest, Romania

[2] Politehnica University of Bucharest, Mechanical Engineering, Mechatronics and Robotics Department, Bucharest, Romania

[3] National Institute of Research – Development for Machines and Installations Designed to Agriculture and Food Industry- INMA, Bucharest, Romania

* bogdan.serban3105@gmail.com

Abstract: *This paper presents a dynamic simulation model of an intelligent wood splitter. The numerical simulation was performed using the Simcenter AMESim simulation environment. Libraries of mechanical, hydraulic and control signal components were used; the time variation of cylinder rod displacement, cylinder rod speed rate, piston force and power used by the whole equipment were determined. The hydraulic fluid model used in numerical simulation is ISO VG46 oil.*

Keywords: *Wood splitting, hydraulic cylinder, hydraulic drive, intelligent hydraulic drive*

1. Introduction

With more than 3.5 million households using stoves and chimneys in the cold season, wood is one of the main sources of home heating in Romania. In rural areas, about 85% of households use wood for heating. [1]
Considering that the need for heating houses starts in October and ends in April, so for 6 months, the consumption of wood for heating homes is very high. With a very large quantity of wood, it is necessary to make the process of supplying wood to households more productive, splitting logs into smaller sizes and splitting them for storage to burn them for heating living spaces. Mainly, in the rural areas of Romania, the cutting of the timber is done with a hand saw and splitting logs is done using an axe. The intelligent mechanization of household activities, including the splitting of firewood, leads to an easier life for Romanian household residents [2].
Splitting consists of driving a wedge into the wood, in the direction of the fibers. The wedge is inserted in the wood and causes it to split. With the increase of the contact surfaces between the wedge and the wood, elastic deformation of the log fibers occurs, followed by the breaking of the connections between them, the parts resulting from the splitting separating from each other [3,4].
The hydraulic cylinder serves to convert the energy of the hydraulic fluid into useful mechanical work. The flow rate generated by the hydraulic pump produces a linear displacement of the piston rod, inside the cylinder bore, with the load on the opposite side of the force imposed by the pressure of the fluid medium [5]. Thus, hydraulic energy is transformed into a controllable force acting in a straight line [6, 7].
Splitters are classified according to several criteria: their mobility, type of construction and the way the wood drive mechanism moves, or the position of the wood during the splitting process. In terms of mobility, splitters can be fixed or mobile. In terms of the design of the drive mechanism, the splitter may have a conveyor chain, a crank mechanism or hydraulic cylinders. In terms of the movement of the drive mechanism, the splitter may perform a rotating motion or a continuous movement. Depending on the type of splitting element, the splitter may be a wedge or a helical cone, the most commonly used being wedge-shaped splitters. In terms of the position of the wood to be split, splitters can be horizontal or vertical [3].
This paper presents, for the process of splitting wood mass, the optimization and development of a fixed horizontal hydraulic system, which performs an alternative rectilinear movement of the cylinder

wedge. To be energy efficient, the system uses a low-power electric motor to drive the hydraulic pump and it is possible to achieve high pressure in the hydraulic cylinder, thus generating the force needed for splitting a log.

2. Material and method

The physical system developed so far is shown in Fig.1, and consists of the metal structure of the system, the hydraulic cylinder, the wedge for splitting the wood mass and 4 elements for supporting the wood mass, another role of which is to position the center of the log at the same level as the tip of the wedge; thus splitting is done correctly; and in the future, the system will be fully functional.

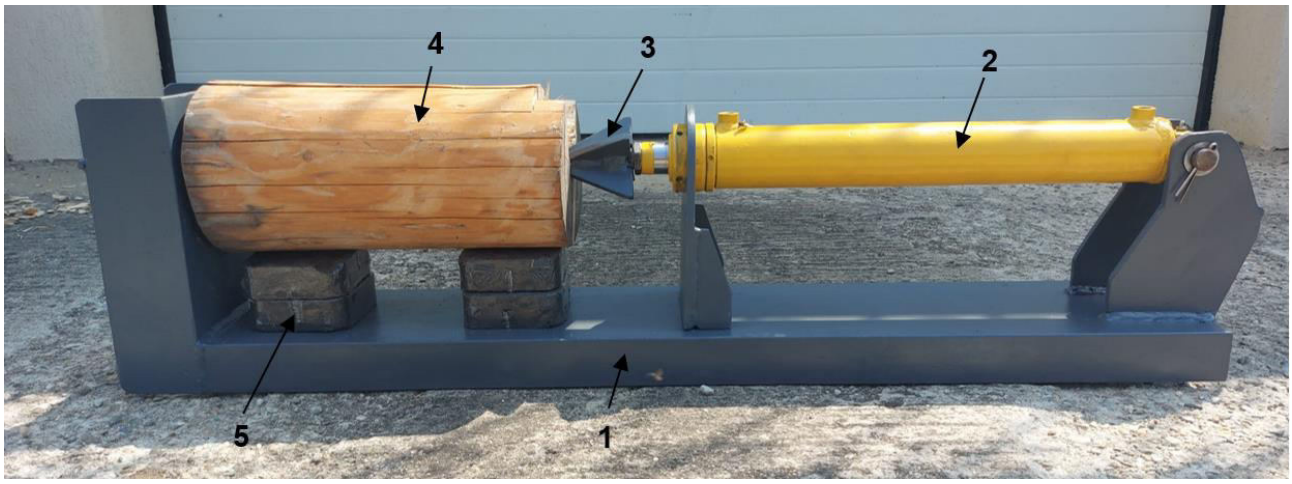

Fig. 1. The hydraulic splitting system
1 - System's metal structure, 2 - Hydraulic cylinder, 3 - Splitting tool (Wedge); 4 - Splitting object (wooden mass, log), 5 - Supporting and positioning elements.

The support on which the log will be positioned to be split will be equipped with two contacts and a spring that indicates the presence of the log in the space intended for its splitting. When the spring is compressed, a contact will send a signal to the hydraulic distributor, indicating the presence of the log.
We have taken some safety measures against possible accidents, namely the introduction of working parameters for the weight of the log. If its weight is in the range of 20-60 kg, the hydraulic cylinder will be activated and the splitting will be performed. If the weight of the log is outside this range, then the control system will not operate the hydraulic directional control valve, and consequently the hydraulic cylinder. This range represents the minimum and maximum weight of the wood mass. The maximum weight of the log was calculated according to its density and volume, and the result is that its maximum weight is 60 kg, because anything over this weight can represent the weight of the handler or other objects that happen to be in the space intended for splitting and could result in injuries or process related accidents. The minimum weight of 20 kg is set because after the entire splitting cycle, fragments of the split wood may remain, and the idle operation of the hydraulic cylinder represents a higher energy consumption. Also, for reduced energy consumption, two contacts will be placed at the end of the stroke of the cylinder rod. The purpose of those contacts is to send command signal to the directional control valve when the cylinder rod has reached 1%, respectively 90% of its maximum stroke.
The system was designed based on the data obtained by the simulation network, being evaluated and optimized virtually first. This was done in the integrated multidisciplinary technical systems simulation platform, namely the AMESim software, through which we combined elements of mechanics, electronics and hydraulics. The result is shown in Fig. 2.

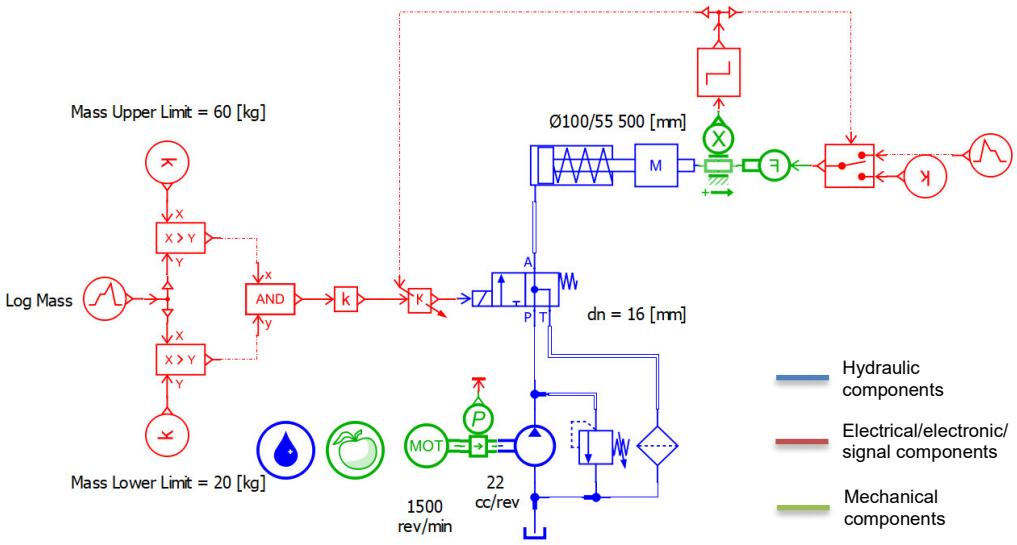

Fig. 2. Numerical simulation network of the hydraulic system for wood splitting

The hydraulic sub-system consists of a hydraulic gear pump with a fixed flow rate of 22 cc/rev. Between the hydrostatic pump and the electric motor there is a power sensor which is used to measure the power consumed by the system. The pressure relief valve, which acts as a safety relief valve, together with the filter are other hydraulic components of the equipment. The nominal diameter of the hydraulic directional control valve chosen is 16 mm. The hydraulic cylinder chosen has a diameter of 100 mm, the cylinder rod is 55 mm in diameter and the maximum stroke is 500 mm. Between the two there are two contacts, mounted at both ends of the cylinder rod, which limit the displacement of the cylinder rod, but also send a feedback signal to the directional valve to retract when the rod reaches its minimum or maximum stroke.
The electronic sub-system consists of an electric motor with a speed of 1500 rpm, a control block made of electrical signals, logic operators and signal amplifiers in the numerical simulation. Physically, this mechanism is composed of a spring and two contacts. It operates according to a simple logic. If the mass of the wood is in the required range, a signal will be sent to the hydraulic directional valve, the hydraulic cylinder will be actuated, and the wood will be split. If the mass of the wood does not fall within this range, then the directional valve remains in the preferred position, so the system will not act in any way. This can also be seen in Fig. 3, which represents the logic behind the whole process.

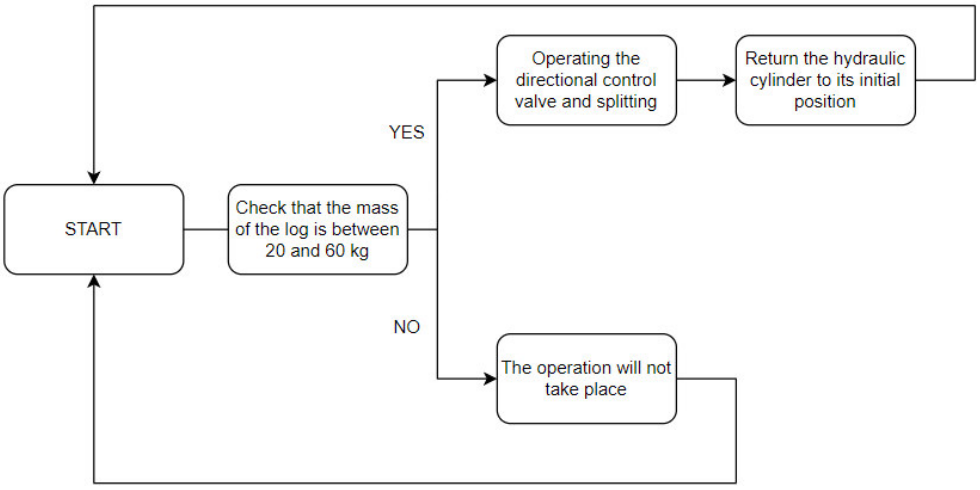

Fig. 3. The ladder diagram of the intelligent command system

3. Results of virtual experimentation

Based on the AMESim simulation network from the previous chapter, the results presented below were obtained:

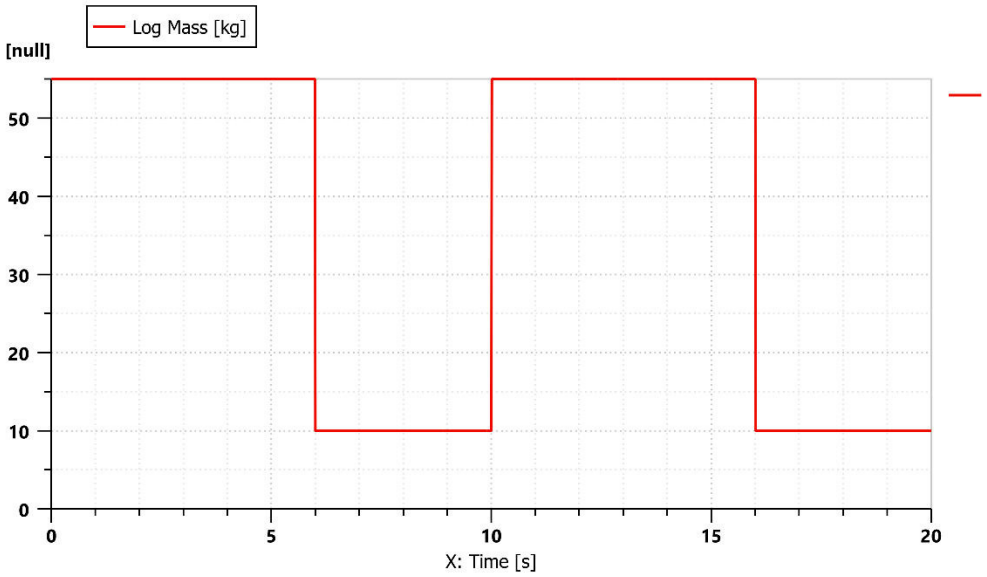

Fig. 4. Time variation in log mass during the splitting process

As one can see in figure 4, after the log is positioned in the splitting space and is included within the weight range - in the figure the weight is 55 kg – one can see how the mass of the log reaches 10 kg after 6 seconds as the wood chipping falls off the support due to the splitting process, the log separating into smaller fragments. It is also observed that the duration of one cycle is 10 s, the splitting time is 6 s and the withdrawal of the cylinder rod takes 4 s.

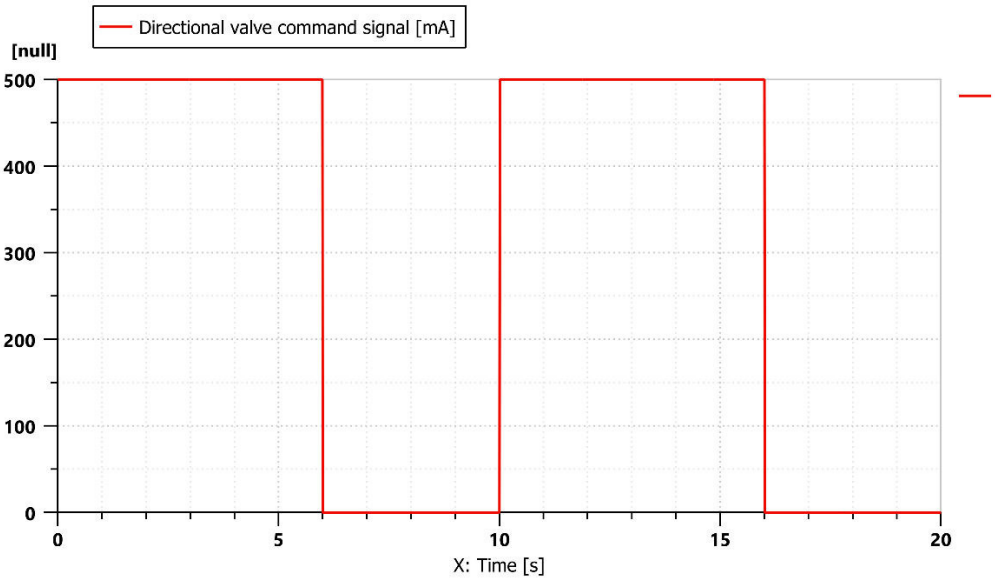

Fig. 5. Time variation in the hydraulic directional valve control signal

As one can see in Fig. 5, the hydraulic directional valve receives a command signal and starts to operate the system for splitting wood. In this graph, the control signal during 6 s, namely during the

splitting process, is 500 mA. When the rod retracts, the control signal reaches zero, after which the cycle starts again.

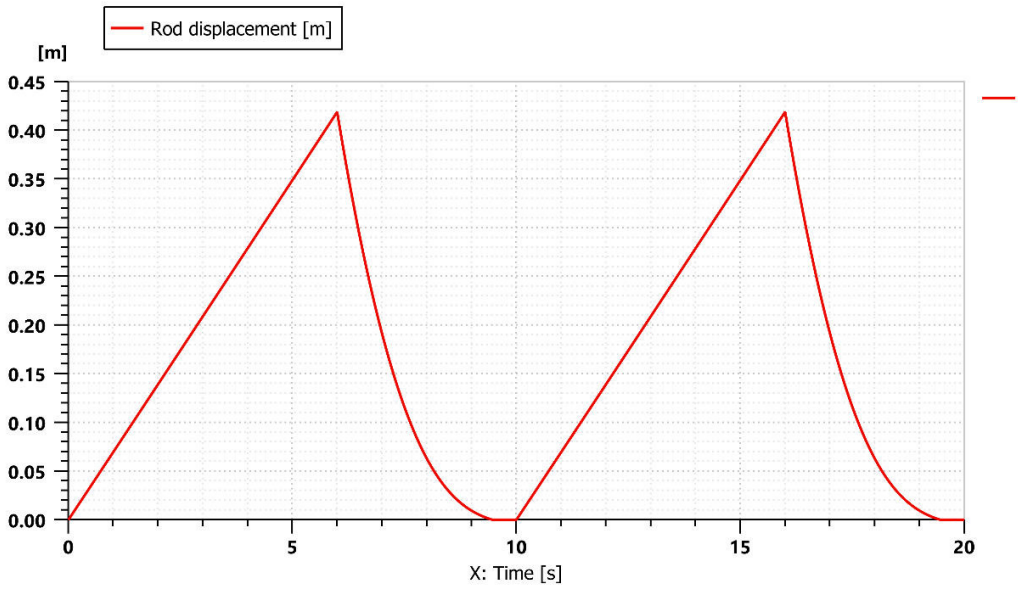

Fig. 6. Time variation in hydraulic cylinder rod displacement

Figure 6 shows the variation over time of the hydraulic cylinder rod displacement, and as one can see, the advance of the cylinder rod into the wood mass to be split is a slower one because the resistance of the log fibers is high. At the same time, the contact located at the end of stroke of the cylinder rod does not make it possible to move it to the end, and in this way, the energy consumed by the whole system is less. Cylinder rod retraction is faster because there are no relevant pressure drops in the system.

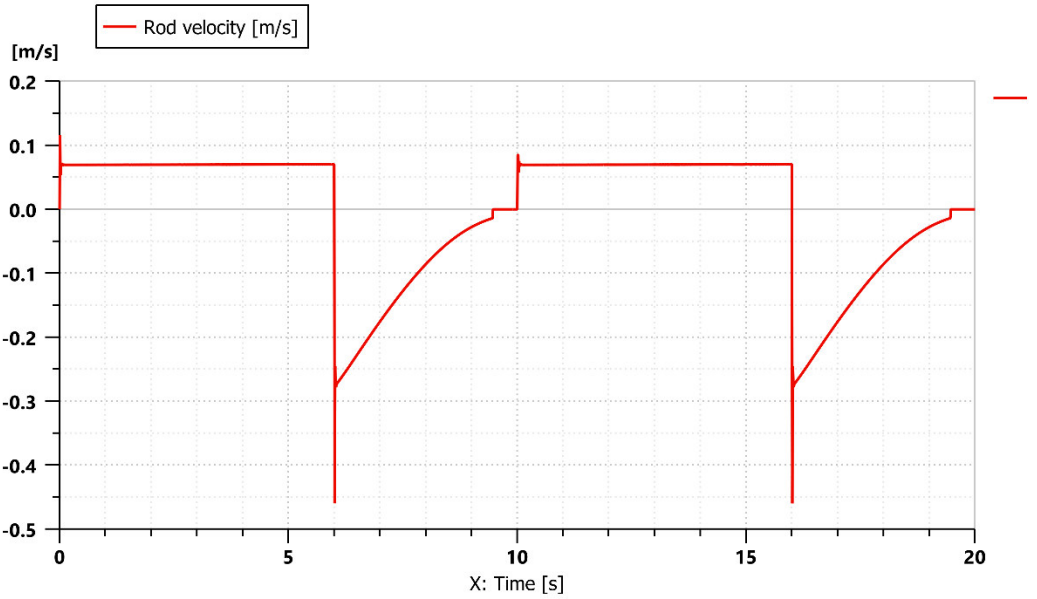

Fig. 7. Time variation in hydraulic piston speed rate

As one can see in the graph in Figure 7, the speed of the hydraulic piston when splitting is constant. It can be noticed that the speed rates achieved by the hydraulic piston are the usual kind, smaller than 0.5 m/s.

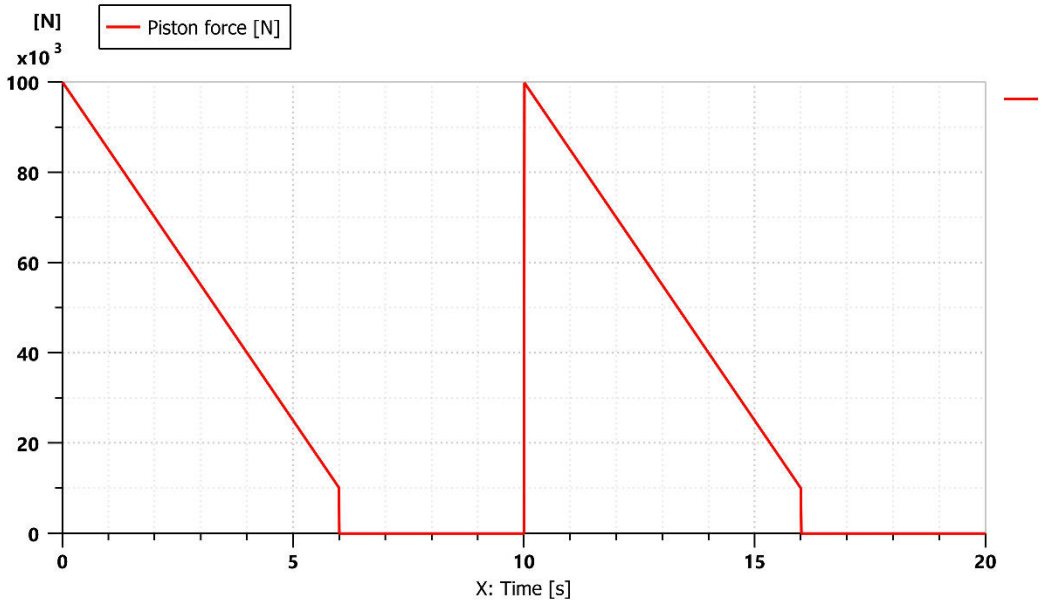

Fig. 8. Time variation in piston force

Figure 8 shows that at the moment of splitting, namely when the tip of the wedge is tangent to the wood mass, the force of the hydraulic piston is maximum, because the fibers resisting the splitting are resistant. When the splitting is complete, the force of the piston gradually decreases to 0 as the log is split; after 6 seconds it's split completely; the piston starts retracting and is waiting to receive a signal from the electronic control block, after which, if another log to be split is within the parameters, the cycle resumes.

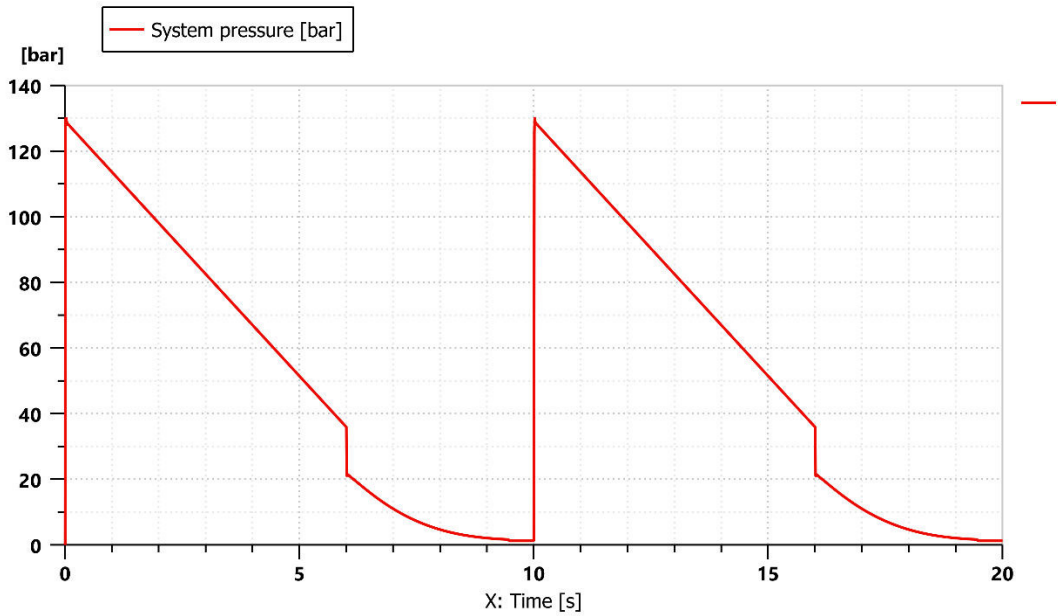

Fig. 9. Time variation in system pressure

Figure 9 shows the variation in system pressure over time. When there is no wood for splitting in the splitting proximity, the system pressure is 0. When the log is positioned and is to be split, the system pressure decreases throughout the splitting process, and when the hydraulic piston is no longer compressed, the system pressure gradually decreases.

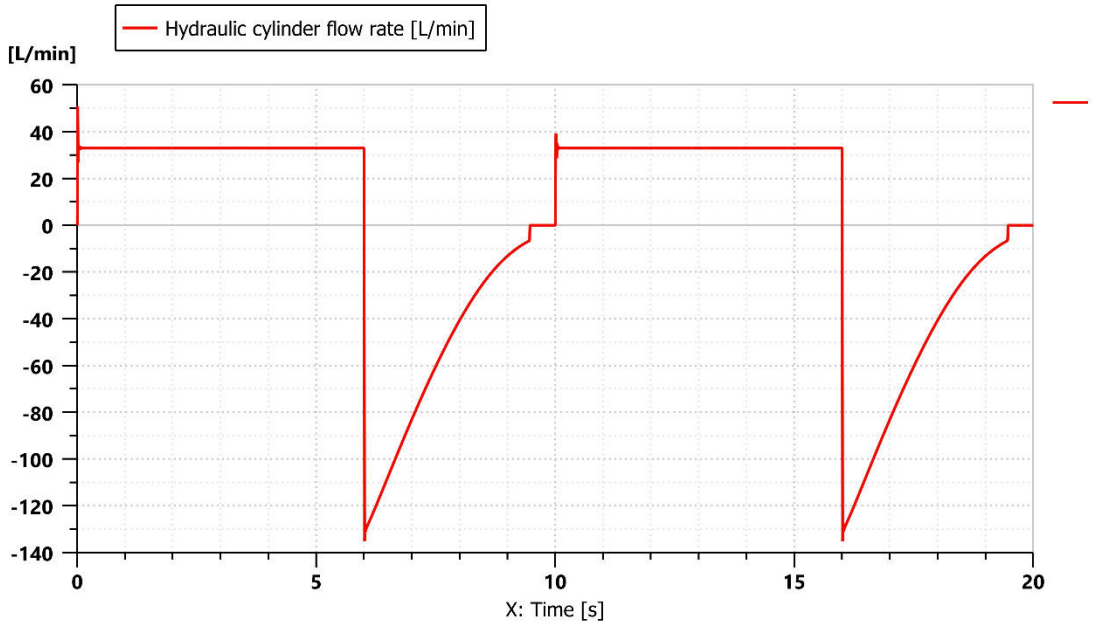

Fig. 10. Time variation in hydraulic cylinder flow rate

As one can see in the graph in Figure 10, the hydraulic cylinder flow rate remains constant during the splitting process because the whole system is optimized to operate under the correct conditions. When there is no more wood mass for splitting, the oil flow rate is redirected to the tank, which is necessary to retract the cylinder rod to its initial position, after which the cycle is resumed.

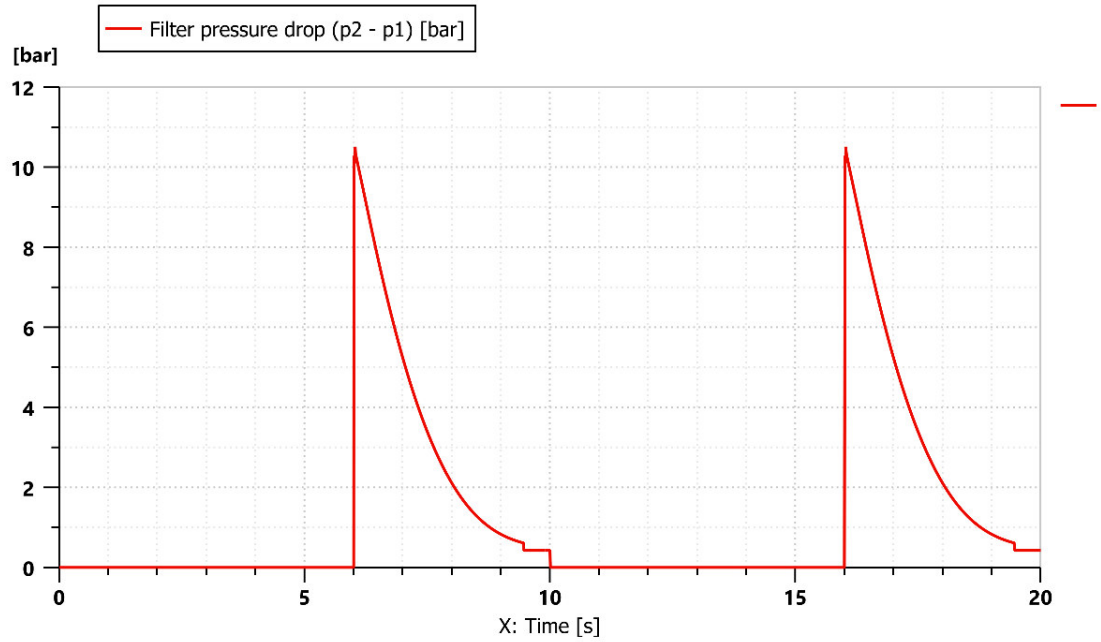

Fig. 11. Time variation in the pressure drop on the hydraulic system filter

As one can see in the graph above, the pressure drop on the system is quite small and there are no significant losses in the system that would prevent the whole system from functioning properly.
The graph in Figure 11 shows that at the moment of splitting, the whole system needs a lot of power to operate the cylinder rod. The higher the resisting forces, the higher power transmitted by the hydraulic pump is needed for the splitting process to take place properly.

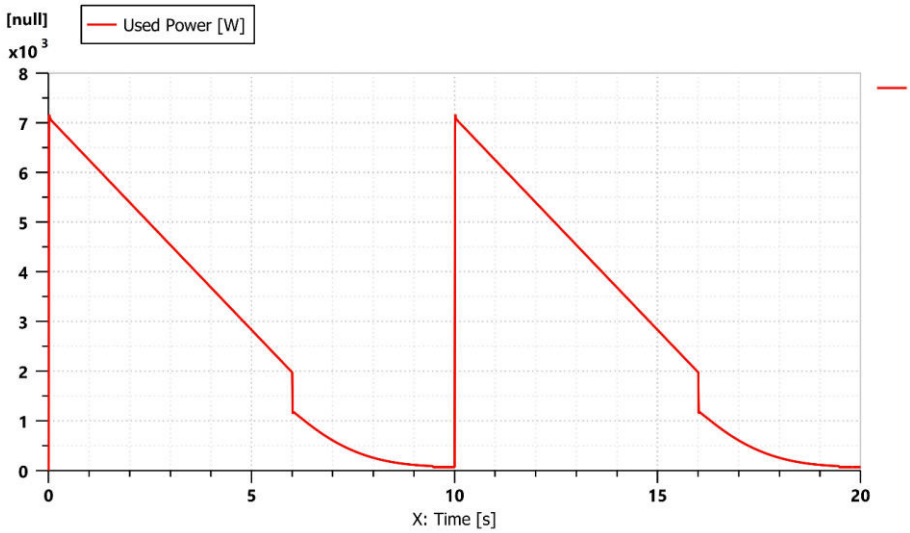

Fig. 11. Time variation in the power used by the hydraulic pump

4. Conclusions

- One of the most important results of this paper is the analysis and development of a system that mainly increases productivity due to the automation of a simple process, which previously required intensive labor, done in most households. More splits can be achieved with this intelligent hydraulic system in less time than with mechanical devices.
- The system was designed to offer the performance required for the process of wood splitting, without fancy components; the simple hardware used results in a lower purchase price if the system was placed on the market. In addition, energy consumption is kept as low as possible resulting in high reliability that is needed for household uses, the main targeted purchaser being country people from rural areas, where income is low.

Acknowledgments

This paper has been financed under a project funded by the Ministry of Research, Innovation and Digitalization through Programme 1- Development of the national research & development system, Sub-programme 1.2 - Institutional performance - Projects financing the R&D&I excellence, Financial Agreement no. 18PFE/30.12.2021. European funding has also been granted, under Competitiveness Operational Programme POC 2014-2020, call POC-A1-A.1.1.3-H-2016, Financial agreement no. 253/02.06.2020, signed between INOE 2000 and the Ministry of Education and Research for the project titled “Horizon 2020 Support Center for European project management and European promotion PREPARE”, MYSMIS2014 code 107874.

References

[1] National Institute of Statistics of Romania. “Volume of Wood Exploited / Volumul de lemn exploatat”. Last updated September 28, 2015. Accessed October 21, 2022. https://insse.ro/cms/ro/content/volumul-de-lemn-exploatat.
[2] Avram, Mihai, and Andrei Benescu. *Calculul si proiectarea unui dispozitiv hidraulic pentru despicat masa lemnoasa / Calculation and Design of a Hydraulic Device for Splitting Wood*. Bachelor thesis. Politehnica University of Bucharest, 2022.
[3] Gassner, Timothy. *“Hydraulic wood splitter”* (US patent 0055585 A1), 2012.
[4] Wirsbinski, James L., and Dale A. Manteufel. *“Hydraulic wood splitter”* (US patent 4470441), 1984.
[5] Avram, Mihai. *Hydraulic and Pneumatic Drives: Classic and Mechatronic Equipment and Systems / Actionari Hidraulice si Pneumatice: Echipamente si Sisteme Clasice si Mecatronice.* Bucharest, University Publishing House, 2005.
[6] Kováč, Ján, Jozef Krilek, Marián Kučera, and Štefan Barcík. “The Impact of Design Parameters of a Horizontal Wood Splitter on Splitting Force.” *Wood Industry / Drvna industrija* 65, no. 4 (2014): 263-271.
[7] Maier, Anton. “*Hydraulic drive with rapid stroke and load stroke”* (US patent 9771957 B2), 2017.

ISSN 1454 - 8003
Proceedings of 2022 International Conference on Hydraulics and Pneumatics - HERVEX
November 9-10, Băile Govora, Romania

RHEOLOGICAL BEHAVIOR OF BIODEGRADABLE FLUIDS USED IN HYDRAULIC POWER INSTALLATIONS

Andreea Mirela TELEAȘĂ[1], Alexandru Valentin RĂDULESCU[1], Cătălin DUMITRESCU[2], Sorin CĂNĂNĂU[1]

[1] University POLITEHNICA Bucharest, Romania, andreea.teleasa@upb.ro

[2] INOE 2000 - IHP, HYDRAULICS AND PNEUMATICS RESEARCH INSTITUTE, Bucharest, Romania, dumitrescu.ihp@fluidas.ro

Abstract: *This paper presents the rheological properties for two hydraulic fluids: a hydraulic fluid based on mineral oils (H46) and a biodegradable hydraulic oil based on vegetable oils (HETG46). From a rheological point of view, the models used for these tests were the Newtonian model and the power law model, and from a thermal point of view, the model used is the Reynolds model.*
The tests were carried out with the help of the BROOKFIELD CAP 2000+ stand and the interpretation of the results was done with the help of the CAPCALC32 calculation program.
Following the experimental results, we can conclude that the biodegradable hydraulic fluid HETG46 has the same rheological behavior as the mineral fluid H46, but a viscosity reduced by approx. 20% For both fluids, the thermal Reynolds model of viscosity variation with temperature is found to approximate the experimental values with the same accuracy, leading to correlation coefficients greater than 96%.

Keywords*: rheology, hydraulic fluids, Newtonian model, power law model, viscosity*

1. Introduction

Lubricants are usually petroleum-based products and are considered to be a source of new carbon dioxide through their extraction, production and post-use in components and equipment. With global demand for lubricants expected to continue growing at an estimated annual rate of 2.6% through 2015, the importance of reducing environmental impact becomes apparent [1].

2. Hydraulic lubricants

Hydraulic lubricants play a critical role in the operation and performance of hydraulic systems [2]–[4]. In addition to viscosity and oxidative and thermal stability, hydraulic lubricants must protect pumps from wear and enable uninterrupted operation of actuators and valves. In addition, hydraulic oils must perform adequately at high temperatures and pressures; perform to tight tolerances, especially in advanced hydraulic systems; be compatible with a variety of metals and elastomers; protect different types of pumps from wear (piston, gear, vane, etc.); and operates in the presence of moisture that may contaminate the system. In certain operations, hydraulic oils must also be fire resistant [1].
Standard specifications for hydraulic fluids and components serve an important function in the fluid industry. Fluid standards validate the safety, durability, compatibility, cleanliness and functionality of hydraulic fluids [5]. The primary purpose of a hydraulic fluid is power transfer. The concept of fluid power is based on a principle articulated by Blaise Pascal, which is given as follows: "The pressure applied to an enclosed fluid is transmitted undiminished to every portion of that fluid and to the walls of the containing vessel" [6]. In the context of fluid power, pressure is related to the force acting on an enclosed fluid. This principle gave birth to the modern hydraulic system, which involves highly engineered systems for efficiently controlling fluid flow to transfer energy and accomplish work [5].
The heart of any hydraulic system is the pump, which draws fluid through its inlet and forces fluid through its outlet, usually against the pressure created by valves, plumbing, and actuators downstream of the pump. Pumps, actuators, and other system components have surfaces that

move relative to each other, often at high speeds, pressures, and temperatures. These components require cooling and lubrication for efficient performance and durability. Consequently, hydraulic fluids not only transmit power, but also have a critical function as a lubricant and heat transfer medium [5].
Most hydraulic fluids consist of a base fluid and a combination of additives that have been optimized to impart chemical characteristics and functionality to the finished product. Operating conditions and equipment manufacturer specifications generally dictate the type of fluid that is required and therefore the type of base stocks and additives that must be used [5].

2.1 Mineral oils

It is not known when mineral oil was first produced, but as a petroleum derivative, it must have been after the discovery of crude oil, but even that has already been known for thousands of years. Mineral oil is known by many different names. The reason for this is probably historical, as the product was created long before the common nomenclature was implemented. Synonyms include heavy mineral oil, light mineral oil, liquid paraffin, liquid petroleum jelly, mineral oil mist, paraffin oil, paraffinum liquidum, liquid petroleum jelly, petroleum oil, white mineral oil, and white oil. This is a complex mixture of highly refined saturated branched chain naphthenic hydrocarbons [7].

2.2 Vegetable oils (biodegradable)

Biodegradable hydraulic fluids are currently formulated with renewable products such as rapeseed, sunflower, corn, soybean and canola or synthetic ester. These types of fluids are now considered less toxic and more biodegradable than conventional hydraulic fluids.
Vegetable oils have excellent lubricating qualities, are non-toxic and biodegradable. Their chemical structures are triglycerides in which a variety of saturated, monounsaturated, or polyunsaturated fatty acids are esterified to a glycerol backbone. The physical properties of a vegetable oil depend on the nature of its fatty acid composition. These oils tend to oxidize at temperatures above 90°C and have a shorter life compared to conventional petroleum-based fluids [5].

3. Experimental procedure

3.1 The experimental stand and the mathematical models used

The experimental test stand is a Brookfield CAP 2000+ viscometer, shown in Fig. 1. This is a viscometer that measures the flow behavior of fluids and the viscosity of both liquid and semi-solid materials, using the cone-plane coupling as working geometry, shown in Fig. 2.

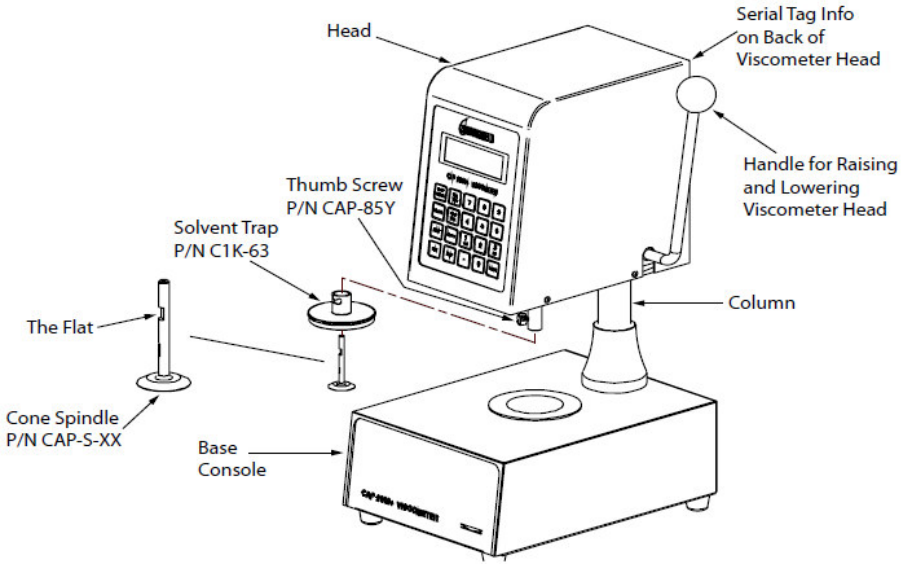

Fig. 1. Cone-plate Brookfield viscometer

Fig. 2. Work geometries

Table 1 shows the characteristics of the cones used at the Brookfield stand. In our case, the cone used is no. 8, characterized by a diameter of 15.11 mm and an angle of 3°.

Tabel 1: Geometry and viscosity range of testing cones

Cone number	Cone radius, [mm]	Cone angle, [°]	Viscosity range, [Pa·s]
3	9.53	0.45	0.083...1.87
5	9.53	1.8	0.333...7.50
6	7.02	1.8	0.833...18.7
8	15.11	3	0.312...3.12

To highlight the thixotropy of the fluids, a loading test was carried out starting from the minimum velocity gradient to a maximum velocity gradient, from where its discharge begins. The temperature range at which the tests were performed was 20-75°C.
From a rheological point of view, the models proposed to determine the rheological properties and to describe their behavior are:

- Newtonian model:

$$\tau = \eta \cdot \dot{\gamma}, \tag{1}$$

Where τ is shear stress, η is viscosity, $\dot{\gamma}$ is shear rate,

- Power Law model:

$$\tau = m \cdot \dot{\gamma}^{n}, \tag{2}$$

Where “m” and “n” are material constants, τ is shear stress, $\dot{\gamma}$ is shear rate, m- consistency index, n- flow index
From a thermal point of view, the proposed model is:

- Reynolds model:

$$\eta = \eta_{50} \cdot e^{-m(t-50)}, \tag{3}$$

Where η- dynamic viscosity of the fluid at temperature, η_{50}- viscosity at a temperature of 50°C, m- coefficient of variation of viscosity with temperature, t- temperature, 50- reference temperature.

3.2 The oils used

In this work, the oils used were [8]:

- H46 - It is a mineral oil that has been used as a benchmark. It has a density of 871 kg/m^3, and the kinematic viscosity at 40°C is between 41.4 - 50.6 cSt.
- HETG 46 - It is a hydraulic fluid based on vegetable oils, slightly biodegradable, environmentally friendly. The additives used provide excellent properties related to resistance to oxidation, corrosion, low temperature and extreme pressure. The density is 918 kg/m^3, the kinematic viscosity at 100ºC is 10 cSt.

3.3 Results

A change of the rheological properties induced by temperature or deformation in the structure of fluids refers to the phenomenon of thixotropy (thermal or deformation hysteresis). The phenomenon consists in the fact that the relationships between apparent viscosity and temperature or the velocity gradient measured when one of these parameters increases or decreases are not identical [9].
Figure 3 and Figure 4 show the variation of the tangential stress depending on the shear rate at a temperature of 20°C for H 46 and HETG 46 hydraulic fluids.

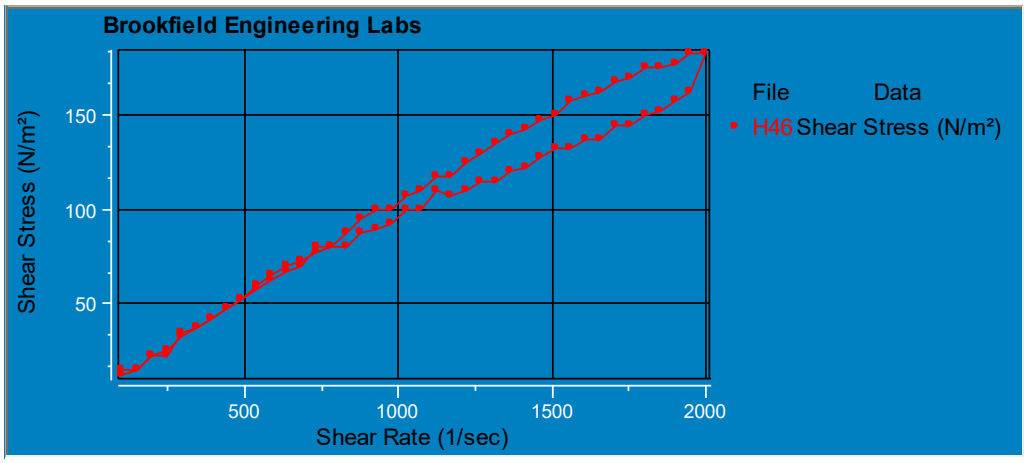

Fig. 3. Variation of the tangential stress versus shear rate at temperature of 20°C for the hydraulic oils H 46

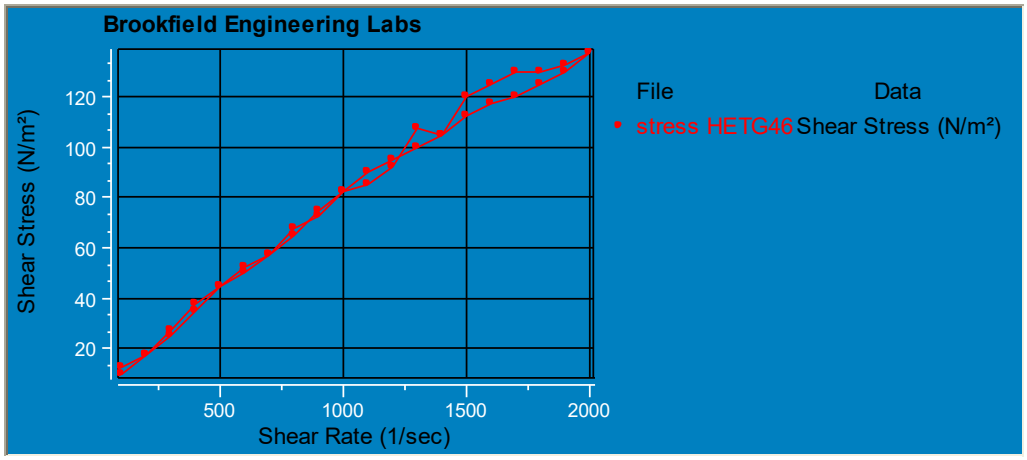

Fig. 4. Variation of the tangential stress versus shear rate at temperature of 20°C for the hydraulic HETG 46

For both fluids, the variation of viscosity with temperature at different speed gradients can be done in the area of speed gradients from 0 to 1000 s^{-1}, an area where the thixotropy of the lubricant is negligible (the hysteresis loop does not exist).

If the velocity gradient exceeds 1000 s^{-1}, thixotropy becomes much more obvious, which implies a limitation of the velocity gradient range on which the experimental determination of the viscosity variation with temperature will be made.

Figure 5 shows the comparison of the two hydraulic fluids based on the variation of the tangential stress and the shear rate.

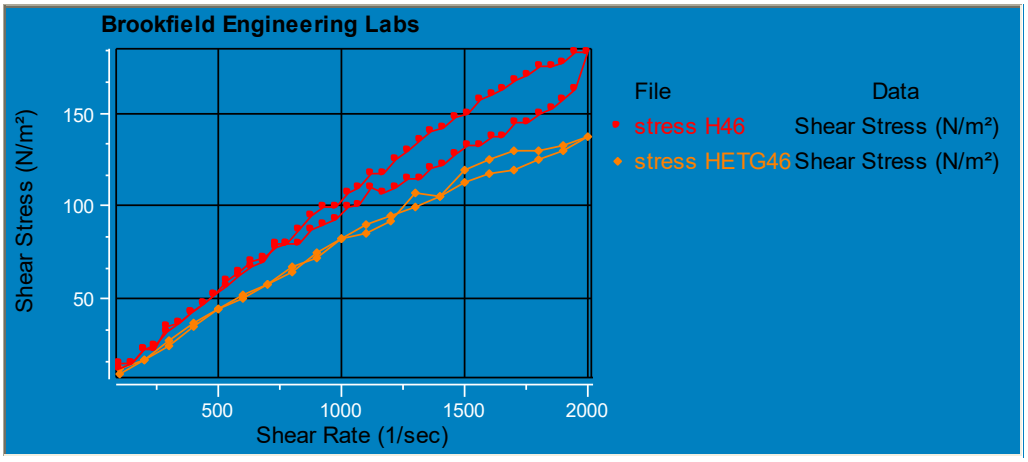

Fig. 5. Comparison of the two hydraulic fluids based on the variation of the tangential stress and the shear rate

Analyzing the two curves, we can see that the H46 fluid has a higher slope and the thixotropy is much more pronounced than that of the HETG46 fluid, which means that the viscosity of the H46 fluid is higher than that of the HETG46 fluid, where the slope and thixotropy are lower.
From the point of view of homogeneity, we can say that HETG46 fluid is much more stable than H46 because its thixotropy is very low.
Figure 6 and Figure 7 show the rheograms of H46 and HETG 46 hydraulic fluids at a temperature of 20°C using the power law rheological model. These were performed using the numerical regression of the experimental data, using CAPCALC 32 software, to determine the rheological parameters under the assumption of power law model variability.

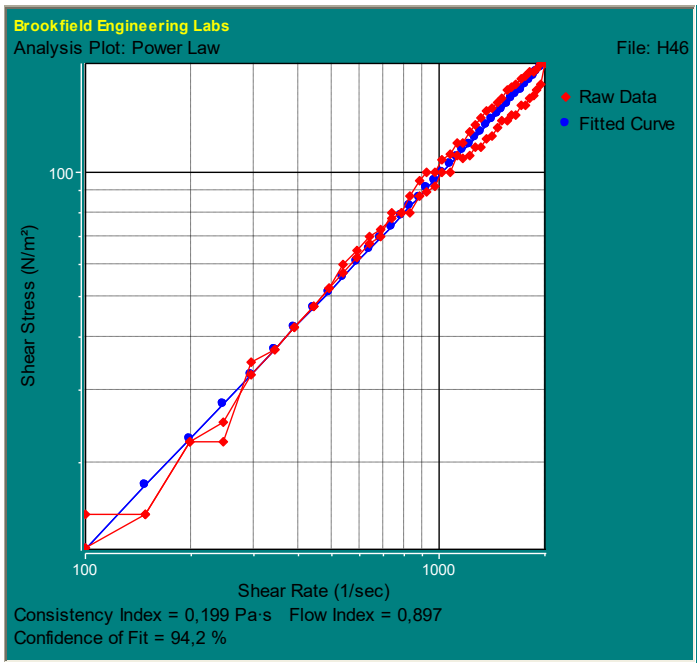

Fig. 6. Rheogram of hydraulic fluids H46 at a temperature of 20°C using the power law rheological model

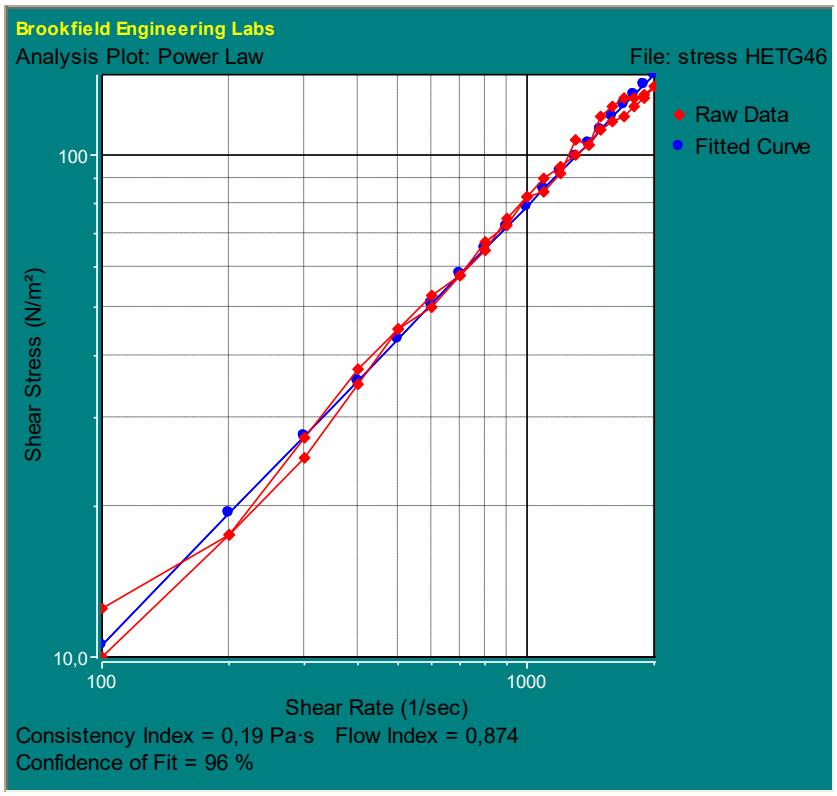

Fig. 7. Rheogram of hydraulic fluids HETG 46 at a temperature of 20°C using the power law rheological model

Figure 8 and Figure 9 show the variation of viscosity with temperature at four speed gradients (125 s^{-1}, 250 s^{-1}, 375 s^{-1}, 500 s^{-1}) for the two fluids. The observation we can make about the H46 fluid is that the viscosity decreases with the increase of the velocity gradient, where we can say that we have a strong pseudoplastic behavior. For the HETG 46 biodegradable fluid, this is a little obvious.

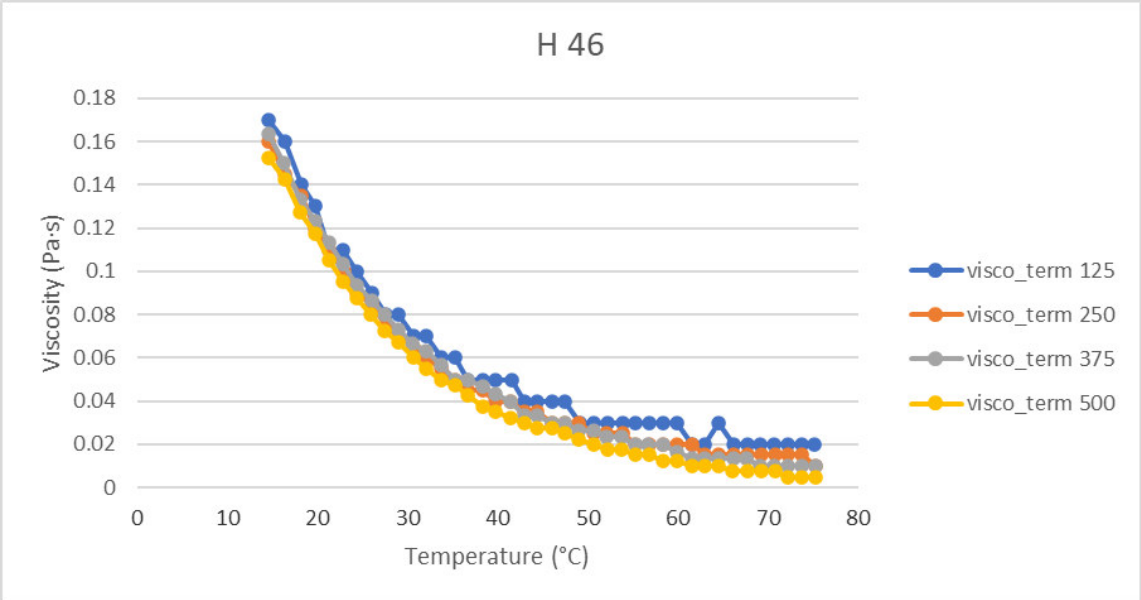

Fig. 8. Variation of the viscosity versus temperature for hydraulic oils H46

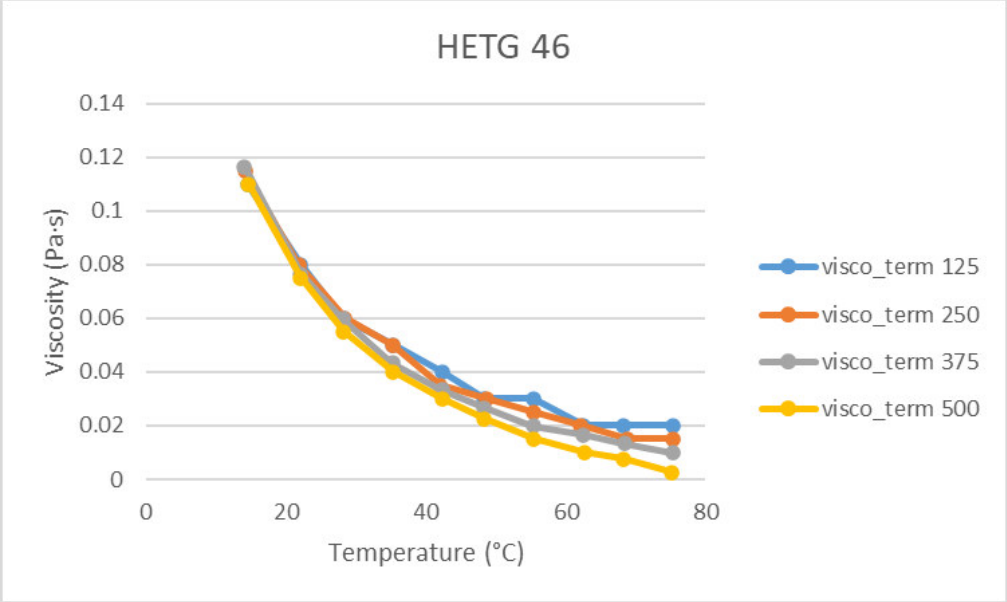

Fig. 9. Variation of the viscosity versus temperature for hydraulic oils HETG 46

Table 2 shows the parameters of the Reynolds model corresponding to the four viscosity variations for the two fluids. The observation we can make about these results is that the viscosity at the temperature of 50°C and the temperature coefficient decrease with the increase of the velocity gradient.

Table 2: Characteristic parameters for the variation of viscosity as a function of temperature using the Reynolds model for hydraulic fluids

Parameters / Shear rate [1/s]	H 46		
	$\eta_{50^\circ}[Pa \cdot s]$	Temperature parameter, $m[°C^{-1}]$	Correlation coefficient, $\rho[\%]$
125	0.030	-0.039	96.71
250	0.025	-0.045	98.40
375	0.027	-0.048	99.51
500	0.020	-0.057	99.89
Parameters / Shear rate [1/s]	HETG 46		
125	0.030	-0.031	97.62
250	0.025	-0.034	98.64
375	0.020	-0.037	98.93
500	0.015	-0.049	99.83

4. Conclusions

The aim of the work is to test the two hydraulic fluids (mineral oil and biodegradable oil) from a rheological point of view.
Regarding the rheological models, the most appropriate is the Newtonian model, which has a correlation coefficient over 98%.
Both oils show a high correlation coefficient of up to 95% for the power law model.
Following the experimental results, we can conclude that the biodegradable hydraulic fluid HETG46 has the same rheological behavior as the mineral fluid H46, but a reduced viscosity with approx. 20%
For both fluids, it is found that the Reynolds thermal model of viscosity variation with temperature approximates the experimental values with the same accuracy, leading to correlation coefficients higher than 96%.

Acknowledgments

The authors wish to express thanks to the INOE 2000 - IHP Hydraulics And Pneumatics Research Institute for supporting this work within the frame work of the research.

References

[1] Sharma, Brajendra K., and Girma Biresaw (Eds.). *Environmentally friendly and biobased lubricants*. Boca Raton, CRC Press, Taylor & Francis Group, 2017.
[2] Pirro, D. M., and A. A. Wessol. *Lubrication Fundamentals*. Second Edition, Revised and Expanded. Mechanical Engineering-New York and Basel-Marcel Dekker, 2001.
[3] Givens, W. A., and P. W. Michael. “Hydraulic fluids.” Totten, G., S. Westbrook, and R. Shah (Eds.). *Fuels and Lubricants Handbook: Technology, Properties, Performance and Testing*. Glen Burnie, ASTM International, 2003.
[4] Rudnick, Leslie R. *Synthetics, mineral oils, and bio-based lubricants: chemistry and technology*. CRC Press, 2020.
[5] Totten, George E., and Victor J. Negri. *Handbook of hydraulic fluid technology*. 2nd ed. Boca Raton, CRC Press, 2012.
[6] Bishop, M. *Makers of Modern Thought*. NY, American Heritage Publishing, 1972.
[7] Rawlings, A. V., and K. J. Lombard. “A review on the extensive skin benefits of mineral oil." *International Journal of Cosmetic Science* (2021): 511–518.
[8] Dumitrescu, L., Ş.M. Şefu, I.M. Baciu, and M. Blejan. “Intelligent Hydraulic System for Comparative Functional Testing of Biodegradable Working Fluids.” *Hidraulica Magazine*, no. 2 (2021): 97–102.
[9] Malkin, A. Ya., and S. N. Khadzhiev. "On the rheology of oil (Review)." *Petroleum Chemistry* 56 (2016): 541–551.

ISSN 1454 - 8003
Proceedings of 2022 International Conference on Hydraulics and Pneumatics - HERVEX
November 9-10, Băile Govora, Romania

SYSTEM FOR ADJUSTING THE LINEAR DISPLACEMENT VELOCITY AND CONTROLLING AN ELECTROHYDRAULIC SERVO CYLINDER

Radu Iulian RĂDOI[1,*], Alexandru Polifron CHIRIȚĂ[1], Bogdan Alexandru TUDOR[1], Robert BLEJAN[1], Vlad BUZOIANU[2]

[1] National Institute of Research & Development for Optoelectronics / INOE 2000 – Subsidiary Hydraulics and Pneumatics Research Institute

[2] S.C. PROFLEX AUTOMOTIVE S.R.L.

*radoi.ihp@fluidas.ro

Abstract: *Certain industrial applications such as machinery, automated production lines or robots require a precise control of the movement speed of some mechanisms or tools. Hydraulic drives are suitable for applications where high power is required due to advantages such as high power-to-weight ratios, low speed torque, accurate control with servo proportional electro-hydraulic valves and compact design. For a precise control of applications with linear movement based on hydraulic cylinders, it is necessary to use closed loop systems. Closed loop systems involve the use of feedback transducers and servo controllers. The paper presents the results of the experiments of a velocity adjusting system for hydraulic servo cylinder, which uses a data acquisition board and a virtual instrument application made in the LabVIEW environment.*

Keywords: *Servo cylinder, servo valve, linear velocity, PID control*

1. Introduction

Hydraulic drives are widely used in large machinery and heavy industry applications due to possibility to scale the power and ability to change direction, torque and speed across a system very simple, without mechanical transmissions. Servo systems with closed loop control are used for positional adjustments, repeated movements with a certain adjustable stroke or a movement profile of some applications from machine tools. Closed loop control systems can use dedicated servo amplifiers, control cards or PLCs. These systems receive the setpoint variable as command input, the process variable at the feedback input, and the controller delivers a command signal to the execution element. The most widespread closed loop control system is made with PID controllers. Other authors have carried out research on the control performance of an electro-hydraulic actuator using AMESim [1] or the analysis of the speed control of a hydraulic actuator using digital hydraulics [2]. Another paper [3] proposes an electrohydraulic actuator where the speed variation is done with an EHU electrohydraulic unit equipped with an electric motor with variable speed. Also in [4] leakage compensation was studied for maintaining constant speed for a drive system with a hydraulic actuator, based on the control of a proportional directional valve and control of the input speed for pump.
In this work, a laboratory stand-type application was created with a servo cylinder and controller made with a data acquisition board and a software application developed in the LabVIEW environment. With the help of the application, a certain travel speed can be set and the evolution of the position, speed, pressures in the hydraulic cylinder chambers and the system error can be visualized on the diagrams.

2. Electrohydraulic system

The electrohydraulic system of the stand consists of a hydraulic servo cylinder with a Moog type D761 servo valve (Fig. 1) coupled with a hydraulic load cylinder and installed on a metal frame. The servo cylinder is fed from a pumping group with an axial piston pump. In the diagram in Fig. 2 one can see the load cylinder provided with two filling / venting valves (HT) and throttle valve (TV). The power supply of the servo cylinder is done through the F filter, a relief valve (RV) being

connected in the derivation. The servo cylinder is equipped with two pressure transducers (PT) for the two chambers and a magnetostrictive stroke transducer (LT) for the cylinder rod. The scheme also includes the acquisition board (DAQ), a signal conditioner (SC) for the transducers with output signal 4 ÷ 20 mA and an amplifier for the control of the servo valve (VA). Signal conditioner and valve amplifier are supplied with voltage from a 24 Vdc source (PS). The valve amplifier is a modular type produced by Bosch Rexroth and has been calibrated for a maximum control signal of ±40 mA for the servovalve coils connected in parallel, the control input being a differential type with ±10 V.

Fig. 1. Hydraulic servo cylinder equipped with transducers

The characteristics of the hydraulic cylinder are:
- Piston diameter: 50 mm;
- Rod diameter: 20 mm;
- Stroke: 200 mm;

The characteristics of the servo valve are:
- Size: 04;
- Maximum supply pressure: 315 bar;
- Rated flow: 38 l/min;
- Signal for 100 % spool stroke: ±40 mA (coils connected in parallel).

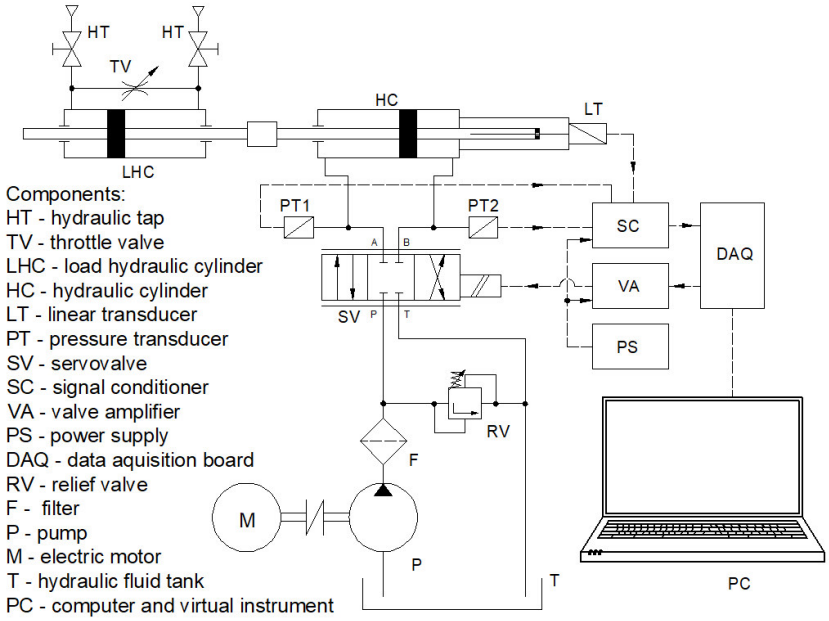

Fig. 2. Schematic of the speed adjusting system of the servo cylinder

3. Control system

A closed loop control system has the process variable as the controlled variable. The process variable is measured using a sensor. In the case of the application in this paper, the process variable is the speed and a position transducer is used to measure it, the speed being obtained by deriving the displacement according to (1).

$$v(t) = \frac{dx(t)}{dt} \tag{1}$$

The process variable enters the control system as feedback [5, 6]. The setpoint value is the desired command value for the process variable. At any moment, the process variable is compared with the setpoint value, and the difference between the two values is used by the controller to generate an output quantity to drive the system. If it is desired, at a given moment, to change the speed (setpoint) up or down, the controller commands the system (servovalve) to increase or decrease the flow rate supplied to the hydraulic cylinder chamber. Because the monitoring process of the process variable for the provision of feedback and the calculation of the order size to the system is a continuous one, the system is one in a closed loop.
The control system for adjusting the speed of a servo cylinder has been created with a LabVIEW virtual instrument, which uses an NI USB-6008 data acquisition board to transmit the setpoint command signal and to read the process variable from a displacement transducer of magnetostrictive type, incorporated in the servo cylinder (Fig. 3). To read the signals from the transducers, a DAQ Assistant block was used in which the analog channels were configured. Three analog inputs (AI0, AI1, AI2) were used, one for the displacement transducer and two for the pressure transducers connected to ports A and B of the hydraulic cylinder. The analog signal from the position transducer in the 1...5 V range is scaled in mm to display the displacement and after derivation the signal is scaled in m/s. Scaling was done by defining tables with interpolation points in Scaling and Mapping blocks. The Setpoint and Process Variable signals, which enter the PID block (Fig. 4) were scaled in the same range of variation, and the output signal that enters the valve amplifier type VT 11021 that controls the servo valve was scaled in the ±10 V range. To generate the command signal with the acquisition board, a DAQ Assistant block was used in which the analog output channel AO0 was configured. For the graphic display of the signals: setpoint, cylinder speed (process variable), pressure ports, cylinder movement and error, Waveform Chart blocks were used.
After several iterations regarding tuning the controller, the following values for PID Gains were established: proportional gain K_p = 1; integral gain K_i = 0; derivative gain K_d = 0.1.

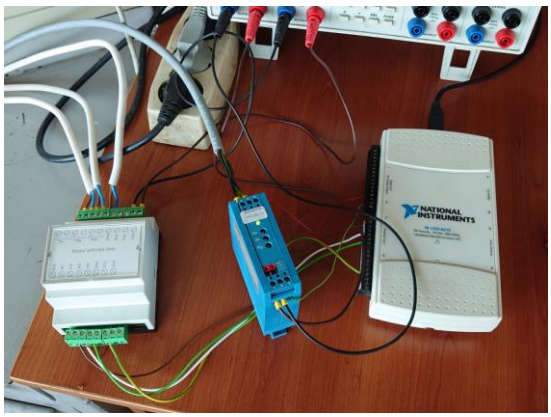

Fig. 3. Data acquisition system

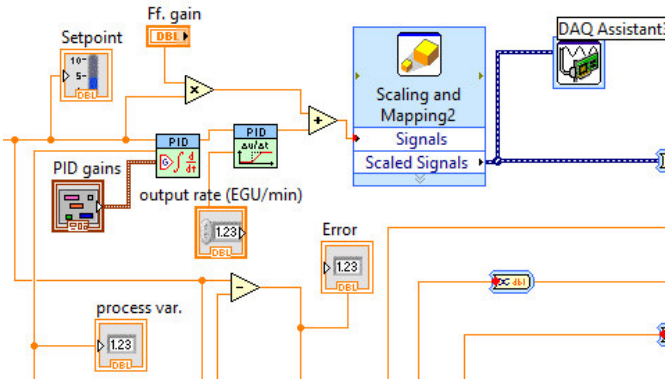

Fig. 4. LabVIEW controller network

PID tuning allows obtaining P, I, D parameters for optimizing control objectives such as disturbance rejection and setpoint tracking. The Kp parameter is used to increase the response speed, and if it increases too much it leads to oscillations. The Ki parameter is used to obtain

steady-state response with the disadvantage that large oscillations can be obtained over a long period. The Kd parameter is used for damping purposes with the disadvantage that high frequency oscillations and sensitivity to noisy signals can be obtained.

4. Experimental results

After installing the actuation system with servo cylinder and tuning the PID controller, tests were done to obtain experimental data. A random signal was generated (Fig. 5) for the setpoint and the evolution of the response from the hydraulic cylinder was followed as precise as possible.

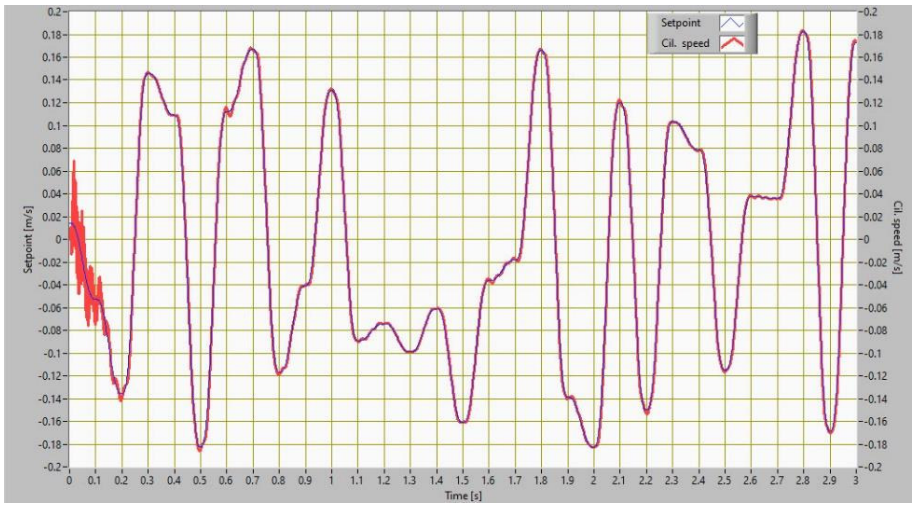

Fig. 5. Setpoint and process variable - cylinder speed

The pressure variation in the hydraulic cylinder chambers during the test can be seen in figure 6.

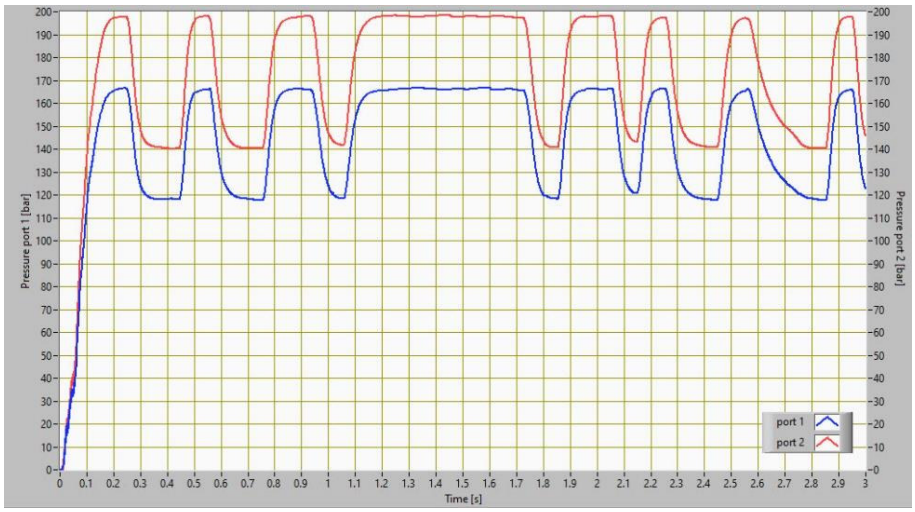

Fig. 6. Pressure at cylinder ports

The stroke profile of the hydraulic cylinder, during testing, can be found in figure 7. The maximum amplitude of the stroke was 70 mm.
The variation of the error of the speed control system during testing can be found in figure 8. When the system is put into operation, a slight oscillation is observed, which is dampened by the derivative gain set to the controller.

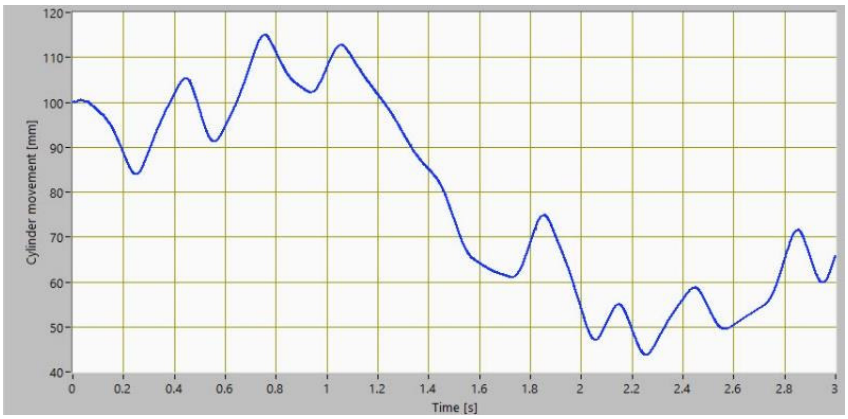

Fig. 7. Hydraulic cylinder movement

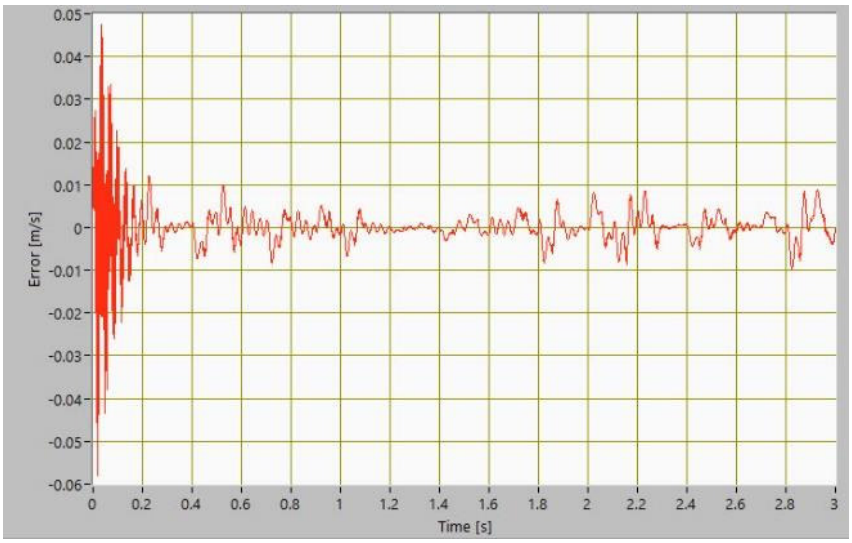

Fig. 8. System error variation

5. Conclusions

For laboratory applications that require closed-loop control, virtual instruments and data acquisition boards can be successfully used, without the use of controllers that can add additional costs.
The electrohydraulic system with speed regulation controller, made with a software application, can also be used for testing the dynamic performance of certain applications such as robotics, machinery drives, etc.
For industrial applications in the field of hydraulic actuations, numerical controllers implemented with the help of PLCs or industrial PID servo controllers can be used. The tuning of these controllers can be done by various methods such as Ziegler-Nichols, Cohen-Coon, etc. or with the help of PID tuning software.

Acknowledgments

This paper has been developed in INOE 2000-IHP, as part of a project co-financed by the European Union through the European Regional Development Fund, under Competitiveness Operational Programme 2014-2020, Priority Axis 1: Research, technological development and innovation (RD&I) to support economic competitiveness and business development, Action 1.2.3 – Partnerships for knowledge transfer, project title: *Development of energy efficient technologies in niche applications of the manufacture of on-demand mechanical-hydraulic subassemblies and maintenance of mobile hydraulic equipment*, project acronym: MENTEH, SMIS code: 119809, Financial agreement no. 6/25.06.2018, subsidiary contract no. 45/17.01.2022. The paper has been funded by the Romanian Ministry of Research and Innovation under

NUCLEU Programme, Financial Agreement no. 18N/2019, Ad 16/2022, Project code PN 19-18.01.01, Phase 12 “Research on the development of intelligent hydraulic control, adjustment and automation methods using standard electronic blocks and specific computer applications”. Financing has also been received under a project funded by the Ministry of Research, Innovation and Digitalization through Programme 1- Development of the national research & development system, Sub-programme 1.2 - Institutional performance - Projects financing the R&D&I excellence, Financial Agreement no. 18PFE/30.12.2021.

References

[1] Hu, Jing, Ming Liu, and Wei Li. “Position and Speed Double Closed Loop Control Performance of Electro-Hydraulic Actuator System Research Based on AMESim.“ *Applied Mechanics and Materials* 779 (July 2015): 220-225.

[2] Kalaiarasan, G., Giriraj Mannayee, Boopathi Marimuthu, S. Mayakoti, and K. Krishnamurthy. “Analysis of hydraulics actuator speed control using digital hydraulics.“ *International Journal of Mechanical Engineering and Technology (IJMET)* 8, no. 7 (July 2017): 213-224.

[3] Qu, Shaoyang, Federico Zappaterra, Andrea Vacca, Zifan Liu, and Enrique Busquets. “Design and Verification of An Open-Circuit Electro-Hydraulic Actuator System with An Integrated Electro-Hydraulic Unit.“ Paper presented at the The 13th International Fluid Power Conference 13. IFK, Aachen, Germany, March 21-23, 2022.

[4] Abou El-Azm Aly, A., M. Pascal, and R. Taher. “Experimental Study of Leakage Compensation for Actuator Speed Control in Electro-Hydraulic Systems.“ *International Journal of Engineering Research & Technology (IJERT)* 4, no. 12 (December 2015): 129-138.

[5] Rydberg, Karl-Erik. *Feedbacks in Hydraulic Servo Systems*. IEI / Fluid and Mechanical Engineering Systems, Linköpings Universitet, 2008.

[6] Hu, Dongming, Shoubao Ding, Huaiqiu Zhu, Bing Xu, and Huayong Yang. “Velocity-tracking Control of the Variable-speed Controlled Hydraulic System: Using Compound Algorithm of PD & Feedforward-feedback Control.“ Paper presented at the Third International Conference on Measuring Technology and Mechatronics Automation ICMTMA, Shanghai, China, January 6-7, 2011.

ISSN 1454 - 8003
Proceedings of 2022 International Conference on Hydraulics and Pneumatics - HERVEX
November 9-10, Băile Govora, Romania

PREDICTIVE MONITORING OF HORIZONTAL AXIS WIND TURBINE ROTOR BLADES STRENGTH

Prof. PhD. Dr.Sc. **Viorel BOSTAN**[1], Prof. PhD. Dr.Sc. **Valeriu DULGHERU**[1,*], Assoc. prof. PhD. **Marin GUȚU**[1]

[1] Technical University of Moldova

* valeriu.dulgheru@bpm.utm.md

Abstract: *Wind turbine blades are subjected to complex environmental and mechanical loads during the operating period. To reduce and optimize maintenance costs, a detailed understanding of the degradation and failure mechanisms of wind turbines is required. This is important for reliable prediction of failure events, planning of maintenance activities and mitigation of degradation processes. The paper presents the main failures of mega wind turbine blades, their analysis methods, performing extensive numerical modeling of a blade and determining areas with stress and deformation concentrations, establishing with higher precision the location of critical areas in order to implement the predictive monitoring system of the wind turbine blades state.*

Keywords: *Wind turbine, blade, numerical modeling, stresses, strains, predictability*

1. Introduction

Wind turbine blades are subjected to complex environmental and mechanical loads during their service life, including cyclic deformation, precipitation, erosive particles, freezing, high humidity and temperature variations, but also extraordinary events such as shipping damage, bird strikes and electric discharges [1, 2]. To reduce and optimize maintenance costs, a detailed understanding of the degradation and failure mechanisms of wind turbines is required. This is important for reliable prediction of failure events, planning of maintenance activities and mitigation of degradation processes. For wind turbine blades, life extension is one of the best strategies for using them after 25 years of operation.
However, accidents involving structural failures of wind turbine blades are not uncommon. It is reported [2] that, with approximately 700,000 blades in service globally, there are an average of 3800 blade failure incidents each year.

2. Wind turbine blades failure mechanisms

2.1 Methods of analyzing the failure mechanisms of wind turbine blades

Wind turbine blade damage can be classified as surface damage (surface microcracks and coatings), resin and/or interface damage (delamination, resin defects), and structural element damage (fiber breakage or bending) [1,2]. Surface defects can be caused by erosion (caused by rain, sand and hail) or impacts with small objects. The damaged and rough surface reduces the aerodynamic performance of the blade. It does not disrupt the operation of the wind turbine, but surface defects grow and can lead to structural damage of the blade.
In general, the failure mechanisms of wind turbine blades are analyzed using the following main methods:

- post-destruction analysis of damaged blades;
- full-scale testing of blades in laboratories with video observation and structural condition monitoring;
- analysis of databases and collection of incident reports;
- direct monitoring of blade deformation and degradation during operation (e.g. using non-destructive testing and structural condition monitoring methods);

- testing the design of sub-components (e.g. beam), reproducing parts or elements of the blades (e.g. joints or sandwiches);
- computational modeling of blade deformation and damage.

Direct monitoring of wind turbine blade deformation and damage can be performed using non-destructive testing methods and structural health monitoring methods [3]. Sensors are attached or embedded in the blades and deformation and damage events are monitored. While structural health monitoring is typically developed for blade control, it can also be used to understand failure mechanisms. Such experiments are undertaken to investigate blade surface erosion. A more detailed analysis is provided in the paper [3].

While **computational modeling of wind turbine blade degradation** is one of the most effective approaches to failure mechanism analysis, the models typically include some predefined and assumed damage mechanisms. For example, a static analysis is done to establish the critical area of the blade and then fatigue crack propagation in that area is simulated.

Computational models are quite efficient and have a wide range of applications. However, their application requires a prior knowledge of the expected damage mechanisms.

2.2 The critical areas of the wind turbine blade

Several segments of wind turbine blades are particularly susceptible to degradation. Among them, the segments subjected to the most intense loads (tip and leading edge), transition sectors (for example, the transition zone from the cylinder to the aerodynamic surface and the transition of the composite layer to a lower thickness), interface portions (with adhesive layers, e.g. trailing edge). According to research [4] the most affected areas of the blade are: near the root (30–35% of the chord length from the root) and near the tip (70% in the chord length from the root of the blade), the root of the blade, the trailing edge on the high pressure side and leading edge.

The main damage mechanisms in critical areas:

Blade tip. Because the tip velocity is the highest, the erosion and resulting damage to the leading and trailing edges is much more intense near the tip. Moreover, lightning can strike the blades near the tip and cause the skin to separate near the tip or from the spar [5].

Leading edge. As a rule, it is subjected to raindrops, hail, sand and frequent impacts. If surface erosion is not repaired quickly, it can lead to laminates cracking or allow water to enter the bonding area [5].

Trailing edge. The trailing edge of wind turbine blades can fail by peeling of the adhesive joint (e.g. due to peel stresses) and/or by buckling of the sandwich panels. Buckling can lead to final failure of the adhesive joint on the running board at much lower than maximum loads.

Areas of thickness transitions, hub portion: Other potentially damaging sectors are in the transition zone from circular section to airfoil, due to the sudden transition from thick laminate to fine geometry and large laminated panels in the area of the maximum chord section that can be susceptible to buckling [5].

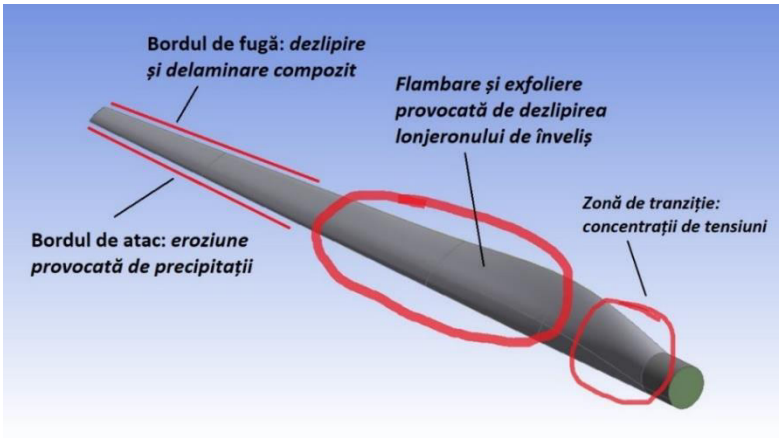

Fig. 1. The locations of the damage mechanisms of a wind turbine blade

Adhesive joints/Bond Lines: The leading and trailing edge joints between the skin and the internal stiffeners can deteriorate or peel off, leading to buckling of the structures [5]. Blade destruction can occur if the spar detaches from the skin and buckles. According to [4], the blade failure mechanism most often observed are transverse cracks in the area of the maximum chord section (initiated as a detachment of the outer layer from the sandwich core) and detachment of the stiffening ribs from the blade shell in

the transition zone from base (triggered by peel stresses on the adhesive bonding portions). These effects are amplified by manufacturing defects and blade torsional stresses [4]. Figure 1 shows a sketch of the locations of commonly observed damage mechanisms of a wind turbine blade.
Thus, the most endangered sectors of the blades of a wind turbine are the protruding parts (tip, trailing edge), areas with transition sections and those where structural elements are bonded. Fortifying these areas can significantly increase the durability and service life of wind turbine blades.
Figure 2 shows some images of damaged wind turbines with the power of over 1 MW. As can be seen, the location of blade damage is in the buckling zone, at a distance between 0.3 and 0.5 of the rotor radius. According to the research results presented by the authors [2] blade failures occur most of the time in operating conditions that fall within nominal parameters such as wind speed and operating period. Such destructions are consequences of non-compliance with manufacturing technology. Good interaction between material selection, structural design and manufacturing process is required to improve the structural integrity of blades.

Fig. 2. Location and appearance of damage on operating wind turbine blades

A finite element calculation model of the strength of a typical blade is presented below. The purpose of this numerical simulation of blade stress conditions is to establish the critical areas and determine the equivalent stresses and strains.

3. Numerical modeling of a blade and determination of stress and strain concentration areas

The rotor geometry designed in SolidWorks software was then imported into the DesignModeler program in the ANSYS Workbench environment where the fluid domain was created. To simplify CFD (Computational fluid dynamics) analysis and to save calculation time, 1/3 of the entire domain was modeled.

Table 1: Constructive-functional parameters of the analyzed rotor

Nominal power, MW	1.5 - 3
Nominal rotor speed, min-1	18 - 20
Wind speed, m/s	10 - 20
Rotor diameter, m	83
Variation of shell and spar thickness, m	0.1 – 0.005

A CFD volume including 120° of the rotor was created with a single blade assuming periodic conditions. At the same time, the tower and the ground were neglected. The dimensions of the computational fluid domain were chosen taking into account the best practices and recommendations presented in research [6, 7] to ensure free flow without influencing the domain boundaries. A typical wind turbine rotor with the following input parameters was considered for the simulations (table 1).
To simplify the structural analysis it has been assumed that the composite material can be homogenized by the following orthotropic material properties, Table 2. These values are representative of the properties of composite materials used in real wind turbine blades.

Table 2: Properties of the used material

Density (kg/m^3)	*1550*
Young-X Modulus (Pa)	*1.1375E+11*
Young-Y Modulus (Pa)	*7.583E+09*
Young-Z Modulus (Pa)	*7.583E+09*
Poisson's ratio-XY	*0.32*
Poisson's ratio-YZ	*0.37*
Poisson's ratio-XZ	*0.35*
Shear Modulus-XY(Pa)	*5.446E+09*
Shear Modulus-YZ (Pa)	*2.964E+09*
Shear Modulus-XZ (Pa)	*2.964E+09*

Among all the simulation steps, the finite element mesh generation step is the most important. The accuracy of the numerical calculation is determined, first of all, by the quality of the mesh, the density and distribution of nodes in key areas of the computational domain. Such area is near the blade surface where the boundary layer forms. In these areas the elements have been properly refined to correctly capture the strong variations in the flow parameters. Also, transitions from fine mesh to coarse mesh areas have been handled carefully, as too abrupt a transition can alter the accuracy of the calculation. The fluid domain was divided into ~3000 000 elements.

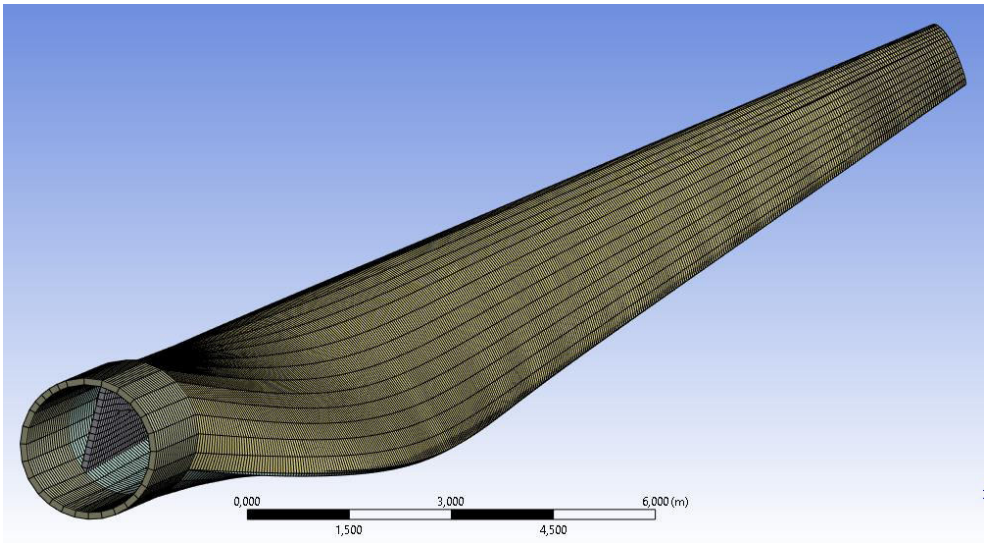

Fig. 3. Wind turbine blade mesh details

This value was accepted according to the mesh refinement study presented in the research [8]. Details of the blade shell discretization are shown in figure 3. The rotor was simulated under different boundary conditions, such as wind speed of 10 - 20 m/s and rotation speed corresponding to the nominal one 18 - 20 min^{-1}. To check the correctness of the settings, Fig. 4 illustrates the velocity vectors distributed over the blade surface at the nominal speed of 18 min^{-1} (wind speed of 10 m/s).
The air pressure variation diagram passing through the rotor was also drawn, Fig. 5. This corresponds to the physical model according to indications of the researchers [8].

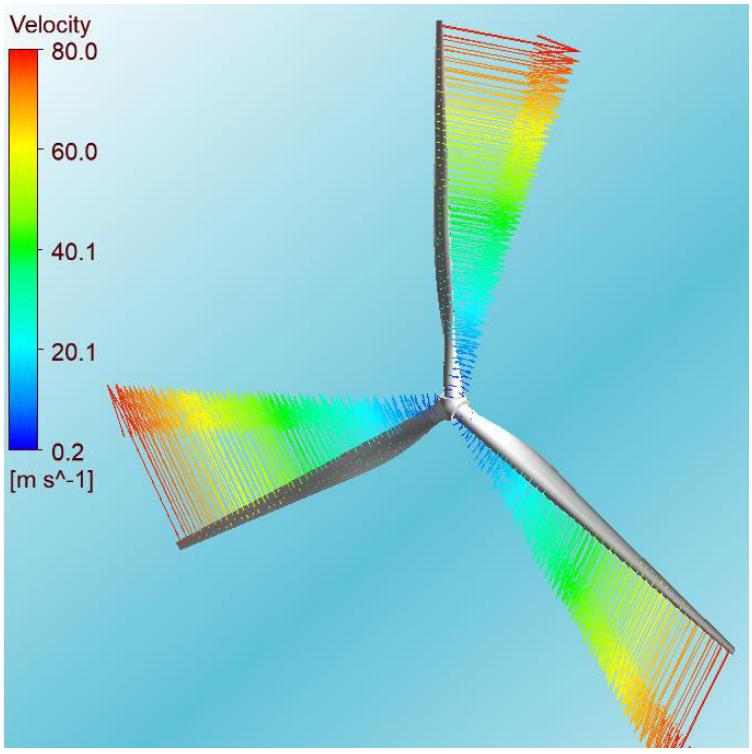

Fig. 4. Wind turbine rotor model simulated at 10 m/s wind speed

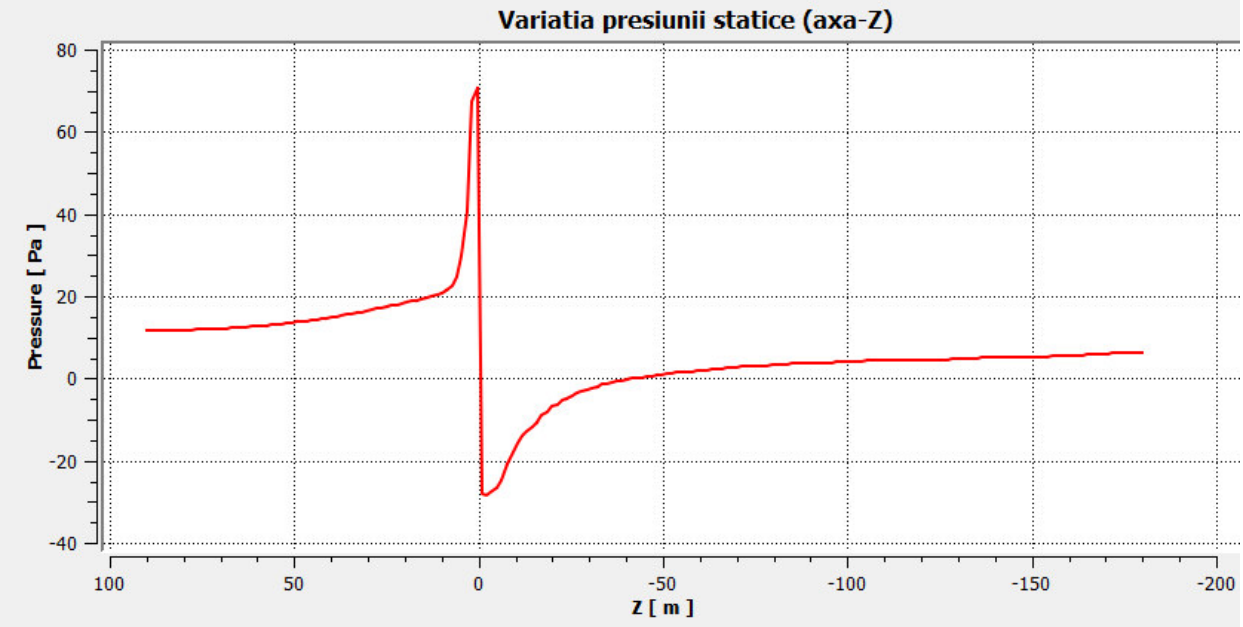

Fig. 5. Variation of air pressure in the turbine rotor section

Figure 6 shows the pressure distribution on the blade surface at the wind speed of 10 m/s. Such pressure distribution obtained as a result of aerodynamic effects for the whole range of wind speeds was considered as the main task in the calculation model. Thus, the blade is subjected to complex bending-torsional stresses. Compared to the real loads that include the gravity, in the simulations it was neglected.

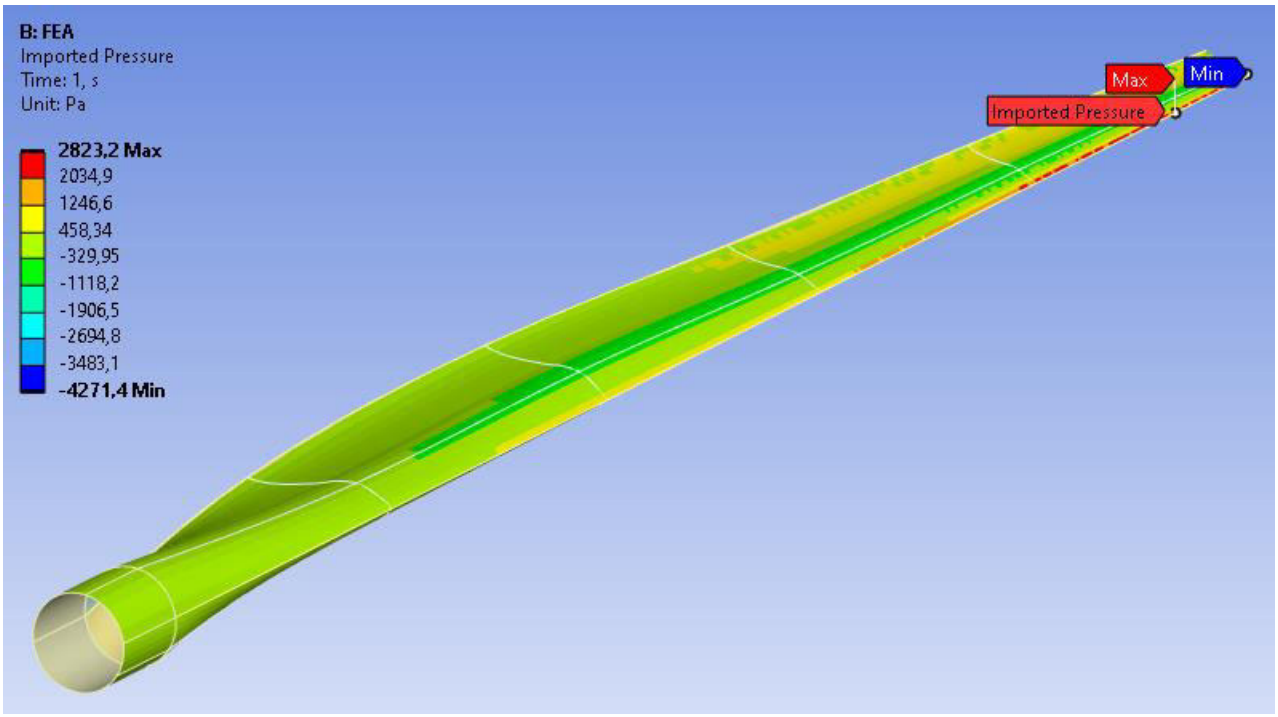

Fig. 6. Fluid pressure distribution on the blade surface

After performing the blade simulations, the results of interest were extracted. The distribution of the equivalent stresses (von-Misses) and the location of the concentrations are shown in figure 7. These are the maximum values (≈ 48 MPa) corresponding to the wind speed of 16 m/s. For the nominal wind speed (≈ 11 m/s) the value of the equivalent stresses is ≈ 35 MPa. For comparison, the tensile strength of the epoxy resin adhesive used in the blades structures is 30 – 40 MPa. It is obvious that the operation of the wind turbine at slightly higher than nominal wind speeds must be limited.

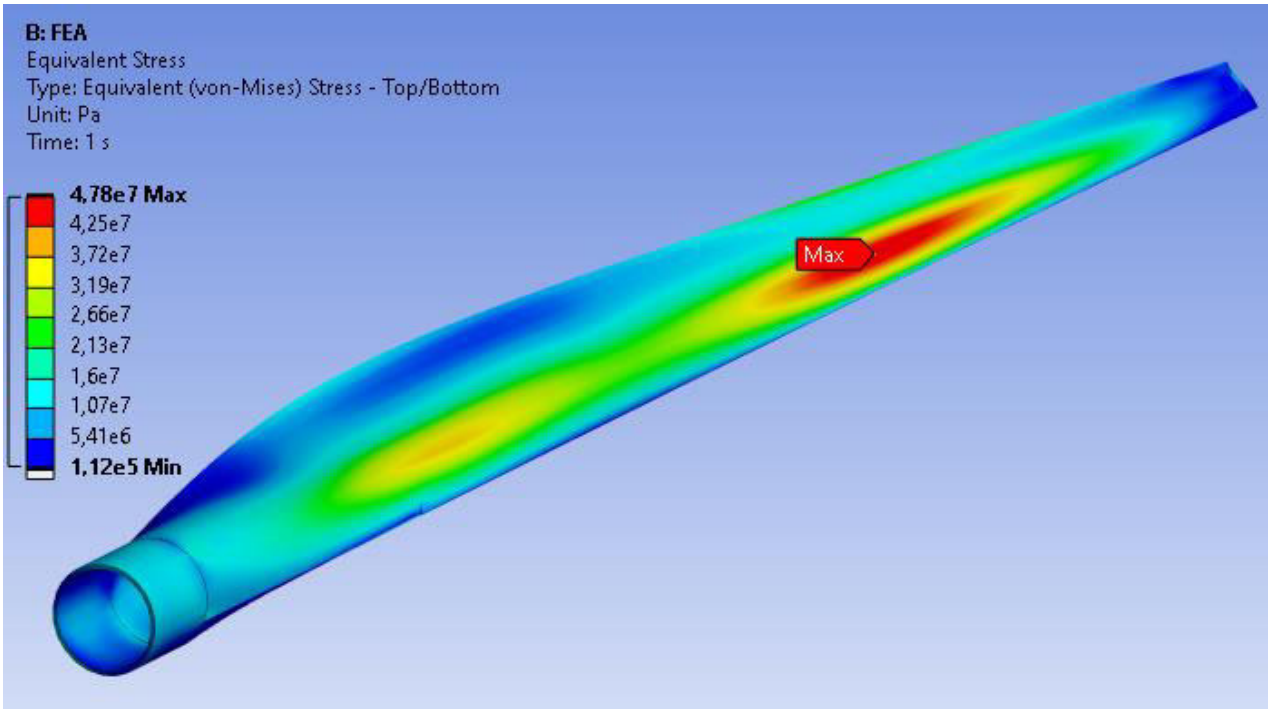

Fig. 7. Equivalent (Von-Mises) stresses distribution on the blade shell

Figure 8 shows the equivalent elastic strain in the blade shell and certain locations where concentrations occur. An illustrative case is presented for wind speed V =12 m/s. For the other wind speeds the locations of the critical areas are the same.

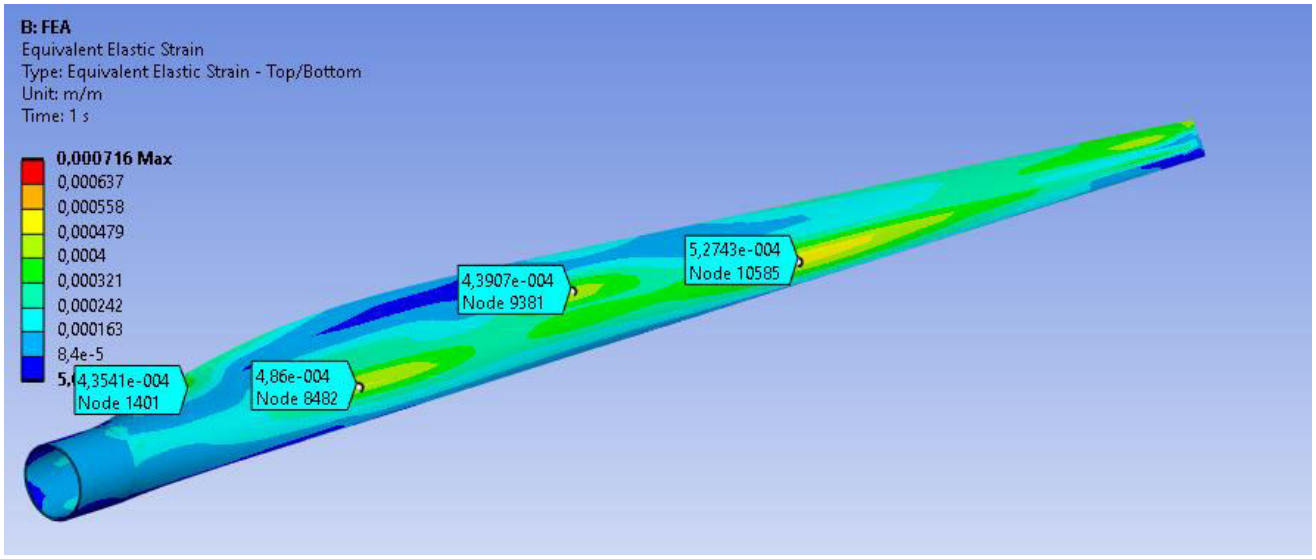

Fig. 8. Equivalent elastic strain distribution (a case for V =12 m/s)

Below is a diagram containing all the values of the equivalent elastic strain depending on the wind speed, figure 9. The distribution of the equivalent elastic strain in the blade shell is presented for the minimum and maximum values that coincide with the locations along the longitudinal axis (radius rotor – 0.17r and 0.68r). The diagram also shows the wind turbine rotor power values obtained from the relationship: P = ω ·T, where ω = 2 rad/s is kept constant at wind speeds greater than 12 m/s, and T – the torque developed by the turbine rotor depending on the wind speed.

Fig. 9. Results diagram of wind turbine blade simulation

Determination of the critical areas with higher precision for a particular blade model requires the direct simulation of it. However, with the help of the information in Figures 1, 2 and 8, priority locations can be established in order to implement the wind turbine blade condition predictive monitoring system.

References

[1] Mishnaevsky, L., Jr. "Root Causes and Mechanisms of Failure of Wind Turbine Blades: Overview." *Materials (Basel)* 15, no. 9 (April 2022): 2959. https://doi.org/10.3390/ma15092959.

[2] Chen, X. "Fracture of wind turbine blades in operation - Part I: A comprehensive forensic investigation." *Wind Energy* 21, no. 11 (November 2018): 1046– 1063. https://doi.org/10.1002/we.2212.

[3] McGugan, M., and L. Mishnaevsky, Jr. "Damage Mechanism Based Approach to the Structural Health Monitoring of Wind Turbine Blades." *Coatings* 10, no. 12 (2020): 1223. https://doi.org/10.3390/coatings10121223.

[4] Jensen, Find, et al. *Cost and Risk Tool for Interim and Preventive Repair (CORTIR)*. Bladena Report. EUDP Project 64018-0507 – Final Report, 2021.

[5] Robinson, C. M. E., E. S. Paramasivam, E. A. Taylor, A. J. T. Morrison, and E. D. Sanderson. *Study and Development of a Methodology for the Estimation of the Risk and Harm to Persons from Wind Turbines.* London, Health and Safety Executive, 2013.

[6] Wang, Z., G. C. Tsai, and Y. B. Chen. "One-Way Fluid-Structure Interaction Simulation of an Offshore Wind Turbine." *International Journal of Engineering and Technology Innovation* 4, no. 3 (2014): 127-137.

[7] Kelele, Hailay Kiros, Torbjørn Kirstian Nielsen, Lars Froyd, and Mulu Bayray Kahsay. "Catchment Based Aerodynamic Performance Analysis of Small Wind Turbine Using a Single Blade Concept for a Low Cost of Energy." *Energies* 13, no. 21 (2020): 5838. https://doi.org/10.3390/en13215838.

[8] Lachance-Barrett, S., and E. Corona. "Wind Turbine Blade FSI (Part 1) - Numerical Solution." September 27, 2019. Accessed October 12, 2022. *Fluent Learning Modules*. https://confluence.cornell.edu/.

ISSN 1454 - 8003
Proceedings of 2022 International Conference on Hydraulics and Pneumatics - HERVEX
November 9-10, Băile Govora, Romania

EXPERIMENTAL ACHIEVEMENTS IN THE FIELD OF DIGITAL HYDRAULICS

Bogdan Alexandru TUDOR[1,*], Ștefan Mihai ȘEFU[1], Radu Iulian RĂDOI[1], Ioan PAVEL[1]

[1] National Institute of Research & Development for Optoelectronics / INOE 2000 – Subsidiary Hydraulics and Pneumatics Research Institute

* btudor.ihp@fluidas.ro

Abstract: *Digital hydraulic actuation systems have had a resounding success in the scientific world since the beginning and have had good results, regarding the degree of intelligence, integration, energy losses, etc. In recent years, the phenomenon has gained momentum and attracted more and more researchers to this field, and with them, the interest of companies to introduce such systems to the market has also developed. In this work, the authors intend to review the achievements in Romania in this field and bring a national update of the level of knowledge of the field.*

Keywords: *Digital hydraulics, energy efficiency*

1. Introduction

Hydraulic systems developed rapidly starting with the 20th century, along with the evolution of microprocessor technology, so that hydraulic systems could integrate microprocessors, electro power amplifiers and sensors, in order to improve dynamic control, intelligence and reliability. With the entry into the 21st century, the huge cost of labor and energy forced the industry to develop in the direction of energy conservation and increasing the degree of intelligence of the systems. However, the cost of hydraulic equipment and low energy efficiency are key factors that limit the development of this field and future applications. In addition, with the introduction of the concept of Industry 4.0 by Germany in 2013, there was even more pressure for industrial hydraulic systems to be even smarter and to be integrated into the concept of the Intelligent Factory [1].
Considering all these general trends, if hydraulic systems want to survive in this competition on the industrial market, they must inevitably develop in the direction of high energy efficiency and low acquisition cost, and digital hydraulics offers the possibility to achieve this.

2. Definition of digital hydraulics

The definition of digital hydraulics is still not a stable one, and the current definitions can only partially reflect the characteristics of digital hydraulics, so the definition of digital hydraulics can be ambiguous.
That being said, the definition of digital hydraulics is based on the views of researchers around the world. We define digital hydraulics as a system that realizes an active and intelligent control of the system output. Hydraulic components with such technical characteristics can be defined as digital hydraulic components. In addition, the essential feature of digital hydraulics is intelligent control; technology that can only achieve on/off control cannot be classified as digital hydraulics.
Digital hydraulics is defined by the active control of the system outputs of a hydraulic component (directional valve, pump, actuator). Digital hydraulics is not limited to digital control of analog components, but relies on intelligent control using PWM (Pulse Width Modulation) signals and achieving flow and speed adjustments using the on/off directional valve, coded either PNM (Pulse Number Modulated), or PCM (Pulse Code Modulated).

3. Types of digital hydraulics

Digital hydraulics is divided into two categories, the parallel digital hydraulics and the switching one,

as well as that with a stepper motor, which comes as a subdivision of digital switching hydraulics.

3.1. Digital hydraulics in parallel and switching

At the European level, two types of digital hydraulics are known, the parallel one, developed by the University of Tampere in Finland, under the leadership of Matti Lindjama [2] and digital switching hydraulics, developed at the University of Linz in Austria under the leadership of Rudolf Scheidl [3].
Digital hydraulic systems in parallel are realized by connecting the components in parallel, and the value of the flow passing through each component must be in the progression made by one of the PNM (Pulse number Modulated) and PCM (Pulse Coded Modulated) series.
Digital hydraulic systems in parallel have a fixed number of discrete outputs that depend on the nature of the components and do not require continuous switching of the components between the closed and the open position.
On the other hand, the digital switching hydraulics uses components that can quickly switch between the closed and the open position, in order to obtain a discrete adjustment of the flow at the exit from the system. The high-frequency switching of digital switching systems is performed with a PWM (Pulse Width Modulated) signal.

3.1.1. Stepping digital hydraulics

These digital hydraulic systems use a precise stepper motor controlled by discretely modulated digital signals. The rotation of the stepping motor is transmitted to the directional valve spool through a mechanical structure, so that a discrete adjustment of the flow rate is obtained in order to realize the intelligent control of the output from the system.
Because the stepper motor has no accumulated error and almost no hysteresis, the digital stepping directional valve has higher spool movement accuracy. Four typical forms of stepping digital hydraulic directional valve are shown in Fig. 1.
However, the stepping motor produces rotary motion, which must be converted into linear motion to drive the spool. Therefore, conversion mechanisms such as cam and ball screws are indispensable. However, all conversion mechanisms have high friction and inertia, which act on the frequency response characteristics of a stepping digital hydraulic directional valve. In addition, the stepping motor is prone to overstepping at high frequency. These problems limit the application of these methods and it is a much more difficult method to implement than the digital switching hydraulics proposed by Rudolf Scheidl.

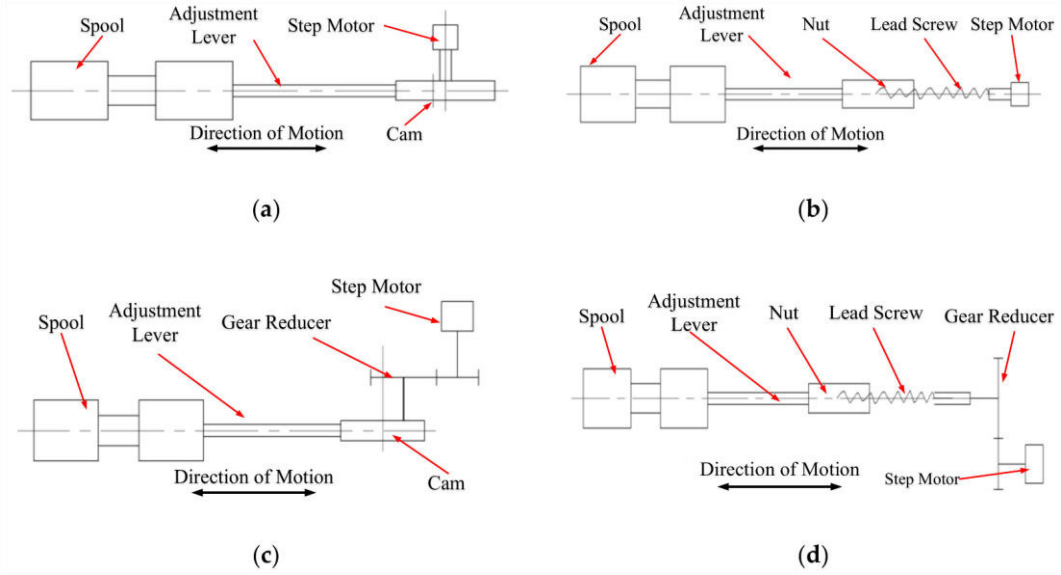

Fig. 1. Four typical forms of stepping digital hydraulic valves

4. Digital hydraulic equipment developed in National Institute of Research & Development for Optoelectronics / INOE 2000 – Subsidiary Hydraulics and Pneumatics Research Institute (IHP)

Within the Research and Development Institute INOE 2000 - IHP, the authors have until now developed various digital hydraulic systems, some up to the concept level, others up to the demonstrator level, and in the following these systems will be presented.

4.1. DFCU with five binary coded directional valves

DFCU shown in Fig. 2 consists of the following components: internal combustion engine marked M; fixed flow pump (HP); hydraulic accumulator (HA); 2/2 directional valve (DV6); 5 directional valves (on/off) DV1- DV5 type 2/2, which are transited by different flow rates in binary progression; the directional valve DV7 type 4/2 that changes the direction of rotation of the hydraulic motor; HM hydraulic motor; FM flow transducer; PT pressure transducer; F filter, and PLC that controls the operation of the entire system.

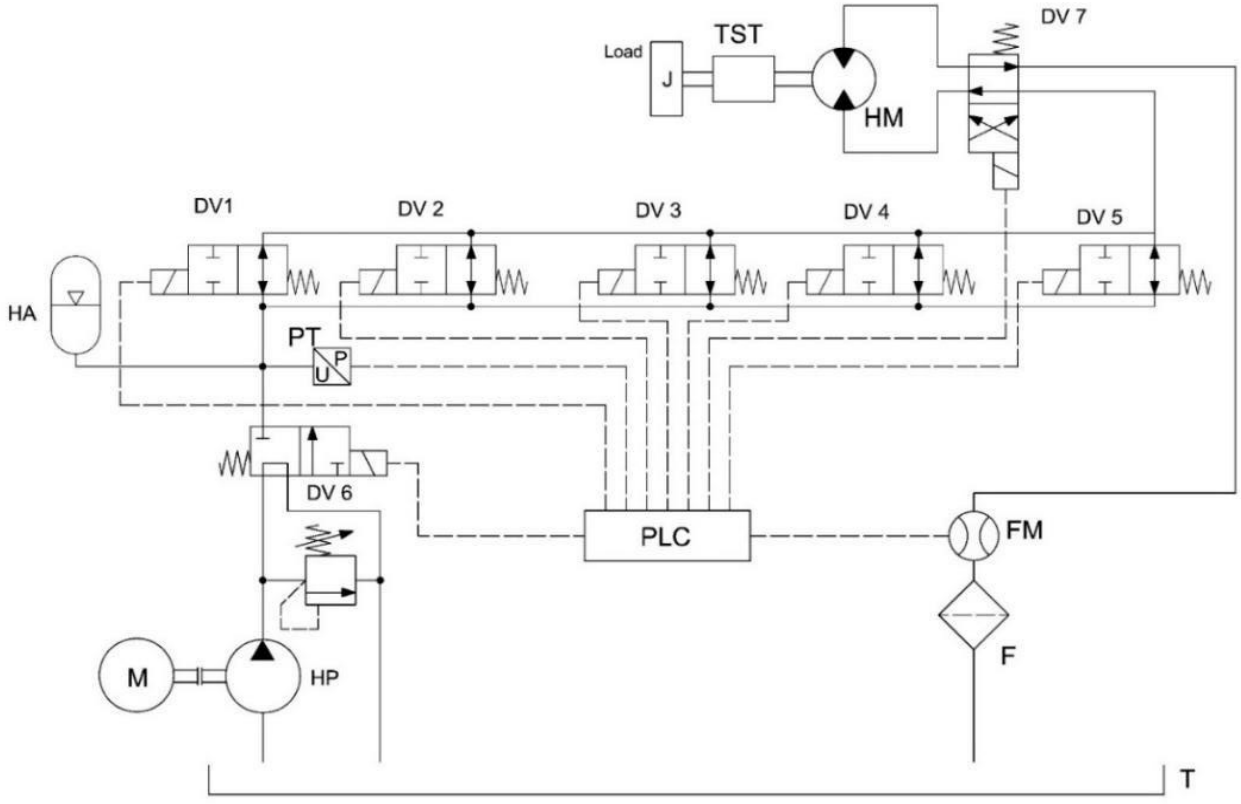

Fig. 2. DFCU with 5 binary coded directional valves [4]

The status of each directional valve and the achieved flow rate for each of the 31 adjustment steps can be seen in Table 1.

Table 1: The status of each directional valve and how to obtain the 31 adjustment steps

Q State	q=2 [l/min]	q=4 [l/min]	q=8 [l/min]	q=16 [l/min]	q=32 [l/min]	Qt [l/min]
0	-	-	-	-	-	0
1	+	-	-	-	-	2
2	-	+	-	-	-	4
3	+	+	-	-	-	6
4	-	-	+	-	-	8
5	+	-	+	-	-	10
6	-	+	+	-	-	12
7	+	+	+	-	-	14
8	-	-	-	+	-	16
9	+	-	-	+	-	18
10	-	+	-	+	-	20
11	+	+	-	+	-	22
12	-	-	+	+	-	24
13	+	-	+	+	-	26
14	-	+	+	+	-	28
15	+	+	+	+	-	30
16	-	-	-	-	+	32
17	+	-	-	-	+	34
18	-	+	-	-	+	36
19	+	+	-	-	+	38
20	-	-	+	-	+	40
21	+	-	+	-	+	42
22	-	+	+	-	+	44
23	+	+	+	-	+	46
24	-	-	-	+	+	48
25	+	-	-	+	+	50
26	-	+	-	+	+	52
27	+	+	-	+	+	54
28	-	-	+	+	+	56
29	+	-	+	+	+	58
30	-	+	+	+	+	60
31	+	+	+	+	+	62

4.2. Digital switching directional valve

The directional valve developed for digital switching hydraulics is composed of the electromagnet (2) supplied with an electrical signal through the connector (1), which is attached to the steering valve body (4) by four screws (3). The coil is marked with the position (5) and the position of the return spring (6) is located depending on the construction version (NC - normally closed, Fig. 3.a, or NO - normally open, Fig. 3.b) towards the electromagnet or at the opposite end of the electromagnet. In the picture one can also see the spring plate (7) and nut (8) for the NC version.

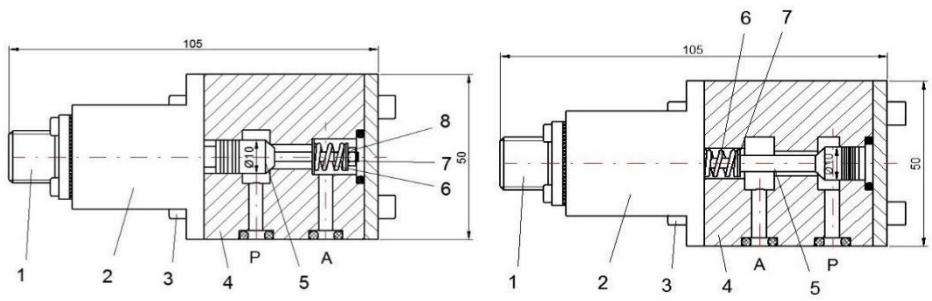

a. b.

Fig. 3. Variants of digital switching hydraulic directional valve - a. normally closed, and b. normally open [5]

4.3. DHPS – Digital Hydraulic Pumping System

The hydraulic system (Fig. 4) uses 4 fixed flow coaxial pumps connected to an electric motor (3). Pump selection is done with a normally open on/off directional valve (6). When one of the on/off directional valves is switched to the closed position, the flow is directed from the tank to the consumer through the directional valve (7). The safety valve (8) provides system overload protection. Each directional valve is transited by a different flow (Q1, Q2, Q3, Q4) from which we can select for the system one, two or even all of them to achieve flow regulation with the help of a programmable logic controller (9) (P.L.C.).
Q1 = First pump with the flow displacement of 4 cm^3/rev
Q2 = Second pump with the flow displacement of 8 cm^3/rev
Q3 = Third pump with the flow displacement of 16 cm^3/rev
Q4 = Forth pump with the flow displacement of 32 cm^3/rev.

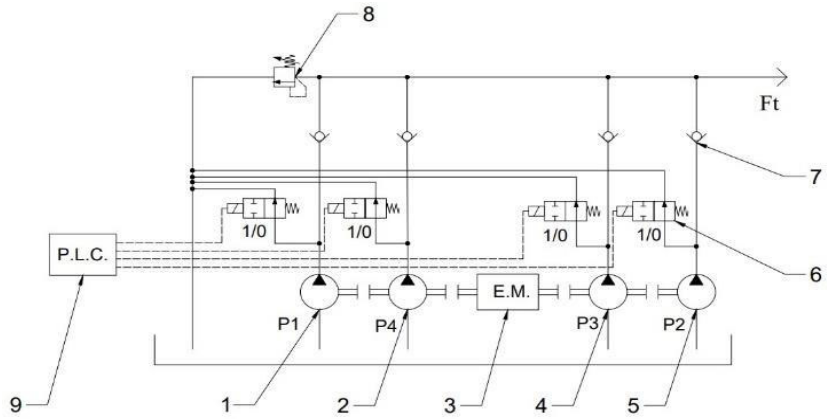

Fig. 4. Hydraulic system with four fixed displacement pumps consists in: (1, 2, 4, 5) fixed displacement pumps, (3) biaxial electric motor, (6) 2/2 directional valve, (7) one-way valve, (8) pressure relief valve

4.4. VDLA – Variable Displacement Linear Actuator Hybrid with binary coded surfaces

The hybrid VDLA (Fig. 5) was so named because its construction uses two types of coding, namely PNM coding and PCM coding, and consists of a large diameter piston (13), driven by 9 smaller diameter pistons (4) positioned symmetrically around the axis of the main piston (13), and their operation is carried out according to the table below.

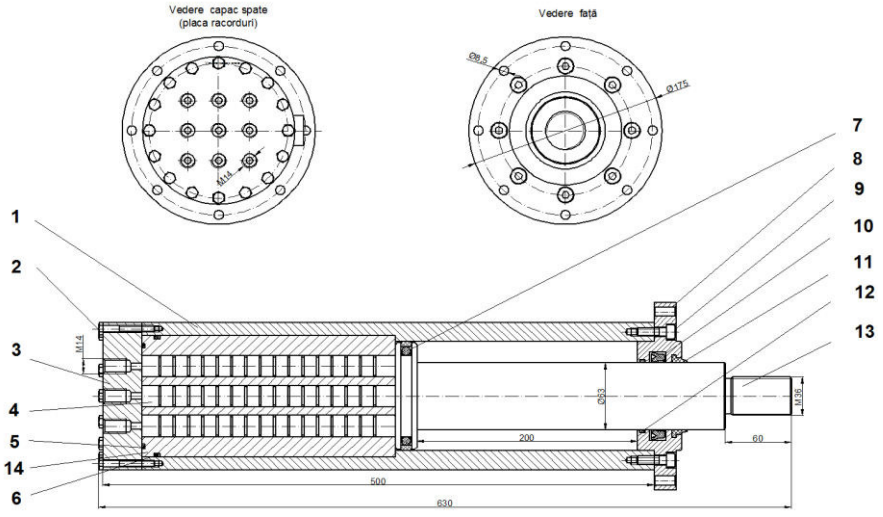

Fig. 5. VDLA Hybrid with binary coded surfaces [6]

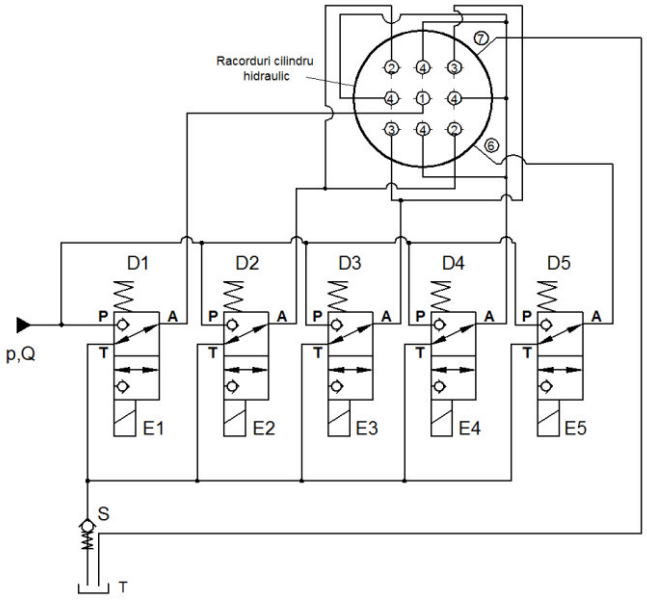

Fig. 6. Hybrid VLDA actuation diagram consists in: 5 2/2 directional valves (D1, D2, D3, D4, D5), 1 one way valve (S), and the VDLA

Table 2: The state of each directional valve depending on the desired setting

Elmg. Motion	E1	E2	E3	E4	E5
Advance 1	+	-	-	-	-
Advance 2	-	+	-	-	-
Advance 3	+	+	-	-	-
Advance 4	-	-	-	+	-
Advance 5	+	-	-	+	-
Advance 6	-	+	-	+	-
Advance 7	+	+	-	+	-
Advance 8	-	+	+	+	-
Advance 9	+	+	+	+	-
Withdrawal	-	-	-	-	+

4.5. VDLA with three binary coded surfaces

VDLA with three concentric zones, binary coded, thus, A2 = 2A1, A3 = 2A2, thus obtaining 23-1 = 7 different variations of force and speed. This type of VDLA allows by separately supply the 3 concentric zones, using on/off type directional valves, to obtain a relatively linear force and speed variation curve.

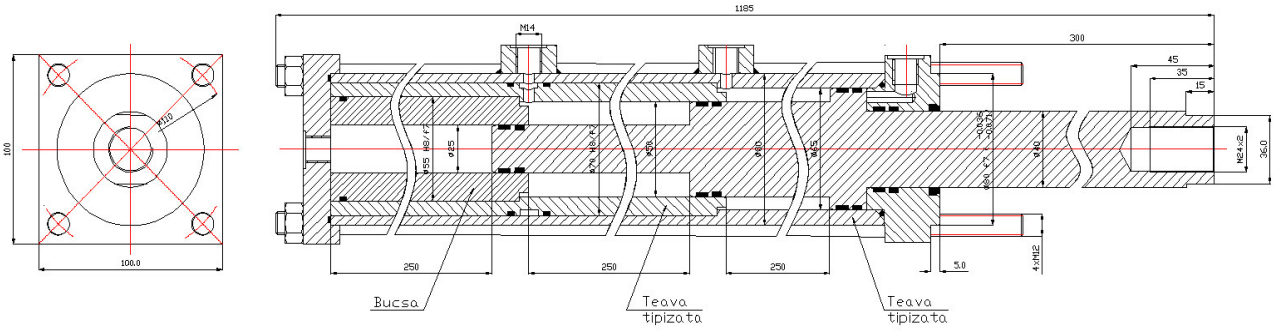

Fig. 7. VDLA with 3 binary coded surfaces

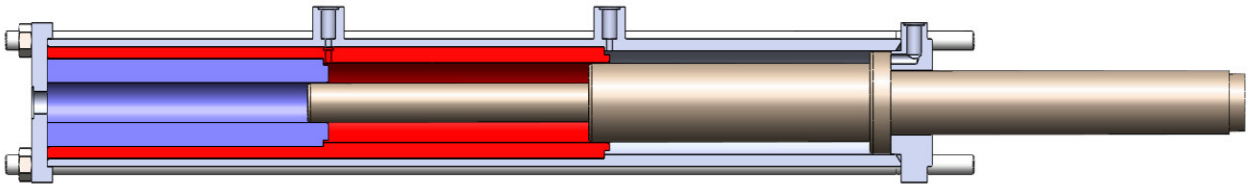

Fig. 8. Section through VDLA, where one can see the three chambers colored with blue, red and gray

Table 3: The variation of the three surfaces of the VDLA

The cylinder with three surfaces binary multiplied		The cylinder with three surfaces with typical diameters	
Area [cm²]	Diameter [mm]	Area [cm²]	Diameter [mm]
4.906	25	4.906	25
9.812	43.3	14.712	50
19.624	61.24	19.503	65

5. Conclusions

The development of digital hydraulic systems is on an upward slope at the moment and they are becoming more and more appreciated in the field.
From year to year, more and more articles and solutions appear in this field both in the country and worldwide. Digital hydraulics is a modern, reliable solution with a low purchase cost compared to classic hydraulic solutions.
Digital hydraulics reduces energy losses as it can deliver the necessary flow to the work point without the need for additional adjustments and sending energy-carrying flows to the tank.
At this moment, some of these systems are already implemented in the industry and we expect that in the coming years their number will increase considerably and they can be directly purchased from traditional manufacturers of hydraulic equipment.

Acknowledgments

This paper has been financed under a project funded by the Ministry of Research, Innovation and Digitalization through Programme 1- Development of the national research & development system, Sub-programme 1.2 - Institutional performance - Projects financing the R&D&I excellence, Financial Agreement no. 18PFE/30.12.2021.

References

[1] Zhang, Qiwei, Xiangdong Kong, Bin Yu, Kaixian Ba, Zhengguo Jin, and Yan Kang. "Review and Development Trend of Digital Hydraulic Technology." *Applied Sciences* 10, no. 2 (2020): 579. https://doi.org/10.3390/app10020579.

[2] Scheidl, Rudolf, Matti Linjama, and Stefan Schmidt. "Is the future of fluid power digital?" *Proceedings of the Institution of Mechanical Engineers, Part I: Journal of Systems and Control Engineering* 226, no. 6. (2012): 721-723. doi:10.1177/0959651811435628.

[3] Messner, F., and R. Scheidl. "Development and experimental results of a small fast switching valve derived from fuel injection technology." Paper presented at the Eighth Workshop on Digital Fluid Power (DFP16), Tampere, Finland, May 24-25, 2016.

[4] Șefu, Ștefan Mihai, Bogdan Alexandru Tudor, Radu Iulian Rădoi, Ioan Bălan, and Mario Cristea. "Optimizing consumption in agricultural machines and installations by using digital hydraulics." *Acta Technica Corviniensis – Bulletin of Engineering* XV, Fascicule 3 (July – September 2022): 111-116.

[5] Drumea, P., R. Rădoi, B. Tudor, Al. Hristea, and I. Bălan. "Normally closed switching valve for high frequency." Paper presented at the 22nd Int. Conf. on Hydraulics and Pneumatics Hervex, Baile Govora, Romania, November 9-11, 2016.

[6] Drumea, P., I. Pavel, G. Matache, and I. Bălan. "Digital linear hydraulic motors." Paper presented at the 23rd Int. Conf. on Hydraulics and Pneumatics Hervex, Baile Govora, Romania, November 8-10, 2017.

ISSN 1454 - 8003
Proceedings of 2022 International Conference on Hydraulics and Pneumatics - HERVEX
November 9-10, Băile Govora, Romania

MECHATRONICS - TECHNOLOGY COMPATIBLE WITH THE INFORMATION SOCIETY

Prof. PhD. Dr.Sc. **Valeriu DULGHERU**[1,*]

[1] Technical University of Moldova

* valeriu.dulgheru@bpm.utm.md

Abstract: *We are witnessing the dawn of the Fourth Industrial Revolution, generically called Industry 4.0. The paradox of progress - it's something completely unexpected: we get more and more from less, a phenomenon called dematerialization. One of the important achievements of this phenomenon are the mechatronic products, designed as systems not components.*
Mechatronic technology brings to the center of attention the problem of information, which is the dominant component in relation to the other components (material and energy). Arguments: information ensures the satisfaction of man's spiritual needs; only information increases the newly added value of all things; information is culture.

Keywords: *Mechatronics, dematerialization, system design, transdisciplinary*

1. Introduction

"The strongest argument for the integration of disciplines
is the very fact that life is not divided by subject".
(J. Moffett)

The 21st century marked the beginning of the Knowledge Society with the following dimensions: Social, Educational, Environmental, Cultural, Economic. As a consequence of this Knowledge Society according to a considerable number of personalities we are witnessing the dawn of the Fourth Industrial Revolution, generically called Industry 4.0 with its basic components (intelligent autonomous robots, simulation and prototyping, virtual reality, 3D printing/additive manufacturing, culture E Integration and processes, cyber-physical systems, Internet of things, technologies Data centers, cloud computing). What was the major consequence of these two remarkable decades of the 21st century? Something completely unexpected – the paradox of progress: we get more and more from less, a phenomenon called dematerialization. One of the important achievements of this phenomenon are mechatronic products [1].
We live perhaps more than ever in history, in a "civilization of products". The products generate a standard of living, fuel a level of cultural conduct. Products of great complexity often embody a spirituality comparable to a book or a work of art. One of the basic trends of the 21st century is the development of industrial products as "intelligent with major scientific intensive content" and "multifunctional". This, in fact, fits perfectly into the paradox of this century - to "get more from less". So, industrial products are becoming more and more multifunctional. The most characteristic multifunctional product is the iPhone, which replaces more than 50 other products. In this context, the following important trends in engineering education are more and more prominent: the need to reengineer engineering education; creative learning; systemic design. The new, extremely dynamic realities demand the creation of a specialist capable of self-improvement, capable of proposing solutions, making decisions. "That's a book case. So what?" is the phrase that no longer works.
The computer revolution marked the leap from the industrialized society to the informational society, generating a wave of innovations in technology and education. Mechatronics is a transdisciplinary field of engineering, a synergistic combination of precision mechanics, electronic command and control systems and informatics, which serves the design, realization, commissioning and exploitation of intelligent automatic systems. The Japanese defined the

meaning of these renewal movements, patenting the term mechatronics at the beginning of the 8th decade of the last century.
The content of the term has been constantly enriched as a natural result of the evolution in technological development, becoming a philosophy, a multidisciplinary science of intelligent machines and the environment of integrated design and manufacturing. The mechatronics philosophy marked the leap from traditional, sequential engineering to simultaneous or concurrent engineering. But until the appearance of the first mechatronic products, the mechanical and electrical systems and the steering components experienced a genuine evolution (fig. 1).

Purely mechanical systems	*Until 1900*	*1788 – the steam engine;* *1872 – the Otto engine;* *1887 – Daimler engine; Babbage's calculating machine;* *Mechanical typewriter.*
1870 – the d.c. motor 1889 – the AC motor		
Mechanical systems with electric drive	*1920*	*Machine tools;* *Pumps.*
↓ Electric relays AMPS Regulators		
Mechanical systems with automatic control	*The 1930s*	*Airplanes;* *Automobiles;* *Steam turbines;* *Electric typewriter.*
↓ 1948, 1952 – the transistor 1955 – the thyristor 1959 – the integrated circuit 1971- the microprocessor		
Mechanical systems with: *- Electronic analogue control;* *- Sequential control;* *- Numerical control.*	*Beginning in the 1950s through the mid-1980s.*	*Elevators with automatic control;* *Numerically controlled machine tools;* *Industrial robots;* *Computer peripherals.*
↓ 1978 – the microcontroller 1981 the PC Process mains New sensor and actuators Integration of components		
Mechatronic systems: - Mechanical and electronic integration and calculation technique → Synergy; - The software determines the functions; - New design tools.	*Since the mid-1980s.*	*Mobile robots;* *Flexible lines;* *Electronic vehicle control (ABS, ESP);* *CD-ROM drives.*

Fig. 1. Evolution of mechanical, electrical and mechatronic systems

2. Design of non-component systems – a new direction

An increasingly widespread direction in design is the design of systems rather than separate components. A systemic design of a product means [1]:

- optimal operation within a system;

- fulfilling the pre-established functions within the limits of the life span;
- possibility of recycling after end of life.

Design itself is a science, which includes a set of goals for exploring design processes, for organizing and memorizing all design-related knowledge. In order to create a real and optimal system, it is necessary to be nominated, mainly, two decisions:

- *about the content, elements, terminology, etc. and through this about the system border;*
- *about the internal structure, relationships, taxonomy, etc.*

A number of paradigms have been proposed to describe the design process:

- *design → search. From a systemic point of view, a project is based on a lot of input parameters and "objects", which must be positioned according to some functional relationships so that the output value represented by the product model can be defined. The design process consists of a search for options and solutions;*
- *design → satisfaction of some conditions;*
- *design → compilation;*
- *design → optimization*.

There is knowledge that can be designated as traditional design knowledge. Knowledge about the strength of materials, constructive elements, technology or other fields is strictly necessary for mechanical design. This knowledge is not always presented in a form convenient for designers. Existing knowledge must be sorted and reviewed. A large part of knowledge about systems and design must complete the knowledge base of a designer, forming the designer's own informational background. Starting from these aspects, four fundamental concepts for the content of design science are stated:

- *Traditional knowledge and extensions;*
- *Selections from traditional knowledge and extensions, additions;*
- *Revised selections from traditional knowledge and extensions, additions;*
- *Only expansions.*

The first concept *includes all engineering sciences within the science of design. In the second concept the domain is improved only if common knowledge is selected. The third concept can fulfill the goal of relevant knowledge for designers in a convenient form. The last concept is attractive because no contradictions appear for the existing order. Furthermore, researching the design process seems to be just the right research task. This point of view is possible only if one assumes that designers are the only basic executive powers of the actual design process. No complete basis can appear in this way, describing the general transformations of information as they occur in the design process, including those made with the computer.*

Thus, new fields based on multidisciplinary, multifunctionality such as Mechatronics, Bionics, Adaptronics, Integronics etc. appeared.

3. Mechatronics

Mechatronics is a transdisciplinary field of engineering, a synergistic combination of precision mechanics, electronic command and control systems and informatics, which serves the design, realization, commissioning and exploitation of intelligent automatic systems. The revelation of the engineer from the "Yaskawa" concern was inevitable, given that electronics had become a component that could no longer be separated from mechanical systems. The term was used to describe the technological fusion: mechanical-electronic-informatics [2] (fig. 2). *"Mechatronics is the synergistic integration of mechanical engineering with electronic and intelligent computer control in the design and manufacture of products and processes".*

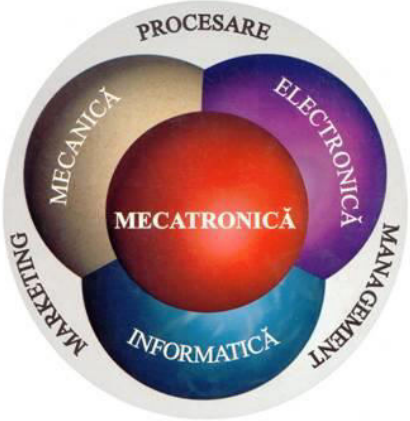

Fig. 2. Mechatronics concept

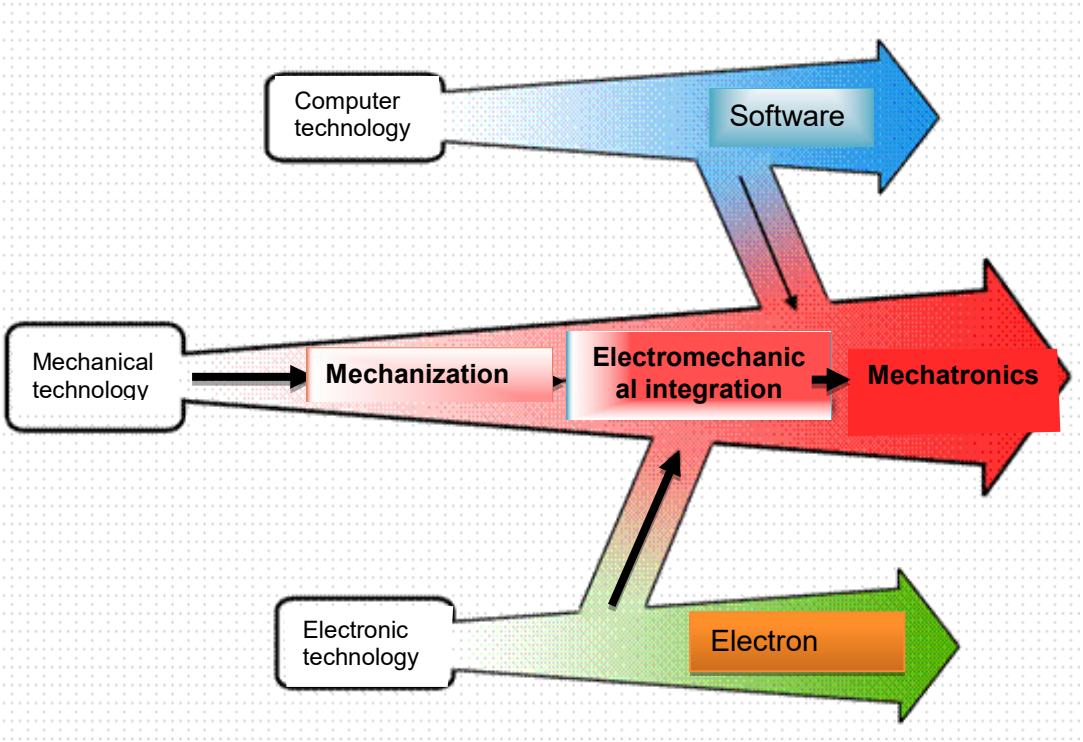

Fig. 3. Flow towards mechatronic integration.

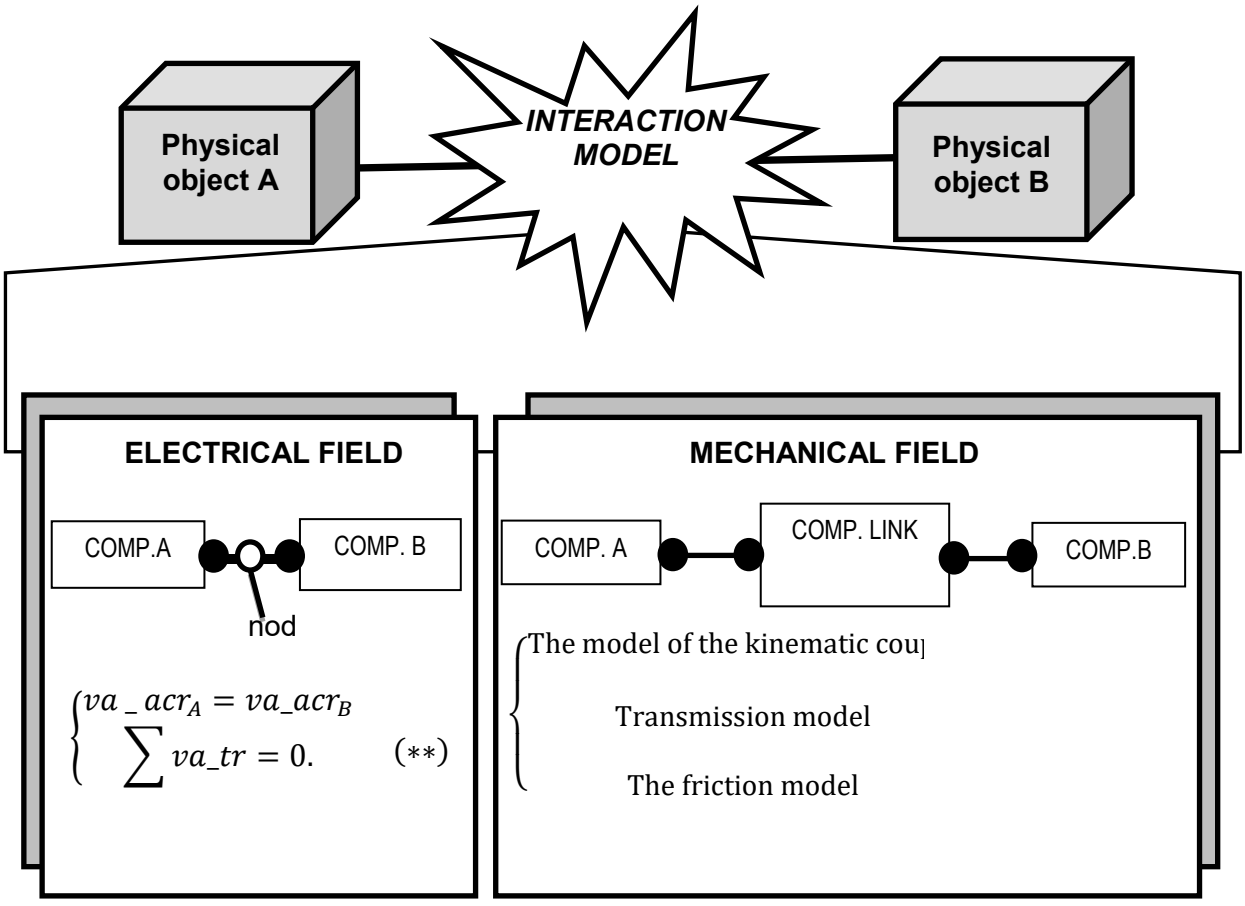

Fig. 4. Example of interaction of objects in a mechatronic system.

One can observe that the integration of the main components is carried out on the basis of efficient management, in accordance with the needs of the consumer. Mechatronics is the result of a transdisciplinary process, the result of the natural evolution in technological development. Electronic technology has spurred this evolution. The development of microelectronics has allowed electromechanical integration with microprocessors, so that electromechanical structures become intelligent, reaching mechatronics (fig. 3).

Mechatronic technology brings to the center of attention the problem of information, which is the dominant component in relation to the other components (material and energy). Arguments [2]:
- information ensures the satisfaction of man's spiritual needs;
- only information increases the newly added value of all things;
- information means culture.

The promotion of information links in the structure of technical systems ensures their flexibility and reconfigurability. Quantitative and qualitative evaluation of information is an essential issue in education, research and production activities [3]. In fig. 4. An example of the interaction of objects in a mechatronic system is presented.

4. Priority areas of use of mechatronic products

Starting from the premise that the consumer is increasingly demanding systems, not separate components, mechatronic products are increasingly widespread in all fields. The consumer no longer wants to purchase, for example, an electric motor, a gearbox, a working machine and the steering system produced separately. He wants a mechatronic product optimized in all aspects (efficiency, dimensions, ecological).

The nomenclature of mechatronic products is very large and varied (fig. 5): automobiles; toil; aircraft with ground infrastructure; satellite systems; computing; biomedical equipment; appliances; modern agricultural machinery; cine-photo and audio-video equipment; telecommunications technique; intelligent transport systems; research equipment etc. [4]. All are representative examples of mechatronic products. Practically everything we call a high-tech product is a mechatronic product. The modern car is getting smarter. Until around the 1970s-1980s, mechanical components, many of them true technical "jewels", represented an overwhelming weight in the whole of a car, the electrical part and electronics being limited to a limited number of engines (starter, alternator, windshield wipers) , sensors (for oil temperature, antifreeze, oil pressure, fuel level), relays (for signaling, ignition) bulbs. The development of microelectronics, materialized in logic and analog integrated circuits, power integrated circuits, digital processors (microprocessors, microcontrollers, DSPs), the realization of high-performance conventional and non-conventional actuation systems, new types of sensors, etc., have opened perspectives wide to satisfy some requirements, which were imposed more and more frequently, related to: traffic safety; economy; reliability; comfort; environment protection.

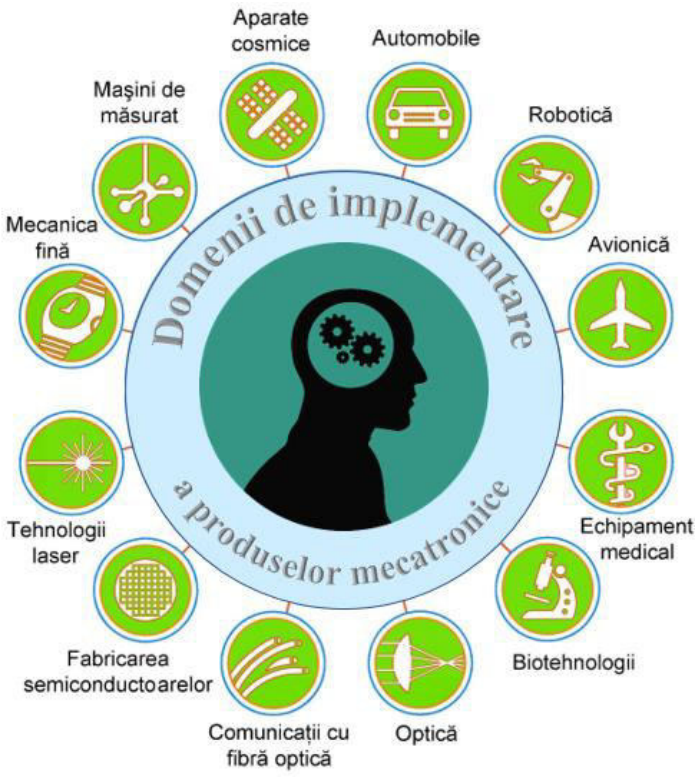

Fig. 5. Priority areas of use of mechatronic products

In addition to mechatronic systems for engine management, ABS, ESP, active suspension, interconnection of subsystems with appropriate buses – for example, CAN-Bus, navigation systems, X-by Wire, telematics, etc. A modern car of a medium class includes about 60 - 70 mechatronic products (electric motors, reducers, execution mechanisms, equipped with sensors and sensory systems. An eloquent example is the major differences between the highly successful "frog" of the Volkswagen company, from the 1960s (136 W–maximum power consumed; 150 m of electrical cables and about 80 electrical contacts) and its successor from 2001, the "New Beetle" car (2050 W, 1500 m of cables and 1200 electrical contacts). Robots, in general, are the systems that include the most advanced mechatronic products. Mobile robots (wheeled, humanoid and animaloid), in addition to the mechatronic products characteristic of stationary robots, which include a "brain", made up of one or more processors to control the entire system, also include sensors and mechatronic systems that allow it to orientate, identifying or avoiding obstacles. A particularly dynamic field of mechatronic applications is that of micro-robots, which are in a continuous race of miniaturization worldwide: walking micro-robots; micro-robots for inspections in hard-to-reach areas; micro-robots for military applications; magnetic micro-robots for the body etc. According to researchers from the Massachusetts Institute of Technology, by 2020, there will be micro-robots capable of uniting with each other to form tools or tools and then separating again. To demonstrate this, they created test modules with microprocessors and magnets. Mechatronic systems are becoming more intelligent as artificial intelligence advances.

5. Mechatronic education

Developing systems thinking is especially important for today's engineers. For the training of mechatronics specialists in accordance with the requirements of new technologies, the basic mechatronic principles in education were outlined, aiming [5]:

- *development of systemic thinking;*
- *training skills to work in a team.*

This is largely achieved through mechatronic education, which ensures flexibility in action and thought. By offering effective solutions to promote interdisciplinarity, mechatronics has become the support of efforts to stimulate initiative and creativity. The interdisciplinary mechatronics laboratories constitute the basis for the materialization of the principles: "education through practice", "education through research", transferring the emphasis from the information side to that of training skills at all stages of the educational process. The first graduation of mechatronic engineers took place in Great Britain in 1989. The content of the term mechatronics has been continuously enriched as a natural consequence of the evolution in technological development. Mechatronics became philosophy. For engineering practice, the mechatronics philosophy marked the leap from traditional, sequential engineering to simultaneous or concurrent engineering.

Mechatronics is a high degree of integration of disciplines synthetically called transdisciplinarity, a term introduced in 1970 by Jean Piaget who defines it as "what is at the same time between disciplines, within different disciplines and beyond any discipline", its purpose being the understanding of the world through the unity of knowledge. "Because today we are in the midst of an intellectual revolution, we must understand that transdisciplinarity reveals to us the poetic dimension of existence, crossing, as I said, all the disciplines, beyond them. Not to be confused, however, with multidisciplinarity and interdisciplinarity" says Basarab Nicolescu. Transdisciplinarity is seen as a superior form of integrated learning and involves concepts, methodology and language, which tend to become universal (systems theory, information theory, cybernetics, mechatronics, integronics, etc.). The interpenetration of disciplines and the coordination of research can end up with the adoption of the same set of fundamental concepts or general methodical elements, that is, a new field of knowledge or a new discipline.

Starting from the premise that today engineers must be trained at a high interdisciplinary level at the Technical University of Moldova within a cross-border project, a Mechatronics Laboratory was created (fig. 6), and the education plan for engineering specializations completes a discipline nine - "Applied Mechatronics".

Extensions of mechatronics in other fields such as: hydronics, pneutronics, thermotronics, autotronics, agromechatronics (precision agriculture) are increasingly common. The evolution in the micro- and nano-fields means: micromechatronics, nanomechatronics, and at the junction of the fields of natural and artificial systems - biomechatronics. The general trend is to "intellectualize machines and systems".

6. Conclusions

- The integration of electronics and computer technology has led to the substantial simplification of mechanical components and cheaper systems. Mechanical parts have been replaced by electronic components, cheaper, more reliable, more precise and easier to maintain.

Robotic arm JAKA

3D printer Raise 3DE2

Modular training equipment in mechatronics for Industry 4.0

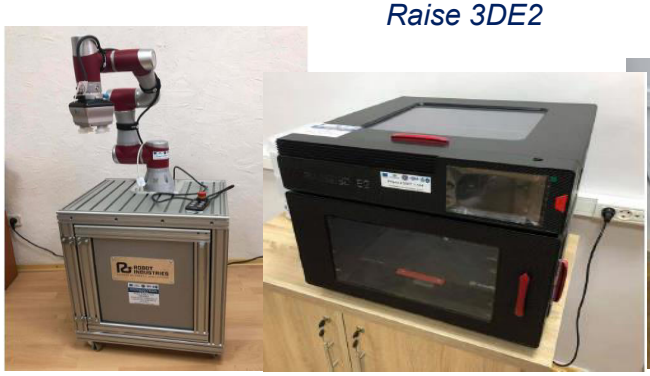

Assistance, safety and control systems for motor vehicles

Modular system for rapid prototyping of flight mechatronic system (drone) Aircraft Kit F450-V2

Fig. 6. Mechatronics Laboratory: Technical University of Moldova

- In the perspective of lighter constructions, relatively elastic systems were made, with a reduced mechanical damping, but in which a command with adequate reaction, based on electronics, sensors and adequate actuators, ensures an electronic damping.
- Introduction of regulation systems for position, speed, force, etc. it allows not only to maintain the programmed quantities within reasonable precision limits, but also to obtain a quasi-linear behavior, even if the mechanical system is non-linear.
- Mechatronic products are increasingly ubiquitous in all fields: aerospace, robots, industry, medicine, domestic, etc.

References

[1] Dulgheru, Valeriu. *Basics of Creative Product Development / Bazele elaborării creative a produselor.* Vol. 2. Chișinău, Bons Offices Publishing House, 2020.
[2] Cungi, Charly. *Knowing how to be assertive in all circumstances* / *Savoir s'Affirmer en Toutes Circonstances.* 2nd edition. Paris, Editions Retz Publisher, 2007.
[3] Olaru, Dumitru, and Ciprian Vasile Stamate. *Mechatronic microsystems. Basic principles, manufacturing technologies and constructive solutions* / *Microsisteme mecatronice. Principii de bază, tehnologii de fabricaţie şi soluţii constructive*. Iași, 2016. Accessed October 19, 2022. https://mec.tuiasi.ro/diverse/MICROSISTEME%20MECATRONICE.pdf.
[4] Bernardi, Mauro, et al. “New approaches for developing mechatronical products in multidisciplinary teamwork.” Paper presented at the 35th CIRP Intern. Sem. on Manufacturing Systems, Seoul, South Korea, 2002.
[5] Mătieş, Vistrian, Dan Mândru, and Radu-Nicolae Bălan. *Mechatronic technology and education* /*Tehnologie şi educaţie mecatronică*. Cluj-Napoca, Todesco Publishing House, 2001.

ISSN 1454 - 8003
Proceedings of 2022 International Conference on Hydraulics and Pneumatics - HERVEX
November 9-10, Băile Govora, Romania

THE INVOLVEMENT OF FLUID POWER IN THE FIELD OF RENEWABLE ENERGY

Liliana DUMITRESCU[1], Radu RĂDOI[1], Cătălin DUMITRESCU[1,*], Ana-Maria Carla POPESCU[1], Dragoș PREDA[2]

[1] National Institute of Research & Development for Optoelectronics / INOE 2000 – Subsidiary Hydraulics and Pneumatics Research Institute

[2] SC Rolix Impex Series SRL, Bucharest

[*] dumitrescu.ihp@fluidas.ro

Abstract: *Exploitation of renewable energy sources is the most convenient solution for reducing the negative effects of the use of fossil fuels: pollution, temperature rise, vegetation change, etc. Although there are numerous targets set worldwide, the concrete results are not at the expected level. This is why more and more technical fields are involved in finding solutions for increasing the amount of useful energy from renewable sources, as well as for solving other problems associated with energy production, such as its storage. The paper presents some achievements in which the field of fluid power is involved, with an emphasis on the systems developed in recent years, and which have been put into operation or have a high potential for this.*

Keywords: *Compressed air, hydraulic system, renewable energy, digital hydraulics*

1. Introduction

Renewables generated 28.3% of global electricity in 2021, similar to 2020 levels (28.5%) and up from 20.4% in 2011. Despite the progress of renewables in the power sector, the surge in global energy demand was met mostly with fossil fuels [1]. This amount of energy is produced with total installed capacities of 3146 GW, of which 314 GW were added in 2021, 17% more than the previous year. The conversion from solar and wind energy covers more than 10% of the total electrical energy consumed, the completion of up to 28.3% being provided by hydro energy (15%) and bio + geothermal (approx. 3%). Unfortunately, the burning of fossil fuels still provides a significant share of the electricity consumed, 62%, and the rest is produced in nuclear power plants, which are also the subject of some controversies.
There are also positive aspects: one of them is that, 10 years ago, the share covered by renewable sources was only 20% of electricity consumption, while the absolute values were significantly lower. However, the current trend of increasing the share of renewable energy and conversion capacities in the total of plants for the production of electricity is far from that required to reach the targets proposed for the years 2030 or 2050; this is why the forceful approach of commissioning as many renewable energy conversion units of various types as possible is necessary.
Hydraulic and pneumatic systems can be found, in recent decades, in various installations for the production of energy from renewable sources, and the number of fields in which they are involved is constantly increasing, as the technological advance and the appearance of new materials solve certain problems. One example is the emergence and use of biodegradable oils, making hydraulic systems compatible with onshore or off-shore applications.
In the following, some systems will be presented in which fluids under pressure (mainly air, water or oil) play an important role in various phases related to the production or storage of energy.

2. Pneumatic systems in the structure of energy production facilities

2.1 CAES system

The most well-known system based on energy storage in compressed air is the CAES system (Compressed Air Energy System); it solves the problem of the imbalance between energy production

and its consumption, by storing part of the energy produced in the form of compressed air, during the production surplus period. When energy demand exceeds production, compressed air is used to drive electric power generators, often with the help of gas turbines.
The first utility-scale diabatic compressed air energy storage project was the 290 megawatt Huntorf plant opened in 1978 in Germany using a salt dome with 580 MWh energy, 42% efficiency.

Fig. 1. Huntorf plant (Germany) and the principle of operation [2]

As one can see in the figure above, energy storage is based on air compression in special enclosures, at a pressure of several tens of bar (50...70 bar in operation); the compressors are powered by surplus energy, produced during periods of low consumption. Air is held in the reservoirs until consumption increases and requires the commissioning of additional capacity (turbines). These turbines, in which natural gas is mixed with pressurized air, use approx. 2/3 of the energy produced for air compression; therefore, using already compressed air, all the energy produced is delivered to consumers.
Other technical characteristics of the plant:
- It uses 2 caverns of approx. equal shapes and volumes (140,000 and 170,000 m^3, respectively)
- Vertical location between 650 and 800 m depth
- Maximum air flow used by the turbine: 417 kg/s.

The location and shape of the two caverns is shown in figure 2.

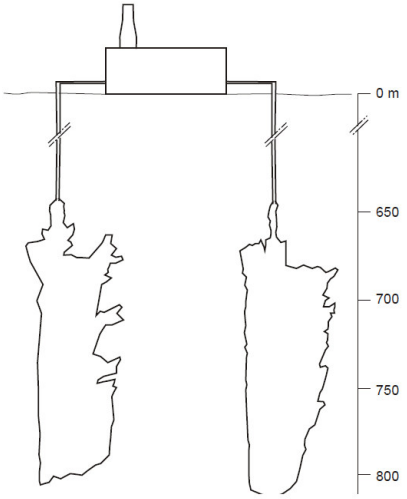

Fig. 2. The shape and location of the two caverns of the Huntorf plant [3]

Following the success registered in operation, a 110-megawatt plant with a capacity of 26 hours (2,860 MWh energy) was built in McIntosh, Alabama (1991). It uses a 540,000 m^3 solution mined salt cavern to store air at up to 75 bar. The stored energy is enough to cover the electricity consumption of 11,000 American homes for 26 hours.
Both of these plants use diabatic processes, and the technology is called D-CAES; starting from this and using the heat resulting from air compression, the A-CAES (Adiabatic – CAES) technology was developed, which is still at an experimental level.
In D-CAES applications, the energy stored in compressed air is used indirectly, the compressed air being mixed with natural gas for combustion; however, there are also applications where compressed air is used directly, to drive a pneumatic motor that, further, drives a generator. In this case it is of interest to know the amount of energy that can be stored in compressed air; a preliminary calculation can be made using the formula:

$$W = p_B V_B \ln\frac{p_A}{p_B} + (p_B - p_A)V_B \tag{1}$$

where: W – stored energy (MJ), P_A, P_B – initial and final pressures in the enclosure, (MPa), V_B – volume of the enclosure (m^3). The formula can be used for isothermal processes.
If we consider the compression of air from atmospheric pressure to 100 bar, in an enclosure with a volume equal to 1 m^3, taking into account that 1MPa = 10 bar, we will get:

$$W = 10.0\ MPa\ \cdot 1\ m^3 \cdot \ln(0.1\ \text{MPa}/10.0\ \text{MPa}) + (10.0\ \text{MPa} - 0.1\ \text{MPa}) \cdot 1\ m^3 = \\ = 10 \cdot (-4.6) + 9.9 = -36.1\ \text{MJ} \tag{2}$$

Given that

$$1\ MJ = 0.2778\ \text{kWh} \tag{3}$$

it results:

$$W = -36.1 \cdot 0.2778 = -10.03\ \text{kWh} \tag{4}$$

the "–" sign shows that the gas absorbs energy.
Air compression in storage plants can be of three types: isothermal, adiabatic and diabatic. In storage plants that use isothermal compression, the heat produced during compression is removed at the same rate as it is produced, in order to maintain a constant temperature. An air cooler is used to remove the heat in the atmosphere, and a heater is used to use the stored air. In storage plants that use adiabatic compression, heat is stored and reused when exhausting the air towards a gas turbine. These plants can have an efficiency of up to 90 percent. Storage plants that use diabatic compression remove heat with the help of an air cooler, and when the stored energy is needed, the compressed air is released and heated by combustion to be used to drive a gas turbine. Nowadays all the companies are trying new methods to store the heat produced when compressing the air to be fully reused to maximize efficiency [4].

2.2 Ground-Level Integrated Diverse Energy Storage (GLIDES) technology

A step forward from the CAES principle and technology is the use of pressurized air only for energy storage, and an intermediate fluid (water, oil, etc.) is used to convert the stored energy into mechanical energy. In the following, two examples of such technologies are presented.
GLIDES is a laboratory technology, developed at Oak Ridge National Laboratory, USA, in the experimental model stage, intended to store energy in the form of compressed air, with the help of a "liquid piston", which is actually water under pressure [5].
The main parts of the system are: a reservoir for maintaining the liquid at atmospheric pressure, vessels containing air (or other gas) at an initial pressure, a pump with which the vessels are charged, as well as a mechanical energy generator (turbine of special construction). To these main components, some specific hydraulic components are added, to carry out the processes. For energy storage, liquid is pumped from the storage tank into pressure vessels using excess energy. The process takes place until the maximum storage pressure is reached. To use the stored energy, pressurized water is sent to a hydraulic turbine, which drives an electric generator.

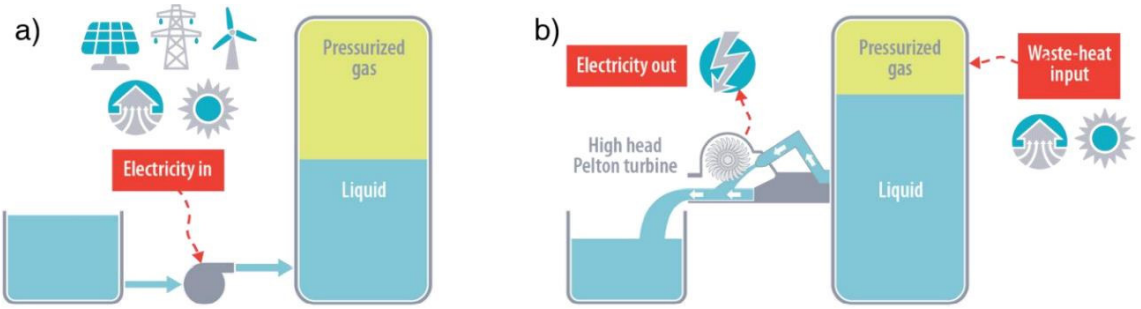

Fig. 3. "Liquid piston" technology - the working principle
a) storage phase; b) the phase of recovery / reuse of stored energy

The figures below show two phases of the operation of the experimental plant. In figure 4, the installation is in the energy storage phase, when the water is pumped into the storage containers; the water from the large capacity external tank (approx. 2000 l) is pumped into 4 tanks of 500 l each, up to a pressure of 130 bar. When this pressure is reached the water pump is stopped and the energy can be maintained without loss as long as needed.

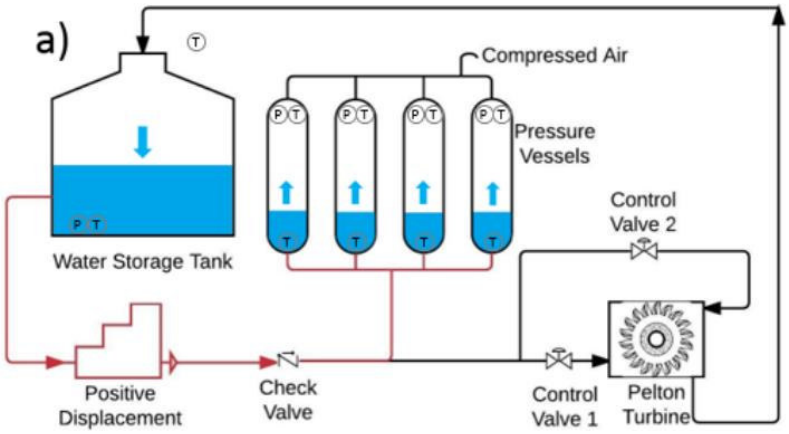

Fig. 4. GLIDES experimental installation - energy storage phase

In Figure 5, the installation supplies the stored energy and converts it from pneumatic energy to mechanical energy by means of a specially constructed 2-jet Pelton turbine capable of delivering 5.5 kW per jet. The unloading of the storage containers is done until the pressure reaches 70 bar. The water that drives the turbine is collected and returned to the outer tank without being lost. The minimum pressure in the storage tanks is monitored and restored whenever necessary.

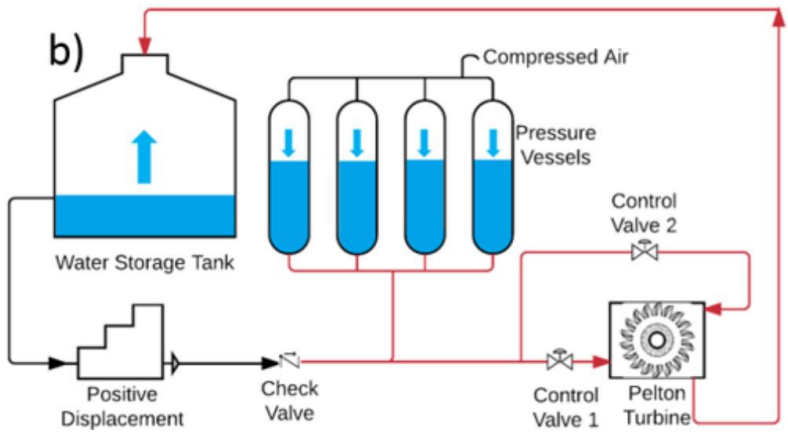

Fig. 5. GLIDES experimental installation – delivery of stored energy

This installation is experimental; there are also industrial applications, of significantly higher powers, but they must solve certain problems when moving from the phase of experimental installation to that of a functional solution. Such a solution was developed by the AUGWIND company.

2.3 AUGWIND air battery

The Israeli company AUGWIND was founded in 2012 by two researchers who started from the premise that the progress made in the conversion of renewable energy is not also found in the storage of the resulting energy, so that the energy is available for longer periods of time. The solution developed by the company is a combination of pumped hydro and compressed air energy storage. The system has the commercial name of AirBattery and has been implemented in several energy storage projects, which accumulate over 200 MWh [6].
The principle diagram is shown below; the pre-compressed air is found in some tanks placed in the ground, in which water is introduced until the air reaches a pressure of 40 bar. The pumps are powered by electricity from a renewable source (wind, solar, etc.); since the water is introduced gradually, the process is isothermal. Water pumped into pressurized tanks is stored in above-ground tanks.
After reaching the working pressure, the pumping process stops and the "battery" is charged; the supply of the stored energy is done by sending water under pressure to a hydro-mechanical converter, of the water turbine type, which drives an electric generator.
The key element of this system is the pressure tank, in which the water compresses the air; for large tanks, classic solutions such as metal tanks are not sustainable, due to high costs. The solution proposed by AUGWIND is based on an inner polymer lining, surrounded by a metal mesh with mechanical resistance. The resulting assembly, shaped like a classic cylindrical tank, is mounted below ground level and covered with concrete; this results in a pressure-resistant container with a long service life.

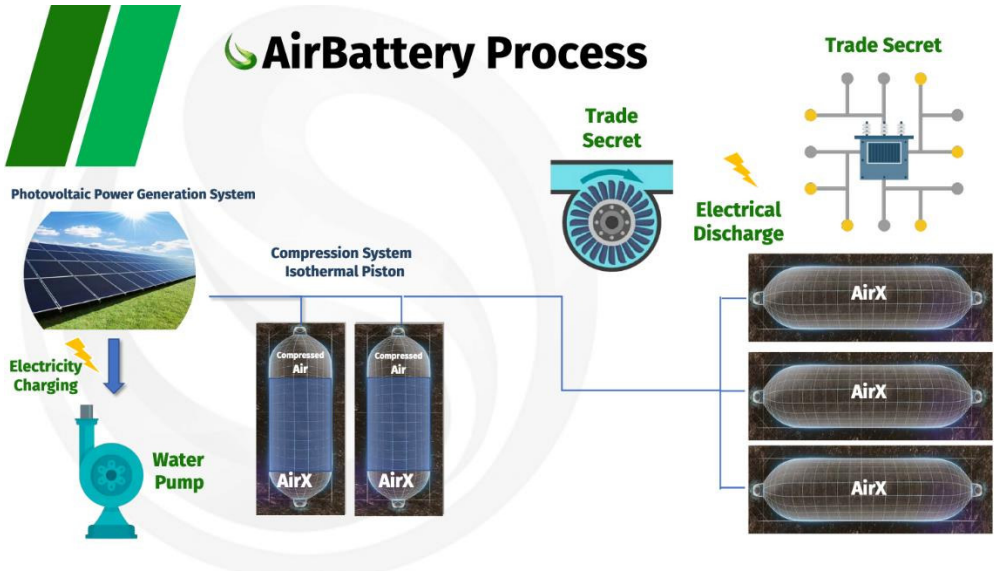

Fig. 6. Structure of the AUGWIND compressed air energy storage facility

The main advantages are presented below; it is important to note that since there are no components in relative motion, wear is very low and therefore the theoretical number of charge-discharge cycles is very high. The efficiency estimated by the company exceeds 80%.
Another advantage is given by the possibility of scaling the installation by adding a corresponding number of tanks; regardless of the number of buried tanks, the soil above them can be used for agriculture or energy production with solar panels or other technologies. However, a technical-economic analysis carried out by the company indicated that, for maximum efficiency, the storage capacity must be at least 5 MW.

Fig. 7. Advantages of the AirBattery system

3. Hydraulic systems in renewable energy conversion facilities

3.1 Hydrostatic transmissions with applications in the field of wind turbines

The previously presented solutions were based on energy storage in pressurized air, hence pneumatic applications; hydraulic systems, in turn, have a significant involvement in the conversion and storage of renewable energy, in various forms. However, the most widespread applications are those related to the transmission of energy with hydraulic sub-systems in the structure of wind turbines.

These turbines, mainly the horizontal axis ones, have the electrical generator mounted coaxially with the rotor, which significantly increases the mass of the assembly placed at height, which can reach tens of tons of weight. For this reason, the expenses related to the construction housing this assembly are high and are reflected in the final price of the turbine; another problem is the price of maintenance operations, which is higher if it is carried out at height.

The platform (excluding the rotor) represents between 20 ... 35% of the total weight of a large turbine reaching in some cases the order of hundreds of tons. In the case of the VESTAS V90/3000 turbine, with a power of 3 MW, the nacelle weighs 75 tons, the rotor 28 tons, and the tower minimum 155 tons.

At the level of 2022, the largest horizontal axis turbines have reached powers of 15...16 MW. Even if it is considered that the mass placed at height does not increase proportionally with the installed power of the turbine, the weight of the components is a significant one, and any reduction of it has favorable effects on the final price of the turbine and subsequent maintenance.

One of the possibilities to reduce the mass located at height is to mount the generator on the ground and transmit the energy from the rotor through a hydrostatic transmission; in this way the rotor and some hydraulic components remain located in the nacelle and the rest are located below. Research in this direction began in the 1970s, with the Rybak company putting into operation, in December 1980, the turbine model SWT-3, with an installed power of 3 MW.

In this turbine, the hydrostatic transmission is composed, at the level of the flow generators, of 14 hydrostatic pumps with constant flow, which feed a group of 18 motors with variable flow; a speed multiplier is used to increase the speed of the rotor, to be compatible with the drive speed of the pumps. Another gear transmission is mounted between the hydraulic motors and the generator.

In 2010, in Germany, the RWTH Aachen University developed an experimental platform that simulates a variable speed wind turbine and carried out experimental research with modeling and simulation [7].

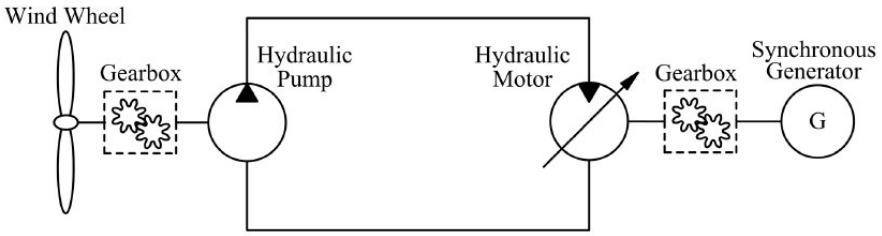

Fig. 8. Operating principle of the wind turbine with hydrostatic transmission

As in the case of the Rybak turbine, the pumping group is made with fixed flow pumps, and fixed and variable flow motors are used to drive the generators; one or both engines can be used to drive each generator, according to figure 9 (a).
The results indicated that this hydraulic transmission of wind power can compensate the influence of the fluctuation of the wind speed on the output power, but also achieve an optimal efficiency of 85%.

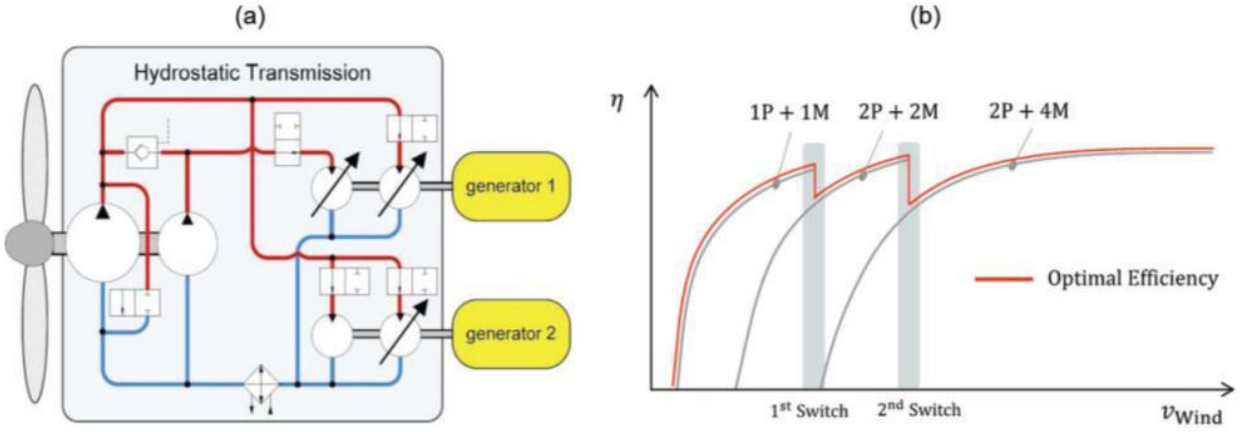

Fig. 9. Hydrostatic transmission (HST) for a 1 MW turbine developed at IFAS

A more complex scheme, using both pump and motor in digital construction, is shown in figure 10 [8].

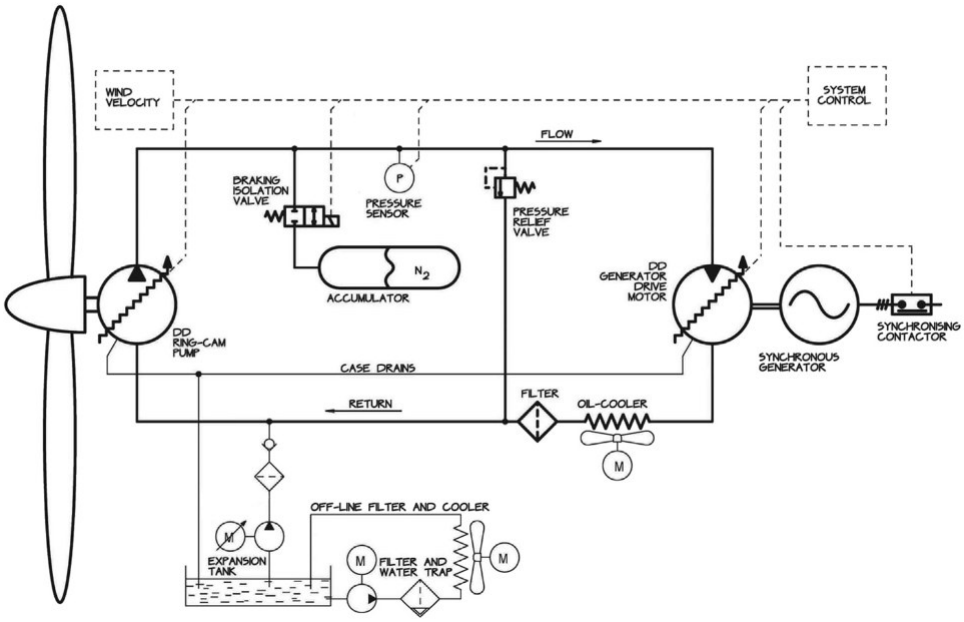

Fig. 10. Diagram of a hydrostatic transmission with digital elements integrated in a wind energy conversion system

The mechanical energy produced by the rotor is transmitted to the hydrostatic pump, which supplies high-pressure flow to a hydraulic motor that rotates the electric generator. This system works in a closed circuit and includes all the specific components; the oil in the circuit is cooled and filtered and water is removed, using an off-line circuit. A central control unit manages the operation of the system. The construction using the principles of digital hydraulics of the pump and the motor is based on 2 technological peculiarities: 1) intake and discharge valves with electromagnetic control, and 2) the parallel coupling of banks of cylinders to create digital pumps and motors of desired capacity. The solution was put into practice by the company Artemis Intelligent Power.
In 2009, this company made the first version of the digital pump designed to equip a hydraulic transmission for a turbine with an installed power of 1.6 MW. The test results indicated an efficiency of the turbine equipped with this transmission of over 90%, close to the efficiency of a classic turbine [9].
Artemis Digital Displacement (ADD) drivetrain is formed by a hydrostatic transmission followed by two parallel synchronous generators. For the 1.6 MW system (rated power), one low speed pump drives two 800 kW hydraulic motors. The hydraulic motors each drive one electrically excited high voltage synchronous generator. The most important optimization for the pump and motors consists in making the valve's operation independent of the angular displacement of the rotor shaft. This unconstrained dependence allows individual operation of each cylinder.

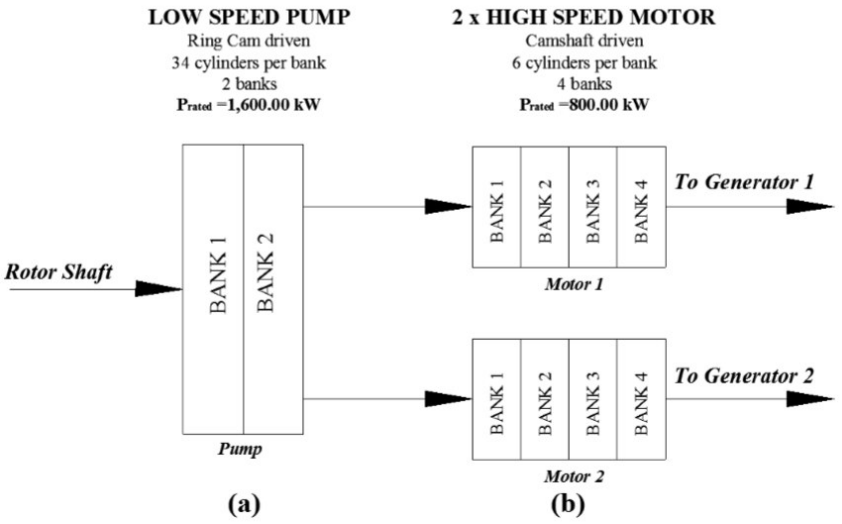

Fig. 11. Hydrostatic transmission for wind turbines proposed by Artemis Intelligent Power

The ADD low speed pump has a total of 68 cylinders (pistons) contained in two parallel banks; to drive the pump pistons, a cam ring is used, which is similar to a ring with lobes on the outer surface, but without any eccentricity. The pump pistons are forced to follow the lobes of the ring and in this way they perform their oil pumping function. The pump ring in the 1.6 MW transmission has 24 lobes, which actuate 34 pumping pistons; to achieve the required geometric volume, 2 packages of pistons are mounted together, according to figure 11.
Artemis Digital Displacement motor has a total of 24 cylinders of the same geometry. They are distributed in 4 banks. Each bank includes 6 cylinders equally radially distributed. The banks are stacked over each other. One single camshaft drives the 24 cylinders so each cylinder had one full stroke any single revolution.

3.2 The use of various working fluids

The energy transmission systems from the offshore turbine component have certain constructive peculiarities, which take into account their location; an important problem related to the use of hydrostatic transmissions is the pollution that can occur when oil is lost in the circuit; to avoid this

problem, some researches turn to the use of biodegradable fluids or even sea water, as is the case of the two examples below.
Figure 12.a shows the operating principle of an offshore turbine, where the electric generator is connected to a water turbine, driven by a jet of sea water that is pressurized with the help of a pump; it is driven by a hydraulic motor fed from a pump connected to the rotor of the wind turbine. If the hydrostatic transmission is located above sea level (on a platform, for example), the danger of pollution is eliminated or greatly mitigated. The solution was proposed and developed by Delft University.

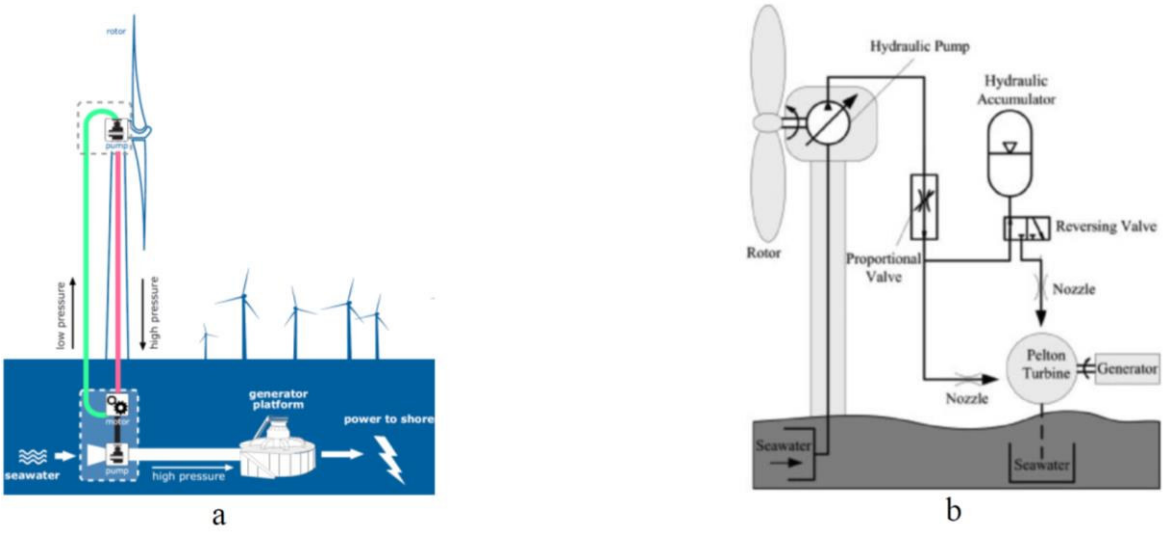

Fig. 12. Wind turbines that use sea water

A step further is achieved if hydrostatic transmissions are used that work with sea water as the working fluid, as shown in figure 12.b [10]; in this case, the hydraulic pump driven by the rotor works with sea water in an open circuit, sending the water to a Pelton turbine that drives the electric generator. For the (limited) compensation of the decrease in wind speed, a pneumo-hydraulic accumulator is installed, which is charged during periods of strong wind. The amount of stored energy is limited by the capacity of the accumulator; if this one is permanently connected, it can reduce the unevenness of the flow that drives the Pelton turbine.

4. Conclusions

Fluid power applications in the field of renewable energy are very diverse and constantly expanding. The compressibility of gases recommends them for storage applications in natural or artificial reservoirs, at pressure rates of 50...100 bar; with capacities in the order of hundreds of thousands of cubic meters, the tanks can store significant amounts of energy and have the advantage of a long operating life, while maintaining performance. The first plant of this type was commissioned in 1978 and is still active, proving the reliability of the CAES concept.
Along with the development of new materials and manufacturing solutions, the range of applications has also expanded; in addition to purely pneumatic applications, a current trend is that of "liquid piston" solutions, in which water compresses the air in the tank.
Regarding hydraulics, its involvement in renewable energy applications was initially found in pitch adjustment, yaw and rotor braking, lubrication; a newer direction is energy transfer. The involvement of hydraulics in these fields is due to the advantages it has over other types of systems (mechanical, electrical) - safe, reliable, with a good power density and competitive prices.
Regarding hydraulic power transfer, the future seems to belong to digital systems, at least for the main components of a transmission: the pump driven by the turbine rotor and the rotating hydraulic motor that drives the electric generator. If the initial solutions, such as the Rybak turbine that

appeared in the 80s, had a large number of pumps and motors that were actuated in turn, taking into account the transmitted power, today digital technology has penetrated the interior of rotating hydrostatic machines, as can be seen in the achievements of the ARTEMIS company.

Acknowledgments

The paper has been developed in INOE 2000-IHP, as part of a project co-financed by the European Union through the European Regional Development Fund, under Competitiveness Operational Programme 2014-2020, Priority Axis 1: Research, technological development and innovation (RD&I) to support economic competitiveness and business development, Action 1.2.3 – Partnerships for knowledge transfer, project title: *Development of energy efficient technologies in niche applications of the manufacture of on-demand mechanical-hydraulic subassemblies and maintenance of mobile hydraulic equipment*, project acronym: MENTEH, SMIS code: 119809, Financial agreement no. 6/25.06.2018, subsidiary contract no. 119/08.02.2022. It has also received financing under a project funded by the Ministry of Research, Innovation and Digitalization through Programme 1- Development of the national research & development system, Subprogramme 1.2 - Institutional performance - Projects financing the R&D&I excellence, Financial Agreement no. 18PFE/30.12.2021.

References

[1] REN21 (Renewable Energy Policy Network for the 21st Century). “Renewables 2022. Global Status Report.” Accessed September 15, 2022. https://www.ren21.net/wp-content/uploads/2019/05/GSR2022_Full_Report.pdf.

[2] Solar Edition. “World’s First Utility-Scale CAES Plant was Built-in 1978 in Northern Germany.” February 16, 2020. Accessed September 15, 2022. https://solaredition.com/worlds-first-utility-scale-caes-plant-was-built-in-1978-in-northern-germany/.

[3] Crotogino, F., K.-U. Mohmeyer, and R. Scharf. “Huntorf CAES / More than 20 years of successful operation.” Paper presented at the Solution Mining Research Institute (SMRI) Spring Meeting, Orlando, Florida, USA, April 15-18, 2001.

[4] Whitlock, Robin. “Compressed Air Energy Storage (CAES) Systems.” *Interesting Engineering*. March 12, 2016. Accessed September 16, 2022. https://interestingengineering.com/science/compressed-air-energy-storage-caes-systems.

[5] Odukomaiya, Adewale, Ahmad Abu-Heiba, Samuel Graham, and Ayyoub M. Momen. “Experimental and Analytical Evaluation of a Hydro-Pneumatic Compressed-Air Ground-Level Integrated Diverse Energy Storage (GLIDES) System.” *Applied Energy* 221(C) (July 2018): 75-85.

[6] Augwind. Accessed September 21, 2022. https://www.aug-wind.com/about-us.

[7] Vukovic, Milos, and Hubertus Murrenhoff. “The Next Generation of Fluid Power Systems.” *Procedia Engineering* 106 (2015): 2 – 7. doi: 10.1016/j.proeng. 2015.06.002.

[8] Silva, P., Antonio Giuffrida, Nicola Fergnani, Ennio Macchi, Matteo Cantù, Roberto Suffredini, Massimo Schiavetti, and Gianluca Gigliucci. “Performance prediction of a multi-MW wind turbine adopting an advanced hydrostatic transmission.” *Energy* 64 (2014): 450 – 461.

[9] Popescu, Teodor Costinel, and Ionaș Cătălin Dumitrescu. “Considerations regarding the use of hydrostatic transmissions in wind turbines.” Paper presented at the 25th International Conference on Hydraulics and Pneumatics HERVEX 2019, Băile Govora, Romania, November 13-15, 2019.

[10] Fan, Yajun, Anle Mu, and Tao Ma. “Study on the application of energy storage system in offshore wind turbine with hydraulic transmission.” *Energy Conversion and Management* 110 (February 2016): 338-346.

ISSN 1454 - 8003
Proceedings of 2022 International Conference on Hydraulics and Pneumatics - HERVEX
November 9-10, Băile Govora, Romania

INTELLIGENT HYDRAULICS USING ARTIFICIAL INTELLIGENCE

Ștefan Mihai ȘEFU[1,*], Bogdan Alexandru TUDOR[1]

[1] National Institute of Research & Development for Optoelectronics / INOE 2000 – Subsidiary Hydraulics and Pneumatics Research Institute

* sefu.ihp@fluidas.ro

Abstract: *With the progress made in the fields of programming and electronic systems, the next step was taken, artificial intelligence. By using AI in modern systems, we want to support man in all his activities by introducing systems that can process a certain set of information by themselves without man intervening in the process. Although the use of AI comes to the aid of humans, it increases the level of knowledge necessary for the operator to be able to operate such systems. In this paper, the authors want to bring an update on the field of intelligent hydraulics and the degree of use of AI in modern hydraulic systems.*

Keywords: *Intelligent hydraulics, artificial intelligence, modernization, intelligent hydraulic pump, smart hydraulic, energy efficiency*

1. Introduction

A first attempt to define artificial intelligence (AI) was given by its parents Minsky and McCarthy, who considered it to be any activity that is now done by a machine and was previously done by a human. Researcher Francois Chollet said that artificial intelligence is related to the ability of a system to adapt and improvise in a new environment, to generalize its knowledge and apply it to unknown scenarios. Intelligence is the efficiency with which new skills are acquired to solve non-specific tasks. Intelligence is often thought of as the ability of humans, or in the case of artificial intelligence, of machines to learn, but we are actually discussing how effectively new things can be learned. According to specialist Lynne Parker A.I. is basically an umbrella term for a broad set of methods, algorithms, and technologies made by appropriate software, such as machine learning, natural language processing, or robotics. Since the industry has already entered the era of artificial intelligence, hydraulics could not remain outside the phenomenon. Even if the definition of intelligent hydraulics is still under discussion, it has been accepted that in any variant to ensure features such as the existence of a programmable block, a system of communication with the outside world of the machine, the existence of a hard suitable for the purpose, the existence of a diagnostic capacity. The level of intelligence is different from machine to machine and is basically given by the level of control, command, monitoring and organology of the equipment. The faster, more precise and more capable the cars are of self-adaptation to specific conditions, the smarter the car is considered to be. It is already evident that the level of intelligence required and accepted is also constantly increasing, that is, there will be a visible increase in the ability to store, transmit and process data, in addition to the development of actuation and acquisition equipment [1].
Smart products are defined by a number of basic characteristics, usually codified and divided into static and passive or dynamic and active.
When the concept of Industry 4.0 began to be used more often in the real economy, it was switched to an identification of products - smaller milestones and especially passive ones through unique codes such as the serial number, to which a quantity of information is attached in depending on the level of digitization.
The transition to production based on intelligent technologies has made the manufacturing phases to be taken over and recorded digitally, which essentially serves to streamline the assembly and maintenance of equipment and systems.
Even if the introduction of artificial intelligence knows an intense development, the role of the operator will not disappear, but his activity will be modernized and adapted to new technologies. The

unfortunate problem is that this process will be done primarily to optimize profits and quite a bit for the public good.
In order for the ethical elements of development to be respected, it is necessary for the use of artificial intelligence to be made transparent and responsible in compliance with laws and legal norms, and the technologies and procedures to be easily explainable and aimed at solving the expectations of the population. Ethics is applicable in all sub-fields of manufacturing including design, operation and maintenance. It is important that products are designed to be safe and reliable right from the design stage. It cannot be accepted that manufacturers can bypass or exclude the good of buyers by blaming artificial intelligence that would apply all the laws and regulations in force too strictly. Damage or accidents caused by automated machines cannot be accepted as the fault of the technology and not the manufacturer. For example, technology based on artificial intelligence that has penetrated the medical field cannot be held responsible for possible errors and accidents, given the obligation of producers and users for special human supervision, in all phases, from conception to the exploitation of the results [2].
The relationship between artificial intelligence and intelligent hydraulics:
The area of use of artificial intelligence is very large, but even more important is the permanent increase in the number of fields in which it is applied. Very important are the applications in technology, and in this direction essential are the applications in the subassemblies that ensure the movement. In principle, the movement is ensured by electric drive or by hydraulic drive. In recent years, intelligent hydraulic equipment has emerged as the basis of artificial intelligence involved in the technologies of mobile machinery industries, agricultural machinery production, aviation, metallurgy and steelmaking, machine building, etc. Interestingly, both hydraulic equipment and systems are used, as well as hydraulically actuated test stands. Practically all ideas, methods, solutions valid for artificial intelligence are also valid for intelligent hydraulics.

2. The importance of intelligent hydraulics

Intelligent hydraulic systems help end users gain better insight into their equipment, which improves machine performance and increases productivity.

Intelligent hydraulics is a necessity and not a technological fad to which hydraulic actuation also aligns. Among the elements that show the importance of intelligent hydraulics are the following:

a) Creates new jobs that involve knowledge from modern technical-scientific fields. Traditional operators who often have elementary training will no longer find easy work, instead the number of jobs that require workers to know some elements of electronics, mechanics, electricity, hydraulics and Informatics.

b) Reduces unnecessary energy consumption in areas such as transport, metallurgy, manufacturing technologies. The fact that the intelligent hydraulics will adapt the energy consumption to the necessary, optimize the energy balance of the machine and solve the energy efficiency shows the modernity and usefulness of the concept.

c) Saves the person from performing operations that require great effort and repetitive, physically tiring, but especially mentally.

d) Essentially contributes to the modernization of machinery drive systems. Over time, the specialists have worked, are working and will work on energy efficiency and increasing productivity from the design, production and maintenance phases of both the technological lines and the final products that reach clients, individuals or legal entities. There is no variant of development without the involvement of artificial intelligence, therefore also of intelligent hydraulics.

3. The advantages of intelligent hydraulics

Lately it has been accepted that intelligent hydraulics is important in the process of technological modernization of the economy. However, companies have been restrained in its industrial application, although there are many economic advantages such as:

- Intelligent hydraulics create competitive advantages that can be vital for manufacturers. The level of economic efficiency of intelligent hydraulic systems leads to the creation of competitive advantages, which very often can drive some firms out of the market, or produce an unexpectedly high demand from the market. The fact that intelligent hydraulics increases efficiency and productivity has made many companies active in the field in order not to be excluded from the market. In the near future, the market will no longer accept products with low efficiency or low productivity. The price of energy will drive out of the market producers who do not adapt to trends and customer demands.
- Obtaining special economic results as a result of modern equipment and systems, which have acceptable expenses for the activities that give intelligence. With the reduction and stabilization of the prices of intelligent hydraulic equipment, electronic calculation blocks and data transmission and reception systems, the reluctance to use AI (and therefore also intelligent hydraulics) of manufacturers has been reduced very seriously.
- Easy access to high class computing systems. For a long time and in many countries, difficult economic, technical and scientific access to high-performance technologies and equipment was a decisive factor blocking progress. Today, the unrestricted existence on the market of methods, equipment and high-performance computing systems, such as processors and PCs, but also cloud systems, allow anyone fairly easy access to everything necessary for smart technologies.
- The ability to solve concrete problems. Intelligent hydraulics make an essential contribution to reducing the risks of important functional errors, especially in workplaces that are dangerous for humans.

Intelligent hydraulics have the ability to work faster than humans, to be available at any time of the day, but above all to perform difficult and repetitive work.
The fear that intelligent technical systems will reduce the number of jobs is unfounded, although those requiring lower professional training will be reduced, but the number of those requiring higher qualifications will increase significantly.

4. General applications of intelligent hydraulics

Intelligent hydraulics began to be used more and more in almost all industrial fields.

- In the field of car, rail, naval or air transport, it must be specified that the modernization involves the fields of planning, the fields of tracking, the technological fields of actuation of various sub-assemblies and devices and even the actuations of energy-efficient tractions.
- In the field of machines and automatic machines such as robots and manipulators, hydraulics and pneumatics equipped with artificial intelligence occupy a dominant position in opposition to electric variants.
- In the field of agricultural machinery and machinery, intelligent hydraulics will allow a revolutionary development of the entire agricultural sector.
- In the fields of machine tools and technological manufacturing lines, with all directives without technical support to favor electric drives, a special involvement of intelligent hydraulics is foreseen.
- In all technical fields where there are complex machines that need powers greater than 20kw.

The need to move to intelligent technology in the field of hydraulic drives is for machines and machines in manufacturing technologies to become even smarter, so to increase efficiency and productivity it is necessary to improve connectivity. Intelligent hydraulic systems are always prompter and can provide general intelligence either by using only intelligent equipment or by selecting areas

with important influence in the operation of the assembly and only those will be equipped with intelligence. The intelligence of hydraulics allows better communication not only with the central command and control system but with all the machines in the entire plant. Also important is the compatibility with the Internet of Things-IoT, one of the bases of the Industry 4.0 process, which makes full use of the individual performances of each installation.
The life of the machinery is essential for the user of the hydraulic installation, which is why intelligent systems are needed to detect faults before they occur to reduce downtime. It's good to know when the uses become dangerous, when the filtration starts getting worse, or when the machines start going out of tune. In this way, we can talk about a timely service and a low repair time [3].
As a result, the intelligence of the hydraulics allows the transition to a proactive maintenance, through which the danger of a failure is detected in time, so the operators can plan to stop the machine only when necessary and often this allows the full supply to be made and on time, thus reducing stocks.
Another motivation for switching to intelligent hydraulics is that problem identification, so diagnosis becomes easier and thus maintenance becomes cheaper, as well as minimizing machine downtime.
The increase in costs with the modernization of machines and the introduction of intelligent components is amortized quite quickly by reducing the downtime and increasing the quality of the products.
Using intelligent hydraulics in figure 1 we can see parameters that we can measure and the benefits of knowing them [4].

5. Intelligent hydraulics

The trend of recent years in hydraulic drives has been and still is towards smarter components and systems that have greater freedom, flexibility and efficiency. It finds that manufacturers of complex machinery are looking for smarter hydraulic drive components and subassemblies. Hydraulic drive suppliers need to know that the level of intelligence is changing extremely quickly. Users of hydraulic pumps take into account their efficiency, the controllability that increases the precision and dynamics of the pumping systems, the versatility that ensures good operational flexibility of them, but also the level of noise and vibrations that can negatively influence the whole machine. Beneficiaries want intelligent hydraulics to lead to smooth and efficient hydraulic response.

6. Intelligent hydraulic equipment

6.1 Smart pumps and pumping units

The most important hydraulic equipment that has been equipped with artificial intelligence are pumps and pumping units. The intelligent drive and control of hydraulic pumps required by industrial applications ensures not only the efficiency, controllability and versatility of the system but also the control of noise, temperature and vibration. Intelligent pumps created for Industry 4.0 allow the visualization of operational information regarding flows, pressures, yields, temperatures, speeds at any time. The fact that this data, as well as others, can be accessed not only directly but also via the cloud enables efficient control of mobile machinery as well. Crucially, the sensors and control system elements are integrated into the pump allowing easy connection to both the hydraulic system and the large machine. This allows the variation of the flow (speed) and the adjustment of the initial settings according to the requirements of the machine and the situation at each moment of the mechano-hydraulic parameters, existing on the machine. The advantages of using this type of pump can be concentrated in:
- Remote control and command
- Good functional efficiency
- Predictive maintenance that improves uptime and reduces maintenance costs

Figure 1 shows the hydraulic pump and its control and data acquisition elements. The PLC module can be connected to the Internet and controlled remotely or by Artificial Intelligence.

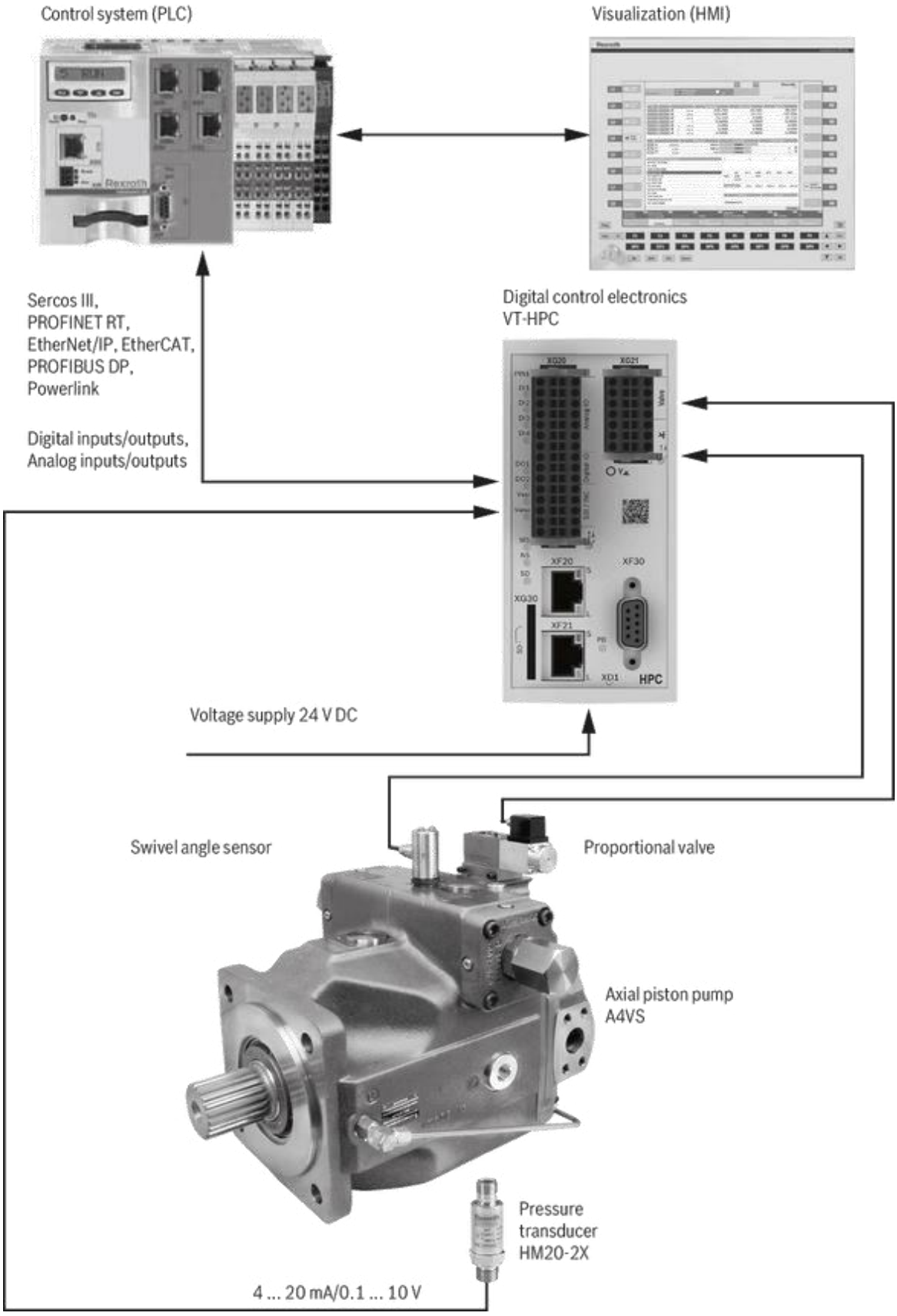

Fig. 1. Smart hydraulic pump [5]

6.2 Actuators and pipelines

The hydraulic actuator is a piece of equipment that converts the energy of a fluid under pressure into mechanical energy. The actuator can be linear, rotary or semi-rotary, so a cylinder or a rotary motor. The actuator has become from a simple piece of equipment to a complex one by adding sensors and command and control blocks. If we only refer to the intelligent hydraulic cylinder, it is composed of an ordinary cylinder to which a linear sensor and an electronic block are attached inside or outside to ensure the commanded position or speed. It accurately provides distances within the stroke (typically from 0 to 3m), forces (from 1 to 500kN) or fixed or adjustable speeds. The cylinder's intelligence allows it remote control which is very important in many applications.
The actuator combines the intelligence of electronic servoing with the power density of hydraulic actuation. Although the system of smart cylinders is complex, as it allows good precision, but also predictability, repeatability and safety, it is surprising that users can be at an average level of professional training in the field. This advantage helps users reduce expenses related to the professional level of maintenance specialists.
Smart actuators are complex hydraulic equipment, consisting of cylinder, transducers, electronic control block and a suitable computer system.
The most important advantages of intelligent hydraulic actuators are:

- It represents a compact assembly with all the components tested by the manufacturers
- Maximum energy density and adaptation of consumption to demand
- Permanent and precise position control, speed, force, noise and low leakage.
- High reliability and minimal maintenance
- Acceptable price

The use of intelligent hydraulic actuators is becoming more and more intensive in a wide range of industries, from agricultural applications where even the depth of plowing or seeding is controlled, to heavy equipment for construction and mining.
Referred to by many names such as: electronic position-sensing, electro-hydraulic control, intelligent cylinders and smart cylinders; this technology utilizes linear transducers (sensors) to communicate the cylinder's piston position back to the overall hydraulic system.
Increased control, functionality and sensor-instrumented cylinders are becoming more important and more common in heavy industrial, mobile, and agricultural equipment.

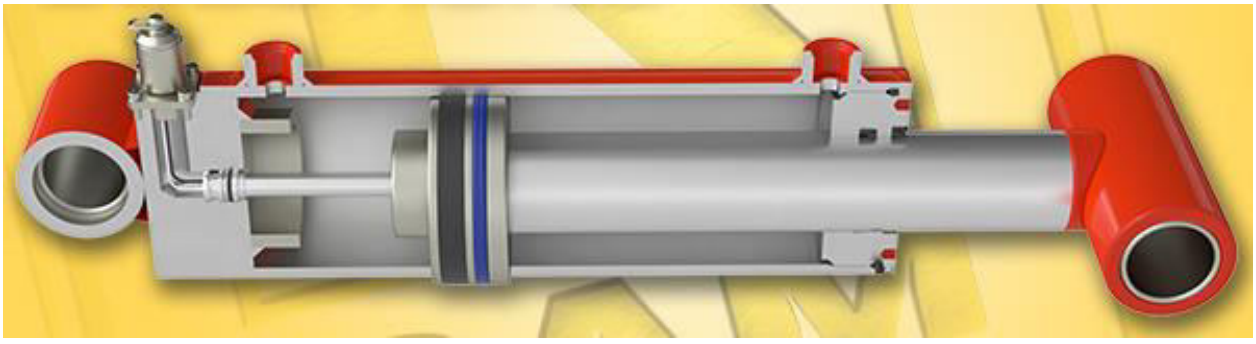

Fig. 2. Intelligent hydraulic cylinder [6]

6.3 Smart sensors

Sensors provide feedback on output based on factors such as speed, distance, pressure, temperature, fluid quality, etc. Sensors help ensure that equipment such as cranes or trailers are level. This is useful to confirm that the equipment is stabilized. In addition, position sensors can tell the operator when it is safe to move only when the outriggers or outriggers are disengaged.
Eaton’s LifeSense hydraulic hose includes a sensor that can detect hose failure or problems and send a notice through a wireless or wired network, to alert machine operators of impending failure.

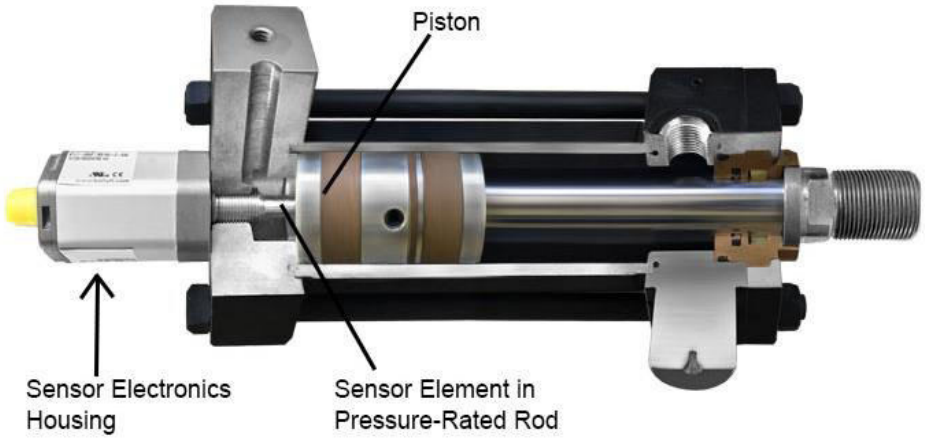

Fig. 3. Sensors for hydraulic cylinders [7]

The classic linear position feedback solution for hydraulic cylinders is the rod-style magnetostrictive sensor installed from the back end of the cylinder. The cylinder rod is gun-drilled to accept the length of the sensor probe, and a target magnet is installed on the face of the piston. A hydraulic port on the end cap provides installation access to thread in the pressure-rated sensor tube. This type of installation carries several advantages but also some potential disadvantages depending on the application.

7. Intelligent hydraulic equipment

All specialists know that precision in components is needed to minimize losses and ensure that the operator gets a "real-time" feel for the operations being undertaken. As a result, intelligent instrumentation helps achieve intelligent hydraulic systems that generate highly relevant information for the entire machine.
Intelligent hydraulic systems:
A typical intelligent hydraulic drive system is based on 4 mandatory subassemblies: (see figure 4).

1. A hydraulic pump driven by an electric or thermal engine
2. Pipes, hydraulic steering and control elements, sensors and transducers, filters and auxiliary equipment
3. A linear or rotary actuator.
4. Electronic control block

Fig. 4. Intelligent hydraulic drive system [1]

Two important clarifications must be made:

- Without a modern electronic control there is no intelligent hydraulics, so the computer has already become a basic component of the hydraulic system.
- An intelligent hydraulic system can have centralized intelligence or distributed intelligence on components and only a centrally concentrated part

The intelligent system design methodology is supported by process elements for processing and storage, cloud technologies, Internet of Things (IoT), communication technology, machine learning, simulation analysis, real data analysis, artificial intelligence and of intelligent components such as hydraulic pumps, actuators and sensors.

8. Conclusions

Intelligent hydraulics together with artificial intelligence have a superior energy efficiency compared to classic drives. At the same time, this modernization will not cause the loss of jobs for operators, but will increase the level of knowledge required by the operator. The modernization of the components of the hydraulic installations helps to measure the functional parameters in real time, and with artificial intelligence the installations can be stopped from operation so that the system does not fail completely.

Acknowledgments

This paper has been financed under a project funded by the Ministry of Research, Innovation and Digitalization through Programme 1- Development of the national research & development system, Sub-programme 1.2 - Institutional performance - Projects financing the R&D&I excellence, Financial Agreement no. 18PFE/30.12.2021.

References

[1] Jensen, Sara. “Intelligent Hydraulic Systems Enhance Machine Connectivity and Performance.” *OEM Off-Highway - Fluid Power*. November 30, 2020. Accessed October 18, 2022. https://www.oemoffhighway.com/fluid-power/article/21200293/intelligent-hydraulic-systems-enhance-machine-connectivity-and-performance.

[2] Müller, Vincent C. “Ethics of Artificial Intelligence and Robotics.” In Zalta, Edward N. (ed.). *Stanford Encyclopedia of Philosophy (Summer 2020 Edition)*. Palo Alto, CSLI, Stanford University, 2020.

[3] Javdanitehran, Mehdi, and Thorsten Brecht. “Intelligent systems in mobile hydraulics. Leadership in hydraulic solutions.” Paper presented at 9. Kolloquium Mobilhydraulik, Karlsruhe, Germany, September 22-23, 2016.

[4] Casoli, Paolo, Mirko Pastori, and Fabio Scolari. “A multi-fault diagnostic method based on acceleration signal for a hydraulic axial piston pump.” *AIP Conference Proceedings* 2191 (December 2019): 020037. https://doi.org/10.1063/1.5138770.

[5] Bosch Rexroth Pty Ltd. “Digital control electronics for axial piston pumps. VT-HPC-1-1X.” October 24, 2022. Accessed October 25, 2022. https://www.boschrexroth.com/en/au/products/product-groups/industrial-hydraulics/electronics/pump-control/vt-hpc-1-1x.

[6] Ram Industries Inc. “Smart Sensing Hydraulic Cylinder Solutions.” October 20, 2020. Accessed October 25, 2022. https://www.ramindustries.com/blog/post/smart-sensor-cylinders.aspx.

[7] Menke, Henry. “External Position Feedback for Hydraulic Cylinders.” *Automation Insights*. Accessed October 17, 2022. https://automation-insights.blog/2017/07/19/external-position-feedback-for-hydraulic-cylinders-2/.

ISSN 1454 - 8003
Proceedings of 2022 International Conference on Hydraulics and Pneumatics - HERVEX
November 9-10, Băile Govora, Romania

LIGNOCELLULOSIC BIOMASS - NEW RESOURCES FOR BIOPOLYMERS PRODUCTION

Lăcrimioara ȘENILĂ[1,*], Eniko KOVACS[1], Daniela SCURTU[1], Lucian DORDAI[1], Cecilia ROMAN[1]

[1] INCDO-INOE 2000, Research Institute for Analytical Instrumentation ICIA Cluj-Napoca

* lacri.senila@icia.ro

Abstract: *Lignocellulosic biomass is a renewable and abundant material that can be used as raw material to obtain biopolymers. In this paper, the production of carbohydrates from lignocellulosic biomass was investigated in order to obtain raw materials for biopolymer production. A technological methodology for polylactic acid (PLA) and polyhydroxyalkanoate (PHA) production from lignocellulosic biomass was proposed. The autohydrolysis pretreatment of peach orchards leads to carbohydrates separation at high temperatures (160, 180, and 200°C) and pressure (80 bar). The effect of pretreatment methods for carbohydrate production was evaluated. The structural characterization of lignocellulosic biomass, before and after pretreatment, was carried out by reflected light microscopy.*

Keywords: *Lignocellulosic biomass, biopolymers, pretreatment*

1. Introduction

Considering the availability of fossil fuels and their impact on the atmosphere, i.e., the greenhouse effect, developing alternative renewable energy becomes imperative for sustainable development. Therefore, biomass becomes the major source of “green energy”. Lignocellulosic biomass is an abundant source, affordable, renewable, and available in large quantities, which received considerable attention as a promising alternative to fossil fuels [1]. Lignocellulosic biomass comes from the following sources: crop residues, wood, herbaceous biomass, agro-industrial residues, and vegetable waste. In recent years, biofuels and bioenergy production from lignocellulosic raw materials was considerably developed. In contrast, the production of chemicals and biomaterials from renewable raw materials remains limited [2,3]. The major components of lignocellulosic biomass, namely cellulose and hemicellulose, can be converted into bioethanol and bioplastics, whereas lignin can be converted into polymers. Cellulose is a complex consisting of 3000 or more glucose units, whereas hemicellulose is formed from pentoses (xylose and arabinose), hexoses (mannose, glucose, and galactose) and uronic acids. Lignin is a complex polymer consisting of three types of precursor alcohols: p-coumaric, coniferyl and p-synapic alcohols [4].
White biotechnology is an industrial biotechnology for durability, in which microorganisms or enzymes are used to produce fuels and chemicals from renewable resources. Biopolymers are biodegradable and non-biodegradable (fossil fuel). Biodegradable polymers are cellulose, hemicelluloses, polylactic acid, poly succinic acid, polyhydroxyalkanoates, gluten, and algal biopolymers [5].
The main components of lignocellulosic biomass (cellulose and hemicelluloses) need to be extracted and subjected to pretreatment and hydrolysis to obtain biopolymers.
Over the last few years, many pretreatment, hydrolysis, and fermentation methods have been developed, but each presents advantages and disadvantages. Most plastics start out as hydrocarbons derived from crude oil, the global plastic production extending every year. The growing production of petroleum-based plastics has a negative impact on the environment. Therefore, bioplastic innovation and research activities, which provide alternatives to conventional plastics are needed. In recent years, global innovative biopolymers such as polyhydroxyalkanoates (PHA), polyhydroxy butyrate (PHB) and polylactic acid (PLA) have been the most used alternatives. The production of biopolymers from lignocellulosic waste consists of four steps:

(1) pretreatment for cellulose and hemicellulose separation, (2) hydrolysis to break down the molecules of cellulose and hemicellulose in sugars, (3) fermentation of sugars into biopolymers (PLA and PHA) by using specific bacteria and (4) a polymerization/polycondensation process [6,7]. Lactic acid has two enantiomeric forms: lactic acid L (+) and lactic acid D (-) (Figure 1).

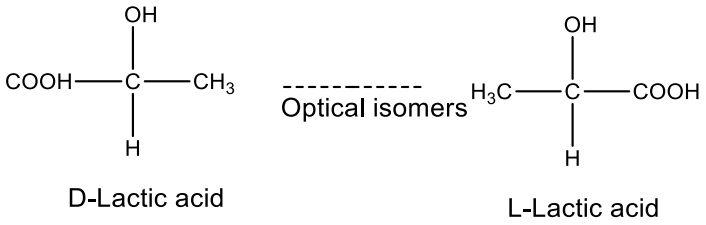

Fig. 1. Lactic acid isomers

The strains used for PLA production by microbial fermentation are *Bacillus strains*, such as *Lactobacillus*, *Bavaricus, Casei, Caltaromicus, Salivarius, Carno-bacterium, Enterococcus, Lactococcus, Leuconostoc, Pediococcus, Streptococcus, Tetragenococcus, Vagococcu*s, and *Weissella* [8].
Polyhydroxyalkanoates are bioplastics and have a great interest due to their potential to replace the fossil plastic. PHAs are biodegradable aliphatic polyesters that have a structure based on 3-hydroxyalkanoate acid. Due to its composition and polymer nature, PHAs are biocompatible, biodegradable, water-insoluble, non-toxic and thermoplastic, which makes them competitive with synthetic plastics. The bacterial species used to generate PHAs are: *Ralstonia eutropha, Aspergillus eutrophus, Cupriavidus necator, Rhodobacter sphaeroides, Wautersia eutropha, Pseudomonas* sp., *Thermus thermophiles, Hydrogenophaga pseudoflava, Haloferax mediterranei, Saccharophagus degradans, Bacillus* sp*., Halomonas* sp., *Azohydromonas lata, Chromobacterium* sp., *Methylobacterium* sp., *Azotobacter* sp., *Burkholderia* sp., *Zobellella denitrificans, Dechloromonas* sp*., Comamonas* sp., *Aeromonas* sp., *Erwinia* sp. and *E. Coli [9].*
The problem with the use of lignocellulosic biomass in the production of biopolymers is the extraction of carbohydrates. Thermochemical or biochemical processes are required to transform polymers (cellulose and hemicellulose) from the lignocellulosic biomass structure into monomers. The pretreatment method is the most critical step, there are different methods presented in the literature [10]. Currently, green techniques are used for the extraction of carbohydrates from biomass, such as supercritical fluid extraction, autohydrolysis, and steam-explosion that do not use chemicals.
Therefore, enzymatic hydrolysis and fermentation are the most promising alternative for converting lignocellulosic waste into sugars, being also green technologies. Separate hydrolysis and fermentation (SHF) and simultaneous saccharification and fermentation (SSF) are two processes that can be used for bioplastic production with high yield and low production cost [11].
The paper aims to demonstrate the valorisation of lignocellulosic biomass by developing value-added biobased products through green methods and chemicals, as much as possible. Separation of cellulose from lignocellulosic biomass will be performed in order to use it as raw material for bioplastics obtainment.

2. Materials and Methods

2.1. Chemicals and reagents

All chemicals used were of analytical reagent grade and were purchased from Merck (Darmstadt, Germany). All solutions were prepared by using ultrapure water (18.2 MΩcm−1 at 20 °C) obtained from a Direct-Q3 UV Water Purification System (Millipore, Molsheim, France).

2.2. Sample description

The lignocellulosic biomass samples were purchased from the Research Station of the University of Agricultural Sciences "Ion Ionescu de la Brad" from Iași, farm no. 3 „Vasile Adamachi" (Romania). The samples were collected immediately after the cutting operations of peach trees, dried and shredded to a diameter of 0.2 mm.

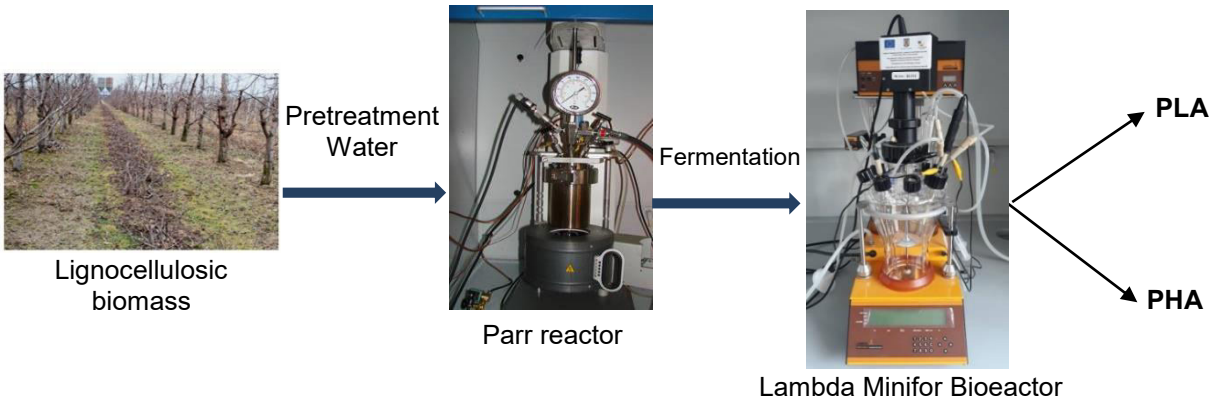

Fig. 2. Schematic representation of the technological approach of this paper

2.3 Pretreatment of lignocellulosic biomass

The pretreatment method was carried out according to our recent publication [4]. Carbohydrates were extracted at three different temperatures (160, 180, and 300°C) for 15, 30, and 45 min. At the end of the experiments, the solids and liquid samples were collected and separated by filtration. Cellulose, lignin, and hemicellulose content was determined according to the reference [12].

2.4 Structural characterization of lignocellulosic biomass by using reflected light microscopy

The lignocellulosic biomass, before and after pretreatment, was characterized by a reflected light microscope (Kern OKN-1, Germany). The microscope is an infinity optical system and has a 50 W halogen incident illumination unit. The samples were analyzed by a light microscope at up to 40 x magnification.

3. Results and discussion

The chemical composition of lignocellulosic biomass (peach orchards) used in this study is presented in Table 1. Cellulose is the most abundant component of lignocellulosic biomass (30.8 ± 0.8%). The moisture content was 10%. The high content of holocellulose (57.1%) recommends the peach orchard biomass as raw material for bioplastic production.

Table 1: Chemical composition of lignocellulosic biomass (peach orchards)

Component	Amount (%, w/w)
Cellulose	30.8 ± 0.8
Hemicelluloses	26.3 ± 0.4
Lignin	29.5 ± 0.3
Ash	2.5 ± 0.01
Extractables	1.3 ± 0.01

When synthesizing biopolymers such as PHA and PLA from lignocellulosic biomass, the first step is to obtain carbohydrates. The use of autohydrolysis pretreatment for the separation of cellulose from lignocellulosic biomass led to hemicellulose solubilized in liquid fraction and cellulose and lignin separated in the solid fraction. The separation of biomass components depends on the pretreatment method used.
Pretreatment with water at high temperatures and pressure is an ecological pretreatment that uses as solvent only water. The efficiency of the pretreatment depends on temperature, time, and pressure. The mechanism involves the formation of hydrogen ions that act as Lewis acids. Humidity can generate carbonic acid, which improves the hydrolysis of hemicelluloses in the liquid phase [8]. The experiments were carried out at different temperatures (160, 180, and 200°C), reaction times (15, 30 and 45 min), and the same pressure (80 bar). The chemical composition of the solid fractions resulted after the pretreatment are presented in Figure 3 (a-c).

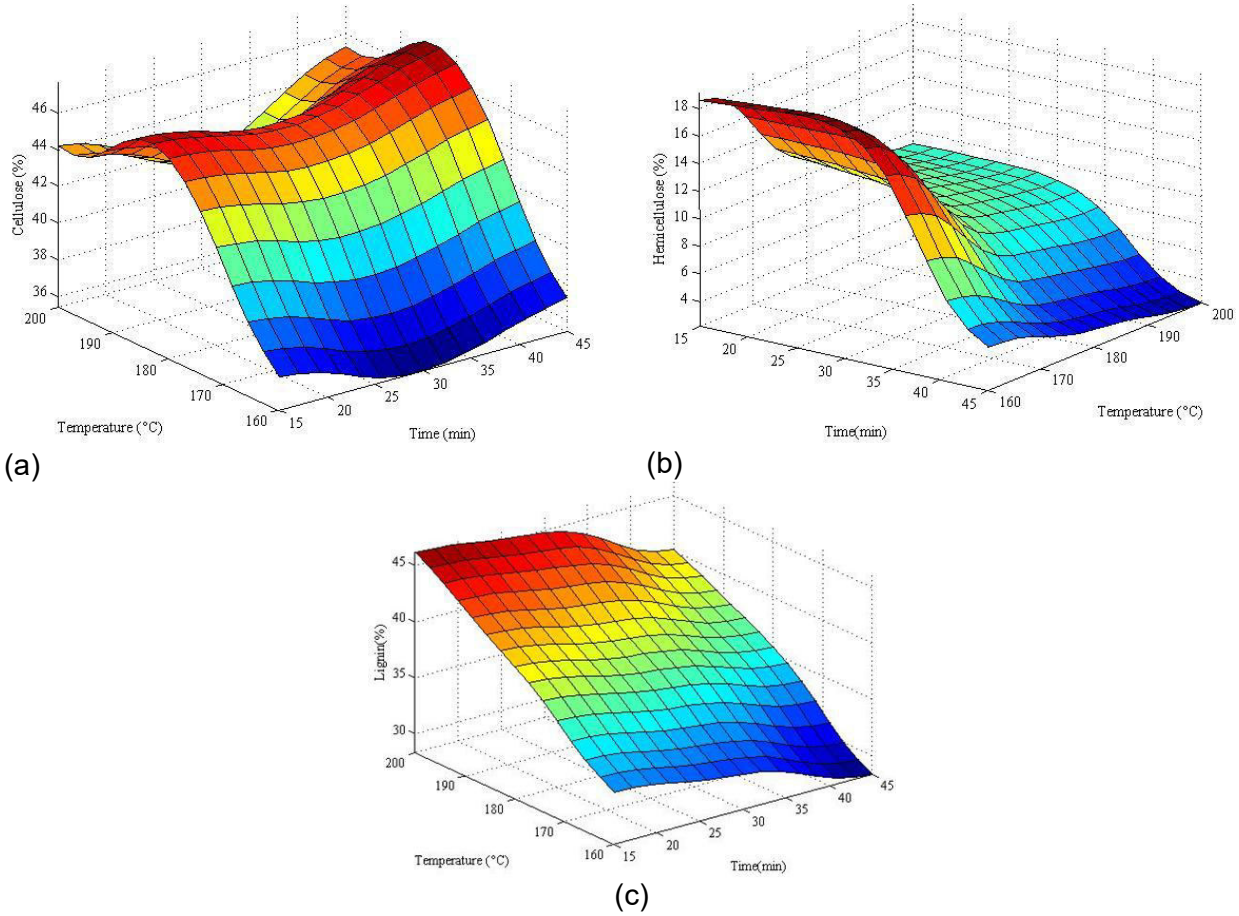

Fig. 3. (a) Content of cellulose, (b) hemicelluloses and (c) lignin in solid fraction separated after pretreatment, at different conditions

The solid yield of the fraction recovered after pretreatment varied between 55.2 -70.1%. It decreased with the temperature increase and reaction time. This is caused by the solubilization of the hemicellulose in the liquid fraction. The solid fraction composition was analyzed after each experiment to determine the cellulose, hemicellulose, and lignin content. The cellulose content ranged from 32.0 to 45.1/100 g of pretreated biomass, while the lignin content ranged from 35.0 to 48.1/100 g of pretreated biomass. The hemicellulose content decreases with the temperature increase and reaction time from 15 min to 45 min. Autohydrolysis pretreatment can separate cellulose from lignocellulosic waste, which can be used as a raw material in the production of bioplastics. For a maximum efficiency of cellulose, the separation is recommended as a pretreatment of lignocellulosic biomass, at a temperature of 180°C for 30 minutes.

Structural characterization of lignocellulosic biomass by using reflected light micrographs

Autohydrolysed biomass has a different texture than untreated biomass. The structure of the untreated biomass shows resistance, while the autohydrolysed structure indicates degraded biomass after the pretreatment. Untreated biomass structure is rigid and has longitudinal sections and a fibrous structure, whereas the treated biomass shows crystalline form. Reflected light microscopy confirms the efficiency of the autohydrolysis pretreatment.

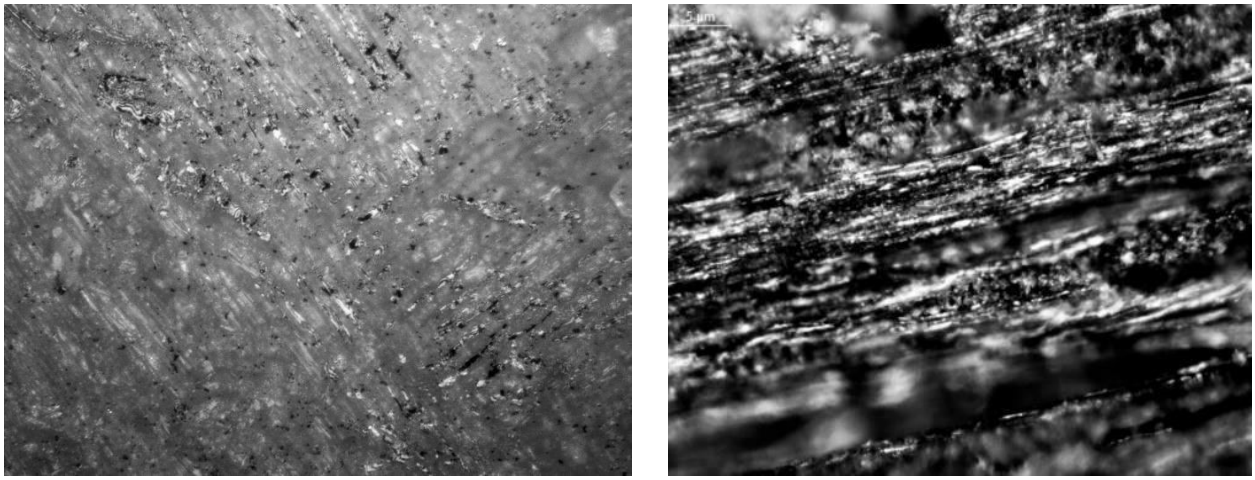

(a) (b)

Fig. 4. Reflected light micrographs of the: (a) untreated (b) pretreated biomass (180°C, 30 min)

Technological approach proposed

The obtained cellulose could be further used for PLA and PHA production. The technology of obtaining PLA from cellulose will contain the following main steps: (i) enzymatic hydrolysis of cellulose and simultaneous fermentation with specific bacteria for the production of lactic acid; (ii) purification and separation of lactic acid from the fermentation medium; (iii) lactic acid polycondensation with the PLA obtainment and (iv) separation and characterization of the obtained PLA bioplastic (Figure 5).

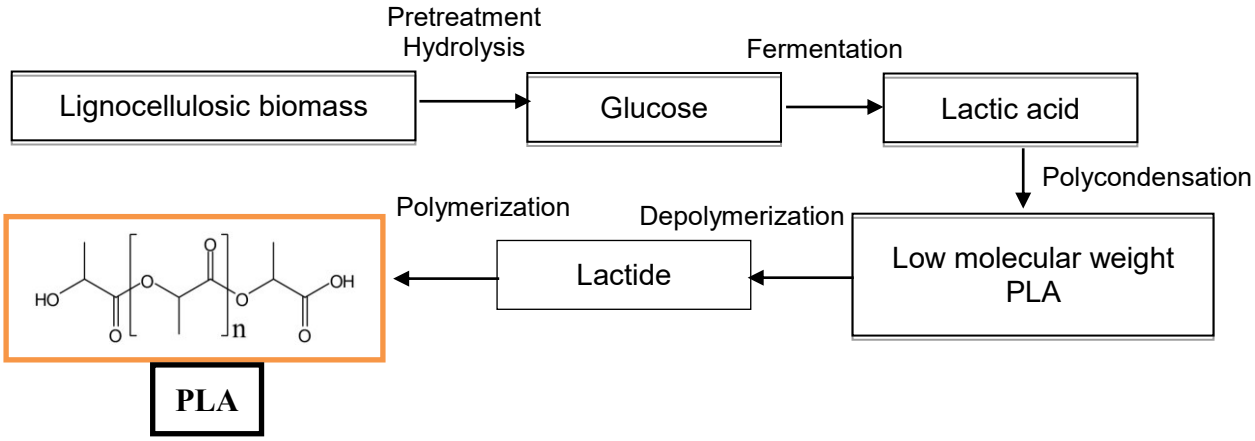

Fig. 5. Schematic representation of the biosynthetic partway for the production of PLA from lignocellulosic biomass

The technology of PHA production from lignocellulosic biomass contains the following main stages: (i) fermentation with specific bacteria for direct production of PHA, (ii) purification and separation of PHA from the fermentation medium and (iii) characterization of the obtained PHA bioplastic.

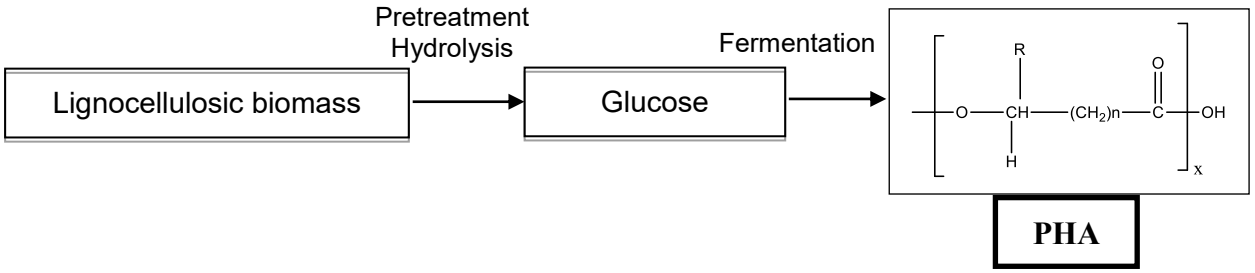

Fig. 6. Schematic representation of the biosynthetic partway for the production of PHA from lignocellulosic biomass

4. Conclusions

Extraction of carbohydrates from lignocellulosic biomass was performed using an autohydrolysis pretreatment. The lignocellulosic biomass used in this study has a high content of cellulose and hemicelluloses, recommended as raw material for bioplastics production. Two new technologies for bioplastics (PLA and PHA) were proposed.

Acknowledgments

This work was supported by a grant of the Ministry of Research, Innovation and Digitization, CNCNS-UEFISCDI, project number PN-III-P1.1.1-TE-2021-0179, within PNCDI III, LIGNOBIOPLAST.

References

[1] Senila, Lacrimioara, Simona Costiug, Anca Becze, Dalma Kovacs, Eniko Kovacs, Daniela Alexandra Scurtu, Otoo Tudor-Boer, and Marin Senila. “Bioethanol production from Abies Alba wood using adaptive neural fuzzy interference system mathematical modelling.” *Cellulose Chemistry and Technology* 54 (2020): 53-64. doi:10.35812/cellulosechemtechnol.2020.54.06.

[2] Cheikhyoussef, Natascha, and Ahmad Cheikhyoussef. “Chapter18 - Industrial polymer synthesis using supercritical carbon dioxide.” *Green Sustainable Process for Chemical and Environmental Engineering and Science*. Elsevier, 2020.

[3] Pontes, Rita, Aloia Romaní, Michele Michelin, Lucília Domingues, José Teixeira, and Joao Nunes. “L-lactic acid production from multi-supply autohydrolyzed economically unexploited lignocellulosic biomass.” *Industrial Crops and Products* 170 (October 2021): 113775.

[4] Senila, Lacrimioara, Eniko Kovacs, Daniela Alexandra Scurtu, Oana Cadar, Anca Becze, Marin Senila, Erika Andrea Levei, Diana Elena Dumitras, Ioan Tenu, and Cecilia Roman. “Bioethanol Production from Vineyard Waste by Autohydrolysis Pretreatment and Chlorite Delignification via Simultaneous Saccharification and Fermentation.” *Molecules* 25, no. 11 (June 2020): 2606. doi:10.3390/molecules25112606.

[5] Yan, Xu, Dongna Li, Xiaojun Ma, and Jianing Li. “Bioconversion of renewable lignocellulosic biomass into multicomponent substrate via pressurized hot water pretreatment for bioplastic polyhydroxyalkanoate accumulation.” *Bioresource Technology* 339 (November 2021): 125667.

[6] Nduko, John Masani, and Seiichi Taguchi. “Microbial Production of Biodegradable Lactate-Based Polymers and Oligomeric Building Blocks from Renewable and Waste Resources.” *Frontiers in Bioengineering and Biotechnology* 8 (February 2021): 618077. doi: 10.3389/fbioe.2020.618077.

[7] Senila, Lacrimioara, Daniela Alexandra Scurtu, Eniko Kovacs, Erika Andrea levei, Oana Cadar, Anca Becze, and Cerasel Varaticeanu. “High-Pressure supercritical CO_2 pretreatment of apple orchard waste for carbohydrates production using response surface methodology and method uncertainty evaluation.” *Molecules* 27, no. 22 (November 2022): 7783. https://doi.org/10.3390/molecules27227783.

[8] Rahman, Md Hafizur, and Prakashbhai R. Bhoi. “An overview of non-biodegradable bioplastics.” *Journal of Cleaner Production* 294 (April 2021): 126218.

[9] Rehakova, Veronika, Iva Pernicova, Xenie Kourilova, Petr Sedlacek, Jana Musilova, Karel Sedlar, Martin Koller, Michal Kalina, and Stanislav Obruca. “Biosynthesis of versatile PHA copolymers by thermophilic members of the genus *Aneurinibacillus*.” *International Journal of Biological Macromolecules* (November 2022): S0141-8130(22)02774-X (In press). https://doi.org/10.1016/j.ijbiomac.2022.11.215.

[10] Guo, Kai-Ning, Chen Zhang, Ling-Hua Xu, Shao-Chao Sun, Jia-Long Wen, and Tong-Qi Yuan. “Efficient fractionation of bamboo residue by autohydrolysis and deep eutectic solvents pretreatment.” *Bioresource Technology* 354 (June 2022): 127225.

[11] Kawaguchi, Hideo, Kenji Takada, Taghreed Elkasaby, Radityo Pangestu, Masakazu Toyoshima, Prihardi Kahar, Chiaki Ogino, Tatsuo Kaneko, Akihiko Kondo. “Recent advances in lignocellulosic biomass white biotechnology for bioplastics.” *Bioresource Technology* 344(Pt B) (October 2021): 126165.

[12] Teramoto, Yoshikuni, Seung-Hwan Lee, and Takashi Endo. “Pretreatment of woody and herbaceous biomass for enzymatic saccharification using sulfuric acid-free ethanol cooking.” *Bioresource Technology* 99, no. 18 (December 2008): 8856-8863.

ISSN 1454 - 8003
Proceedings of 2022 International Conference on Hydraulics and Pneumatics - HERVEX
November 9-10, Băile Govora, Romania

EXPERIMENTAL RESEARCH ON AN INNOVATIVE HORTICULTURAL TECHNICAL SYSTEM OF ANALYSIS, PREDICTION AND BIODYNAMIC ACTION

Mihai Gabriel MATACHE[1,*], Iuliana GĂGEANU[1], Alexandru IONESCU[1], Ana-Maria TĂBĂRAȘU[1], Andrei Alexandru BENESCU[2]

[1] National Institute of Research – Development for Machines and Installations Designed for Agriculture and Food Industry – INMA Bucharest / Romania, gabimatache@yahoo.com

[2] INOE 2000-IHP Bucharest / Romania

* gabimatache@yahoo.com

Abstract: *The research carried out in this paper aimed to test the operation of an innovative horticultural technical system (intelligent equipment) for analysis, prediction and biodynamical action, which is an electrically driven equipment intended for spraying and applying phyto-sanitary treatments in a various range of crops using an algorithm for weed and diseased plant detection. The experiments conducted focused on testing the autonomy and charging time for the system, verifying the power consumption and testing the volumetric yield, but also on the algorithm. The results showed good functioning for both the hardware and the software parts of the system, encouraging to further the experiments for a larger variety of applications in agricultural crops.*

Keywords: *Intelligent system, electrically driven, detection algorithm, weed detection, crop maintenance*

1. Introduction

The "attack" of weeds, diseases and pests implies the reduction of the quantity and quality of crops, regardless of their nature (agricultural, horticultural and, why not, forestry). To combat diseases, pests and weeds in agricultural crops, pesticides are frequently used, which according to their purpose can be: fungicides, used to combat diseases caused by parasitic fungi; insecticides, used to fight insects and herbicides, used to fight weeds. The timely, fast and effective application of pesticides can save a potentially compromised crop and is crucial in modern agriculture [1,2].
From the complex of works that make up the maintenance technology of agricultural and horticultural crops, the works for combating diseases and pests have a special significance for the quantity and quality of production. It can be estimated that production losses due to diseases and pests can reach up to 35%, and in some cases, production can be completely compromised. Reducing production losses per hectare is possible only within the framework of integrated control, the method in which chemical treatments occupy the most important place [3].
Machines and equipment for the application of treatments ensure the optimal use of protection products, minimize the risks for the crop, man and the environment, intervene quickly where necessary and as often as necessary, they can apply emulsions, solutions or suspensions of chemical products, the application is made in the form of drops small for maximum coverage effectiveness can be applied before, during or after sowing [4].
Currently, hydraulic sprayers, pneumatic sprayers, mechanical sprayers and hydro-pneumatic combined sprayers are used. In general, a spraying machine consists of: the frame of the machine; liquid tank; hoses and liquid transport pipes; the filtration system; liquid pump(s); liquid agitators (homogenizers); the command group with control, dosing and distribution equipment; the spraying boom with the spraying equipment; various auxiliary equipment (for washing, preparation of solutions, etc.) [5].
Agricultural machines can be equipped with different equipment that allows them to be automated, and they can be handled as easily as possible. Such equipment can be the GIS localization

systems and the machine vision systems that promote efficient coordination and guidance of machines [5,6,7].
Also, new technologies are based on the use of modern sensors that remotely transmit valuable information that can prevent the appearance of diseases of agricultural crops. An important application in this regard are unmanned aircraft systems (UAS) that can be equipped with optical sensors (e.g., multispectral, thermal, hyperspectral cameras, etc.), which provide high-precision data about the field of interest (identification of plant diseases, weed recognition, terrain mapping, etc.) [8].
Automatic intelligence (machine learning) is an essential element in precision agriculture, it is used in the processing of data generated by detection systems, using different statistical and mathematical models. The fields of application of automatic intelligence in agriculture are diverse, it can be used in crop prediction, species identification, pest recognition, soil moisture and temperature estimation, etc. [9,10,11].
The paper presents the experimental research conducted on innovative horticultural technical system of analysis, prediction and biodynamic action, both from a mechanical point of view and for its the capacity to analyse crops and distinguish weeds from plant crops in order to perform treatments.

2. Material and methods

The experimental model of innovative horticultural technical system (intelligent equipment) for analysis, prediction and biodynamical action is an electrically powered equipment intended for the distribution of phyto-pathological treatments for onion, carrot, potato, parsley, parsnip, and celery crops. Being powered by electricity, it can be used without restrictions both in closed spaces and in open spaces. The drive wheels are placed on the rear axle.
The experimental model of innovative horticultural technical system (intelligent equipment) for analysis – Figure 1, prediction and biodynamical action if composed of:
1. SME electrically operated mobile structure;
2. DSP dosage system and biological protection of plants.
The system it is equipped with a KIT of hardware-software system, neural network for automatic control of its functionality.

Fig. 1. Experimental model of innovative horticultural technical system (intelligent equipment) for analysis, prediction and biodynamical action

The main technical characteristics of the experimental model of the innovative horticultural technical system (intelligent equipment) for analysis, prediction and biodynamical action are:

Table 1: Main system characteristics

Characteristic	M.U.	Value / characterization
Rear wheel track	mm	1320
Wheelbase	mm	2600
Electric drive motor	kW	12
li-ion battery	Vcc	96
Solution tank capacity	l	400 l
Tank material	-	glass fiber reinforced resin
Pump motor	kW	3
Maximum flow rate of the pump	l /min	86 l/min
Maximum working pressure	bar	20 bar
Line filter	-	with self-cleaning and discharge based on hydraulic agitator
Agitation system	-	with hydraulic agitator
Boom length	m	8
No. boom sections	-	3
Nr. Port-nozzles	-	31
Pressure and flow regulator	-	3-way
Clean water tank capacity for the human operator	l	10
Solution indicator	-	through transparency
Platform structure	-	steel, galvanized

The tests for the innovative horticultural technical system (intelligent equipment) of analysis, prediction and biodynamic action, were carried out under the following conditions:
- the land used was cultivated agricultural land and the test track which is a flat surface covered with concrete,
- air temperature: 23.1 °C;
- air humidity: 45%;
- wind speed 0.6 m/s.

The charging time of the batteries was measured with the help of a multimeter and a timer but also with the help of the communication interface with the PC connected to the BMS. The charging times corresponding to the three power regimes were determined.
The movement speed is determined by calculation, timing the time required to cover the distance of 50 m. Three measurements were made, reporting the average of the measured data. The speed is calculated with the formula:

$$V = (3.6\ x\ d)/t \text{ [km/h]} \quad (1)$$

where: *V* – movement speed [km/h];
d - travelled distance [km];
t - travel time [s].

Determination of electricity consumption from the network

The power absorbed (*P*) from the network is measured, then the electrical energy consumed (*W*) is calculated with the formula:

$$W = (P\ x\ t)/3600 \text{ [kWh]} \quad (2)$$

where: *P* - is the power absorbed from the network [kW];
t - operating time [s].

The charging energy that ends up being stored in the battery is determined by a charger efficiency coefficient (μ).

$$\boldsymbol{Pb} = W\ x\ \mu \tag{3}$$

where: Pb - is the energy with which the battery is charged;
W – consumed energy, [kW];
μ - the efficiency coefficient of the charger [0.93].

The flow rate of the pump was determined by the volumetric method at the input speed of 540 rpm. The liquid discharged by the pump was captured through the hoses that lead it to the boom for 1 minute in a vessel and was measured with capacity units from the laboratory's equipment. The tests were performed at a pressure of 2 bar.
The volumetric yield of the pump was determined by calculation using the relation:

$$\boldsymbol{\eta_v} = Q_r/Q_t\ \ x\ 100\ [\%] \tag{4}$$

where: Q_t = the real flow rate of the pump [l/min];
Q_r = the theoretical flow [l/min];
$Q_t = \pi ø^2 / 4\ s{\cdot}n{\cdot}i$ – where:
Ø = (interior) pump cylinder diameter [dm];
s = piston stroke [dm];
n = pump crankshaft speed [rot/min];
i = number of pump cylinders (i=3).

Image classification is a key component in the field of artificial vision algorithms to develop applications such as: surveillance, traffic monitoring, collision avoidance, face recognition, augmented reality, eye tracking, medical imaging, agricultural industry, etc. The evolution of cameras on the market and the emergence of new cameras requires the development of new algorithms that produce similar results, regardless of camera brand, in the same quality class. The artificial vision algorithm testing procedure must take into account testing on different cameras but also in specific situations that appear in reality.
The algorithm proposed for the intelligent system is running on the laptop which processes the data from the camera. Depending on whether weeds are detected, the command is sent to the Arduino control board, which controls the relays to operate the spray heads.
The recognition process takes about 100 - 50 ms per image (or 10 - 20 fps) to detect a weed target before a new image is captured and is ready for processing, which allows the data to be processed to enable command in real time for real situations.
To test the robustness of the algorithm, 4 cameras were tested, one of them - Eboda Sj6100, being the adventure camera with angle of view. The camera used is a LOGITECH HD Pro C920 Web camera, but to test the robustness of the developed algorithm, the Eboda Sj6100, VHD J1702C and Microsoft LifeCam HD-3000 Web cameras were also used, only for a limited set of tests.

Fig. 2. Cameras used

3. Results

The results obtained from the measurements performed for the charging times are presented in table 2.

Table 2: Charging time of the system

No.	Characteristic	M.U.	The value of the parameters determined during testing the 96 Vdc battery of the mobile structure electrically operated		
1.	220V 6A power supply	hours	5.6	5.8	5.6
2.	220V 16A power supply	hours	2.07	2.09	2.05
3.	220V 32A power supply	minutes	59	58	58
No.	**Characteristic**	**U.M.**	**The value of the parameters determined during testing the 48 Vdc battery of the dosing system and biological protection of plants**		
1.	220V 6A power supply	hours	2.8	2.7	2.8
2.	220V 16A power supply	minutes	63	61	63
3.	220V 32A power supply	minutes	33	32	33

The results obtained from the determination of the travel speed are presented in table 3.

Table 3: Movement speed results

No.	Characteristic	M.U.	Maximum speed	Average speed
1.	Calculated speed	km/h	25.3	24.6

The results obtained from the determinations for the consumed energy and for the stored energy are presented in table 4.

Table 4: Consumed energy and the stored energy registered for the system

No.	Characteristic 96 Vdc battery of the mobile structure electrically operated	M.U.	Consumed energy [W]	Stored energy [W* μ]
1.	Energy consumed at 220V 6 A	kWh	1320	1227
2.	Energy consumed at 220V 16A	kWh	3520	3273
3.	Energy consumed at 220 V 32 A	kWh	7040	6547
No.	**Characteristic 48 Vdc battery of the dosing system and biological protection of plants**	**M.U.**	**Consumed energy [W]**	**Stored energy [W* μ]**
1.	Energy consumed at 220V 6 A	kWh	1320	1227
2.	Energy consumed at 220V 16A	kWh	3520	3273
3.	Energy consumed at 220 V 32 A	kWh	3612	3360

The innovative horticultural technical system (intelligent equipment) of analysis, prediction and biodynamic action was also tested in the field (figure 3), with all the microvalves turned on in the MANUAL working mode, being equipped with foliar fertilization nozzles and being used for the application of ecological fertilizer in a green crop. The purpose of the experiments was to verify the machine's functionality in the field, its autonomy and its behaviour under maximum load.

Fig. 3. Innovative system - field experiments with fertilization nozzles

Table 5 shows the data corresponding to the autonomy of the intelligent system with a single battery charge of 6.7 kWh. The productivity of the spraying work was calculated using actual working speeds measured during the experiments and the 8 m working width of the machine. Also, the total area was calculated as the productivity of the spraying work multiplied by the autonomy of the machine, considering the assumption of working in a straight line, without taking into account the time required to turn the machine at the end of the field.

Table 5: Autonomy of the intelligent system

Work	**Autonomy of the electrically operated mobile structure, *h***	**Autonomy of the dosing system and biological protection of plants, *h***
Movement	3.00	-
Foliar fertilization/phytosanitary treatments	2.5	2.5

The results obtained from the determinations for the volumetric yield are presented in table 6.

Table 6: Autonomy of the experimental model

Pressure (bar)	**Flow at the pump (l/min)**				**Measurement uncertainty**	**Volumetric yield (%)**	**Measurement uncertainty**
2	R1	R2	R3	Average			
	28.3	28.1	27.6	28	0.42 l/min	17.85	0.42 %

The hardware system together with the software system and the developed neural network form a hardware-software system - KIT, neural network for the experimental model of innovative horticultural technical system (intelligent equipment) of analysis, prediction and biodynamic action which has the role of monitoring, analysis and control for the experimental model of innovative horticultural technical system (intelligent equipment) of analysis, prediction and biodynamic action of dosage and biological protection of plants.

The verification of the system functionality was done in the manual operating mode, starting and stopping each microvalve individually through the graphical user interface. The continuity of the electrical control circuits, the hydraulic circuits of the sprinkler system, the functionality of the microvalves, as well as the communication between the PLC and the touchscreen operating terminal were thus verified.
After testing, in laboratory conditions, (constant brightness) the false-positive detection situation for the cultivated plant, at different rotations, the result was that the algorithm has 100% accuracy for the same plant. 10 different plants were tested for 12 rotations for each plant. It shows from here that the positioning does not lead to false-positive cases.

Fig. 4. a) Placement of the scene in laboratory conditions b) scene filmed by the camera

The algorithm tested for weeds recognition showed a similar precision, with very small differences, which is considered to be due to the positioning of the plants due to natural wind conditions and due to the appearance of the focusing phenomenon when the cultivated plant is very close to the camera. The Eboda Sj6100 type camera presented a lower detective rate because of the distortion errors, due to the large viewing angle, but this case really shows the robustness of the algorithm.

4. Conclusions

From the tests carried out, the following can be stated:
- the system registered good charging times for power supplies of 220V 16A and 220V 32A both for the 96 Vdc battery and for the 48 Vdc battery;
- the system has similarly good autonomy, that can be translated into good crop coverage in one pass with one battery charge;
- the detection algorithm works even if the camera takes information above the plant or above the interval between crop rows, in different situation, the results being less conclusive during night-time, due to the different characteristics of artificial lighting.
- the volumetric yield registered good values, similar to those of conventional spraying machines;
- the system is a viable ecological solution for crop maintenance in terms of fertilization and treatment application, being suitable both for conventional and organic crops.

Acknowledgments

This work was financed by The Ministry of Research, Innovation and Digitalization through Program 1 - Development of the national research-development system, Subprogram 1.2 - Institutional performance - Projects for financing excellence in RDI, Contract no. 1PFE/30.12.2021.

References

[1] Mogârzan, Aglaia. *Phytotechnics / Fitotehnie*. Iași, Ion Ionescu de la Brad Publishing House, 2012.
[2] Berar, Viorel, and Gheorghe Poșta. *Vegetable cropping / Legumicultură*. Timișoara, USAMV Timișoara, 2005.
[3] Jianshu, Chen, Wang Jianlun, Wang Shuting, and Liu Hao. "The Matching Research of Strawberry Diseases Image Features Based on KD-Tree Search Method". Paper presented at Computer and Computing Technologies in Agriculture VII. 7th IFIP WG 5.14 International Conference, CCTA 2013, Beijing, China, September 18-20, 2013.
[4] Rees, S.J., C.L. McCarthy, X.P.B. Artizzu, C.P. Baillie, and M.T. Dunn. "Development of a prototype precision spot spray system using image analysis and plant identification technology." Paper presented at Agricultural Technologies in a Changing Climate: The 2009 CIGR International Symposium of the Australian Society for Engineering in Agriculture, September 13-16, 2009, Brisbane, Australia.
[5] Persu, Catalin et al. "Intelligent system for the active control of phytosanitary treatment works in field crops, depending on their degree of weed infestation / Sistem inteligent pentru controlul activ al lucrărilor de realizare a tratamentelor fitosanitare in culturile de câmp, funcție de gradul de infestare cu buruieni al acestora." Contract PN 16 24 01 05, 2016.
[6] Latha, Mrs., A. Poojith, B. V. Amarnath Reddy, and G. Vittal Kumar. "Image Processing In Agriculture." *International Journal of Innovative Research in Electrical, Electronics, Instrumentation and Control Engineering* 2, no. 6 (June 2014): 1562- 1565.
[7] Wang, Jianlun, Jianlei He, Yu Han, Changqi Ouyang, and Daoliang Li. "An Adaptive Thresholding algorithm of field leaf image." *Computers and Electronics in Agriculture* 96 (2013): 23-39.
[8] Jain, A.K., R.P.W. Duin, and J. Mao. "Statistical pattern recognition: a review". *IEEE Transactions on Pattern Analysis and Machine Intelligence* 22, no. 1 (January 2000): 4–37.
[9] Mustafa, M., A. Hussain, K. Ghazali, and S. Riyadi. "Implementation of Image Processing Technique in Real Time Vision System for Automatic Weeding Strategy." Paper presented at IEEE International Symposium on Signal Processing and Information Technology, Giza, Egypt, December 15-18, 2007.
[10] Shinde, A., and M. Shukla. "Crop detection by machine vision for weed management." *International Journal of Advances in Engineering & Technology* 7 (2014): 818- 826.
[11] Perez, A., F. Lopez, J. Benlloch, and S. Christensen. "Colour and shape analysis techniques for weed detection in cereal fields." *Computers and Electronics in Agriculture* 25 (2000): 197-212.


http://hervex.ro